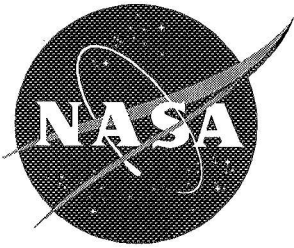


1995108039



NASA Conference Publication 3274

348595

Part 1

FAA/NASA International Symposium on Advanced Structural Integrity Methods for Airframe Durability and Damage Tolerance

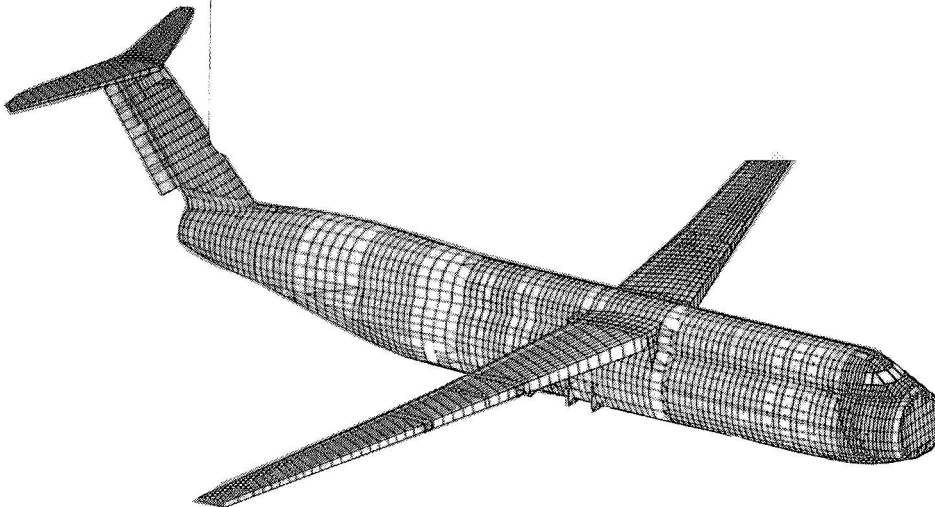
P.10

*Edited by
Charles E. Harris*

(NASA-CP-3274-Pt-1) FAA/NASA
INTERNATIONAL SYMPOSIUM ON ADVANCED
STRUCTURAL INTEGRITY METHODS FOR
AIRFRAME DURABILITY AND DAMAGE
TOLERANCE (NASA Langley Research
Center) 506 p

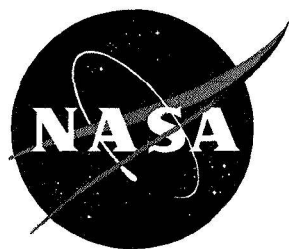
N95-14453
--THRU--
N95-14486
Unclass

H1/39 0023094



Proceedings of a symposium jointly sponsored
by the Federal Aviation Administration,
Washington, DC, and the National Aeronautics
and Space Administration, Washington, DC, and
held in Hampton, Virginia
May 4-6, 1994

September 1994



NASA Conference Publication 3274
Part 1

FAA/NASA International Symposium on Advanced Structural Integrity Methods for Airframe Durability and Damage Tolerance

Edited by
Charles E. Harris
Langley Research Center • Hampton, Virginia

Proceedings of a symposium jointly sponsored
by the Federal Aviation Administration,
Washington, DC, and the National Aeronautics
and Space Administration, Washington, DC, and
held in Hampton, Virginia
May 4-6, 1994

National Aeronautics and Space Administration
Langley Research Center • Hampton, Virginia 23681-0001

September 1994

The use of trade names of manufacturers in this report does not constitute an official endorsement of such products or manufacturers, either expressed or implied, by the National Aeronautics and Space Administration.

Preface

The need to design ultra lightweight airframe structures that are both durable and damage tolerant has historically been a major motivation for the engineering and research community. More recently, transport aircraft are being kept in service well beyond their original design economic life goals. Advanced technologies are under development that will enable the structural engineers to design longer life aircraft and to extend the life of high time aircraft currently in the commercial and military fleets. These technologies include better corrosion prevention, more accurate residual strength and life prediction methodologies, more durable materials, and more reliable and economical in-service inspection techniques. In order to advance civil aviation and to promote continuous airworthiness, the United States Federal Aviation Administration and the National Aeronautics and Space Administration co-sponsored this symposium to review recent research developments and to stimulate the exchange of technical ideas within the international aeronautical engineering community. The focus of the symposium was on advanced durability and damage tolerance methodology for metallic airframe structures.

Technical papers were selected for presentation at the symposium after a review of extended abstracts received by the Organizing Committee from a general call-for-papers. Keynote addresses were given in the opening Plenary Session by Mr. Harvey Safeer, Director of the FAA Technical Center, and Mr. Ray Hood, Manager of the NASA Advanced Subsonic Technology Program. Mr. Safeer gave the FAA perspective on the role of advanced technology in improving aircraft safety and Mr. Hood reviewed NASA's technology development programs for the next generation subsonic and supersonic aircraft. Technical papers were presented in oral briefings or posters on the following topics:

Structural Concepts for Enhanced Durability, Damage Tolerance, and Maintainability
New Metallic Alloys and Processing Technology
Fatigue Crack Initiation and Small Crack Effects
Fatigue Crack Growth Models
Fracture Mechanics Failure Criteria for Ductile Materials
Structural Mechanics Methodology for Residual Strength and Life Prediction
Development of Flight Load Spectra for Design and Testing
Advanced Approaches to Resist Corrosion and Environmentally Assisted Fatigue

Full-length manuscripts were solicited from the authors of papers presented in both oral briefings and posters. These papers are included in the proceedings.

The members of the Symposium Organizing Committee are as follows:

Charles E. Harris, NASA Langley Research Center, Symposium Chairman
Chris C. Seher, FAA Technical Center, Symposium Co-Chairman
Satya N. Atluri, Georgia Institute of Technology
Arij de Koning, National Aerospace Laboratory NLR, The Netherlands
Walter F. Jones, USAF AFOSR, Bolling Air Force Base
John W. Lincoln, USAF ASD/ENFS, Wright-Patterson Air Force Base
Matthew Miller, Boeing Commercial Airplane Group
James C. Newman, Jr., NASA Langley Research Center
Tom Swift, FAA National Resource Specialist

Approximately 300 research scientists and practicing engineers attended the symposium. The affiliations of the participants included 25% from government agencies, 31% from academia, and 44% from industry.

Charles E. Harris
NASA Langley Research Center

CONTENTS

Preface	iii
--------------------------	-----

PART 1

Elastic-Plastic Models for Multisite Damage Ricardo L. Actis and Barna A. Szabó	1-1
Small Crack Test Program for Helicopter Materials Bal Annigeri and George Schneider	17-2
Bending Effects of Unsymmetric Adhesively Bonded Composite Repairs on Cracked Aluminum Panels Cory Arendt and C. T. Sun	33-3
Evaluation of Bonded Boron/Epoxy Doublers for Commercial Aircraft Aluminum Structures Bruce Belason, Paul Rutherford, Matthew Miller, and Shreeram Raj	49-4
Inspecting for Widespread Fatigue Damage: Is Partial Debonding the Key? John Brewer	61-5
Microstructurally Based Model of Fatigue Initiation and Growth J. R. Brockenbrough, A. J. Hinkle, P. E. Magnusen, and R. J. Bucci	71-6
Testing and Analysis of Flat and Curved Panels with Multiple Cracks David Broek, David Y. Jeong, and Douglas Thomson	85-7
Probabilistic Inspection Strategies for Minimizing Service Failures Abraham Brot	99-8
Nonlinear Fracture Mechanics-Based Analysis of Thin Wall Cylinders Frederick W. Brust, Brian N. Leis, and Thomas P. Forte	111-9
Fatigue Analysis of Multiple Site Damage at a Row of Holes in a Wide Panel Kimberley Buhler, Alten F. Grandt, Jr., and E. J. Moukawsher	127-10
A Method of Calculating the Safe Fatigue Life of Compact, Highly-Stressed Components Arthur W. Cardrick and Vera J. Pike	145-11
Corrosion and Corrosion Fatigue of Airframe Aluminum Alloys G. S. Chen, M. Gao, D. G. Harlow, and R. P. Wei	157-12

PROCEEDING PAGE BLANK NOT FILMED

Computational Predictive Methods for Fracture and Fatigue	175
J. Cordes, A. T. Chang, N. Nelson, and Y. Kim	13
Influence of Crack History on the Stable Tearing Behavior of a Thin-Sheet Material with Multiple Cracks	193
D. S. Dawicke, J. C. Newman, Jr., M. A. Sutton, and B. E. Amstutz	14
Study of Multiple Cracks in Airplane Fuselage by Micromechanics and Complex Variables	213
Mitsunori Denda and Y. F. Dong	15
Extracting a Representative Loading Spectrum from Recorded Flight Data	225
Anthony G. Denyer	16
The Role of Fretting Corrosion and Fretting Fatigue in Aircraft Rivet Hole Cracking – A Status Report on Two FAA Grant Programs	241
Charles B. Elliott III, Mark Moesser, and David W. Hoepfner	17
Initiation and Propagation of Small Corner Cracks	247
Fernand Ellyin, Daniel Kujawski, and David F. Craig	18
Statistical Investigation of Fatigue Crack Initiation and Growth Around Chamfered Rivet Holes in Alclad 2024 T3 as Affected by Corrosion	259
M. I. Fadrakas, M. E. Fine, and B. Moran	19
Development of the NASA/FLAGRO Computer Program for Analysis of Airframe Structures	277
R. G. Forman, V. Shivakumar, and J. C. Newman, Jr.	20
Space Shuttle Fatigue Loads Spectra for Prelaunch and Liftoff Loads	289
Judith Goldish and Raphael Ortasse	21
Fatigue Reliability Method with In-Service Inspections	307
H. H. Harkness, M. Fleming, B. Moran, and T. Belytschko	22
Nonlinear Bulging Factor Based on R-Curve Data	327
David Y. Jeong and Pin Tong	23
Development of a Composite Repair and the Associated Inspection Intervals for the F111C Stiffener Runout Region	339
R. Jones, L. Molent, J. Paul, T. Saunders, and W. K. Chiu	24
Recent Advances in the Modelling of Crack Growth under Fatigue Loading Conditions	351
A. U. de Koning, H. J. ten Hoeve, and T. K. Henriksen	25
Axial Crack Propagation and Arrest in Pressurized Fuselage	375
M. Kosai, A. Shimamoto, C.-T. Yu, S. I. Walker, A. S. Kobayashi and P. Tan	26
Fracture Mechanics Validity Limits	393
Dennis M. Lambert and Hugo A. Ernst	27

Challenges for the Aircraft Structural Integrity Program	409-28
John W. Lincoln	
The Effects of Pitting on Fatigue Crack Nucleation in 7075-T6 Aluminum Alloy	425-29
Li Ma and David W. Hoeppner	
Modeling Time-Dependent Corrosion Fatigue Crack Propagation in 7000 Series Aluminum Alloys	441-30
Mark E. Mason and Richard P. Gangloff	
Analysis of Small Crack Behavior for Airframe Applications	463-31
R. C. McClung, K. S. Chan, S. J. Hudak, Jr., and D. L. Davidson	
Full-Scale Testing and Analysis of Fuselage Structure	481-32
M. Miller, M. L. Gruber, K. E. Wilkins, and R. E. Worden	
Advanced Method and Processing Technology for Complicated Shape Airframe Part Forming	497-33
P. V. Miodushevsky and G. A. Rajevskaya	

PART 2*

Flight Parameters Monitoring System for Tracking Structural Integrity of Rotary-Wing Aircraft	505
Jamshid Mohammadi and Craig Olkiewicz	
Fatigue Loads Spectra Derivation for the Space Shuttle – Second Cycle . . .	517
Raphael Ortasse	
Prediction of Fatigue Crack Growth under Flight-Simulation Loading with the Modified Corpus Model	547
U. H. Padmadinata and J. Schijve	
The Characterization of Widespread Fatigue Damage in Fuselage Structure	563
Robert S. Piascik, Scott A. Willard, and Matthew Miller	
Discrete Crack Growth Analysis Methodology for Through Cracks in Pressurized Fuselage Structures	581
David O. Potyondy, Paul A. Wawrzynek, and Anthony R. Ingraffea	
A New Stochastic Systems Approach to Structural Integrity	603
James W. Provan and Khalil Farhangdoost	
Fatigue and Damage Tolerance Scatter Models	621
Veniamin L. Raikher	

* Part 2 is presented under separate cover.

A Probabilistic Fatigue Analysis of Multiple Site Damage	635
S. M. Rohrbaugh, D. Ruff, B. M. Hillberry, G. McCabe, and A. F. Grandt, Jr.	
Evaluation of the Fuselage Lap Joint Fatigue and Terminating Action Repair	653
Gopal Samavedam, Douglas Thomson, and David Y. Jeong	
Fatigue Life until Small Cracks in Aircraft Structures. Durability and Damage Tolerance	665
J. Schijve	
Development of Load Spectra for Airbus A330/A340 Full Scale Fatigue Tests	683
H.-J. Schmidt and Th. Nielsen	
Aircraft Stress Sequence Development A Complex Engineering Process Made Simple	699
K. H. Schrader, D. G. Butts, and W. A. Sparks	
The Load Separation Technique in the Elastic-Plastic Fracture Analysis of Two- and Three-Dimensional Geometries	703
Monir H. Sharobeam	
An Artificial Corrosion Protocol for Lap-Splices in Aircraft Skin	725
Bevil J. Shaw	
The Application of Newman Crack-Closure Model to Predicting Fatigue Crack Growth	741
Erjian Si	
Fatigue Crack Growth under Variable Amplitude Loading	755
Jihad A. Sidawi	
Residual Life & Strength Estimates of Aircraft Structural Components with MSD/MED	771
Ripudaman Singh, Jai H. Park, and Satya N. Atluri	
Ultrasonic Techniques for Repair of Aircraft Structures with Bonded Composite Patches	785
S. H. Smith, N. Senapati, and R. B. Francini	
Near Tip Stress and Strain Fields for Short Elastic Cracks	801
A. H. Soediono, G. A. Kardomateas, and R. L. Carlson	
Widespread Fatigue Damage Monitoring – Issues and Concerns	829
T. Swift	
Microstructurally Based Variations on the Dwell Fatigue Life of Titanium Alloy IMI 834	871
Mark L. Thomsen and David W. Hoepfner	
Fatigue Crack Growth in 2024-T3 Aluminum under Tensile and Transverse Shear Stresses	891
Mark J. Viz and Alan T. Zehnder	

Results of Uniaxial and Biaxial Tests on Riveted Fuselage Lap Joint Specimens	911
H. Vlieger	
On the Measurement of the Crack Tip Stress Field as a Means of Determining ΔK_{eff} under Conditions of Fatigue Crack Closure	933
Ian R. Wallhead, Lyndon Edwards, and Peter Poole	
Analysis of Cold Worked Holes for Structural Life Extension	947
David H. Wieland, Jon T. Cutshall, O. Hal Burnside, and Joseph W. Cardinal	
Fracture Behavior of Large-Scale Thin-Sheet Aluminum Alloy	963
Roland deWit, Richard J. Fields, Leonard Mordfin, Samuel R. Low, and Donald Harne	
Fatigue and Residual Strength Investigation of Arall®-3 and Glare®-2 Panels with Bonded Stringers	985
Ming Wu, Dale A. Wilson, and S. V. Reddy	
Prediction of R-Curves from Small Coupon Tests	999
J. R. Yeh, G. H. Bray, R. J. Bucci, and Y. Macheret	
Aircraft Fatigue and Crack Growth Considering Loads by Structural Component	1015
J. D. Yost	
Stress Intensity Factors for Surface and Corner Cracks Emanating from a Wedge-Loaded Hole	1029
W. Zhao, M. A. Sutton, K. N. Shivakumar, and J. C. Newman, Jr.	
Nonlinear Analysis of Damaged Stiffened Fuselage Shells Subjected to Combined Loads	1045
James H. Starnes, Jr., Vicki O. Britt, Richard D. Young, Charles C. Rankin, Charles P. Shore, and Nancy Jane C. Bains	

ELASTIC-PLASTIC MODELS FOR MULTI-SITE DAMAGE¹

348602

57-39

23095

p. 16

Ricardo L. Actis
Engineering Software Research and Development, Inc.
St. Louis, MO

Barna A. Szabó
Center for Computational Mechanics
Washington University, St. Louis, MO

SUMMARY

This paper presents recent developments in advanced analysis methods for the computation of stress intensity factors and the J-integral under conditions of small scale yielding in structural panels with multi-site damage. The method of solution is based on the p-version of the finite element method. Its implementation was designed to permit extraction of linear stress intensity factors using a superconvergent extraction method (known as the contour integral method) and evaluation of the J-integral following an elastic-plastic analysis. Coarse meshes are adequate for obtaining accurate results supported by p-convergence data. The elastic-plastic analysis is based on the deformation theory of plasticity and the von Mises yield criterion.

The model problem consists of an aluminum plate with six equally spaced holes and a crack emanating from each hole. The cracks are of different sizes. The panel is subjected to a remote tensile load. Experimental results are available for the panel. The plasticity analysis provided the same limit load as the experimentally determined load. The results of elastic-plastic analysis were compared with the results of linear elastic analysis in an effort to evaluate how plastic zone sizes influence the crack growth rates. The onset of net-section yielding was determined also. The results show that crack growth rate is accelerated by the presence of adjacent damage, and the critical crack size is shorter when the effects of plasticity are taken into consideration. This work also addresses the effects of alternative stress-strain laws: The elastic-ideally-plastic material model is compared against the Ramberg-Osgood model.

INTRODUCTION

Reliable stress intensity factor computation of cracked structural components is of major importance in modern design of aircraft structures where requirements for residual strength and fatigue crack propagation must be met. In this paper the problem of computing the stress intensity factors for a structural panel with multi-site damage, with guarantee of reliability, is discussed. This work focuses on the accuracy and reliability of the numerical solution of a proposed mathematical model and on the influence that different modeling assumptions may have on the results of the analysis. Two kinds of error are important in this case:

1. The differences between the exact solution of the mathematical problem formulated to represent a physical system or process and its numerical approximation are called errors of discretization. Is it possible to guarantee that the error of discretization is small?

1. Work supported by NASA Lyndon B. Johnson Space Center under Grant NAG 9-622.

2. The differences between the exact solution of the mathematical problem formulated to represent a physical system and the actual response or behavior of the physical system are called errors of idealization or modeling errors. How does incorporating plasticity in the analysis affect the stress intensity factors?

In some cases the two errors, the errors of discretization and modeling, may partially cancel one another. Therefore it is important to verify by means other than the experiment itself, that the numerical solution is close to the exact solution of the model. Only then is it possible to investigate whether the errors of idealization are large or small by making comparisons with experimental observations. The efficient and reliable control of numerical errors, achieved by the use of a superconvergent method for the computation of the stress intensity factors, makes it feasible to investigate the sensitivity of crack extension to alternative modeling decisions.

In this paper, the effect of plasticity on the values of the fracture mechanics parameters is investigated. First, the finite element implementation is discussed; and second the method is illustrated with the integrity assessment of a row of fastener holes with multi-site damage, for which experimental results are available.

FINITE ELEMENT IMPLEMENTATION

Choice of an Extension Process

In the finite element method the control of the errors of discretization can be achieved by mesh refinement (h-extension), by increasing the polynomial degree of elements (p-extension), or a combination of both (hp-extension).

The size of a finite element is the diameter of the smallest circle (or sphere) that contains the element. This diameter is denoted by h and the diameter of the largest finite element in the mesh is denoted by h_{max} . h-Extension involves letting $h_{max} \rightarrow 0$. Alternatively, we can hold the number of elements constant and increase the polynomial degree of elements. The polynomial degree of elements is a vector p . p-Extension involves letting the smallest polynomial degree $p_{min} \rightarrow \infty$. In hp-extensions mesh refinement is combined with an increase of the polynomial degree of elements. In these processes the number of equations that has to be solved, the number of degrees of freedom, is progressively increased, hence the name 'extension'. Note that h- and p-extensions can be viewed as special cases of hp-extension, which is the general discretization strategy of the finite element method.

An important question is: "Which is the most efficient method of extension with respect to reducing discretization errors?" This question can be answered on the basis of a simple classification of the exact solution of the problem one wishes to solve. The exact solutions (u_{EX}) have been classified into three main categories:

Category A: u_{EX} is analytic. A function is analytic at a point if it can be expanded into a Taylor series about that point on the entire solution domain, including the boundaries of the solution domain. Alternatively, the domain can be divided into subdomains and u_{EX} is analytic on each subdomain, including the boundary of each subdomain. The finite element mesh is so constructed that the boundaries of the subdomains are coincident with element boundaries.

Category B: u_{EX} is analytic on the entire domain, including the boundaries, with the exception of a finite number of points (in three dimensions u_{EX} needs not be analytic along a finite number of lines). The mesh is so constructed that the points where u_{EX} is not analytic are nodal points (in three dimensions the

lines where u_{EX} is not analytic are coincident with element edges). An example of problems in Category B is a cracked elastic body. The crack tip is a singular point.

Category C: Problems for which the exact solution is neither in Category A nor in Category B are in Category C.

Most problems in mechanical and structural design belong in either Category A or Category B. Most problems in fluid dynamics belong in Category C. Knowing the classification of a problem, it is possible to compare h-, p- and hp-extensions on the basis of rate of convergence, that is, the rate of change of the error measured in energy norm with respect to the number of degrees of freedom. For problems in Category A and B the discretization errors are most efficiently controlled by p-extension. Designing a mesh such that when the polynomial degree of elements is uniformly increased then the discretization error decreases exponentially until the required degree of accuracy has been reached; usually it involves grading the mesh in geometric progression in the vicinity of singular points (ref. 1).

The Trunk and Product Spaces

By definition, the standard quadrilateral element $\Omega_{st}^{(q)}$ is the set of points (ξ, η) which satisfy $|\xi| \leq 1$, $|\eta| \leq 1$, see Figure 1. The *trunk space* of degree p is defined as the set of polynomials which can be

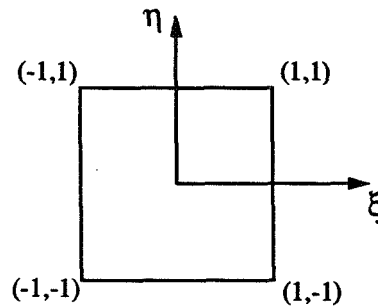


Figure 1. The standard quadrilateral element $\Omega_{st}^{(q)}$.

expressed as linear combinations of $\xi^i \eta^j$, $i, j = 0, 1, \dots, p$; $i + j \leq p$ and supplemented by the monomial term $\xi \eta$ for $p=1$, and the monomial terms $\xi^p \eta$, $\xi \eta^p$ for $p \geq 2$. For example, for $p=4$ the trunk space includes all polynomials up to degree 4, plus two fifth order polynomials. The *product space* of degree p is the set of polynomials which can be expressed as linear combinations of $\xi^i \eta^j$, $i, j = 0, 1, \dots, p$. For example, for $p=4$ the product space includes all polynomials up to degree 8.

The answer to the question: "Which space should be used in a given application?" depends on the accuracy requirements. The following points should be taken into consideration:

1. The number of degrees of freedom increases much more rapidly with respect to p when the product space is used. For example, in the case of $p=8$ there are 47 degrees of freedom per field for the trunk space, and 81 degrees of freedom per field for the product space.
2. For a given polynomial degree the error, measured in energy norm, is always smaller for the product space than for the trunk space. This is because the trunk space is a subset of the product space.
3. For a given number of degrees of freedom the error for the product space, measured in energy norm, may be smaller or larger than the error for the trunk space. There appears to be no way of predicting which space performs better for specific cases.

4. For static analyses, work performed by the computer increases more slowly with respect to increasing p for the product space than for the trunk space. This is because in the case of the product space the increase affects the internal modes only and those modes are eliminated by the solver locally, i.e. no assembly is involved and the front width is unaffected.

In our implementation both the trunk and product spaces are available for quadrilateral elements, and the polynomial degree can be increased up to $p=8$.

Elastic-Plastic Analysis

The implementation of material nonlinearities within the framework of the p -version was considered an essential feature in the assessment of modeling assumptions. The elastic-plastic analysis is based on the von Mises yield criterion and the deformation theory of plasticity. The purpose and scope of this implementation are as follows (for further details see ref. 2):

1. Realistic mathematical models of real physical systems must have a capability to provide initial estimates for the effects of nonlinearities at a low computational cost. The deformation theory of plasticity serves this purpose well for a large class of practical problems.
2. The effects of a single overload event on structures made of ductile materials are of substantial practical importance. Such effects can be well represented by mathematical models based on the deformation theory of plasticity, provided that the plastic flow is contained, i.e., the plastic zone is surrounded by elastic material.
3. The propagation of cracks in strain-hardening materials is generally correlated with the J-integral. The J-integral is based on the deformation theory of plasticity.
4. An important feature of the linear implementation is that engineering data can be conveniently extracted from finite element solutions in the post-solution phase. The deformation theory of plasticity makes it feasible to extend this into the elastic-plastic regime because the data storage requirements are small.
5. The p -version is not susceptible to Poisson ratio locking and hence correct limit loads are obtained. In the conventional (h -version) locking occurs when the displacement formulation is used. For this reason alternative formulations, generally known as mixed methods, must be employed.

Elastic-Plastic Material Properties

An important modeling assumption is the type of stress-strain law used for the elastic-plastic analysis. Four types of stress-strain relationships have been implemented:

Ramberg-Osgood: Material characterized by four parameters (Figure 2): The modulus of elasticity (E), Poisson's ratio (ν), the stress (S_{70E}), which is the stress corresponding to the intersection of the stress-strain curve with a line which passes through the origin and has the slope of $0.70E$, and an exponent n in the expression:

$$\epsilon = \frac{\sigma}{E} + \frac{S_{70E}}{E} \left(\frac{\sigma}{S_{70E}} \right)^n \quad (1)$$

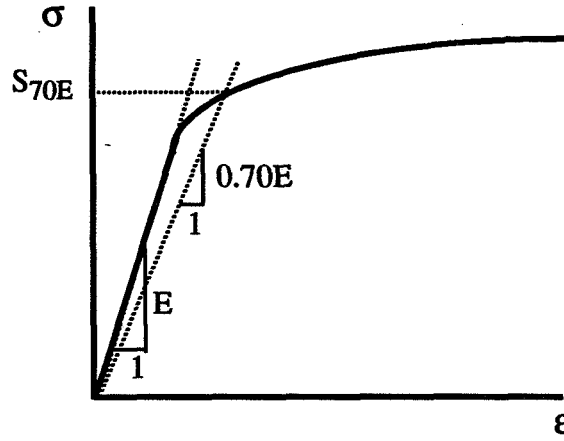


Figure 2. The Ramberg-Osgood stress-strain curve.

Typical values of n range between 4 and 90. Fractional values are permitted for n . In the limit as $n \rightarrow \infty$, an elastic-perfectly plastic material behavior is approached.

Elastoplastic: Elastic-perfectly plastic material characterized by E , ν and the yield stress S_y .

Bilinear: Linear-elastic, linear strain hardening material characterized by E , ν , S_y and the tangent modulus E_t which characterizes strain hardening.

5-Parameter: Material characterized by two linear segments joined by a cubic spline.

Solution Algorithm

The following is an outline of the solution procedure implemented for two-dimensional elastic-plastic problems based on the deformation theory of plasticity. The procedure is known as direct integration. The iteration number is represented by a superscript in brackets:

1. Obtain a linear solution for the problem. Ensure that the relative error in energy norm is small, certainly under 5%, preferably under 1%.
2. Compute the total equivalent strain $\bar{\epsilon}$ in each Gauss point. The elastic equivalent strain is defined as:

$$\bar{\epsilon}^e = \frac{\sqrt{2}}{2(1+\nu)} \sqrt{(\epsilon_1^e - \epsilon_2^e)^2 + (\epsilon_2^e - \epsilon_3^e)^2 + (\epsilon_3^e - \epsilon_1^e)^2} \quad (2)$$

and the plastic equivalent strain is given as:

$$\bar{\epsilon}^p = \frac{\sqrt{2}}{3} \sqrt{(\epsilon_1^p - \epsilon_2^p)^2 + (\epsilon_2^p - \epsilon_3^p)^2 + (\epsilon_3^p - \epsilon_1^p)^2} \quad (3)$$

where ν is Poisson's ratio, $\epsilon_1, \epsilon_2, \epsilon_3$ are the principal strains. The total equivalent strain is:

$$\bar{\epsilon} = \bar{\epsilon}^e + \bar{\epsilon}^p. \quad (4)$$

3. Using $(\bar{\epsilon})^{(k)}$, compute the secant modulus $E_s^{(k)}$ at each Gauss point from the one-dimensional stress-strain curve.
4. In each Gauss point for which $\bar{\epsilon} > \epsilon_Y$ (the uniaxial strain at the onset of yielding), determine the elastic plastic material stiffness matrix using $E_s^{(k)}$. Recompute the stiffness matrices for those elements for which $\bar{\epsilon} > \epsilon_Y$ in one or more Gauss points, and obtain a new finite element solution $u_{FE}^{(k+1)}$.

5. Using $E_s^{(k)}$ and $u_{FE}^{(k+1)}$, compute the strain and stress tensor components and the equivalent stress at each Gauss point. Using expressions (2)-(4), compute the total equivalent strain at each Gauss point $(\bar{\epsilon})^{(k+1)}$. If the equivalent stress $\bar{\sigma}^{(k+1)}$ in each Gauss point satisfies:

$$|\bar{\sigma}_r - \bar{\sigma}^{(k+1)}| \leq \tau |\bar{\sigma}| \quad (5)$$

then stop, else using $(\bar{\epsilon})^{(k+1)}$, compute $E_s^{(k+1)}$, increment k to $k+1$ and return to step 3. In (5), $\bar{\sigma}_r$ is the reference equivalent stress from the uniaxial stress-strain curve corresponding to $(\bar{\epsilon})^{(k+1)}$, and τ is the pre-specified tolerance. The equivalent stress is computed based on the principal stresses as follows:

$$\bar{\sigma} = \frac{\sqrt{2}}{2} \sqrt{(\sigma_1 - \sigma_2)^2 + (\sigma_2 - \sigma_3)^2 + (\sigma_3 - \sigma_1)^2} \quad (6)$$

Fracture Mechanics Parameters

In the neighborhood of the crack tip in an elastic body, the solution becomes singular and the stress values go to infinity at the crack tip. Whether or not a crack will propagate, and at what rate, depends on the energy available to drive crack extension. In linear-elastic fracture mechanics the stress intensity factors are a measure of the stress singularity at the crack tip. They depend on the geometry of the body, the configuration of the crack, the boundary conditions and the loading. In the elastic-plastic regime, the J-integral has been increasingly used to characterize crack initiation and crack growth. J can be interpreted as the energy release rate, and in the linear-elastic case $J=G$ (the energy release rate).

Stress Intensity Factors

The computation of Mode I and II stress intensity factors for linear elastic fracture mechanics was implemented using the Contour Integral Method, as described in ref. 1:

$$K_I = \sqrt{2\pi} A_1^{(1)}, \quad K_{II} = \sqrt{2\pi} A_1^{(2)} \quad (7)$$

where $A_1^{(m)}$, $m = 1, 2$, is the first term in the asymptotic expansion of the solution in the neighborhood of the crack tip for modes I and II respectively.

Let Γ_ρ be a circle of radius ρ centered on the crack tip (Figure 3), and assume that ρ is sufficiently close to the crack tip. Then we can write:

$$A_1^{(m)} \approx \int_{\Gamma_\rho} (W^{(m)} T_{FE} - u_{FE} T^{W^{(m)}}) ds \quad (8)$$

where $W^{(m)}$ is an extraction function, T_{FE} is the traction vector along Γ_ρ computed from the finite element solution u_{FE} , and T^W is the traction vector along Γ_ρ due to the extraction function.

The J-integral

The J-integral provides a mean to determine an energy release rate for cases where plasticity effects are not negligible. In the case of plane stress and plane strain the J-integral is defined by:

$$J = \int_{\Gamma_\rho} (W dy - T \frac{\partial u}{\partial x} ds) \quad (9)$$

where Γ_ρ is a contour around the crack tip, W is the strain energy density:

$$W = W(x, y) = \int_0^\epsilon \sigma_{ij} d\epsilon_{ij}. \quad (10)$$

T is the traction vector (with components T_x, T_y) along Γ_ρ , u is the displacement vector (u_x, u_y) and ds is an element of Γ_ρ . The coordinate system is located such that the origin is in the crack tip, the x-direction is parallel to the crack face (see Figure 3).

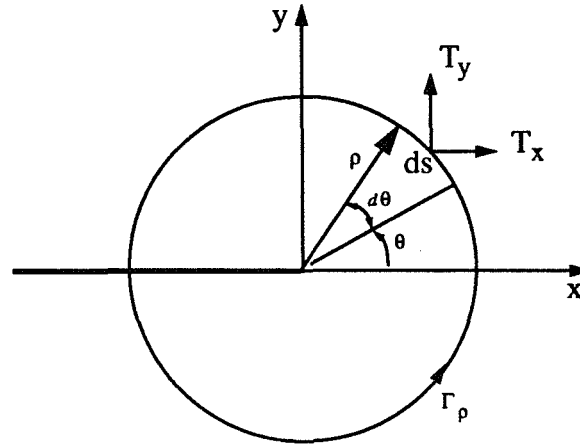


Figure 3. Path around the crack tip.

If the integration is performed along a circular path of radius ρ centered at the crack tip, equation (9) can be written as:

$$J = \int_{-\pi}^{\pi} (W \cos \theta - T_x \frac{\partial u_x}{\partial x} - T_y \frac{\partial u_y}{\partial x}) \rho d\theta. \quad (11)$$

The J-integral can be computed for linear and nonlinear isotropic or orthotropic materials. For the case of elastic-plastic materials, the integration path should be selected in such a way that it does not cut through the plastic zone around the crack tip. In the plastic region the strain energy density (W) is not defined.

EXAMPLE PROBLEM

Problem Description

The model problem consists of a 2024-T3 aluminum alloy plate with six equally spaced holes and a crack emanating from each hole. The cracks are of different sizes and the panel is subjected to a remote tensile load. The panel was selected from ref. 3, and corresponds to an MSD test coupon for constant ampli-

tude crack growth testing. Numerical and experimental crack growth data are available for the panel. Figure 4 shows the configuration of the panel for the example problem.

The objective of the analysis is to compute the stress intensity factors and the J-integral for each crack at different stages during crack propagation. The results are compared with the experimental values. The elastic-plastic analysis is performed using two different stress-strain laws: Ramberg-Osgood and elastic-ideally-plastic. The length of each crack (measured from the edge of the hole) for the four cases analyzed is

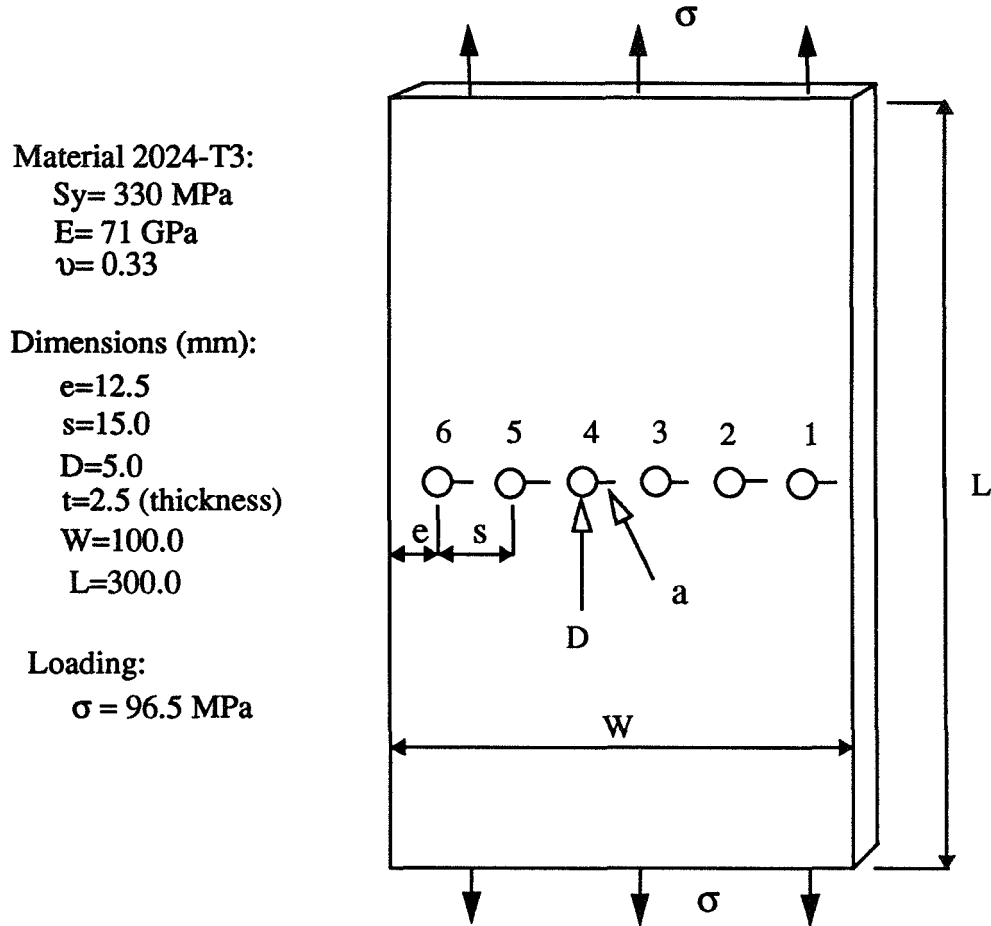


Figure 4. Panel configuration for example problem.

shown in Table 1. Case 1 corresponds to the initial crack length values; Case 2 represents the crack lengths after 6000 loading cycles; Case 3 after 12000 cycles; and Case 4 represents the crack lengths at failure (~13500 cycles).

Table 1: Crack Length (mm) for Each Case

Case	a_1	a_2	a_3	a_4	a_5	a_6
1	3.00	2.08	2.38	2.47	2.00	2.03
2	4.35	3.48	3.70	3.70	3.26	3.26
3	6.74	5.87	6.09	5.87	5.09	4.78
4	7.78	7.90	7.90	6.89	5.78	5.11

Discretization

In designing the finite element mesh and selecting the other discretization parameters, the smoothness of the exact solution of the mathematical model representing the physical system should be considered. For the example problem, the following modeling aspects are relevant:

1. Two-dimensional (plane stress) analysis is considered appropriate for this case.
2. Due to symmetry conditions, only half of the panel needs to be analyzed.
3. Elastic-plastic material properties are used to assess the influence of crack tip plasticity on the fracture mechanics parameters.

The solution of the mathematical model just described is smooth inside the domain and on the boundaries, except at the crack tips where the stresses are unbounded in the linear case. For the nonlinear case when the material is elastic-perfectly plastic, the stresses are finite but the strains are singular at the crack tips. The design of the finite element mesh should account for the nature of the exact solution. Geometrically graded meshes toward the singular points are known to be optimal in conjunction with p-extension for problems of this type. However, the design of geometrically graded meshes for domains with multiple cracks emanating from holes with sizes comparable to the hole diameters is very cumbersome and in many cases impractical. For that reason, the use of very simple meshes combined with high order elements (product space) is selected. This strategy has been tested and documented in refs. 3 and 4.

The finite element mesh consisting of 38 quadrilateral elements is shown in Figure 5. Each crack has been defined parametrically, so that the same mesh could be used for the four cases shown in Table 1 by adjusting the crack length parameters. Note that no mesh refinement around the crack tips has been used. Due to symmetry, only half the panel was discretized.

Two elastic-plastic stress-strain relations were investigated. The Ramberg-Osgood material characterized by: $E=71$ GPa, $\nu=0.33$, $S_{70E}=320$ MPa, $n=12$, and the elastic-perfectly plastic material characterized by $S_y=330$ MPa. The linear solution was computed for the product space and polynomial degree ranging from 1 to 8. Four nonlinear solutions were computed for each case in order to obtain an assessment of the discretization error for the nonlinear analysis. The linear runs corresponding to p-levels 5, 6, 7 and 8 were used to start the nonlinear iterations. The number of iterations required to complete any given analysis was based on a specified tolerance of 1.0% (see Eq. 5).

Results

Discretization Errors

For each linear analysis, the estimated relative error in energy norm was computed from the eight available solutions. Table 2 shows a typical result which corresponds to Case 1. The reported rate of convergence is typical for the p-extension in the case of category B type problems without geometrically graded meshes towards the singular points. For cases 1, 2 and 3, the estimated relative error in energy norm corresponding to p-level=5 and above was less than 5%.

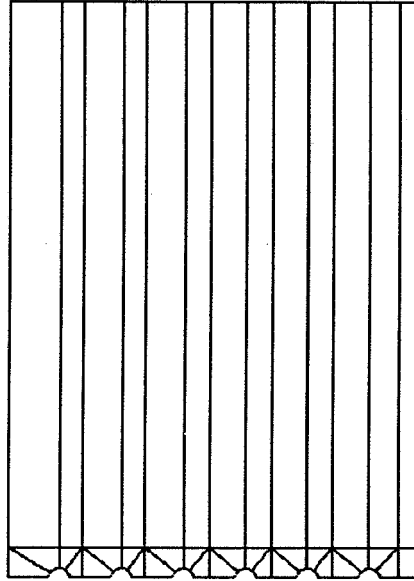


Figure 5. Finite element mesh.

Table 2: Estimated Relative Error in Energy Norm. Linear Solution for Case 1

p-Level	DOF	Potential Energy [N mm]	Rate of Convergence	Estimated % Error
1	117	-2490.4413	0.00	10.23
2	392	-2504.4379	0.31	7.02
3	819	-2510.8236	0.50	4.86
4	1398	-2513.3046	0.51	3.71
5	2129	-2514.6060	0.56	2.93
6	3012	-2515.3562	0.62	2.37
7	4047	-2515.7996	0.64	1.96
8	5234	-2516.0703	0.64	1.66

The fracture mechanics parameters were computed for the available sequence of linear and nonlinear solutions: Eight runs for each linear case and 4 runs for each nonlinear case. Convergence of the extracted results was assessed in each case. Typical convergence data are shown in Table 3 for the linear and nonlinear fracture mechanics parameters of Case 2, Crack 1.

Fracture Mechanics Parameters

Tables 4 to 6 show the values of the fracture mechanics parameters (FMP) for each crack and for cases 1 to 3 respectively. They include the stress intensity factor (K_I), the J-integral (J_e) computed from the linear solution and the values of the J-integral computed from the elastic-plastic solution for the Ramberg-Osgood material (J_p^{RO}) and the elastic-perfectly plastic material (J_p^{EP}). The relative difference between the elastic

and plastic (Ramberg-Osgood) values of J is also included. All values included in the tables correspond to the linear or nonlinear solutions for p -level=8.

Table 3: Convergence Data for Case 2, Crack 1

p-Level	K_I [MPa m ^{1/2}]	J_e [N m ⁻¹]	J_p^{RO} [N m ⁻¹]	J_p^{EP} [N m ⁻¹]
1	11.26	1148	---	---
2	14.43	2567	---	---
3	13.84	2647	---	---
4	13.41	2531	---	---
5	13.90	2681	2737	2683
6	14.28	2822	2881	2825
7	14.22	2827	2925	2859
8	14.15	2815	2927	2864

Table 4: FMP for Case 1 (N=0)

Parameter	Value of the Parameter for Crack #					
	1	2	3	4	5	6
K_I [MPa m ^{1/2}]	12.65	12.40	12.49	12.49	12.11	11.95
J_e [N m ⁻¹]	2242	2151	2186	2185	2059	2000
J_p^{RO} [N m ⁻¹]	2276	2200	2236	2231	2097	2031
J_p^{EP} [N m ⁻¹]	2256	2176	2219	2218	2084	2015
$(J_p^{RO}-J_e)/J_e$ [%]	1.8	2.3	2.3	1.8	1.9	1.5

Table 5: FMP for Case 2 (N=6000)

Parameter	Value of the Parameter for Crack #					
	1	2	3	4	5	6
K_I [MPa m ^{1/2}]	14.15	14.20	14.17	14.04	13.62	13.24
J_e [N m ⁻¹]	2815	2817	2818	2769	2592	2448
J_p^{RO} [N m ⁻¹]	2927	2905	2900	2843	2653	2491
J_p^{EP} [N m ⁻¹]	2864	2840	2837	2785	2609	2458
$(J_p^{RO}-J_e)/J_e$ [%]	4.3	3.3	2.8	2.5	2.3	1.6

Table 6: FMP for Case 3 (N=12000)

Parameter	Value of the Parameter for Crack #					
	1	2	3	4	5	6
K_I [MPa m ^{1/2}]	18.78	19.26	19.04	18.21	16.67	15.39
J_e [N m ⁻¹]	4885	5152	5019	4604	3893	3325
J_p^{RO} [N m ⁻¹]	6292	7057	6681	5786	4504	3603
J_p^{EP} [N m ⁻¹]	5585	6072	5771	5151	4196	3497
$(J_p^{RO}-J_e)/J_e$ [%]	28.6	37.1	33.1	25.9	15.7	8.1

These results clearly indicate that the stress intensity factors are not substantially affected by crack tip plasticity until the number of cycles is sufficiently high (near the end of the life of the panel). This is in agreement with the experimental observation: Towards the end of the life, the actual fatigue crack propagation rate is larger than that predicted by using the linear stress intensity factors. Tables 7 to 9 show a comparison of the experimental crack propagation rate (ref. 3) with those computed from the expression:

$$\frac{da}{dN} = C (\Delta K)^m \quad (12)$$

for the linear solution and from the expression:

$$\frac{da}{dN} = C (\sqrt{E \cdot \Delta J_p})^m \quad (13)$$

for the nonlinear solution. C and m are material constants ($C=4.15 \times 10^{-8}$, $m=2.2$ when ΔK is given in ksi, and da/dN is given in inch/cycle). The values of J_p for the Ramberg-Osgood (R-O) and for the elastic-perfectly-plastic material (E-P) are considered in Eq. 13.

Table 7: Fatigue Crack Propagation Rates for Case 1 (N=0)

Propagation Rate given by	da/dN [10 ⁴ mm/cycle] for Crack #					
	1	2	3	4	5	6
Eq. 12	2.28	2.18	2.21	2.21	2.07	2.01
Eq. 13(R-O)	2.30	2.21	2.25	2.25	2.10	2.03
Eq. 13 (E-P)	2.28	2.19	2.23	2.23	2.09	2.01
Experimental	2.10	2.20	2.16	2.00	1.75	1.80

Table 8: Fatigue Crack Propagation Rates for Case 2 (N=6000)

Propagation Rate given by	da/dN [10^4 mm/cycle] for Crack #					
	a ₁	a ₂	a ₃	a ₄	a ₅	a ₆
Eq. 12	2.92	2.93	2.92	2.86	2.68	2.49
Eq. 13(R-O)	3.03	3.01	3.00	2.94	2.72	2.54
Eq.13 (E-P)	2.96	2.93	2.93	2.87	2.69	2.50
Experimental	2.91	2.69	2.92	2.64	2.52	2.20

Table 9: Fatigue Crack Propagation Rates for Case 3 (N=12000)

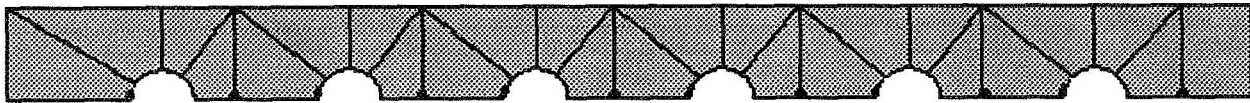
Propagation Rate given by	da/dN [10^4 mm/cycle] for Crack #					
	a ₁	a ₂	a ₃	a ₄	a ₅	a ₆
Eq. 12	5.43	5.74	5.60	5.08	4.18	3.49
Eq. 13 (R-O)	7.03	7.98	7.51	6.41	4.87	3.81
Eq. 13 (E-P)	6.17	6.76	6.40	5.64	4.50	3.69
Experimental	7.12	8.95	7.56	6.40	5.30	3.47

The Plastic Zone Size

Figure 6 shows the extent of the plastic zone at each crack tip for cases 1, 2 and 3 for the Ramberg-Osgood stress-strain law. The plastic zone is the set of all points for which the total equivalent strain is greater than or equal to the uniaxial yield strain $\bar{\epsilon} \geq \epsilon_Y$, where $\epsilon_Y = S_Y/E$.



Case 1: N=0



Case 2: N=6000



Case 3: N=12000

Figure 6. Plastic zone sizes for Ramberg-Osgood material.

Limit Load

The limit load was computed for the elastic-perfectly plastic material, by imposing a uniform normal displacement along the top edge of the panel, and computing the stress resultant along that edge. The crack configuration of Case 4 (failure condition) was used, and a nonlinear solution was obtained for each value of the imposed displacement. The results are shown in Figure 7. The limit load for this problem can be estimated as:

$$P_L = S_Y \left(W - 6d - \sum_{i=1}^6 a_i \right) t = 330 (100 - 30 - 41.36) 2.5 = 23628 \text{ N}$$

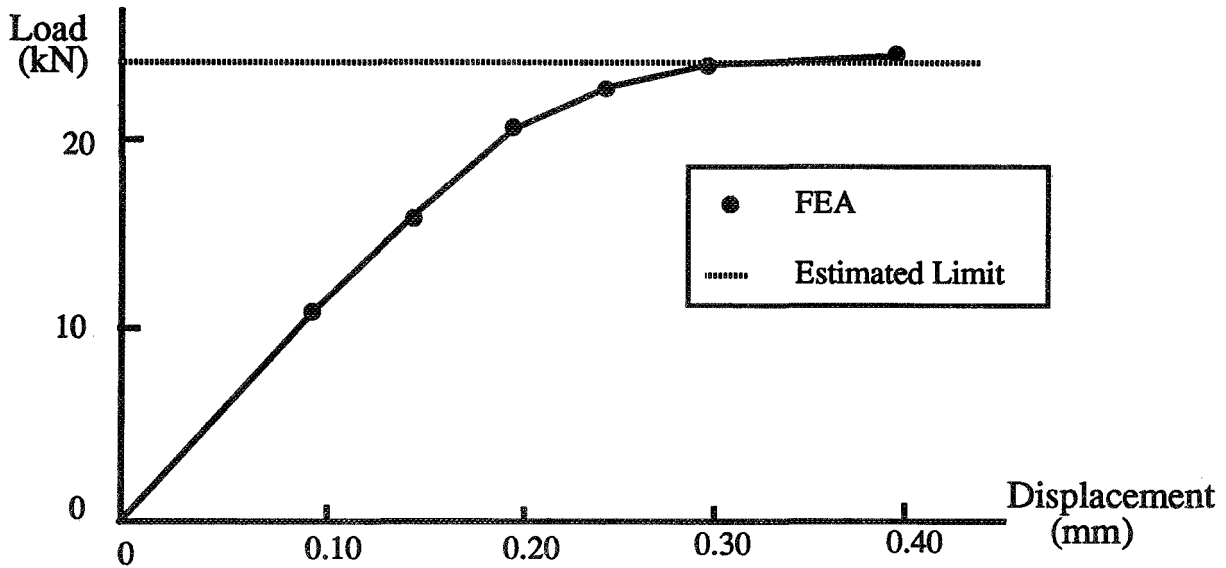


Figure 7: Load-displacement relation for case 4, elastic-perfectly plastic material.

Time Requirements

One important consideration in the utilization of an analysis tool incorporating advanced methodology is the amount of time required to analyze a problem of substantial complexity like the one discussed in this paper. To address this issue, we report in this Section the amount of time spent in the linear and nonlinear analyses. The computer runs were performed on a HP 9000/715 workstation using the finite element code STRESS CHECK¹ developed by the authors. The total time is the sum of the time required to perform three main activities: (1) preparation of input data, (2) execution of analyses, and (3) extraction of results.

The preparation of input data consists of the description of the solution domain, the design of the finite element mesh, the specification of the material properties, and the assignment of the boundary conditions (loads and constraints). This involves almost exclusively engineering time which will depend on the level of training of the analyst, and on the characteristics of the software tool used. The preparation of input data for the problem shown in Figure 5 required approximately 20 minutes of wall clock time. Since the crack

1. STRESS CHECK is a trademark of Engineering Software Research and Development, Inc., 7750 Clayton Rd., Suite 204, St. Louis, MO 63117.

lengths were defined in parametric form, and since the same description can be used to perform linear and nonlinear analyses, only one mesh was used for all cases analyzed.

The execution time depends on the analysis type. To obtain a sequence of linear solutions (p-level=1 to 8), 1.5 minutes of CPU time were required for each case. For the nonlinear solutions, the CPU time depends on the number of iterations necessary to achieve the desired tolerance level (see Eq. 5), which in turn depends on the amount of plasticity associated with the solution. To obtain a sequence of nonlinear solutions (p-level=5 to 8) for the crack configuration of case 1, 9.5 minutes of CPU were required; for case 2, 10.4 minutes of CPU; for case 3, 18.0 minutes of CPU.

The extraction of the results (the fracture mechanics parameters) involves mostly analyst's time. To compute the six crack tip stress intensity factors and J-integral (both elastic and plastic) for each case analyzed, about 30 minutes of wall clock time were required.

In summary, a complete analysis of a multiple-site damage panel for one crack configuration, including preparation of input data, execution of a sequence of linear and nonlinear solutions, and extraction of the data of interest, can be performed in about 1.5 hours of wall clock time.

The Importance of Controlling Discretization Errors

Intrinsic control of discretization errors by finite element programs is very important for properly correlating computed information with experimentally observed data and for using computed data in engineering decisions which cannot be measured directly, and/or exploring a range of loadings and constraint conditions, not covered by the experiment.

To illustrate this point, let Φ_{EXP} be some experimental information, for example a measured displacement or strain, Φ_{MOD} the same information predicted by a mathematical model, for example the equations of elasticity together with the appropriate material properties, boundary conditions and loading data; Φ_{FEA} the same information predicted by a finite element approximation of the mathematical model. Φ_{MOD} is generally not known, nevertheless the purpose of an experiment is to determine whether the mathematical model correctly describes the physical system being modeled, that is, whether Φ_{MOD} is sufficiently close to Φ_{EXP} . Writing:

$$|\Phi_{EXP} - \Phi_{MOD}| \equiv |\Phi_{EXP} - \Phi_{FEA} + \Phi_{FEA} - \Phi_{MOD}| \leq |\Phi_{EXP} - \Phi_{FEA}| + |\Phi_{FEA} - \Phi_{MOD}| \quad (14)$$

it is seen that if the quality of a mathematical model is to be assured then it is necessary to ensure that $|\Phi_{FEA} - \Phi_{MOD}|$ is not larger, and preferably much smaller, than $|\Phi_{EXP} - \Phi_{FEA}|$, which is known from measurement and computation. The quality control procedures of any finite element program should make it possible to ascertain that $|\Phi_{FEA} - \Phi_{MOD}|$ is smaller than $|\Phi_{EXP} - \Phi_{FEA}|$.

Unfortunately, there are many examples in industrial practice where close correlation with experimental results is achieved through skillful manipulation of the discretization parameters. The sensitivity of the approximate solution to discretization parameters is a strong indication that the numerical error is large, or the model is improperly defined. In the absence of intrinsic procedures designed for controlling approximation errors, it is possible to correlate computed data with experimental observations through near cancellation of two large errors:

$$\Phi_{EXP} - \Phi_{FEA} \equiv \underbrace{\Phi_{EXP} - \Phi_{MOD}}_{\pm M} + \underbrace{\Phi_{MOD} - \Phi_{FEA}}_{\pm M} \approx 0 \quad (15)$$

where M is some big number. Such models are unreliable and can be very misleading when the model is used for drawing general conclusions from experimental information.

CONCLUSIONS

Control of errors of discretization and modeling can be achieved if the analysis tools provide sufficient flexibility and are easy to use. It is also required that complex problems, both linear and nonlinear, be solved in hours instead of days.

Advanced analysis methods for the computation of stress intensity factors and the J-integral under conditions of small scale plasticity have been implemented within the framework of the p-version of the finite element method. The implementation makes it possible for practicing engineers to assess damage in structural components under elastic-plastic conditions with guaranteed reliability. The key elements which make this implementation unique can be summarized as follows:

1. The use of the product space and superconvergent extraction for the stress intensity factors allows the use of very simple (coarse) meshes to obtain extremely reliable results for the linear elastic fracture mechanics parameters.
2. The use of the deformation theory of plasticity with the von Mises yield criterion and the high-order finite elements (product space) makes it possible to use the same coarse meshes for the elastic-plastic analysis. Plastic zone sizes, J-integrals and limit loads can be easily and reliably computed from the finite element solutions.
3. The availability of various representations for nonlinear material makes it possible to assess the influence of different stress-strain laws in the results.
4. The possibility of using spring boundary conditions, bearing loads, and precise geometric representations allows for closer representation of actual problems.

The application of these techniques to a multi-site damage panel clearly demonstrates that the investigation of different modeling assumptions can be accomplished in a reasonable amount of time, and that the results obtained can be used to assess the influence of plasticity on the residual strength of the panel.

REFERENCES

1. Szabo, B. A.; and Babuska, I.: *Finite Element Analysis*. John Willey and Sons, Inc., 1991.
2. Szabo, B. A.; Actis, R. L.; and Holzer, S. M.: Solution of Elastic-Plastic Stress Analysis Problems by the p-Version of the Finite Element Method. Center for Computational Mechanics, Washington University, St. Louis, MO 63130, Report WU/CCM-93/3, November 1993.
3. Nathan, A.; and Brot, A.: An Analytical Approach to Multi-Site Damage. 17th Symposium of the International Committee on Aeronautical Fatigue, Stockholm, Sweden, June 10, 1993.
4. Actis, R. L.; and Szabo, B. A.: Computation of Stress Intensity Factors for Panels with Multi-Site Damage. Center for Computational Mechanics, Washington University, St. Louis, MO 63130, Technical Note WU/CCM-92/3, December 1992.

1995108041

N95-14455

SMALL CRACK TEST PROGRAM FOR HELICOPTER MATERIALS • 348606

52-39

Bal Annigeri
United Technologies Research Center
East Hartford, CT

23096

R 16

George Schneider
United Technologies, Sikorsky Aircraft
Stratford, CT

ABSTRACT

Crack propagation tests were conducted to determine crack growth behavior in five helicopter materials for surface cracks between 0.005 to 0.020 inches in depth. Constant amplitude tests were conducted at stress ratios $R = 0.1$ and 0.5 , and emphasis was placed on near threshold data (i.e. 10^{-8} to 10^{-6} inches/cycle). Spectrum tests were conducted using a helicopter spectrum.

The test specimen was an unnotched tension specimen, and cracks were initiated from a small EDM notch. An optical/video system was used to monitor crack growth. The material for the test specimens was obtained from helicopter part forgings. Testing was conducted at stresses below yield to reflect actual stresses in helicopter parts.

INTRODUCTION/BACKGROUND

At the present time helicopters are generally "Safe Life" designed and maintained. This means that conservative structural component replacement times are defined based on SN fatigue data, and parts are removed at these replacement times. Inspections may be performed at periodic intervals based on experience with service problems such as wear and corrosion.

The Air Force damage tolerance approach, in which inspection intervals are quantified through crack growth analysis, has been applied to some helicopter structures to define inspection intervals in instances of service problems. Sikorsky Aircraft has also been investigating the general application of damage tolerance to the H-53 helicopter under Air Force contracts.

- * Test program performed by United Technologies Sikorsky Aircraft and Research Center under contract F09603-89-G-0096-0014.

As part of the Air Force damage tolerance investigations crack propagation data was generated for the actual materials used in the H-53. Initial crack propagation data was obtained for large cracks using compact tension specimens, and for somewhat smaller corner cracks (greater than 0.015 inches) using edge notch specimens.

This crack propagation data was then used to assess crack growth times and inspection intervals in H-53 rotor and airframe structure. These structures are subjected to significant vibratory loading at frequencies of the main and tail rotor rpm (approximately 3 and 12 hz, respectively), and sometimes at two to four times these frequencies. As a result crack growth analyses often involved initial crack depths at the limit of detectability (0.005 inches); and, even at these small crack sizes, crack growth times in some structures were relatively short.

One concern in these crack growth assessments was the validity of the crack growth rate data at crack depths as small as 0.005 inches. A test program was therefore conducted under Air Force funding with the objective of obtaining crack growth rate data for surface cracks between 0.005 and 0.020 inches in depth in H-53 dynamic system and airframe materials. Emphasis was placed on constant amplitude near threshold data (i.e. 10^{-8} to 10^{-6} inches/cycle). Some spectrum testing was also performed to examine load interaction effects.

MATERIAL SELECTION AND DESCRIPTION

Five materials were chosen for the test program based on a survey of materials in primary H-53 rotor and airframe structure. The materials are as follows:

1. Al7075-T73 forging
2. 4340 (150 ksi) steel forging
3. Ti-6Al-4V alpha-beta forged, annealed
4. Ti-6Al-4V alpha-beta forged, solution heat treated and annealed
5. Ti-6Al-4V beta STOA forged

These materials encompass most of the H-53 structure, and are also common in many other Sikorsky helicopters such as the H-60 series (Black Hawk, Sea Hawk, and Night Hawk). The Al7075-T73 forgings are used in a number of main and tail rotor parts, and most of the major frames and fittings in the airframe are fabricated from this material. The 4340 steel and three titaniums are used primarily in main and tail rotor parts.

All the materials are die forgings and they were all obtained from actual helicopter parts bought to Sikorsky specifications as

indicated in Table 1. Conformance to the specifications was verified through standard Sikorsky materials process evaluations. The use of actual parts for material sources was considered essential in providing proper material form, microstructure, and properties.

Tensile ultimate and yield strengths for the materials are provided in Table 2. The Al7075-T73 and 4340 steel properties are "S" basis design properties from Mil-Hdbk-5E. The titanium properties are the average of the properties measured in the Sikorsky material conformance tests.

EXPERIMENTAL METHODS

The test facility at the United Technologies Research Center (Fig. 1) consists of a 3310 series "Interlaken" test system which includes a fully automated servo-hydraulic, closed loop test machine and a model 3200 controller. A Universal Test Program Series 3110, which is a menu driven software system, was used to control the test under both constant amplitude and spectrum loading.

Crack Detection And Monitoring

An optical/video crack detection and monitoring system was selected and developed for this program. This method was selected over other methods such as replicate (refs. 1,2) and electric potential drop (ref. 6) based on efficiency in developing the test procedures and performing the tests. Similar optical methods for crack detection using a camera instead of a video system had been successfully used in references 3,4, and 5. The major components in this system consisted of a macrophoto lens, a CCD video camera, video recorder, strobed fiber optic lighting, and a video monitor. The use of a strobed lighting system provided the ability to capture the image of the crack at the maximum load without stopping the tests. It was therefore possible to video monitor and record the crack growth in real time. Crack lengths were measured on the video monitor which was calibrated against measurements taken in the microscope. The crack length measurements were taken as the projected crack length along a straight line in the crack direction.

Specimen Configuration

In the selection of the test specimen the two types shown in Figure 2 (refs 1,2,4,5) were considered. Both of these specimens provided small test sections which facilitated the detection and tracking of naturally initiated cracks. As shown in Fig 2a the

notched specimen (refs. 1,2) consists of single edge notch plate with overall dimensions of 12 x 2 inches and a semicircular notch of radius of .125 inches. The unnotched specimen in Figure 2b (refs. 4,5) is a smoothly tapered specimen, and therefore it has no significant stress concentration. Its overall dimensions are 6 x 0.3 inches. Although both specimens appeared reasonable, the unnotched specimen was chosen for the following reasons:

1. The smaller overall specimen size facilitated specimen manufacture from actual helicopter parts.
2. It would not have to be stabilized at $R = -1$ testing as would the larger notched specimen.
3. It had no stress concentration. This results in a simpler stress intensity solution. It was also believed that the notched specimen might require higher stresses at the crack origin to naturally initiate a crack.

The regions of the specimen in which cracks initiated were manufactured to minimize residual stresses and provide a surface suitable for visualization of small cracks. The specimen preparation involved an initial EDM process to form the taper shape in the gage section. The specimens were then hand polished with a 240 to 320 grit wet sand paper to remove the EDM remelt and heat affected areas. The next step was chemical milling of the steel and titanium specimens and electro polishing of the aluminum specimens. The final preparation involved wet sanding with 600 to 1000 grit sand paper, and then polishing with 30, 15 and 3 micron diamond paste in a Varsol solution.

Test Method Development

The test method development consisted of modifications to the specimen geometry, surface preparation, optical magnification, and specimen lighting. The specimen geometry was modified to that shown in Figure 3 to lower grip loads and thus prevent slip and failure at the grips. It was also determined that highly polished surfaces, and specialized fiber optic lighting were necessary for tracking the crack. In early testing, naturally initiated cracks were attempted using a 30X magnification. However, problems in detecting the crack led to a final magnification of 200x, and the use of a very small EDM starter notch to facilitate and localize crack initiation. Very small EDM notches (0.006 to 0.009 inch surface lengths) were achieved by introducing an initial EDM notch, and then polishing the specimen to reduce the notch size.

EXPERIMENTAL PROGRAM

Test Plan

The test plan was to perform eight tests for each of the five selected H-53 materials. These tests consisted of two constant amplitude tests at each of three stress levels $R = \sigma_{\min}/\sigma_{\max} = -1, 0, \text{ and } 0.5$ and two spectrum tests. Due to budget and technical constraints the $R = -1$ tests were not performed. The objective was to provide crack growth rate data for surface cracks from 0.005 to 0.020 inches in depth in the near threshold region. It was desired that the cracks be naturally initiated to obtain the best possible data, but, as noted, it was necessary to use small EDM starter notches. Another important consideration was to perform the tests for stresses below yield to reflect stress levels typical of helicopter structure.

Stress Intensity Considerations

One of the problems in the test program was to perform propagation tests for 0.005 to 0.020 depth cracks at low stress intensity values. The problem is illustrated in Table 3. This table shows the maximum stresses (based on Sikorsky SN data) needed to initiate a crack in a reasonable number of cycles (0.5 to 1 million); the stress intensity ranges ΔK at these stress levels and crack depths of 0.005, 0.010, and 0.020; and the large crack threshold stress intensities. As shown the stress intensities at the crack sizes of interest are all well above the large crack thresholds.

The method used to overcome this problem for stress ratios $R = 0$ and .5 was to initiate the crack at $R = -1$ (compression fatigue) as suggested in reference 4. If the crack propagation tests are then performed at $R = 0$ and 0.5 without changing the maximum stress, lower ΔK 's than those in Table 3 may be realized. Using this method ΔK values near the large crack threshold were obtained for $R = 0$ and 0.5. However, no solution was obtained for $R = -1$.

Another possibility for obtaining lower stress intensities is that the EDM starter notch might reduce the stress required for crack initiation from those shown in Table 3. However during the development testing it was found that even with the EDM notch it was difficult to initiate cracks at stresses much below those in the table.

Spectrum Considerations

A number of helicopter stress spectra were examined for use in the spectrum crack growth tests. These spectra included the two standard helicopter rotor spectra HELIX28 and FELIX32 which were developed in a European collaborative effort for hinged and fixed rotor systems, respectively. Three spectra used in Sikorsky crack propagation assessments of the H-53 were also examined. These spectra included those for the airframe pylon fold hinge, the main rotor spindle (blade retention component), and the outboard blade spar.

Significant variability was found in these spectra. The HELIX32 spectrum showed very little variation in maximum stress and its predominate stresses (stresses at which most cycles occur) are at $R = 0.4$. The FELIX28 spectrum has overloads in maximum stress around 1.5 times the predominate stresses, and its predominate stresses are at $R = 0.1$ to 0.3 . The H-53 pylon fold spectrum has overloads in maximum stress of 1.2 to 2.4 times the predominate stresses, and its predominate stresses are at R values of 0.6 to 0.8 . The H-53 main rotor spindle has little variation in maximum stress, and its stress ratios are mostly between 0.7 and 0.8 . The H-53 main rotor outboard blade spectrum has the most variability in maximum stress of all the spectra examined with some overloads as high as 3 to 4 times the predominate stress levels. The outboard blade spectrum has a wide range of R values from 0.1 to 0.6 for high frequency stresses.

In this test program a modified H-53 pylon fold spectrum was selected for use in the spectrum tests. The spectrum was modified to maintain all R values below 0.6 . This spectrum is representative of helicopter spectra with reasonably high overload factors.

TEST DATA AND TEST RESULTS

Table 4 provides a summary of the constant amplitude tests performed. At least two constant amplitude tests were performed for each of the five materials at stress ratios $R = 0.1$ and 0.5 . The cracks were initiated from the EDM notch in compression fatigue ($R = -1$), and the maximum stress was either maintained or slightly increased for the crack propagation testing at $R = 0.1$ or 0.5 . As explained, the initiation of cracks at $R = -1$ resulted in lower stress intensities than could be achieved by initiating the cracks at positive R ratios. The maximum stress is maintained the same for crack propagation to avoid overload effects.

Table 5 provides a summary of the spectrum tests performed. One spectrum test was performed for each material using the H-53 airframe pylon fold spectrum. The cracks were initiated using

constant amplitude compression fatigue ($R = -1$). As shown in the table the maximum crack initiation stress was well below the maximum spectrum stress, and it was even below some of the high cycle maximum stresses in the spectrum.

Crack length (a) versus cycle data (N) was recorded using the calibrated optical/video system for each constant amplitude and spectrum test. The constant amplitude data was converted to crack propagation rate data (da/dN vs ΔK) using the ASTM secant method for determining da/dN , and a simple infinite plate solution for stress intensity K . The infinite plate solution assumes a semicircular crack, and examination of the fracture surface verified that this was a reasonable assumption. The mathematical expressions are:

$$da/dN = (a_{i+1} - a_i) / (N_{i+1} - N_i)$$

and

$$K = 0.7\sigma(\pi a)^{1/2}$$

At the present time a limited amount of data analysis has been performed for the constant amplitude test. The results for $R = 0.1$ are plotted in Figures 4 through 7. In all but Figure 4 (Al7075-T73) the small crack data is compared with large crack compact tension test data obtained about eight years ago in another Air Force funded test program. The Al7075-T73 is compared with large crack propagation rate curves used in the crack propagation computer program FLAGRO.

The AL7075-T73 $R = 0.1$ crack growth rate data (Fig 4) shows considerable scatter. The Al-2 specimen shows the most reasonable behavior with generally increasing da/dN with ΔK . The Al-16-1 and Al-3 specimens show erratic crack growth behavior. The Al-16-1 specimen generally showed a decreasing da/dN with increasing ΔK . This may be due to the small initial crack size (Table 4) and interaction with the EDM notch. The Al-3-1 specimen was tested at the highest ΔK values and its behavior is also erratic. The Al-2 test specimen shows reasonable agreement with the FLAGRO curve.

Some preliminary evaluation of the Al7075-T73 $R = 0.5$ data shows good agreement between the two specimens. The crack propagation rate da/dN is also generally increasing with increasing ΔK , but there is still a considerable amount of data scatter.

The 4340 steel $R = 0.1$ crack growth rate data (Fig 5) shows much less scatter than the aluminum, and remarkable agreement with the large crack compact tension threshold test results conducted eight years ago. The material sources for both the small and large crack specimens were H-53 main rotor hinge pins, but separate forgings were purchased from inventory and heat treated eight years apart.

The Ti-6Al-4V beta STOA small crack $R = 0.1$ data is shown in Figure 6 along with large crack compact tension threshold test data. The small crack data shows considerable scatter, and faster crack propagation rates than the large crack data. The material sources for the large and small crack specimens were a UH-60 main rotor retention spindle forging, and a large H-53 elastomeric main rotor hub forging, respectively.

The Ti-6Al-4V alpha-beta $R = 0.1$ small crack data is shown in Figure 7, along with large crack compact tension threshold test data. As with the 4340 steel the Ti-6Al-4V alpha-beta crack growth rate data shows little scatter, and excellent agreement between large and small cracks. The small crack data contains both annealed and solution heat treated and annealed forgings, and shows no difference in their crack growth rates. The large crack specimens were obtained from a large H-53 conventional main rotor hub forging, and the small crack specimens were obtained from smaller retention components (Table 1).

CONCLUSIONS

This test program has provided constant amplitude and spectrum crack propagation data for small surface cracks 0.005 to 0.020 inches in depth for five common helicopter forged materials. The test specimens were obtained from helicopter part forgings, and the materials were checked against Sikorsky material conformance specifications. The tests were conducted at stresses well below the yield stress to be representative of stresses in helicopter parts.

Preliminary analysis of the constant amplitude test data indicates that the 4340 steel and Ti-6Al-4V alpha-beta data show little crack growth rate data scatter when using the ASTM secant method to calculate da/dN . These materials also showed good agreement with large crack compact tension threshold test data. The Al7075-T73 and Ti-6Al-4V beta STOA materials show considerable data scatter when using the ASTM secant method to calculate da/dN . The aluminum data showed erratic behavior possibly due to interaction with the EDM notch. The Ti-6Al-4V beta STOA data tended to show faster crack propagation rates than that from large crack compact tension specimens.

Further data analysis needs to be performed to evaluate the constant amplitude $R = 0.5$ and spectrum data, and to compare this with other Air Force funded test program data for helicopter materials. These other test programs include the compact tension data referenced in this paper, and some notched specimen corner crack data for initial crack radii between 0.015 and 0.030 inches. Other methods for crack growth rate calculations should be evaluated, such as the modified polynomial regression technique (refs. 4 and 5).

Further testing is recommended to obtain naturally initiated crack propagation data to avoid possible interaction with the EDM starter notch, and to perform tests at $R = -1$. It is also recommended that tests be performed at lower stress intensities to determine if 0.005 inch deep cracks will grow below the large crack threshold.

Performing tests at lower stress intensities and at $R = -1$ for 0.005 to 0.020 inch deep cracks is a difficult problem. A load shedding test was performed for one of the constant amplitude $R = 0.1$ Al-7075-T73 specimens (specimen Al-16). In this test the loads were shed abruptly, and the data indicates that the crack propagated below the large crack threshold. The crack growth rates (da/dN) calculated by the secant method showed considerable data scatter.

ACKNOWLEDGEMENTS

The work in this report was funded by the U.S. Air Force under contract no. F09603-89-G-0096-0014 to Sikorsky Aircraft with Mr. Gary Chamberlain of Warner Robins ALC as the program manager. This support is gratefully acknowledged. Thanks are also due to L. H. Favrow for directing the test program, R.I. Holland for performing the tests, P. Inguanti for material conformance evaluations, R.J. Haas for assistance in selection and design of the optical/video system, and M. Winter and J. Wegge for development of computer image processing.

REFERENCES

1. Edwards, P.R. and Newman J.C. Jr., Short-Crack Growth Behavior in Various Aircraft Materials, AGARD Report No. 767, August 1990.
2. Newman, J.C., Jr, and Edwards, P.R., Short-Crack Growth Behavior in an Aluminum Alloy -An AGARD Cooperative Test Programme, AGARD Report No. 732, December 1988.
3. Iyyer, N.S. and Dowling, E., Fatigue Growth and Closure of Short Cracks, AFWAL-TR-89-3008, June 1989. (VPI)
4. Larsen, J.M., The Effects of Slip Character and Crack Closure on the Growth of Small Fatigue Cracks in Titanium-Aluminum Alloys, WRDC-TR-89-4094, February 1990.
5. Larsen, J.M., et. al., Measurement of Small Cracks by Photomicroscopy: Experiments and Analysis, ASTM STP 1149, 1992.
6. Hudak, S.J.Jr., and Bucci, R.J., Fatigue Crack Growth Measurement and Data Analysis, ASTM STP 738, 1979.

Table 1. Materials For Small Cracks Program

Material	Source	Part Number/Quantity
Al7075-T73 Die Forging	SH-60 STA 295 Side Fuselage Frame	70209-222054-002 1
Steel 4340 (150 ksi) Die Forging	H-53 Main Rotor Horizontal Hinge Pin	65103-11020-006 2
Ti-6Al-4V Beta STOA Die Forging	H-53 Main Rotor Elastomeric Hub	65103-11501-103 1
Ti-6Al-4V Alpha-Beta Die Forging, Annealed	H-53 Main Rotor Hub	65102-11541-002 2
Ti-6Al-4V Alpha-Beta Die Forging, Solution Heat Treated and Annealed	S-76 Main Rotor Spindle/Cuff	65102-11541-002 1

Table 2. Material Properties

Material	Ultimate (ksi)	Yield (ksi)
Al7075-T73 Die Forging	66	54
Steel 4340 (150 ksi) Die Forging	150	132
Ti-6Al-4V Beta STOA Die Forging	133	145
Ti-6Al-4V Alpha-Beta Die Forging, Annealed	139	129
Ti-6Al-4V Alpha-Beta Die Forging, Solution Heat Treated and Annealed	155	147

Table 3. Fatigue Stresses and Threshold Stress Intensity Factor

Material	R Ratio	Fatigue Vibratory Stress (ksi) for Initiation in 0.5 to 1.0 x 10 ⁶	ΔK (ksi ($\sqrt{\text{in}}$))			Large Crack ΔK_{th} (ksi ($\sqrt{\text{in}}$))
			$a = .005$ in	$a = .01$ in	$a = .02$ in	
Al7075-T73 Forged	-1	29-34	5.1-6.0	7.2-8.4	10.1-11.9	
	0.0	20-22	3.5-3.9	5.0-5.5	7.0-7.7	2.5-3.5
	0.5	13-14	2.3-2.5	3.2-3.5	4.6-4.9	1.5-2.2
Steel 4340 (150 ksi) Forged	-1	70-74	12.3-13.0	17.3-18.3	24.6-26.0	
	0.0	58-60	10.2-10.5	14.4-14.9	20.4-21.0	4-7
	0.5	35-36	6.1-6.3	8.7-8.9	12.2-12.6	3-4
Ti-6Al-4V Beta STOA Forged	-1	80-85	14.0-14.9	19.8-21.1	28.0-29.8	
	0.0	55-59	9.7-10.4	13.6-14.6	19.3-20.7	4.6
	0.5	34-35	6.0-6.1	8.4-8.7	11.9-12.3	2.5-4.0
Ti-6Al-4V Alpha-Beta Forged	-1	40-60	7.0-10.5	9.9-14.9	14.0-21.0	
	0.0	30-50	5.3-8.7	7.4-12.4	10.5-17.5	3-4
	0.5	20-30	3.5-5.3	5.0-7.4	7.0-10.5	2-3

$$\Delta K = 0.7(2Sv)\sqrt{\pi a}$$

Table 4. Small Crack Constant Amplitude Test Summary

Material	Specimen Number	R	Max Stress (ksi)	Vibratory Stress (ksi)	EDM Notch (in)	Half Crack Length Range (c/2, inches)	Delta K Range (ksi(in)**0.5)
Al7075-T73 Forged	A1-3	0.1	45	20.25	0.0095	.0048-.0169	3.5-6.5
	A1-16	0.1	45	20.25	0.005	.0025-.0056	2.5-3.8
	A1-2	0.1	30	13.5	0.0075	.0045-.0229	2.2-5.1
	A1-R6	0.5	24	6	0.0085	.0056-.220	1.1-2.2
	A1-M7	0.5	24	6	0.00875	.0048-.0217	1.0-2.2
Steel 4340 (150 ksi) Forged	S1-2	0.1	70	31.5	0.0077	.0042-.0211	5.1-11.3
	S1-3	0.1	70	31.5	0.0068	.0047-.0217	5.3-11.5
	S1-1	0.5	86	21.5	0.006	.0050-.0224	3.0-6.5
	S3-1	0.5	66	16.5	0.0075	.0061-.0218	3.1-6.0
Ti-6Al-4V Beta STOA Forged	T-13	0.1	80	36	0.0093	.0054-.0183	6.5-12.1
	Ti-4	0.1	67.5	30.4	0.009	.0053-.0218	5.5-11.1
	Ti-6	0.1	70	31.5	0.0084	.0049-.0229	5.4-11.8
	T-20	0.5	80	20	0.0085	.0068-.0238	4.1-7.7
	T-21	0.5	75	18.75	0.0085	.0049-.0226	3.3-7.0
Ti-6Al-4 Alpha-Beta Forged Annealed	1-1038-2A	0.1	45	20.25	0.0085	.0075-.0225	4.3-7.5
	1-1013-1	0.1	50	22.5	0.00985	.0058-.0206	4.2-8.0
	1-1038-5A	0.5	52.5	13.13	0.00875	.0075-.0205	2.8-4.7
	1-1013-3A	0.5	50	12.5	0.008	.0067-.0210	2.5-4.5
Ti-6Al-4V Alpha-Beta Forged Solution Heat Treated & Annealed	1-1037-1	0.1	50	22.5	0.008	.0068-.0228	4.5-8.4
	1-1037-4	0.1	65	29.25	0.0071	.0044-.0230	4.8-11.0
	1-037-5	0.5	60	15	0.008	.0051-.0201	2.6-5.3
	1-037-9	0.5	50	12.5	0.0085	.0065-.0210	2.5-4.5

Table 5. Small Crack Spectrum Test Summary

Material	Specimen Number	Crack Initiation			Crack Propagation		
		EDM Notch (in)	Max Stress (ksi)	R	Max Stress	Half Crack Length Range (c/2, inches)	Total Cycles
Al7075-T73 Forged	Al-M6	0.0078	24	-1	53	.0044-.0204	340179
Steel 4340 (150 ksi) Forged	S1-5	0.0055	70	-1	106	.0049-.020	515424
Ti-6Al-4V Alpha-Beta Forged	T1-12	0.0085	70	-1	106	.0054-.0219	53019
Ti-6Al-4V Alpha-Beta Forged Annealed	1-1013-6	0.0099	55	-1	92	.0055-.0214	220896
Ti-6Al-4V Alpha-Beta Forged Solution Heat Treated and Annealed	1-037-7	0.00685	57.5	-1	92	.0049-.0203	533832

ELASTIC-PLASTIC MODELS FOR MULTI-SITE DAMAGE ¹

Ricardo L. Actis
Engineering Software Research and Development, Inc.
St. Louis, MO

Barna A. Szabó
Center for Computational Mechanics
Washington University, St. Louis, MO

SUMMARY

This paper presents recent developments in advanced analysis methods for the computation of stress intensity factors and the J-integral under conditions of small scale yielding in structural panels with multi-site damage. The method of solution is based on the p-version of the finite element method. Its implementation was designed to permit extraction of linear stress intensity factors using a superconvergent extraction method (known as the contour integral method) and evaluation of the J-integral following an elastic-plastic analysis. Coarse meshes are adequate for obtaining accurate results supported by p-convergence data. The elastic-plastic analysis is based on the deformation theory of plasticity and the von Mises yield criterion.

The model problem consists of an aluminum plate with six equally spaced holes and a crack emanating from each hole. The cracks are of different sizes. The panel is subjected to a remote tensile load. Experimental results are available for the panel. The plasticity analysis provided the same limit load as the experimentally determined load. The results of elastic-plastic analysis were compared with the results of linear elastic analysis in an effort to evaluate how plastic zone sizes influence the crack growth rates. The onset of net-section yielding was determined also. The results show that crack growth rate is accelerated by the presence of adjacent damage, and the critical crack size is shorter when the effects of plasticity are taken into consideration. This work also addresses the effects of alternative stress-strain laws: The elastic-ideally-plastic material model is compared against the Ramberg-Osgood model.

INTRODUCTION

Reliable stress intensity factor computation of cracked structural components is of major importance in modern design of aircraft structures where requirements for residual strength and fatigue crack propagation must be met. In this paper the problem of computing the stress intensity factors for a structural panel with multi-site damage, with guarantee of reliability, is discussed. This work focuses on the accuracy and reliability of the numerical solution of a proposed mathematical model and on the influence that different modeling assumptions may have on the results of the analysis. Two kinds of error are important in this case:

1. The differences between the exact solution of the mathematical problem formulated to represent a physical system or process and its numerical approximation are called errors of discretization. Is it possible to guarantee that the error of discretization is small?

1. Work supported by NASA Lyndon B. Johnson Space Center under Grant NAG 9-622.

2. The differences between the exact solution of the mathematical problem formulated to represent a physical system and the actual response or behavior of the physical system are called errors of idealization or modeling errors. How does incorporating plasticity in the analysis affect the stress intensity factors?

In some cases the two errors, the errors of discretization and modeling, may partially cancel one another. Therefore it is important to verify by means other than the experiment itself, that the numerical solution is close to the exact solution of the model. Only then is it possible to investigate whether the errors of idealization are large or small by making comparisons with experimental observations. The efficient and reliable control of numerical errors, achieved by the use of a superconvergent method for the computation of the stress intensity factors, makes it feasible to investigate the sensitivity of crack extension to alternative modeling decisions.

In this paper, the effect of plasticity on the values of the fracture mechanics parameters is investigated. First, the finite element implementation is discussed; and second the method is illustrated with the integrity assessment of a row of fastener holes with multi-site damage, for which experimental results are available.

FINITE ELEMENT IMPLEMENTATION

Choice of an Extension Process

In the finite element method the control of the errors of discretization can be achieved by mesh refinement (h-extension), by increasing the polynomial degree of elements (p-extension), or a combination of both (hp-extension).

The size of a finite element is the diameter of the smallest circle (or sphere) that contains the element. This diameter is denoted by h and the diameter of the largest finite element in the mesh is denoted by h_{max} . h-Extension involves letting $h_{max} \rightarrow 0$. Alternatively, we can hold the number of elements constant and increase the polynomial degree of elements. The polynomial degree of elements is a vector p . p-Extension involves letting the smallest polynomial degree $p_{min} \rightarrow \infty$. In hp-extensions mesh refinement is combined with an increase of the polynomial degree of elements. In these processes the number of equations that has to be solved, the number of degrees of freedom, is progressively increased, hence the name 'extension'. Note that h- and p-extensions can be viewed as special cases of hp-extension, which is the general discretization strategy of the finite element method.

An important question is: "Which is the most efficient method of extension with respect to reducing discretization errors?" This question can be answered on the basis of a simple classification of the exact solution of the problem one wishes to solve. The exact solutions (u_{EX}) have been classified into three main categories:

Category A: u_{EX} is analytic. A function is analytic at a point if it can be expanded into a Taylor series about that point on the entire solution domain, including the boundaries of the solution domain. Alternatively, the domain can be divided into subdomains and u_{EX} is analytic on each subdomain, including the boundary of each subdomain. The finite element mesh is so constructed that the boundaries of the subdomains are coincident with element boundaries.

Category B: u_{EX} is analytic on the entire domain, including the boundaries, with the exception of a finite number of points (in three dimensions u_{EX} needs not be analytic along a finite number of lines). The mesh is so constructed that the points where u_{EX} is not analytic are nodal points (in three dimensions the

Figure 4. da/dN For Al7075-T73 Forged, $R = 0.1$

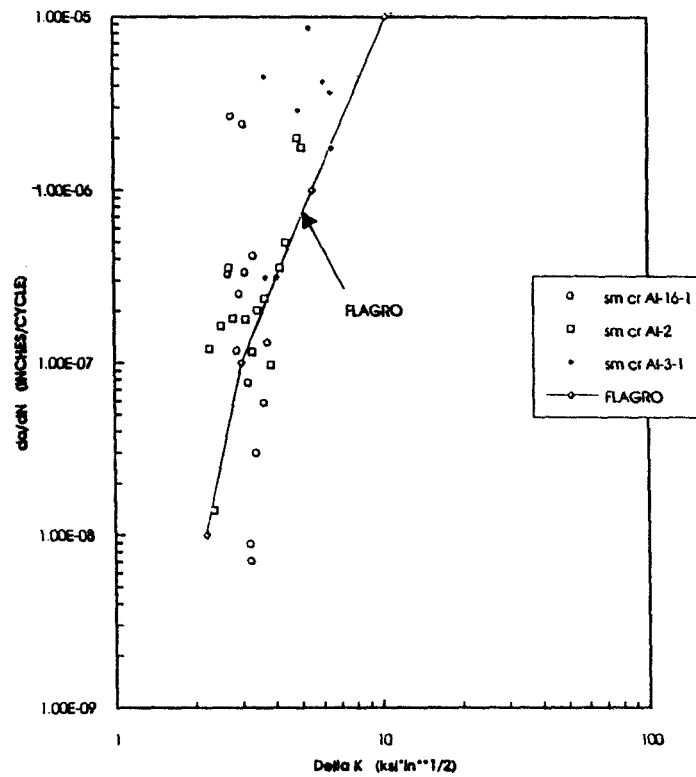


Figure 5. da/dN For 4340 (150 ksi) Steel Forged, $R = 0.1$

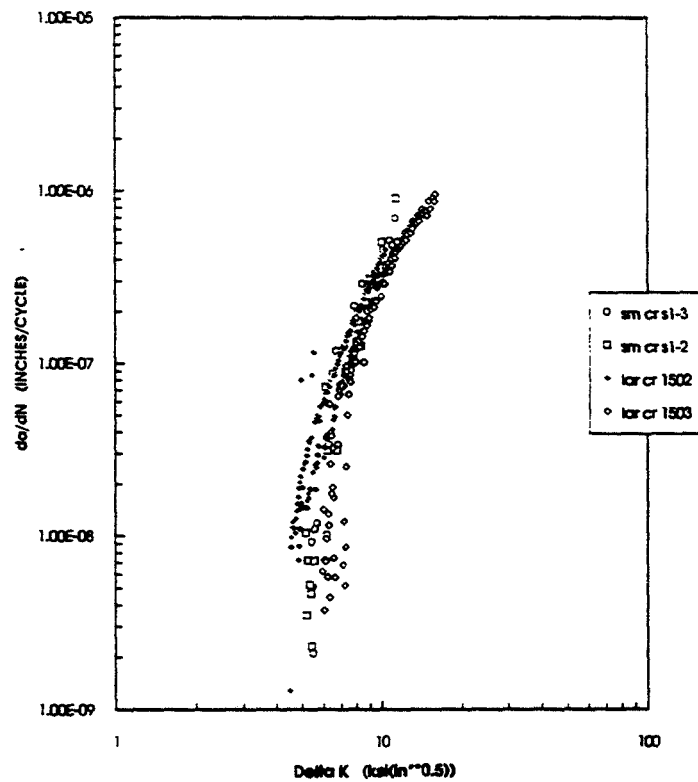


Figure 6. da/dN For Ti-6Al-4V Beta STOA Forged, $R = 0.1$

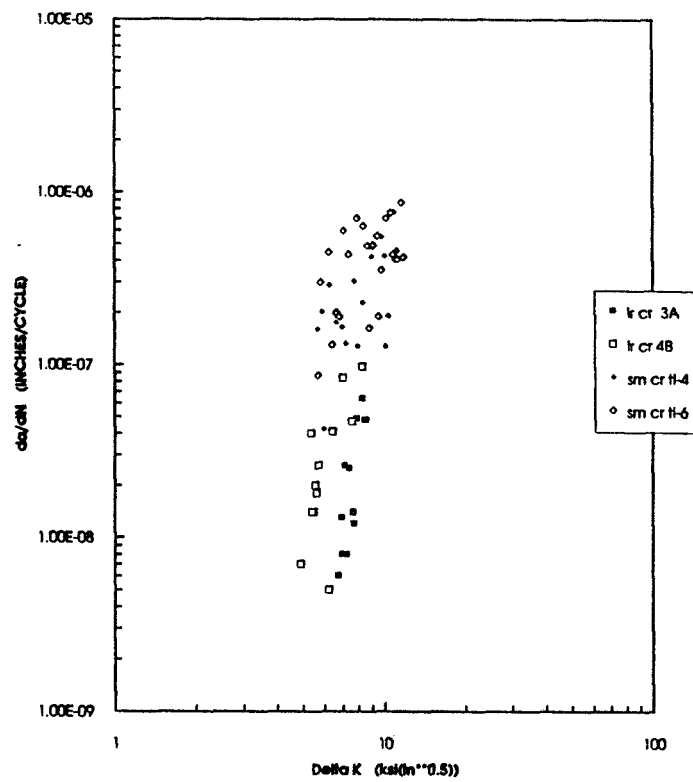
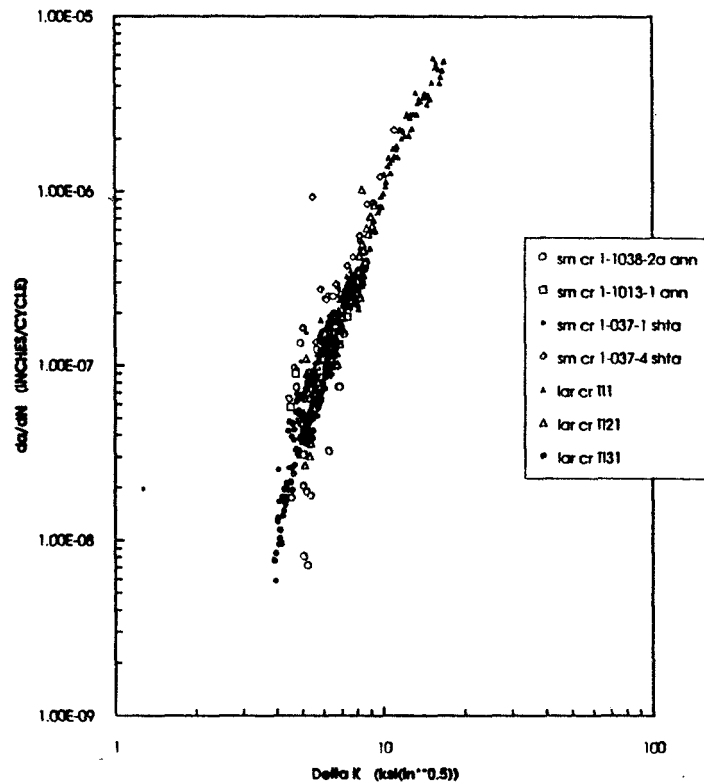


Figure 7. da/dN For Ti-6Al-4V Alpha-Beta Forged, $R = 0.1$



**BENDING EFFECTS OF UNSYMMETRIC ADHESIVELY BONDED
COMPOSITE REPAIRS ON CRACKED ALUMINUM PANELS**

348608

Cory Arendt and C.T. Sun
School of Aeronautics and Astronautics
Purdue University
West Lafayette, IN 47907

53-39

23097

p. 16

SUMMARY

The bending effects of unsymmetrically bonded composite repairs on cracked aluminum panels were quantified using a plate linear finite element model. Stress intensity factors and strain energy release rates were obtained from the model using the modified crack closure method. The bending effects were quantified by running the model twice, once with out-of-plane displacement suppressed and another time without these restrictions. Several configurations were examined. The effect of the thickness and strength of the adhesive and repair layer was determined, crack growth stability was identified, and the effect of a debond was considered. The maximum stress intensity factor was also analyzed. Previous work by other authors was found to underpredict the bending effect.

INTRODUCTION

In the late 1970's the Royal Australian Air Force developed a method to arrest fatigue and corrosion crack growth in their aircraft through the application of adhesively bonded composite repairs. Since then, many researchers have addressed the problem from a theoretical standpoint and developed methods to predict the stress intensity factors at the crack tip for various patch configurations. Tierang Liu and Weixun Fan[3], Poole, Brown, and Young[4], and Young, Cartwright, and Rooke[5] have used either finite element, boundary element, or numerical analysis to calculate the stress intensity factors using 2-D models without considering out-of-plane deformation. In the actual application of a repair to the fuselage or wing section of an aircraft, the repair can only be applied to the outer accessible side. Hence, the repair is applied unsymmetrically with respect to the loading axis. With the application of the unsymmetric repair, the neutral axis of loading has shifted outward from the cracked plate, resulting in localized bending of the repaired region. This localized bending leads to further opening of the crack face farthest from the repair. Because of this out-of-plane deformation, the 2-D solutions are no longer valid unless a bending correction factor is included. Jones, Callinan, and Aggrawal[6] developed their own finite element code based upon the shear stress profile of a symmetrically patched configuration. In their development, they acknowledged the bending effect and adjusted the shape functions to account for the single sided patched configurations. However, they made no attempt to actually account for the difference in stress intensity factors for unsymmetric and symmetric repair configurations.

Ratwani[1] was the first to address the bending effect from a strength of materials approach. He utilized the finite element code NASTRAN to calculate the stress intensity factor with a specialized crack

tip element. In the model, the plate and repair were composed of 2-D plate elements while the adhesive layer was composed of prismatic shear elements. As a result, the adhesive layer was not an elastic continuum, but rather a layer which only transferred shear loads. An elliptical debond between the cracked plate and the adhesive layer was introduced into the model. The repair and plate were considered to be of the same material and size. The results, which did not account for out-of-plane deformation, were then adjusted to correct for the bending effect. The difference between the load carried by the cracked layer and the load carried by the repaired layer resulted in a global moment. This moment was then applied to the entire structure and the increased stress due to bending was included in the stress intensity factor. Experiments were performed and the bending effect was found to have an average of 27% increase in the normalized stress intensity factor.

Rose[2] used a theoretical basis to develop a solution for a finite length patch configuration. In this he used shear lag analysis to calculate an effective adhesive load transfer length. The adhesive layer was removed and the crack extended an amount over which the shear load could not transfer. To simplify the theory, the repair was assumed to be of infinite length. From slender beam deflection theory, and equilibrium, Rose developed expressions for the deflection of the repair and unrepaired section in the out-of-plane direction. These deflections were transformed into moment expressions for the patched and unrepaired region. A total reaction moment at the crack location was calculated. By integrating the reaction moment over the thickness of the repair, the strain energy caused by bending was calculated. The total strain energy release rate was then obtained by superimposing the energy needed to close the crack in the in-plane direction with the strain energy needed to bend the structure back to its original position.

Ratwani and Rose's solution cannot be compared because they are derived for entirely different patch configurations. It is the object of this study to use a plate finite element model to accurately predict the 3-D bending effects. Comparisons between the results of the present model and both Ratwani's and Rose's work were made.

The effects of a debond, variations in adhesive and repair properties were investigated. Crack stability along with extrapolation of the maximum stress intensity factor from the average value finite element results were discussed.

PRESENT MODEL

Using the commercial finite element code ANSYS, a 2-D bonded repair model was created. The aluminum plate and repair were modeled using 4-noded shell elements with five degrees of freedom (u_x, u_y, u_z, θ_x , and θ_y) at each node. The adhesive layer was represented by shear springs in the x and y directions. Attempts were made to model the adhesive layer as an elastic continuum using 3-D, 8-noded brick elements. However, due to the adhesive layer's relatively small thickness, severe numerical errors were encountered. This occurred because the aspect ratios of these elements far from the crack tip grew to unreasonably high proportions. The plate and repair were modeled using rectangular elements. The nodes of each layer coincided identically in space with respect to the x and y directions as shown in Figure1. The spring elements used to model the adhesive layer were one dimensional. Only the two

shear springs at each node were included in the model. The spring constants were developed on the assumption that the adhesive layer would transfer only shear loads. The relation between the shear nodal forces and in-plane nodal displacements is given by:

$$\frac{F}{A} = \mu \frac{(u_{\text{Upper}} - u_{\text{Lower}})}{t_{\text{Adhesive}}} \quad (1)$$

where μ is the shear modulus of the adhesive and A is the area represented by the shear spring. These shear spring constants in the x and y directions were found to be a function of the element's area and were distributed evenly among the four nodes.

$$k_x, k_y = \frac{\mu A}{4t_{\text{Adhesive}}} \quad (2)$$

Since each element consists of a different area, the spring constants varied from node to node.

In order to connect the outer layers to the inner spring elements, constraint equations were imposed. These constraint equations provided continuity along the adhesive/plate interface and adhesive/repair interface. The equations related the rotational deformation and in-plane displacement of the shell elements to the displacement of the spring elements (see Figure 1). Four nodes existed in the z direction for each x - y coordinate. The outer two nodes were part of the plate and repair layers, while the 2 springs were connected to the inner two nodes. The constraint equations were implemented in the x , y , and z directions. For the x -direction:

$$u_{x2} = u_{x1} - \frac{t_{\text{Repair}}}{2} \theta_{y \text{ Repair}} \quad u_{x3} = u_{x4} + \frac{t_{\text{Plate}}}{2} \theta_{y \text{ Plate}} \quad (3)$$

y -direction:

$$u_{y2} = u_{y1} + \frac{t_{\text{Repair}}}{2} \theta_{x \text{ Repair}} \quad u_{y3} = u_{y4} - \frac{t_{\text{Plate}}}{2} \theta_{x \text{ Plate}} \quad (4)$$

z -direction:

$$u_{z2} = u_{z1} \quad u_{z3} = u_{z4} \quad (5)$$

STRAIN ENERGY RELEASE RATE CALCULATIONS

The modified crack closure method [7] was used to calculate the strain energy release rate. The crack closure method allows for the calculation of the strain energy release rate by calculating the strain energy at a single crack length. The crack size was increased a finite amount when the model was run a second time. The difference in strain energy between these two cases divided by the increase in crack length produced the desired strain energy release rate. Since this method was time consuming, the modified crack closure method was developed. It assumed that the strain energy release rate could be obtained in one run of the model if the widths of the two crack tip elements were identical and the ratio of the width of the crack tip element to the length of the crack, itself, was less than 10%. In this model crack opening was considered to be Mode I. Without the out-of-plane bending effect, the crack growth was entirely Mode I. However, when out-of-plane deformation did occur, the crack opening increased on the side furthest from the repair. This caused the crack face to rotate, allowing the crack to open even more. Thus, for out-of-plane deformation, two strain energy release rates had to be calculated: One to

close the crack tip in terms of the displacement and a second to rotate the crack face back to its original position.

The strain energy release rate due to translational displacement was calculated by:

$$G_{lu} = \frac{1}{2\Delta a} \{F_{yA} (u_{yB} - u_{yC})\} \quad (6)$$

The strain energy release rate due to rotation was calculated by:

$$G_{lr} = \frac{1}{2\Delta a} \{M_{xA} (\theta_{xB} - \theta_{xC})\} \quad (7)$$

The total strain energy release rate is the sum of these two calculations. By calculating the total strain energy release rate for different mesh configurations, convergence could be examined. Figures 2 and 3 demonstrated mesh convergence with respect to element size along the x and y directions. The converged mesh properties chosen for all models were $\Delta a / a = .075$ and $\Delta L = .005$.

MODEL VERIFICATION

In an effort to verify the constraint equations and spring constants, the model was altered to compare it to the results generated by Young [8]. In [8], center cracked plates were subjected to uniform bending moments. A single plate finite element model was used to calculate the normalized strain energy release rate. In the present study, a similar finite element mesh was created using ANSYS. Verification of the constraints came about by removing the adhesive layer in the spring model and comparing the results of this two plate model to a single plate. The adhesive layer in the spring model was removed because the shear springs were not designed to undertake large scale bending deformation. The two plate configuration was tied together solely by constraint equations and gave identical results to the single plate solution. The difference between Young's results [8] and the single and double plate configurations differed by less than .5% (see Figure 4).

The spring constants were verified by checking if the spring model would converge to the two plate configuration. Figure 5 demonstrates how the spring model successfully converged to the two plate solution.

COMPARISONS

Comparison to Ratwani's [1] finite element results was performed. Ratwani experimented with several different repair configurations, but only one model considered the bending effect. The center cracked aluminum plate under axial tension was repaired with an aluminum patch. The repair was the same size as the plate. Utilizing symmetry, only a quadrant of the plate was modeled. An elliptical debond between the plate and the adhesive layer existed in order to facilitate the use of the specialized crack tip element.

The present model was built to the same specifications as in Ratwani's work. The model was then run twice for each crack length, once with the following boundary conditions for having no out-of-plane deformation :

$$\begin{aligned}
 @x = 0 & \quad u_x = 0 \quad \theta_y = 0 \\
 @y = 0, x > a, z = \frac{t_{\text{Plate}}}{2} & \quad u_y = 0 \quad \theta_x = 0 \\
 @y = 0, z \neq \frac{t_{\text{Plate}}}{2} & \quad u_y = 0 \quad \theta_x = 0 \\
 @ \text{all nodes} & \quad u_z = 0
 \end{aligned} \tag{8}$$

In the second run the constraints in the z direction at all the nodes except for the one at the origin of the plate were released. An elliptical debond with semi-minor to semi-major axis ratio of $b/a = .10$ was included (see Figure 1). The semi-major axis coincided with the crack length a . The debond was simulated by removing the constraints between the plate and adhesive layer. The results are presented in Figure 6.

With no consideration for bending, the present model underpredicted Ratwani's results, that also did not include bending, by an average of 6% over a set of five crack lengths. This discrepancy could be accounted for by the difference in convergence directions. Ratwani's use of the specialized crack tip element resulted in convergence from above the actual value. The modified crack closure method, on the other hand, reached a converged solution from below the actual value. Once Ratwani's results were corrected for bending and compared to the present model, which was allowed to displace in the out-of-plane direction, the present model overpredicted Ratwani's results by more than 11.5%. Ratwani's results also showed that the bending effect could increase the normalized stress intensity factor by over 27%, while the present model demonstrated a 52% increase. Thus on average, Ratwani underpredicted the present model's bending effect by about 25%.

Rose [2] developed an analytical expression to calculate the value of the strain energy release rate for a patched configuration undergoing out-of-plane deformation. Rose developed his solution based upon a patch of a finite length instead of a full length patch. His expression was a function of all the thicknesses and material properties involved. In order to make a valid comparison of Rose's expression, the present model was run for several different cases to find possible regimes where the theory broke down. Figure 7 demonstrated how the two models compared when examining the trends in the adhesive layer. Both accurately predicted the increasing trend in total strain energy release rate as the adhesive thickness increased and adhesive shear modulus decreased. The average difference between all three cases resulted in the present model overpredicting the total strain energy release rate by 176%. A similar test was run for the variation in repair properties (see Figures 8a and 8b). In this case, the present model results showed a definite decreasing trend as the repair stiffness increased. Rose's model, in this case, did not provide a consistent trend indicating that his model was not able to predict expected values in all regimes.

CRACK STABILITY

Rose's model was based upon a prediction that the strain energy release rate would reach a limiting value as the crack grew. Because of this limiting value, a characteristic crack length could be calculated. This limitation was based upon the maximum displacement allowed by the cracked surface derived in the shear lag analysis. This derivation was performed for the case when bending was suppressed. However, when calculating the increase in strain energy release rate due to bending, this assumption remained true. Therefore, Rose assumed a characteristic crack length would also exist when bending was introduced. When the models that accounted for bending were run for various crack lengths, the strain energy release rate failed to reach a limit (see Figure 9). The values for the spring model increased, while Rose's model was not affected by the variation in crack length. In the case where bending was suppressed for the present model, it was demonstrated that the strain energy release rate remained constant. Thus, it was proven that Rose's application of the shear lag analysis was correct in the case where bending was suppressed, but not applicable in the case when bending did exist.

An increase in the strain energy release rate indicated crack growth instability. This result was viewed with skepticism. In order to determine the validity of this finding, the patch was removed and the model was re-run. Figure 10 demonstrated the increasing rate of instability of the single plate. With this plot, the boron repair configuration with out-of-plane bending was also found to be relatively stable on this new scale. Therefore, it could be concluded that unsymmetric patch configurations may possess crack growth instability. However, comparison of this instability for the unsymmetric patch configuration to the instability for a single plate was found to be relatively minor.

DEBOND EFFECTS

The effects of the debond size were next considered. Following Ratwani's experimental finding [1] that the elliptical debond begins at the crack tip, different elliptical debond sizes were considered. Having fixed a semi-major axis of the ellipse as the crack length a , the semi-minor axis b was varied. It can be seen in Figure 11 that a change in the debond's elliptical shape produced a negligible increase in the strain energy release rate for a certain crack length. When the effect of the inclusion of a debond was considered, the effect was much more pronounced. Figure 12 depicted the difference in a boron repair model with and without a debond and with and without bending. When bending was not considered, the inclusion of a debond increased the strain energy release rate by an average of 200%. In a similar manner, the debond for the case where bending was included increased the strain energy release rate by 88%.

MAXIMUM STRESS INTENSITY FACTOR

The total strain energy release rate calculated from the finite element model was based upon the displacement and rotation at the mid-plane of the crack plate. When bending occurred, the crack opening

increased on the side furthest from the repair. This caused the crack face to rotate, allowing the crack to open further. The amount of energy gone into opening the crack face in the in-plane direction was 97%, while the remaining 3% went into rotating the crack face. From the finite element results, the rotation seen by the mid-plane node was less than a fraction of a degree. From these results, it was concluded that the rotation of the crack face was minor. Therefore, the variation in the strain energy release rate through the thickness of the plate varied a negligible amount. This also indicated that the bending effect does not deform the local crack tip region in the out-of-plane direction. Instead, the bending effect is a global phenomenon. Thus, plane stress relationships held near the crack tip. From plane stress fracture mechanics, the stress intensity factor was obtained from:

$$K = \sqrt{\frac{G_{\text{Total}} E_{\text{Plate}}}{t_{\text{Plate}}}} \quad (9)$$

The variation in the stress intensity factor through the thickness is negligible.

When the normalized stress intensity factor was plotted against the crack growth of a boron repair configuration, the values decreased (see Figure 13). In terms of the normalized stress intensity factor, the effect of bending on a model without a debond was an increase of 520%, while a model with a debond experienced a 400% increase.

CONCLUSIONS

This paper has presented a successful development of a plate finite element model which can be used to predict the bending effects of a bonded composite repair configuration. Constraint equations and shear springs were incorporated into the model to accurately represent the out-of-plane deformation that occurs in unsymmetric patch configurations. The modified crack closure method produced results within 6% of Ratwani's in-plane deformation results obtained through the use of special crack tip elements.

The following conclusions were obtained:

- Ratwani's model underpredicted the present models results by 25% in terms of the normalized stress intensity factor.
- Rose's analytical solution underpredicted the total strain energy release rate for several adhesive thicknesses by an average of 176%.
- For the repair variation analysis, Rose's theory produced an inconsistent trend.
- The total strain energy release rate increased as the adhesive thickness increased and shear modulus decreased.
- The total strain energy release rate decreased as the stiffness of the repair increased.
- Crack growth instability occurred for the unsymmetric repair. However, it was relatively stable as compared to the instability of an unrepaired crack.
- A debond increased the total strain energy release rate by 200% when no bending occurred, and 88% when bending was present.
- The variation of stress intensity factor over the thickness of the cracked plate is negligible.

REFERENCES

1. Ratwani, M.M.: Characterization of Fatigue Crack Growth in Bonded Structures. AFFDL-TR-77-31 Volume II, June 1977, pp.55-64.
2. Baker, A.A.; and Jones, R.: Bonded Repair of Aircraft Structures. Martinus Nijhoff Publishers, 1988, pp. 77-98.
3. Liu, Tierang; and Fan, Weixun.: Analysis for an Adhesively Bonded Finite Strip Repair to a Cracked Plate. *Engineering Fracture Mechanics*. vol.47, no. 5, pp. 629-637.
4. Poole, P.; Brown, K.; and Young, A.: Adhesively Bonded Composite Patch Repair of Thick Sections. *Fatigue and Fracture Mechanics*. 1988.
5. Young, A.; Cartwright, D.J.; and Rooke, D.P.: The Boundary Element Method for Analysing Repair Patches on Cracked Finite Sheets. *The Aeronautical Journal of the Royal Aeronautical Society*, December 1988.
6. Jones, R.; Callinan, R.J.; and Aggrawal, K.C.: *Analysis of Bonded Repairs to Damaged Fibre Composite Structures*. *Engineering Fracture Mechanics*. vol.17, no.1, pp.37-46.
7. Rybicki, E.F.; Kanninen, E.F.: A Finite Element Calculation of Stress Intensity Factors by a Modified Crack Closure Integral, *Engineering Fracture Mechanics*, 1977 vol.9 pp.931-938.
8. Young, Min Jho: Analysis of Cracked Plates Subjected to Out-of-Plane Loadings, Ph. D. Thesis, Purdue University, 1991.

ACKNOWLEDGMENT

This work was supported by the Air Force Office of Scientific Research through a University Research Initiative Grant No. NTP1397 to Purdue University.

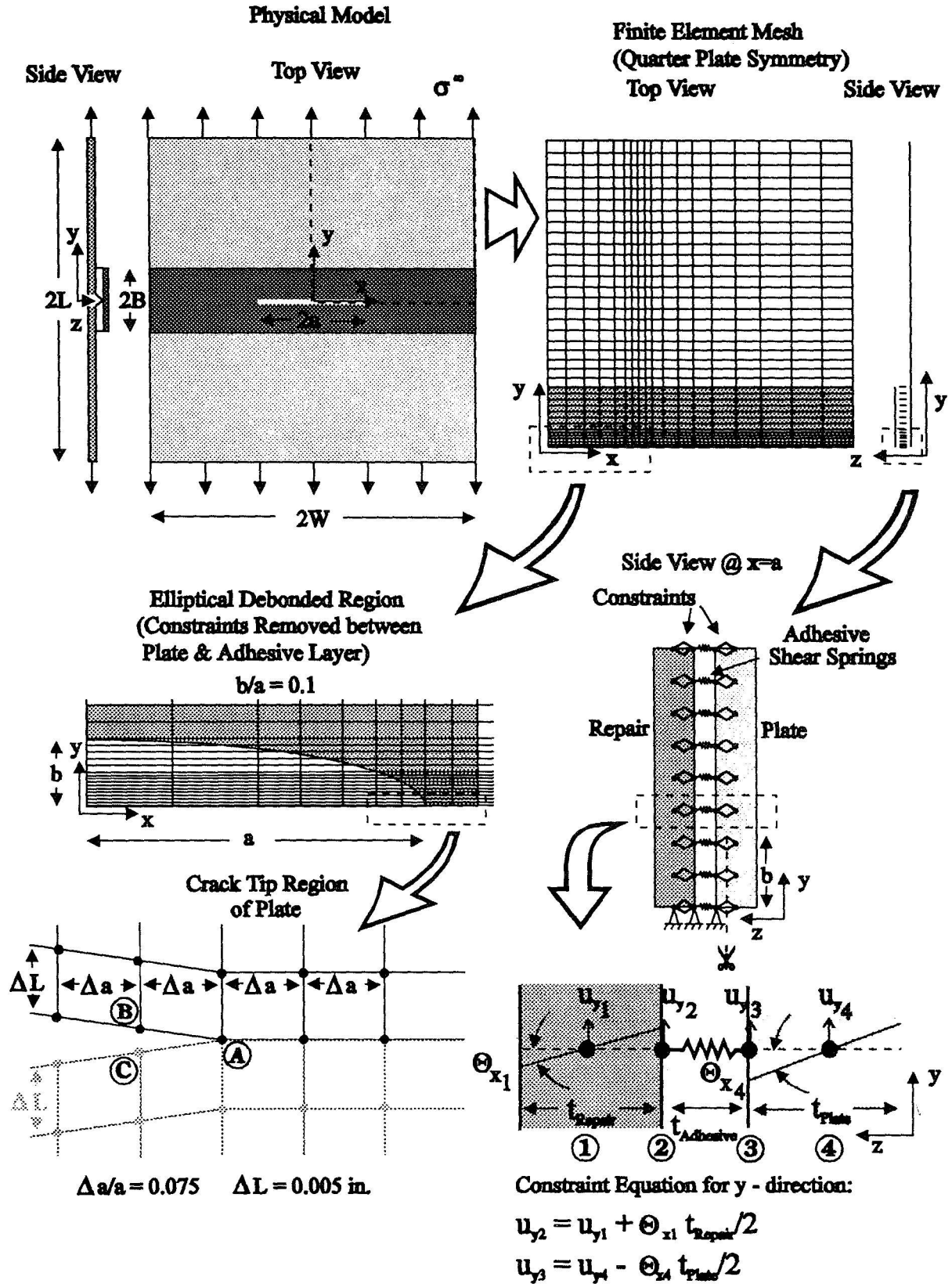


Figure 1. Finite Element Model for the Adhesively Bonded Repair of Cracked Aluminum Plates.

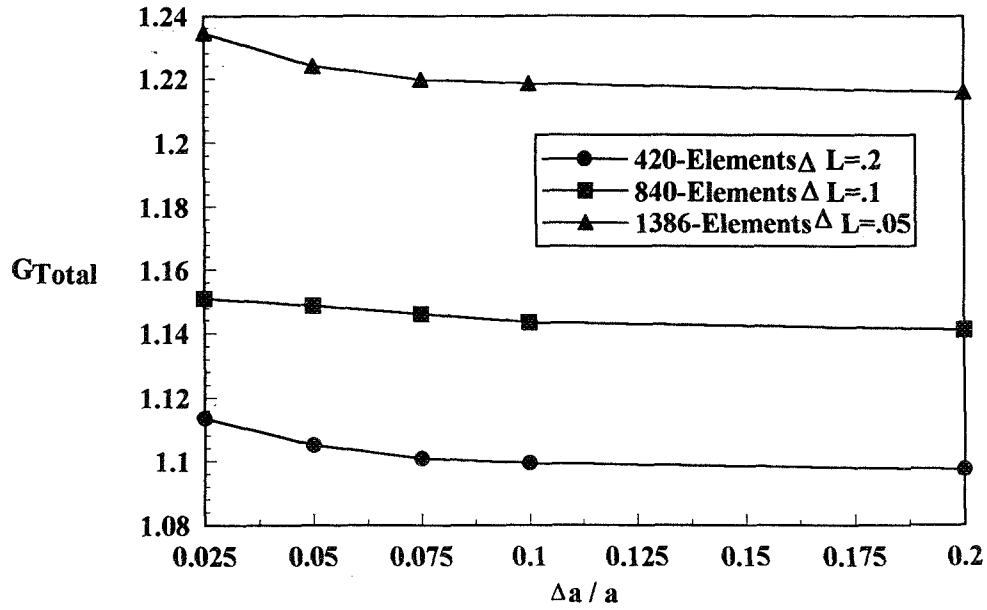


Figure 2

Mesh Convergence with respect to element size along x-axis.

$E_{\text{Re pair}} = 10.3 \times 10^6 \text{ psi}$. $E_{\text{Plate}} = 10.3 \times 10^6 \text{ psi}$. $\mu_{\text{Adhesive}} = 3.872 \times 10^6 \text{ psi}$.

$t_{\text{Re pair}} = .1181 \text{ in}$. $t_{\text{Plate}} = .1181 \text{ in}$. $t_{\text{Adhesive}} = .009 \text{ in}$. $\sigma^\infty = 16935 \text{ psi}$. $\nu = .33$

$L = 10 \text{ in}$. $W = 10 \text{ in}$. $B = 2.0 \text{ in}$. $a = 3.0 \text{ in}$.

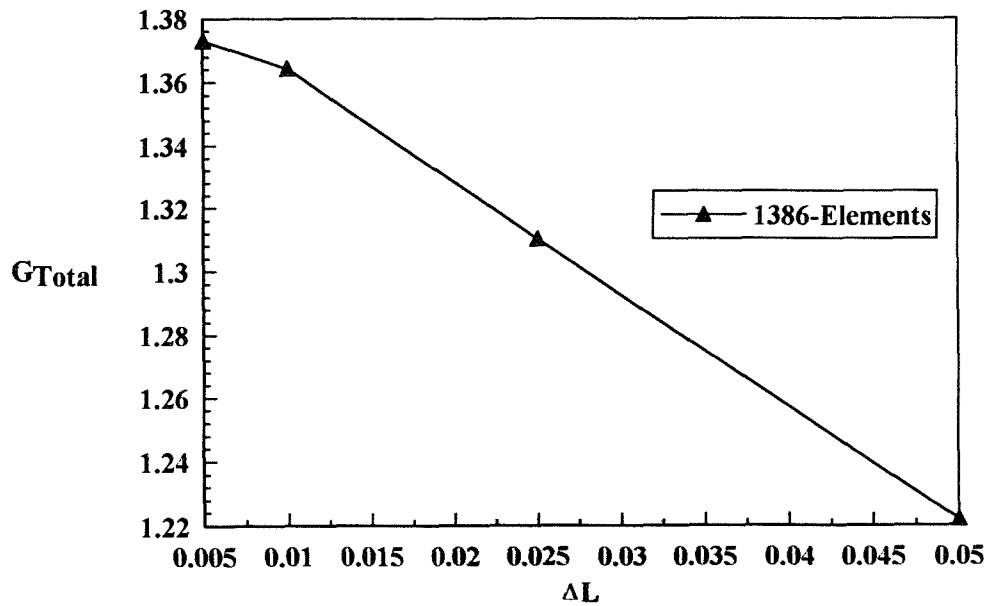


Figure 3

Mesh convergence with respect to element size along y-axis.

$\Delta a / a = .075$.

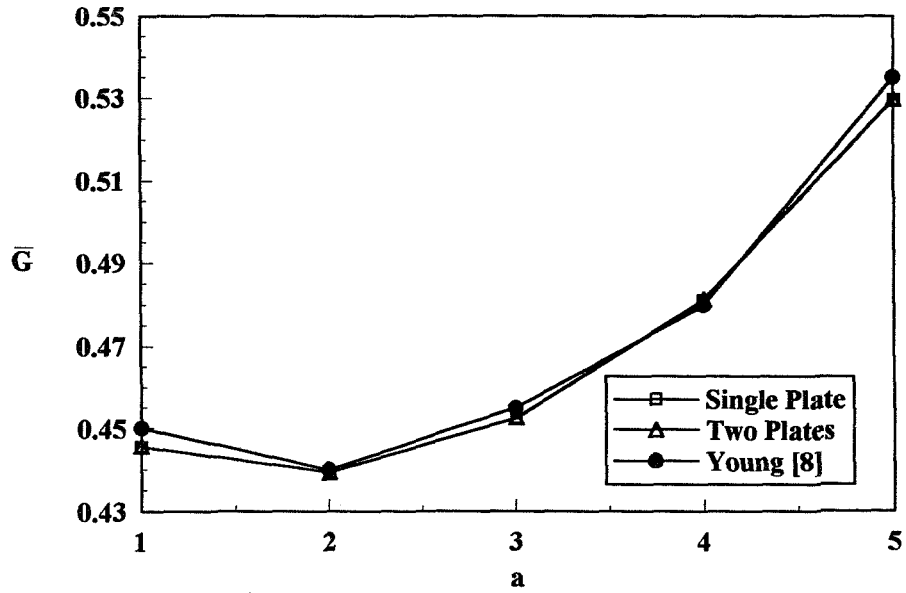


Figure 4 Comparison of normalized $\bar{G} = G_{Total} E h^3 / 12 M^2 a \pi$ for a center cracked plate subjected to uniform bending moment. $\Delta a / a = .10$
 $E = 3.0 \times 10^6$ psi. $h = .3$ in. $M = 1500$ in.lb. $L = 10.0$ in. $W = 10.0$ in.

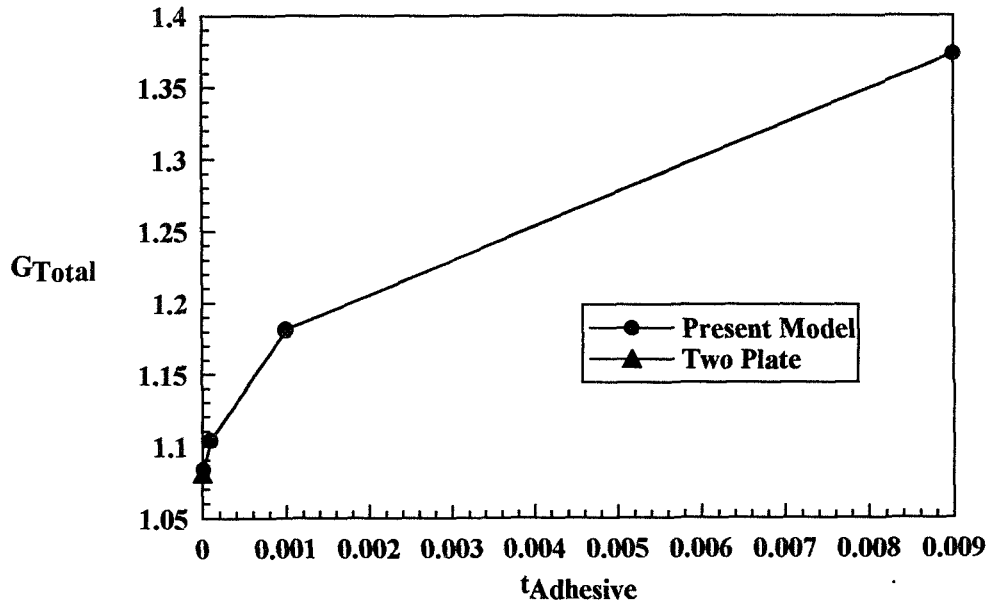


Figure 5 Convergence of Present Model to Two Plate Solution.
 $E_{Repair} = 10.3 \times 10^6$ psi. $E_{Plate} = 10.3 \times 10^6$ psi. $\mu_{Adhesive} = 3.872 \times 10^6$ psi.
 $t_{Repair} = .1181$ in. $t_{Plate} = .1181$ in. $\sigma^\infty = 16935$ psi. $\nu = .33$
 $L = 10$ in. $W = 10$ in. $B = 2.0$ in. $a = 3.0$ in.

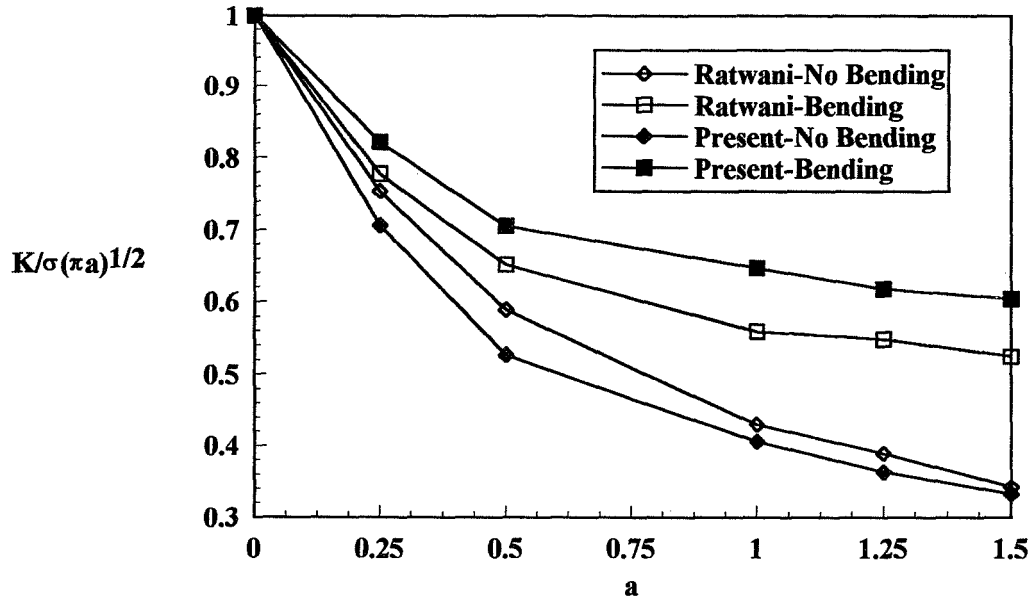


Figure 6

Comparison to Ratwani's Bending Correction Factor.

$E_{\text{Repair}} = 10.3 \times 10^6$ psi. $E_{\text{Plate}} = 10.3 \times 10^6$ psi. $\mu_{\text{Adhesive}} = 6.0 \times 10^4$ psi.
 $t_{\text{Repair}} = .063$ in. $t_{\text{Plate}} = .063$ in. $t_{\text{Adhesive}} = .008$ in. $\sigma^\infty = 16935$ psi. $\nu = .33$
 $L = 6$ in. $W = 3$ in. $B = 6$ in. Elliptical Debond $b/a = .10$

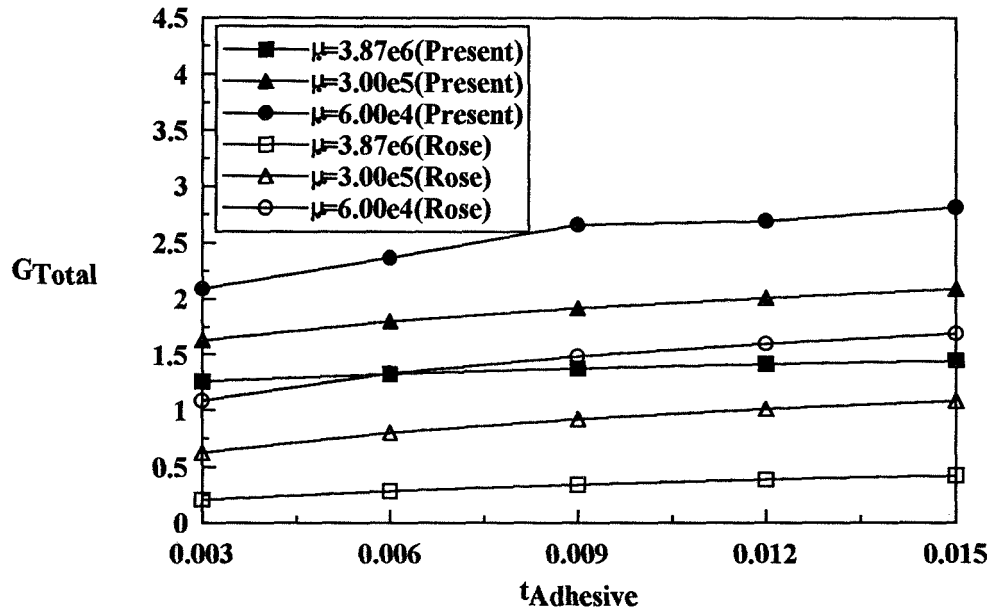


Figure 7

Comparison to Rose's Analytical Solution for variations in adhesive thickness and adhesive shear modulus.

$E_{\text{Repair}} = 10.3 \times 10^6$ psi. $E_{\text{Plate}} = 10.3 \times 10^6$ psi.
 $t_{\text{Repair}} = .1181$ in. $t_{\text{Plate}} = .1181$ in. $\sigma^\infty = 16935$ psi. $\nu = .33$
 $L = 10$ in. $W = 10$ in. $B = 2.0$ in. $a = 3.0$ in.

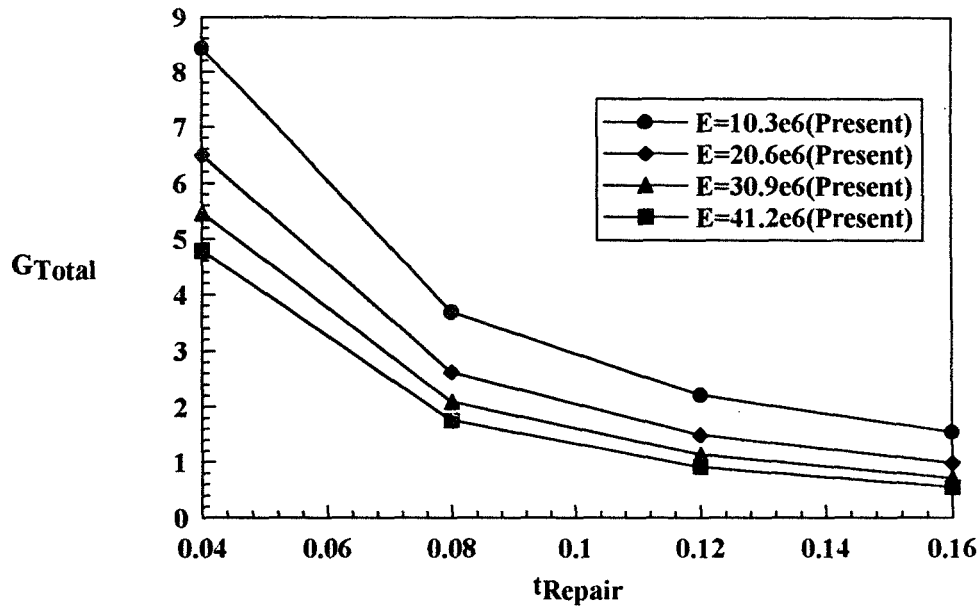


Figure 8a Present solution for variations in repair thickness and repair modulus.

$E_{Plate} = 10.3 \times 10^6$ psi. $\mu_{Adhesive} = 1.015 \times 10^5$ psi
 $t_{Plate} = .1181$ in. $t_{Adhesive} = .008$ in. $\sigma^{\infty} = 16935$ psi. $\nu = .33$
 $L = 10$ in. $W = 10$ in. $B = 2.0$ in. $a = 3.0$ in.

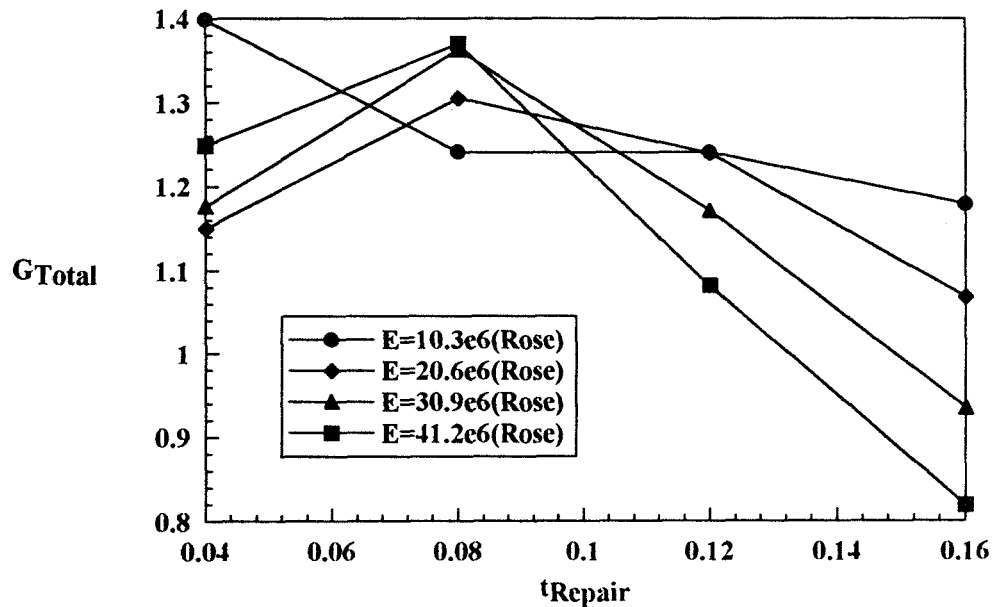


Figure 8b Rose's analytical solution for variations in repair thickness and repair modulus.

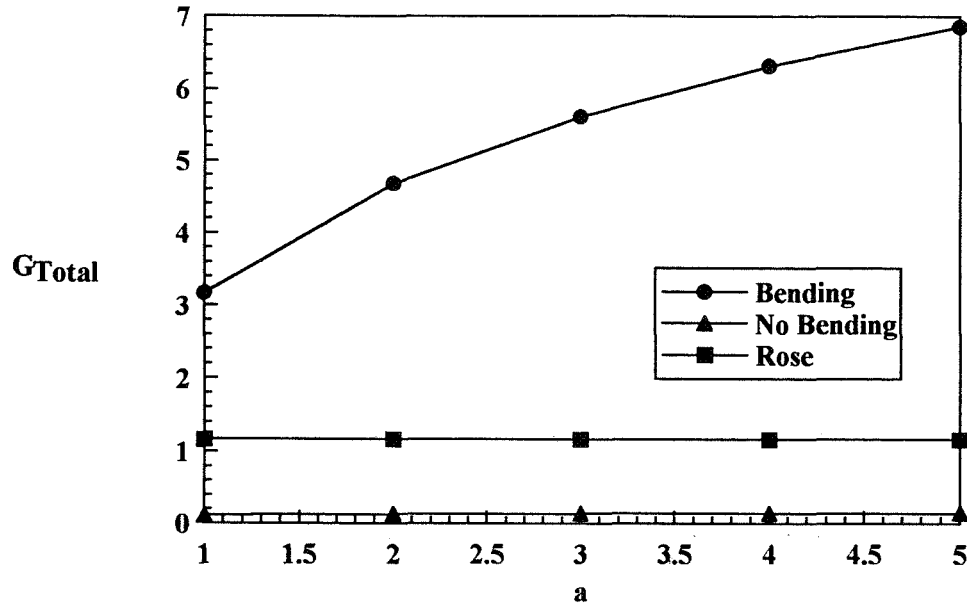


Figure 9

Crack Trend for Boron Repair Scheme.

$E_{\text{Repair}} = 29.0 \times 10^6 \text{ psi}$, $E_{\text{Plate}} = 10.3 \times 10^6 \text{ psi}$, $\mu_{\text{Adhesive}} = 1.015 \times 10^5 \text{ psi}$
 $t_{\text{Repair}} = .04 \text{ in.}$, $t_{\text{Plate}} = .1181 \text{ in.}$, $t_{\text{Adhesive}} = .008 \text{ in.}$, $\sigma^\infty = 16935 \text{ psi}$, $\nu = .33$
 $L = 10 \text{ in.}$, $W = 10 \text{ in.}$, $B = 2.0 \text{ in.}$

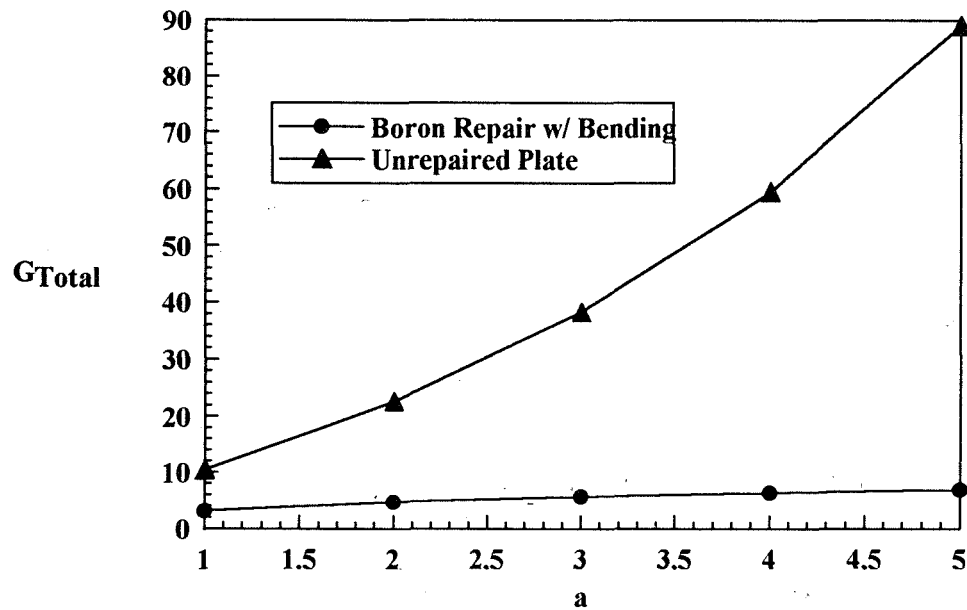


Figure 10

Crack Stability for various crack lengths.

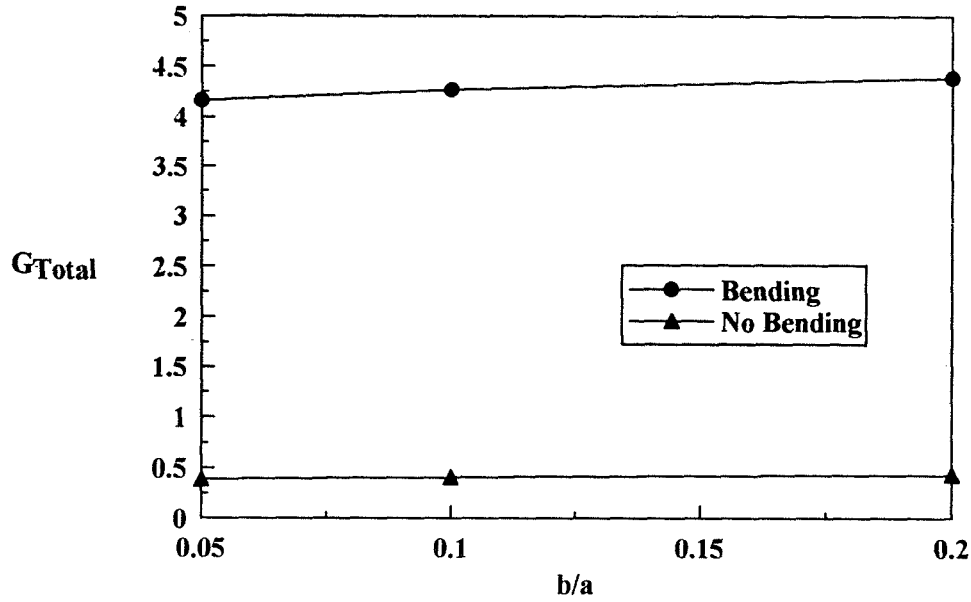


Figure 11

Comparison of elliptical debonds of various aspect ratios.

$E_{\text{Repair}} = 29.0 \times 10^6 \text{ psi}$. $E_{\text{Plate}} = 10.3 \times 10^6 \text{ psi}$. $\mu_{\text{Adhesive}} = 1.015 \times 10^5 \text{ psi}$
 $t_{\text{Repair}} = .04 \text{ in.}$ $t_{\text{Plate}} = .1181 \text{ in.}$ $t_{\text{Adhesive}} = .008 \text{ in.}$ $\sigma^\infty = 16935 \text{ psi}$. $\nu = .33$
 $L = 10 \text{ in.}$ $W = 10 \text{ in.}$ $B = 2.0 \text{ in.}$ $a = 1.0 \text{ in.}$

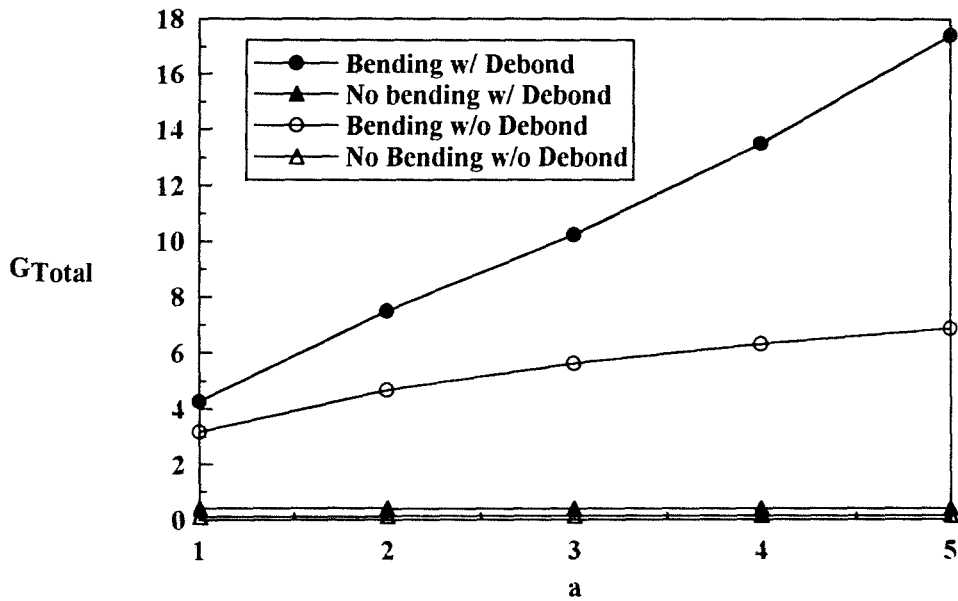


Figure 12

Crack Growth for boron repair scheme with elliptical debond. $b/a = .10$

$E_{\text{Repair}} = 29.0 \times 10^6 \text{ psi}$. $E_{\text{Plate}} = 10.3 \times 10^6 \text{ psi}$. $\mu_{\text{Adhesive}} = 1.015 \times 10^5 \text{ psi}$
 $t_{\text{Repair}} = .04 \text{ in.}$ $t_{\text{Plate}} = .1181 \text{ in.}$ $t_{\text{Adhesive}} = .008 \text{ in.}$ $\sigma^\infty = 16935 \text{ psi}$. $\nu = .33$
 $L = 10 \text{ in.}$ $W = 10 \text{ in.}$ $B = 2.0 \text{ in.}$

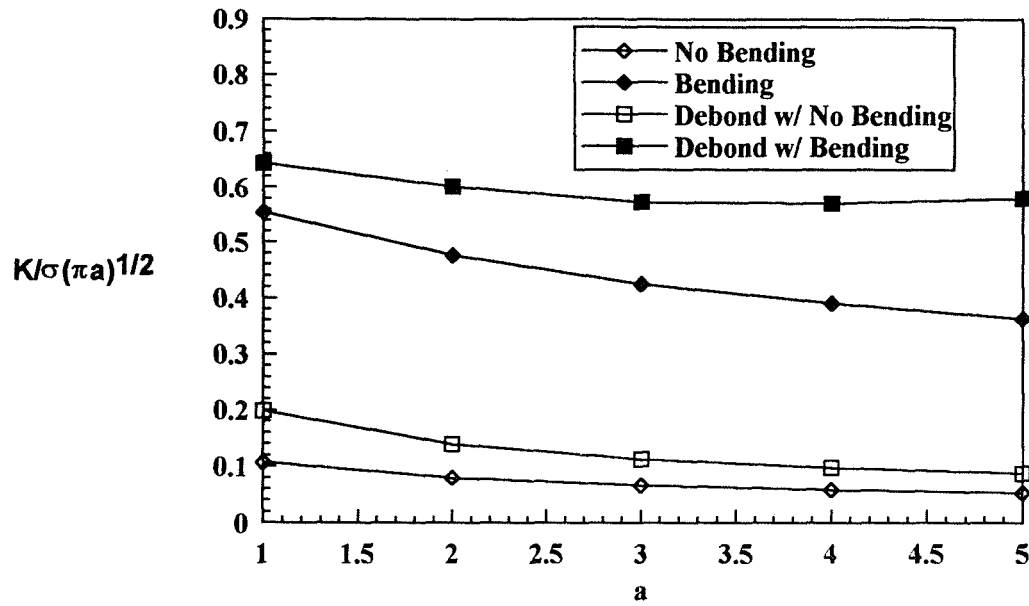


Figure 13 Crack growth trend for a boron repair scheme. Debond $b/a = .10$
 $E_{\text{Repair}} = 29.0 \times 10^6$ psi. $E_{\text{Plate}} = 10.3 \times 10^6$ psi. $\mu_{\text{Adhesive}} = 1.015 \times 10^5$ psi
 $t_{\text{Repair}} = .04$ in. $t_{\text{Plate}} = .1181$ in. $t_{\text{Adhesive}} = .008$ in. $\sigma^\infty = 16935$ psi. $\nu = .33$
 $L = 10$ in. $W = 10$ in. $B = 2.0$ in.

1995108043

N95- 14457

**EVALUATION OF BONDED BORON/EPOXY DOUBLERS FOR COMMERCIAL
AIRCRAFT ALUMINUM STRUCTURES**

348612

54-39

2-3098

p. 12

Bruce Belason, Textron Specialty Materials

Paul Rutherford and Matthew Miller, The Boeing Company

Shreeram Raj, Integrated Technologies

ABSTRACT

An 18 month laboratory test and stress analysis program was conducted to evaluate bonded boron/epoxy doublers for repairing cracks on aluminum aircraft structures. The objective was to obtain a core body of substantiating data which will support approval for use on commercial transports of a technology that is being widely used by the military. The data showed that the doublers had excellent performance.

DISCUSSION

About 2000 bonded boron/epoxy doublers have been successfully flying on U.S. and Australian aircraft since the mid-1970s, with another 2000 being installed by the U.S. Air Force in 1993-1994 on the C141 fleet (wing weep-hole riser cracks). The advantages include reduced installation cost and increased fatigue life, as well as other performance benefits.

There are also about 50 boron/epoxy doublers successfully flying for ~~evaluation~~ on U.S. and Australian commercial aircraft, including 25 on 2 Federal Express 747s since early 1993 (these are demonstration "decal" doublers on undamaged structure -- see Chart #2 for locations).

To help accelerate the transition of the bonded boron/epoxy doubler technology to commercial aircraft, Textron Specialty Materials sponsored a program to obtain a core body of test data which was projected to be required by the FAA and its international counterparts for approval for commercial aircraft applications. This program was conducted by the Boeing Company. The mechanical properties and performance tests were performed at Integrated Technologies (Intec).

This paper presents a synopsis of the results. There were four basic efforts in the program, as summarized in Chart #3 and described below.

- 1) Materials Specification. Materials properties data were obtained on three lots of 225°F cure boron/epoxy (designated #5521 by Textron) to support an existing Aerospace Materials Society specification (AMS # 3867/4A). Chart #4 summarizes the tests conducted.
- 2) Doubler Installation Process Specification. A doubler installation specification was written which included surface preparation (degrease, abrade, phosphoric acid anodize, and prime); adhesive; boron ply lay up and cure; and inspection (ultrasonic) including reference standards. Existing Boeing specifications for all procedures and materials (other than boron) were used (e.g., BMS 5-101 for 180°F performance structural adhesive; BMS 5-89 for primer; etc.). Chart #5 summarizes the process. It is available in written form and a training video has also been made and is available.

The effects of various deviations from the doubler curing process (pressure, temperature, heat-up rate) and primer cure rate were evaluated on bond strength (lap shear). The results are summarized in Chart #6. The doubler cure process is quite robust in that relatively large variations from the baseline process do not significantly affect the lap shear bond strength. Note: based on these tests, 15" Hg (vacuum bag) cure was established as the baseline cure pressure.

- 3) Finite Element Analyses (FEA). 2-D and 3-D linear elastic FEA were conducted to support the performance test program (see Item #4 below). Key items investigated were the stresses in the bondline, the aluminum, and the boron/epoxy for three loads and two structural boundary conditions. The three loads were (1) thermal load due to the differential coefficients of thermal expansion (CTE) and the 225°F cure, (2) 15 ksi applied tensile load, and (3) combined thermal and tensile load. The two structural boundary conditions were for the doubler edge ending near-to (1.3") and far-from (4.3") an underlying stringer. Chart #7 presents a summary of the results.

The key observation is that the shear and peel stresses in the adhesive due to the thermal load are of about the same value, but act in the opposite direction, to those stresses from the 15 ksi applied tensile load. A possible important implication of this is that a higher adhesive stress exists when the aircraft is on the ground vs in flight (for tensile-loaded structures), which could lead to increased inspection confidence of the bond. More sophisticated analyses (e.g., elastic-plastic using temperature-varying adhesive properties) are recommended to investigate this point further.

Another key observation was that the peak axial stress concentrations in the aluminum and boron/epoxy were both lower for the combined load than for the 15 ksi applied tensile load. Thus, again, the residual thermal stresses have a beneficial effect.

- 4) Performance Tests (Laboratory). This was the largest effort of the program. It consisted of 110 static ultimate tension and 143 tension fatigue tests of boron/epoxy doublers bonded to 7075-T6 aluminum sheet (i.e., a relatively brittle aluminum) which had a 0.5" long sawcut (to simulate a crack) with a 0.25" diameter stop-drill. Chart #8 defines the test protocol. In general the specimens were fabricated per the installation specification of Item #2 above.

The tests were very successful and the results are summarized in Charts #9 through #11. The boron/epoxy doublers restored the static ultimate strength of the aluminum (80 ksi A/B statistical minimum value). Failure was almost always in the aluminum outside the doubler.

The fatigue tests were conducted at 3 ksi to 20 ksi (sine wave) at 5Hz, with 300,000 cycles being considered runout. (See Chart #8 for rationale for this condition which is considered a relatively severe "envelope" condition). Runout was successfully achieved with no crack re-initiation for the baseline boron/epoxy doubler geometry as long as the stop-drill was defect-free (e.g., no burrs). For reference, control specimens with no doubler (but with the stop-drilled 0.5" long sawcut) failed at 3100 cycles (average) -- thus more than a factor of 100X lower life. Post-fatigue static ultimate tension tests on the baseline configuration showed no degradation in static strength.

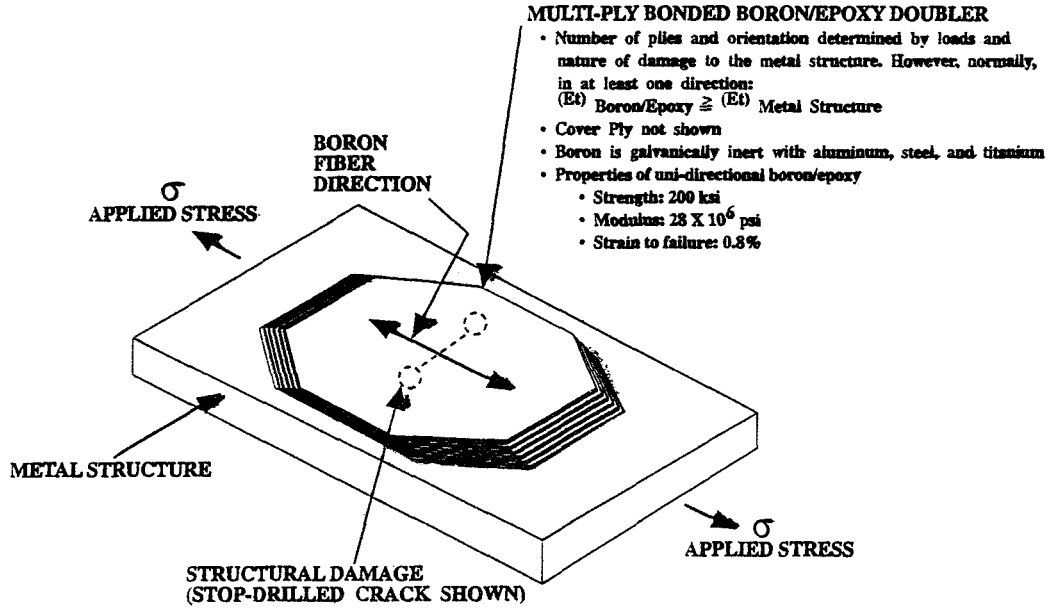
The effects of a number of variables and conditions on fatigue life were also evaluated. For many of these variables, the effect was negligible (i.e., no crack re-initiation after 300,000 cycles). These variables included: doubler geometry and ply lay up; 1.0 inch long crack; thinner aluminum; impact of 100 and 300 inch lbs. in line with the crack just beyond the stop drill; 1 month at 185°F - 85% humidity hot wet environment; 1 week immersion at 120°F in Skydrol; 1 Hz (sine and square wave) and Spectrum (with no compression) fatigue cycles; cure pressure (5 inch to 28 inch of Hg vacuum); and the presence of 0.5" diameter (deliberate) voids at the edge of the bondline and over the stop-drilled hole.

Variables which did result in crack re-initiation (but not necessarily crack propagation across the width of the specimen) included too few plies; no stop-drill; -65°F and cycle hot-cold (a 3 to 18 ksi stress cycle may eliminate crack initiation at these conditions); and 0 to 18 ksi load with no lateral restraint. Chart #11 summarizes the results. For those conditions where the crack re-initiated (from the stop-drilled hole), the crack grew at a linear reproducible rate, independent of crack length, and the boron/epoxy doubler carried the full load and had a post-fatigue (runout) static ultimate strength greater than 80 ksi for 96% of the specimens for which the crack did not emerge from under the doubler. In no case did the boron/epoxy doubler globally debond prior to the crack propagating the full width of the aluminum -- and most times, not even then, despite high twist loads (Ref Chart #8: the aluminum was 4 inches wide, the boron doubler was about 3 inches wide). In fact, 4 specimens with intact boron doublers on fully-cracked aluminum had a residual static ultimate strength of over 40 ksi (based on the original cross-sectional area of the aluminum). -- See Chart #10.

The overall conclusion of the test program is that viable materials and installation specifications have been written; the laboratory test data shows excellent performance; and the FEA help understand the interaction of the residual thermal stresses with the applied loads. This data should be very useful in supporting commercial aircraft applications of bonded boron/epoxy doublers. This laboratory data has also been successfully supported in flight evaluation of 25 "decal"* doublers on two Federal Express 747s (see chart #2). These doublers were installed in early 1993 and had over 700 flights as of late February 1994 and have performed excellently.

*The term "decal" means the doublers were applied to undamaged structure. The doublers, however, do carry about half the load in the primary load-carrying direction.

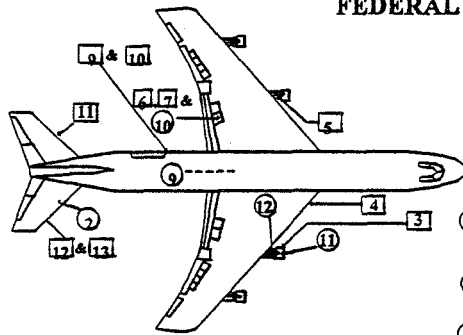
BONDED BORON/EPOXY DOUBLERS FOR REINFORCEMENT OF METALLIC AIRCRAFT STRUCTURES



- THERE ARE ABOUT 4000 BORON/EPOXY DOUBLERS FLYING ON MILITARY AIRCRAFT AND 50 ON COMMERCIAL AIRCRAFT

CHART #1

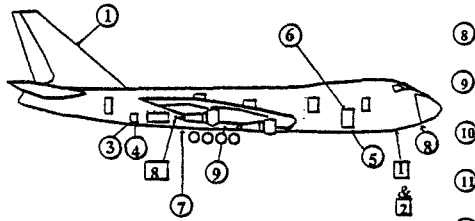
LOCATION OF 25 BONDED BORON/EPOXY "DECAL" DOUBLERS ON 2 FEDERAL EXPRESS 747-200s



("Decal" Means The Doubler Is On Undamaged Structure, The Doubler Does Carry - 1/2 The Load In The Principal Stress Direction)

Aircraft: Fed Ex. #N639FE
Line Number 354
Installation Date:
Jan. 8-12, 1993

Aircraft: Fed Ex. #N631FE
Line Number 406
Installation Date:
March 1-5, 1993



FLIGHT STATUS

- Planes Are In Daily Service - 700 Flights As Of February 1994
- Doublers Are Performing Excellently

Vertical Stabilizer, Lower Forward Leading Edge, RH Side

Horizontal Stabilizer, RH Side Of Leading Edge

Bulk Cargo Door Cut-out, Aft Side & Bottom

Lower Cargo Door Cut-out, Bottom & Forward Side

Fuselage Belly Skin (6:00 Position)

Nose Wheelwell Cutout, Forward Edge

Main Landing Gear Wheelwell Canted Bulkhead Web

Wing-Mid Flap, Upper Skin

Nacelle, Engine #3, Thrust Reverser Translating Sleeve

Pylon, Engine #3, Inboard Side

1 & 2

Fuselage Belly Skin (6:00 Position) AFT of Nose Wheelwell

3

Nose Cowling Inlet Lip Skin (8:00 Position)

4

R/H Wing Leading Edge, Upper Airfoil Surface

5

No. 2 Engine Pylon, Inboard Skin Structure

6 & 7

L/H Inboard Wing Mid-Flap, Upper Skin

8

R/H Aft Fuselage Skin (3:30 Position)

9 & 10

Main Cargo Door Cut-out, Forward Side

11

L/H Horizontal Stabilizer Leading Edge

12 & 13

R/H Horizontal Stabilizer Leading Edge

CHART #2

LABORATORY TEST PROGRAM ON BONDED BORON/EPOXY DOUBLERS

OVERVIEW

- CONDUCTED BY THE BOEING COMPANY
- FUNDED BY TEXTRON SPECIALTY MATERIALS
- PERFORMANCE PERIOD: OCTOBER '92 THROUGH JULY '94

OBJECTIVE

- OBTAIN THE CORE BODY OF SUBSTANTIATING DATA REQUIRED FOR FAA APPROVAL

KEY EFFORTS

1) MATERIALS SPECIFICATION TESTS (AMS SPEC. #3867/4A)

- PHYSICAL
- MECHANICAL
- CHEMICAL
- BOND STRENGTH

2) INSTALLATION PROCESS SPECIFICATION

VIDEO &
WRITTEN
SPEC. AVAILABLE

- SURFACE PREPARATION
- ANODIZE (PAA)
- PRIMER
- ADHESIVE
- CURING PROCEDURE
- NDI PROCEDURES & REFERENCE STANDARDS
- SENSITIVITY EFFECTS OF PROCESS DEVIATIONS

3) PERFORMANCE TESTS

SEE CHARTS
#3, 4, 5 & 7

- 110 STATIC TENSION
- 143 TENSION-TENSION FATIGUE
- GOAL: 300,000 CYCLES EACH
- BORON/EPOXY DOUBLERS BONDED TO 7075-T6 ALUMINUM WITH PRE-INDUCED CRACKS

4) FEM STRUCTURAL DESIGN ANALYSIS/GUIDELINES FOR BONDED BORON DOUBLERS

SEE
CHART#6

- LOAD TRANSFER
- STRESS CONCENTRATIONS
- EFFECTS OF BOUNDARY CONDITIONS (e.g. UNDERLYING RIBS, ETC.)
- EFFECTS OF DIFFERENTIAL COEF. OF THERMAL EXPANSION (ALUMINUM VS. BORON/EPOXY)

CHART #3

PROPERTIES TESTS ON BORON/EPOXY TO VALIDATE AMS SPEC. #3867/4A

PHYSICAL ¹

- RESIN CONTENT
- VOLATILE CONTENT
- RESIN FLOW
- GEL TIME
- DENSITY
- POROSITY
- FLAMMABILITY

MECHANICAL ¹

- COMPRESSION
 - -67°F
 - ROOM TEMP.
 - 180°F WET
- SHORT BEAM SHEAR
 - -67°F
 - ROOM TEMP.
 - 180°F WET

CHEMICAL ¹

- INFRARED SPECTROSCOPY
- LIQUID CHROMATOGRAPHY
- FLUID RESISTANCE
 - JP-4
 - DEICER
 - CLEANER
 - MIL-H-83282
 - SKYDROL

TENSION

- -75°F
 - ROOM TEMP.
 - 180°F WET
 - SKYDROL IMMERSION
- } • 0° LAYUP
&
• 0° ± 45° LAYUP

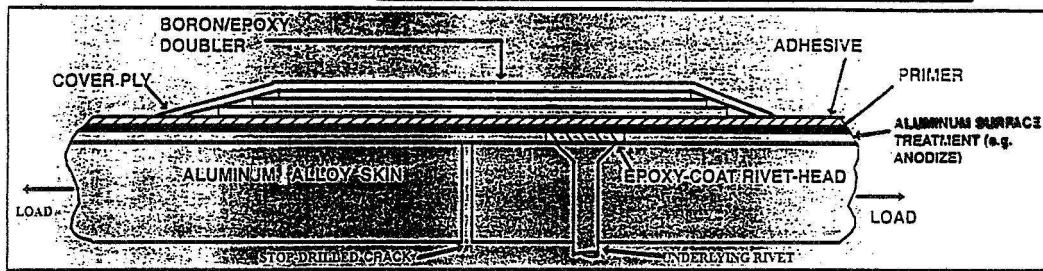
NOTE: 1) ALL TESTS WILL BE ON 3 BATCHES OF MATERIAL

TEXTRON Specialty Materials

CHART #4

Installation Process For Bonding Boron Epoxy Doublers Onto Aluminum

- Uses Existing Technology, Materials, Specifications, and Equipment
- Uses Experienced Composites Personnel
- To Assure Proper Adhesion Requires Process Control



1) TRIAL RUN

- LOCATE DOUBLER
- SOLVENT CLEAN
- CURING UNIT RUN:
 - MEASURE SUBSTRATE TEMPERATURE PROFILE
 - CHECK ABILITY TO PULL VACUUM

2) SURFACE PREPARATION

- CLEAN
- REMOVE PAINT
- ABRASE (WATER BREAK-FREE)
- EPOXY-COAT UNDERLYING RIVET HEADS
- ANODIZE
 - ACID ETCH } PORTABLE EQUIPMENT:
15 MINUTES } VACUUM BAG AND CONTAINERS,
• RINSE } AND ANODE (Ref. Charts #9 & 10)
 - POLARIZED LIGHT INSPECTION TEST
 - PRIME (AIR DRY)
 - COVER

3) DOUBLER INSTALLATION

- CUT AND LAY-UP BORON/PLIES } GENERALLY IS PREASSEMBLED
- PRE-CONSOLIDATE (IF THICK)
- APPLY ADHESIVE
- CO-CURE: BORON, ADHESIVE & PRIMER
 - RAMP TO 225°F @ 5°F/MIN
 - 90 MINUTES AT 225°F (107°C)
 - RAMP DOWN (~20 MINUTES)

4) INSPECT FOR BOND VOIDS AND DELAMINATIONS (ULTRASONIC & VISUAL)

5) SEAL AND PAINT TO OWNER'S SPECIFICATION

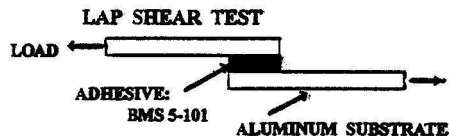
Written Specifications Exist For The Entire Process Shown. And All Materials

TEXTRON Specialty Materials

(Original figure unavailable at time of publication)

CHART #5

SENSITIVITY OF BOND STRENGTH TO VARIATIONS IN INSTALLATION PROCESS



BASELINE CURE CONDITION

- TEMPERATURE: 90 MINUTES @ 225°F
- HEAT-UP RATE: 5°F PER MINUTE
- CURE PRESSURE: 15" Hg (i.e. ~ HALF ATMOS. VACUUM)
- PRIMER CURE: AIR DRY

1) EFFECTS OF CURE PRESSURE

PRESSURE	BOND STRENGTH*
5" Hg	5190 PSI
10" Hg	5230 PSI
15" Hg	5730 PSI
15" Hg	5420 PSI
28" Hg	4100 PSI

(2 DATA SETS)

2) EFFECT OF CURE TEMP. & TIME (AT 28" Hg)

CONDITION	BOND STRENGTH*
90 MIN. @ 225°F	4100 PSI
90 MIN. @ 250°F	4230 PSI
180 MIN. @ 225°F	4390 PSI

*ALL VALUES SHOWN ARE THE AVERAGE OF 5 TESTS

3) EFFECTS OF CURE HEAT-UP RATE

HEAT-UP RATE	BOND STRENGTH*
5°F PER MINUTE	4230 PSI
1°F PER MINUTE	5140 PSI
10°F PER MINUTE	3960 PSI

4) EFFECTS OF PRIMER CURE RATE

PRIMER CURE COND.	BOND STRENGTH*
HEAT LAMP CURE	4230 PSI
<30 MIN. AIR DRY	3960 PSI
AIR DRY (15" Hg CURE)	5730 PSI
BOIL PRIMER WITH HOT AIRGUN	4990 PSI

5) EFFECTS OF BORON PLY INSERTED IN MIDDLE OF ADHESIVE (15" Hg CURE)

CONDITION	BOND STRENGTH*
NO BORON PLY	5730 PSI
WITH BORON PLY	5160 PSI

CONCLUSION: VERY ROBUST INSTALLATION PROCESS

CHART #6

ORIGINAL PAGE IS
OF POOR QUALITY

FINITE ELEMENT STRESS ANALYSES

OBJECTIVE

FIRST ORDER ESTIMATE OF CRITICAL STRESSES:

- IN BONDLINE
- IN ALUMINUM



DUE TO

- THERMAL LOAD (I.E., RESIDUAL CURE STRESSES DUE TO DIFFERENTIAL COEFFICIENTS OF THERMAL EXPANSION)
- APPLIED 15 KSI TENSILE LOAD
- COMBINED THERMAL + TENSILE LOADS

ANALYSES CONDUCTED

MODELS USED:

- 2-D: ANSYS + COSMOS M
- 3-D: NIKE

LINEAR ELASTIC

USED ROOM TEMPERATURE PROPERTIES

KEY CONCLUSIONS

- RESIDUAL THERMAL STRESSES ARE SIGNIFICANT
- HOWEVER, IN THE ADHESIVE, SHEAR AND PEEL STRESSES ACT IN OPPOSITE DIRECTIONS FOR THERMAL VS TENSILE LOADS, AND ARE OF SIMILAR MAGNITUDE. THUS:
 - ADHESIVE LOADS ARE LOWER FOR COMBINED LOAD (E.G., IN FLIGHT).
 - AN AS-APPLIED DOUBLER ON UNLOADED STRUCTURE HAS HIGH ADHESIVE STRESSES -- IMPLIES IN-SITU "PROOF TEST" OF SORTS . . . NEEDS MORE SOPHISTICATED ANALYSIS.
- MAXIMUM TENSILE STRESSES IN ALUMINUM AND BORON ARE LOWER FOR COMBINED LOAD THAN FOR 15 KSI TENSILE LOAD ONLY.

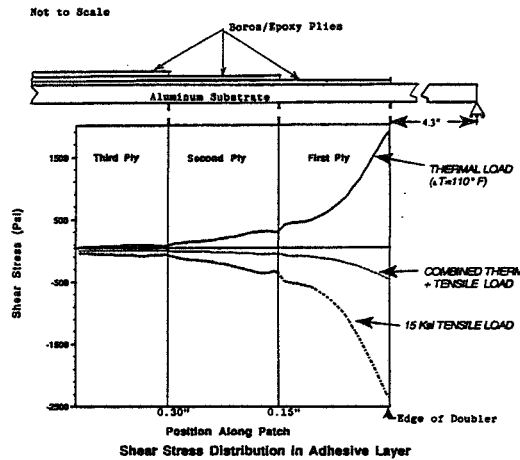
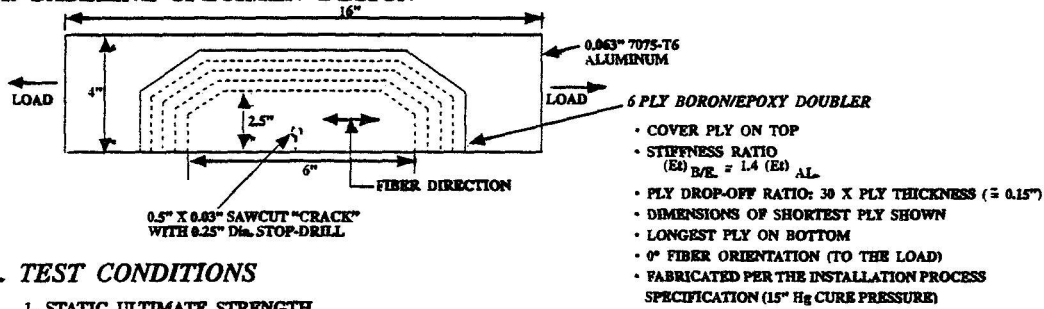


CHART #7

TEST PROTOCOL FOR PERFORMANCE TESTS

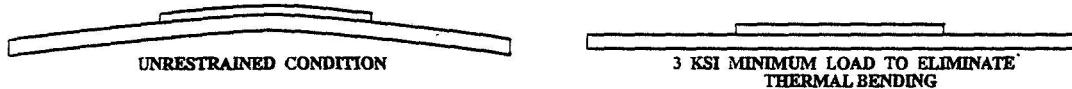
A. BASELINE SPECIMEN DESIGN



B. TEST CONDITIONS

1. STATIC ULTIMATE STRENGTH
 - GOAL: > 80 ksi: RESTORE A/B STATISTICAL MINIMUM FOR 7075-T6 ALUMINUM
 2. FATIGUE LIFE^①
 - 3 KSI TO 20 KSI @ 5 Hz
 - 300,000 CYCLES CONSIDERED RUNOUT
 - UNRESTRAINED SPECIMEN
- RELATIVELY CONSERVATIVE "ENVELOPE" CONDITION:
- HIGH CYCLE FATIGUE LIFE @ HIGH STRESS
 - RELATIVELY BRITTLE ALUMINUM

①. RATIONALE FOR FATIGUE TEST CONDITION



AIRCRAFT	AIRCRAFT DESIGN OBJECTIVE	COUPON TEST FATIGUE OBJECTIVE	DESIGN STRESS	ESTIMATED EQUIVALENT DESIGN STRESS
737	75,000 CYCLES	300,000 CYCLES	0 TO 15 ksi	3 TO 17 ksi
747	20,000 CYCLES	80,000 CYCLES	0 TO 18 ksi	3 TO 20 ksi

CHART #8

KEY CONCLUSIONS FROM PERFORMANCE TESTS

OVERALL:

- EXCELLENT PERFORMANCE

STATIC ULTIMATE STRENGTH (TENSILE):

- THE BORON/EPOXY DOUBLER RESTORES THE PRE-CRACKED ALUMINUM TO ITS STATISTICAL A/B MINIMUM STRENGTH (80 KSI FOR 7075-T6 AL), INCLUDING ON POST-FATIGUED SPECIMENS (300 K CYCLES) WHERE THE CRACK HAS GROWN SIGNIFICANTLY (BUT IS STILL UNDER THE DOUBLER).

FATIGUE PERFORMANCE:

- BASELINE CONFIGURATION: NO CRACK RE-INITIATION AT 300,000 CYCLES (RUNOUT). (CONTROL SPECIMEN WITH NO DOUBLER FAILED AT 3100 CYCLES).
- BASELINE PERFORMANCE NOT AFFECTED BY:
 - VARIOUS DOUBLER GEOMETRIES
 - 0° VS 0° ± 45° BORON PLIES
 - LONGEST PLY ON BOTTOM VS. TOP
 - CURE PRESSURE (5" TO 28" Hg VACUUM)
 - ENVIRONMENTS: HOT-WET; SOLVENT
 - CRACK LENGTH OF 1.0"
 - THINNER ALUMINUM (0.032")
 - IMPACT @ 100 & 300 INCH-LBS.
 - 0.5" DIAMETER VOIDS OVER STOP-DRILL AND EDGE OF DOUBLER
 - 1 Hz AND SPECTRUM FATIGUE CYCLES
- CRACK RE-INITIATION¹ DOES OCCUR:
 - IF THERE WAS A DEFECT (E.G., BURR) IN THE STOP-DRILL
 - IF THE CRACK IS NOT STOP-DRILLED
 - IF THERE ARE TOO FEW PLIES (ESPECIALLY AS ALUMINUM GETS THICKER)
 - AT -65°F
 - AT LOAD OF 0 TO 18 KSI WITH NO LATERAL RESTRAINT
- IF/WHEN CRACK RE-INITIATION OCCURS:
 - THE BORON DOUBLER REMAINED INTACT (NO GLOBAL DISBONDS) AND CARRIED THE LOAD
 - CRACK GROWTH WAS AT A LINEAR REPRODUCIBLE RATE INDEPENDENT OF CRACK LENGTH

¹ THIS MEANS THE CRACK EMANATED FROM THE STOP-DRILL. IT DOES NOT NECESSARILY MEAN THE SPECIMEN FAILED.

CHART #9

SUMMARY OF STATIC ULTIMATE TENSION TEST RESULTS

BASELINE

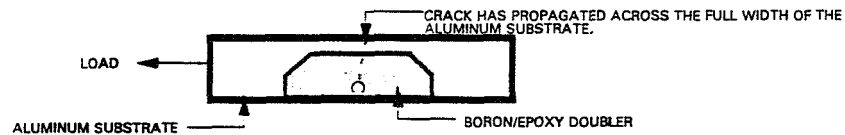
- 11 TESTS
- BORON/EPOXY DOUBLER RESTORES 80 KSI MINIMUM STRENGTH TO THE PRE-CRACKED ALUMINUM
 - ALMOST ALL SPECIMENS BROKE IN THE ALUMINUM OUTSIDE OF THE BORON/EPOXY DOUBLER
 - INCLUDES TESTS ON VARIOUS DOUBLER GEOMETRIES (NO EFFECT)

POST-IMPACT

- 2 TESTS
- GOOD STRENGTH RETENTION AT HIGH IMPACT (43 KSI @ 1200 INCH-LBS)

POST-FATIGUE (300,000 CYCLES)

- BORON DOUBLER RESTORES STATIC ULTIMATE STRENGTH -- EVEN IF THE CRACK PROPAGATES THE FULL WIDTH OF THE ALUMINUM BENEATH THE DOUBLER.
 - 97 TESTS (MANY VARIABLES -- SEE "SUMMARY OF FATIGUE TESTS" CHART)
 - 87 TESTS: ≥ 80 KSI
 - 25 HAD CRACK RE-INITIATION
 - 4 TESTS: 69 TO 76 KSI
 - 4 TESTS: 42 TO 44 KSI EQUIVALENT STRESS IN 4" X .063" ALUMINUM: THE CRACK HAD PROPAGATED ACROSS THE FULL WIDTH OF THE ALUMINUM. THE BORON DOUBLER WAS INTACT AND CARRIED THE INDICATED LOAD.



- 2 TESTS: 76 KSI: SAME AS ABOVE, BUT DIFFERENT BORON DOUBLER CONFIGURATION (I.E., FULL WIDTH OF THE 4" ALUMINUM)

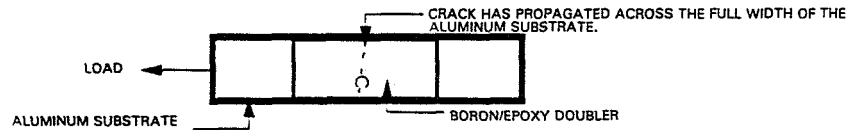


CHART #10

SUMMARY OF FATIGUE TEST RESULTS

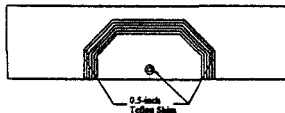
SUMMARY OF TEST RESULTS				RESULTS	
PARAMETER/VARIABLE	NO. OF TESTS	NO. TO 300K CYCLES, NO CRACK RE-INIT. ¹	NO. TO 300K CYCLES, WITH CRACK RE-INIT. AT NO. CYCLES SHOWN ²	NO. TO < 300K CYCLES, WITH FAILURE @ NO. OF CYCLES SHOWN	REMARKS/CONCLUSIONS
1. BASELINE CONFIGURATION ³	13	10	1 @ 113K	1 @ 232K } GRIP 1 @ 284K } FAILURES	• 300K RUNOUT ACHIEVED WITH MINIMAL CRACK RE-INIT.
2. CONTROL; NO DOUBLER	3	--	--	3 @ 3.1K AVG.	• LIFE DROPS BY FACTOR OF > 100
3. DOUBLER GEOMETRY EFFECTS • 0°VS 0° ±45° PLY LAYUP • LONGEST PLY ON BOTTOM VS TOP • SMALLER LATERAL SIZE (1.5" X 4") • WIDER DOUBLER (4" X 4") • 15:1 PLY DROP-OFF	30	14 ⁴ 1	6 TOTAL, 1 EACH @ 87K*, 90K*, 168K, 244K*, 270K, & 283K	9 TOTAL, 1 EACH @ 141K, 145K, 134K, 141K, 74K, 202K, 181K, 212K & 225K	• DEFECTS FOUND IN STOP-DRILL IN ALL 9 SPECIMENS TO < 300K CYCLES, PLUS THOSE WITH ¹ • NO EFFECT OF VARIOUS GEOMETRIES
4. DOUBLER CURE PRESSURE (5" & 28" Hg)	6	6	--	--	• NO EFFECT
5. FEWER BORON PLIES (4 VS 6 IN BASELINE)	3	1	--	1 @ 254K; 1 @ 265K	• CLEAR DROP IN PERFORMANCE
6. ENVIRONMENTAL EXPOSURE • -65°F	6	2	4 TOTAL, 1 EACH @ 44K, 47K, 84K, & 188K	--	• CLEAR DROP IN PERFORMANCE @ -65°F
• -65°F WITH LATERAL RESTRAINT SET AT R.T. 3 KSI POSITION	2	--	1 @ 69; 1 @ 102	--	• NO CHANGE VS. NO RESTRAINT
• 165°F AFTER 1 MO. @ 180°F + 85% HUMIDITY	3	2	1 @ 287K	--	• NO EFFECT
• CYCLIC: -65°F TO 165°F	3	1	1 @ 152K; 1 @ 217K	--	• SOME EFFECT
• 1 WEEK IN SKYDROL @ 120°F	3	3	--	--	• NO EFFECT
7. IMPACT ⁵ • 100 INCH-LB @ RT • 100 INCH-LB @ -65°F; RT FATIGUE • 100 INCH-LB @ 160°F; RT FATIGUE • 300 INCH-LB: REPEAT OF 100 INCH-LB MATRIX	3 3 3 9	3 3 3 8	-- -- -- --	-- -- -- 1 @ 192K. FAILURE WAS OUTSIDE OF THE DOUBLER	• NO EFFECT

CHART #11. Pg. 1 of 3

PARAMETER/VARIABLE		NO. OF TESTS	NO. TO 300K CYCLES, NO CRACK RE-INIT. ¹	NO. TO 300K CYCLES, WITH CRACK RE-INIT. AT NO. CYCLES SHOWN ²	NO. TO < 300K CYCLES, WITH FAILURE @ NO. OF CYCLES SHOWN	REMARKS/CONCLUSIONS
8. NO STOP DRILL		3	--	3 ⁶	--	• CRACK CLEARLY PROPAGATES, BUT BORON-DOUBLER KEEPS SPECIMEN INTACT (2 SPECIMENS CRACKED ACROSS ENTIRE WIDTH)
9. 1.0" LONG CRACK		3	3	--	--	• NO EFFECT
10. OTHER FATIGUE SPECTRA						• NO EFFECT
• 1 Hz SINE WAVE		1	1	--	--	
• 1 Hz SQUARE WAVE		1	1	--	--	
• SPECTRUM LOAD (NO COMPRESSION)		3	3	--	--	
11. ALTERNATE LOADS						• CLEAR DROP IN PERFORMANCE IF NO LATERAL RESTRAINT.
• 0 TO 18 KSI		3	1	--	1 @ 175K; 1 @ 238K	
• 0 TO 18 KSI WITH LATERAL RESTRAINT SET AT 3 KSI POSITION		2	2	--	--	
12. VOIDS (0.5"D) IN BOND OVER STOP-DRILL HOLE AND AT DOUBLER EDGE (SEE B-2 CONFIG)						• MODEST EFFECT ON CRACK RE-INIT. (MOSTLY @ -65°F -- SEE ITEM #6 ABOVE). NO TENDENCY TO CAUSE DOUBLER DEBOND.
• TEST @ RT		3	2	1 @ 149K	--	
• CYCLIC: -65°F to 185°F		3	1	1 @ 147K; 1 @ 211K	--	
13. RIVET (PLUG) AT OUTSIDE EDGE OF DOUBLER (AT HIGH STRESS POINT IN AL.) (SEE B-3 CONFIG)		1	1	--	--	• NO EFFECT
14. THINNER ALUMINUM (0.032")						• NO EFFECT OF THINNER AL
• CONTROL: NO BORON DOUBLER		3	--	--	AVG OF 3: 4.3K	• REPEAT OF ≥ 100X INCREASE IN PERFORMANCE.
• 0.5" CRACK BORON DOUBLER		3	3	--	--	
• 1.0" CRACK HAD 4 PLIES ⁷		3	3	--	--	

		RESULTS			
PARAMETER/VARIABLE	NO. OF TESTS	NO. TO 300K CYCLES, NO CRACK RE-INIT. ¹	NO. TO 300K CYCLES, WITH CRACK RE-INIT. AT NO. CYCLES SHOWN ²	NO. TO < 300K CYCLES, WITH FAILURE @ NO. OF CYCLES SHOWN	REMARKS/CONCLUSIONS
15. THICKER ALUMINUM (0.10")					
• CONTROL: NO BORON DOUBLER	3	--	--	AVG. OF 3: 5.1K	<ul style="list-style-type: none"> REPEAT: LOW LIFE WITH NO DOUBLER 8 PLIES OF BORON (ON 1 SIDE) INSUFFICIENT. (THIS SUPPORTS CONCLUSION OF ITEM #5 ABOVE). NOTE THAT 8 PLIES GIVES BORON: AL. STIFFNESS RATIO OF ONLY 1.1 VS 1.4 FOR 6 PLIES ON .063" AL. (SEE NOTE #8). INCREASE TO 10 PLIES HELPS GREATLY (1.4 STIFF. RATIO). 11 OR 12 PROBABLY BEST DESIGN, OR 4 PLIES ON EACH SIDE.
• 0.5" CRACK 8 PLY BORON DOUBLER ⁸	3	--	--	AVG. OF 3: 129K	
• 1.0" CRACK DOUBLER ⁸	3	--	--	AVG. OF 3: 48K	
• 0.5" CRACK, CYCLIC: -65°F TO 185°F	3	--	--	AVG OF 3: 111K	
• 0.5" CRACK: 10 PLY DOUBLER ⁹	3	1	1 @ 134K	1 @ 144K	
• 0.5" CRACK 0 TO 18 KSI	3	--	--	AVG. OF 3: 126K	
• 0.5" CRACK: 8 PLY DOUBLER, WITH 4 PLIES ON EITHER SIDE	3	2	--	1 @ 210: FAILED OUTSIDE OF DOUBLER	
TOTAL	143				
NOTES: ¹ RE-INIT. IS ABBREVIATION FOR RE-INITIATION. ² ALL CYCLES ROUNDED TO NEAREST 1000. ³ SEE CHART #3 FOR DEFINITION. ⁴ 3 TESTS WERE AT 3 TO 15 KSI. ⁵ THE IMPACT SITE WAS ON THE BORON IN LINE WITH THE STOP DRILL ABOUT 0.25" BEYOND THE STOP DRILL. ⁶ NO. OF CYCLES TO CRACK RE-INITIATION NOT MEASURED. ⁷ THIS RESULTS IN A STIFFNESS RATIO OF 1.8 ((E) _{B.E.} + (E) _{AL}) VS 1.4 FOR 6 PLIES OF BORON EPOXY ON 0.063" AL. ⁸ THIS RESULTS IN A STIFFNESS RATIO OF 1.1 ((E) _{B.E.} + (E) _{AL}) VS 1.4 FOR 6 PLIES OF BORON EPOXY ON 0.063" AL. ⁹ THIS INCREASES THE STIFFNESS RATIO TO 1.4					

Configuration B-2



Configuration B-3

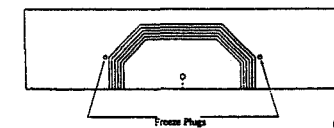


CHART #11, Pg. 3 of 3

1995108044

N95-14458

**INSPECTING FOR WIDESPREAD FATIGUE DAMAGE:
IS PARTIAL DEBONDING THE KEY?**

John Brewer
Volpe National Transportation Systems Center
Cambridge, MA

348613
55-39
23099
P-10

SUMMARY

Experimental and analytical results indicate that cracks can initiate, grow, and coalesce more rapidly in fuselage lap joints that have experienced partial or complete debonding. Computational analysis in this paper shows that stress concentrations and stress intensity factors at the rivet holes are far less severe when the bond is intact. Debonding hastens the initiation of widespread fatigue cracks and significantly increases crack growth rate. Thus, debonded regions serve as "breeding grounds" for widespread fatigue damage. Therefore, the effectiveness of lap joint inspection programs may be enhanced if detailed inspections are focused on areas in which debonding has been detected.

INTRODUCTION

The Federal Aviation Administration has defined a damage tolerant structure as one "that has been evaluated to ensure that, should serious fatigue, corrosion, or accidental damage occur within the operational life of the airplane, the remaining structure can withstand reasonable loads without failure or excessive structural deformation until the damage is detected [1]." An important aspect of aircraft maintenance, therefore, is to increase the effectiveness of inspections.

Substantial research has been conducted in the area of widespread fatigue damage (WFD). WFD can take the form of multiple site damage (MSD) cracks at rivet holes along the fuselage lap joint [2]. These cracks seem to form predominantly in areas of adhesive bond failure. In the first 291 Boeing 737's manufactured, a cold bond adhesive was used that was found to debond in as few as 3000 cycles [3]. Boeing has also shown experimentally that "the fatigue life of a lap joint with a large area of delamination is reduced [3]."

A fatigue test of a full scale fuselage panel with no adhesive bonding was conducted by Foster-Miller, Inc. [4]. The first detection of damage occurred at approximately 37,000 pressurization cycles. At approximately 73,700 cycles, there were only two cracks more than an inch long. However, over the next 1600 cycles, another crack grew from under one inch to over 50 inches long, resulting in loss of pressurization. A record of the visible damage in that experiment is shown in Figure 1.

The Foster-Miller experiment showed that cracking associated with WFD can advance with disconcerting speed. The 1600 cycles between two relatively small cracks and pressurization failure

is less than the normal C-check inspection interval. Nonetheless, we do not regularly see fuselage failures in aircraft with 75,000 flight cycles. A protective mechanism must be at work. That protective mechanism is the action of the adhesive bond. This paper will explore the potential benefits of this form of load transfer in terms of the life needed for WFD crack initiation and growth.

EFFECT OF PARTIAL DEBONDING ON CRACK INITIATION

"Crack initiation" is perhaps an ill-defined term that describes an intuitive series of events. It qualitatively describes the transition from uncoalesced micromechanical damage to a single through-the-thickness crack that grows predictably. The precise definition is not critical to this paper, but, for convenience, it can be defined as that point when the crack tip emerges from under the countersunk rivet head.

Intact adhesive bonds transfer the load between skin panels in small regions at the edge of the joint rather than at the rivet holes. Bonded sheets therefore have similar strain distributions (and, consequently, stress distributions) over most of the joint. Thus, the stress in two equal thickness sheets is essentially equal to half the nominal stress. Little load is actually transferred by the rivets.

In contrast, the top skin in the debonded lap joint carries the entire circumferential load to the first row of rivets. From there, some load is transferred by the rivets into the other sheet and the rest bypasses the first row. Thus, there is one component of the stress concentration factor at the edge of the hole that results from the rivet bearing load and another that arises from the bypass stress, as shown in Figure 2. The magnitudes of these stress concentrations are mitigated somewhat by the biaxial nature of the load on the joint.

The stress concentration factor was calculated by a linear finite element analysis. Three-dimensional 20-noded "brick" elements were used. The three layers (the top and bottom skins and the adhesive layer) were each one element thick. The skins were 0.036 inch thick 2024-T3 aluminum. The adhesive layer was 0.004 inches thick. There were 4356 solid elements. The finite element mesh is shown in Figure 3.

Symmetry boundary conditions were employed such that a periodic repeating pattern was created as shown in Figure 4. Although this configuration of debonding is unlikely in service, it gives an indication of the state of stress experienced in circumstances of interest. Obviously, the calculations are more representative of cases with similar distance from the point of interest to the debond front and approximately the same fraction of debonded area in the vicinity.

The rivet spacing was one inch in both the circumferential and axial directions. The rivet holes were assumed to be cylindrical rather than countersunk. The rivets were modeled with beam elements that were attached to the face of the hole with an array of smaller beam elements. The flexibility of each rivet structure was matched to the value given by the method proposed by Swift [5].

Several configurations of debonding were considered, as shown in Figure 5. Debonding was

simulated by limiting the region in which nodes associated with adhesive layer elements and nodes associated with top sheet elements were "merged" at the interface to enforce displacement continuity.

A biaxial load was applied to the model. The tensile circumferential stress was 1000 psi. The tensile axial stress was 500 psi. This 2:1 ratio is the classical value for a pressurized cylinder. The effects of stiffening substructure were not included in this model. Geometric nonlinearities arising from bending and rotation of the lap joint were suppressed.

The maximum stress concentration occurred in the debonded region in the upper row in the top sheet. By the symmetry of the model, the value was repeated at the lower rivet row in the bottom sheet. The maximum stress concentration factor for each case is given in Table 1. There is a factor of 4.55 between the values for the completely bonded and completely debonded cases.

The service life required for crack initiation can be estimated using a model by Broek [6]. He asserts that Miner's cumulative damage, D , can be used to correlate crack initiation. That is, the number of initiated cracks follows a Weibull distribution when plotted against D , where D is defined as:

$$D = \sum \frac{n_i}{N_i} \quad (1)$$

where n_i is the number of cycles experienced at a given nominal stress level and N_i is the corresponding number of cycles to failure of a lap joint specimen at that stress level. In a related report [7], Broek presents data by Hartman [8] as a source for estimates of N_i . From that fatigue failure data for a similar lap joint, it can be seen that there is a factor of approximately six between the number of cycles to failure of lap joints with and without adhesive bonding. The implication is therefore that it will take approximately six times as long to initiate any crack.

Broek [6] assumed a functional fit for N_i of the form:

$$N_i = \exp \left(\frac{A - (\Delta \sigma)_i}{B} \right) \quad (2)$$

If one assumes that the effective change in stress for each cycle is proportional to the stress concentration factor, then estimates of the relative initiation life can be calculated. The initiation lives normalized by the value for the completely bonded case are given in Table 1.

EFFECT OF PARTIAL DEBONDING ON CRACK GROWTH

Crack growth models usually relate the rate of crack extension to the stress intensity factor. A linear finite element analysis was conducted of the lap joint to determine the Mode I stress intensity factor, K_I , of a crack extending from a rivet hole in the upper row. The crack extended from the edge of the rivet hole to the midpoint between the rivets. The mesh is the same as in Figure 3 except that a discontinuity was introduced to model the crack face and singular elements were used at the crack

tip. The same five configurations of debonding were studied. In each case, the crack emanated from the hole on the debonded side of the model, as shown in Figure 6. The normalized Mode I stress intensity factor is K_I divided by the nominal value for a center-cracked plate with the same tip-to-tip crack size and uniaxial loading:

$$\text{normalized } K_I = \frac{K_I}{\sigma \sqrt{\pi a}} \quad (3)$$

where σ is the nominal circumferential stress level and a is half the tip-to-tip crack length. The results of the normalized stress intensity factor as a function of the fraction of the bond area intact are given in Table 2. The components of stress intensity factor from the other modes (shearing and tearing) were calculated, but never contributed more than one percent to the total stress intensity factor.

The stress intensity factor increases by a factor of 5.7 when the section has completely debonded. This results both from the increase in stress in the top sheet and from the inability of the adhesive and bottom sheet to act as a "patch" to limit the crack opening displacement. Crack growth models usually assume crack extension per cycle is proportional to the stress intensity factor raised to a power. In Reference 9, the parameters for the Walker model of crack growth in 2024-T3 aluminum include the exponent 4. The calculated increase in crack growth rate would therefore be proportional to the ratio of stress intensity factors raised to the fourth power. These values of stress intensity factor (normalized in this case by the completely bonded value) raised to the fourth power are also reported in Table 2. It is seen that crack growth is accelerated by approximately three orders of magnitude for the completely debonded case.

DISCUSSION

The experimental study of a lap joint with no adhesive bond resulted in fast crack initiation and growth. The fact that such behavior is not commonly observed in service demonstrates that the bond is effective in retarding such damage growth. The analyses in this paper show that moderate bonding can provide substantial benefit.

The computational results illustrate some underlying mechanisms of damage acceleration once the adhesive bond is lost in the lap joint. The load is no longer transferred near the edge of the lap joint. Therefore, the circumferential stress level above the upper row of rivets is the full nominal far field stress rather than half that value. Significant load is transferred by bearing load on the rivets. This raises the stress concentration at the edge of the hole and promotes crack initiation there. Once a crack has formed, the failed adhesive bond can no longer act to limit the maximum crack opening displacement and, therefore, the stress intensity factor. Thus, crack growth rates increase dramatically.

The situation in the fleet is, of course, more complex. The debonded area changes over time and strongly affects crack behavior as it does. There are significant effects of the supporting structure in load redistribution. There is also a need to understand the effect of partial debonding on crack

coalescence ("linkup") and any interaction between crack growth and debond growth.

IMPLICATIONS FOR INSPECTION

The implications for maintenance and inspection of fuselage lap joints of these calculations for crack initiation and growth could be significant. If a large section of a lap joint were completely debonded, an incubation period of about 40,000 cycles and a subsequent slow crack growth period of about 30,000 cycles would be followed by extremely rapid growth. Damage tolerance assessments would rely on detecting cracks during the slow growth period. Since cracks are quite small during this phase, detection is not necessarily assured. It would not be conservative for analyses to rely on the existence of intermittent bonded regions to retard or arrest crack growth.

The calculations in this paper indicate that joints with reasonably intact adhesive bonds can expect much longer crack initiation and growth periods. With the rapid growth experienced in the Foster-Miller experiment [4], it is plausible that detection and close inspection of debonded regions before rapid growth begins would be easier and more effective than trying to detect cracks with no regard to the state of the bond. A carefully prepared inspection program might not require frequent detailed inspection of every lap joint rivet.

CONCLUSIONS

The analyses confirm the experimental results that, in a completely debonded lap joint, the stress distribution speeds up the processes of crack initiation and growth. The extent of that acceleration depends on the crack configuration.

This striking contrast in behavior suggests a possible screening during inspection for WFD. If an area inspection can detect debonds with some certainty, then the relative likelihood of WFD formation can be assessed. More informed decisions can then be made about whether a detailed inspection, such as eddy current, is necessary.

REFERENCES

1. Federal Aviation Administration: Advisory Circular 25.571-1B
2. National Transportation Safety Board: Aircraft Accident Report NTSB/AAR-89/03, Aloha Airlines Flight 243, June 1989.
3. Boeing Service Bulletin No. 737-53A1039, Revision 3, August 20, 1987.

4. Thomson, D.; Samavedam, G.; Hoadley, D.; and Jeong, D. Y.: Aircraft Fuselage Lap Joint Fatigue and Terminating Action Repair. Federal Aviation Administration Technical Center Report, August 1993.
5. Swift, T.: Repairs to Damage Tolerant Aircraft. International Symposium on the Structural Integrity of Aging Airplanes, Atlanta, GA, March 1990.
6. Broek, D.: Outline of Risk Analysis to Establish Requirements for Inspection Interval. FractuREsearch TN 9104, July 1991.
7. Broek, D.: Analysis Concerning the Inspection Threshold for Multi-Site Damage. FractuREsearch TR 9104, June 1991.
8. Hartman, A.: Fatigue Tests on Three-Row Lap Joints in Clad 2024-T3 Manufactured by Riveting and Adhesive Bonding. National Aerospace Laboratory of the Netherlands (NLR), Amsterdam, Report TN M-2170, 1967.
9. Damage Tolerance Assessment Handbook, Vol. I. NTIS Report DOT/FAA/CT-93/69.I, October 1993.

Table I. Results of the Stress Concentration Factor Analyses

Percentage of Lap Joint Area with Intact Bond	Maximum Stress Concentration Factor	Normalized Initiation Life
0	4.96	0.17
25	2.42	0.54
50	1.79	0.73
75	1.34	0.89
100	1.09	1.00

Table II. Results of the Stress Intensity Factor Analyses

Percentage of Lap Joint Area with Intact Bond	Normalized Mode I Stress Intensity Factor	Normalized Crack Growth Rate
0	1.04	1083
25	0.74	275
50	0.52	8.3
75	0.21	1.6
100	0.18	1.0

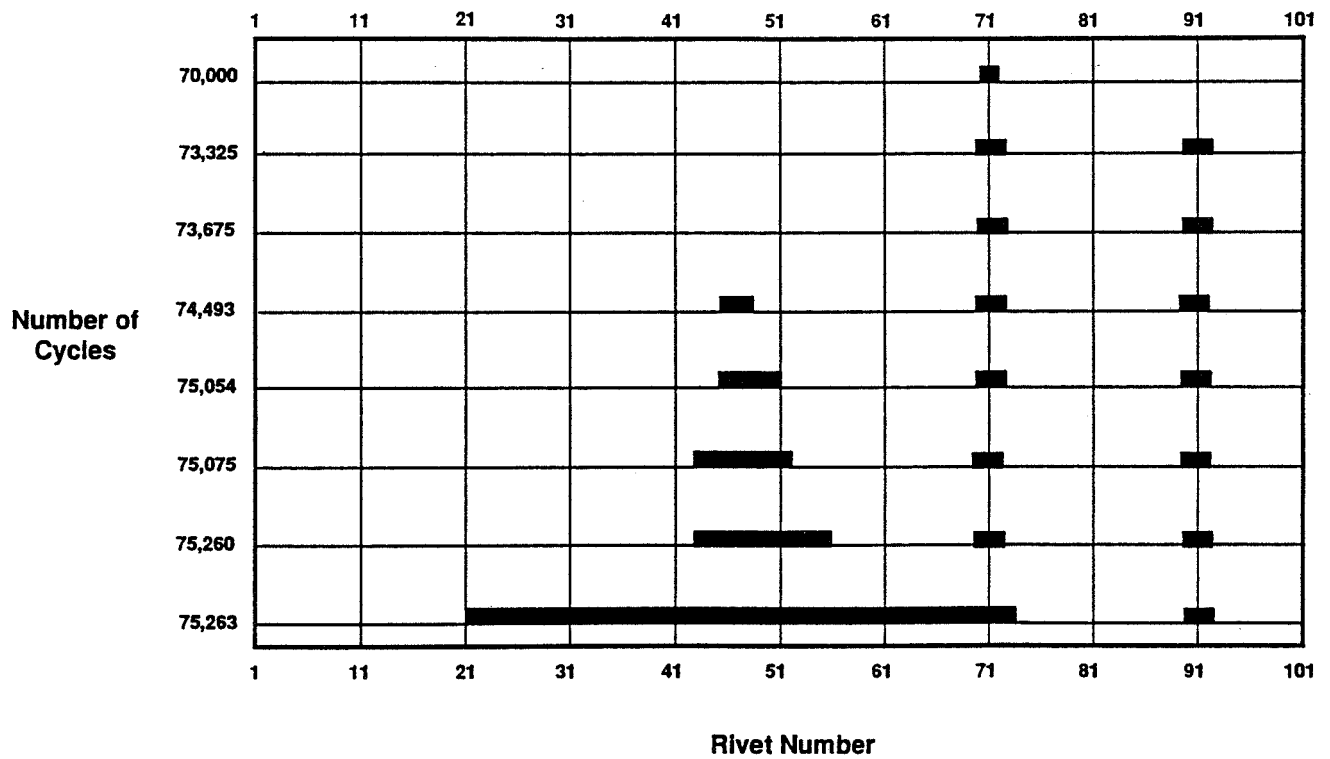


Figure 1. Visible cracks in Foster-Miller experimental full scale fuselage fatigue panel [4].

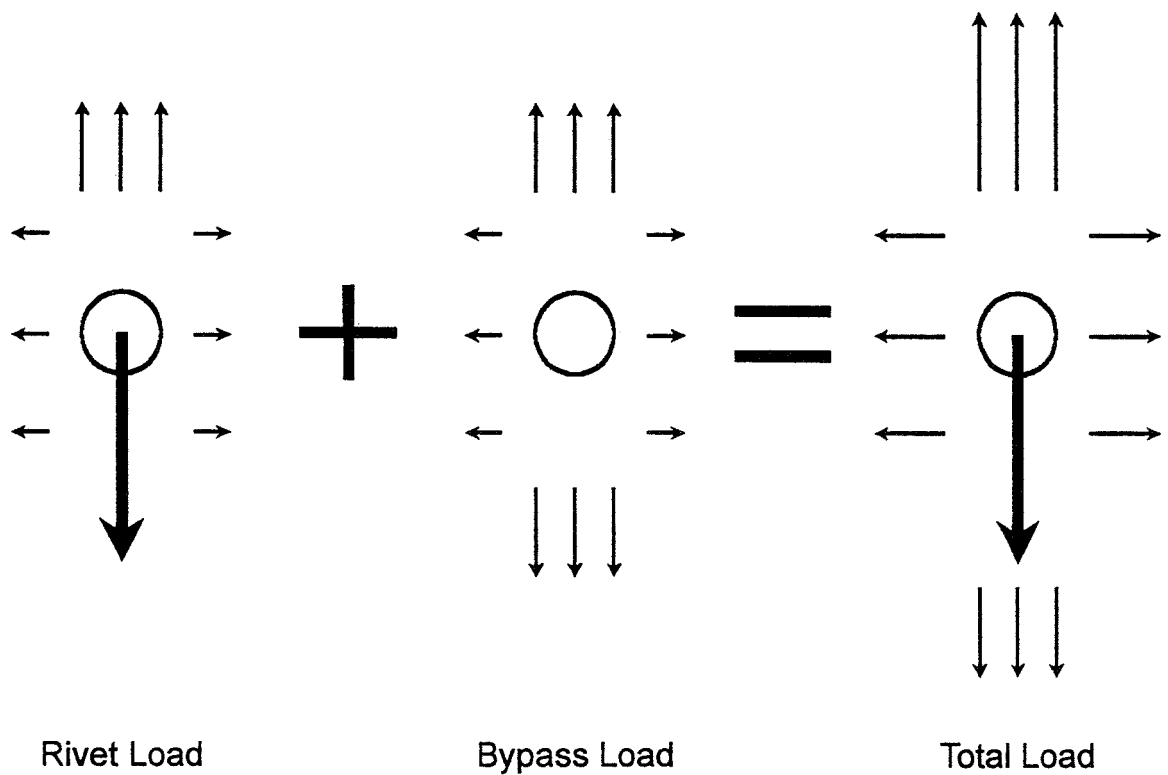


Figure 2. Components of the stress concentration factor.

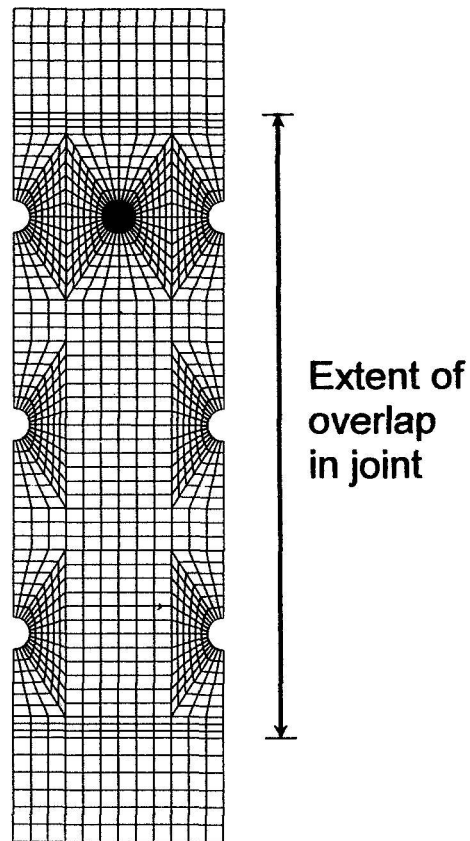


Figure 3. Finite element mesh in the computational analysis.

This model:

represents this structure:

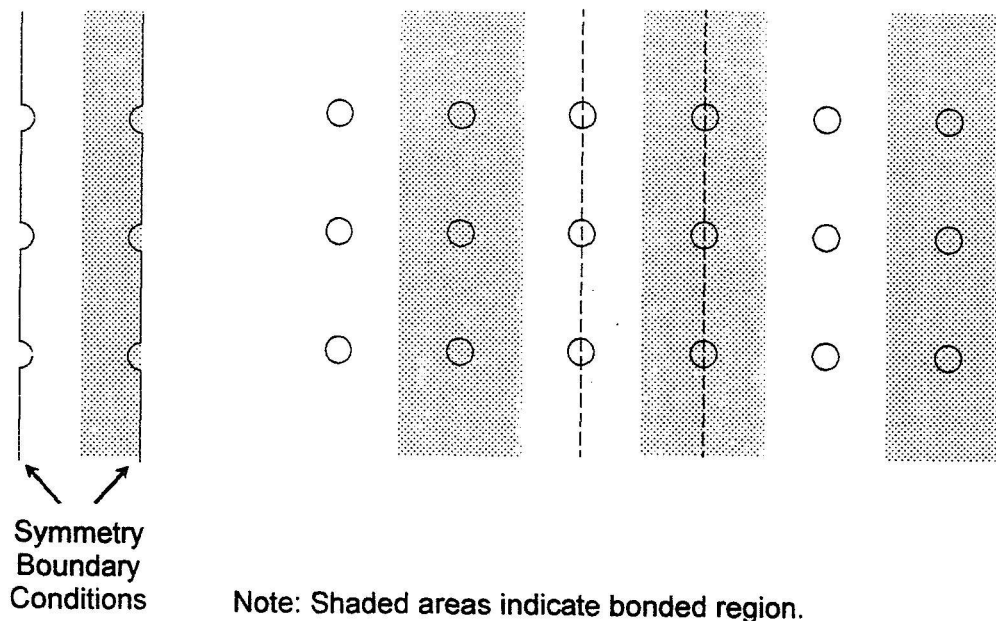
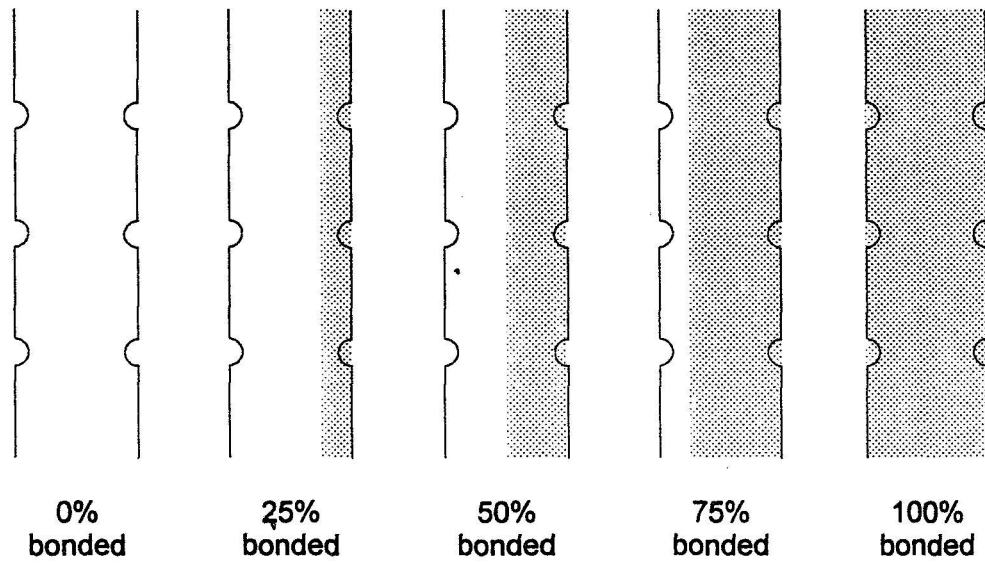
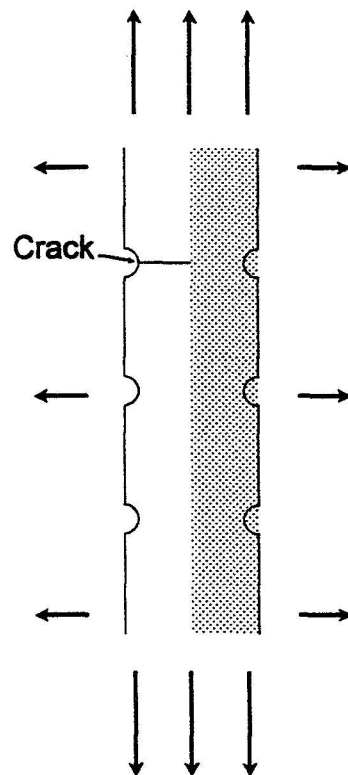


Figure 4. Model of an infinitely repeating strip with symmetry boundary conditions.



Note: Shaded areas indicate bonded regions.

Figure 5. Configurations of debonded areas.



Note: Shaded area indicates bonded region.

Figure 6. Crack location relative to debonded area.

MICROSTRUCTURALLY BASED MODEL OF
FATIGUE INITIATION AND GROWTH348615
56-39

23/00

p- 14

J. R. Brockenbrough, A. J. Hinkle, P. E. Magnusen, R. J. Bucci
Product Design and Mechanics Division
Alcoa Technical Center, PA 15069-0001

ABSTRACT

A model to calculate fatigue life is developed based on the assumption that fatigue life is entirely composed of crack growth from an initial microstructural inhomogeneity. Specifically, growth is considered to start from either an ellipsoidal void, a cracked particle, or a debonded particle. The capability for predicting fatigue life from material microstructure is based on linear elastic fracture mechanics principles, the sizes of the crack-initiating microstructural inhomogeneities, and an initiation parameter that is proportional to the cyclic plastic zone size. A key aspect of this modeling approach is that it is linked with a general purpose probability program to analyze the effect of the distribution of controlling microstructural features within the material. This enables prediction of fatigue stress versus life curves for various specimen geometries using distributional statistics obtained from characterizations of the microstructure. Results are compared to experimental fatigue data from an aluminum alloy.

INTRODUCTION

Classically, the fatigue life of a metallic specimen or structure has been thought of in three stages: crack initiation, crack growth and final fracture. As crack measurement techniques have improved and researchers have examined small crack growth, microcracks have been discovered which grow from very early in a structure's life. This period of small crack growth can be 50 to 90% of the fatigue life. This suggests that fatigue life can be considered as a two stage process of growth and fracture. Due to the length of time that a structure spends in this early phase of fatigue crack growth it is important to accurately model this behavior.

In metallic structures there is generally a hierarchy of features which can control fatigue. Various researchers have identified some of these features. In 2024-T4 and 7075-T6, Erhardt et. al. [1], indicate cracks started at surface inclusions; Wang [2] in a study of 2024-T3

identified inclusions and tool marks as key initiators; Lukasak and Koss [3] in a study of a particle reinforced MMC identified two failure modes associated with the reinforcing particle; Lankford and Kusenburger [4] linked high strength steel crack initiation to cavitation caused by particle debonding; Goto, et al. [5] identified particles and surface scratches as fatigue initiators in heat-treated 0.45% C steel; Fischmeister, et al. [6] determined pores and particles to be the initiation sites of a Ni superalloy; Magnusen, et al. [7] indicated that in 7050-T7451 pores and particles act as initiators. Fracture mechanics and damage tolerant methodologies have been shown to work well for rogue inspectable flaws on the order of 0.01-0.05 inches. The motivating force behind this work is to model the role of alloy microstructure on fatigue durability as identified by cracking that originates from a feature of the microstructure approximately 0.0005-0.01 inches in diameter. The crack is then grown to an inspectable dimension of economic consequence (i.e., a crack requiring diagnostic or corrective action during the operational life of a part).

The principal types of microstructural features of concern are micropores and constituent particles. These microstructural inhomogeneities act as sites for the initiation of fatigue cracks. The next section discusses the basic fracture mechanics approach used to model early fatigue growth. Following sections then discuss the infinite life stress sensitivity and sensitivities of the model to material parameters. Finally, life predictions using the model are compared to experimental lives on an aluminum alloy.

MICROSTRUCTURAL BASED FATIGUE MODELING

The method used for the fatigue life analysis is based on the assumption that fatigue life is entirely composed of crack growth from an initial inhomogeneity [8]. Specifically, growth is considered to start from either an ellipsoidal void, a cracked particle, or a debonded particle. It is assumed that each type of inhomogeneity contains a pseudo crack of equatorial length b . As shown in Figure 1, the particle or void height is h and its width is $2R$. The remote stress, σ , is applied in the z direction, perpendicular to the plane of crack growth. It is assumed that for a given far-field cyclic stress, $\Delta\sigma$, the pseudo crack forms in the first few cycles. The pseudo crack can be considered a perturbation of the surrounding stress field for the purpose of calculating the available energy for crack extension in the vicinity of a local pore/particle stress concentration. The length of this pseudo crack is assumed to be proportional to the cyclic plastic zone size ahead of the crack as illustrated in Figure 1. To make these ideas more precise, consider the Trantina-Barishpolsky effective stress intensity factor [9], for the flaw geometry

shown. The stress intensity factor associated with the crack surrounding the inhomogeneity can be expressed as,

$$K_{T-B} = \beta \sigma \sqrt{\pi b} \quad (1)$$

where the dimensionless term β addresses the local microfeature and is given by,

$$\beta = \frac{2}{\pi} + B \left(1.12k_t - \frac{2}{\pi} - 1 \right) \left(\frac{R}{b+R} \right)^{10} + \left(\frac{R}{b+R} \right)^{1.8} \quad (2)$$

Here B is a constant that has the value 1 for a void, 2 for a bonded cracked particle, and 0.3 for an debonded particle; k_t is the local elastic stress concentration factor for the ellipsoidal void or particle without the crack. Note that β depends on the geometry through the ratio $R/(b+R)$, so that for $b \gg R$, Equations 1 and 2 reduce to the stress intensity factor solution for an embedded elliptical crack, where the void or particle lacks influence on the stress intensity factor. At the other extreme, for $b = 0$, from Equation 1, the stress intensity factor is zero. Under the imposition of a far-field cyclic stress range $\Delta\sigma$, the cyclic stress intensity factor is,

$$\Delta K_{T-B} = \beta \Delta\sigma \sqrt{\pi b} \quad (3)$$

An estimate of the cyclic plastic zone size associated with ΔK_{T-B} is, [10]

$$r^* = \frac{1}{\pi} \left(\frac{\Delta K_{T-B}}{2\sigma_y} \right)^2 \quad (4)$$

where σ_y is the yield strength of the material. The procedure used to calculate the parameter, b, is to equate it to this measure of plastic zone size. Thus, solve Equation 3 for b and equate it to the plastic zone size of Equation 4. This amounts to finding the ratio $R/(b+R)$ that satisfies

$$\frac{\beta \Delta\sigma}{2\sigma_y} = 1 \quad (5)$$

THRESHOLD STRESS FOR INHOMOGENEITY INITIATED FATIGUE

Equation 5 can be used directly to estimate the fatigue threshold stress, or the stress which yields infinite life, $\Delta\sigma_\infty$. For infinite life, $b = 0$, and

$$\Delta\sigma_\infty = \frac{2\sigma_y}{\frac{2}{\pi} + B\left(1.12k_t - \frac{2}{\pi} - 1\right) + 1} \quad (6)$$

Although the number of cycles to failure is sensitive to the initial void or particle size, Equation 6 suggests that if fatigue life is controlled by the growth of a crack from an inhomogeneity, then the infinite life stress is independent of void or particle size. It is proportional to yield strength and shows a strong dependence on local stress concentration factor, k_t , and the type of inhomogeneity through B . For voids, $B = 1$ and Equation 6 becomes,

$$\Delta\sigma_{\infty-\text{voids}} = \frac{2\sigma_y}{1.12k_t} \quad (7)$$

For cracked particles, $B = 2$ and Equation 6 becomes,

$$\Delta\sigma_{\infty-\text{particles}} = \frac{2\sigma_y}{2.24k_t - 1 - \frac{2}{\pi}} \quad (8)$$

A plot of the sensitivity of the infinite life stress to the local stress concentration factor is shown in Figure 2 for both voids and cracked particles. Figure 2 shows that voids affect the infinite life stress more severely than uncracked particles. For voids, a lower limit on the stress concentration factor is a smooth sphere for which k_t is about 2. At this point the ratio of infinite life stress to yield stress is about 0.9. For Equations 7 and 8 it is assumed that the yield strength is an upper limit on the infinite life stress for the mechanism of fatigue crack growth from a void or particle. This assumption sets limits on the stress concentration factors below which little improvement in infinite life stress is expected. For voids, improvements are possible up to the point at which the void is the shape of a smooth sphere which is the minimum stress concentration possible. For non-spheres there is a dramatic drop in the infinite life stress for small increases in the local stress concentration. For a stress concentration of 3, the ratio of infinite life stress to yield strength has dropped to about 0.6. This corresponds to a circular

cavity of elliptical cross-section with aspect ratio 2.5, as depicted in Figure 3. For particles, the value of stress concentration factor at which the infinite life stress begins to decrease is 1.62. The stress concentration of the particle depends both on particle shape and particle elastic modulus. For a bonded uncracked particle, stress concentrations in the matrix are typically less than 2 [11]. A plot of the stress concentration factor for an isolated rigid elliptical cylindrical particle is shown in Figure 4. For far-field uniform tension, the stress concentration factor for tangential tension is less than 2 for aspect ratios ranging up to 30. This suggests that particle cracking will typically be required before particles can control the infinite life stress. In previous studies on the effects of cracked particles [12,13], it has been shown that cracked particles behave like high aspect ratio voids. This is expected to severely limit the infinite life stress, as shown in Figure 2.

Since the stress concentration factor, k_t , is taken to be a local value at the point where a crack starts to grow, Equation 6 shows that the infinite life stress is sensitive to the smoothness of the void or particle.

SENSITIVITY OF FATIGUE LIFE CURVE TO MODEL PARAMETERS

Crack growth emanating from a metallurgical inhomogeneity is assumed to follow a power law,

$$\frac{da}{dN} = A\Delta K^m \quad (9)$$

where $\frac{da}{dN}$ is the crack growth rate, ΔK is the cyclic stress intensity, and A and m are material constants. For the aluminum plate used in this study, the coefficients obtained by fitting the equation to long crack growth data were, $A = 3.9 \times 10^{-9}$, $m = 4.18$ for an R-ratio of 0.1. ΔK is in units of ksi $\sqrt{\text{in}}$.

The sensitivity of the fatigue model to changing material and microstructural parameters can be assessed by calculating the cyclic stress versus life (S/N) curves for the varying material conditions. Specimen failure occurs when $K_{\max} = K_{1c}$; a value of $K_{1c} = 25 \text{ ksi } \sqrt{\text{in}}$ was used. The influence of particle size on fatigue life is shown in Figure 5 for particle sizes ranging from 0.001 in. to 0.01 in. at a stress concentration value of 2. The yield strength was fixed at 70 ksi. The effect of increasing particle size is to decrease life throughout the range of stress levels.

The infinite life stress, however, is insensitive to particle size. Similar trends hold for increasing void size at constant aspect ratio. The sensitivity of fatigue life to yield strength is shown in Figure 6. Here the particle size is fixed at 0.005 in. and the yield strength is varied from 60 ksi to 80 ksi. As seen, there is almost no change in fatigue life with stress level above the infinite life stress, $\Delta\sigma_{\infty}$. The effect of yield strength on $\Delta\sigma_{\infty}$ is strong; for this mechanism, increasing yield strength increases the threshold stress for fatigue. The results shown in Figures 5 and 6 show that if simultaneously particle (void) size is decreased while increasing yield strength, fatigue life is expected to increase at all stress levels. The inhomogeneity aspect ratio or stress concentration has a similar effect on the fatigue life curve as yield stress does. Figure 7 shows a comparison of fatigue S/N curves for particles and voids at different shapes for a yield strength of 70 ksi. The particle or void size is fixed at 0.005 in. It is seen that increasing the stress concentration has a large effect on decreasing the infinite life stress.

COMPARISON OF MODEL CALCULATIONS TO TEST DATA

Open hole fatigue tests were performed to quantify the influence of the various microstructural features on fatigue performance of a high strength aluminum alloy. The fracture surfaces from the failed specimens were then examined in a scanning electron microscope and the size, location and type of crack initiating inhomogeneity were recorded. Failures in material A were controlled by microporosity, while the failures for material B were generally controlled by cracked particles located at or near the corners of the bore hole. Despite the change in initiation mechanism from material A, where micropores dominated, open hole lifetimes of the two materials are similar.

The model described in the previous sections has been used to calculate open hole fatigue performance of these materials. These calculations have been made using data obtained from the failed fatigue specimen fracture surfaces. Additional input for the calculation included the yield strength, crack growth properties of the material and the local stress concentration factor at the microstructural feature. The local stress concentration factor was determined empirically from fitting the model with the infinite fatigue life data for each material variant. The values obtained for the local stress concentration factor for material A and B are 7.5 and 4.25, respectively. These values can be interpreted to say that the local stress concentration factor became less severe as the microstructural feature changed. The growth model was linked to the program PROBAN [14] to permit use of statistical information on particle and pore

distributions. PROBAN is a general purpose probability analysis program which can be linked to user-defined subroutines to predict crack growth.

The calculated stress versus life curves for each material variant, along with the open hole fatigue test data are shown in Figures 8 and 9. The model was used to calculate the 5%, 50%, and 95% fractiles for each material. (The curves shown are not smooth because only a limited number of stress levels have been analyzed with the model.) In general, the results of the model are in good agreement with the test data. Additional refinement of the model is expected to yield improvement in the ability to predict fatigue behavior of the material variants.

CONCLUSIONS

- Fracture mechanics principles can be applied to microstructural features (0.0005-0.01 inch) that govern fatigue life for both smooth axial and open hole specimen geometries.
- The effects of the initial inhomogeneity size, shape, and location distributions on specimen fatigue life distributions can be analytically predicted.
- Calculations of specimen fatigue S/N curves agree well with actual test data.
- Typically cracked particles are required before particles will control the infinite life stress.
- A particle's or pore's local stress concentration factor is important. The infinite life stress is a maximum when the local stress concentration factor is small.

FUTURE WORK

A goal of modeling is to predict material performance based solely on characterization of the microstructure rather than a postmortem analysis of fatigue failures. Therefore, it is necessary to take metallographic characterizations of the microstructure obtained on random planes and scale the distributions of controlling features to obtain the extreme distributions that are observed through fractography. Extreme value statistics will be used to establish the relationship between the random plane characterizations and the extreme value distributions of constituent particles or voids. Future work will develop capability to predict material fatigue performance based on material microstructure.

ACKNOWLEDGMENTS

The authors wish to acknowledge H. J. Konish, S. M. Miyasato, and R. L. Rolf for many technical discussions and suggestions throughout the course of this work. The authors wish to thank Dr. A. K. Vasudevan and the Office of Naval Research.

REFERENCES

1. Erhart, K. and Grant, N. J., "Behavior of 2024 Aluminum in Low Cycle Fatigue at Low Strain Rates as a Function of Temperature," Fracture 1969, Proceeding of the 2nd International Conference, April 13-18, 1969.
2. Wang, D. Y., "An Investigation of Initial Fatigue Quality," *Design of Fatigue and Fracture Resistant Structures*, ASTM STP 761, P. R. Abelkis and C. M. Hudson, Eds., American Society for Testing and Materials, 1982, pp. 191-211.
3. Lukasak, D. A. and Koss, D. A., "Microstructural Influences on Fatigue Crack Initiation in a Model Particulate-reinforced Aluminum Alloy MMC," *Composites*, Volume 24, Number 3, 1993, pp. 262-269.
4. Lankford, J. and Kusenberger, F. N., "Initiation of Fatigue Cracks in 4340 Steel," *Metallurgical Transaction*, Volume 4, Number 2, 1973, pp. 553-559.
5. Goto, M., Yanagawa, Y., and Nisitani, H., "Statistical Property in the Initiation and Propagation of Microcracks of a Heat-Treated 0.45% C Steel," *JSME International Journal*, Series I, Volume 33, Number 2, 1990, pp. 235-241.
6. Fischmeister, H., Quadfasel, U., Banhardt, V., Bruckner-Foit, A., Jackels, H., Eblinger, P. and Konig, G., "Towards a Probabilistic Lifetime Prediction Model for Aircraft Engine Disks," Translated from *Zeitschrift fur Metallkunde*, Volume 81, October 1990, pp. 707-714.

7. Magnusen, P. E., Hinkle, A. J., Rolf, R. L., Bucci, R. J., and Lukasak, D. A., "Methodology for the Assessment of Material Quality Effects on Airframe Fatigue Durability," Presented at Fatigue 90, Honolulu, HA, July 15-20.
8. A. J. Hinkle, A. F. Grandt, and L. E. Forsythe, "Predicting the Influence of Initial Material Quality on Fatigue Life," Presented at ICAF 93, Stockholm, Sweden, June 07-11, 1993.
9. G. G. Trantina and M. Barishpolsky, "Elastic-Plastic Analysis of Small Defects - Voids and Inclusions," *Engineering Fracture Mechanics*, Vol. 20, No. 1, 1984, pp. 1-10.
10. S. Suresh, Fatigue of Materials, Cambridge University Press, 1991.
11. R. E. Peterson, Stress Concentration Factors, John Wiley, 1974.
12. W. H. Hunt, Jr., J. R. Brockenbrough, P. E. Magnusen, "An Al-Si-Mg Composite Model System: Microstructural Effects on Deformation and Damage Evolution," *Scripta Metallurgica Et Materialia*, Vol. 25, p. 15, 1991.
13. J. R. Brockenbrough, F. Zok, "On the Role of Particle Cracking in Flow and Fracture of Metal Matrix Composites," Alcoa Report # 57-14-93, 1993.
14. Det norske Veritas, PROBAN: General Purpose Probabilistic Analysis Program, Veritas Sesam Systems, Hovik, Norway, January 1992.

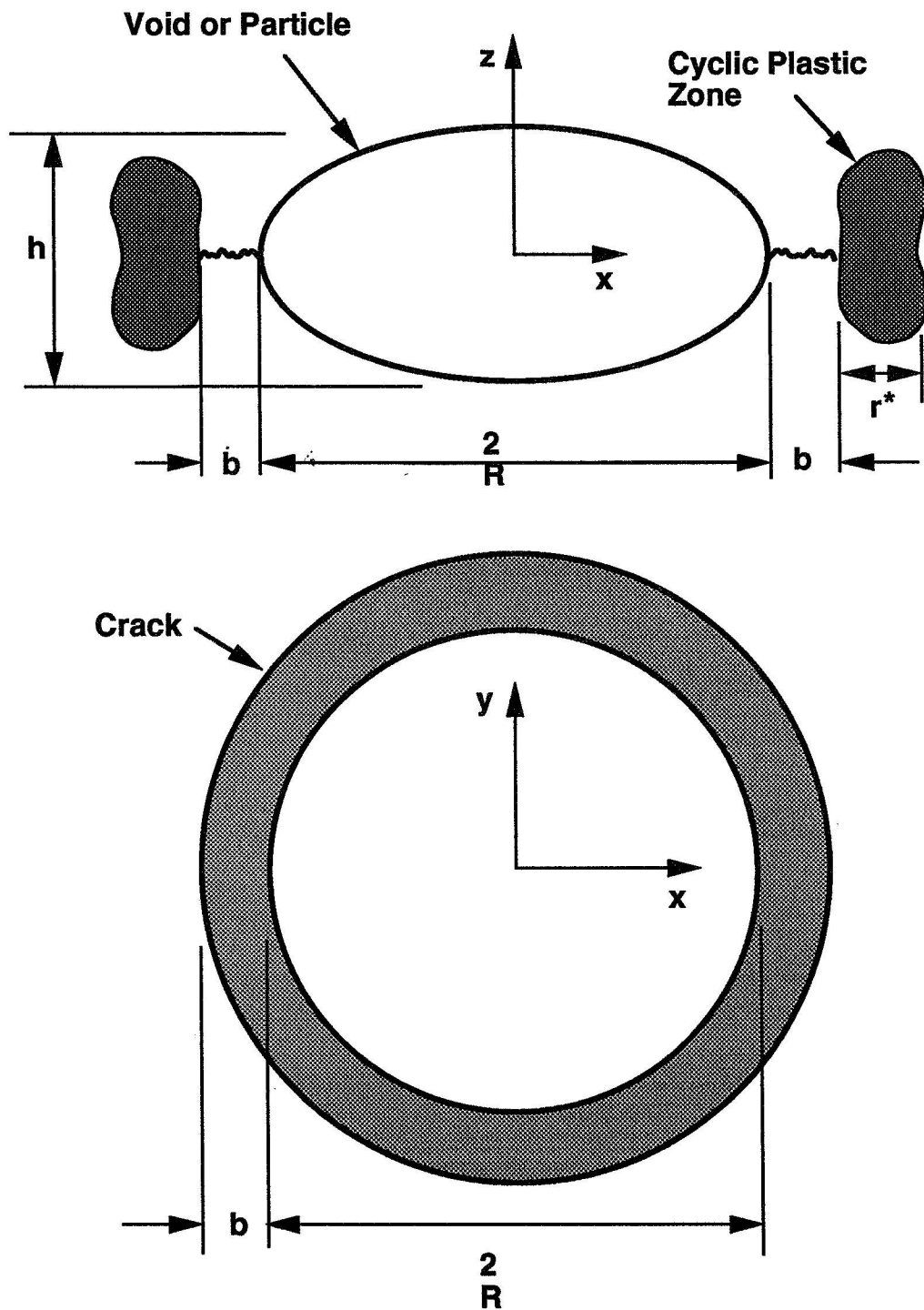


Figure 1. Model for the initial crack size from an ellipsoidal inhomogeneity.

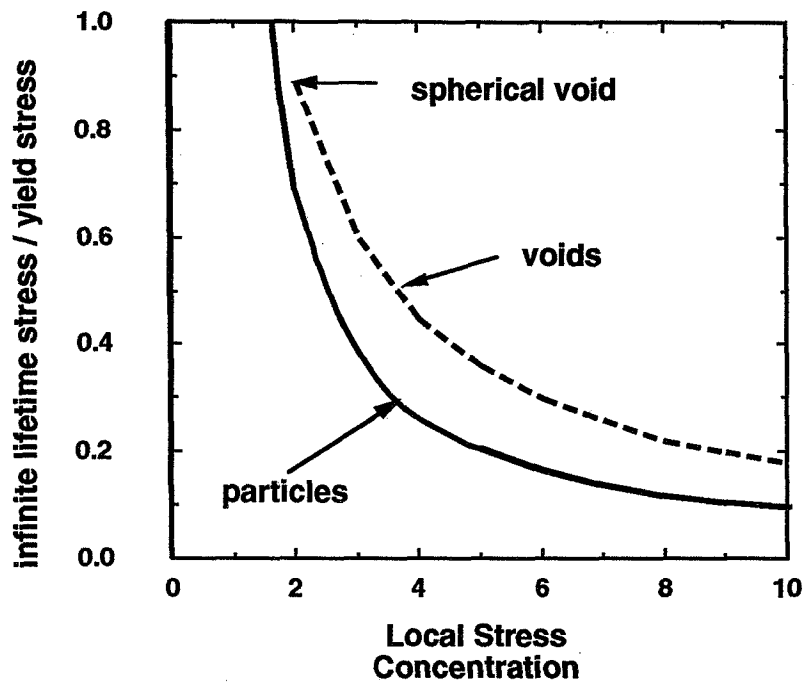


Figure 2. Sensitivity of threshold stress to stress concentration.

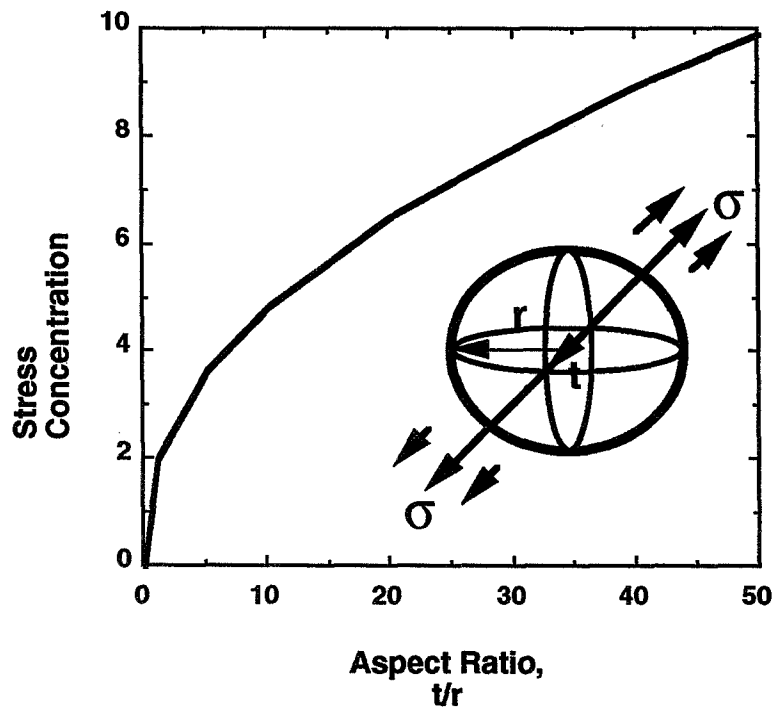


Figure 3. Stress concentration for a circular cavity of elliptical cross-section.

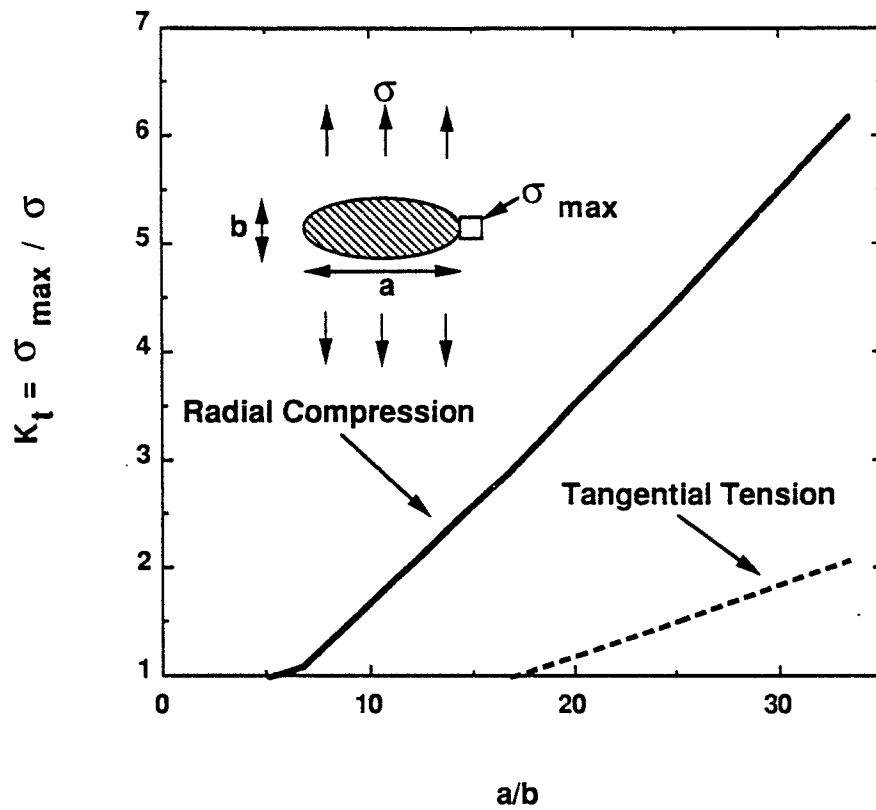


Figure 4. Stress concentration factors for isolated rigid, elliptical, cylindrical inclusion

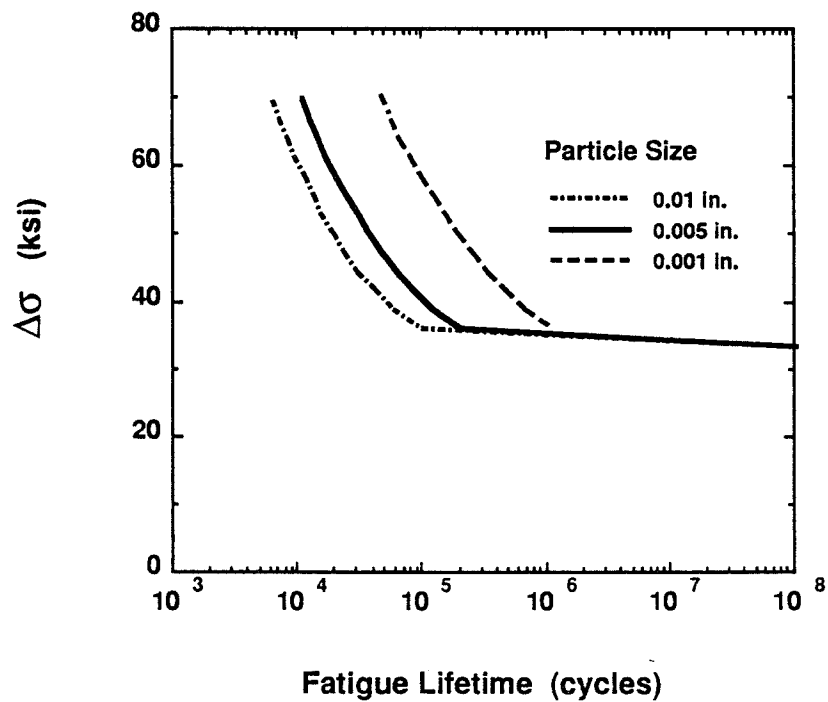


Figure 5. Sensitivity of fatigue lifetime curve to particle size for yield strength of 70 ksi.

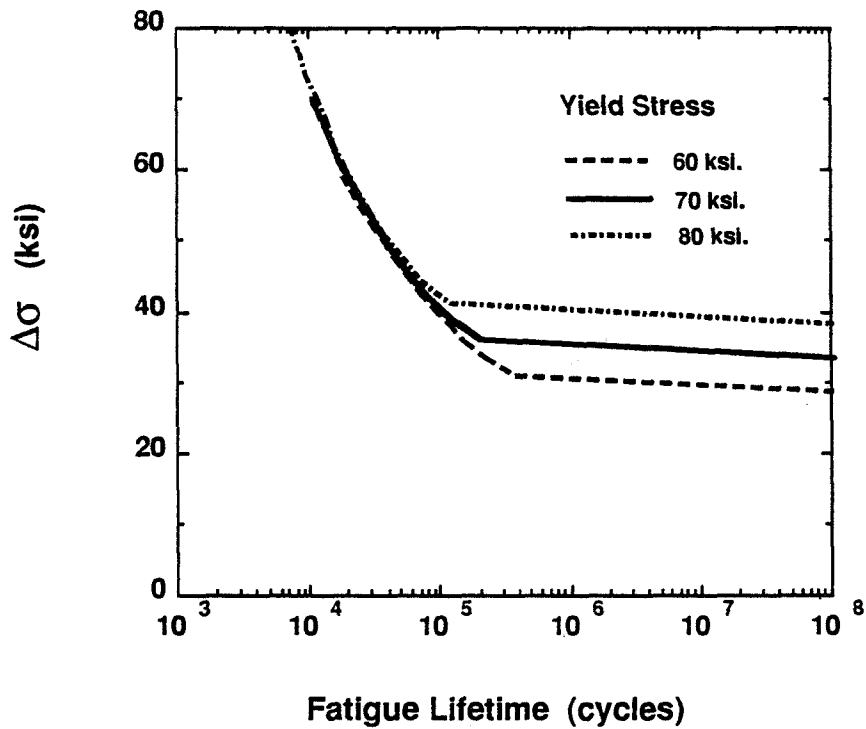


Figure 6. Sensitivity of fatigue lifetime curve to yield stress for particle size of 0.005 in., $k = 2$.

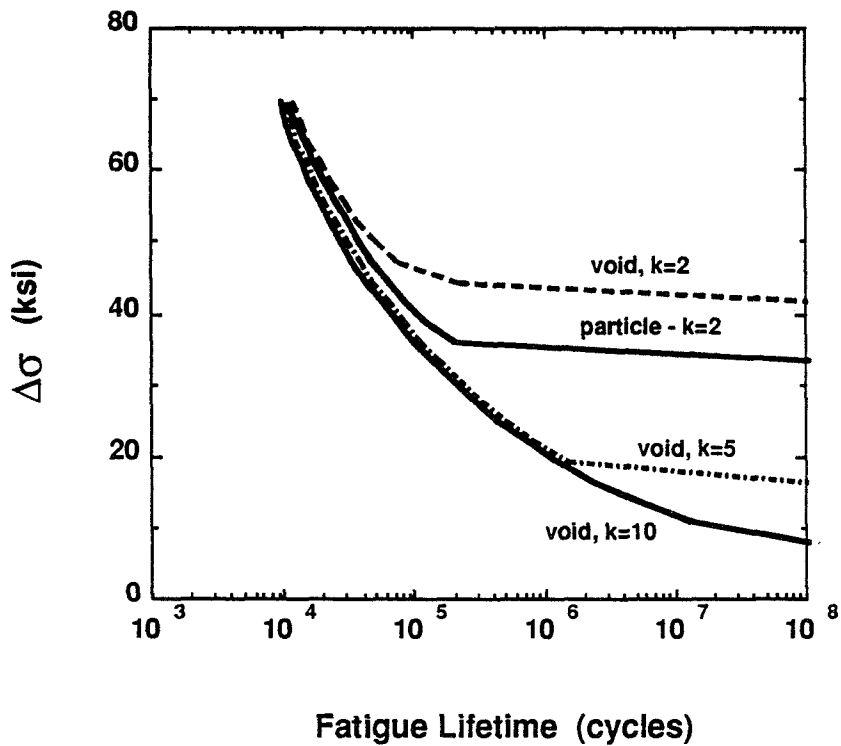


Figure 7. Comparison of fatigue lifetime curves for particles and voids at different particle shapes for yield strength 70 ksi., particle size = 0.005 in.

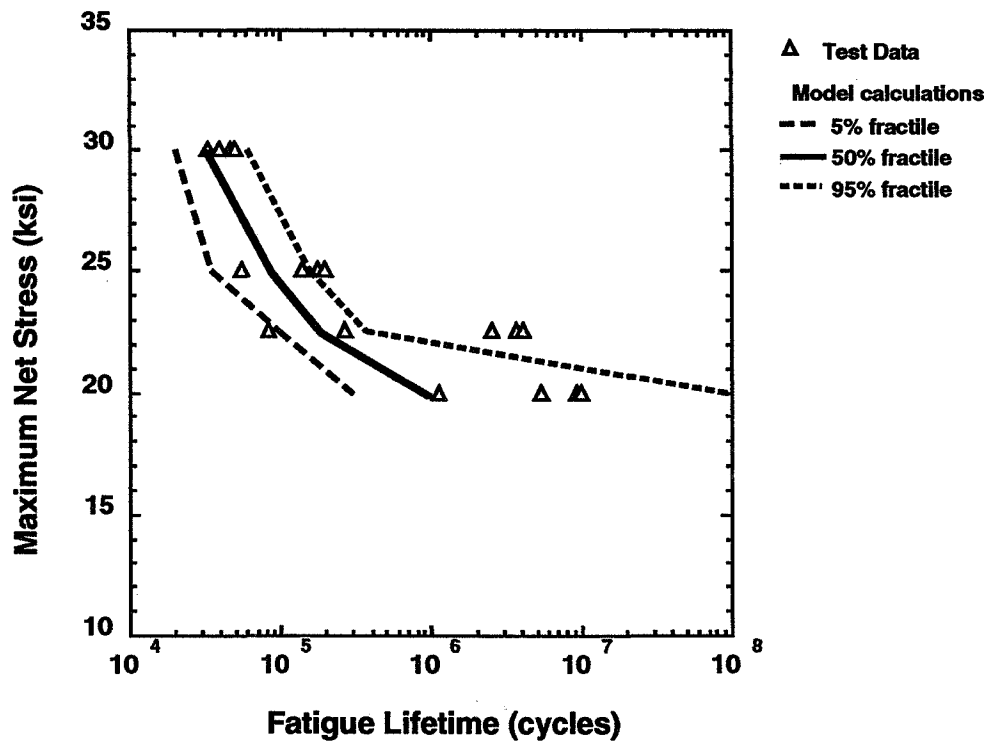


Figure 8. Calculated stress versus life curves for Material A along with the open hole fatigue test data. Tests conducted at $R=0.1$, LT orientation, $\text{freq.}=30$ Hz, lab air.

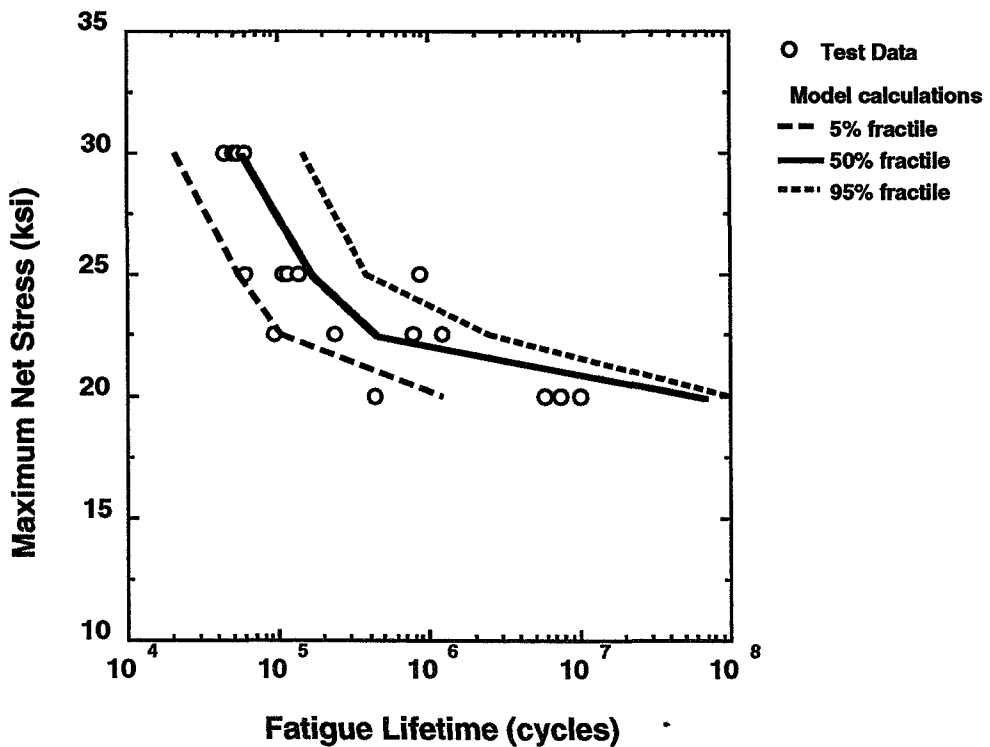


Figure 9. Calculated stress versus life curves for Material B along with the open hole fatigue test data. Tests conducted at $R=0.1$, LT orientation, $\text{freq.}=30$ Hz, lab air.

David Broek
FractureResearch, Inc.
Galena, OH 43021 USA

David Y. Jeong
U.S. Department of Transportation
Research and Special Programs Administration
Volpe National Transportation Systems Center
Cambridge, MA 02142 USA

Douglas Thomson
Foster-Miller, Inc.
Waltham, MA 02154 USA

SUMMARY

An experimental and analytical investigation of multiple cracking in various types of test specimens is described in this paper. The testing phase is comprised of a flat unstiffened panel series and curved stiffened and unstiffened panel series. The test specimens contained various configurations for initial damage. Static loading was applied to these specimens until ultimate failure, while loads and crack propagation were recorded. This data provides the basis for developing and validating methodologies for predicting linkup of multiple cracks, progression to failure, and overall residual strength.

The results from twelve flat coupon and ten full scale curved panel tests are presented. In addition, an engineering analysis procedure was developed to predict multiple crack linkup. Reasonable agreement was found between predictions and actual test results for linkup and residual strength for both flat and curved panels. The results indicate that an engineering analysis approach has the potential to quantitatively assess the effect of multiple cracks on the arrest capability of an aircraft fuselage structure.

INTRODUCTION

Multiple cracking has been observed in several airplanes that have been in service for sometime. The term "Widespread Fatigue Damage" (WFD) is commonly used to refer to a type of multiple cracking that degrades the damage tolerance capability of an aircraft structure. Laboratory testing of flat [1] and curved panels [2] has demonstrated that residual strength is reduced when a lead crack is accompanied by several smaller collinear cracks, compared to the case of a single lead crack only. Moreover, the in-flight failure of the fuselage of Aloha Airlines Flight 243 in 1988 is believed to have been caused by the linking of multiple cracks [3] and the associated degradation of the structure's crack arrest capability.

The Federal Aviation Administration Technical Center (FAATC) has initiated several research programs to investigate the effect of multiple cracking on the structural integrity of the aging fleet. One area of research is to quantify the reduction of residual strength due to multiple cracking in various aircraft components. Analytical predictions of residual strength, however, require the application of appropriate criteria to determine coalescence or linkup of multiple cracks. Swift [4] has hypothesized that a lead crack will linkup with smaller, collinearly aligned cracks when the plastic zones from adjacent crack tips join together. Other linkup criteria, such as the crack tip opening angle [5], have also been proposed, but a generally accepted criterion for multiple crack linkup has not been established.

A test program was designed by FractuREsearch, Inc. [6], and implemented by Foster-Miller, Inc., under contract with the John A. Volpe National Transportation Systems Center, to generate data which could be used to validate results from analytical models. These data are especially appropriate for verification of proposed multiple crack linkup criteria. This paper summarizes the test program and some of the analyses that were performed to correlate the experimental data with linkup predictions. Additional details of the experimental and the analytical phases of this work can be found in References [6], [7] and [8].

EXPERIMENTAL PROGRAM

The Foster-Miller test program may be divided into 3 separate series: (1) basic coupon testing, (2) flat panel testing, and (3) curved panel testing. Thus, the test specimen in each test series had an increased level in complexity as testing progressed. The material of the panels in each test series was 2024-T3 alclad aluminum.

Basic Coupon Tests

The first series of tests was conducted on 1-inch wide coupons to determine basic material properties of 2024-T3 alclad aluminum. Nine (9) coupons were used with varying skin thickness and grain orientation. Average values of yield strength, ultimate strength, and percent elongation for each coupon combination are listed in Table 1.

Table 1. Mechanical Properties of 2024-T3 Aluminum.

Direction/ Thickness (inch)	Yield Strength (ksi)	Ultimate Strength (ksi)	Percent Elongation
Longitudinal/0.040	51.9	64.4	13.9
Transverse/0.040	43.7	63.8	13.7
Transverse/0.080	44.1	66.6	13.8

Flat Panel Tests

The flat panel series was comprised of 12 panels with various multiple crack configurations, shown schematically in Figure 1. These flat panels were unstiffened, with a width of 20 inches and thickness of 0.040 inch. The first three panels contain single cracks only, while the other nine contain a lead crack with one, two or three smaller collinear cracks

ahead of each crack tip. Figure 1 also lists the stresses at linkup and at failure for each panel. In some cases, panel failure and linkup occurred simultaneously. For example, the stress at failure in Panel 7 coincides with the stress at linkup for all three ligaments.

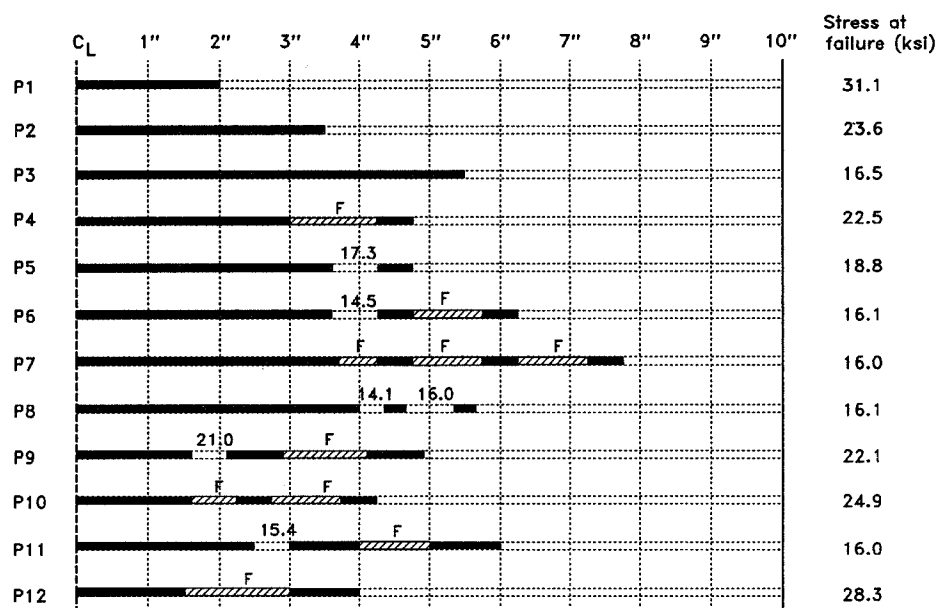


Figure 1. Summary of flat panel tests.

Curved Panel Tests

The full-scale test facility designed and built by Foster-Miller, Inc. was utilized in the curved panel test series. A description of this unique facility can be found in References [2] and [9].

Both unstiffened and stiffened panels were used in this series. The panels have a radius of curvature of 75 inches. The dimensions of the panel test section are 68 inches along the circumference by 120 inches along the width. The curved panels were made from the same batch of 0.040-inch thick 2024-T3 alclad aluminum as the flat panels. Three unstiffened curved panels were tested. The crack configurations for these panels are shown schematically in Figure 2. Six (6) stiffened curved panels were tested. Crack arresters in

the form of tear straps were attached to the skin by two columns of rivets as well as an adhesive bond. Two different tear strap designs, referred to as "light" and "heavy" were used - 4 panels had "light" tear straps and 2 with "heavy" tear straps (see Figure 3). Table 2 lists the relevant dimensions of these two tear strap designs.

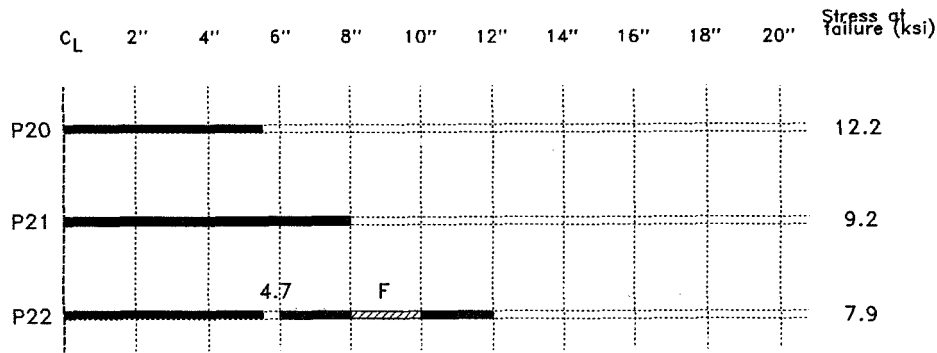


Figure 2. Summary of unstiffened curved panel tests.

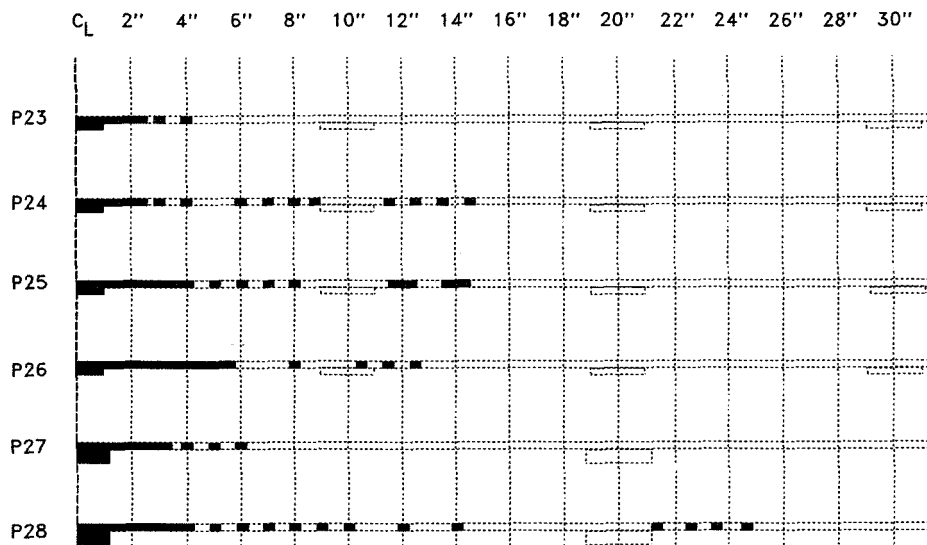


Figure 3. Summary of stiffened curved panel tests.

Table 2. Dimensions of Tear Strap Designs

	Light	Heavy
Thickness (inch)	0.04	0.08
Width (inches)	2.00	2.50
Cross sectional area (inch ²)	0.08	0.20
Longitudinal spacing (inches)	10.0	20.0

CORRELATION OF TEST DATA WITH ANALYSIS

Swift's criterion [4] for linkup of multiple cracks can be expressed mathematically as

$$r_p(\alpha) + r_p(b) = L \quad (1)$$

where $r_p(\alpha)$ and $r_p(b)$ refer to the extent of the plastic zones ahead of the two adjacent cracks and L is the distance between crack tips or the ligament length (Figure 4). Note that in Figure 4, the lead or main crack has a total length of 2α , while the length of the smaller crack is $2b$. One approach¹ to determine the extent of crack tip plasticity is to use the Dugdale equation [10]:

$$r_p = \frac{\pi}{8} \left(\frac{K_I}{\sigma_p} \right)^2 \quad (2)$$

where σ_p is the yield strength of the material. Also, K_I is the stress intensity factor which can be written as

$$K_I = \sigma_o \beta \sqrt{\pi \alpha} \quad (3)$$

where σ_o is the far field stress and β is a geometric correction factor that accounts for effects such as crack interaction, finite width, and crack face bulging.

¹ References [6] and [8] describe other models that can be used to determine the size of the plastic zone ahead of the crack tip.

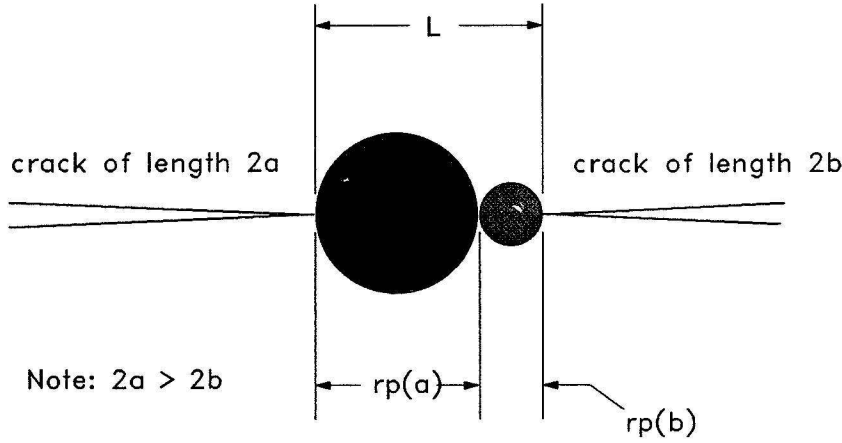


Figure 4. Schematic of linkup criterion based on plastic zone size.

The far field stress at linkup can be determined by combining equations (1), (2), and (3):

$$\sigma_o = \sigma_p \sqrt{\frac{8L}{\pi^2 [\beta(a)^2 a + \beta(b)^2 b]}} \quad (4)$$

The correction factors for crack interaction, $\beta(a)$ and $\beta(b)$, can be found in handbooks such as Reference [11]. Predictions for multiple crack linkup have been made using equation (4) assuming the yield strength of 2024-T3 aluminum to be 50 ksi. Table 3 compares linkup predictions with the experimental results for the various flat panels. On average, the predictions overestimate the actual linkup stresses by 4.7%. The accuracy of the linkup predictions appears to be affected by the ligament length; the percent difference between predicted stresses and test data increases with ligament length.

Predictions for multiple crack linkup can be modified to include the effect of stable tearing [12]. Stable tearing affects the linkup analysis by reducing the distance between cracks which also increases the stress intensity factors due to interaction. The amount of stable tearing can be calculated using the following two-parameter R-curve equation that was derived from a regression analysis of the flat panel test data:

$$K_R = 106.1 \Delta \alpha^{0.212} \quad (5)$$

When the effect of stable tearing is included in the analysis, an iterative procedure must be used to solve equation (4) because the distance between crack tips, L , depends on the amount of stable tearing, Δa , which is a function of the far field stress, σ_o . Table 3 also lists the linkup predictions when stable tearing is included in the analysis. Predictions with stable tearing included are within 2% of the experimental data, on average.

Table 3. Correlations Between Flat Panel Test Data and Analysis

(a) First Linkup

Specimen	Crack Dimensions (inches)			Prediction σ_o (ksi) and Percent Difference from Test Result				Test Result
	a	b	L	<i>NO Stable Tearing</i>		<i>With Stable Tearing</i>		σ_{EXP} (ksi)
P4	3.00	0.25	1.25	26.8	+18.9%	23.8	+5.9%	22.5
P5	3.60	0.25	0.65	17.0	-2.0%	16.1	-6.8%	17.3
P6	3.80	0.25	0.45	13.3	-8.6%	12.9	-11.3%	14.5
P7	3.70	0.25	0.55	15.2	-5.2%	14.6	-9.0%	16.0
P8	4.00	0.15	0.35	11.8	-16.1%	11.6	-18.0%	14.1
P9	1.60	0.40	0.50	19.3	-8.1%	18.8	-10.7%	21.0
P10	1.60	0.25	0.65	24.7	+1.0%	23.4	-5.9%	24.9
P11	2.50	0.50	0.50	15.2	-1.5%	14.8	-4.2%	15.4
P12	1.50	0.50	1.50	36.8	+30.1%	32.8	+15.8%	28.3

(b) Second Linkup

Specimen	Crack Dimensions (inches)			Prediction σ_o (ksi) and Percent Difference from Test Result				Test Result σ_{EXP} (ksi)
	a	b	L	<i>NO Stable Tearing</i>		<i>With Stable Tearing</i>		
P6	4.75	0.25	1.00	19.0	+18.1%	17.4	+8.3%	16.1
P8	4.65	0.15	0.70	16.3	+2.2%	15.4	-3.8%	16.0
P9	2.90	0.40	1.20	25.3	+14.6%	22.9	+3.8%	22.1
P11	4.00	0.50	1.00	19.1	+19.2%	17.7	+10.5%	16.0

Pressurization of a curved panel containing a longitudinal crack creates in-plane and out-of-plane deformations of the crack faces which is generally referred to as bulging. Physically, crack face bulging causes local bending at the crack tips which increases the effective stress intensity factor. In an engineering analysis, the stress intensity factor for a curved panel can be calculated by multiplying the stress intensity factor for a flat panel by an appropriate bulging factor. Thus, the same approach used to predict multiple crack linkup in flat panels can be applied to curved panels if the bulging factor is known. The following bulging factor was used in the subsequent analyses of curved panels [13]:

$$\beta_B = \sqrt{1 + \alpha \left[\left(\frac{E}{\sigma_o} \right) \left(\frac{\alpha}{R} \right)^2 \right]^{\frac{2}{3}}} \quad (6)$$

where E is the modulus of elasticity of the panel material (10 msi), σ_o is the far field stress, α is the half-crack length, R is the radius of curvature (75 inches), and α is an empirical constant (0.671)². This bulging factor was derived by assuming that the R-curve data for unstiffened flat and curved panels is the same [13]. The applicability of other bulging factors is also discussed in Reference [13].

Table 4 lists the linkup predictions for curved unstiffened panels based on using Swift's criterion [4] with the Dugdale plastic zone model and equation (6) for the bulging factor. The yield strength of 2024-T3 alclad aluminum was assumed to be 50 ksi. The agreement between test data and analysis is reasonable, and improves when the effect of stable tearing is included.

Table 4. Correlations Between Unstiffened Curved Panel Test Data and Analysis

	Crack Dimensions (inches)			Prediction σ_o (ksi) and Percent Difference from Test Result				Test Result
	a	b	L	<i>NO Stable Tearing</i>		<i>With Stable Tearing</i>		σ_{EXP} (ksi)
1st Linkup	5.50	1.00	0.50	5.0	+6.4%	4.8	+2.1%	4.7
2nd Linkup	8.00	1.00	2.00	9.9	+25.3%	7.3	-7.6%	7.9

² The numbers in parentheses refer to the values assumed in the analysis.

Analyses were also performed to account for the effect of stiffening in curved panels due to tear straps. Stiffening affects the calculation of the stress intensity factor and the bulging factor. A displacement compatibility approach [14] was employed to calculate stress intensity factors in cracked stiffened panels. This approach can be used to account for such effects as rivet flexibility, biaxial stress, and broken or intact center stiffeners. Rivets are modelled as springs with linear flexibility in the circumferential direction³. Swift [15] has derived an empirical formula to calculate the linear flexibility ($1/k$) of aluminum rivets:

$$\frac{1}{k} = \frac{1}{Ed} \left[5.0 + 0.8d \left(\frac{1}{t_1} + \frac{1}{t_2} \right) \right] \quad (7)$$

where E is the modulus of elasticity of the sheet material, t_1 and t_2 are the thicknesses of the joined sheets, and d is the rivet hole diameter.

Since the displacement compatibility method calculates stress intensity factors for a flat, cracked, stiffened panel, an appropriate bulging factor must be assumed. In the present analysis, equation (6) was modified by using a damping factor that was proposed by Swift [16]. This damping factor assumes that bulging is greatest at midbay, and is minimized at the stiffener locations. Thus, the following bulging factor was used to account for stiffening:

$$\beta_B = \sqrt{1 + \alpha \left[\left(\frac{E}{\sigma_o} \right) \left(\frac{\alpha}{R} \right)^2 \right]^{\frac{2}{3}} \left[1 - \cos \left(\frac{2\pi\alpha}{L} \right) \right]} \quad (8)$$

where L is the tear strap spacing (from Table 2, this spacing is 10 inches for light tear straps and 20 inches for heavy tear straps).

Table 5 lists the results from the correlations between analytical predictions and test data for curved panels. While most of these panels contained more than two cracks (recall Figure 3), only the first two linkup stresses are included in Table 5 for brevity. The effect

³ Nonlinear rivet flexibility can also be modelled in the displacement compatibility approach by implementing an iterative solution procedure and a piecewise linear flexibility curve.

of stable tearing has been included in the analytical predictions listed in Table 5. In general, the agreement between analysis and experiment for linkup stress is good. The engineering analysis predicts linkup stresses with 10% of the test results in the cases where the ligament length is less than 0.5 inch. When the distance between cracks is 0.5 inches or greater, the linkup predictions differ from the test result by more than 20%. These differences are comparable to those observed in the flat correlations. In terms of overall panel failure, predictions for panels with light tear straps are within 25% of the experimental results. Predictions for panels with heavy straps overestimate the observed values by as much as 77%. Considering the uncertainty associated with the bulging factor, the general trend of the results produced by the engineering approach described in this paper appears encouraging.

*Table 5. Correlations Between Curved Panel Test Data and Analysis
(Far field stress, in ksi)*

Panel	First Linkup			Second Linkup			Panel Failure		Comments
	<i>Predict</i>	<i>Test</i>	<i>L(a)</i>	<i>Predict</i>	<i>Test</i>	<i>L(a)</i>	<i>Predict</i>	<i>Test</i>	
22	4.8	4.7	0.5	7.3	7.9	2.0	7.3	7.9	Unstiffened
23	10.6	11.3	0.2	11.9	15.2	0.6	23.1	22.1	Light tear straps
24	10.6	11.3	0.2	11.9	15.2	0.6	20.9	18.0	Light tear straps
25	11.4	11.1	0.	11.4	11.1(b)	0.6	21.1	16.9	Light tear straps
26	-	N/A	-	-	N/A	-	15.9	16.9(b)	Light tear straps
27	10.9	10.9	0.3	12.4	11.8	0.6	20.0	13.3(d)	Heavy tear straps
28	11.9	9.9	0.5	11.9	9.9	0.6	17.5	9.9	Heavy tear straps

NOTES:

- (a) L = Ligament length or distance between cracks (in inches).
- (b) Stress at linkup for first 4 ligaments.
- (c) Initially, test was conducted with INTACT center stiffener. The test was restarted after the center stiffener was intentionally cut.
- (d) Test fixture ran out of stroke before panel failure. Therefore, the recorded failure pressure is probably too low.

CONCLUSIONS

- (1) Tests on 20-inch wide, flat, unstiffened panels demonstrated that residual strength is reduced when a lead crack is accompanied by several smaller, collinear cracks.
- (2) Using Swift's proposed criterion for multiple crack linkup [4] and Dugdale's plastic zone model, predictions can be obtained to give reasonable agreement with experimental data. Predictions of multiple crack linkup for flat panels averaged within 5% of the experimental data.
- (3) The effect of stable tearing can be included in predictions of multiple crack linkup by using an iterative solution procedure. Using the Dugdale plastic zone model, predictions of linkup in flat panels averaged within 2% of the experimental data when stable tearing was included.
- (4) Ligament length or distance between crack tips appears to affect the accuracy of predictions for multiple crack linkup. Predictions are more accurate when the ligament length is less than 0.5 inches.

Acknowledgement - The research described in this paper was performed in support of the Federal Aviation Administration Technical Center's Aging Aircraft Research Program. The support and interest from Dr. Michael L. Basehore at FAATC is gratefully appreciated by the authors.

REFERENCES

- [1] Maclin, J.R.: Performance of Fuselage Pressure Structure, *1991 International Conference on Aging Aircraft and Structural Airworthiness*, NASA CP-3160, Washington, D.C., 1992, pp. 67-75.
- [2] Samavedam, G.; Hoadley, D.; and Thomson, D.: Full-Scale Testing and Analysis of Curved Aircraft Fuselage Panels, Final Report, DOT/FAA/CT-93/78, DOT-VNTSC-FAA-93-10, December 1993.
- [3] National Transportation Safety Board: Aircraft Accident Report - Aloha Airlines, Flight 243, Boeing 737-200, N737-200, N73711, near Maui, Hawaii, April 28, 1988, NTSB/AAR-89/03, PB89-910404, June 1989.
- [4] Swift, T.: Damage Tolerance Capability, *Specialists Conference on Fatigue of Aircraft Materials*, Delft University of Technology, October 1992.
- [5] Newman, J.C.; Dawicke, D.S.; Sutton, M.A.; and Bigelow, C.A.: A Fracture Criterion for Widespread Cracking in Thin-Sheet Aluminum Alloys, *17th ICAF Symposium on Durability and Structural Integrity of Airframes*, Stockholm, Sweden, June 1993.
- [6] Broek, D.: The Effects of Multi-Site Damage on the Arrest Capability of Aircraft Fuselage Structures, FractuREsearch Report No. TR 9302, June 1993.
- [7] Thomson, D.; Hoadley, D.; and McHatton, J.: Load Tests of Flat and Curved Panels with Multiple Cracks, Foster-Miller Draft Final Report to Volpe Center, September 1993.
- [8] Jeong, D.Y.: Analysis of Residual Strength Tests on Flat and Curved Panels with Multiple Cracks, Volpe Center Draft Final Report, October 1993.
- [9] Samavedam, G.; and Hoadley, D.: Fracture and Fatigue Strength Evaluation of Multiple Site Damaged Aircraft Fuselages - Curved Panel Testing and Analysis, Final Report, DOT/FAA/CT-94/10, DOT-VNTSC-FAA-93-8, January 1994.
- [10] Dugdale, D.S.: Yielding of Steel Plates Containing Slits, *Journal of the Mechanics and Physics of Solids* 8, 1960, pp. 100-108.
- [11] Tada, H.; Paris, P.; and Irwin, G.: *The Stress Analysis of Cracks Handbook*, Second Edition, Paris Productions, Inc., 1985.
- [12] Tong, P.; Greif, R.; Chen, L.; and Jeong, D.Y.: Damage Tolerance of Fuselage Panels with Widespread Fatigue Damage, *17th ICAF Symposium on Durability and Structural Integrity of Airframes*, Stockholm, Sweden, June 1993.

- [13] Jeong, D.Y.; and Tong, P.: Nonlinear Bulging Factor Based on R-Curve Data, *FAA/NASA International Symposium on Advanced Structural Integrity Methods for Airframe Durability and Damage Tolerance*, NASA CP-3274, 1994.
- [14] Swift, T.: The Effects of Fastener Flexibility and Stiffener Geometry on the Stress Intensity Factor in Stiffened Cracked Sheet, *Prospects of Fracture*, Noordhoff International, Leyden, The Netherlands, 1974, pp. 419-536.
- [15] Swift, T.: Development of the Fail-Safe Design Features of the DC-10, *Damage Tolerance in Aircraft Structures, ASTM STP 486*, American Society for Testing and Materials, Philadelphia, PA, 1971, pp. 164-214.
- [16] Swift, T.: Design of Redundant Structures, *Fracture Mechanics Design Methodology*, AGARD-LS-97, North Atlantic Treaty Organization, London, England, 1979.

PROBABILISTIC INSPECTION STRATEGIES FOR MINIMIZING SERVICE FAILURES 348619

Abraham Brot
TASHAN Engineering Center
Israel Aircraft Industries
Ben-Gurion Airport, Israel

58-39

23/02

P-10

SUMMARY

The **INSIM** computer program is described which simulates the "limited fatigue life" environment in which aircraft structures generally operate. The use of **INSIM** to develop inspection strategies, which aim to minimize service failures, is demonstrated. Damage-tolerance methodology, inspection thresholds and customized inspections are simulated using the probability of failure as the driving parameter.

INTRODUCTION

Aircraft structures generally have a limited fatigue life. Sooner or later, cracks develop at critical locations. These cracks propagate and, unless detected and repaired, will eventually result in a failure. There are three, mutually exclusive, possible outcomes of the fatigue process:

- (1) The aircraft may reach the end of its operational life and be retired from service. The retired aircraft may or may not have undetected cracks at critical locations.
- (2) A crack may be detected during maintenance operations. The affected part is usually repaired or replaced.
- (3) A crack reaches its critical size undetected and the structure fails in service.

It is the aim of the fatigue engineer to minimize the probability of failure during the service life. Damage-tolerance methodology serves this purpose by requiring or encouraging the following:

- (1) Moderate stress levels resulting in long crack initiation and propagation lives;
- (2) rationally determined NDI methods and intervals;
- (3) fail-safe or crack-arrest design features to avoid catastrophic failures.

However, over the past 10-15 years, a trend has developed in which aircraft are being operated much longer before retirement. For many aircraft models, high-time aircraft greatly exceed original design life goals (Reference 1). With increased service usage, the NDI methods and

intervals originally specified may prove to be inadequate for avoiding failures and new strategies must be developed in order to minimize failures in service.

SIMULATION OF THE FATIGUE PROCESS AND ITS DETECTION

A simulation method has been developed to provide strategies for the optimum scheduling of structural inspections. The **INSIM** (**IN**spection **SIM**ulation) computer program has been written to simulate the "limited fatigue life" environment. Using **INSIM**, various inspection methods and intervals can be evaluated for selected parameters, and the resulting probability of failure can be determined.

INSIM contains four probabilistic simulations:

- (1) Service life variation is provided by a normal distribution defined by a mean and high-time ($+3\sigma$) expected service life.
- (2) Crack initiation life is described by a two-parameter (shape factor and characteristic life) Weibull distribution.
- (3) Crack growth variation is characterized by a normal distribution defined by a mean rate and an extreme ($\pm 3\sigma$) variation.
- (4) NDI probability of detection is modelled by a three-parameter (shape factor, characteristic length and minimum detectable length) Weibull distribution.

INSIM performs a simulation of a single critical location in an entire fleet of aircraft. Cracks initiate at various times and grow at variable rates in each aircraft. Inspections are performed according to a predetermined schedule, using as many as six different NDI methods. Cracks are detected during these inspections according to the statistical expectation of detection. As the simulation proceeds from aircraft to aircraft, cracks are detected, aircraft are retired from service or failures occur. The computer acts as a scorekeeper, amasses the statistics and summarizes the results. In order to provide statistical significant results, a large number of simulations must be performed. In a typical simulation, 100,000 inspections will be performed for a fleet of 30,000 aircraft.

The program determines, for the parameters selected:

- (1) The probability of an aircraft reaching retirement, uncracked at the critical location.
- (2) The probability of an aircraft retiring with an undetected crack.
- (3) The probability of detecting a crack before it reaches the size dictated by the damage-tolerance regulations.

(4) The probability of detecting a crack larger than the above, but less than the size required for failure.

(5) The probability of a failure occurring during the service life.

Based on these results, optimum NDI methods and intervals can be selected to provide a required level of safety and cost effectiveness. A typical **INSIM** output is shown in Table 1.

The method is especially well suited for developing inspection strategies for multiple-site or widespread fatigue damage situations.

Table 1. A Typical Example of INSIM Results

SUMMARY & STATISTICS

Fleet size:	30000	Threshold:	10000	Interval(s):	4000
Mean service life:	29965			High-time aircraft:	45463
Min. crack initiation:	7104			Max. crack initiation:	150598
Min. crack growth:	11376			Max. crack growth:	17285
Inspections performed:	164488			Inspections per aircraft:	5.48

	Number of Aircraft	Percent
Aircraft retired uncracked:	29309	97.70%
Aircraft retired cracked:	494	1.65%
Cracks < A_p detected:	187	0.62%
Cracks > A_p detected:	3	0.0100%
Failures:	7	0.02333%

SELECTING INSPECTION STRATEGIES USING INSIM

The **INSIM** computer program can be used to select inspection strategies that minimize the probability of failure in service. Several examples will be shown to demonstrate this feature.

The Primary Strategy -- Damage-Tolerance Methodology

The damage-tolerance regulations implicitly require the use of moderate stress levels and rationally determined NDI methods and intervals. This results in several benefits such as: long crack initiation lives, long crack growth lives, relatively large critical crack sizes and ample opportunities to detect cracks. Thus, damage tolerance methodology can be considered to be the primary strategy for minimizing service failures.

Figure 1 compares the probability of failure for a typical location designed to damage-tolerance requirements compared to one designed to safe-life requirements.

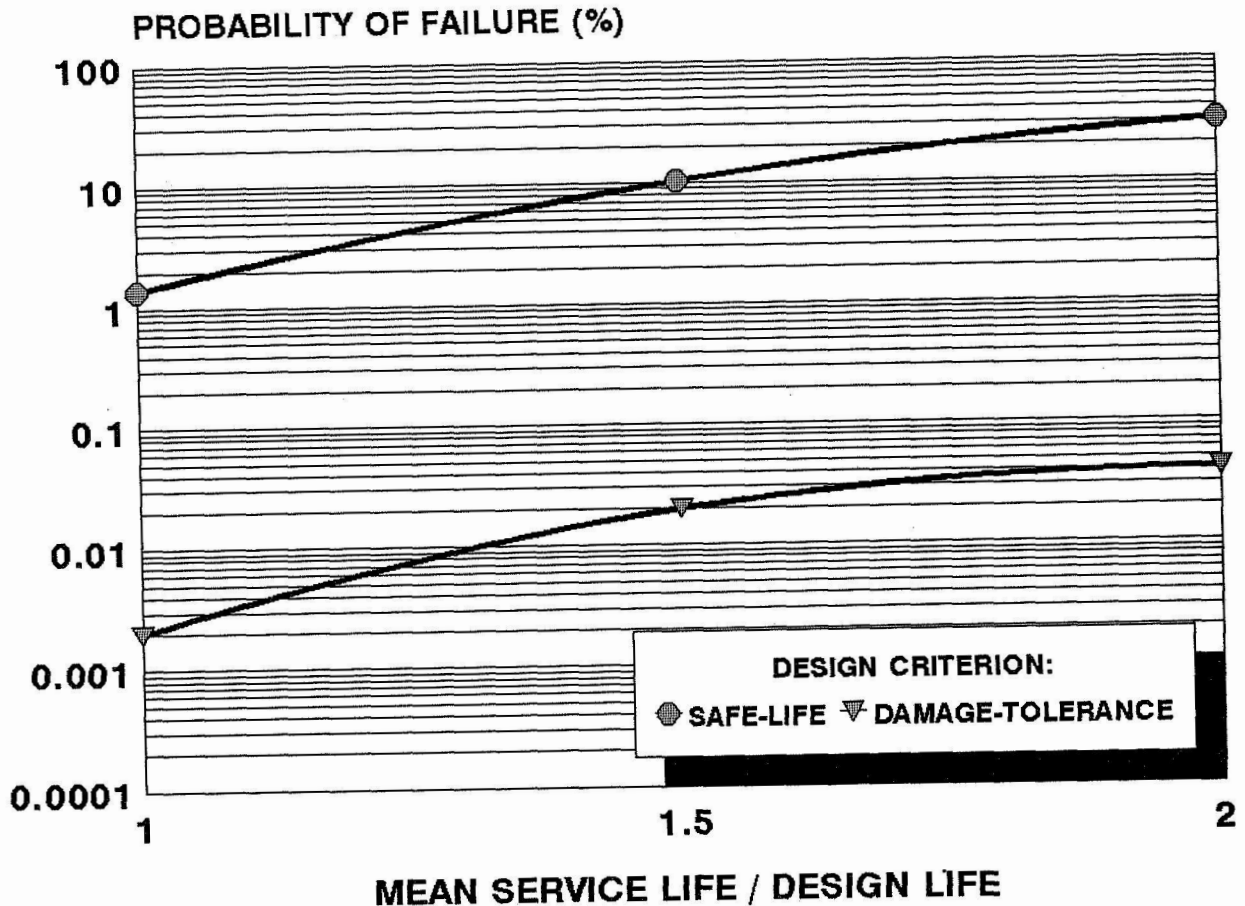


Figure 1. Effect of mean service life on the probability of failure.

The safe-life requirements assume a mean crack initiation life of two design lifetimes and an inspection interval of half the design lifetime. Implementation of the FAR-25 damage-tolerance requirements resulted in a 21% reduction in allowable stress level and set an inspection interval of 20% of the design lifetime.

Figure 1 shows that the probability of failure, for a mean service life equal to the design life, is 1.4% for the safe-life design while it is only 0.002% for the location designed according to the damage tolerance criterion. As the mean service life of the fleet increases, so does the probability of failure. Figure 1 indicates, for a mean service life equal to twice the design life, the probability of failure is 31% for the location designed to the safe-life criterion. The corresponding value for the location designed to be damage-tolerant is only 0.04%.

There is a commonly expressed belief that a structure, designed to the damage-tolerance requirements, is not affected by an extension in service life, since the assumed fatigue damage reverts to a predetermined value after each inspection that did not detect a crack. If this is true, there need not be any limitations on the acceptable service life of an aircraft. Even without considering corrosion damage, which is time dependant, the total life view of **INSIM** shows that this premise is not true, and the probability of failure increases with increased service life. This is obviously due to the fact that, for the overwhelming number of locations (more than 99%), aircraft can be expected to retire from service without any cracks being detected, as is shown in Table 2. As the service life increases with respect to the design life, less aircraft retire without cracks being detected. Most of the difference is reflected by the number of cracks detected by NDI. However, it is inevitable that some of the difference is accounted for by unsuccessful inspections which lead to service failures. Therefore, it is clear that the probability of failure increases with service usage -- even in locations designed according to the damage-tolerance criteria.

TABLE 2. Typical Distribution of Possible Outcome at a Location

POSSIBLE OUTCOME AT LOCATION	MEAN SERVICE LIFE / DESIGN LIFE		
	1.0	1.5	2.0
Retired from service before detection of crack	99.97%	99.73%	99.06%
Crack detected by NDI	0.03%	0.25%	0.90%
Failure in service	0.00%	0.02%	0.04%
T O T A L	100.00%	100.00%	100.00%

As usage severity increases, it can be expected that the probability of failure will increase. This is illustrated in Figure 2 for locations designed according to the safe-life and damage-tolerance criteria. Usage severity is characterized here by an increase in the spectrum stress level. As is shown in Figure 2, under a 20% increase in usage severity, the probability of failure for the safe-life design can reach 55%. For the damage-tolerance design, even under these adverse conditions, the probability of failure only reaches 0.13%.

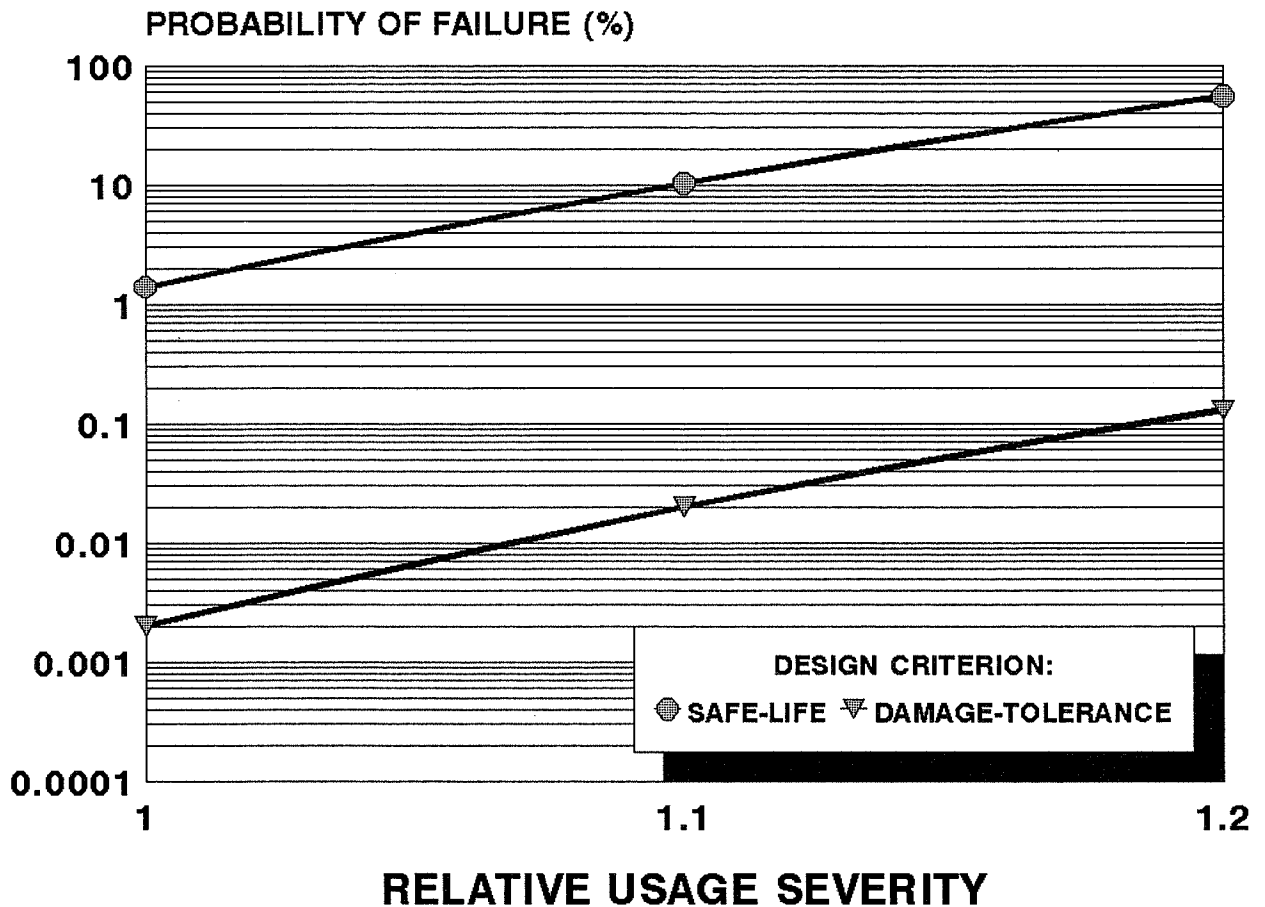


Figure 2. Effect of usage severity on probability of failure.

These studies, assisted by the **INSIM** program, demonstrate that the damage-tolerance methodology can be considered to be the primary strategy for minimizing service failures. As is shown in Figures 1 and 2, even under adverse conditions of extended service life and usage severity, reasonable probabilities of failures can still be achieved.

The Inspection Threshold -- Friend or Foe?

It is FAA practice to permit, under certain circumstances, delaying the initial inspection to 50% of the design life (See Reference 2). This initial inspection is often called the "inspection threshold".

The concept of an inspection threshold obviously appeals to the manufacturer and operator, who can delay maintenance to a later date. It is assumed that there is only a very small probability that cracks will be detected early in an aircraft designed to be damage-tolerant. Therefore, the initial inspection can be safely delayed until 50% of the design life has been reached.

This premise has been studied, using the **INSIM** computer program, and the results are shown in Figure 3. The parameters used are typical results for a location designed to be damage-tolerant. The mean service life was taken to be equal to the design life. Inspections are performed, after the threshold inspection, at intervals of 20% of the design life.

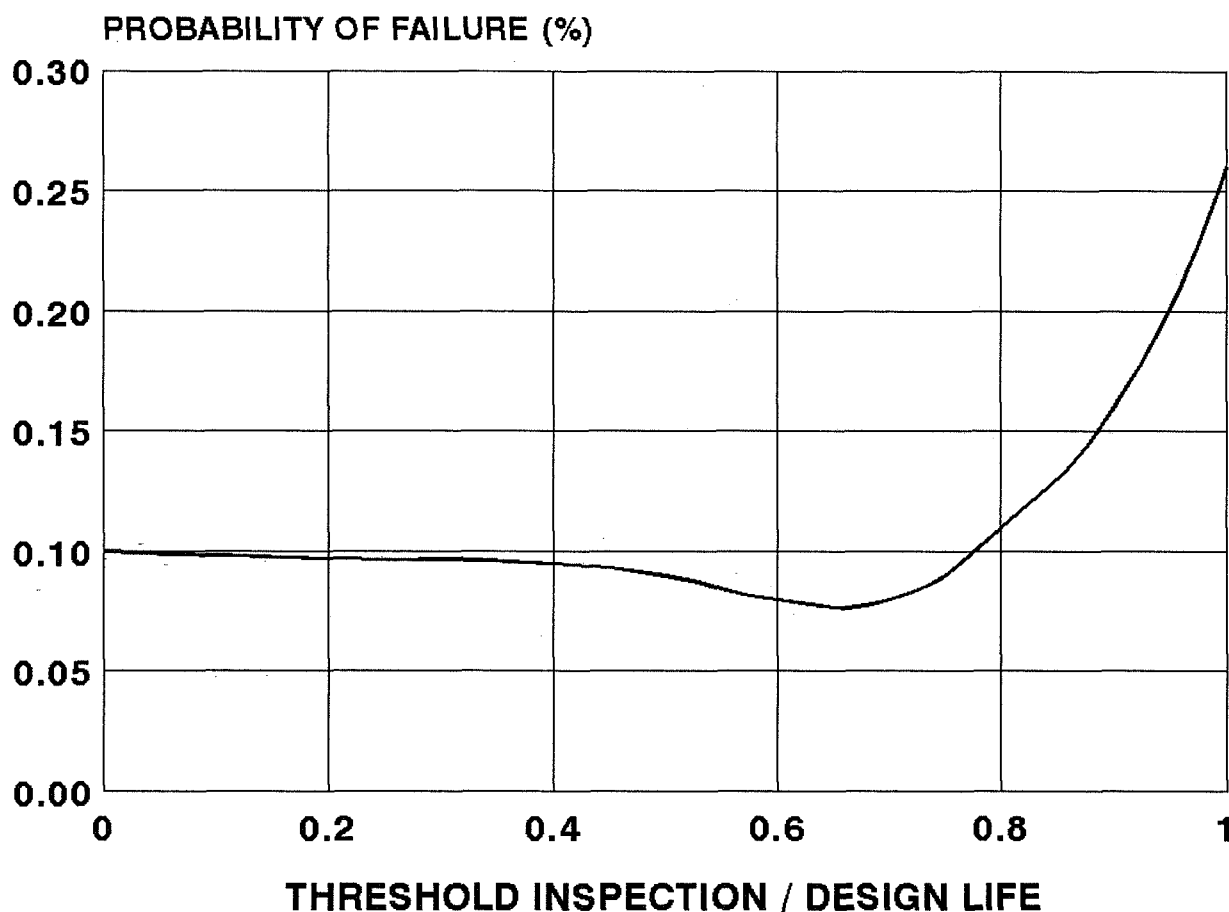


Figure 3. Effect of threshold inspection on the probability of failure.

Figure 3 indicates that the probability of failure remains nearly constant for conditions ranging from no threshold inspection to delaying the threshold inspection to 75% of the design life. In fact, for threshold inspections between 40% and 70% of the design life, there is a slight reduction in the probability of failure. This unexpected phenomenon can be explained by the fact that the presence of a threshold inspection may place the remaining inspections at points on the crack growth curve where crack detection is more probable. Only when the threshold inspection is scheduled for later than 75% of the design life does the probability of failure begin to rise rapidly.

As a result of this study, and similar studies performed using **INSIM** over a wide range of parameters, it can be concluded that there is no adverse effect in scheduling the threshold inspection at 50% of the design life for aircraft that have been designed to damage-tolerance requirements.

Customized Inspections for Minimizing the Probability of Failure

In spite of the virtues of the damage-tolerance methodology in minimizing the probability of failure, adverse situations exist in which conventional inspection intervals are insufficient. In such a case, **INSIM** can be used to select a customized inspection schedule which will reduce the probability of failure to an acceptable level. This will be demonstrated using two examples.

The first example deals with a 2024-T3 plate having several fastener holes. A crack will develop at one fastener hole, eventually severing the ligament and then continue to grow from the opposite side of the hole. The crack continues to grow until it reaches a size critical under service loads, and then failure occurs. Using conventional damage tolerance criteria, the threshold inspection was selected to be 50% of the design life and subsequent inspection intervals were selected to be 20% of the design life, using a liquid penetrant NDI method. Figure 4 indicates the probability of failure for this location which is designated location "A".

When the mean service life equals the design life, Figure 4 indicates that the probability of failure would be 0.05% without any inspections. This is due to the relatively large mean crack initiation life of nearly four design lifetimes. When the inspections prescribed by the damage tolerance criteria are applied, the probability of failure drops to 0.01%.

As the mean service life increases, the probabilities of failure likewise increase, as is illustrated in Figure 4. When the mean service life reaches twice the design life, the probability of failure is 0.55%, even though the inspections are performed in accordance with the damage tolerance requirements. This probability of failure is excessive, and should be reduced. Several customized inspection schedules were studied with the assistance of **INSIM**. Table 3 describes the customized inspection schedule which seemed to be the most cost-effective.

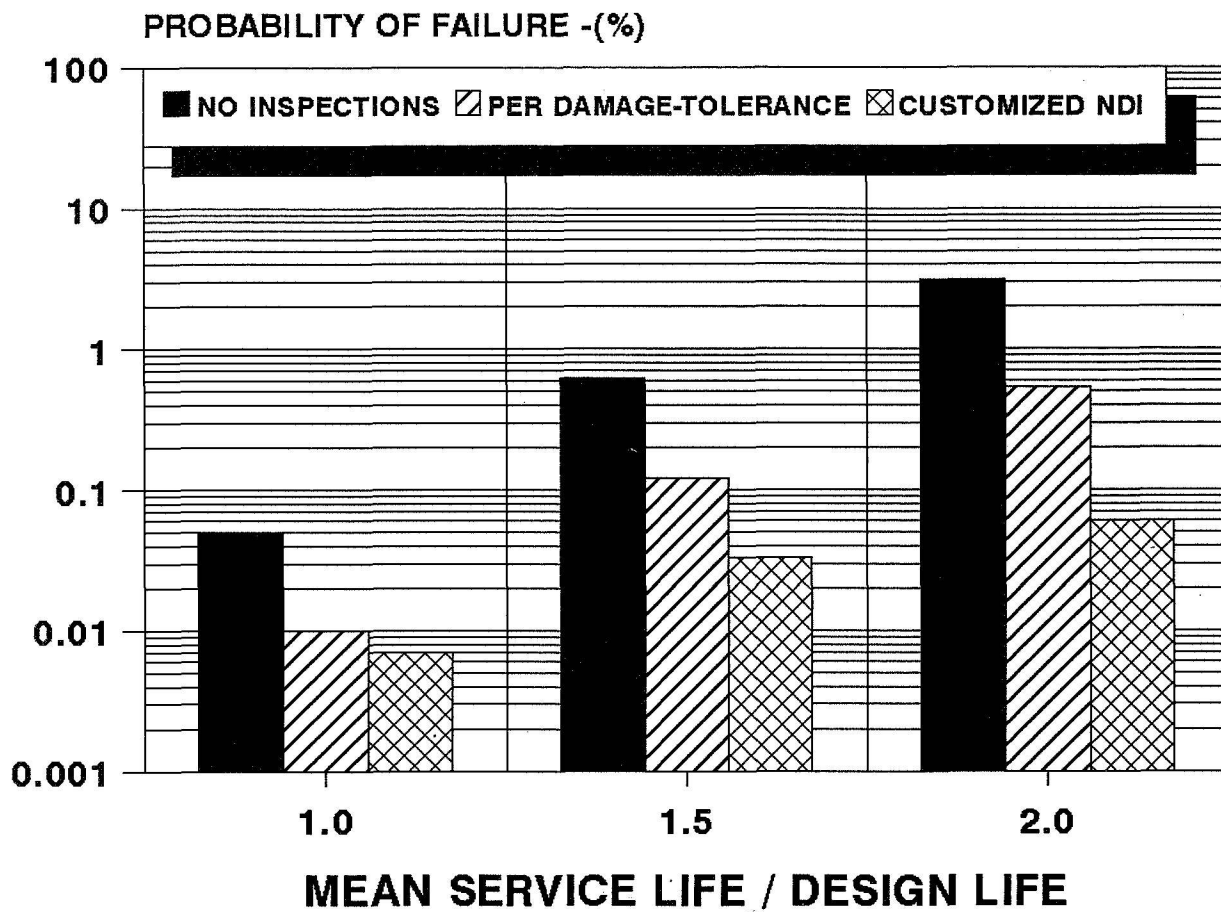


Figure 4. Probability of failure for location "A".

TABLE 3. Customized Inspection Schedule for Location "A"

(All inspections are performed using liquid penetrant)

SERVICE LIFE / DESIGN LIFE	INSPECTION INTERVAL / DESIGN LIFE
0.50	Threshold Inspection
0.50 - 1.00	0.20
1.00 - 1.50	0.15
1.50 - 2.00	0.10
2.00 -	0.05

The customized inspection begins with the conventional threshold and inspection interval, as dictated by damage-tolerance requirements. With each extension in service life, the interval is reduced, as is shown in Table 3. Figure 4 describes the effect of the customized inspection schedule on the probability of failure. When the mean service life equals the design life, the customized schedule has no real effect. However, when the mean service life reaches 1.5 times the design life, the probability of failure is reduced from 0.12% to 0.033%, as is shown in Figure 4. When the mean service life reaches twice the design life, the customized inspections reduce the probability of failure from 0.55% to 0.06%. This is a very significant reduction in the probability of failure. This example demonstrates how a specific inspection strategy, of reducing the inspection interval as service life is extended, can be selected to minimize the probability of failure.

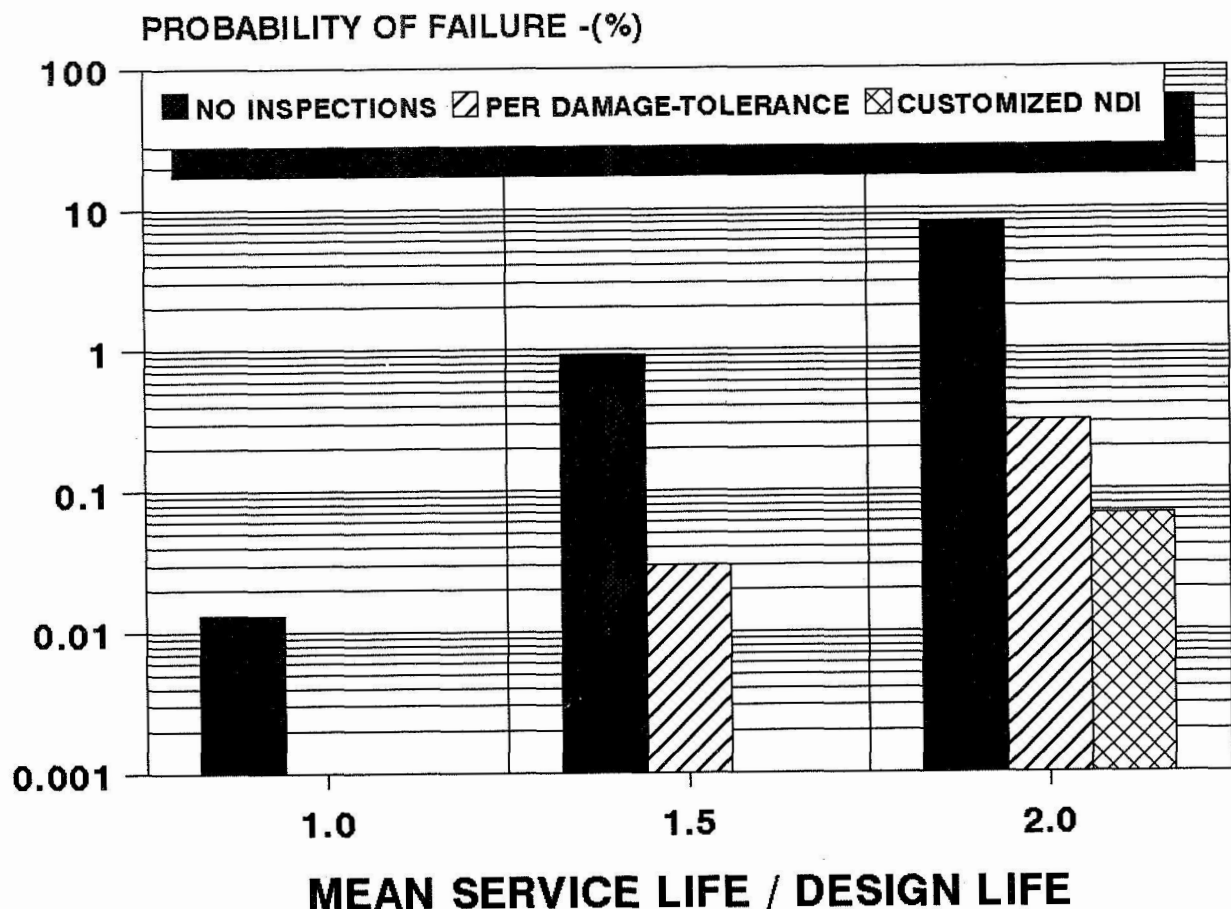


Figure 5. Probability of failure for location "B".

The second example deals with a 7475-T73 wing skin panel at an access hole. Cracks developing at the edge of the hole will propagate and eventually result in a failure of the panel. Conventional damage tolerance analysis set the threshold inspection at 50% of the design life and the inspection interval at 15% of the design life. Inspections are to be performed visually. Figure 5 describes the probability of failure for this area, which is designated location "B".

When the mean service life equals the design life, Figure 5 indicates that the probability of failure is only 0.013% even without any inspections. When the above inspections are performed, the probability of failure is virtually zero.

However, as the service life increases, the situation begins to deteriorate. When the mean service life equals twice the design life, the probability of failure increases to 8.0% for no inspections and 0.31% when the prescribed inspections are performed, as is shown in Figure 5. By using **INSIM** to study various inspection strategies, it was concluded that the addition of an ultrasonic inspection, at the end of each design life, would reduce the probability of failure significantly.

Figure 5 indicates that when the mean service life is twice the design life, this supplementary inspection will reduce the probability of failure from 0.31% to 0.067%.

These two examples demonstrate two ways that customized inspections can be used to reduce the probability of failure significantly. The first method is to continuously reduce the inspection interval as the service life increases beyond the originally determined design life. The second method is to add supplementary inspections at specific intervals of service usage. In both cases the **INSIM** computer program was used to evaluate the improvement to the probability of failure.

REFERENCES

1. Whittaker, I. C., et al, "Fleet Fatigue Cracking Threshold Prediction", Proceedings of the 16th Symposium of the International Committee on Aeronautical Fatigue (ICAF), Tokyo, Japan, 1991.
2. Swift, T., "Verification of Methods for Damage Tolerance Evaluation of Aircraft Structures to FAA Requirements", Proceedings of the 12th Symposium of the International Committee on Aeronautical Fatigue (ICAF), Toulouse, France, 1983.

**NONLINEAR FRACTURE MECHANICS-BASED ANALYSIS
OF THIN WALL CYLINDERS**

348622

59-39

23103

P. 16

Frederick W. Brust
Brian N. Leis
Thomas P. Forte
Battelle Memorial Institute
Columbus, Ohio

SUMMARY

This paper presents a simple analysis technique to predict the crack initiation, growth, and rupture of large-radius, R , to thickness, t , ratio (thin wall) cylinders. The method is formulated to deal both with stable tearing as well as fatigue mechanisms in applications to both surface and through-wall axial cracks, including interacting surface cracks. The method can also account for time-dependent effects. Validation of the model is provided by comparisons of predictions to more than forty full scale experiments of thin wall cylinders pressurized to failure.

INTRODUCTION

This paper summarizes the results of a series of papers (refs. 1-9) which describe the development, application, and verification of a simple methodology to predict failure in large R/t cylinders (greater than 40). While the methodology was developed for the natural gas pipeline industry, where failures can lead to serious consequences, it should be equally applicable to the airline industry since the toughness of line pipe steel and aircraft aluminum are quite similar. The methods are applicable for both through-wall and surface cracks, although the main focus here is on the surface cracks. The general methodology has been developed for time-dependent primary creep crack growth, with the special case of the elastic-plastic crack growth incorporated. The method has been programmed into a user friendly personal computer-based code (ref. 10), which is currently being used by non-experts to devise line pipe hydro-proof test strategies to certify line pipe.

The paper first discusses the importance of time-dependent effects, first on gas line pipe steel and then for aluminum, at and below room temperature. The predictive model is described next, as developed to predict fracture for surface cracked cylinders. The method is based on classical J-Tearing theory, with J estimated via a plastic zone correction technique for the surface crack problem. Next, two examples are discussed, one which deals with a through-wall crack in a pipe which experiences time-dependent crack growth, and then a summary of more than forty predictions compared to experimental data. Finally, a discussion of multiple interacting surface cracks and the extension of the model to multiple interacting cracks is considered.

IMPORTANCE OF TIME DEPENDENCE

Because of its usual association with thermally activated creep, time-dependent deformation and its corresponding effect on the crack growth and failure process are often considered to be important only at high temperatures. However, an increasing body of experimental evidence suggests that, for many materials, time-dependent effects cannot be neglected for quasi-static loading rates even at room temperature or below. Primary creep will occur in these situations if the stress is sufficiently high. Obviously, near a crack tip the stresses are very high, so that near a crack tip time dependent deformation may be manifest in the form of primary creep. Time- dependent deformation near a crack tip may lead to creep crack growth in addition to the time-independent (plastic) crack growth which is usually considered.

Since prediction of failure loads is usually performed by neglecting time- dependent deformation (at lower temperatures), non-conservative predictions may often result. This is particularly true for structures which are routinely subjected to proof tests such as gas pipelines, or certain aerospace structures. Indeed, proof tests are performed to ensure service reliability for a structural component by assuming that cracks which may lead to catastrophic failure in service will be removed during the test. Parts which fail during the proof test are then replaced, thus presumably avoiding catastrophic service failures.

Unfortunately, for ductile materials, proof tests may cause a crack to grow without failing the component. In fact, the crack may grow to a length which will lead to component failure during service at relatively moderate loads due to the history-dependent damage which occurs at the crack tip during the proof test. Time- dependent crack growth greatly enhances this effect. Hence, it is very important to be able to quantify the effects of time-dependent, as well as time-independent, crack growth and damage which occur during a proof test and, correspondingly, the effect of this damage on the subsequent service loading must be understood.

A somewhat detailed summary of time-dependent deformation of steels has been provided in refs. 4, 6-9 and, as such, will not be repeated here. However, because this behavior is not unique to steels and has been observed for some time in aluminum and other materials used in aerospace applications, a brief discussion of some of the earliest data to document the time dependent behavior of aluminum at and below room temperature (ref. 11) follows here before the model to deal with coupled creep and plasticity is presented. Tiffany and Masters in 1964 presented some of the earliest data that indicate the relative effects of high stress induced creep and its effect on crack growth, specifically for surface-flawed 2219-T87 aluminum specimens tested in liquid nitrogen. Those results showed that as the stress intensity increased above some threshold level, sustained loading below K_{Ic} caused failures at times that decreased from the order of hundreds of hours to near zero as the critical value of the stress intensity was approached. For that specific material, the threshold for sustained load cracking at liquid nitrogen temperatures was about $0.9 K_{Ic}$. Similar trends have been developed since for a variety of materials and applications. It follows that care must be taken to ensure that such growth does not confound attempts to ensure integrity through proof testing and to avoid failures due to this mechanism. It is to this end that the following model was developed.

ANALYSIS MODEL - SURFACE CRACKS

The general model for predicting cylinder failure in the presence of surface cracks is presented here. The general theory for predicting elastic-plastic and primary creep crack growth is provided in ref. 4. The extension of the model to handle through-wall axial cracked cylinders is provided in refs. 7-8, and details of the surface crack model are provided in refs. 6 and 9. Here we provide only the final equations for the axial surface cracked cylinder to illustrate the simplicity of, and ease of use for, the model.

Because elastic-plastic estimation schemes are not available for evaluating J for surface cracks in cylinders except for special cases, the model is based on an adaptation of elastic solutions for J . For elliptic surface cracks subjected to tensile loading, detailed compilations of finite element solutions are readily available in the literature if linear elastic conditions prevail. The primary creep model consists of estimating J by using a time-dependent Irwin estimate of the plastic zone in the elastic solution. Referring to fig. 1 for geometric definitions of the pipe and flaw, the elastic component, J_e , is written as:

$$J_e = \sigma^2 \left(\frac{\pi a}{Q} \right) \{ F(c/a, a/t, R/t, \phi) \}^2 \{ E/(1 - \nu^2) \}^{-1} , \quad (1)$$

where σ is the applied stress due to the pressure, P , ($\sigma = PR/t$), Q is the square of the complete elliptic integral of the second kind, and ϕ defines the location along the crack front where J_e is evaluated (see fig. 1). In addition, R , t , c , and a are defined in fig. 1, and E and ν are the elastic modulus and Poisson's ratio, respectively. The F -function in Equation (1) has been compiled in ref. 12 for $R/t = 40$ using the Atluri (ref. 13) SNA version of the finite element alternating method. For present purposes, the value of Q is taken in the form of the Newman and Raju approximation (ref. 14), i.e.,

$$\begin{aligned} Q &= 1 + 1.464 (a/c)^{1.65} , & a/c \leq 1.0 \\ Q &= 1 + 1.464 (c/a)^{1.65} , & a/c \geq 1.0 \end{aligned} \quad (2)$$

Plastic and Primary Creep Component of $J_p(t)$

The time-dependent nonlinear component of J for external axial surface cracked pipes is estimated by including a nonlinear correction to the elastic solution based on the inelastic time-dependent field at the flaw. Resorting to this approximation derives from the fact that the time-dependent component of J could not be interpolated from any known finite element solutions, since no compilation or general

numerical solutions are available for surface cracked pipes with formal consideration of inelastic effects.

The concept of a time-dependent plastic zone at the crack tip is natural given that primary creep rather than secondary creep is considered to occur during the short-time higher pressure excursions during hydrotesting. During the initial loading, a plastic zone develops whose size varies along the length of the flaw. During the hold periods, primary creep develops apparently due to the high stress which occurs at the crack tip all along the crack front. Because the time-independent hardening exponent is greater than the creep exponent, "loading" occurs at the crack tip along the crack front during the hold period (see ref. 4). Hence, during hold periods the crack tip inelastic zone grows along the crack's length. The nonlinear component of J is time dependent since, as the plastic zone grows in size during the hold periods, J increases.

Theoretical considerations indicate that good estimates of J can only be assured if the inelastic zone remains relatively small when using this method of estimating J . Despite this limitation, the method will be applied in cases where the plastic zone is large compared to the crack depth, as occurs, for example, for deep cracks near failure load. In such limiting cases, the calculated size of the inelastic zone may be larger than the remaining uncracked ligament in front of the crack tip at the deepest point along the crack front. This is physically unrealistic, so that, under these circumstances, the use of a plastic zone-type correction to the elastic solution to estimate J is viewed as a compliance correction technique.

The size of the plastic zone ahead of the crack tip has been estimated by analogy to the approach suggested by Kujawski and Ellyin (ref. 15): viz,

$$r_p = \frac{2 \hat{n}}{\hat{n} + 1} \left[\frac{K^2}{\beta \pi s_y^2} \right] \quad (3)$$

$\beta = 2$ Plane σ (at tips, $\phi = 90^\circ$ fig. 1)

$\beta = 6$ Plane ϵ (at tips, $\phi = 0^\circ$ fig. 1).

The value of \hat{n} in Equation (3) is calculated as:

$$\hat{n} = \frac{W_y^e + W_y^p}{W_y^e + W_y^p/n} \quad (4)$$

with the partitioned energy densities defined as:

$$W_y^e \equiv \frac{s_y^2}{2E} \quad , \quad (5a)$$

and

$$W_y^p \equiv \left[\frac{n}{n+1} \right] s_y \epsilon_y^p \quad (5b)$$

In Equation (5), s_y is the yield stress and ϵ_y^p is the amount of plastic strain at yield, which is often defined as the 0.2 percent offset strain. For a Ramberg-Osgood stress-strain law :

$$\frac{\epsilon}{\epsilon_o} = \frac{\sigma}{\sigma_o} + \alpha \left[\frac{\sigma}{\sigma_o} \right]^n \quad (6)$$

The value of ϵ_y^p is given by:

$$\epsilon_y^p = (\alpha \epsilon_o) \left[\frac{\sigma_y}{\sigma_o} \right]^n, \quad (7)$$

where, as detailed earlier, α and n are correlated through σ_o , and are history dependent.

It follows that the nonlinear component of J , $J_p(t)$ is given by:

$$J_p(t) = (\sigma)^2 \left\{ \frac{\pi(r_p(t))}{QE/(1 - \nu^2)} \right\} \{F^2(a/t, c/a, \phi)\}, \quad (8)$$

where $r_p(t) = r_p(n(t), \alpha(t))$. The value of J is then found as the sum of Equations (1) and (8).

The Material Resistance Curve. In a series of tests on compact tension specimens, Kuhnle and Riedel (ref. 16) have shown that the J -resistance curves are independent of load-hold effects for thermal conditions between room temperature and 300 F. The specimens were each subjected to various types of loading conditions, such as varying load-hold times, varying displacement rates, constant load, and in all cases the J -resistance curves are very similar. However, there is a temperature dependence, with the J -R curves lowering as temperature increases. Our results (see refs. 4-9) have also shown the same trend as observed in ref. 16.

This means that once a J -resistance curve is developed at a given temperature, it may be used to predict the crack growth behavior of cracked bodies experiencing creep deformation, provided that the creep is mainly primary. For our model, the J -resistance curves were developed using standard elastic-plastic loading rates and conditions and are assumed to be valid for analysis during creep conditions. This is important since it allows only one resistance curve to be developed and this curve is independent of loading rate. This, of course, assumes that dynamic loading of the specimens does not occur; i.e., the loading is typical for quasi-static conditions.

MODEL PREDICTIONS AND COMPARISONS WITH EXPERIMENTAL DATA

This section provides two example comparisons of model predictions to experimental data. The first example illustrates the predictive ability of the model for a case where time-dependent behavior is important for an axially through-wall cracked cylinder. The second example shows a comparison of model predictions compared to experimental results for more than 40 full-scale pipe experiments where time dependence was not important.

Axial Through-Wall Cracked Cylinder

A 22-inch outer diameter by 0.27-inch-thick pipe made of X52 line pipe steel was subjected to the pressure-time history shown in fig. 2. As seen here, the pipe was subjected to a series of load-hold sequences until failure occurred at 1100 psi. Initially, it took some time (about 100 minutes) to load the pipe to the first hold pressure of 775 psi. However, after the initial load was applied, subsequent load times required between 45 and 120 seconds, and these appear as vertical lines (step functions) in fig. 2. The analysis model assumes that the load periods occur instantaneously, and then the hold period begins. The implications of this assumption in terms of predicted failure pressure and crack growth versus time predictions are small. However, for history-dependent loading situations, the time it takes to load the specimen may be important. A discussion of the implications of history-dependent loading on the primary creep model is provided in ref. 8.

The estimation scheme for an axial through-wall cylinder is somewhat different from that summarized above for a surface-cracked cylinder and is provided in refs. 4 and 7. The material properties, both time-dependent tensile properties and the J-Resistance curve, are listed in ref. 7 and are not provided here so that the results may be emphasized.

For the pressure-time history imposed to the pipe shown in fig. 2, the predicted pressure versus crack growth history is illustrated in fig. 3. Also shown in fig. 3 are plots of the experimental pressure versus crack growth history. Note that the experimental results for both crack tips are shown here since symmetric crack growth did not occur at both crack tips in the experiment. Good prediction of the experimental behavior is evident. Also plotted in fig. 3 is the predicted behavior neglecting time-dependent damage accumulation. It is clear that neglecting the primary creep behavior which occurs in the highly stressed crack tip region can result in non-conservative prediction of failure pressure. Neglecting time-dependent damage mechanisms in the flaw growth process overpredicts the failure pressure by about ten percent here. This has serious implications with regard to proof-test methodology.

The predicted crack length versus time behavior is compared to the experimental data for both crack tips in fig. 4. Very good comparison is observed up to about 25,000 seconds. Reasonable predictions are also observed beyond this point although slightly shifted in time. Near failure, and at failure, where the amount of crack growth precludes valid J-Tearing theory, it is seen that predicted crack growth underestimates the experimental data. This underprediction of crack growth is also observed for time-independent analyses based upon J-theory (see, for instance, ref. 17). However, the predicted failure pressure compares quite well with experimental results. Predictions are compared to experiments for several other crack sizes and cylinder dimensions and loading conditions, as discussed in refs. 7 and 18.

Axial Surface-Cracked Cylinder Analysis

The experimental database in ref. 19 is considered tentatively to represent an average pool of data, and predictions are based on the average fracture trends. The J-Resistance curves for the test data in ref. 19 are not available since, at the time of these tests, other fracture parameters were used to characterize fracture. As such, average J-resistance behavior was characterized in terms of flow stress and CVP (Charpy) full-size energy, which were routinely determined for these materials at the time of these tests. The equation used to convert these parameters to a usable J-Resistance curve was developed in ref. 20. The time-dependent Ramberg-Osgood relations were developed from isochronous stress-strain tests, as discussed in refs. 6-9. The analyses are performed free of "selective calibration" that might be used (inappropriately) on a case-by-case basis to enhance the quality of the predictions, i.e., only one set of material data were used for all cases about to be discussed.

Values of predicted and observed failure pressure are shown in fig. 5 for comparison and evaluation of the analysis method. Figure 5a directly compares failure pressures with the predicted result on the ordinate, P_p , and the observed experimental result on the abscissa, P_e . This figure does not show any particular bias as a function of observed pressure nor is there a particular bias in regard to steel grade or processing history. The mean slope is 1.0415, with a standard deviation of 0.0977. This means that, on average, the model predictions are slightly conservative, which, in turn, means that the average J-resistance behavior is slightly overpredicted by the average trends representing the relationship between flow stress and Charpy data, as developed in ref. 20. Fig. 5b shows that there is no bias in the predictions as a function of a/t . That is, the ratio of predicted to observed failure pressure scatters evenly for all values of the abscissa, a/t . Likewise, this figure shows no particular bias as a function of c/a . Finally, fig. 5c shows these results reasonably fit a normal distribution consistent with the assumption that this pooled experimental database represents an average collection of observed failure pressures. Note that the J-tearing theory (Equations 1 to 8) was found to control all but one of the predictions in this dataset. Only the test for $a/t = 0.92$ was controlled by the net-section criterion.

The analysis of these test results has assumed that all flaw growth in these tests is time-independent. The pressure increased in these tests at about 20 psig-minute (ref. 19), so that some creep-tearing is possible as the pressure approaches the failure pressure. This time-dependent growth can only occur at or above pressures causing $J \sim J_{Ic}$. Analysis of a series of typical flaw depths and lengths indicated this occurred over the last 5 to 10 percent of the pressurizing. Calculations with time dependence during this interval showed little difference in the predicted failure pressure, as compared to the behavior predicted assuming elastic-plastic conditions only. Accordingly, the difference between the predicted and observed results is, on-average, not due to the idealization of neglecting time dependent effects. The difference is therefore ascribed to the definition of "average" fracture properties in ref. 18, using that rather limited database for pipe steels to represent the average behavior for this larger dataset.

INTERACTING SURFACE CRACKS

Because many practical failure situations involve multiple cracks, with failure being a consequence of the interaction and coalescence of such cracks, the present model for primary creep is currently being extended to address this class of problem. To date, analyses have been completed exploring this problem idealized in terms of a pair of cracks (ref. 21). This work has explored this problem through a range of analyses that again have been made using the finite-element alternating method (FEAM). The numerical procedure as adapted to this class of problem is detailed elsewhere (refs. 12 and 21), while ref. 21 provides some of the available results.

Fig. 6 provides an overview of the crack-pairs geometry discussed in ref. 21. With regard to fig. 6, note that the geometry addressed represents a surface-cracked flat-plate which, as detailed in ref. 12, can be used to represent the cracking behavior in cylinders with diameter-to-wall thickness ratios that are greater than about 40, so that the related results encompass many aerospace situations. Analysis has been done for cases where the axial and circumferential spacing between the tips of a pair of geometrically identical cracks have been systematically varied for a limited set of crack length-to-depth ratios. These analyses were done to determine the relative spacings between tips for (1) positive interaction (i.e., K increases) or shielding (i.e., K decreases) and (2) to assess conditions for coalescence. The length-to-depth ratios studied were selected to represent typical stress-corrosion cracking (SCC) geometries, which was the motivation for much of this work (ref. 22). This consideration led to flaw length-to-depth ratios (i.e., $2c/a$) in the range of $1 \leq 2c/a \leq 6$. With reference to fig. 6, the analysis for crack-pairs has been done to represent axial tip spacings in the range $-3 \leq 2d/t \leq 1$ for circumferential tip spacings in the range $0 \leq 2b/t \leq 1$.

Figs. 7a through 7c show typical results for Mode I, II, and III cracking, respectively. These mixed-mode results are used here to illustrate the role of Modes II and III as drivers for trends observed in SCC coalescence. Results in fig. 7 represent $a/t = 0.5$ (i.e., depth = half the wall thickness) and $c/a = 3$ (i.e., length = 6 times the depth), for $2d/t = -3$, which in this case defines co-parallel cracks (i.e., cracks stacked above each other). With reference to fig. 6, $\phi = 0$ represents the intersection of the crack with the surface while $\phi = 90$ is the location of maximum depth. Decreasing values of $2b/t$ denote a decreasing circumferential spacing while increasing values of $2d/t$ indicate increasing axial spacing.

Note by comparing the results for Modes II and III with the Mode I trends that K_{II} is about 0.1 K_I , whereas K_{III} is still smaller and shows a sign change around the crack front. The nature of the shear modes is to cause the tips of vertically stacked (co-parallel) cracks to grow toward each other for the portions of these cracks near the surface. Analysis similar to that shown in fig. 7 for other flaw spacings indicates the tendency for nearly co-linear cracks to hook toward the other crack. As with the case of the co-parallel (stacked) cracks, the shear components (Modes II and III) drive this process. Both features are observed in patches of SCC. Such features also occur for mutually adjacent crack tips for fatigue crack growth, which indicates that the mechanics of the process rather than the mechanism controls such features. It follows that fracture mechanics should provide a viable basis to characterize coalescence and failure for SCC.

Results similar to those shown in fig. 7 for Modes I, II, and III across a range of other lateral spacings continue to be developed to assist in formulating criteria for coalescence and failure in

situations where the local and global compliance are altered by the presence of multiple surface cracks. These studies currently include idealized arrays of cracks as well as specific configurations typical of failures in thin-walled cylinders (ref. 23).

SUMMARY and CONCLUSIONS

This paper has presented and discussed an engineering analysis technique to predict the crack initiation, growth, and rupture of large-radius, R , to thickness, t , ratio (thin wall) cylinders. The method was discussed in terms of stable tearing although it has been formulated to also deal with fatigue mechanisms in applications to both surface and through-wall axial cracks, including interacting surface cracks. The method was formulated and discussed with reference to the analysis of time-independent as well as time-dependent effects. Validation of the model was discussed in terms of comparisons of predictions to the actual failure behavior of more than forty full-scale experiments of thin-wall cylinders pressurized to failure. Validation beyond that discussed herein indicates the suitability of this same engineering concept for fatigue loadings in thin-walled cylinders as well as for more complex loading histories. Finally, the extension of this concept to serve as a failure criterion in applications involving multiple cracks was discussed.

The primary conclusion of this work is that an engineering model has been developed that provides reasonably accurate solutions for the stability and growth of cracks in thin-walled cylinders. While the majority of the applications of this model have been to steel structures, the underlying concepts can be extended to most engineering materials in otherwise comparable situations.

REFERENCES

1. Leis, B. N.; and Brust, F. W.: Hydrotesting Effects - 1. *Oil and Gas Journal*, February 12, 1990, pp. 45-48.
2. Leis, B. N.; and Brust, F. W.: Hydrotesting Effects - Conclusion. *Oil and Gas Journal*, February 19, 1990, pp. 52-54.
3. Brust, F. W.; and Leis, B. N.: A Study of Primary Creep Crack Growth at Room Temperatures. *Numerical Methods in Fracture Mechanics*, Editors Luxmoore & Owen, Proceedings of the 5th ICNMF, Freiburg, West Germany, April, 1990.
4. Brust, F. W.; and Leis, B. N.: A New Model for Characterizing Primary Creep Damage. *Int. Journal of Fracture*, vol. 54, pp. 45-63, 1992.
5. Brust, F. W.; and Leis, B. N.: The Effects of Primary Creep on Elastic-Plastic Crack Growth. *Fatigue, Degradation, and Fracture*, 1990, ASME Special Publication, vol. 195, June, 1990.

6. Brust, F. W.; and Leis, B. N.: Primary Creep Crack Growth at Room Temperature in Surface Cracked Pipes. *Int. Journal of Pressure Vessels and Piping*, vol. 52, pp. 273-298, 1992.
7. Brust, F. W.; and Leis, B. N.: A Model for Predicting Primary Creep Damage in Axial Cracked Cylinders, Part I, Theory. *Engineering Fracture Mechanics*, vol. 4, pp. 615-627, 1992.
8. Brust, F. W.; and Leis, B. N.: A Model for Predicting Primary Creep Damage in Axial Crack Cylinders, Part II, Applications, *Engineering Fracture Mechanics*, vol. 43, no. 4, pp. 629-639, 1992.
9. Leis, B. N.; and Brust, F. W.: Validation of Room-Temperature Primary Creep Crack-Growth Analysis For Surface Cracked Pipes, *Nuclear Engineering and Design*, vol. 142, pp. 69-75, 1993.
10. Leis, B. N.; and Ghadiali, N.D.: *Pipe Axial Flaw Failure Criteria -- PAFFC Version 1.0 User's Manual and Software*. American Gas Association, NG-18 Report No. 211, April 26, 1994.
11. Tiffany, C. F.; and Masters, J. N.: *Applied Fracture Mechanics*. ASTM STP 381, pp. 249-278, 1964.
12. Stonesifer, R. B.; Brust, F. W.; and Leis, B. N.: Stress-Intensity Factors for Long Axial Outer Surface Cracks in Large R/t Pipes. *Fracture Mechanics: Twenty-Second Symposium*, Vol. II, ASTM STP 1131, 1992, pp. 29-45.
13. Nishioka, T.; and Atluri, S. N.: Analytical Solution for Embedded Elliptical Cracks, and Finite Element Alternating Method for Elliptical Surface Cracks Subjected to Arbitrary Loadings. *Engineering Fracture Mechanics*, vol. 17, no. 3, pp. 247-268, 1983.
14. Newman, J. C.; and Raju, I. S.: An Empirical Stress-Intensity Factor Equation for the Surface Cracks. *Engineering Fracture Mechanics*, vol. 15, no.1-2, pp. 185-192, 1981.
15. Kijawski, D.; and Ellyin, F.: On the Size of Plastic Zone Ahead of Crack Tip. *Engineering Fracture Mechanics*, vol. 25, no. 2, pp., 229-236.
16. Kuhnle, V.; and Riedel, H.: Time-Dependent Deformation and Fracture of Steel Between 20 and 400 C. *International Journal of Fracture*, vol. 34, pp. 179-194, 1987.
17. Hutchinson, J. W.; and Paris, P. C.: *Stability of Analysis of J Controlled Crack Growth*. ASTM STP 668, pp. 37-64, 1979.
18. Leis, B. N.; Brust, F. W.; and Scott, P. M.: *Development and Validation of a Ductile Flaw Growth Analysis for Gas Transmission Line Pipe*. American Gas Association, Cat. No. L51543, June 1991.

19. Kiefner, J. F.; Maxey, W. A.; Eiber, R. J.; and Duffy, A. R.: *Failure Stress Levels of Flaws in Pressurized Cylinders*. ASTM STP 536, pp. 461-481, 1973.
20. Leis, B. N.; and Brust, F. W.: *Ductile Fracture Properties of Selected Line Pipe Steels*. American Gas Association, Catalog No. L51604, January 1990.
21. Stonesifer, R. B.; Brust, F. W.; and Leis, B. N.: Mixed Mode Stress Intensity Factors For Interacting Semi-Elliptical Surface Cracks In A Plate. *Engineering Fracture Mechanics*, vol. 45, no. 3, pp. 357-380, 1993.
22. Leis, B. N.; and Parkins, R. N.: Modelling Stress-Corrosion Cracking of High-Pressure Gas Pipelines. Paper 19 in Eighth Symposium on Line Pipe Research proceedings, American Gas Association, Catalog No. L51680, September, 1993.
23. Leis, B. N.; and Mohan, R.: Failure Criteria for Pipeline Flaws. Paper 9 in Eighth Symposium on Line Pipe Research proceedings, American Gas Association, Catalog No. L51680, September, 1993.

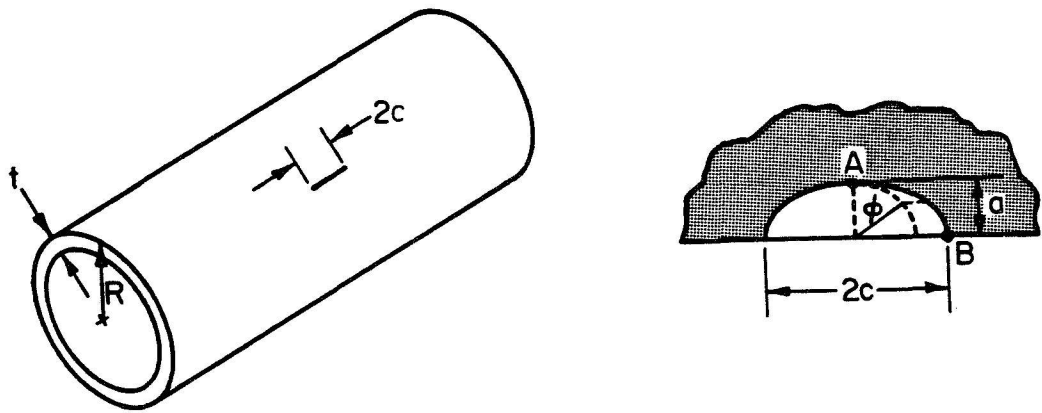


Figure 1. Geometric parameters for part-through-wall flawed cylinders.

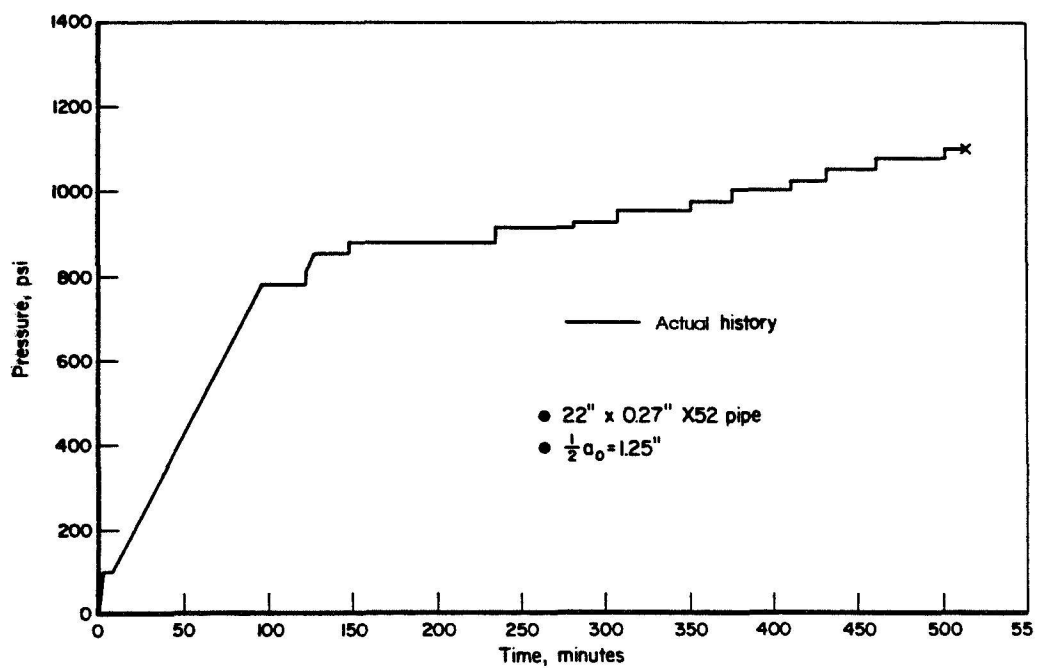


Figure 2. Pressure versus time history applied to 22-inch through-wall cracked pipe.

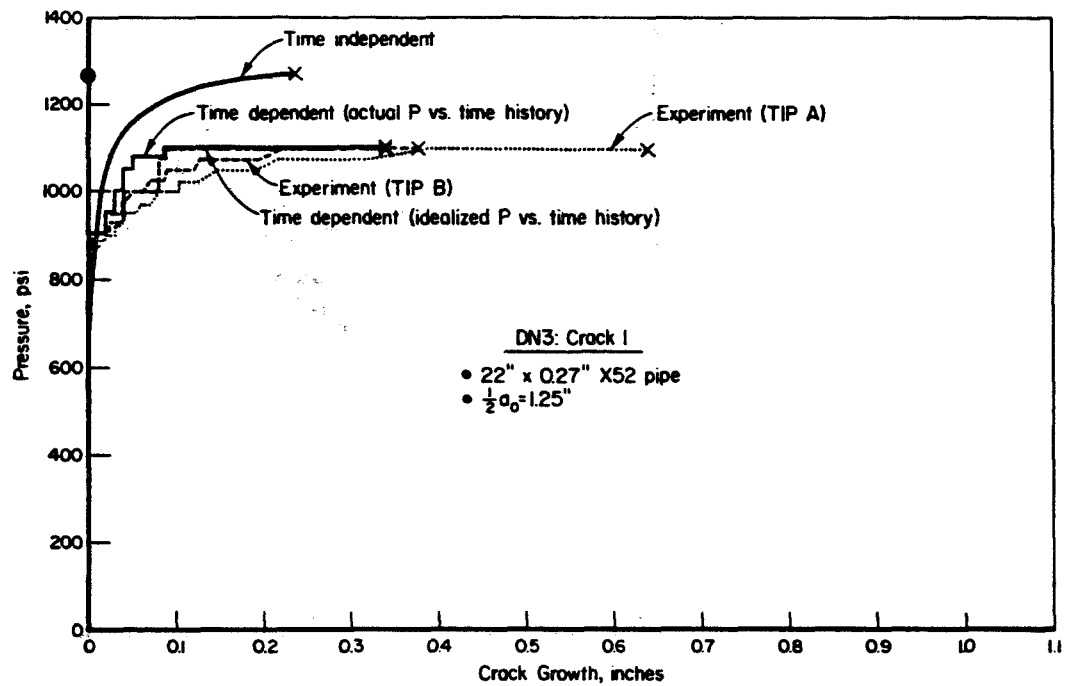


Figure 3. Results for full-scale test DN3.

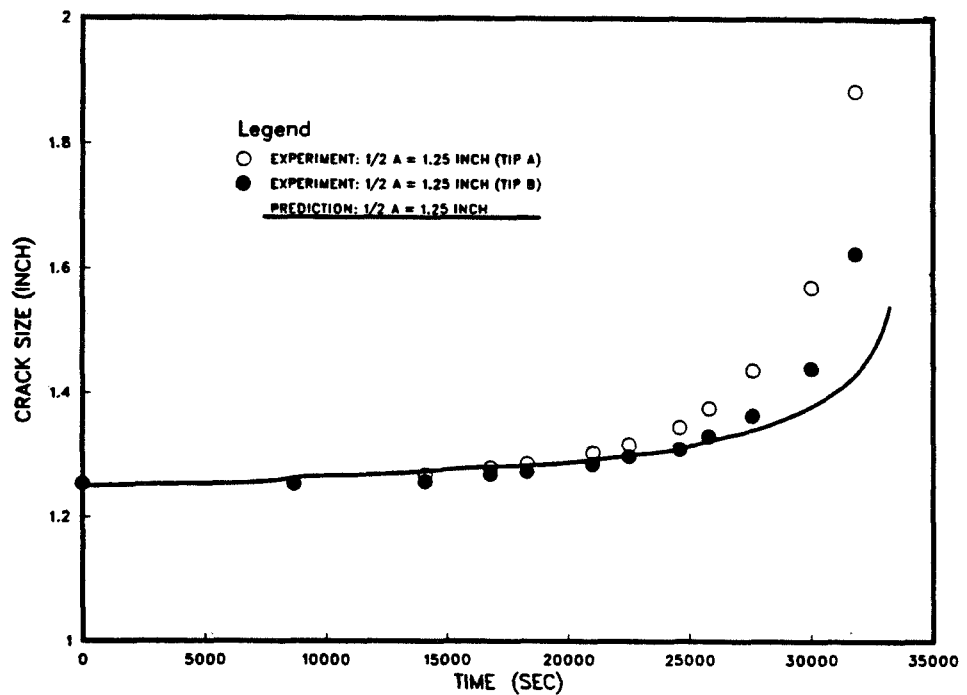
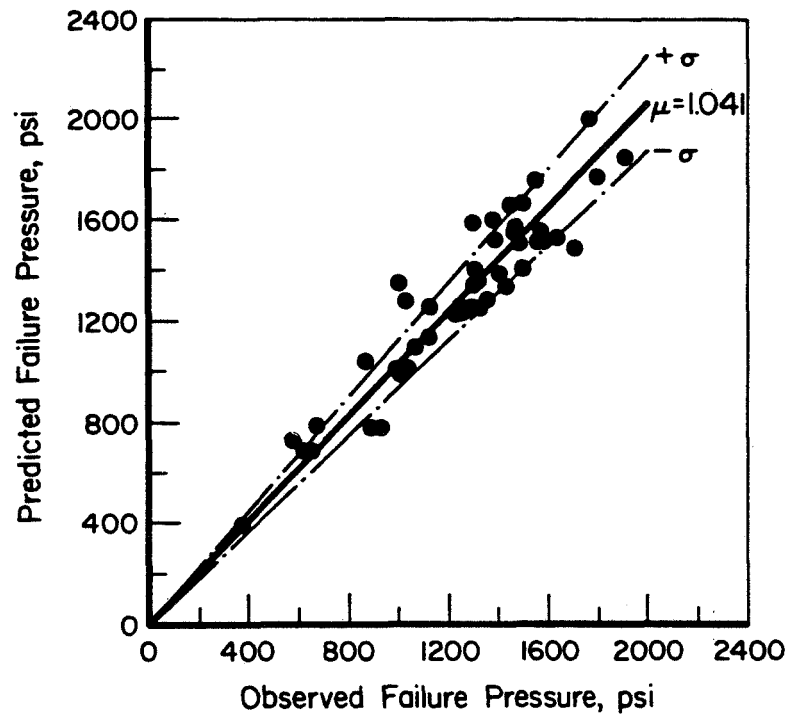
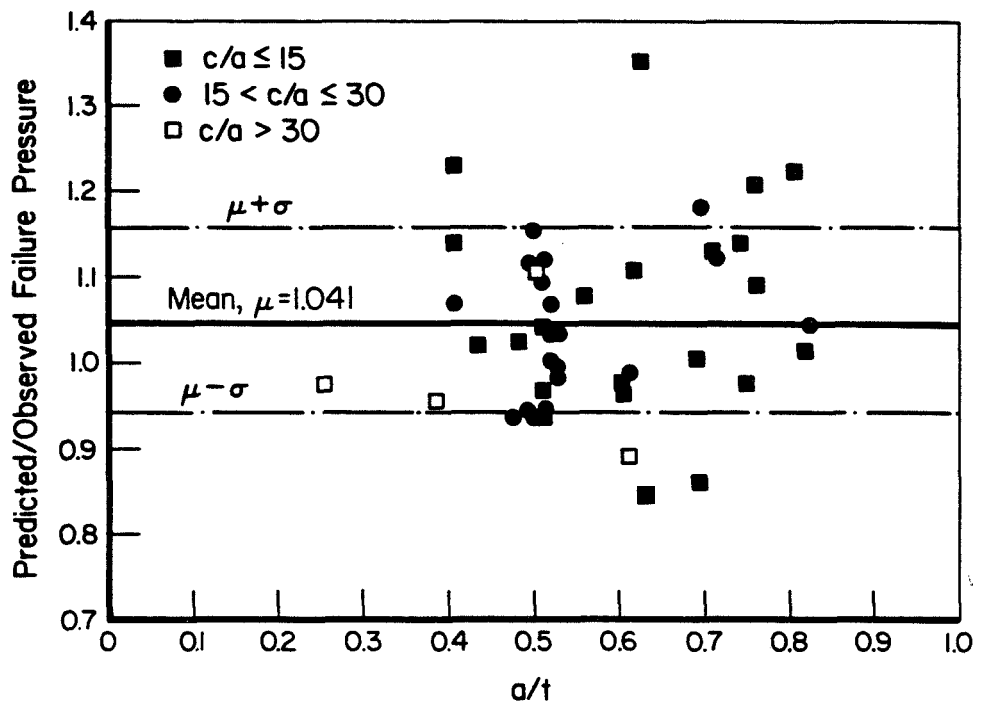


Figure 4. Crack size versus time for 22-inch pipe.

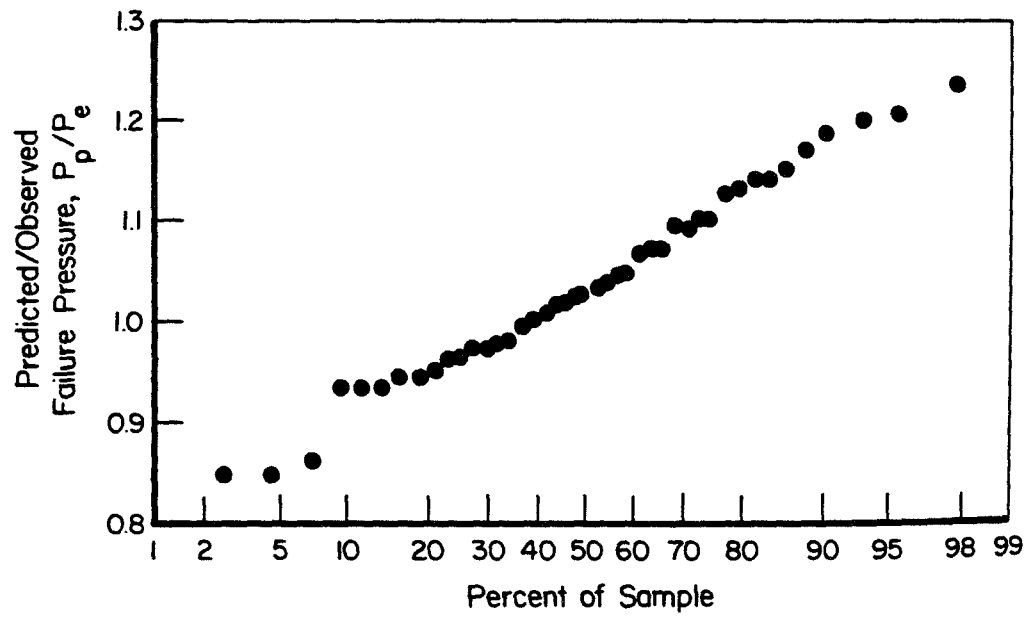


(a) P_p versus P_e



(b) P_p versus a/t and a/c

Figure 5. Comparison of observed and predicted failure pressure for SAPF full-scale tests of PTW flawed line pipe.



(c) P_p versus Frequency of Occurrence

Figure 5. Concluded.

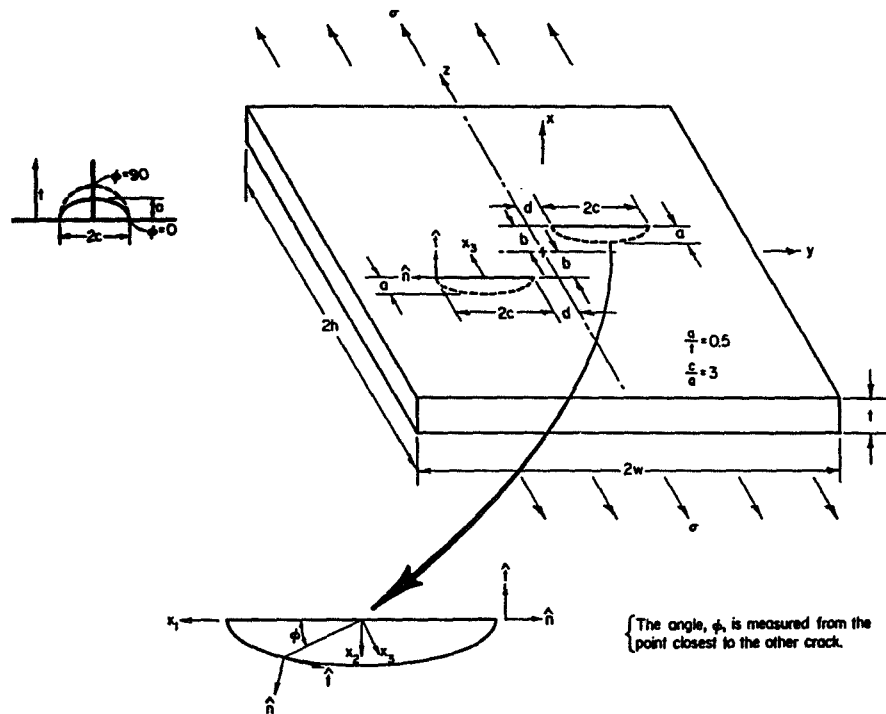
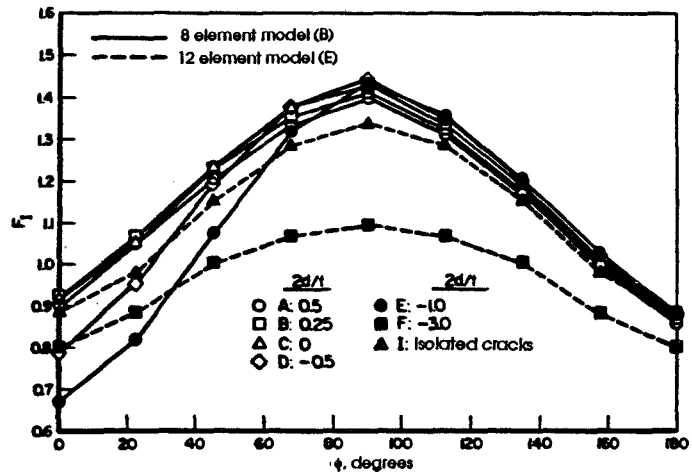
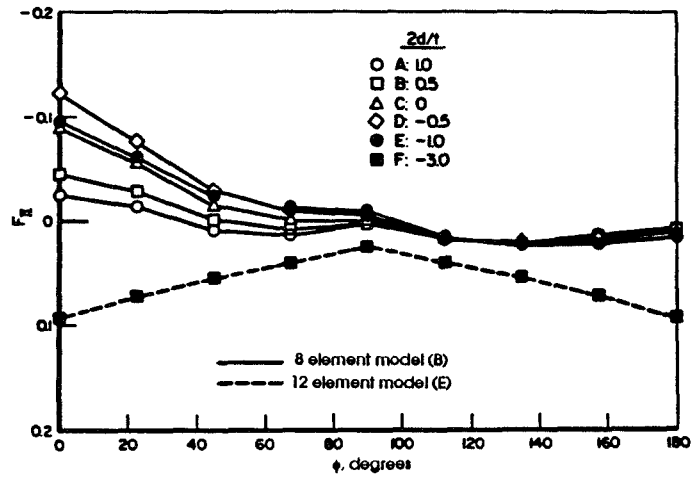


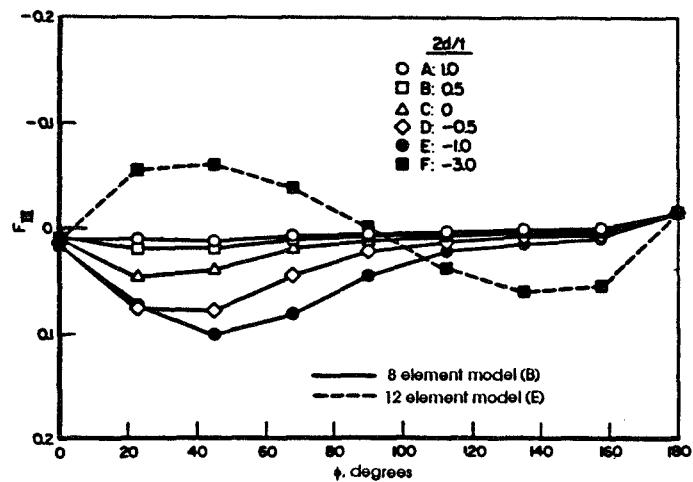
Figure 6. Geometric parameters for a pair of arbitrarily located cracks.



(a) Mode I cracking



(b) Mode II cracking



(c) Mode III cracking

Figure 7. Normalized crack driving force as a function of position along the crack front for a pair of cracks for a range of crack positions and depths.

**FATIGUE ANALYSIS OF MULTIPLE SITE DAMAGE
AT A ROW OF HOLES IN A WIDE PANEL**

Kimberley Buhler*
Warner Robins Air Logistics Center
Robins AFB, GA 31098.

Alten F. Grandt, Jr.
School of Aeronautics and Astronautics, Purdue University
W. Lafayette, IN 47907-1282.

E. J. Moukawsher*
US Coast Guard Repair and Supply Center
Elizabeth City, NC 27909.

ABSTRACT

This paper is concerned with predicting the fatigue life of unstiffened panels which contain multiple site damage (MSD). The initial damage consists of through-the-thickness cracks emanating from a row of holes in the center of a finite width panel. A fracture mechanics analysis has been developed to predict the growth, interaction, and coalescence of the various cracks which propagate in the panel. A strain-life analysis incorporating Neuber's rule for notches, and Miner's rule for cumulative damage, is also employed to predict crack initiation for holes without initial cracking. This analysis is compared with the results of a series of fatigue tests on 2024-T3 aluminum panels, and is shown to do an excellent job of predicting the influence of MSD on the fatigue life of nine inch wide specimens. Having established confidence in the ability to analyze the influence of MSD on fatigue life, a parametric study is conducted to examine the influence of various MSD scenarios in an unstiffened panel. The numerical study considered 135 cases in all, with the parametric variables being the applied cyclic stress level, the lead crack geometry, and the number and location of MSD cracks. The numerical analysis provides details for the manner in which lead cracks and MSD cracks grow and coalesce leading to final failure. The results indicate that MSD located adjacent to lead cracks is the most damaging configuration, while for cases without lead cracks, MSD clusters which are not separated by uncracked holes are most damaging.

*This research was performed while K. Buhler and E. J. Moukawsher were graduate students at Purdue University.

INTRODUCTION

The problem of Multiple-Site Damage (MSD) in aging aircraft has motivated development of a computer program to predict the fatigue life of a panel containing a row of holes with an arbitrary arrangement of small cracks [1-3]. A typical MSD specimen which the program is designed to analyze is shown in Fig. 1. Here a row of open holes are assumed to contain various combinations of initial radial through-thickness cracks. Small cracks located at multiple holes are referred to as multiple-site damage (MSD), while the term "lead crack" is used to describe a large crack connecting two or more holes. This section overviews the computational algorithm, and summarizes a set of experiments conducted to verify the ability to predict the effect of MSD on fatigue life. Additional details of the analysis and experiments are provided in Refs. 1-3. Once the predictive capabilities of the algorithm are established, subsequent sections describe results from a parametric analysis performed to study the effects of various crack combinations on the fatigue life of a 31.0 inch wide panel containing 30 open holes.

Description of the Crack Growth Algorithm

The crack growth algorithm is conceptually quite simple. Given the initial specimen geometry (dimensions and hole layout), MSD configuration (location and lengths of cracks), and loading conditions (constant amplitude load only), the cracks are grown incrementally until they link together or the panel fails. The first step is to calculate the stress intensity factors for all cracks. One crack tip is then assumed to advance a small amount, and the cycles required for this increment of growth are calculated. The remaining cracks are then grown a distance corresponding to this cyclic interval by employing a user selected fatigue crack growth model to relate the cyclic stress intensity factor and fatigue crack growth rate. After each incremental growth the current crack geometry is compared to one of several failure criteria to determine whether the panel fails. For holes which are initially uncracked, cumulative damage is summed at these locations in conjunction with a Neuber notch analysis. Miner's rule is applied to determine when a crack is initiated at these holes. When this strain-life analysis determines that "crack initiation" has occurred at a given hole, a crack equal to Dowling's "transition" crack length [4] is introduced, and the crack growth calculations continue at that location. This routine is repeated until the failure criterion is satisfied. Throughout the analysis storage arrays are used to monitor the crack tip properties (stress intensities and growth rates), and changing panel configuration (as cracks link together).

A form of the compounding method is used to determine the stress intensity factors for the various MSD specimen cracks. The cracks are treated as either edge, center or radial hole cracks [5]. Cracks which link together are considered as either center or edge cracks (the holes are ignored). Once the crack type is designated (initiated by the user and automatically updated with crack growth) an initial solution for ΔK is calculated for each crack. The final cyclic stress intensity factor employs an interaction factor which is based on the Kamei-Yokobori K solution [6] for two interacting cracks.

Several different failure criteria have been incorporated into the program including:

- a. K exceeds the critical stress intensity factor (K_C) for the material

- b. The crack growth rate exceeds a user specified amount
- c. The total crack length exceeds a user specified amount
- d. The net section stress in the uncracked ligament exceeds the tensile yield stress of the material
- e. The ligament between two adjacent cracks yields by a criterion proposed by Swift [7].

Swift's ligament yield criterion accounts for the significant plastic zone ahead of long lead cracks which limit the ability to carry additional load. Failure of the panel is predicted when the plastic zone at the tip of the lead-crack reaches a point where it 'touches' the plastic zone of the nearest approaching crack tip from the adjacent holes. If this condition occurs, then the panel fails as the large lead crack 'unzips' through the remaining row of holes.

Experimental MSD Fatigue Tests

A series of experimental tests were conducted with nine inch wide 2024-T3 aluminum panels to verify the program analysis. The 0.09 inch thick specimens contained a single row of 8 to 11 open holes with a 0.16 inch diameter. Some specimens contained large lead cracks (obtained by cutting the ligament between two or more central holes), and all specimens contained small radial MSD cracks (on the order of 0.05 to 0.10 inches long) at two or more of the remaining holes. These specimens were cycled to failure using a constant amplitude loading spectrum with an R ratio of 0.01 and at a frequency of 5 hertz. Measurements of the growth and coalescence of initial fatigue cracks, as well as cycles required to develop cracks at initially uncracked holes, were recorded and compared with results of the LEFM based numerical analysis. Figure 2 compares measured and predicted crack growth for a typical MSD specimen, while Fig. 3 summarizes measured and predicted life for the 12 tests conducted. A separate set of experiments with similar precracked MSD specimens indicated that the Swift [7] ligament yield criterion gave a good estimate of residual strength for those test specimens. Further details of the test results are included in Refs. 1-3.

PARAMETRIC STUDY OF A WIDE PANEL WITH MSD

Having established confidence in the ability to analyze the influence of MSD on fatigue life, it was decided to employ the numerical model for a parametric study of the influence of various MSD scenarios in an unstiffened panel. To conduct this study, a 31.0 inch wide panel containing 30, 3/16 inch diameter holes was selected as the test model. This size panel was chosen to allow analysis of many different MSD/lead crack combinations. Two basic crack configurations were considered in this study: panels containing a 'lead' crack in the presence MSD cracks growing from other holes, and panels containing arbitrary combinations of MSD without a lead crack. Typical examples of the starting crack configurations are shown in Fig. 4. The main goal here was to determine how reasonably expected MSD

scenarios affect the life of a large panel. Furthermore, trends in the crack growth and coalescence were sought.

Parameters Associated With MSD

A summary of the parameters investigated are shown in Table 1. Some parameters were fixed to limit the total number of feasible combinations, with the main variables being the applied loading and the crack geometries. The assumed stress-strain and fatigue material properties were extracted from Ref. 1. The 0.2% yield strength was determined to be 54.3 ksi, while the ultimate strength was 60.0 ksi. Additionally, the material da/dN versus ΔK relationship was experimentally determined and converted to a mathematical representation consisting of a series of line segments [1].

The initial crack geometry defines the size of the initial cracks and their location relative to the holes and other cracks. To bound the number of combinations to a reasonable maximum, the initial sizes and configurations were limited to a selection which were considered reasonably expectable. As the initial predictions were analyzed some configurations were refined to focus on critical areas. Two basic crack sizes were selected to resemble typical MSD fatigue cracks growing from a hole. The lengths of these two radial cracks were 0.05 inches and 0.1 inches, and they were placed at opposite sides of a hole (Fig. 5) to approximate the general randomness of fatigue crack lengths which normally stem from differing initiation periods.

The panels were divided into five zones, each containing six holes (Fig. 4), to enable an ordered approach to the placement of the various crack combinations. Three different lead crack configurations were selected, and in all cases the lead cracks were located in zone three (which was centered in the panel). The different lead crack configurations are shown in Fig. 6. For each lead crack type, various combinations of other cracks were started at holes in the other zones. Both symmetrically and nonsymmetrically placed cracks in the overall panel were studied. Examples of the starting configurations with lead cracks are shown in the top part of Figs. 7 and 8. For the cases without lead cracks, various numbers of cracked holes in each zone were considered. An example is shown at the top of Fig. 9. The clusters of cracks in each zone were positioned in adjacent holes, and also with uncracked holes between the cracked ones. Additionally, a cluster of six cracked holes was moved to various locations in the panel and the resulting fatigue behavior considered.

Constant amplitude cyclic loading was applied to the parametric models. Typical fuselage hoop stresses, which are generated from internal pressurization, are reported in the literature as ranging from 10.0 to 15.0 ksi [8-10]. This study considered the following three maximum applied cyclic loads: 10.0, 12.5 and 15.0 ksi. The variations in the applied loading was seen to greatly affect the fatigue lives of the cracked panels.

DISCUSSION OF RESULTS

The results from the study are presented in three forms. Tables 2 and 3 present the total panel lives for specific cases considered, as well as the number of cracked holes in each zone. Figures 7-9

show example crack tip propagation plots for all the holes in the panel, and include plots for panels with or without lead cracks. Above the main plot is a figure which illustrates the initial panel crack configuration. Figures 10 and 11 are bar charts of the total panel life versus the number of cracked holes. These charts include results for all the three applied loading cases.

Typical Crack Growth Trend in Panels Containing a Lead Crack

The parametric study revealed a typical crack growth trend which leads to the panel failure. This is best described for the panels containing lead cracks by considering Fig. 7. This panel contained a type 1 lead crack with cracks growing from all other holes in zone 3. No other holes in the panel were initially cracked. The propagation plot shows dominant crack growth from the holes on the left side of the lead crack. The crack on the right side of hole 14 grows quickly in the presence of the lead crack tip to the left of hole 15. These cracks link after about 19,000 cycles resulting in a much longer crack with its left tip on the left side of hole 14, and the right end still uncracked at hole 16. This process continues with the crack growth accelerating through the other MSD cracks in holes 13 and 12.

While the initial cracks on the left of the lead crack have been linking, the cracked holes on the right side of the lead crack (holes 17 and 18) have grown comparatively slower. These cracks have not been so strongly influenced by the lead crack which does not extend past the right side of hole 16. After hole 12 and 13 link at 26,000 cycles, there is a period up until 30,500 cycles where only the cracks from holes 17 and 18 grow in a slow stable manner. At this point none of the other holes in the panel contain cracks. During this time the uncracked holes are accumulating "initiation" damage until 30,500 cycles when a crack initiates at the right side of hole 16. This results in a large central crack extending from holes 12 to 16. At this stage the large central crack has reached a critical length where unstable extension occurs. This causes the central crack to link with the cracks growing from holes 17 and 18 almost immediately after the initiation at hole 16, which results in an even longer central crack which is temporarily stopped by the uncracked holes 12 and 19. Within another 1,000 cycles the cracks in the remaining uncracked holes begin to initiate causing the excessively large central crack to instantly 'unzip'. This is only temporarily halted by further uncracked holes which are remotely located from the center of the panel. Once the unzipping process starts, cracks rapidly initiate in the remaining holes causing the panel to fail.

Typical Crack Growth Trend in Panels Containing No Lead Crack

Figure 9 is a sample crack propagation plot for a panel without an initial lead crack. For this case the panel contained a pair of adjacently cracked holes in each of the five zones. The plot shows the cracks between the pairs of cracked holes growing and linking after about 47,000 loading cycles. The resulting longer cracks grow and link with the adjacent holes after about 64,000 cycles. Following this, cracks start to initiate at previously uncracked holes, and the panel soon fails. Reference 11 further describes similar trends for various other configurations.

The patterns described above suggest that regardless of the initial crack configuration, crack growth and coalescence will tend to result in a much larger crack, which will control the failure of the panel as it extends through other holes. Additionally, the number of cycles required to fail the panel after the larger crack has reached some critical length is a small portion of the total panel life, and is affected by

the initiation times of the initially uncracked holes. Based on this pattern the life of the panel is dependent on how long it takes for a particular crack configuration to generate the larger critical crack. The next section discusses the effects of the various configurations, and the different applied loads.

Effects of Different Crack Configurations on Panels Containing a Lead Crack

For the lead cracked panels a series of predictions were made with varying numbers of other holes cracked. The number of cracked holes remotely located from the lead crack ranged from 0 to 12, and was selected to simulate the initial onset of a MSD scenario. For each crack configuration, predictions were made for the three different cyclic load levels (10, 12.5, and 15.0 ksi). Referring to Table 2, the results show that the type of lead crack and the magnitude of applied load have a great effect on the total panel life. For the 10.0 ksi applied load case, the panel with the type 1 lead crack and 8 other cracked holes (MSD334) had a total life of 73,021 cycles. By comparison, the same case with the type 2 lead crack (MSD335) had a life of 40,921 cycles which is approximately 40 percent less than the life of the type 1 case. Similarly, the same case with the type 3 lead crack (MSD336) had a total life of 30,616 cycles, which is approximately 25 percent less than the type 2 life.

The magnitude of the applied loading also has a large effect on the panel lives. For example the life of the panel containing the type 1 lead crack with 8 other cracked holes (MSD334), ranged from 73,021 cycles for 10.0 ksi applied load, to 7,054 cycles for the 15.0 ksi load. Similarly the type 3 lead crack case (MSD336) ranged from 30,616 cycles to 2,988 cycles. The fatigue life for the panel when loaded at 15 ksi was approximately 10 percent of the life when loaded at 10 ksi.

Table 2 also indicates that moving the same number of cracked holes remote from the lead to various zones has a negligible effect on the total panel life. For example moving three other cracked holes to different zones in the type 1 lead crack panel (MSD316, MSD322), causes the total life to vary from 91,291 cycles to 91,281 cycles. This is due to the dominance of the lead crack controlling the panel life.

The apparent dominance of the lead crack on the panel lives motivated several predictions where holes located closely to the lead crack were initially cracked. A typical example is shown in Fig. 8. As expected the lives are markedly reduced in these cases. For example, referring to Table 2 (MSD326, MSD332), the panel life for the type 2 lead crack case containing 4 other cracked holes is more than halved when the four other holes are located in zone 3 (adjacent the lead crack) compared to the MSD being located in the other zones, remote from the lead crack location. Furthermore, predictions were made where a cluster of three cracked holes were located on the immediate left side of the lead cracks. This cluster was separated from the lead crack by both one and two initially uncracked holes. (Refer to Fig. 8 example). Table 2 shows that for this situation the magnitude of the effect on the total lives depends on the type of lead crack. For example, for the type 1 lead crack (MSD322), the panel life for three other initially cracked holes remotely located from the lead crack was 91,281 cycles. This compares to 55,821 cycles when a cluster of three cracked holes was separated from the lead crack by two uncracked holes (MSD340), and 52,721 cycles when the cluster was separated from the lead by one uncracked hole (MSD343). The same comparison for the type 2 lead crack case resulted in 46,935 cycles for the remote crack locations, compared to 45,250 cycles for the two hole separation, and 42,299 cycles for the single hole separation (results not included in Table 2). A similar result for the type 3 lead crack case as the type 2 case occurred. Figure 8 shows how the cracks coalesce to form the controlling large central crack. The

close proximity of the cluster of three cracks to the lead crack tends to reduce the time taken to generate large central crack, which in turn reduces the total panel life.

Figure 10 is an example bar chart of the total panel life versus the number of cracked holes remotely located from the lead crack. From this figure it is apparent that:

- a. there is a large reduction in the panel life with increasing applied load,
- b. the lives of the panels loaded at 10.0 ksi decrease quite considerably as the number of initially cracked holes increases, but by comparison the lives for the panels loaded at 12.5 ksi and particularly 15.0 ksi are not as sensitive to the number of initial cracked holes.

In summary the lives of these panels are strongly controlled by the type of lead crack, the location of the other MSD relative to the lead crack, and the magnitude of the applied loading.

Effects of Different Crack Configurations on Panels Without a Lead Crack

A similar crack growth pattern for panels with lead cracks was found to be applicable to the panels without lead cracks. The cracks grow and coalesce to form a large central crack which rapidly extends to panel failure. Predictions were made for increasing numbers of cracked holes. In some cases the cracked holes were clustered together while in others they were separated by uncracked holes. Additionally, predictions were made for a cluster of six initially cracked holes which were moved about the panel. Some specific results for these cases are listed in Table 3.

The results show that the panel lives are strongly influenced by the number of cracked holes clustered together. Referring to Table 3, the results from case numbers MSD406 and MSD402 show that there is a considerable difference in panel lives when the cracked holes are adjacent to one another as opposed to being separated by an uncracked hole. For example, if a total of 15 cracked holes are initially clustered together in groups of three, the panel life was 50,336 cycles. When the same number of holes are separated by an uncracked hole, the panel life was 79,407 cycles, which is 58% greater than for the clustered case.

Figure 11 is a bar chart of the total panel life versus the number of clustered holes in these panels. Similarly to the lead crack case, the plot shows the large reduction in the panel life as the applied loading increases. Additionally, it shows that for a particular applied load there is some minimum number of cracked holes which may be clustered together after which the total panel life is insensitive to additionally cracked holes. Referring to the bar chart, for a load level of 10.0 ksi, the panel life is about the same when there are clusters of 4 and 6 holes. For a load level of 12.5 ksi the chart shows that the panel life is insensitive to additional MSD once three holes are cracked, while for a load of 15.0 ksi two holes is the critical minimum.

Finally, within the limitations of this simplified study, it is worth noting that the most damaging case leading to the shortest panel life consisted of a lead crack in the presence of cracks at all the other holes in the immediate vicinity and subject to a 15.0 ksi applied load. For this case the total panel life was 1,270 cycles, which compares with the least damaging case which was a panel containing no lead crack

and several separately located cracked holes, remotely loaded at 10.0 ksi. The panel life for this case was 124,025 cycles, which is two orders of magnitude higher.

A Note On Predicted Crack Initiation Times

As explained, the predictive program applies a cumulative damage rule to determine when cracks initiate at uncracked holes. At zero life the initial accumulated damage is assumed to be zero, and is subsequently summed to 1.0 before cracks are initiated. In reality, the accumulated damage is not zero when the MSD problem starts. While it is possible to initialize the accumulated damage to some value between 0.0 and 1.0, there is no reasonable basis to select or calculate an appropriate value. It does, however, seem reasonable that since MSD is associated with aging aircraft subjected to thousands of pressurization loading cycles, then initially uncracked holes in any type of predictive scenario will probably have an accumulated damage closer to 1.0 than 0.0. (In this study 0.0 was selected and applied consistently throughout). Furthermore, since the application of Miner's rule to predict crack initiation is generally considered to have a large scatter band, it was not deemed necessary to fine tune it by adjusting the initial accumulated damage.

CONCLUSIONS

This paper described the development of a computer program to predict the fatigue crack growth, coalescence, and ultimate failure of a flat, unstiffened panel with a row of holes containing MSD. The numeric analysis was verified by a series of experimental test results which agreed well with the predictions. The program was then used to study the fatigue behavior of a wide panel containing many open holes and various crack configurations.

Within the limitation on considering every conceivable crack case, several conclusions were drawn from the parametric study. For panels with a lead crack plus MSD:

- a. MSD fatigue growth and coalescence forms a large crack which causes the panel to fail. Crack initiation delays the unstable extension of the longer cracks.
- b. The lead crack type has a strong effect on the fatigue life.
- c. MSD located immediately adjacent to a lead crack presents the most damaging crack configuration.
- d. The maximum applied cyclic stress greatly affects the total panel fatigue life.

For panels without lead cracks:

- a. A similar fatigue crack growth pattern as for the lead crack case applies.

- b. Panels containing clusters of cracked holes not separated by uncracked holes present the most damaging crack configuration.

REFERENCES

1. E.J. Moukawsher, "Fatigue Life and Residual Strength of Panels With Multiple Site Damage", M.S. Thesis, School of Aeronautics and Astronautics, Purdue University, May 1993.
2. E. J. Moukawsher, A. F. Grandt, Jr., and M. A. Neussl, "A Fatigue Analysis of Panels With Multiple Site Damage," *1992 USAF Structural Integrity Program Conference*, San Antonio, Texas, December 1-3, 1992
3. E. J. Moukawsher, A. F. Grandt, Jr. and M. A. Neussl, "Analysis of Panels with Multiple Site Damage," AIAA Paper No. 94-1459, *AIAA SDM Conference*, Hilton Head, SC, April 18-21, 1994.
4. N. E. Dowling, "Notched Member Fatigue Life Predictions Combining Initiation and Propagation," *Fracture of Engineering Materials and Structures*, Vol. 2, 1979, pp. 129-138.
5. D. P. Rooke and D. J. Cartwright, "Compendium of Stress Intensity Factors," *Her Majesty's Stationery Office*, London, 1976.
6. A. Kamei and T. Yokobori, "Two Collinear Asymmetrical Elastic Cracks," *Report of the Research Institute for Strength and Fracture of Materials*, Tohoku University, Vol. 10, Section 1-4, pp 41-42, December 1974.
7. T. Swift, "Effect of MSD on Residual Strength", from a presentation given at the U.S. Air Force Symposium on Multi-Site Damage, February 1992.
8. T. Swift, "Widespread Fatigue Damage Monitoring Issues and Concerns", 5th International Conference on Structural Airworthiness of New and Aging Aircraft, June 1993.
9. P. Tong, R. Grief, L. Chen, D.Y. Jeong, "Damage Tolerance of Fuselage Panels With Widespread Fatigue Damage", ICAF Conference, Stockholm Sweden, June 1993.
10. R.J. Bucci, H.J. Konish, "Test/Evaluation Protocols for Corrosion Damage Assessment - C/KC135 Corrosion Fatigue Round Robin Test Program", Report 57-93-24, October 1993.
11. K. Buhler, "A Study of Fatigue Crack Growth of Panels Containing Multiple Site Damage," M.S. Thesis, School of Aeronautics and Astronautics, Purdue University, December 1993.

Table 1. Parameters Associated With The Numeric Study

FIXED PARAMETERS:	
Panel Width	31.0 inch
Panel Thickness	3/32 inch
Material	2024-T3 Aluminum Alloy
Hole Diameter	3/16 inch
Hole Pitch	1.0 inch
MSD Lengths	0.05, 0.1 inch
VARIABLES:	
Applied Load	10.0, 12.5, 15.0 ksi
Lead Crack Geometry	three different configurations
MSD Locations	total 135 cases considered

Table 2: Highlights of Specific Results For Panels Containing Lead Cracks and MSD

CRACK CONFIGURATION								PANEL LIFE (CYCLES)		
LEAD CRACK TYPE	TEST REFER. NO.	TOTAL NO. OTHER CRACK HOLES	ZONE 1 NO. OF CRACK HOLES	ZONE 2 NO. OF CRACK HOLES	ZONE 3 NO. OF CRACK HOLES	ZONE 4 NO. OF CRACK HOLES	ZONE 5 NO. OF CRACK HOLES	LOAD: 10.0 KSI	LOAD: 12.5 KSI	LOAD: 15.0 KSI
1	MSD316	3	1	1	2	1	-	91,291	29,192	8,393
1	MSD322	3	1	1	2	-	1	91,281	-	-
1	MSD325	4	1	1	2	1	1	86,306	28,088	8,060
1	MSD331	4	-	-	6	-	-	32,414	10,034	3,082
1	MSD334	8	2	2	2	2	2	73,021	24,437	7,054
1	MSD340	3	-	3	2	-	-	55,821	23,606	8,438
1	MSD343	3	-	2	3	-	-	52,721	22,911	8,106
2	MSD326	4	1	1	2	1	1	45,578	13,133	3,241
2	MSD332	4	-	-	6	-	-	15,250	5,358	1,270
2	MSD335	8	2	2	2	2	2	40,921	12,051	2,988
3	MSD336	8	2	2	4	2	2	30,616	9,020	2,360

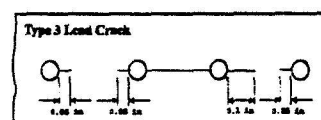
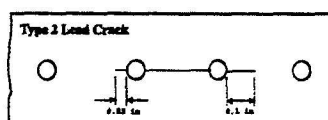
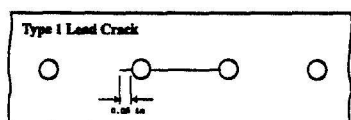
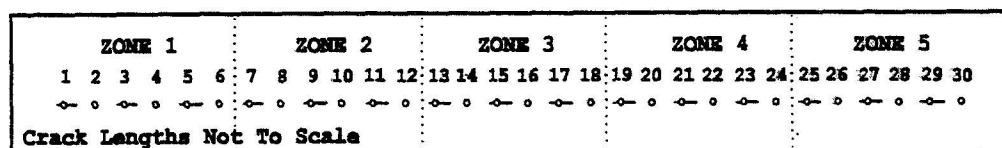


Table 3. Highlights of Specific Results For Panels Containing MSD Without a Lead Crack

CRACK CONFIGURATION								PANEL LIFE (CYCLES)		
TEST REFER. NO.	TOTAL NO. OF CRACK HOLES	ZONE CRACK CONFIG	ZONE 1 NO. OF CRACK HOLES	ZONE 2 NO. OF CRACK HOLES	ZONE 3 NO. OF CRACK HOLES	ZONE 4 NO. OF CRACK HOLES	ZONE 5 NO. OF CRACK HOLES	LOAD: 10.0 KSI	LOAD: 12.5 KSI	LOAD: 15.0 KSI
MSD401	30	GROUP	6	6	6	6	6	41,596	20,394	11,478
MSD406	15	GROUP	3	3	3	3	3	50,336	21,797	12,237
MSD402	15	APART	3	3	3	3	3	79,407	37,992	20,668
MSD405	10	GROUP	2	2	2	2	2	67,010	27,369	12,981
MSD403	10	APART	2	2	2	2	2	97,727	40,146	20,956
MSD404	5	APART	1	1	1	1	1	124,025	54,066	27,986

Note: GROUP = clusters of initially cracked hole grouped together,
 APART = cracked holes initially separated by one or more uncracked holes.



Example: MSD402 - Cracked holes separated by uncracked holes.

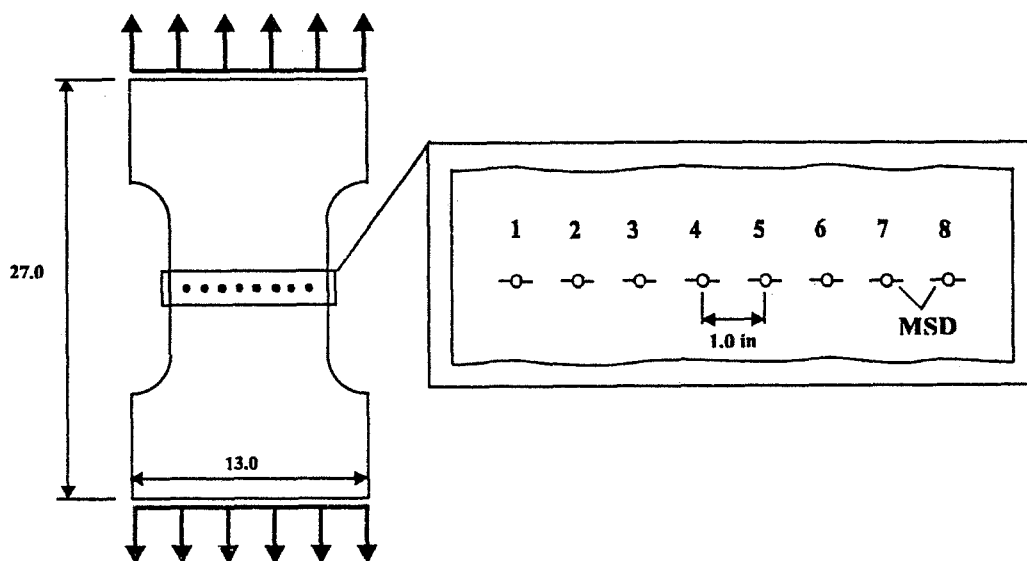


Figure 1. Typical fatigue specimen with cracks at all holes.

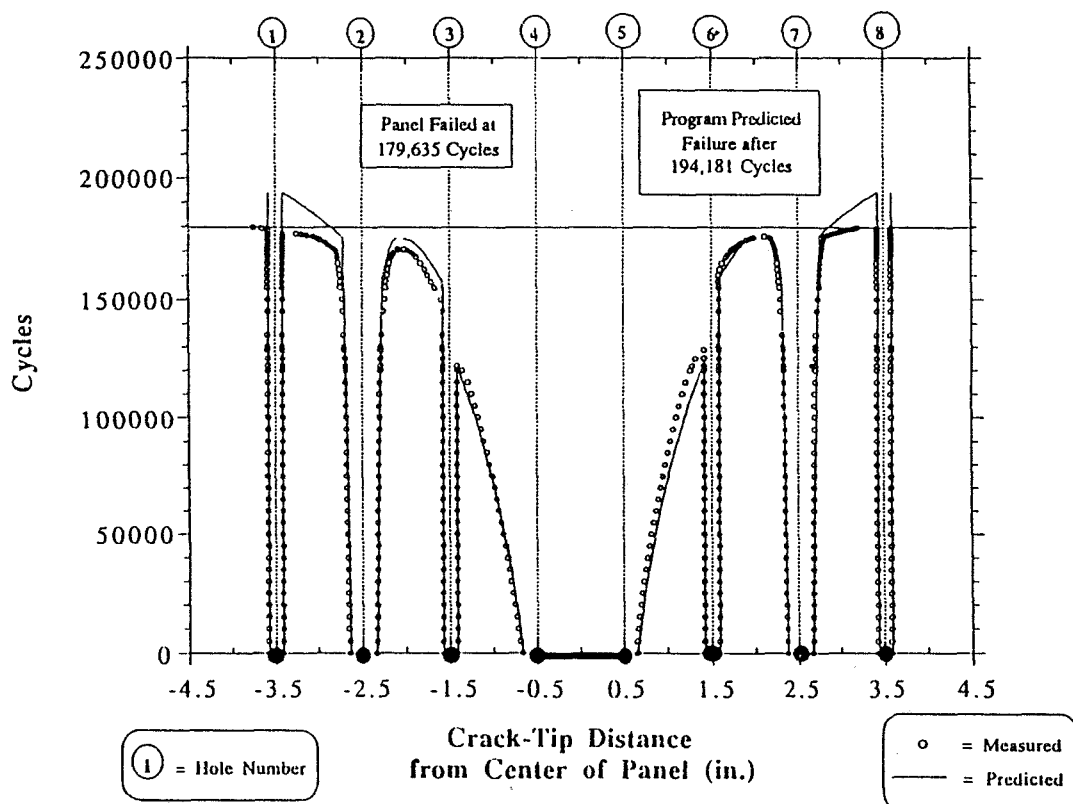


Figure 2. Sample comparison of measured and predicted MSD crack propagation diagram.

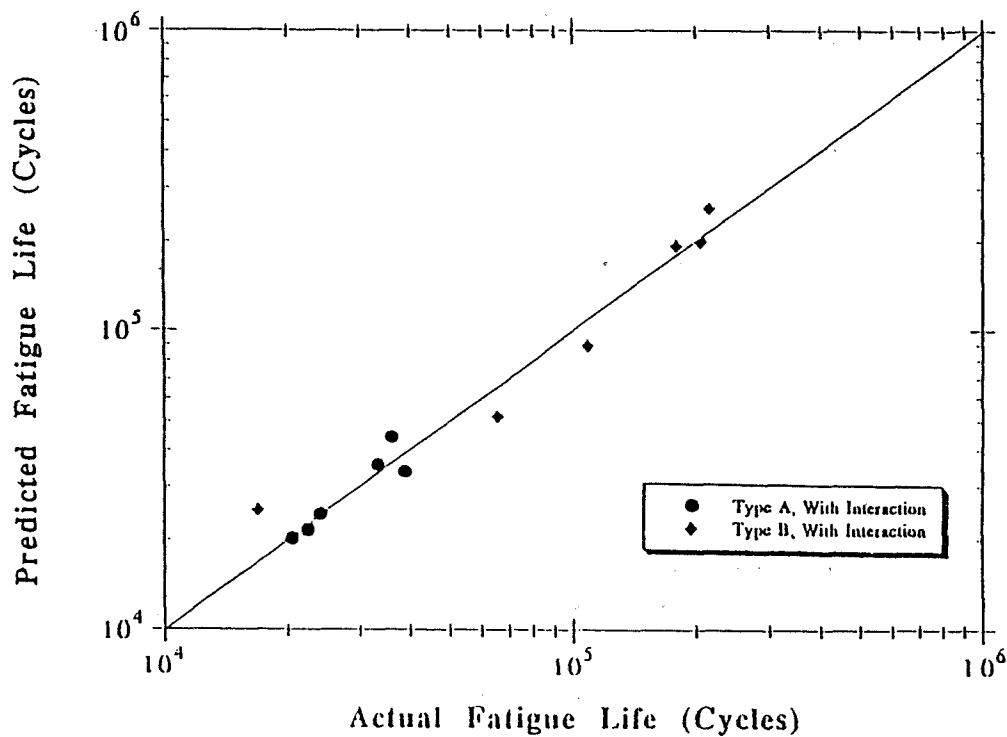
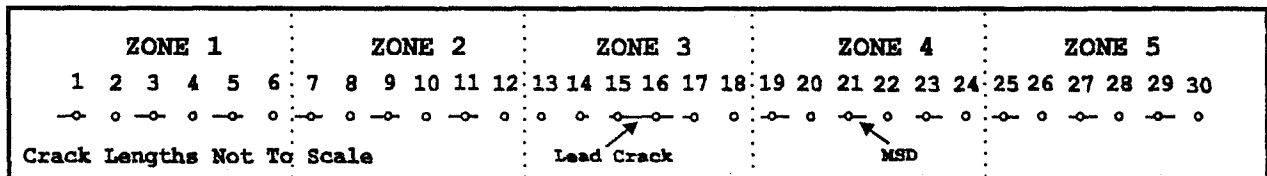
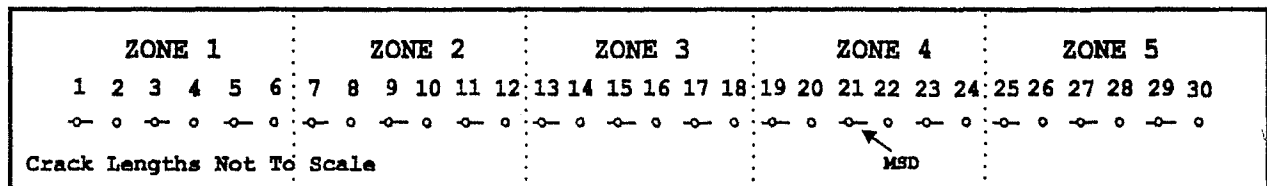


Figure 3. Predicted versus actual fatigue lives for 12 test specimens.



Example of a cracked panel containing MSD and a lead crack.



Example of a cracked panel containing MSD at every alternate hole.

Figure 4. Typical starting configurations considered in numeric study.

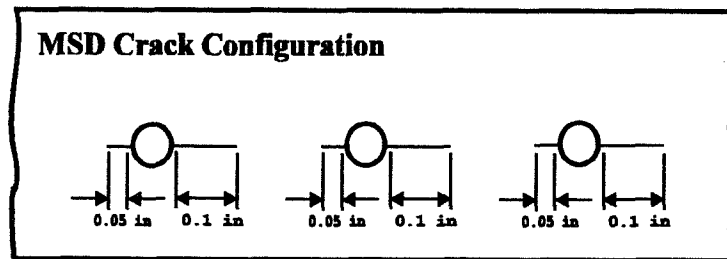


Figure 5. Details of MSD crack configuration.

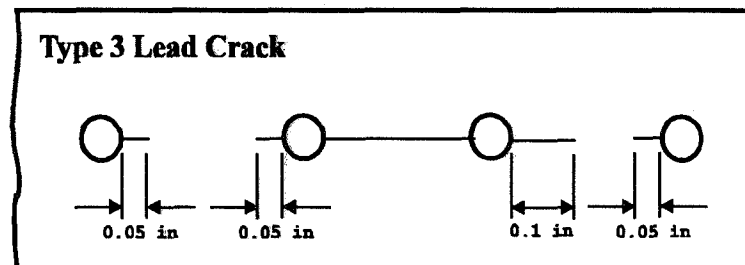
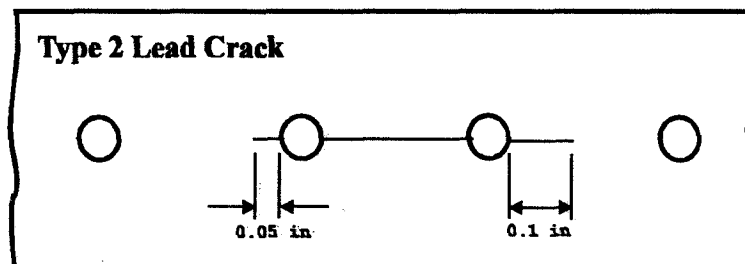
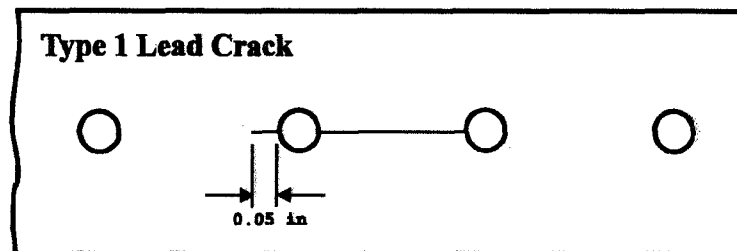
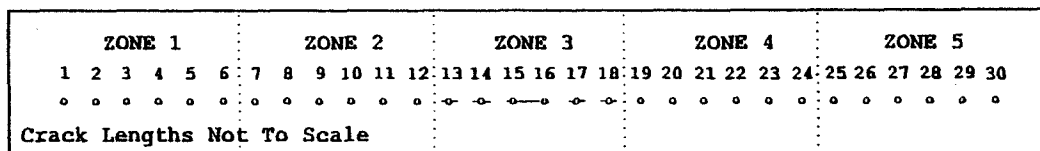


Figure 6. Details of the lead crack configurations.



Initial Crack Configuration

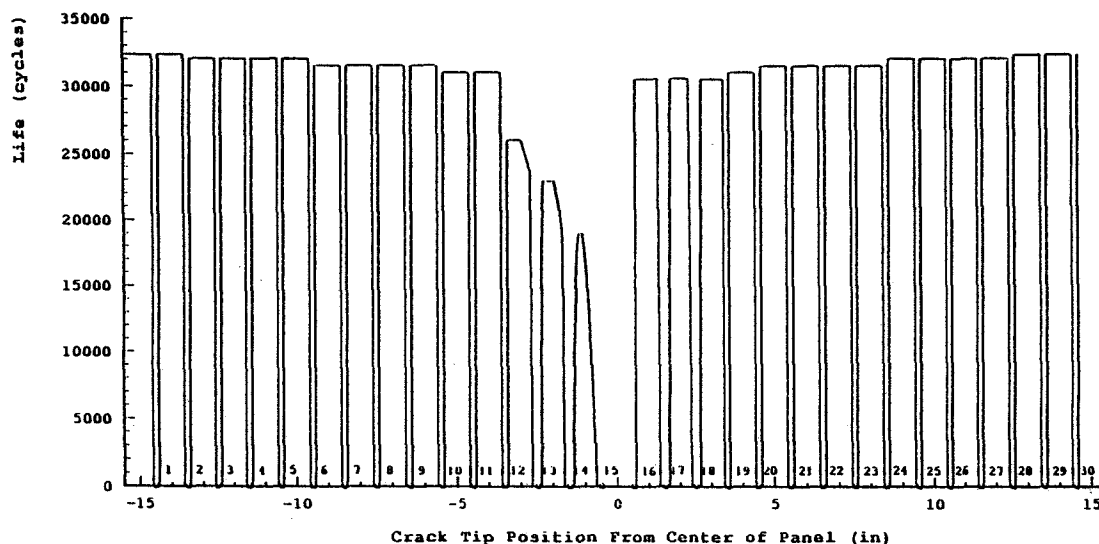
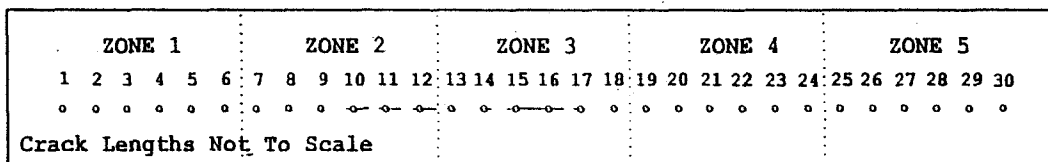


Figure 7. Sample crack propagation diagram for a panel containing a lead crack.



Initial Crack Configuration

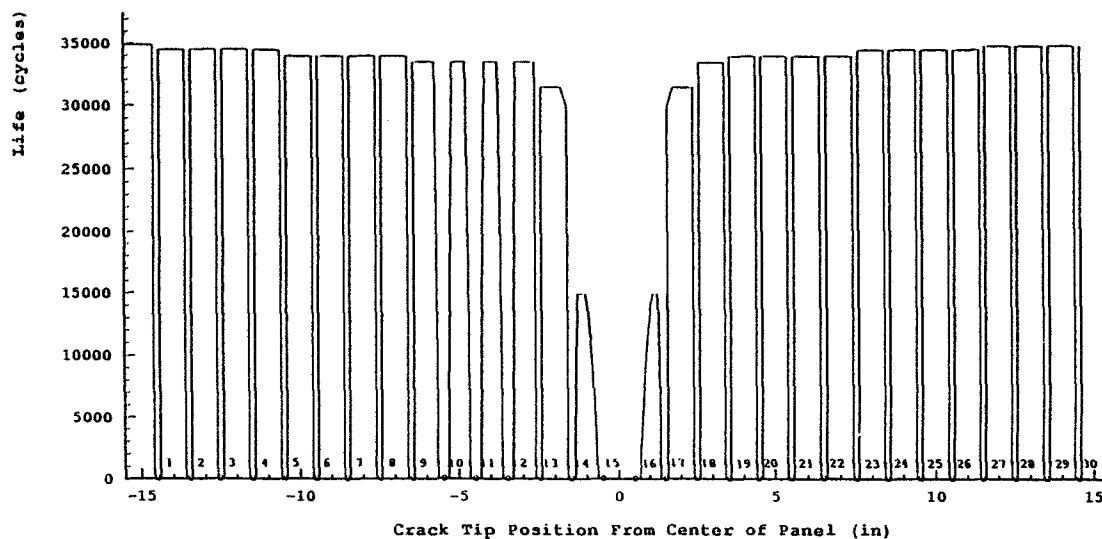


Figure 8. Sample crack propagation diagram for a panel containing a lead crack and adjacent MSD.

ZONE 1						ZONE 2						ZONE 3						ZONE 4						ZONE 5					
1	2	3	4	5	6	7	8	9	10	11	12	13	14	15	16	17	18	19	20	21	22	23	24	25	26	27	28	29	30
o	o	o	o	o	o	o	o	o	o	o	o	o	o	o	o	o	o	o	o	o	o	o	o	o	o	o	o	o	o

Crack Lengths Not To Scale

Initial Crack Configuration

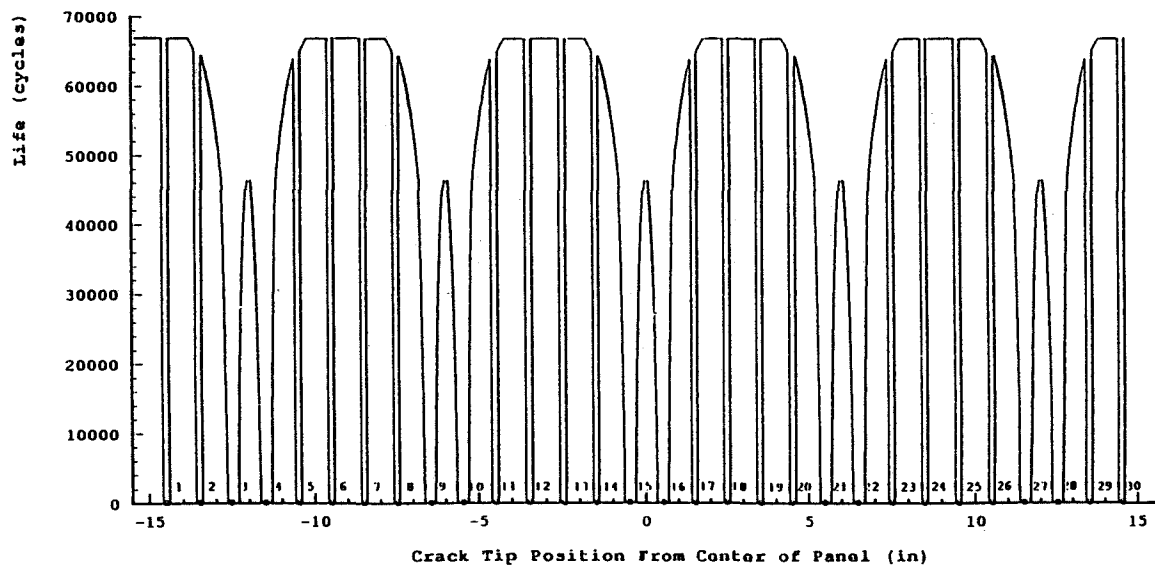


Figure 9. Sample crack propagation diagram for a panel containing pairs of holes with MSD.

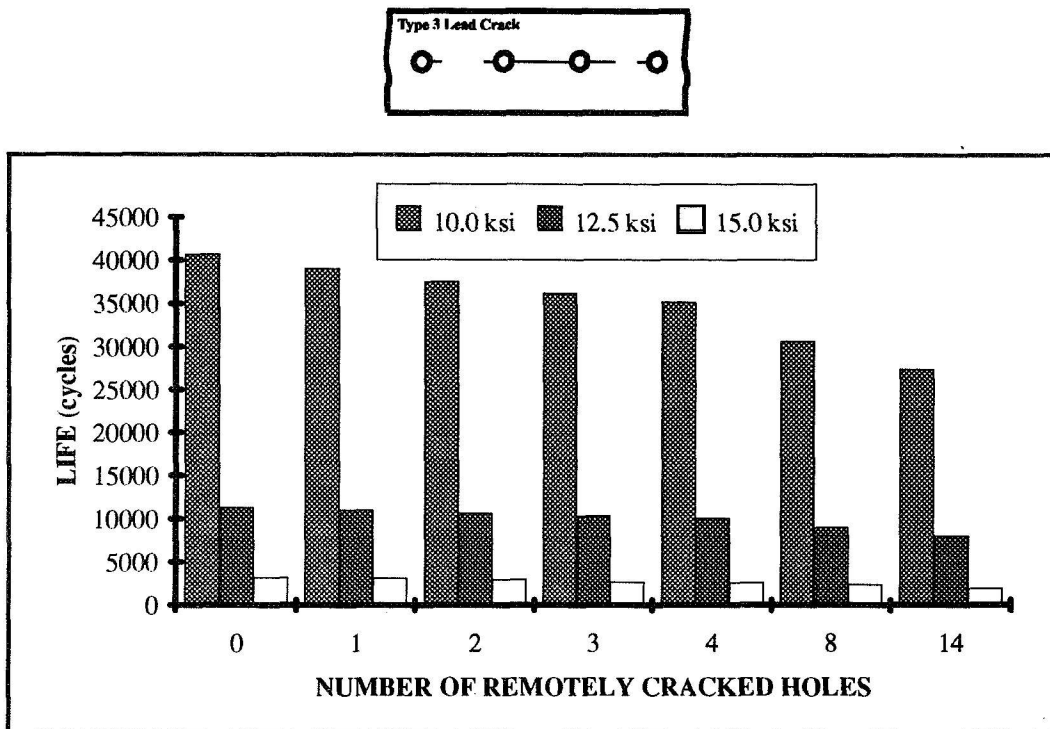


Figure 10. Total panel life versus number of cracked holes remotely located from the lead crack for the type 3 lead crack.

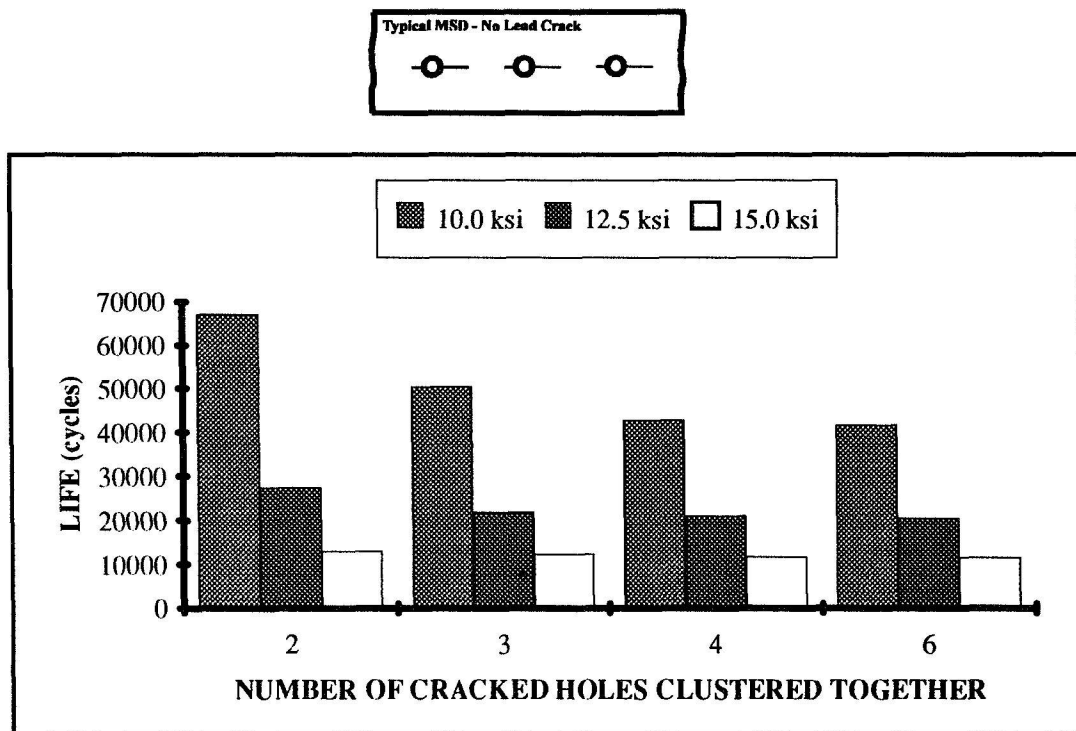


Figure 11. Total life versus number of clustered holes for panels containing no initial lead crack.

**A METHOD OF CALCULATING THE SAFE FATIGUE LIFE
OF COMPACT, HIGHLY-STRESSED COMPONENTS**

348628

511-39

23105

p. 12

Arthur W Cardrick
Defence Research Agency
Farnborough, Hampshire, England

Vera J Pike
Defence Research Agency
Farnborough, Hampshire, England

SUMMARY

This paper describes a method which has been developed for estimating the safe fatigue life of compact, highly-stressed and inaccessible components for aeroplanes and helicopters of the Royal Air Force. It is explained why the Design Requirements for British Military Aircraft do not favour the use of a damage-tolerance approach in these circumstances.

INTRODUCTION

Performance considerations dictate that the structures of many types of military aircraft are compact and highly stressed. In consequence, many components are relatively inaccessible for inspection and stresses are often so high that cracks which are only just perceptible can cause appreciable reductions in strength.

Good practice dictates that the materials used for these inaccessible components must be of consistently high quality with high toughness and good corrosion resistance as well as good fatigue performance. Additionally, the design of the components must be such that the desired fatigue performance can be achieved using standard manufacturing processes which do not themselves leave room for inconsistencies. The consistency that is inherent in a good design is achieved in service by providing protection against corrosion and accidental damage and ensuring that this protection is maintained throughout the life.

The Airworthiness Division of DRA, formerly RAE, Farnborough is the principal architect of the Fatigue Design Requirements for British Military Aircraft (1) and so we begin by explaining why we have retained a safe-life [S-N] procedure for estimating the fatigue performance of compact, highly-stressed and inaccessible components rather than moving to a damage-tolerance approach. We then outline an advanced method of life estimation [providing a best estimate of the mean/typical life] that has been developed for application under the wide range of conditions that must be considered in design (2). Returning to our Design Requirements role, we outline the basis of the factor of 3 1/3 that has been used for major fatigue tests [to allow for the intrinsic scatter in fatigue performance between

one airframe and another] and describe the Safe S-N procedure that has been developed to allow for the changes in scatter that accompany changes in the slope of the S-N curve (3). It is explained how this procedure is used to adjust the test factor of $3 \frac{1}{3}$ when the service loading severity differs appreciably from that used for the major fatigue test and how it is also used to assess the effectiveness of the test in proving the safe life of all fatigue-sensitive features of the structure.

WHY WE HAVE RETAINED A SAFE-LIFE APPROACH FOR ESTIMATING THE LIFE OF COMPACT, HIGHLY-STRESSED COMPONENTS

The safe-life procedure that is used for estimating the fatigue performance of *compact, highly-stressed and inaccessible components* for British military aeroplanes and helicopters has its roots in an approach introduced in the mid fifties to provide a disciplined basis for demonstrating compliance with the increasing fatigue life requirements that were then being specified. The need for loads monitoring has always featured in British safe-life requirements and it is perhaps largely for this reason that we have not suffered the shortcomings which caused the USAF to become dissatisfied with the approach in the mid sixties (4). Indeed, we believe the balance between performance and safety is about right - the chance of losing a British combat aircraft due to a fatigue failure is about as low as the chance of death due to a road accident when driving a car (5), Figure 1 . Like other airworthiness authorities, we accept the use of a damage-tolerance approach for those components which are relatively accessible for inspection and have crack growth characteristics which enable damage to be detected, reliably, before the safety of the structure is seriously impaired.

When, in 1969, an F-111 aircraft was lost from a serious manufacturing defect in a compact, highly-stressed and inaccessible component after only 100 flying hours, the USAF introduced the 'initial flaw' concept and thereby grasped the nettle of applying the damage-tolerance approach to uninspectable structure. [The slow-crack-growth option which forms the basis of this step has always been available in the British Military Requirements, but we have always insisted that there must be an appreciable period during which the crack growth is *inspectable*]. Even today, however, there remain appreciable uncertainties in applying the concept to compact, highly-stressed components in which the period of detectable crack growth is insufficient to provide confidence in the analysis.

Like the USAF, we were concerned at the gap in the safe-life requirements which was exposed so vividly by the loss of the F-111, but in our case (6) we chose to address the problem by making the good practice outlined in the previous section a condition of compliance viz.,

- (i) the materials used must be of consistently high quality with high toughness and good corrosion resistance as well as good fatigue performance,
- (ii) the design of the components must be such that the desired fatigue performance can be achieved using standard manufacturing processes which do not themselves leave room for inconsistencies, and
- (iii) the components must be protected against corrosion and accidental damage throughout their service lives.

Where a compact and highly-stressed component is susceptible to accidental damage, an initial-flaw approach may provide an alternative to re-design, but the validity of the inspection periodicity would need to be demonstrated by test and any inspection penalty would need to be acceptable to the operator.

AN ADVANCED METHOD OF FATIGUE LIFE ESTIMATION

The literature on methods of fatigue life estimation is strewn with good intentions - methods which have worked well for the special conditions under which they were developed, but which have been found wanting when applied over the wide range of conditions which must be considered in design. For this reason, Miner's Rule is still widely used in design and certification - although it is normally used only as a transfer function between a test under realistic loading and the actual loading applied in service.

For some years there has been a realisation that in the absence of realistic test data upon which to adjust the Miner calculation, it is possible to improve the estimate for metal components by taking account of local residual stresses that may be generated by local plastic deformation under extreme cycles in the loading spectrum. It has also been recognised that when most of the fatigue life is occupied by the formation of microcracks, rather than by their propagation, a further 'elastic' interaction may need to be taken into account (7). It is noteworthy that an alternative method of allowing for the interaction effects associated with local plasticity is favoured by the US Navy. This uses the local strain theory due to Neuber together with special test data obtained under constant *strain* amplitude (8). The method makes no specific allowance for elastic interaction, but, as with our own approach, there is provision for calibration factors to be built-in as experience is gained over the wide range of conditions which are encountered in design.

The method of life estimation developed by the authors (2) uses conventional constant [load] amplitude S-N data as a basic building block and this is adjusted to allow for the effects of residual stresses and elastic interaction.

In developing the method, the range of structural features which must be considered in design was represented by lug specimens (high stress concentration and fretting - life occupied largely by *propagation* of microcracks) and open-hole specimens (moderate stress concentration, no fretting - life occupied largely by *initiation* of microcracks), with the addition of double-dog-bone specimens assembled using interference-fit fasteners and interfay. Most of the lugs and all of the open-hole specimens were manufactured from aluminium alloys, titanium alloy (annealed), NiCrMo steel and maraging steel. The specimens were tested to failure, under constant amplitude loading and spectra representing aeroplane and helicopter applications (9). In total, the lives estimated were evaluated against 30 different test conditions, representing data from more than 300 fatigue tests.

For lug specimens (representing fastened joints with high load transfer through the fasteners), the method provided a good estimate of the life in most cases; (achieved life)/(estimated life) = 1.0 on average compared with a figure of 3.6 (conservative) for Miner's Rule. However, for the NiCrMo steel specimens the life was *overestimated* (unconservative) by a factor of between 1.5 and 10.

For all the types of specimen taken together (representing fastened joints, fillets and open holes), the method was equally applicable; (achieved life)/(estimated life) = 1.1 on average compared with a figure of 2.8 (conservative) for Miner's Rule. The life was *overestimated* (unconservative) by a factor of 1.5 or more on only 5% of occasions if the NiCrMo steel lug specimens were excluded.

The main feature of the method is that, without the need for special data, it does seem to provide a more consistent estimate of fatigue performance than Miner's Rule when applied across the range of structural features and loading spectra that must be considered in design. However, in any application we always try to find *some* test data upon which to build confidence in the validity of the estimates.

OBTAINING A SAFE LIFE USING THE SAFE S-N PROCEDURE

In the mid fifties, when most structures were made from aluminium alloys, large numbers of structural components, such as wings and tailplanes, were tested to failure under various fatigue loadings. The results of these tests formed the basis of the our safe-life requirements. Most fatigue failures were found to occur in joints where the effects of fretting were combined with high shear transfer through the fasteners - these features having the lowest ratio of fatigue to static strength. On the basis of this evidence, our predecessors recommended that the test life of an airframe [under realistic loading] should be reduced by a factor of $3 \frac{1}{3}$ to allow for the scatter between one airframe and another. The factor was believed to correspond to the ubiquitous 'three standard deviations down' on the mean fatigue life and also included an allowance for the uncertainty in using only one specimen to estimate the mean. An additional factor of 1.5 was specified for use in cases where loads were unmonitored. Thus, the design of safe-life components for British military aircraft has been driven by the need to satisfy this test requirement.

It is well known that the scatter in fatigue life is lowest at the highest severities of loading, where the S-N curve is steep, and that scatter increases progressively as the loading severity is reduced - eventually becoming so large that it must be handled using a factor on stress. The Safe S-N approach (3) makes an allowance for this variation in scatter and enables the life factor that is applied in interpreting the test loading to be adjusted from $3 \frac{1}{3}$ to a more appropriate value in those cases where the severity of loading in service differs appreciably from that applied on test.

Additionally, the Safe S-N procedure is used to assess the adequacy of the test factor of $3 \frac{1}{3}$ for other components. Where a shortfall is apparent, a supplementary compliance is required.

Derivation of Safe S-N Curves

The factors on life and stress which are specified for the construction of Safe S-N curves are based upon a statistical analysis of the scatter of large numbers of specimens representing structural components made from aluminium alloys, titanium alloy and steels. These specimens were tested to failure under spectra representing aeroplane and helicopter applications (9). Each sample of tests was used to construct an S-N curve of [four-parameter] Weibull form viz.,

$$S = S_{inf}(1 + A/(N+G)^m)$$

where S_{inf} = stress severity at fatigue limit
 A = numerical constant
 G = numerical constant governing low endurances
 m = numerical exponent

For loading severities, S , typical of the lower surface of combat aeroplane wings, the scatter was found to differ appreciably between features and materials, but these large differences tended to disappear when the comparison was based on the local *slope* of the S-N curve. At the fatigue limit the scatter [coefficient of variation in S_{inf}] was not considered to be sufficiently dissimilar for a distinction to be made between the different features and materials.

For aluminium alloy lugs [representing the joints with high shear transfer through the fasteners which featured so prominently in the tests done in the fifties], our tests showed that the customary life factor of 3 1/3 corresponds to a probability of failure of about 1 in 1,000 for a loading severity corresponding to a safe life of between about 6,000 and 9,000 flying hours. At the fatigue limit, this probability of 1 in 1,000 corresponds to factor on stress of about 1.5 [scatter at S_{inf} assumed to be the same in all cases]. Thus, by analysing the scatter observed for aluminium alloy lugs at various loading severities, we were able to construct a continuous 'Safe S-N curve' that corresponds to a probability of failure of 1 in 1,000 and is consistent with the practice of using a factor of 3 1/3 for major tests. By applying the life factor from the steepest part of the curve [2.8] to the steepest part of the curves for the other features and materials, together with the stress factor of 1.5 at the fatigue limit, we were able to construct Safe S-N curves that produced a working approximation to the scatter which had been observed in each case.

In order to use the test factors on life and stress in estimating a safe life, or generating a test spectrum, it is necessary to apply them to an estimated mean S-N curve for *constant amplitude* loading and blend them together to form a continuous curve. The need to blend the curves arises when the shape of the S-N curve for constant amplitude loading differs from that under the spectrum loading from which the scatter data was derived. For S-N curves of Weibull form, as are commonly used in aerospace applications, a numerical method is available to eliminate any inconsistencies in this blending process (10). A Safe S-N curve drawn using this procedure is illustrated in Figures 2 and 3.

The factors specified for the construction of Safe S-N curves (1) enable account to be taken of the number of tests used to estimate the mean fatigue performance and the number of components on the aircraft [normally two nominally identical tests/components per airframe and 6 tests/4 components for helicopter dynamic components]. Corresponding procedures can be used to derive Safe S-N curves for any desired probability of failure.

Applications of the Safe S-N Procedure

The introduction of the Safe S-N approach into the Fatigue Design Requirements for British Military Aircraft has been accompanied by a number of other changes which are designed to enable the most effective balance to be achieved between the often conflicting requirements of performance, durability and safety (11). Notably, all components must now be shown to have a certain minimum fatigue life under the increases in loading severity that are likely to occur in service. In addition, airframe structures - with the exception of those of helicopters - must be subjected to an additional - termed 'preliminary' - fatigue test that will identify any major shortcomings so that these can be corrected before production is established.

Applications to Combat Aeroplanes

The British Aerospace Hawk, Figure 4, is used by the Royal Air Force for flying training of a general nature and for training in the use of tactical weapons (12). The loading spectrum experienced in the tactical weapons role is markedly more severe than the loading applied in the major fatigue test. When life factors for aluminium alloy lugs are derived for the two loadings, we find that the factor for the more severe loading is lower by about 10%. It is noteworthy that in this computation we have used the method of life estimation described earlier in order also to take into account the beneficial effects of the residual stresses generated under the higher loads. Thus, we have recommended that the factor of $3 \frac{1}{3}$ should be reduced to 3 in computing the fatigue life consumed in the tactical weapons role. We estimate that the increase in life resulting from this reduced factor will save the Royal Air Force in the region of £50M.

By contrast, the Panavia Tornado, Figure 5, has been tested to a spectrum that is *more* severe than that encountered in service. When the life factors for aluminium alloy lugs are derived for the two severities of loading we find that the factor for the less severe loading is higher by about 20%. If this increase is applied to the usual factor of $3 \frac{1}{3}$, the factor becomes 4 for Royal Air Force aircraft. However, the increase in mean life at this lower severity is more than sufficient to compensate for the increase in factor.

Applications to Transport Aeroplanes

The structures of transport aeroplanes are relatively accessible for inspection and critical crack sizes are usually such that regular inspections of a general nature can be relied upon to detect damage before the safety of the structure is seriously impaired. However, as fleets of transport aeroplanes have become older there has been an increasing awareness that the damage tolerance of some components can be undermined and so there has been a return to the safe-life concept to provide a guide to the finite life that must be imposed in such cases.

We have calculated that for older aircraft, which were designed for a service life of about 30,000 flights [and for a test life of between about 100,000 and 150,000 flights], the effect of interpreting the major test using the Safe S-N procedure rather than a factor of $3 \frac{1}{3}$ would be to increase slightly the life of the pressure cabin and to decrease slightly the life of joints with high shear transfer through the

fasteners. It is emphasised, however, that the life of the pressure cabin would not be extended unless an exhaustive test had been done and the necessary standard of 'good practice' could be demonstrated. Other features, such as joints with relatively low shear transfer through the fasteners and sculptured fillets would have their safe lives approximately halved. In extreme cases, it is possible that the probability of occurrence of damage of a critical size could rise from about 1 in 1,000 at the reduced safe life to nearer 1 in 20 at the end of the life obtained using a factor of $3^{1/3}$; items for which an insufficient safe life had been demonstrated would be the subject of a supplementary compliance.

Applications to Helicopters

The usage of helicopters is not monitored as closely as that of military aeroplanes and so the fatigue spectrum used for design is necessarily rather conservative.

Wherever practicable, components are designed so that the stress amplitudes associated with normal usage are below the flat portion of the Safe S-N curve. The stress factor of about 1.5 used in the derivation of the Safe S-N curve is somewhat lower than the factor customarily used for the aluminium alloy components of British military helicopters, but slightly higher than the factors used for components manufactured from steels, titanium alloys and fibre composites. Nevertheless, the influence of introducing the Safe S-N approach in this relatively flat region of the S-N curve is likely to be fairly minor in relation to the influence of the various conservatisms that must necessarily be associated with design.

Those components which, exceptionally, experience most damage on the relatively steep part of the S-N curve, are known to have unnecessarily conservative lives if the stress factor is retained in this region. Therefore, in circumstances where the life is found to be too low, it has been usual to adopt the fixed life factors used for aeroplanes. In such circumstances, the effects of introducing the Safe S-N approach will be much the same as those already described.

CONCLUDING REMARKS

Good practice dictates that the materials used for compact, highly-stressed and inaccessible components must be of consistently high quality with high toughness and good corrosion resistance as well as good fatigue performance. Additionally, the design of the components must be such that the desired fatigue performance can be achieved using standard manufacturing processes which do not themselves leave room for inconsistencies. In order to achieve the consistency that is inherent in good design it is, of course, essential to provide protection against corrosion and accidental damage and to maintain this protection throughout the life.

When this good practice is followed, the safe-life [S-N] procedure is considered to provide a satisfactory method of substantiating fatigue life. Indeed, for compact, highly-stressed and inaccessible components we specify that the safe-life procedure *must* be used. Where a compact and highly-stressed component is susceptible to accidental damage, an initial-flaw approach may provide an alternative to re-design, but the validity of the inspection periodicity would need to be demonstrated by test and any inspection penalty would need to be acceptable to the operator.

Given the good practice outlined above and an acceptable procedure for monitoring the service loading, the validity of the safe-life approach centres on the method of life estimation and the procedure used for allowing for the intrinsic scatter between one component and another.

An advanced method of life estimation has been outlined and this is shown to be more consistent than Miner's Rule when applied to a range of conditions that must be considered in design.

Returning to our Design Requirements role, we have outlined the basis of the factor of 3 1/3 that has been used for major fatigue tests [to allow for the intrinsic scatter in fatigue performance between one component and another] and have described the Safe S-N procedure that has been developed to allow for the changes in scatter that accompany changes in the slope of the S-N curve. It has been explained how this procedure is used to adjust the test factor of 3 1/3 [on the basis of data for aluminium alloy lugs tested under realistic loading] when the service loading severity differs appreciably from that used for the major fatigue test and how it is also used to assess the effectiveness of the test in proving the safe life of all fatigue-sensitive features of the structure.

As something of an anecdote, we refer to a problem in fatigue life estimation set by the US Army some years ago (13). The principal helicopter manufacturers were invited to estimate the safe fatigue life of a pitch link - for those unfamiliar with helicopters, this is an axially-loaded item looking rather like a turnbuckle. Details were provided of the design and of the fatigue performance of the component under constant amplitude loading. It was left to the individual manufacturers to choose an appropriate S-N curve, make an allowance for the intrinsic scatter in fatigue performance and estimate the safe life. Before disclosing his estimate of the life, Charles Hardersen of Kaman Aerospace Corporation observed that as fatigue lives were important to both safety and economics, if engineers didn't calculate them then accountants would probably get the job. He also observed that when confronted with a common body of data, accountants generally arrived at the same answer. *The safe lives estimated by the various manufacturers were 58, 191, 470, 6450, 22523 and 24570 hours!* For the record, using the method we have described here, we obtained a safe life of 590 hours.

REFERENCES

1. Joint Airworthiness Committee: *Design and Airworthiness Requirements for Service Aircraft*. Ministry of Defence Def Stan 00-970, Vol 1, Chapter 201 and accompanying leaflets.
2. Cardrick, Arthur W.; and Pike, Vera J.: *An Advanced Method of Fatigue Life Estimation*. Defence Research Agency MS1/93/WP/009, 1993
3. Cardrick, Arthur W.: *The Safe S-N Curve and Its Influence on the Performance, Durability and Safety of British Military Aircraft*. Defence Research Agency MS1/93/WP/001, 1993
4. Lincoln, John W.: *Damage Tolerance - USAF Experience*. Proc. 13th Symposium of the International Committee on Aeronautical Fatigue, EMAS Publ. Co., 1985
5. Cardrick, Arthur W.; and Curtis Paul T.: *The Certification of Composite Structures for Military Aircraft*. Institution of Mechanical Engineers, AeroTech 92, C428/37/198, 1992
6. Cardrick, Arthur W.; Maxwell, Roy D. J.; and Morrow, Sarah M.: *How Future UK Military Aircraft Will Be Designed for Tolerance to Fatigue Damage*. Proc. Institution of Mechanical Engineers ISBN 0 85298 596 7 (Vol 1), 1986, pp. 15-22.
7. Cardrick, Arthur W.: *Fatigue Life Estimation and Material Evaluation Procedures for Structural Components Subjected to Variable Amplitude Loading*. PhD Thesis, City University, London, 1973
8. Impellizzeri, L. F.: *Cumulative Damage Analysis in Structural Fatigue*. ASTM STP 462, 1970
9. Perrett, Brian H. E.: *Fatigue Endurance of Structural Elements in Various Materials under Constant Amplitude and Variable Amplitude Loadings*. Royal Aircraft Establishment TR 77162, 1977
10. Sweeting, T. J.: *A Method for the Construction of Safe S-N Curves*. J. Fatigue and Frac. of Eng. Mats. and Structs., Vol 15, No. 4, 1992, pp. 391-398
11. Cardrick, Arthur W.: *Responding to the Challenge - A Short Guide to the Principles underlying some Recent Changes to the Design Requirements for British Military Aircraft*. Institution of Mechanical Engineers Seminar on the Structural Integrity of Civil and Military Aircraft, Bristol, 1990
12. O'Hara, John: *Fatigue Design, Test and In-Service Experience of the BAe Hawk*. AGARD SMP Symposium, Bordeaux, 1993
13. Arden, Robert W.: *Hypothetical Fatigue Problem*. Proc. American-Helicopter Soc. Specialists' Mtg., St Louis, 1980



Figure 1. The chance of losing a British combat aircraft due to a fatigue failure is about as low as the chance of death due to a road accident when driving a car.

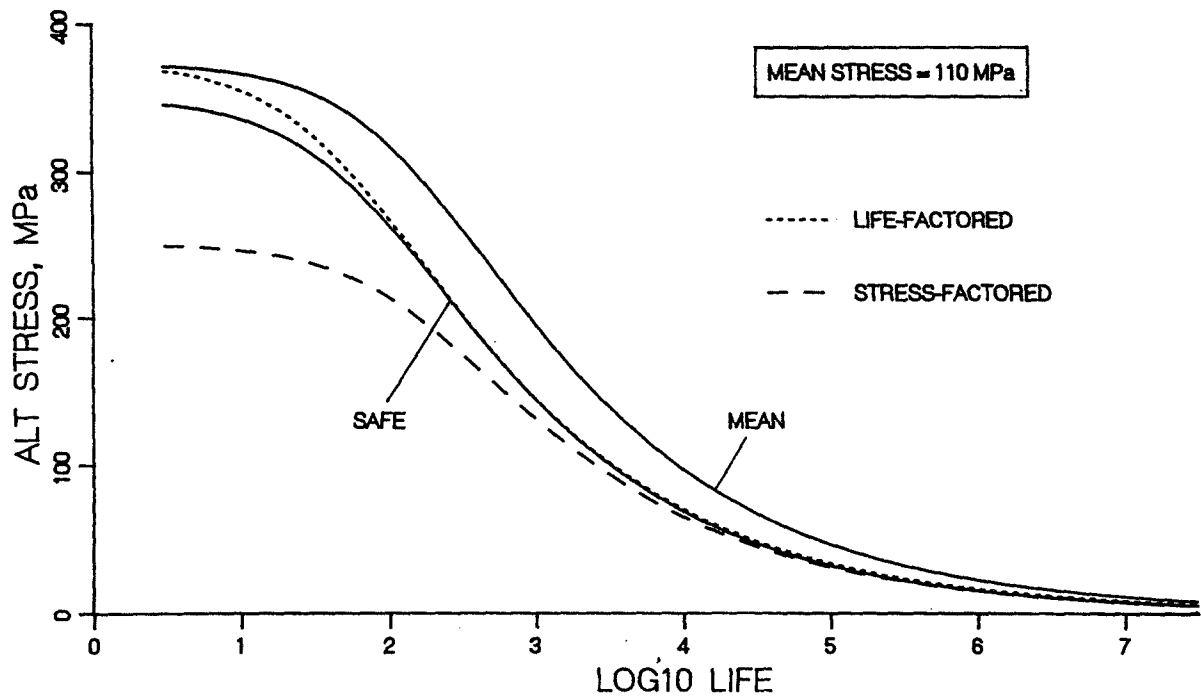


Figure 2. Safe S-N curve of Weibull form - showing compatibility with a safe value of static strength (B value: 460 MPa) - drawn using a numerical method (10).

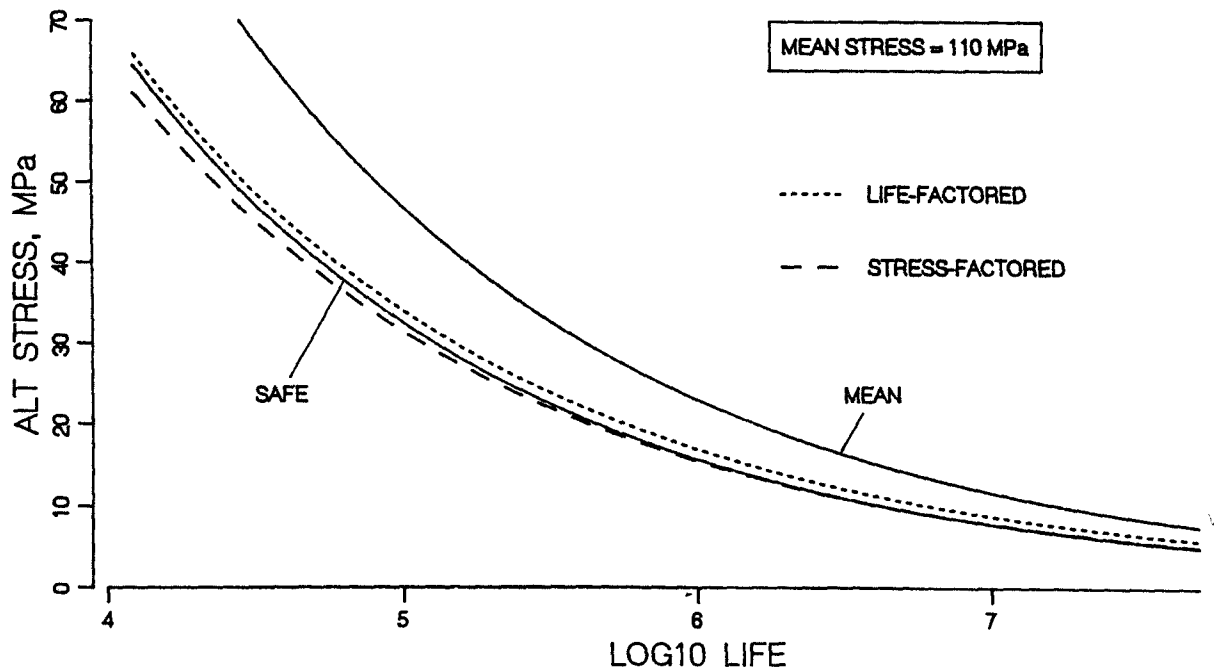


Figure 3. Safe S-N curve of Weibull form - showing transition between life and stress factors in region of most interest - drawn using a numerical method (10).

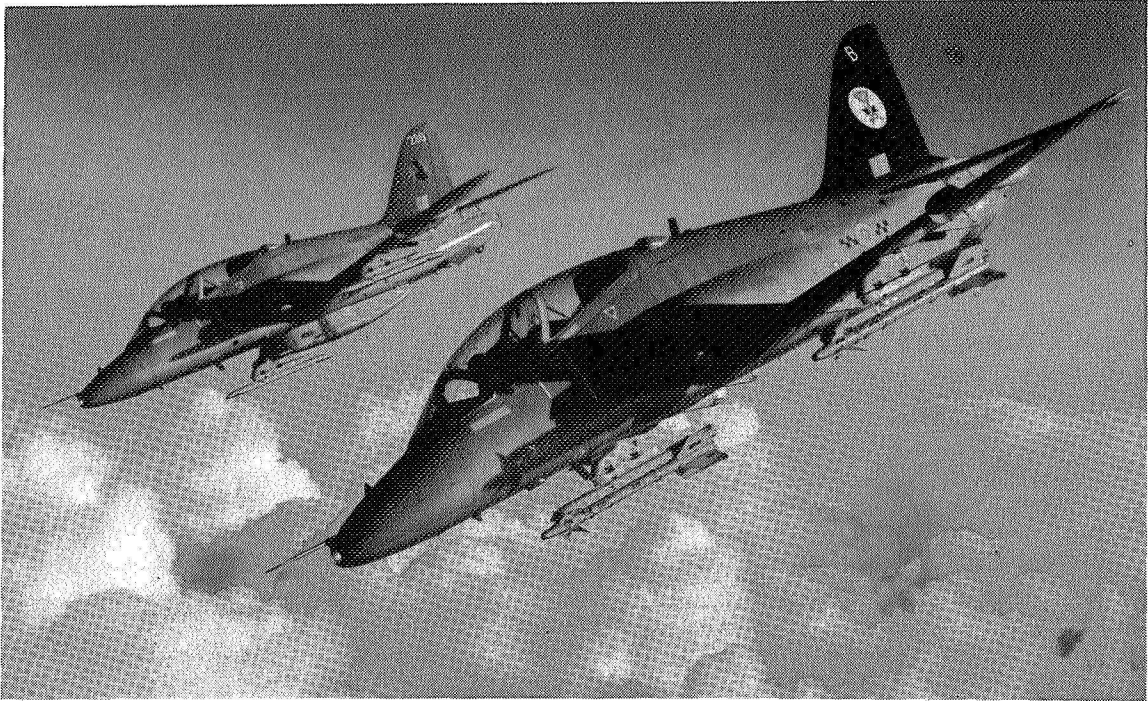


Figure 4. The loading spectrum experienced by the British Aerospace Hawk in the Tactical Weapons role is markedly more severe than that applied in the fatigue test and so a lower scatter factor is needed.

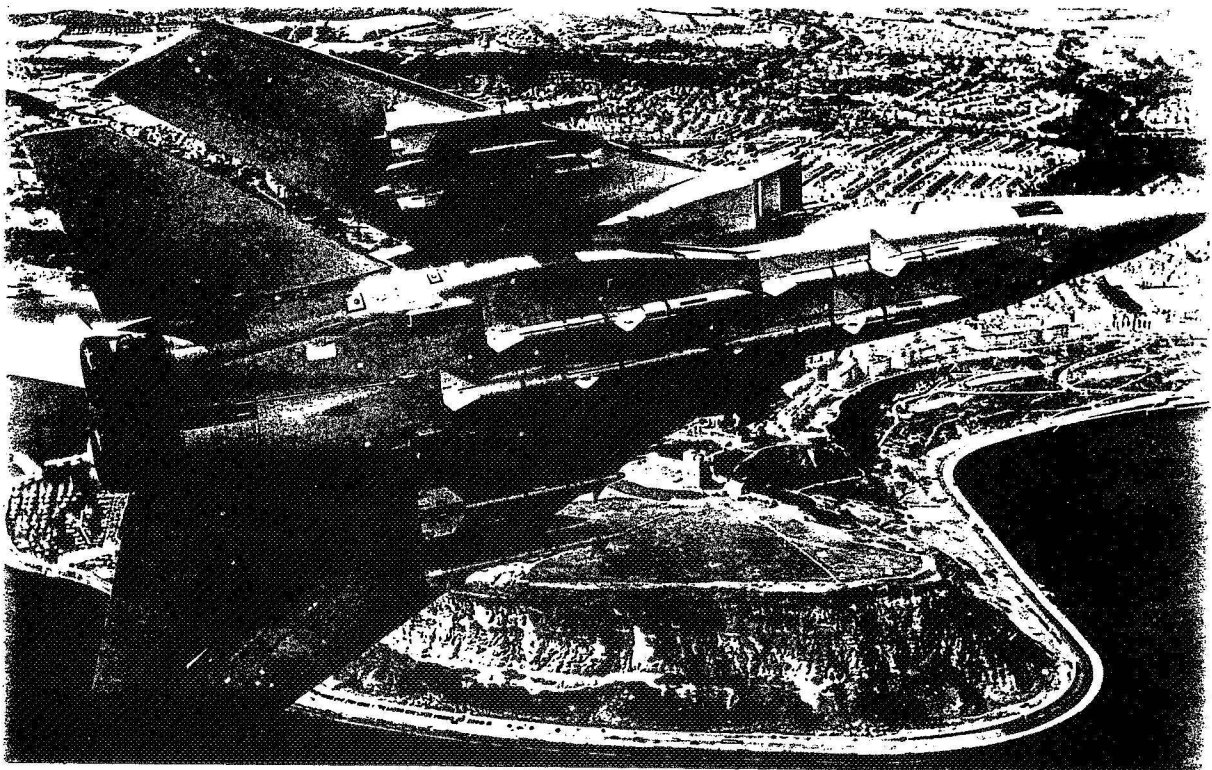


Figure 5. The loading spectrum experienced by the Panavia Tornado is markedly less severe than that applied in the fatigue test and so a higher scatter factor is needed - this is more than compensated for by the higher mean life.

1995108051

N95-14465

348632

CORROSION AND CORROSION FATIGUE OF AIRFRAME ALUMINUM ALLOYS

G. S. Chen, M. Gao, D. G. Harlow and R. P. Wei
Mechanical Engineering and Mechanics
LEHIGH UNIVERSITY
Bethlehem, PA 18015 USA

512-26
23106
p. 17

ABSTRACT

Localized corrosion and corrosion fatigue crack nucleation and growth are recognized as degradation mechanisms that affect the durability and integrity of commercial transport aircraft. Mechanistically based understanding is needed to aid the development of effective methodologies for assessing durability and integrity of airframe components. As a part of the methodology development, experiments on pitting corrosion, and on corrosion fatigue crack nucleation and early growth from these pits were conducted. Pitting was found to be associated with constituent particles in the alloys and pit growth often involved coalescence of individual particle-nucleated pits, both laterally and in depth. Fatigue cracks typically nucleated from one of the larger pits that formed by a cluster of particles. The size of pit at which fatigue crack nucleates is a function of stress level and fatigue loading frequency. The experimental results will be summarized, and their implications on service performance and life prediction will be discussed.

INTRODUCTION

Localized corrosion (in the form of pitting and exfoliation in aluminum alloys), and corrosion fatigue crack nucleation and growth are clearly recognized as degradation mechanisms that affect the durability and integrity of commercial transport aircraft. A quantitative methodology for establishing suitable intervals for inspection and repair, and for assessing the durability and integrity of airframe components, is needed for the effective management of the nation's aging fleet of commercial transport aircraft. The development of such a methodology requires a quantitative understanding, characterization and modeling of the elemental processes of damage, and the integration of the various models into a suitable probabilistic framework for service life prediction. Such an understanding of the damaging mechanisms and the formulation of a predictive methodology will also assist in the design of new aircraft and in the development of suitable "fixes" for the current fleet.

In this paper, a summary of progress is presented for the areas of localized corrosion and corrosion fatigue crack nucleation of an FAA sponsored program on airframe materials. This 3-year program of research is directed at studies of corrosion and corrosion fatigue of airframe materials in support of the FAA Aging Airplanes Program, and was initiated on 15 June 1992. The experimental portion of the program is focused on 2024-T3 (bare) aluminum alloy sheet material.

OBJECTIVES AND SCOPE

The objectives of the program are: (1) to develop basic understanding of the processes of localized corrosion and corrosion fatigue crack nucleation and growth in high strength aluminum alloys used in airframe construction, (2) to develop kinetic models for these elemental processes, and (3) to integrate these models into probabilistic models that can provide guidance in formulating methodologies for service life prediction.

The development of damage is illustrated schematically in Fig. 1, and is shown in a flow diagram in Fig. 2a. The early stage is dominated by corrosion, in the form of pitting or exfoliation, and the later stage by corrosion fatigue crack growth. Within the context of these mechanisms, an upper bound of damage is to be defined in terms of structural reliability and damage tolerance considerations regarding repairs. The research is focused, therefore, on the quantitative understanding and characterization, and kinetic modeling, of the following elemental processes:

- Onset of localized corrosion damage (particularly, mechanisms and kinetics of corrosion pit nucleation and growth).
- Transition from pitting to fatigue crack growth (or crack nucleation).
- Early stages of corrosion fatigue crack growth (short-crack regime).
- Corrosion fatigue crack growth.

Formulation of a predictive model would have to include the probabilistic contributions from material properties and key variables on the rate of corrosion (particularly, pit nucleation and growth, and exfoliation) and corrosion fatigue crack growth, and on the transition from corrosion to cracking.

The following principal issues are being addressed, and the overall modeling framework is shown by the block diagram in Fig. 2b.

- Identification and verification of key internal and external variables that control each of the aforementioned unit processes for corrosion and corrosion fatigue cracking and determination of the stochastic nature of each process
- Quantification of the probability distribution function (including time variance) of each of the key variables
- Development of quantitative understanding of the rate controlling step and mechanism for each damage process, and formulation of a mechanistic (*deterministic*) model for each that describes the functional dependence on the key variables
- Integration of mechanistic models and probability distribution functions, and formulation of mechanistically based probability models for life prediction and reliability assessment

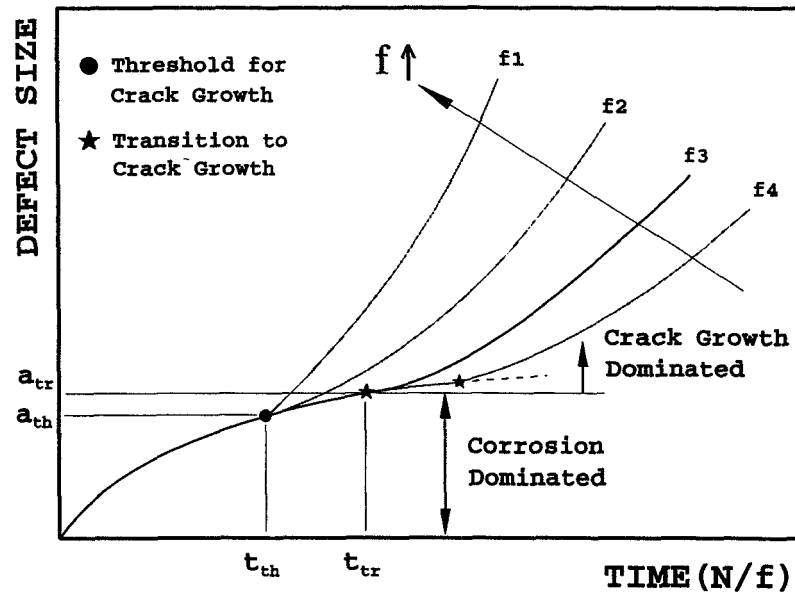


Figure 1. Schematic representation of localized corrosion (pitting or exfoliation) and corrosion fatigue.

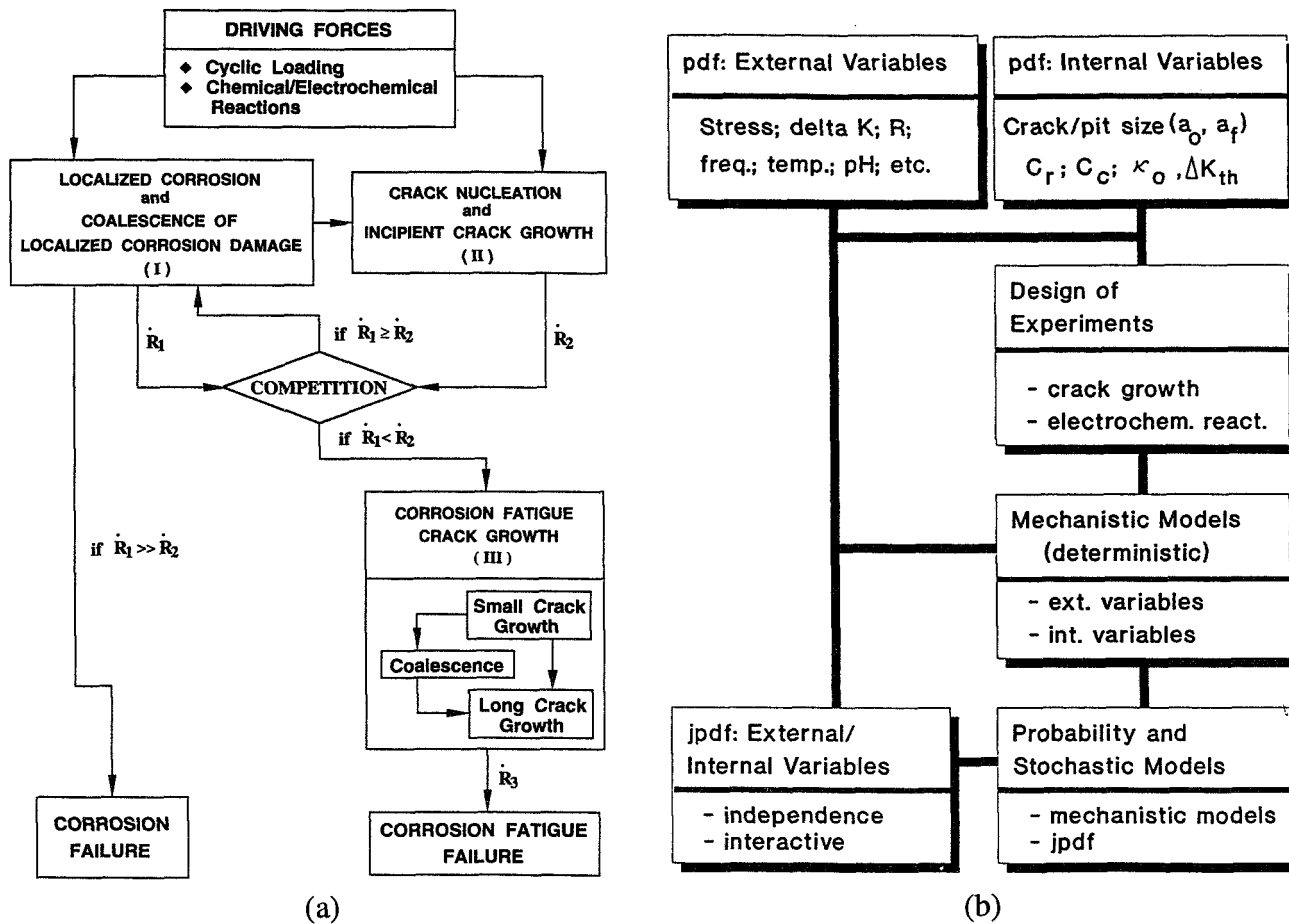


Figure 2. (a) Flow diagram showing the overall processes for corrosion and fatigue damage, and (b) key elements for the formulation of a mechanistically based probability model for life prediction.

The results described herein are restricted to the pitting and crack nucleation (transition) processes. The environment and experimental conditions used (for example, continuous full immersion in an aqueous solution) tend to accelerate damage accumulation. As such, these results should not be applied directly in assessing material performance in service.

PITTING CORROSION

A 1.6 mm (0.06 in.) thick sheet of bare 2024-T3 aluminum alloy is used in this study. The chemical composition is given in Table I, and its microstructure is shown in Fig. 3. Both standard polished and etched sections and back-scattered electron SEM micrographs of un-etched sections are included to show the microstructure and the size and distribution of constituent particles.

Table I. Chemical Composition (wt%) of the 2024-T3 Alloy

Component	Al	Cu	Mg	Mn	Fe	Si	Ti	Cr	Zn
Nominal*	Balance	3.8-4.9	1.2-1.8	0.3-0.9	0.50	0.50	0.15	0.10	0.25
Measured**	93.52	4.24	1.26	0.65	0.15	0.06	0.031	<0.01	0.08

* Metal Handbook, 9th ed., vol. 2, ASM International, Metals Park, OH, 1990, p. 17.

** Laboratory Testing Inc., Dublin, PA.

The as-received material was cut into 10mm x 10mm specimens for corrosion testing. The specimens were ground through a graded series of SiC papers, and then polished with diamond paste and colloidal SiO₂ to achieve mirror-like flat surfaces (~0.05μm rms surface roughness). After polishing, the specimens were cleaned with water and ethyl alcohol, and dried with warm air. Prior to corrosion testing, each specimen was coated with stop-off lacquer so that only the polished surface would be exposed to the test environment. For these studies, 0.5M NaCl (sodium chloride) solution was used. The solution was prepared by mixing reagent grade sodium chloride crystals with de-ionized water. The corrosion experiment was performed by simply immersing the specimen in a covered glass jar containing 200 ml of 0.5M NaCl solution, under free corrosion condition and without mechanical disturbance, principally at room temperature (~23°C) for specific periods of time. Some tests were carried out at 5°, 40°, 65° and 80°C. Before corrosion testing, the solution pH was typically about 5.8 (5.5 to 6) and the oxygen concentration, approximately 7 ppm. A few tests were also conducted at pH of 3 and 11. The solution pH and oxygen level were not controlled during the course of these corrosion tests. After testing for 24 hours at 80°C, for example, the pH increased slightly to 6.7 from 5.8 and the oxygen level dropped to 5.2 from 6.6 ppm.

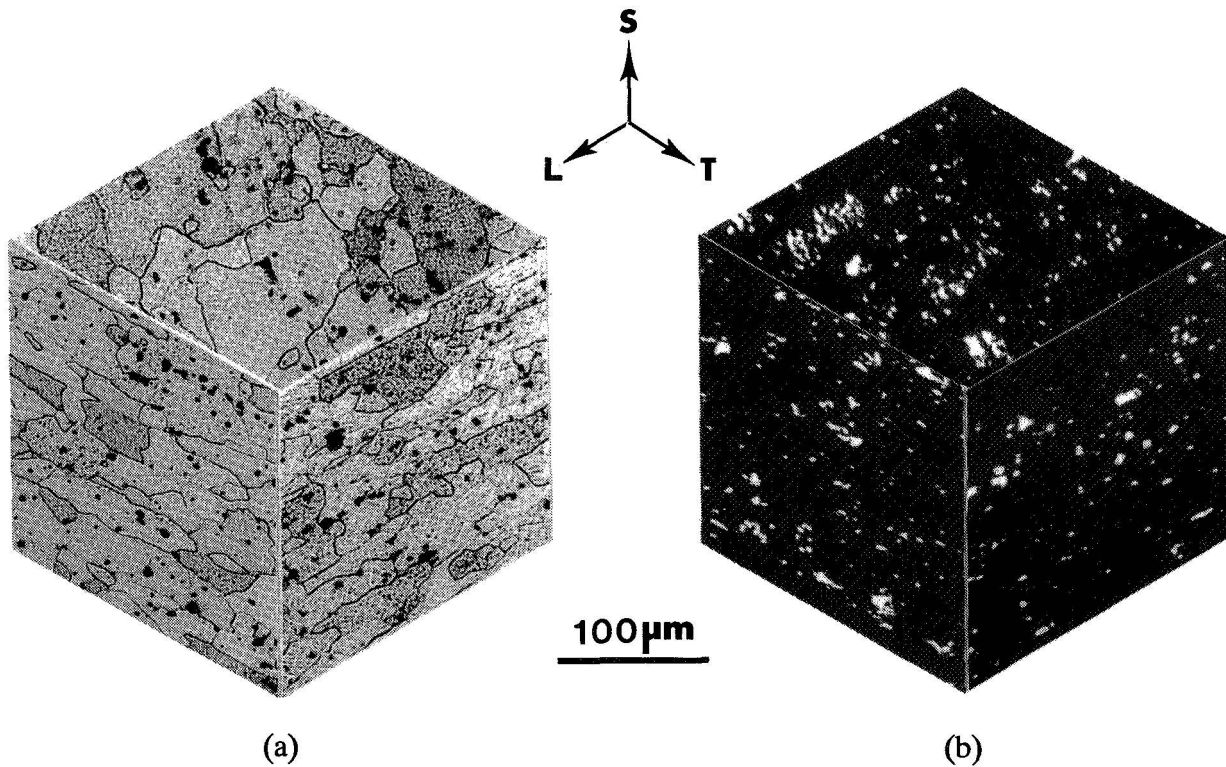


Figure 3. (a) Metallographic features in bright field optical image showing the microstructure of the 2024-T3 aluminum alloy, and (b) constituent particles in SEM backscattered electron contrast showing the particle morphology and distribution.

After corrosion testing, the specimens were washed with deionized water, acetone and ethanol, and dried with warm air. In some cases, a solution containing phosphoric acid (H_3PO_4) and chromic trioxide (Cr_2O_3) was used to remove oxides and corrosion products from the specimen surface. Optical and scanning electron microscopy (OM and SEM) and energy dispersive x-ray spectroscopy (EDX) were then used to investigate the surface morphology and chemical composition of the alloy surface and constituent particles.

Role of Constituent Particles

Figure 4 shows optical micrographs of the same (representative) area of a polished, bare 2024-T3 aluminum alloy surface before and after corrosion. The presence of a large number of constituent particles is evident. It is also clear that early corrosion is associated with these constituent particles. Some clustering of the particles is evident, and there is some banding of particles along the rolling direction of the sheet. The average density of particles with a projected surface area greater than one square micrometer (*i.e.*, $>1 \mu\text{m}^2$) was found to be about 3,230 particles per square millimeter, and the surface areal fraction of the particles was estimated to be about 2.7 percent. Typical size distribution for these particles is shown in Fig. 5 in a Weibull format [1].

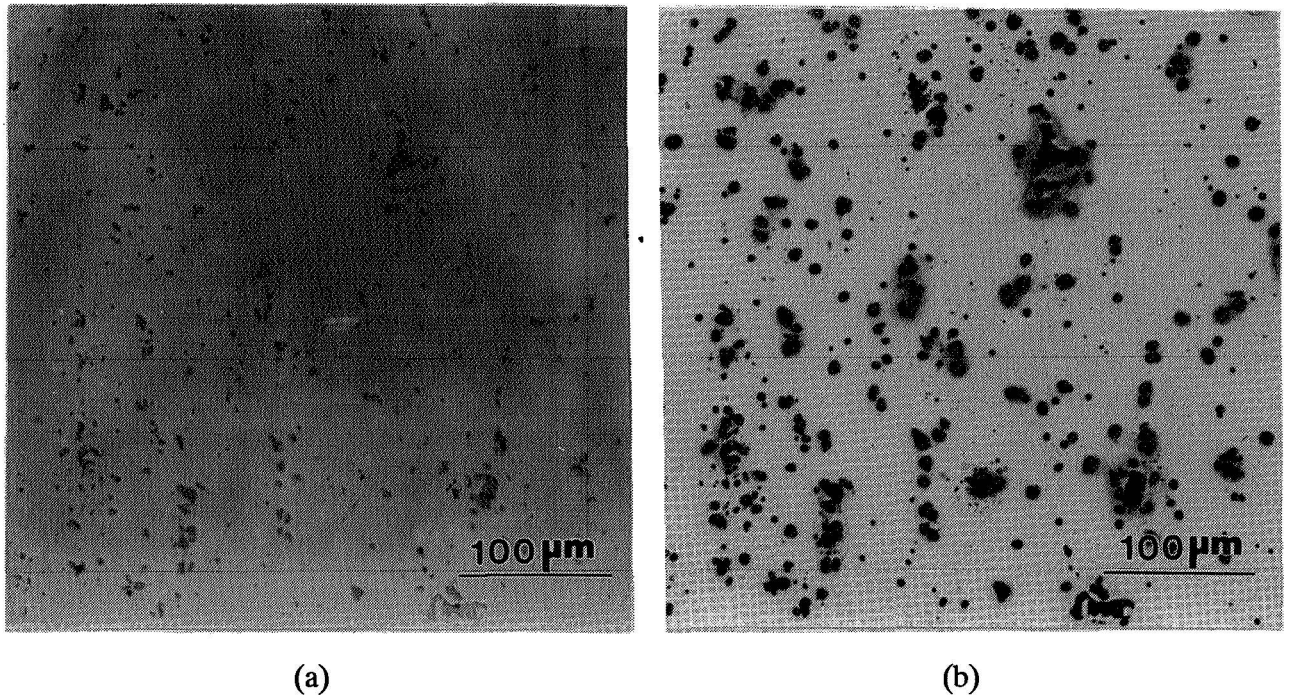


Figure 4. Optical micrographs for the same area of a bare 2024-T3 aluminum specimen showing (a) an as-polished surface, and (b) a corroded surface after 3-hours in 0.5M NaCl solution ($\text{pH} \approx 5.8$) at room temperature.

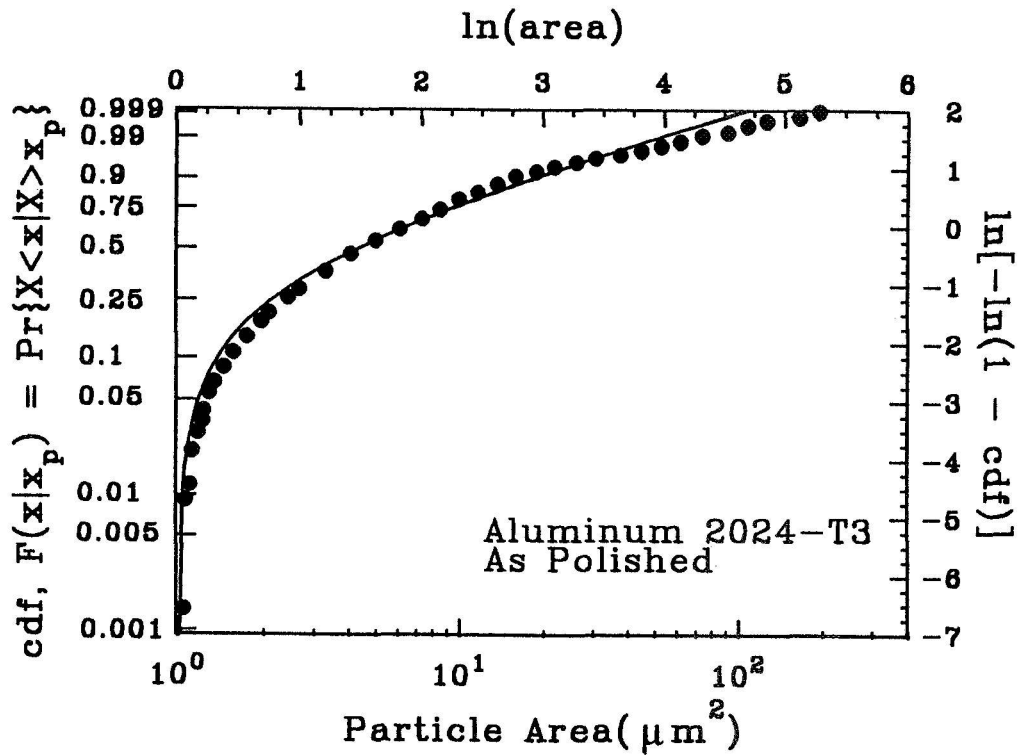


Figure 5. Typical size distribution in a Weibull format for the constituent particles in the 2024-T3 aluminum alloy.

The morphology, chemical composition and corrosion behavior of the particles were examined by SEM and EDX, and typical results are shown in Table II and in Figs 6 and 7. Two types of constituent particles with differing corrosion behavior may be seen from EDX results on selected particles before and after corrosion testing at 80°C, Table II; namely, those that contain only Al, Cu and Mg, before corrosion; and those that contain Al, Cu, Fe and Mn, with no Mg. The distribution and relative concentration of these particles are shown by a comparison of the SEM micrograph and corresponding elemental maps of a typical region, for example, in Fig. 6. Some clustering and mingling of the two types of particles are seen. The fraction of Al-Cu-Mg particles (those not containing Fe in Fig 6) was estimated to be about 75 percent in this alloy.

Table II. Comparison of EDX Results for Individual Particles *Before* and *After* Corrosion in 0.5M NaCl Solution at 80°C for 24 Hours

Particle Type	Corrosion Testing	$K\alpha$ Intensity (counts)				
		M g	M n	Fe	C u	Al
A1	before	678	ND*	ND	9600	2990
	after	ND	ND	495	11362	474
A2	before	804	ND	ND	7086	3516
	after	ND	523	640	5710	1892
A3	before	1437	ND	ND	6593	8411
	after	ND	468	534	6354	840
A4	before	2209	ND	ND	2798	11024
	after	ND	681	619	5061	4671
C1	before	ND	3485	4644	4379	1057
	after	ND	433	1092	9666	4671
C2	before	ND	2132	2972	5541	2086
	after	ND	702	3078	7843	700
C3	before	ND	3280	3960	4067	5057
	after	ND	968	5072	3359	1337
C4	before	ND	2723	3438	4725	5997
	after	ND	689	4997	2443	1470

* ND: not detected.

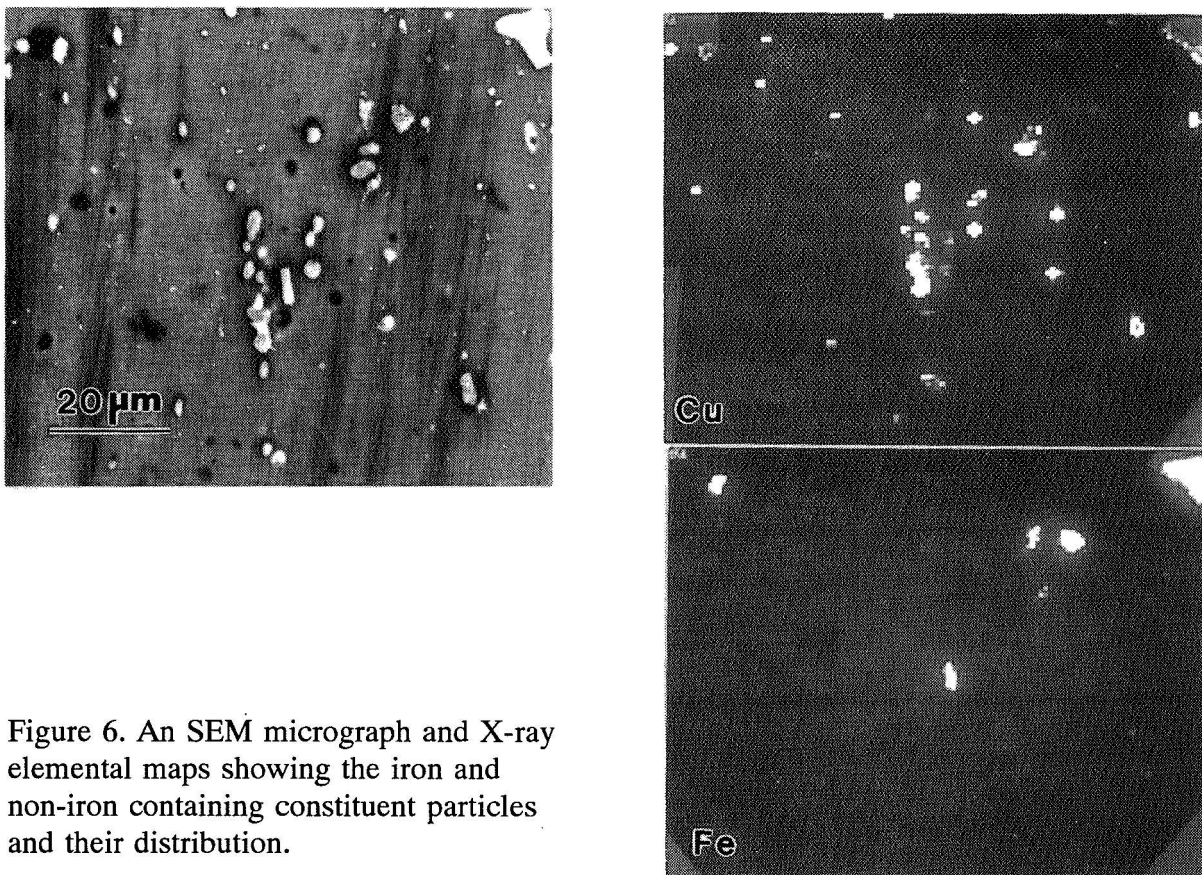


Figure 6. An SEM micrograph and X-ray elemental maps showing the iron and non-iron containing constituent particles and their distribution.

From a comparison of the EDX results in Table II, it is clear that the Mg in all of the Al-Cu-Mg particles was removed by corrosion. Further mechanistic interpretation of these EDX data, however, would require more detailed analyses. Nevertheless, some insight may be gained through a comparison with SEM and EDX analyses of individual particles after corrosion (see Fig. 7). It may be seen that the Al, Cu, Mn and Fe containing particles (e.g., particle at C in Fig. 7a and the corresponding EDX spectra in Fig. 7b) promoted matrix dissolution at their periphery. Those particles that contain Al, Cu and Mg, on the other hand, dissolved (e.g., particles at A in Fig. 7a and the associated spectra in Fig. 7b), and had mostly Cu left. The P and Cr peaks in the EDX spectra (Fig. 7b) are principally residues from chemical cleaning.

The Al-Cu-Mg-containing particles, therefore, acted as anodic sites and lost Mg and Al through dissolution (or dealloying) in the early stage of corrosion, but became more cathodic as copper was left behind (see Table II and particle A in Fig. 7). Dealloying of an intermetallic T_1 phase (Al_2CuLi) and dealuminization of γ_2 (Cu_2Al) compounds have been reported in the literature [2,3]. There is evidence of Fe and Mn deposition onto the Al-Cu-Mg particle sites (though not seen in Fig. 7) during corrosion. On the other hand, copper deposition was observed on the Al-Cu-Mn-Fe containing particles, with nodular copper deposits on these particles irrespective of their size (as indicated by the arrows in Fig. 7a). The phenomenon is similar to that of deposition corrosion [4,5]. This behavior suggests that the Al-Cu-Mn-Fe containing particles served as cathodic sites in the corrosion process, and led to the reduction of cupric ions dissolved in the solution. The data on Fe and Mn (Table II) are less clear because of Cu deposition on some of the particles. The SEM evidence (Fig. 7) suggests that these particles promoted dissolution of the adjacent matrix, but, by and

large, did not dissolve themselves. It is to be noted that no evidence of exfoliation was uncovered in this study.

The form of localized corrosion (i.e. particle-induced pitting) was not altered by temperature, but the degree and rate of pitting damage was enhanced with increasing solution temperature. Particle-induced pitting corrosion was found to be less severe in an acidic (pH = 3) solution, probably because of enhanced general corrosion, and in an alkaline (pH = 11) solution, because of reduced passive film integrity attenuating localized attack.

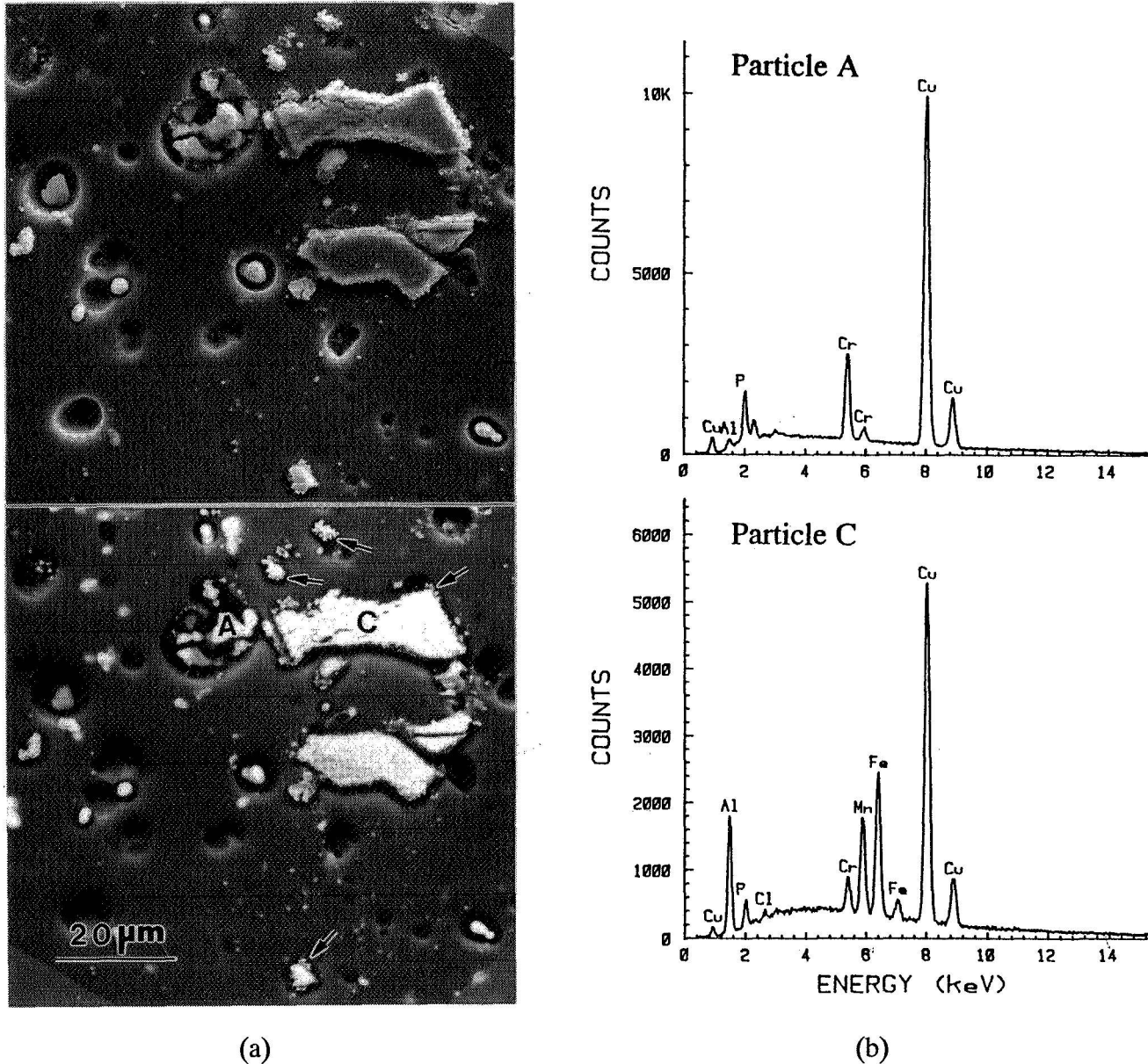


Figure 7. SEM and EDX results for a bare 2024-T3 aluminum alloy specimen tested in 0.5M NaCl solution (pH \approx 5.8) at room temperature for 3 days, showing (a) localized corrosion at constituent particles (top: secondary electron contrast; bottom: backscattered electron contrast), and (b) chemical composition of the particles at A and C in the micrograph. (Arrows point to copper deposition on the Al-Cu-Mn-Fe particles.)

Growth and Coalescence, and Orientation Dependence

The evolution of pitting damage may be seen from a representative SEM micrograph and a Gumbel plot [6] of distributions in pit size at 40°C, Figs 8a and 8b. The results for longer periods of time (e.g., three days or 72 hours, Fig. 8a) confirm the identification of constituent particles as the primary sites for pitting corrosion. Taken together with Fig. 8b, the results provide an indication of the evolution of particle-nucleated pitting damage in the 2024-T3 aluminum alloy. The individual pits grew both in breadth and in depth with time, and can coalesce to form a larger pit (in Fig. 8a). Accelerated pitting may result from this process of pit coalescence rather than through single pit growth.

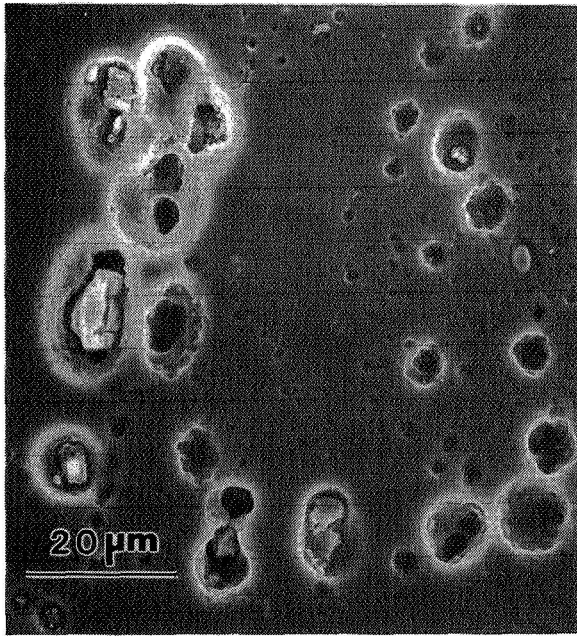
The process is very complex and appears to involve 3-D interactions with constituent particles. Corrosion sensitivity appears to be orientation dependent, being *more severe in the thickness orientation* because of local segregation of constituent particles. Such enhanced pitting at the surface of a drilled and polished hole is shown in Fig. 9, and fatigue cracks have been observed to nucleate from such pits. It is interesting to note that severe corrosion (anodic dissolution) at the large active pit appears to cathodically protect the neighboring surface, resulting in lightly corroded "plateaus" over the surface.

TRANSITION FROM PITTING TO FATIGUE CRACK GROWTH

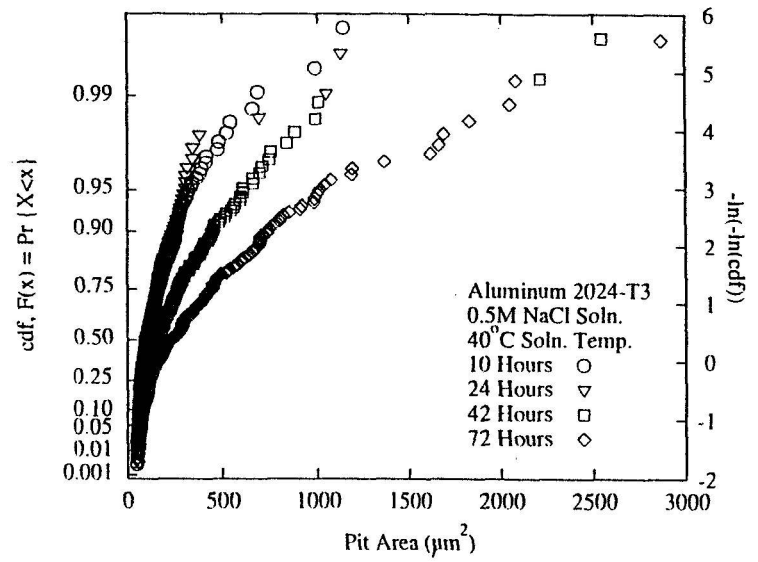
Corrosion fatigue failures often result from the nucleation and growth of fatigue cracks from corrosion induced pits [7,8]. Cracking occurs when the local mechanical condition is adequate for the onset of crack growth. Recently, Kondo [9] and Kondo and Wei [10] considered the competition between corrosion pit and fatigue crack growth in steels, and proposed a criterion for the transition from pitting to corrosion fatigue crack growth, Fig. 1. The criterion is based on the assumption that a corrosion pit may be modeled by an equivalent semi-elliptical (or semi-circular) surface crack. It suggests that transition from pit growth to fatigue crack growth takes place when the stress intensity factor of the equivalent surface crack reaches the threshold stress intensity factor (ΔK_{th}) for fatigue crack growth. Through this criterion a linkage is made between the critical pit size (for a given applied stress) and a fracture mechanics parameter to provide a framework for the prediction of pitting/corrosion fatigue life.

Fatigue experiments were carried out on open-hole specimens of 2024-T3 (bare) alloy in 0.5M NaCl solution at room temperature and different loading frequencies from 0.1 to 10³ Hz. The maximum stress applied at the hole was estimated to be 320 MPa and the load ratio, R, was 0.1. Cracks were found to nucleate from areas of severe local corrosion; namely, *pits* (Figs 10a and 10b). Fatigue failure, by-and-large, resulted from a *single* nucleation site, although many secondary cracks were observed to form at corrosion pits away from the main fatigue crack (Fig. 11). Hence, a dominant flaw model for corrosion and corrosion fatigue appears to be appropriate.

In contradistinction to the original concept of Kondo [9] and Kondo and Wei [10], the pit-to-crack transition size (or crack nucleation size) appears to depend on the cyclic-load frequency being larger at lower frequencies (see Figs 10a and 10b, and Table III). This frequency dependence



(a)



(b)

Figure 8. (a) Coalescence of individual pits taking place laterally and in depth at the specimen surface to form a larger pit, and (b) a Gumbel plot of pit size (projected area) distribution over different corrosion time showing the evolution of pitting damage.

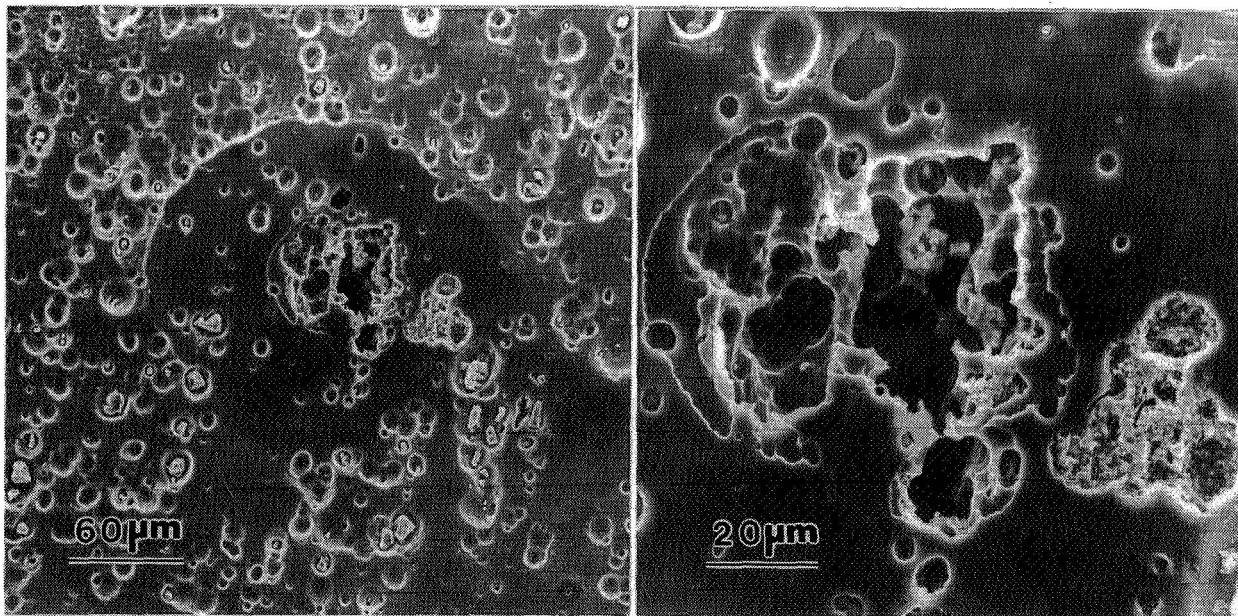
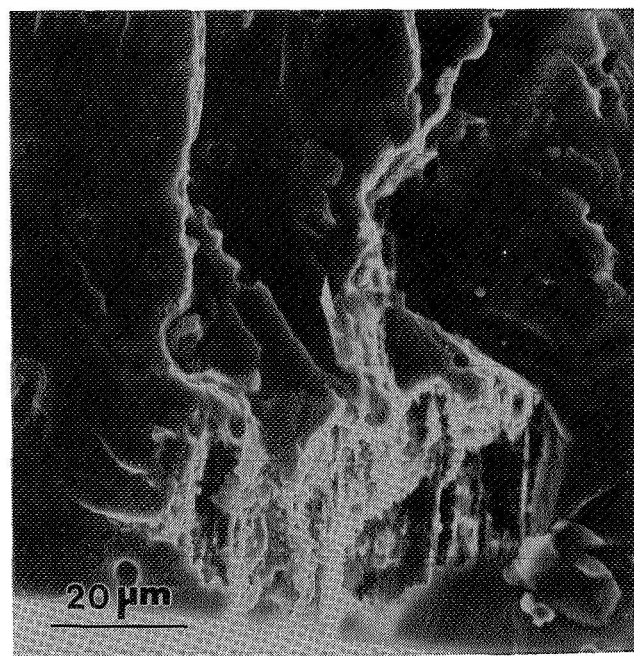
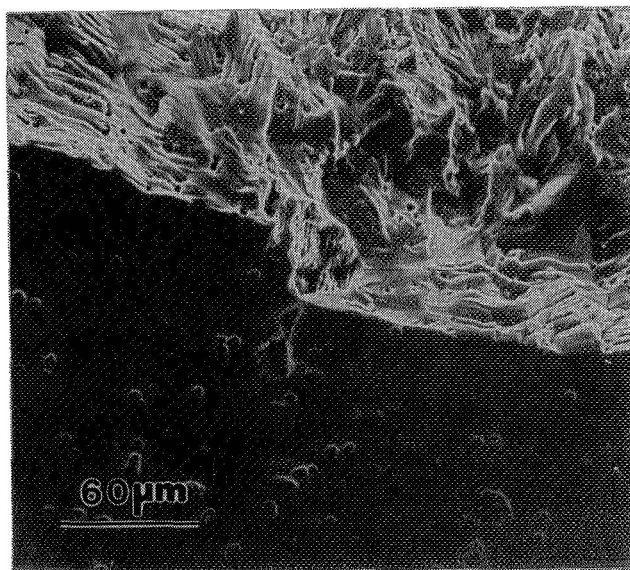
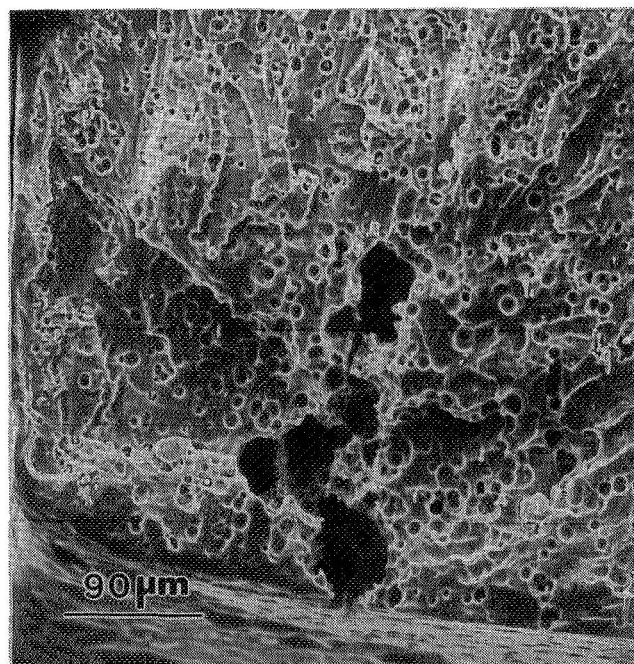
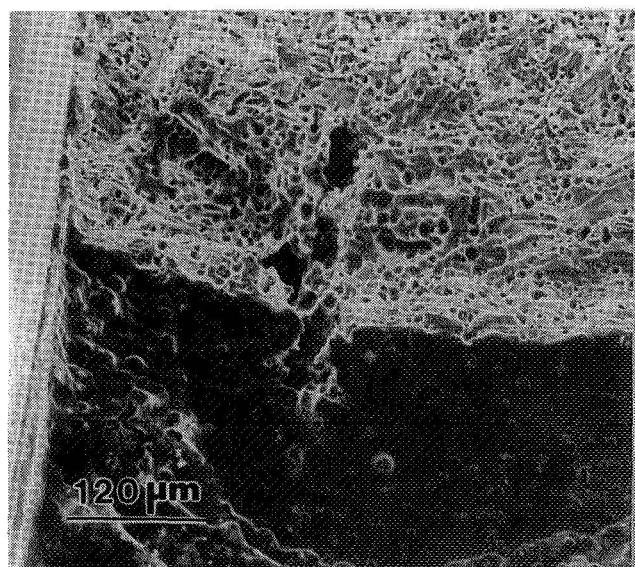


Figure 9. Corrosion features in the thickness orientation of a 2024-T3 aluminum specimen tested in 0.5M NaCl solution (pH = ~5.8) at room temperature for 3 days.



(a)



(b)

Figure 10. Corrosion fatigue crack nucleation associated with pits in 2024-T3 aluminum specimens tested in 0.5M NaCl solution at room temperature with $\sigma_{\max} = 320$ MPa ($R = 0.1$); (a) $f = 10$ Hz, and (b) $f = 0.1$ Hz.

reflected *competition* between pitting corrosion and early corrosion fatigue crack growth. The addition of a growth rate requirement to the transition criterion, therefore, is needed; namely,

$$\Delta K \geq \Delta K_{th}$$

$$(da/dt)_{crack} \geq (da/dt)_{pit}$$

where ΔK_{th} is the threshold for fatigue crack growth, and (da/dt) refers to the appropriate crack and pit growth rates.

The extent of post-crack-growth pitting of the fracture surface also depended on frequency, which reflected the duration of exposure of the fracture surface to the electrolyte. The presence of localized corrosion (pitting) on the fatigue fracture surfaces (see Fig. 10b) further confirmed the competition between localized corrosion and corrosion fatigue crack growth.

A MECHANISTICALLY BASED PROBABILITY APPROACH TO LIFE PREDICTION

It was recognized that a quantitative methodology for life prediction is needed to help define suitable inspection intervals and assess the durability and integrity of aircraft components and structures. To be effective, this methodology must provide statistically accurate estimates of response for conditions not included within the available experimental observations, and account for the influences of key external and internal variables. The external variables include applied stress, environmental chemistry, and temperature; and the internal variables, chemistry within a pit or at the crack tip material properties, initial defect size, etc. (see Fig. 3). The development of such a methodology requires mechanistic understanding and quantification of the processes for damage accumulation. In other words, a mechanistically based probability approach to life prediction (or durability assessment) is needed.

The feasibility and utility of this approach have been demonstrated. A dominant flaw probability model for pitting and corrosion fatigue was developed as an illustrative example [12]. This model was based on an original model proposed by Kondo [9] and Kondo and Wei [10] which assumed pitting corrosion to proceed at a constant volumetric rate. Transition from pit (hemispherical) to crack (semi-circular) was based on a matching of the stress intensity factor for an equivalent semi-circular crack against the fatigue crack growth threshold. A power-law model was used to represent subsequent fatigue crack growth. The elemental models were assumed to capture some of the key mechanistic features, and provide reasonable "predictions" of response. The overall model incorporated initial defect size, corrosion rate, fatigue crack growth rate coefficient, and fatigue crack growth threshold (ΔK_{th}) as random variables, and permitted examinations of the contribution of each of these variables to the distribution in life. This model has been modified to account for corrosion and fatigue from an open circular hole. The modification included a further transition from the pitting initiated semi-circular surface crack at an open-hole to a through-thickness crack. A typical result showing the influence of loading frequency is shown in Fig 12.

These models are reasonably consistent with the foregoing observations of localized pitting corrosion and the subsequent nucleation and growth of a corrosion fatigue crack from a dominant pit.



Figure 11. Secondary cracks forming (away from the main crack) at corrosion pits at the free surface of a fatigue specimen tested in 0.5M NaCl solution at room temperature with $\sigma_{\max} = 320$ MPa ($R = 0.1$) and with $f = 0.1$ Hz.

Table III. Results for Corrosion Fatigue Crack Nucleation of the 2024-T3 Alloy in 0.5M NaCl Solution with $\sigma_{\max} = 320$ MPa ($R = 0.1$) and with $f = 0.1$ to 20 Hz

Sample No.	Frequency [Hz]	N_i [cycles] $/t_i$ [hrs]	N_f [cycles] $/t_f$ [hrs]	(Pit Size)* $2c \times a$ [μm]	$(\Delta K)^{**}$ @ surface [$\text{MPa}\sqrt{\text{m}}$]
A01F29	20	<i>not available</i>	58,629 / 0.81	50 x 80	2.83
A01F14	10	29,700 / 0.83	78,745 / 2.19	45 x 35	2.27
A01F05	5	23,970 / 1.33	59,381 / 3.3	45 x 60	2.60
A01F39	5	27,470 / 1.53	64,800 / 3.6	40 x 60	2.50
A01F51	0.5	39,830 / 22.13	77,875 / 43.26	75 x 200	3.65
A01F08	0.5	41,138 / 22.85	<i>not available</i>	67 x 150	3.41
A01F20	0.1	18,635 / 51.76	57,809 / 160.58	100 x 250	4.20
A01F36 [†]	5	8,000 / 0.44	67,392 / 3.74	100 x 150	3.96

[†] Three day pre-exposure to NaCl solution prior to corrosion fatigue testing.

* $2c$ = maximum width of the pit; a = maximum depth of the pit.

** See ref. [11] for the K estimation for a semi-elliptical surface crack.

The simplified concept of a single pit, however, would require more careful study. A more appropriate model will need to be developed to better represent the three dimensional nature of particle-induced pit nucleation, and their coalescence and growth in breadth and depth into a large pit. The kinetics and probabilistic aspects of pit growth would also require further attention, and are under investigation. In contrast to the simplifying assumption, fatigue crack nucleation from a corrosion pit (or the transition from pit to fatigue crack growth) was found to be dependent on the loading frequency. Additional efforts are underway to better characterize this frequency dependence and the kinetics of fatigue crack growth, and to incorporate them into the life prediction methodology.

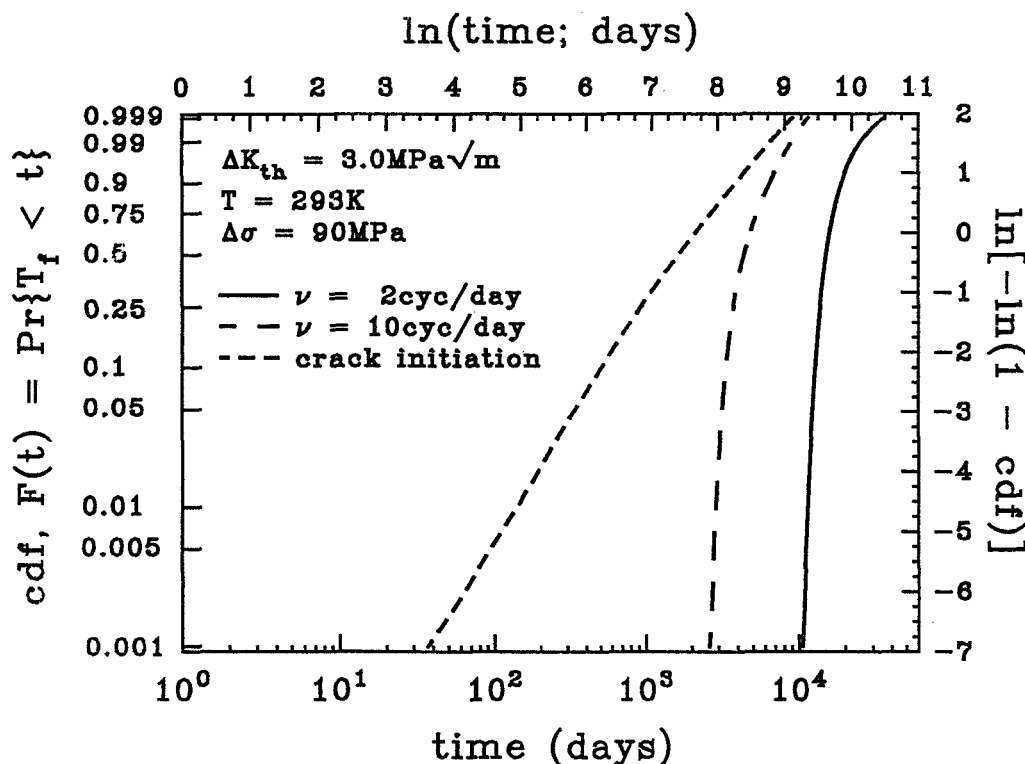


Figure 12. Relative contribution of the time-to-initiation and time-of-crack growth on the *cdf* for the time-to-failure at 293K and 90 MPa.

SUMMARY

The results show that bare 2024-T3 alloys corrode readily in 0.5M NaCl solution. The corrosion is promoted by the presence of constituent particles. The alloy used in this study contained over 3,000 constituent particles per square millimeter with projected area greater than $1 \mu\text{m}^2$. Two types of particles were identified: one containing Al, Cu and Mg, and the other, Al, Cu, Mn and Fe. The Al-Cu-Mn-Fe-containing particles acted as cathodes and resulted in localized dissolution of the surrounding matrix, whereas the Al-Cu-Mg-containing particles acted as anodes and themselves dissolved.

The interactions between the particles, and between the particles and the matrix, result in the nucleation of pits. The growth and coalescence of pits, in depth and in breadth, led to the formation of large corrosion pits, from which corrosion fatigue cracks nucleate. The transition from pit to corrosion fatigue crack growth is determined not only by the need to overcome the threshold K value for fatigue crack growth, but also by the competition between pit and fatigue crack growth rates.

The particle-particle and particle-matrix interactions are complex, and need to be understood as a part of the program in developing models for corrosion damage evolution. A part of the complexity arises from clustering and banding of the particles along the rolling direction, which appear to be more severe in the thickness (S-L and S-T) orientations. The 3-dimensional nature of particle distribution and its influence on the growth of pits in depth as well as in breadth will need to be taken into account. This effort on corrosion and corrosion fatigue crack nucleation, along with studies of corrosion fatigue crack growth, are being continued to provide a mechanistic basis for life prediction.

ACKNOWLEDGMENTS

This research was supported by the Aging Airplane Program of the Federal Aviation Administration under Grant No. 92-G-0006, with Dr. Thomas H. Flournoy as Program Director. Assistance by Dr. Shuchun Chen and Mr. Joseph K.-C. Wan is gratefully acknowledged.

REFERENCES

1. Harlow, D. G.: The Effect of Proof-Testing on the Weibull Distribution. *J. Mater. Sci.*, vol. 24, 1989, p. 1467.
2. Buchheit, R. G. Jr.; Moran, J. P.; and Stoner, G. E.: Localized Corrosion Behavior of Alloy 2090 - The Role of Microstructural Heterogeneity. *Corrosion*, vol. 46, 1990, p. 610.
3. Sury, P.; and Oswald, H. R.: On the Corrosion Behavior of Individual Phases Present in Aluminum Bronzes. *Corrosion Sci.*, vol. 12, 1972, p. 77.
4. Hatch, J. E., ed.: *Aluminum: Properties and Physical Metallurgy*. ASM, Metals Park, OH, 1984, p. 259.
5. Murray, G. A. W.; Lamb, H. J.; and Godard, H. P.: Role of Iron in Aluminum on the Initiation of Pitting in Water. *Br. Corros. J.*, vol. 2, 1967, p. 216.
6. Bury, K. V.: *Statistical Models in Applied Science*. John Wiley & Sons, Inc., NY, 1975, p. 367.
7. Hoepfner, D. W.: Model for Prediction of Fatigue Lives Based upon a Pitting Corrosion Fatigue Process. *Fatigue Mechanisms*. STP 675, Fong, J. T., ed., ASTM, Philadelphia, PA, 1979, p. 841.

8. Muller, M.: Theoretical Considerations on Corrosion Fatigue Crack Initiation. *Met. Trans.*, vol. 13A, 1982, p. 649.
9. Kondo, Y.: Prediction of Fatigue Crack Initiation Life Based on Pit Growth. *Corrosion*, vol. 45, 1989, p. 7.
10. Kondo, Y.; and Wei, R. P.: Approach on Quantitative Evaluation of Corrosion Fatigue Initiation Condition. *Evaluation of Materials Performance in Severe Environments*. Proceedings of International Conference, The Iron and Steel Institute of Japan, Tokyo, Japan, 1989, p. 135.
11. Irwin, G. R.: Crack-Extension Force for A Part-Through Crack in A Plate. *J. Applied Mech. (Trans. ASME)*, December, 1962, p. 651.
12. Wei, R. P.; and Harlow, D. G.: A Mechanistically Based Probability Approach for Predicting Corrosion and Corrosion Fatigue Life. *Durability and Structural Integrity of Airframes*. Blom, A. F. ed., Engineering Materials Advisory Services Ltd., West Midlands, U. K., 1993, p. 347.

ORIGINAL PAGE IS
OF POOR QUALITY

1995108052

N95-14466

Computational Predictive Methods for Fracture and Fatigue

J. Cordes, A.T. Chang, N. Nelson, Y. Kim
Department of Mechanical Engineering
Stevens Institute of Technology
Castle Point on the Hudson
Hoboken, New Jersey 07030

348642
S13-39
23107
P- 18

Abstract

The damage-tolerant design philosophy as used by aircraft industries enables aircraft components and aircraft structures to operate safely with minor damage, small cracks, and flaws. Maintenance and inspection procedures insure that damages developed during service remain below design values. When damage is found, repairs or design modifications are implemented and flight is resumed.

Design and redesign guidelines, such as military specifications MIL-A-83444, have successfully reduced the incidence of damage and cracks. However, fatigue cracks continue to appear in aircraft well before the design life has expired. The F16 airplane for instance, developed small cracks in the engine mount, wing support bulk heads, the fuselage upper skin, the fuel shelf joints, and along the upper wings. Some cracks were found after 600 hours of the 8000 hour design service life and design modifications were required. Tests on the F16 plane showed that the design loading conditions were close to the predicted loading conditions [1]. Improvements to analytic methods for predicting fatigue crack growth adjacent to holes, when multiple damage sites are present, and in corrosive environments would result in more cost-effective designs, fewer repairs, and fewer redesigns.

The overall objective of the research described in this paper is to develop, verify, and extend the computational efficiency of analysis procedures necessary for damage tolerant design. This paper describes an elastic/plastic fracture method and an associated fatigue analysis method for damage tolerant design. Both methods are unique in that material parameters such as fracture toughness, R-curve data, and fatigue constants are not required. The methods are implemented with a general-purpose finite element package. Several proof-of-concept examples are given. With further development, the methods could be extended for analysis of multi-site damage, creep-fatigue, and corrosion fatigue problems.

Introduction

Prediction of fracture and fatigue behavior generally requires a variety of experimentally-generated data points. For elastic/plastic fracture, resistance curves (R-curves) characterize increasing material toughness as a stable crack tip is driven through the crack tip plastic zone. Crack growth resistance curves, such as J-integral versus stable crack growth, are used to predict the onset of fracture

and the stable crack growth behavior in elastic/plastic components. JR-curves depend on thickness, component geometry in the case of center-cracked plates [2], the extent of plasticity [3], and perhaps whether the experiment is load controlled or displacement controlled [4]. Design engineers assessing residual strength must choose material parameters and resistance curves which are determined for similar geometries, thicknesses, and environmental conditions [5-7].

Efforts have been made to predict elastic/plastic fracture and stable crack growth behavior with fewer experimentally-generated data points. Shan et. al. [8] used the crack tip opening angles at crack initiation and at the onset of stable crack growth to predict stable crack growth behavior. Elangovan [9] formulated a method for generating an R-curve using two points on the R-curve. Newman et. al. [10] used a single experimentally-determined parameter, the critical crack tip opening angle, to model stable crack growth behavior in thin aluminum panels. Zhang and Gross [11] used a cohesive stress zone model to predict critical crack tip opening displacement and JR-curve behavior analytically. Fracture parameters were derived from a base fracture parameter, stress/strain diagrams, an assumed micro-damage ahead of the crack tip, and small scale yielding assumptions.

Since the early 1960's, fatigue crack growth rates have been determined using a power-law equation that requires two material constants. The linear-elastic fracture parameter ΔK was introduced by Paris and Erdogan [12] for predicting fatigue crack growth rates (1960):

$$\frac{da}{dN} = C (\Delta K)^n \quad (1)$$

where a = crack size or half-crack size
 da = increment of crack growth
 dN = # of cycles for an increment of crack growth
 C,n = material constants, determined from curve fit
 ΔK = difference in stress intensity factors evaluated at
 the maximum and minimum loading conditions

Paris' equation is limited to problems where C and n are determined for the material, where each loading cycle varies between the same maximum and minimum values, and where the size of the damage zone is small compared to the crack length. Other power-law equations have been introduced to account for the crack growth threshold load or crack initiation load [13,14], to include crack closure effects [15-20], and to include plasticity effects [21]. The crack closure methods have been particularly useful for predicting crack growth behavior under spectrum loading [22,23] and when overloads and underloads are present [24,25]. For all of the power-law equations reviewed, prior knowledge of at least two material constants is required.

The fracture and fatigue methods described in this paper rely only on material stress-strain data; additional experimental parameters and curve matching are not required. The elastic/plastic fracture method

uses a critical crack tip opening displacement curve which is generated during the analysis. The critical VR-curve is used for both the fracture and fatigue analysis method [26,27]. The methods can account for large scale yielding and large amounts of stable crack growth in thin-sheet materials as often used by the aircraft industry. Geometric dependencies are reflected in the finite element modeling. This paper provides an overview of the prediction methods, presents some validation examples, and describes the implications for future research.

Elastic/Plastic Fracture Prediction

Two basic assumptions are used in the elastic/plastic computational procedure: one concerning crack initiation and a second assumption concerning crack propagation. The finite element model incorporates a Dugdale-type cohesive zone at the crack tip and elastic/plastic material properties to model nonlinear material behavior. The cohesive zone replaces the crack-tip singularity and allows relative displacement between the crack tip grid points.

Crack initiation is assumed to occur when the crack opening displacement curve deviates by 5% from initial, linear-elastic behavior. While a mathematical proof is not offered, this assumption is consistent with ASTM specification E-399-83 [5] for brittle fracture and KIC testing. The 5% deviation point is used to determine the crack tip opening displacement at crack initiation V_1 , which occurs at the crack initiation load.

Subsequent crack growth is predicted using a critical crack tip opening displacement curve which is generated during the finite element analysis steps. For subsequent stable crack growth increments, the critical crack tip opening displacement, VR_j is found from:

$$VR_j = V_1 + Vpw_{j-1} \quad (2)$$

where VR_j = the critical crack tip opening displacement for crack propagation at stable crack growth Da_j
 V_1 = the crack tip opening displacement at crack initiation as calculated from the 5% offset,
 Vpw_{j-1} = is the calculated opening displacement at the first node in the crack tip plastic wake, under applied load P_{j-1} .

Fatigue Prediction

The fatigue method uses finite element analysis, elastic/plastic fracture analysis results, and an energy approach to predict fatigue behavior. The governing equations for the fatigue analysis are:

$$N_1 = W_1/E$$

for crack initiation, and:

$$N_p = W_p/E$$

for crack propagation. Where

N_i , N_p = the number of cycles for fatigue crack initiation or propagation

W_i , W_p = required energy for fatigue crack initiation or propagation, determined from elastic/plastic analysis

E = energy dissipated per cycle

The available energy W is determined for each increment of crack growth by considering the available energy in the cohesive stress zone [27].

The dissipated energy ' E ' depends on the applied fatigue loading condition and is an estimate of the energy consumed during each fatigue cycle. It is hypothesized that cyclic energy losses E occur when the residual compressive stress exceeds the negative yield strength of the material. The calculation for E is based on the size of the stable hysteresis loop which occurs in the stress-strain diagram. The resulting fatigue method has the following benefits: 1) Paris-type curve matching coefficients are not required, 2) the fatigue life is predicted from nonlinear analysis which includes plastic tensile strain and plastic compressive strain effects, 3) fracture and fatigue parameters are not required, 4) far-field and near-field effects of the damage are included in the analysis.

Validation of Prediction Methods

A) Elastic/Plastic Fracture Examples --

Description -- A middle-cracked panel, as described in the referenced work by Newman et. al. [10], was used to compare predicted results to experimental results and to Newman's critical crack opening angle (COA) method. The panel measured 76. mm in width, 2.3 mm in thickness, and had a crack-length to width ratio of 0.33. The material was 2024-T3 aluminum. The plate was loaded quasi-statically by an applied displacement at the boundary. The applied load, the stable crack growth increment, and the crack tip opening angle were monitored. In experiments on the middle cracked panel, the crack tip opening angle reached a constant value of 6 degrees after about 2.3 mm of stable crack growth. Newman used this 6 degree value as a single critical parameter, the crack opening angle (COA), for predicting stable crack in a middle-cracked panel.

Implementing the VR-Curve Method -- The analysis using the VR-curve method was completed using ABAQUS [28], a general purpose finite element program. Due to symmetry, one quarter of the panel was modeled using three and four node plane stress elements. An elastic/plastic material model was used for the plane stress elements. The VR-curve method was implemented as a series of load increases and model changes. At each step, the cohesive stress zone was inserted along the crack line at locations where the stress reached the yield

strength. When the critical crack tip opening displacement, as determined from equation (2) was reached, the cohesive stress at the crack tip was removed simulating crack growth.

Implementing Newman's COA Method [10] using ABAQUS -- The VR-curve results were compared to near-field results obtained using Newman's critical COA criteria. The COA method was implemented using ABAQUS, 4-node plane stress elements, and an elastic/plastic material model. The minimum element size was .3968 mm, smaller than the .48 mm element size used in the referenced paper. The critical crack opening angle was determined from the crack surface displacement two nodes behind the crack tip. Using ABAQUS, there was no difference between calculations using all plane stress elements and the recommended calculations using a plane strain core.

Comparison of Results -- Figure 1 shows a comparison of the applied stress versus stable crack growth as determined experimentally, as determined using the VR-curve method described in this paper, and as determined using the COA method. The maximum experimental load was approximately 240. MPa (as determined from points in the referenced paper) and the predicted maximum load using the VR-curve method and stress/strain data only was 260.4 MPa, +8%. The maximum calculated load using the COA method was 239. MPa.

The VR-curve method uses a critical crack tip opening displacement criterial for modeling stable crack growth. At the stable crack growth increments, the COA was determined by considering the displacement approximately 1mm behind the crack tip. (Since the mesh was uneven and not coincident with 1mm increments, the nearest grid point to 1mm was used). Figure 2 shows the calculated crack opening angle for successive crack growth increments. The shape of the curve is similar to the experimental curve, but the calculated critical angle at higher stable crack growth increments was in the 4-5 degree range. Because the displaced shape was nonlinear, the COA calculation was strongly dependent on the distance from the crack tip where the calculation was made.

The shapes of the free crack surface were compared using the VR-curve method and the COA method. Results for applied displacements 0.4589 mm and 0.5848 mm are shown in Figures 3 and 4 respectively. Prior to crack initiation and for small crack growth increments, the shape of the free crack surfaces was similar. Note that at the original crack tip location, 12.7 mm, there is a discontinuity in the slope of the displaced shape. For the COA method, this discontinuity is more pronounced. This change in slope results from the permanent plastic strain at the original crack tip. The results for two different meshes were compared for the COA method and are also shown in the figures. For each of the three methods, the predicted stable crack growth increments differed at a given applied load. For the VR-curve method, the shaded region indicates the damage zone where cohesive forces are acting. As the load became larger, differences in the displaced shapes increased.

Description of 2nd Example -- Results were also compared for a

MIDDLE CRACKED ALUMINUM PANEL: $2A/W=.33$

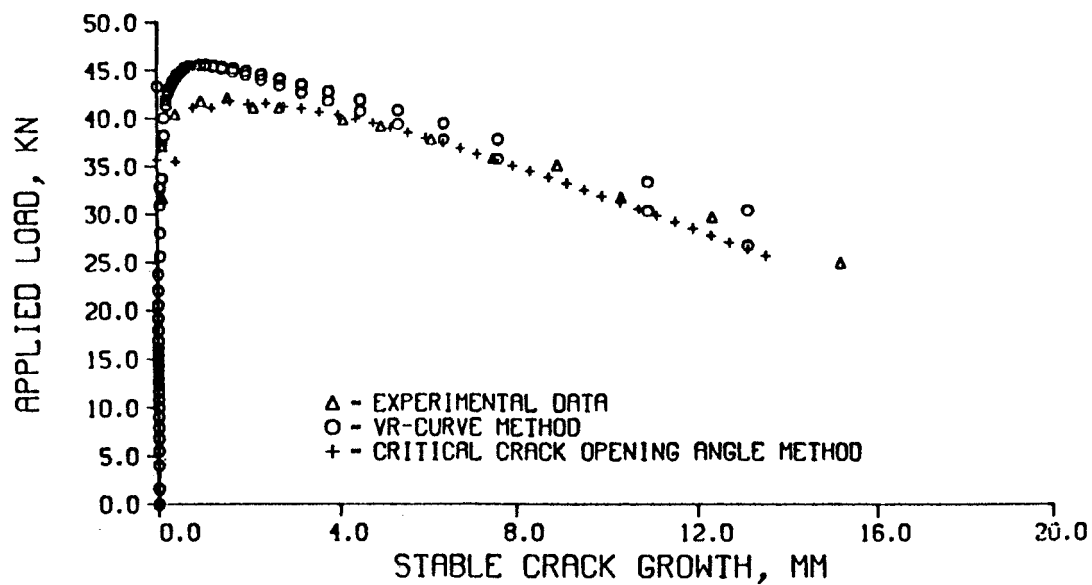


Figure 1: Results for Middle-Cracked Panel

MIDDLE CRACKED ALUMINUM PANEL: $2A/W=.33$

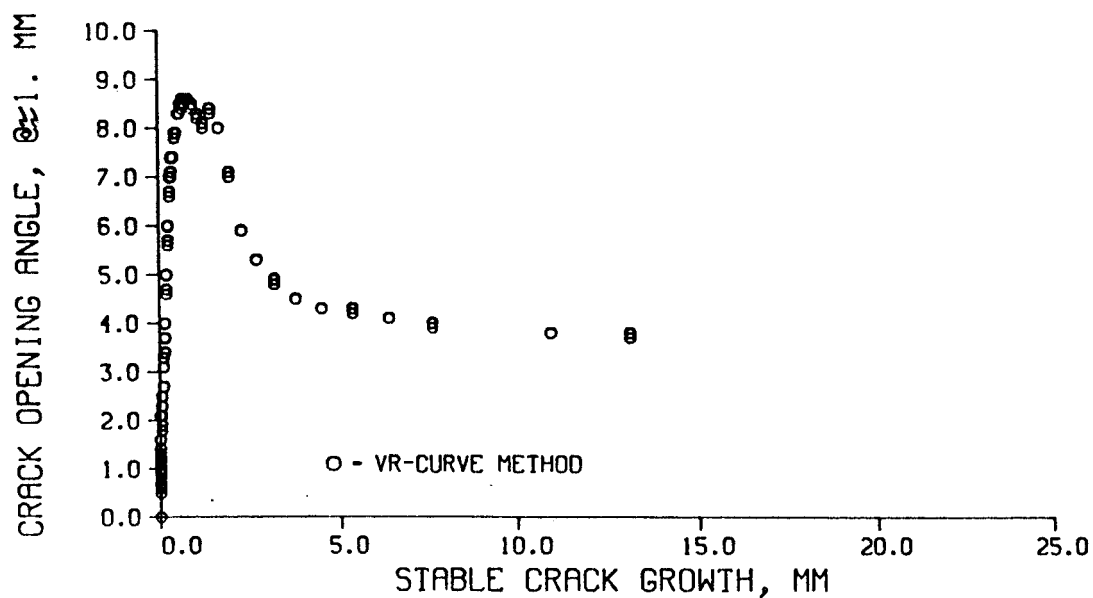


Figure 2: Crack Opening Angle, Middle-Cracked Panel

DISPLACEMENTS ALONG CRACK, YDISP=.4589MM

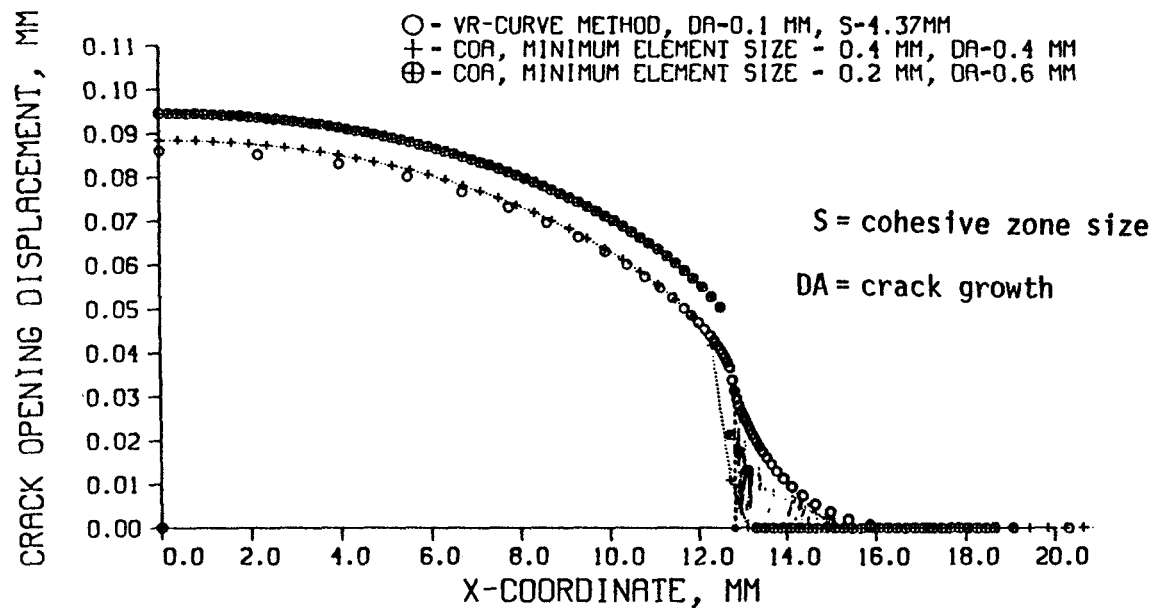


Figure 3: Displacements Along Crack, Middle-Cracked Panel

DISPLACEMENTS ALONG CRACK, YDISP=.5848MM

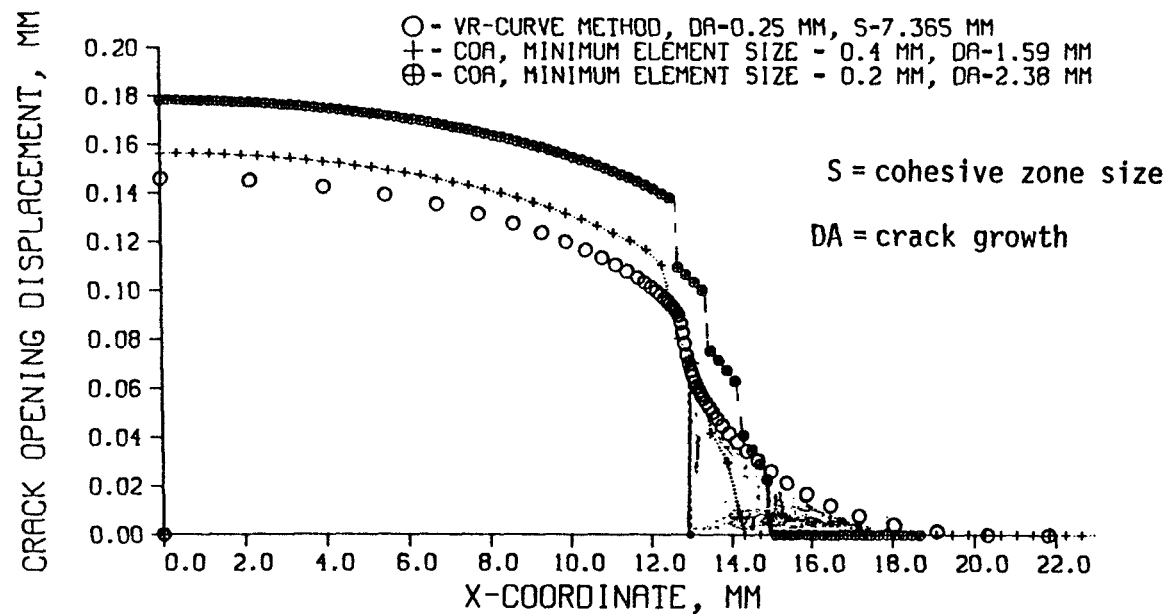


Figure 4: Displacements Along Crack, Middle-Cracked Panel

compact tension specimen fabricated from the same material as Example 1. The geometry of the specimen was described in reference [10] and Figure 5. The applied load versus crack growth behavior is shown in Figure 6. In the experiment, the maximum load of 10.25 kN occurred at 10. mm of crack growth approximately. The VR-curve method predicted a maximum applied load of 10.45 kN at 12.34 mm of stable crack growth. Crack surface displacements before crack initiation and for small increments of crack growth are shown in Figures 7 and 8.

B) Brittle-fracture Example -- For the purposes of analysis, brittle fracture was considered a special case of elastic/plastic fracture. In this example, a compact-tension specimen under plane-strain conditions was evaluated (Figure 9). The load versus crack mouth opening displacement was compared to experimental results [29] and the results are shown in Figure 10. The maximum experimental load was 102.1 kN and the maximum predicted load was 104.0 kN (+1.86). Since the maximum load differed by 1.86% from the experimental load, the KIC value as calculated according to the ASTM specification [5] also differs by 1.86%.

C) Fatigue Examples

Fatigue Crack Initiation Example -- Fatigue examples were used to predict the number of cycles for crack initiation and to predict the stress versus number of cycles curve. The notched steel bar in Figure 11 was used to predict the number of cycles for crack initiation. For the purposes of this analytic method, an assumed initial crack length is required for analysis. Initial crack lengths of .28 mm (.011") and .33 mm (.013") were chosen to be consistent with experimental measurements when the reference was published [30]. Results for notch depths of .381 mm (.15") and 1.27 mm (.05") are shown in Figure 12.

Fatigue Crack Propagation Example -- The double-notched specimen shown in Figure 13 was used to compare the rate of crack growth to experimental values [31]. Two initial notch lengths were investigated. At the lower applied loads, a very fine mesh is required to capture the dissipative energy effects and correctly model the compressive yield zone. As shown in Figure 14, results at the higher load levels are closer to experimental values. Divergence in results at higher load levels is due in part to mesh size; the same mesh was used for all examples but the size of the compressive yield zone was considerably smaller for the higher load levels.

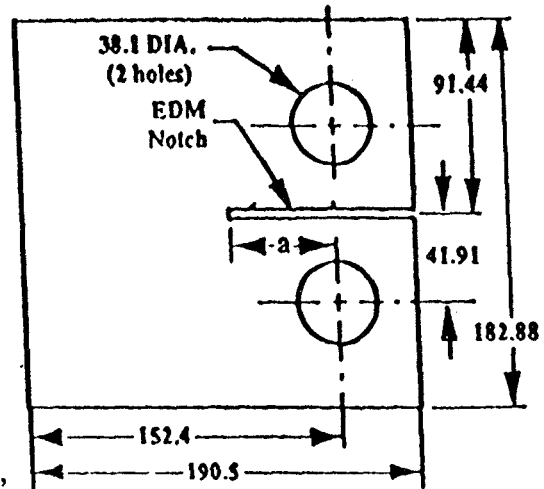
Discussion and Future Research

Elastic/Plastic and Brittle Fracture Analysis -- Although the elastic/plastic method can be implemented using a general-purpose finite element package, special purpose software would be quicker and easier to use.

Several validation examples for aluminum and steel have been completed. The confidence level for the elastic/plastic method would be enhanced by successful completion of additional examples for a

ELASTIC/PLASTIC FRACTURE, EXAMPLE 2

Material: 2024-T3 Aluminum
Yield Stress: $S_y = 345$ MPa
Ultimate Stress: $S_{ult} = 490$ MPa
Compact-Tension
Thickness = 2.3 mm
Panel width = 190.5 mm
 $a = 61$ mm



Reference: Newman, J.C., Jr., Dawicke, D.S., Sutton, M.A., and Bigelow, C.A., "A Fracture Criterion for Widespread Cracking in Thin-Sheet Aluminum Alloys", International Committee on Aeronautical Fatigue, 17 Symposium, Stockholm, Sweden, 1993.

Figure 5: Compact Tension Specimen

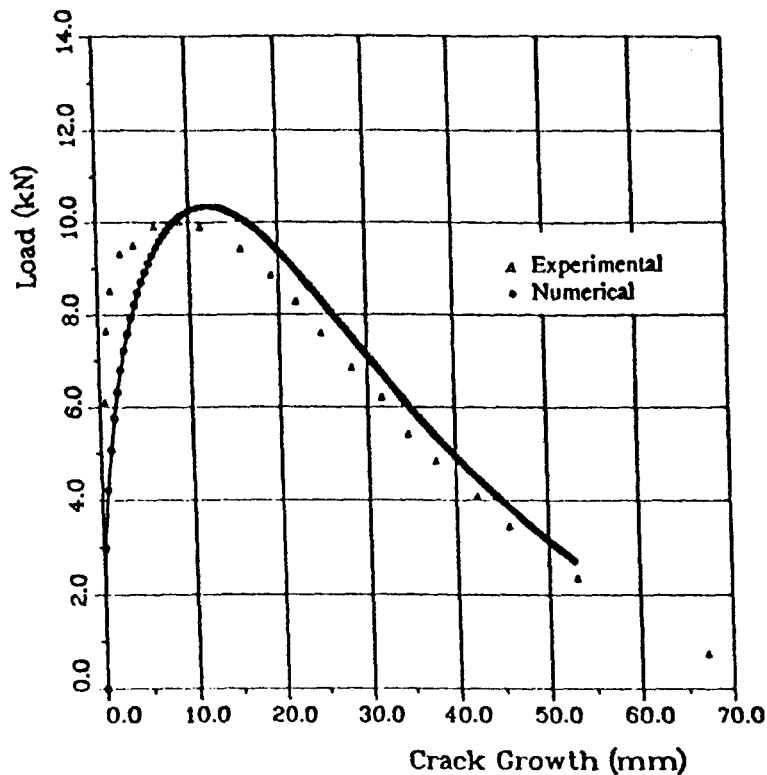


Figure 6: Results, Compact Tension Specimen

COMPACT TENSION SPECIMEN, YDISP=.214 MM

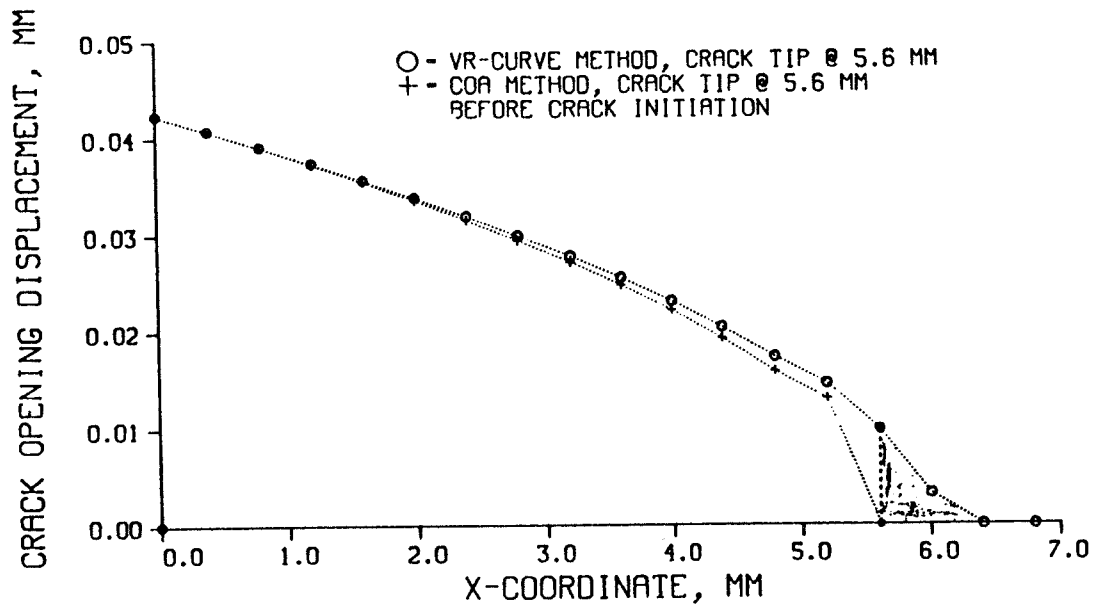


Figure 7: Displacements Along Crack, Compact-Tension Panel (Before Crack Initiation)

COMPACT TENSION SPECIMEN, YDISP=.6852 MM

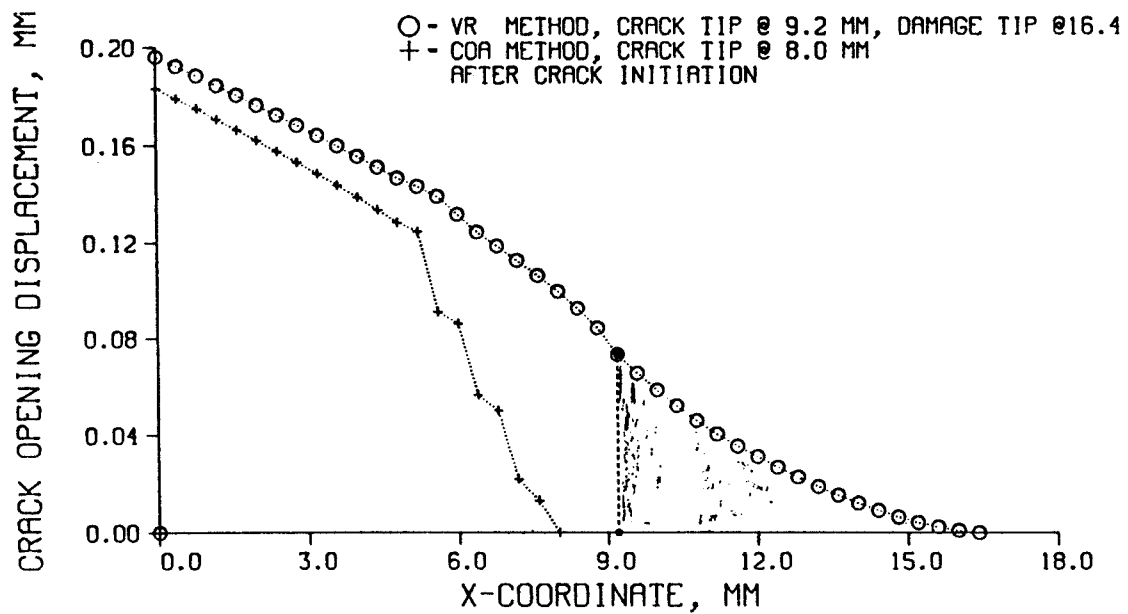


Figure 8: Displacements Along Crack, Compact-Tension Panel (After Crack Initiation)

PLANE STRAIN FRACTURE EXAMPLE

Material: 18Ni Air-Melt Maraging Steel

Yield stress: 190 ksi

Ultimate stress: 196 ksi

Compact tension specimen:

thickness $B = 1.24$ in.

initial crack length $a = 1.95$ in.

width $W = 3.5$ in.

Reference: J.M. Barsom & S.T. Rolfe

Fracture and Fatigue Control in Structures

2nd edition Prentice-Hall, page 89

Figure 9: Brittle Fracture Specimen

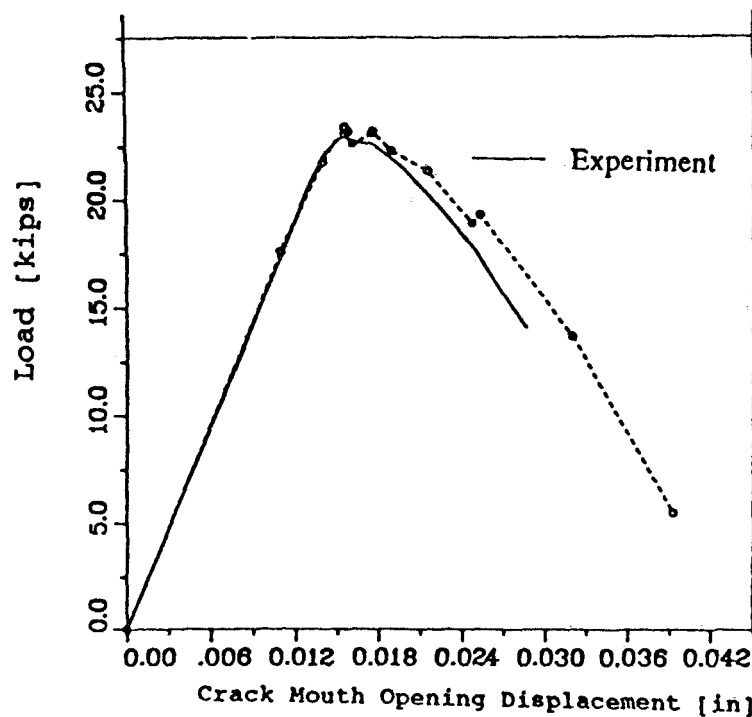
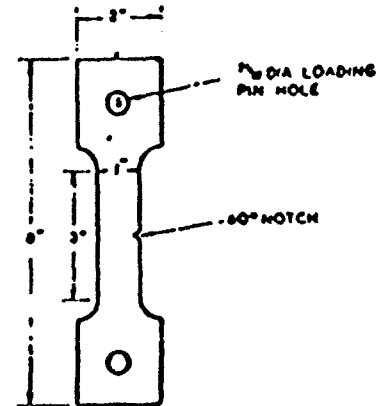


Figure 10: Results, Brittle Fracture

FATIGUE VALIDATION EXAMPLE I

Material: Mild Steel
 Yield Stress: 34,720 psi
 Ultimate Stress: 60,928 psi
 Thickness: 0.2 in.
 Notch root radius: 0.002"
 Two notch depths studied: 0.05" and 0.15"



Reference: A.R.Jack & A.T.Price, International Journal of
 Fracture Mechanics, Vol. 6, No. 4, December 1970

Figure 11: Side Notch Panel

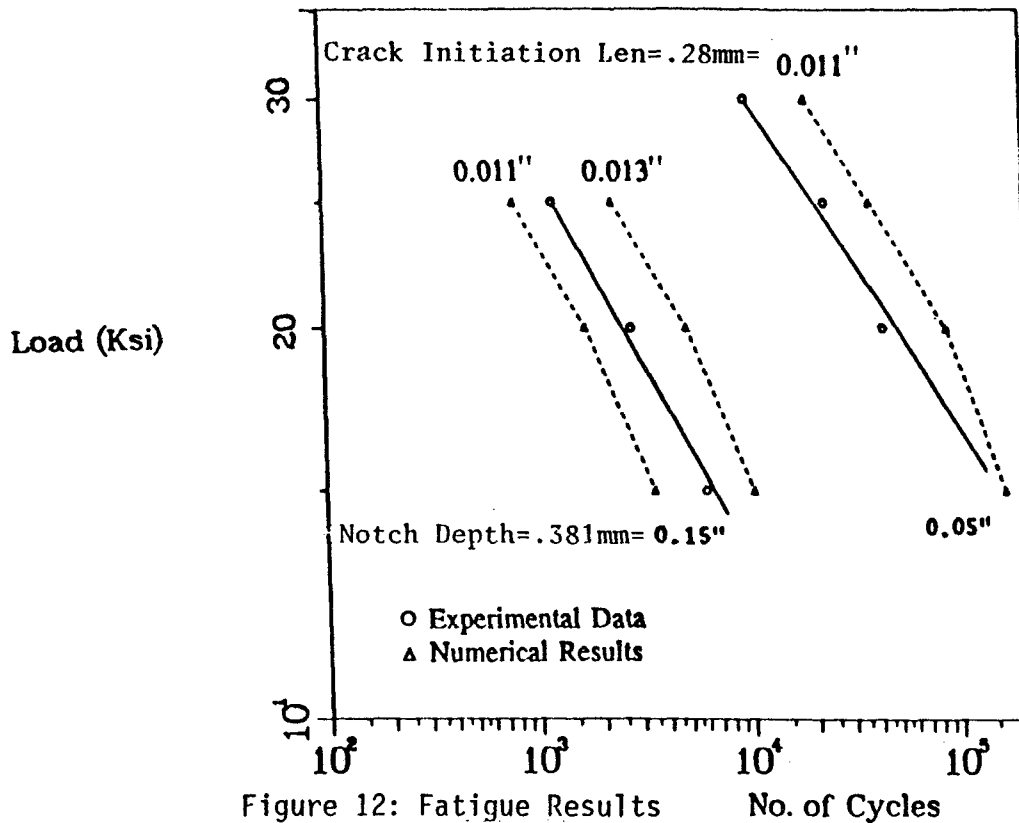
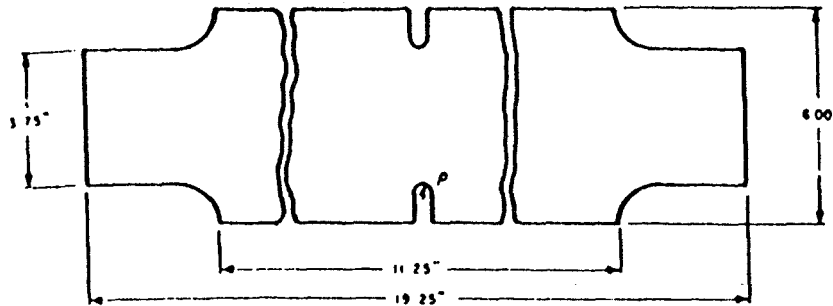


Figure 12: Fatigue Results

(Original figures unavailable at time of publication)

FATIGUE VALIDATION EXAMPLE II



Material: HY130
Yield stress: 146 ksi
Ultimate stress: 153 ksi
Thickness: 0.125"
Two cases studied: root radius 0.016" and 0.064"

Figure 13: Double-Notched Panel

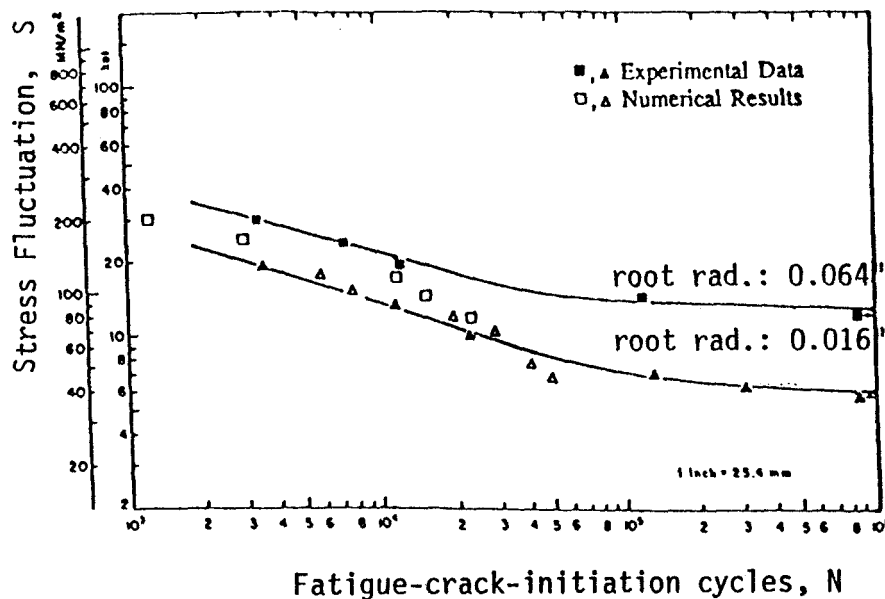


Figure 14: Results, Fatigue Crack Initiation Example
(Double-Notched Panel)

range of metallic alloy materials and geometric shapes. In particular, funding of 'blind' tests for new materials would provide an inexpensive means of increasing the confidence for the method in the engineering community. Similar blind tests would increase the confidence level for predicting KIC.

Fatigue Analysis -- Preliminary results of the fatigue analysis method have been successful. With further development, a special-purpose finite element package could be developed that:

- can be used for either a cracked or flawed specimen
- can predict elastic/plastic crack growth and yield failure
- can predict the critical crack length
- can predict the cycles until crack initiation
- can predict the number of cycles for crack propagation to critical crack length

The package would be applicable to a wide range of geometries and would be designed for use in a range of industries including the automotive, aerospace, and plastics design industries. The package would be written in modular form for expansion into analysis of multi-site damage, creep-fracture, creep-fatigue, and composite materials analysis. Existing special-purpose software such as the programs CRACK IV, FATIGUE and FAST require at least two fatigue constants [32] which would not be required for the proposed software.

Fatigue Crack Initiation -- The research to date indicates that the driving mechanism for fatigue crack growth may be associated with the hysteresis in the stress/strain diagram and the compressive yield zone. The proposed method incorporates this phenomena by use of the E parameter. Additional studies are required to investigate the theoretical basis of this assumption and to determine the optimal means of incorporating this parameter into the fatigue analysis.

Multi-Site Damage -- Unlike most fracture methods which are based on local crack tip damage, the energy parameters used in this analysis method are based on the available and dissipated energy in the structure. The fatigue method is based on two energy parameters W and E. When multiple damage sites are present, the critical crack tip opening displacement curve, generated during the analysis, will be lowered due to the softening effects of multi-site damage and possible crack growth. This softening effect is reflected in the W parameter. Interaction of high stress regions is also captured in the finite element analysis procedure.

The fatigue energy parameter E can also include the effects of multi-site damage. The E parameter sums the energy dissipated at all damage zone nodes experiencing plastic 'shake down' or compressive yield. In the case of multi-site damage, dissipated energy at all damage sites reduces the number of predicted cycles until failure.

Creep-Fatigue -- Presently, predictions of creep fatigue require a material creep law and a series of fatigue constants, each evaluated at a specific state of material creep. Extensive experimental data is

required to determine the C and n constants as a function of the time-dependent creep behavior. The energy-based method proposed in this paper relies on energy assumptions and stress strain diagrams. Material creep law would be required for analysis but fatigue constants would not be required. Nonlinear interactions resulting from cyclic loading under increasing strain due to creep would be incorporated in the critical crack tip opening displacements which are calculated as part of the analysis. A nonlinear creep-fracture method has already been developed by Chang and Kim [33].

Corrosion Fatigue -- Corrosion fatigue cracks have been noted on cargo planes in skin sections with reinforcement straps [34]. The skin section thicknesses are typically within the plane stress region. This type of geometry, thin panels with reinforcing straps, would provide a simple geometry for initial validation of a corrosion fatigue methodology. Corrosion degradation would be incorporated within the material model and corrosion-fatigue constants would not be required.

Composites -- Use of composites in aircraft has increased steadily since the early 1960's. Aircraft such as the F/A 18, the AV 8B, and the V-22 are composed of approximately 10%, 26% and 45% composite materials respectively [35]. Composite materials can result in significant weight savings and an increased resistance to fracture and fatigue. For instance, metal matrix composites with aluminum or titanium matrices have high damage tolerance. Ceramic matrix composites have higher resistance to fracture than unreinforced ceramics while retaining some of the superior high-temperature strength properties.

Existing fracture and fatigue methods are sometimes inappropriate for composite materials due to the lack of standardized ASTM test procedures, the wide variation in material properties, and the likelihood of non-self-similar crack growth. Efforts to evaluate fracture in metal matrix composites and non-self-similar crack growth in glass/epoxy have been initiated [36]. Previous efforts by the authors in predicting Mode II [37] and mixed mode fracture [38] will be helpful for the non-self-similar crack growth problem.

Conclusion

Design engineers typically use finite element methods to check for failure due to buckling and yielding. The method described in this paper uses finite element analysis to predict fracture and fatigue behavior of structures. Once fully developed, the fracture and fatigue methods could find widespread application in aircraft design, engine analysis, bridge design and redesign, and plastics design. The overall safety of fracture-critical designs would be improved without the need for extensive experimental input data.

References

- [1] "F-16 Airframe Structural Integrity Program," from Proceedings of the 1991 USAF Structural Integrity Program Conference, edited by T.D. Cooper, J.W. Lincoln, and R.M. Bader, Wright Patterson Laboratory Report, 1992.
- [2] Landes, H.D., McCabe, D.E., and Ernst, H.A. "Geometry Effects on R-Curve," Nonlinear Fracture Mechanics: Vol II-Elastic-Plastic Fracture, ASTM STP 995, H.D. Landes, A. Saxena, and J.G. Merkle, Eds., American Society for Testing and Materials, Philadelphia, pp. 123-143, 1989.
- [3] Tai, W.H., "An Improvement of CTOD Criterion for Ductile Fracture," Engineering Fracture Mechanics, Vol. 41, pp. 155-157, 1992.
- [4] Kolednik, O., "Loading Conditions May Influence the Shape of J-Da Curves," Engineering Fracture Mechanics, Vol. 41, pp. 251-255, 1992.
- [5] "Standard Method of Test for Plane-strain Fracture Toughness of Metallic Materials," ASTM Designation E-399-83, Vol. 03.01, ASTM Annual Standards, American Society for Testing and Materials, 1985.
- [6] "Standard Practice for R-Curve Determination," ASTM Designation E-561-81, Vol. 03.01, ASTM Annual Standards, American Society for Testing and Materials, 1985.
- [7] "Methods for Crack-tip Opening Displacement (CTOD) Testing," British Standards Institution, BS 5762, 1979.
- [8] Shan, G.X., Kolednik, O., Fischer, F.D., and Stuwe, H.P., "A 2D Model for Numerical Investigations of Stable Crack Growth in Thick Smooth Fracture Mechanics Specimens," Engineering Fracture Mechanics, Vol. 45, pp. 99-106, 1993.
- [9] Elangovan, P.T., "Formulations for Fracture Stress, CTP Zone, and R-Curves," Engineering Fracture Mechanics, Vol. 40, pp. 433-463, 1991.
- [10] Newman, J.C., Jr., Dawicke, D.S., Sutton, M.A., and Bigelow, C.A., "A Fracture Criterion for Widespread Cracking in Thin-Sheet Aluminum Alloys," International Committee on Aeronautical Fatigue, 17 Symposium, Stockholm, Sweden, June 9-11, 1993.
- [11] Zhang, C.H., Gross, D., "Ductile Crack Analysis by a Cohesive Damage Zone Model", Engineering Fracture Mechanics, Vol. 47, pp. 237-248, 1994.
- [12] Paris, P.C., and Erdogan, F., "A Critical Analysis of Crack Propagation Laws, Transactions of the ASME, Journal of Basic Engineering, Series D, Vol. 85, 1963.
- [13] Klesnil, M., and Lukas, P., "Influence of Strength and Stress History on Growth and Stabilization of Fatigue Cracks," Engineering Fracture Mechanics, Vol. 4, pp. 77-92, 1972.

- [14] Mazumdar, P.K., "A Model for High Cycle Fatigue," Engineering Fracture Mechanics, Vol. 21, pp. 907-917, 1992.
- [15] Elber, W., "Fatigue Crack Closure Under Cyclic Tension," Engineering Fracture Mechanics, Vol. 2, pp. 27-45, 1970.
- [16] de Koning, A.U., and Liefting, G., "Analysis of Crack Opening Behavior by Application of a Discretized Strip Yield Model," Mechanics of Fatigue Crack Closure, ASTM STP 982, J.C. Newman, Jr. and W. Elber, Eds., American Society for Testing and Materials, Philadelphia, pp. 437-458, 1988.
- [17] Keyvanfar, F., and Nelson, D.V., "Predictions of Fatigue Crack Growth Behavior Using a Crack Closure Ligament Model," Mechanics of Fatigue Crack Closure, ASTM STP 982, J.C. Newman, JR. and W. Elber, EDS., American Society for Testing and Materials, Philadelphia, pp. 437-458, 1988.
- [19] Dawicke, D.S. , Grandt, A.F. Jr., and Newman, J.C. Jr., "Three-dimensional Crack Closure Behavior," Engineering Fracture Mechanics, Vol. 36, No. 1, pp., 111-121., 1990.
- [20] Kumar, R., "Review on Crack Closure for Constant Amplitude Loading in Fatigue," Engineering Fracture Mechanics, Vol. 42, pp. 389-400, 1992.
- [21] Dowling, N.E., and Begley, J.A., "Fatigue Crack Growth During Gross Plasticity and the J Integral," ASTM STP 590, American Society for Testing and Materials, Philadelphia, pp. 82-103, 1976.
- [22] Newman Jr., J.C. "A Crack-closure Model for Predicting Fatigue Crack Growth Under Aircraft Spectrum Loading," Methods and Models for Predicting Fatigue Crack Growth under Random Loading, ASTM STP 748, J.B. Chang and C.M. Hudson, Eds., American Society for Testing and Materials, pp. 53-84, 1981.
- [23] Newman Jr., J.C. "Prediction of Fatigue Crack Growth Under Variable-Amplitude and Spectrum Loading Using a Closure Model," Design of Fatigue and Fracture Resistant Structures, ASTM STP 761, P.R. Abelkis and C.M. Hudson, Eds. ASTM, pp. 255-277, 1982.
- [24] Drew, M.W., and Thompson, K.R.L., "The Effect of Overload Cycles on Fatigue Crack Propagation in Two Structural Steels," Engineering Fracture Mechanics, Vol. 30, pp. 579-593, 1988.
- [25] Dexter, R.J., Hudak Jr., S.J., Davidson, D.L., "Modelling and Measurement of Crack Closure and Crack Growth Following Overloads and Underloads," Engineering Fracture Mechanics, Vol. 33, NO. 6, pp. 855-870, 1989.
- [26] Cordes, J., Chang, A., Nelson, N., and Kim, Y., "A Computational Method to Predict Elastic/Plastic Fracture," submitted for review and publication, 11/93.

- [27] Chang, A., Nelson, N., Cordes, J., and Kim, Y., "Fatigue Prediction Based on Computational Fracture Mechanics," accepted for presentation, Third Symposium on Advances in Fatigue Lifetime Predictive Techniques, American Society for Testing and Materials, May, 1994.
- [28] ABAQUS, Hibbitt, Karlsson, Sorensen, Inc., Providence, R.I.
- [29] Barsom, J.M., and Rolfe, S.T., Fracture and Fatigue Control in Structures, 2nd. Edition, Prentice-Hall, Inc., Englewood Cliffs, New Jersey, 1987.
- [30] Jack, A.R., and Price, A.T., "The Initiation of Fatigue Cracks from Notches in Mild Steel Plates," International Journal of Fracture Mechanics, Vol. 6, pp. 401-409, 1970.
- [31] Barsom, J.M., and McNicol, R.C., "Effect of Stress Concentration on Fatigue Crack Initiation in HY-130 Steel," ASTM STP 599, pp. 183-204, 1974.
- [32] Akyurek, T., "A Survey of Fatigue Crack Growth Life Estimation Methodologies," Engineering Fracture Mechanics, Vol. 42, pp. 797-803, 1992.
- [33] Chang, A., and Kim, Y., "Creep Fracture by Finite Element Method," Presented at Joint FEEG/ICF International Conference on Fracture of Engineering Materials and Structures, Singapore, 1991.
- [34] Dunn, W., Shaw, L., and Rogers, L., "Vibroacoustic Fatigue and Stress Corrosion Cracks in the Fuselage Skin of a Large Cargo Airplane," from Proceedings of the 1991 USAF Structural Integrity Program Conference, edited by T.D. Cooper, J.W. Lincoln, and R.M. Bader, Wright Patterson Laboratory Report, 1992.
- [35] Isom, J.L., "A Guide for the Consideration of Composite Material Impacts on Airframe Costs," NTIS Technical Report, AFIT/GCA/LSQ/91S-3, Air Force Institute of Technology, Wright Patterson Air Force Base, OH, 1991.
- [36] Cordes, J., Chang, A., Nelson, N., Kalinowski, J., "Predicting Crack Growth in Continuous-fiber Composite Materials," to be presented at the 26th National Symposium on Fracture Mechanics, Idaho Falls, June 1994.
- [37] Cordes, J., and Yazici, R., "Elastic-Plastic Mode II Fracture in an Aluminum Beam," accepted for publication, Fracture Mechanics: 24 Symposium, ASTM STP 1207, edited by J.D. Landes and D.E. McCabe, American Society for Materials Testing, Philadelphia, 1994.
- [38] Cordes, J., Yazici, R., Seo, M., "Mixed Mode Fracture in Plastically Deforming Materials," Journal of Pressure Vessel Technology, ASME, pp. 348-352, 1993.

1995108053

N95-14467

INFLUENCE OF CRACK HISTORY ON THE STABLE TEARING BEHAVIOR OF A THIN-SHEET MATERIAL WITH MULTIPLE CRACKS

D. S. Dawicke
Analytical Services and Materials, Inc.
Hampton, VA

J. C. Newman, Jr.
NASA Langley Research Center
Hampton, VA

M. A. Sutton and B. E. Amstutz
University of South Carolina
Columbia, SC

348615
514-39
23108
P. 21

ABSTRACT

Fracture tests were conducted on 2.3mm thick, 305mm wide sheets of 2024-T3 aluminum alloy with from one to five collinear cracks. The cracks were introduced (crack history) into the specimens by three methods: saw cutting, fatigue precracking at a low stress range, and fatigue precracking at a high stress range. For the single crack tests, the initial crack history influenced the stress required for the onset of stable crack growth and the first 10mm of crack growth. The effect on failure stress was about 4% or less. For the multiple crack tests, the initial crack history was shown to cause differences of more than 20% in the link-up stress and 13% in failure stress. An elastic-plastic finite element analysis employing the CTOA fracture criterion was used to predict the fracture behavior of the single and multiple crack tests. The numerical predictions were within 7% of the observed link-up and failure stress in all the tests.

INTRODUCTION

Commercial jet transport aircraft are designed with economic fatigue design life goals. As the fleet ages and approaches its design life, the possibility for the development of fatigue cracking increases. Analysis tools are needed to assess the influence of fatigue cracks on structural integrity and to define inspection intervals. One of the objectives of the NASA Aircraft Structural Integrity Program [1] is to develop the methodology necessary to predict residual strength of cracked pressurized aircraft fuselage structures. The approach taken is to develop a local fracture criterion that can be used with shell-code finite element analyses. The fracture criterion should be able to predict large amounts of stable crack growth for multiple cracks under conditions of large-scale yielding in thin sheet materials.

The crack tip opening angle (CTOA) [2-6] fracture criterion has been experimentally verified to successfully predict residual strength in laboratory specimens [7-9]. Newman

et al [10] have also applied the CTOA criteria to multiple-site damage (MSD) cracking scenarios, accurately predicting crack link-up and residual strength for 508mm wide sheets of clad 2024-T3 aluminum with 1 to 5 collinear cracks. That study indicated that, as postulated by Swift [11] and demonstrated experimentally by Maclin [12], the residual strength of a structure with a single long crack is significantly reduced by the presence of smaller adjacent cracks. Furthermore, Newman et al [10] indicated that methods used to introduce cracks (fatigue precracking or saw cuts) can significantly influence the residual strength of multiple interacting cracks. The stress required for the onset of stable tearing was greater for saw cuts than for fatigue cracks. Increasing the fatigue precracking stress was also observed to increase the stress required for the onset of stable tearing [8]. These increases may have significant consequences on the link-up and failure of MSD cracking scenarios.

The objective of this study was to experimentally investigate the effect of crack history (including saw cuts) on the residual strength of multiple interacting cracks. Fracture tests were conducted on flat sheet test specimens containing from one to five cracks. The cracks were introduced into the specimens by three methods: saw cutting, fatigue precracking at a low stress range, and fatigue precracking at a high stress range. CTOA and strain field measurements were made on many of the tests. Predictions of the fracture behavior were made using an elastic-plastic finite element analysis and the critical CTOA fracture criterion.

EXPERIMENTAL PROCEDURE

Fracture tests were conducted on 2.3mm thick 2024-T3 aluminum alloy. The yield stress and ultimate strength of the material were 345 and 490 MPa, respectively. The specimens were 305mm wide and had from one to five nearly collinear cracks. The cracks were introduced into the specimen by either fatigue precracking or by saw cuts. Measurements of CTOA were made using the digital image correlation (DIC) and optical microscope (OM) techniques. The strain field measurements were made using the DIC method.

Fracture Tests

All of the specimens were cracked in the L-T orientation (i.e., the load was applied in the longitudinal or rolling direction and the crack was in the transverse direction or perpendicular to the longitudinal direction). The cracks were introduced by fatigue precracking at a high stress range (HS), fatigue precracking at a low stress range (LS), or saw cutting (SC). The saw cuts were made with a jeweler's saw blade that made a square-corner notch with roughly a 0.4mm slot height. The fatigue cracks were obtained by cycling notched specimens at a stress ratio of $R=0.02$ and at a stress range that would result in a stress intensity factor range of about $7 \text{ MPa} \sqrt{\text{m}}$ for the LS tests and about $35 \text{ MPa} \sqrt{\text{m}}$ for the HS tests. The multiple (3 and 5) crack specimens were fatigue precracked by first saw cutting notches at the intended locations of the smaller (MSD) cracks. The notch lengths were roughly 5mm less than the intended crack lengths. A stress range was calculated that resulted in the proper stress intensity factor range for the smaller cracks and the specimen fatigue precracked until the cracks reached the required length. Then,

the longer crack was added by a saw cut, a new stress range calculated, and the specimen was again fatigue precracked until the long crack reached the required length. During the long crack fatigue precracking, the stress intensity factor of the smaller cracks was low enough that no noticeable crack growth was observed. Typical initial crack configurations are shown in Figure 1.

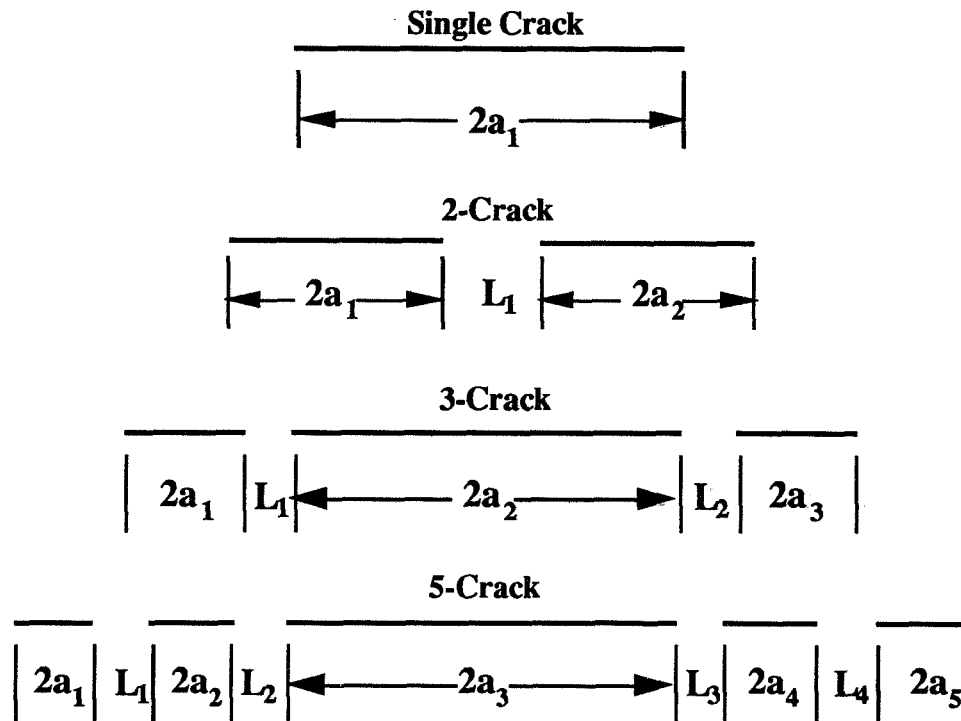


Figure 1. Schematic of crack configurations for fracture tests.

The specimens were fractured under displacement control. The rate of displacement was 3mm/sec. Anti-buckling guides were used in all tests. The anti-buckling guides consisted of two 12mm thick plates of 2024-T3 aluminum that sandwiched the specimen and were held in place by a series of bolts along the vertical edges. A layer of Teflon tape was put on the plates to reduce the friction between the plates and the specimen. The guides had a 10mm high and 250mm long slot in the center of the plate to view the cracks. During each test, measurements of some or all of the following parameters were made: load, crack length, surface CTOA, and surface strain fields.

Measurement Techniques

The critical CTOA during stable tearing was measured by direct observation of the surface using both the DIC and the OM techniques. The OM technique uses a video camera and a long focal length microscope to image the tearing crack. The CTOA is calculated directly from the angle made by points located on the upper surface, the crack tip and the lower surface [8, 9]. Similarly, the DIC technique uses a computer controlled

video camera and lens system to digitize images of the specimen surface. To make measurements with the DIC technique, the specimen surface was coated with a high contrast random speckle pattern. A small region, or subset, is identified in a reference image and the relative displacement of that same subset in a subsequent image is calculated [8, 9, 13-17]. The CTOA measurement is based on displacements of subsets located near the upper and lower crack surfaces and the crack tip [8, 9]. For both the DIC and OM techniques, the CTOA measurements were made within 0.5-1.5mm behind the crack tip.

The surface strain fields were calculated using the DIC technique. A displacement field grid was obtained by systematically measuring the displacements of overlapping subsets ahead of the crack tip. The displacement data was smoothed using a two-dimensional, optimal smoothing method [18]. The smoothing program computed the estimated surface strains ϵ_{yy} , ϵ_{xx} , and ϵ_{xy} at each displacement grid location. The strain field measurements were made in the ligaments between 2 cracks or 2 saw cuts in the 305mm wide specimens.

FINITE ELEMENT ANALYSIS

The elastic-plastic finite element code ZIP2D [19] was used to predict the stable tearing behavior in the fracture tests. The program uses 3-noded, constant strain triangular elements and a critical CTOA criterion to extend the crack. The elastic-plastic analysis employs the initial-stress concept [20] based on incremental flow theory and small strain assumptions. A multi-linear representation of the uniaxial stress-strain curve for 2024-T3, with the data given in Table I, was used in the analysis with a von Mises yield criterion.

TABLE I. Multi-Linear Representation Of The Uniaxial Stress-Strain Curve For 2024-T3

σ (MPa)	ϵ
345	0.00483
390	0.015
430	0.04
470	0.1
490	0.16
490	0.2
E = 71,400 MPa and $\nu = 0.3$	

Finite Element Code and Meshes

The element size along the line of crack extension was $d=0.48\text{mm}$. Symmetry conditions required that only half of the specimen be modeled, with the axis of symmetry along the crack line. Normally, the nodes along the crack line and ahead of the crack tip

are fixed, while those behind are free. This analysis uses springs along the crack line to change boundary conditions associated with crack extension. The spring stiffness is set equal to zero for nodes behind the crack tip and assigned an extremely large value for nodes ahead of the crack tip. Monotonic loading (under displacement control) was applied to the model. Crack growth by stable tearing was governed by the critical CTOA criterion. Reference 7 contains the details of the elastic-plastic finite element analysis used in this work.

Critical CTOA Criterion

The critical CTOA (ψ_c) criterion is equivalent to a critical CTOD (δ_c) value at a specified distance, d , behind the crack tip equal to one element length and is given by:

$$\psi_c = 2 \tan^{-1}(\delta_c/d) \quad (1)$$

The crack-tip node was released and the crack advanced to the next node whenever the CTOA equaled or exceeded a preset critical value (ψ_c) during incremental loading. This process was repeated until crack growth became unstable under load control or the crack reached a desired length under displacement control. The critical CTOA value (ψ_c) was determined experimentally from surface measurements made using both the OM and DIC techniques.

Crack History Simulation

The different crack histories (LS, HS, and SC) were simulated within the finite element analysis. The crack history associated with the low and high fatigue precracking was simulated by cyclic loading of the finite element model. The model was loaded to the appropriate stress level and the crack allowed to advance one element length; then the load returned to zero. The procedure was repeated for another cycle to allow residual stresses to develop ahead of the crack and plasticity deformed material left in the crack wake.

The saw cut was simulated by using the assumption that the saw cut must undergo a deformation, δ_i , at the tip before a crack would initiate. The saw cut tip node would be released once the tip displacement reached δ_i . The value δ_i was obtained by matching the crack growth in the single saw cut fracture tests. Additional information on determining δ_i for the saw cut simulation is given in Reference 10.

RESULTS AND DISCUSSION

Twenty five fracture tests were conducted on the 305mm wide, 2.3mm thick sheets of 2024-T3 aluminum alloy. The tests are summarized in Table II and the initial crack configurations are given in Table III. The critical CTOA was obtained from experimental measurements made on a stably tearing crack.

Single Crack Fracture Tests

Three different types of single crack fracture tests were conducted: low stress range fatigue precracking (LS), high stress range fatigue precracking (HS), and saw cuts (SC). In each test, the crack extension (Δa) was recorded as a function of applied stress. The failure stress was recorded for each test and is shown in Figure 2 as a function of the initial crack length. The LS and HS test had about the same failure stresses. The failure stresses of the SC tests were about 4% higher than the failure stresses in the LS tests.

In each test, the amount of stable crack growth was measured as a function of applied stress, as shown in Figure 3 for the tests with the 127mm initial cracks. The HS and LS tests differed only in the stress range used for the initial fatigue precracking. The high stress range fatigue precracking increased the plastic deformation ahead of the crack and in the crack wake, increasing the stress required to initiate stable crack growth by 16% compared to the LS test. After about 10mm of stable crack growth, the influence of the initial crack history was lost and the behavior of the LS and HS tests were identical, as shown in Figure 3.

The stress required to initiate stable crack growth from a saw cut was about 47% higher than that of the LS test, but the failure stress was only increased by about 4%. The SC test required about 20mm of crack growth before the effect of the saw cut had diminished and the crack growth behavior approached that of the LS and HS tests, as shown in Figure 3.

Multiple Crack Fracture Tests

Three different techniques (LS, HS, and SC) were used to introduce cracks for the multiple crack fracture tests. Three patterns of multiple cracks were examined (Figure 1): two long cracks with a small ligament between them, a long centered crack with a single small crack in front of both crack tips (both small and large ligaments were considered), and a long centered crack with two small collinear cracks in front of both crack tips.

In the tests with three collinear cracks (with small ligaments between cracks), the link-up behavior of all three tests (LS, HS, and SC) was different, as shown in Figure 4. For the LS test, link-up occurred at 136 MPa and the highest stress occurred at a second

TABLE II Test summary for the 304.8mm wide fracture tests

Number of Cracks	Pre-crack Stress Range		Initial Total Crack Length (mm)	Fracture Stress (MPa)	Type ¹	Ligament Link-Up Stress			
	Small Cracks (MPa)	Long Crack (MPa)				L1 (MPa)	L2 (MPa)	L3 (MPa)	L4 (MPa)
1	--	17.2	101.4	215.5	LS	--	--	--	--
5	110.3	22.4	133.5	161.4	LS	161.4	161.4	161.4	161.4
5	--	--	131.8	182.1	SC	182.1	182.1	182.1	182.1
1	--	--	101.7	220.6	SC	--	--	--	--
3	76.6	19.2	126.6	158.3	LS	136.1	135.8	--	--
3	--	--	125.7	166.3	SC	166.3	164.4	--	--
3	63.8	31.9	76.6	258.6	LS	258.6	258.6	--	--
3	--	--	75.8	269.5	SC	269.5	269.5	--	--
1	--	86.2	101.5	219.5	HS	--	--	--	--
3	255.4	83.0	126.2	160.1	HS	146.3	145.7	--	--
5	255.4	83.0	152.6	136.3	HS	136.3	136.3	126.9	126.9
5	255.4	83.0	134.4	161.2	HS	161.2	161.2	161.2	161.2
1	--	16.0	126.1	190.8	LS	--	--	--	--
1	--	16.0	133.4	181.9	LS	--	--	--	--
2	--	21.1	98.5	208.7	LS	91.0	--	--	--
3	76.6	19.2	126.4	171.2	LS	171.2	171.2	--	--
2	--	21.1	100.0	194.5	LS	149.1	--	--	--
2	--	--	97.7	204.7	SC	181.4	--	--	--
2	--	--	95.9	223.4	SC	126.1	--	--	--
1	--	16.0	127.0	186.1	LS	--	--	--	--
1	--	13.3	152.4	160.9	LS	--	--	--	--
1	--	--	150.5	169.2	SC	--	--	--	--
1	--	--	124.8	196.8	SC	--	--	--	--
1	--	63.8	152.4	158.5	HS	--	--	--	--
1	--	76.6	127.1	187.3	HS	--	--	--	--

Note: ¹ LS = low stress range precracking, HS = high stress range precracking, and SC = saw cut

TABLE III Initial Crack Configurations for the 305mm Wide Fracture Tests

2a ₁	L ₁	2a ₂	L ₂	2a ₃	L ₃	2a ₄	L ₄	2a ₅
101.4	--	--	--	--	--	--	--	--
7.4	17.3	8.0	18.3	101.5	18.8	8.4	17.0	8.1
7.4	16.5	9.1	19.9	100.3	17.8	8.0	18.0	7.0
101.7	--	--	--	--	--	--	--	--
13.8	12.3	101.5	14.1	12.3	--	--	--	--
13.6	12.5	100.7	14.9	11.3	--	--	--	--
11.6	51.1	50.7	49.9	14.4	--	--	--	--
11.7	50.3	50.3	49.9	13.8	--	--	--	--
101.5	--	--	--	--	--	--	--	--
14.8	12.6	101.4	14.5	9.9	--	--	--	--
14.2	9.7	16.7	13.7	101.3	18.9	10.9	15.7	9.4
9.4	15.2	9.7	15.1	101.5	15.2	6.6	19.0	6.8
126.1	--	--	--	--	--	--	--	--
133.4	--	--	--	--	--	--	--	--
50.6	5.1	47.9	--	--	--	--	--	--
12.8	24.2	101.4	26.7	12.2	--	--	--	--
47.3	15.2	52.6	--	--	--	--	--	--
51.5	16.0	46.2	--	--	--	--	--	--
48.3	5.2	47.6	--	--	--	--	--	--
127.0	--	--	--	--	--	--	--	--
152.4	--	--	--	--	--	--	--	--
150.5	--	--	--	--	--	--	--	--
124.8	--	--	--	--	--	--	--	--
152.4	--	--	--	--	--	--	--	--
127.1	--	--	--	--	--	--	--	--

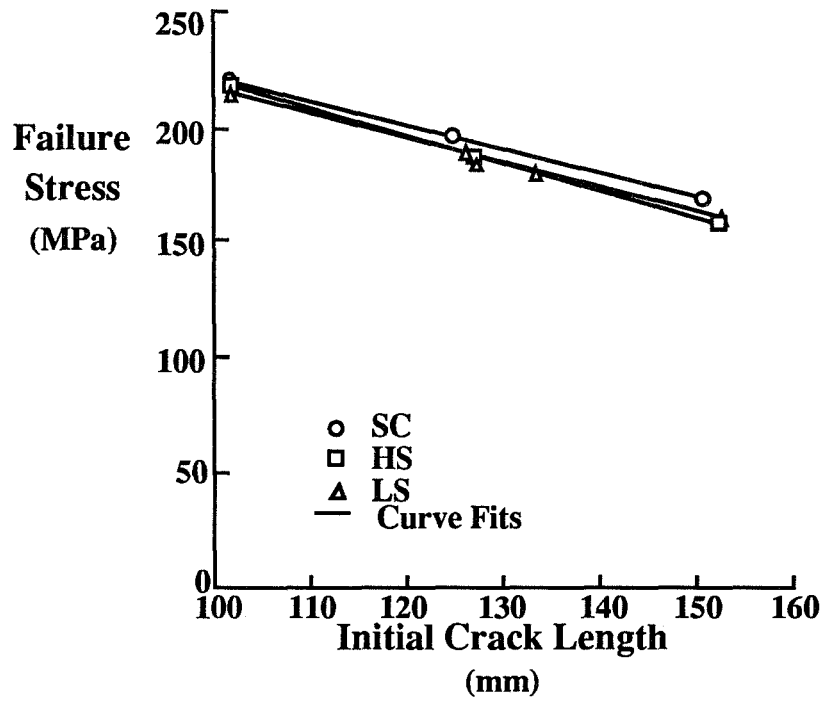


Figure 2. Maximum fracture stress as a function of initial crack length for the single crack fracture tests.

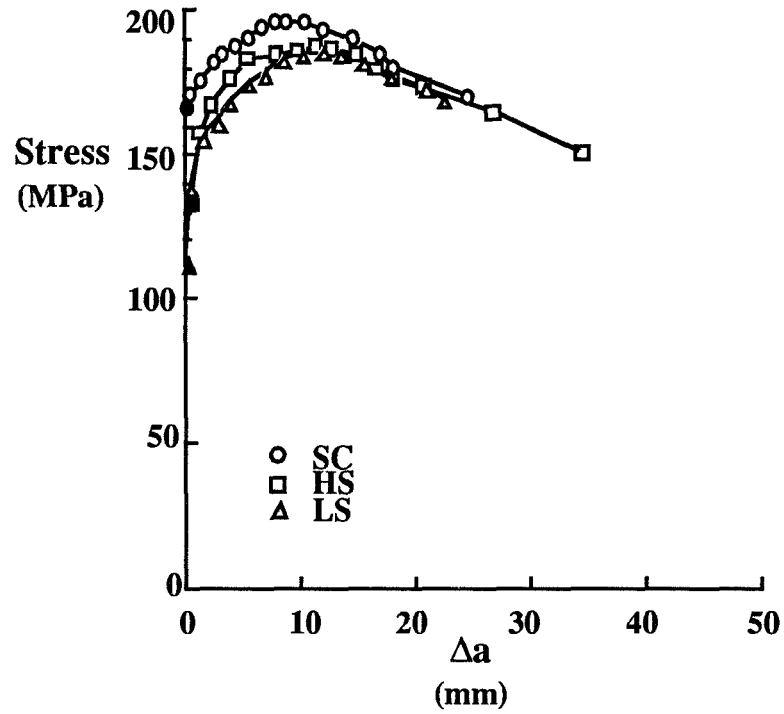


Figure 3. Stress against crack growth behavior for the single 127mm cracks (solid symbols indicate the onset of crack growth).

loading peak, well after link-up. Link-up in the HS test occurred at a stress 7% higher than the stress in the LS test, but after link-up the two tests were nearly identical. The behavior of the SC test was noticeably different. Link-up occurred at 166 MPa, 22% greater than in the LS test, and this was the maximum stress in the test. A second peak stress was observed, but this was less than the link-up stress. The crack growth behavior of the SC test agreed with the LS and HS tests after about 25mm of crack extension. The difference in maximum stresses after link-up for the three tests was only about 5%, but the stable crack growth behavior of the three tests was considerably different.

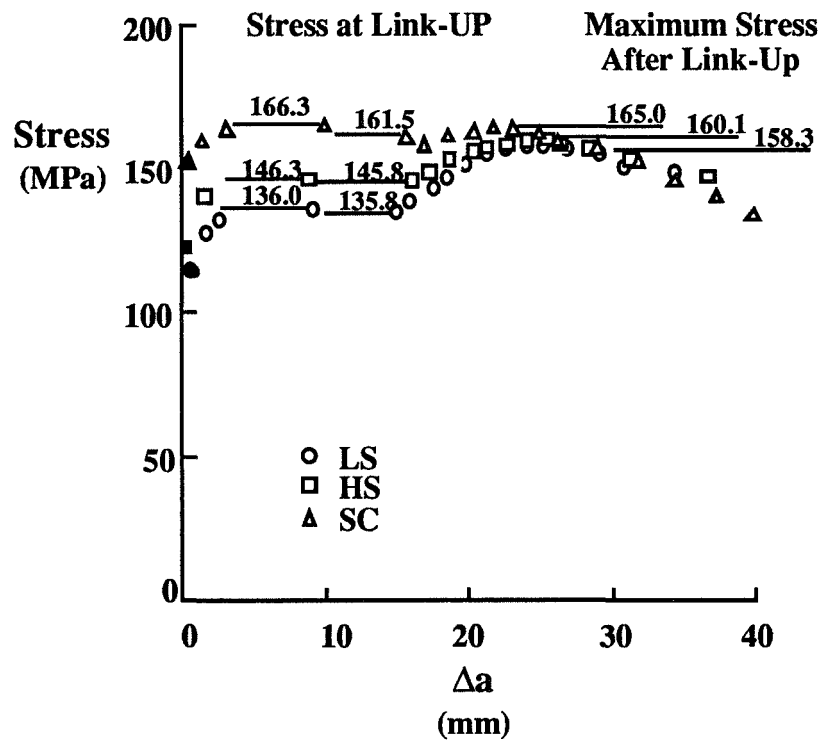


Figure 4 Applied stress against stable crack extension for the 3-crack fracture tests with small ligaments between cracks (solid symbols indicate the onset of crack growth).

In the tests with five collinear cracks, the LS and HS link-up behavior was nearly identical, as shown in Figure 5. In the SC tests, the onset of crack growth occurred at stress level greater than the stress required for failure in the LS and HS tests. First link-up was the critical event (maximum stress) in all three tests, with the link-up in the SC tests at a stress 13% higher than the stress in the LS and HS tests.

Strain Fields

The DIC method was used to measure the strain field in the ligament between two collinear cracks and between two collinear saw cuts. The fatigue cracks and saw cuts

were about 50mm long and both large (15mm) and small (5mm) ligaments were examined. The cracks were fatigue precracked at a low stress level (LS) and the saw cuts (SC) were produced in the same manner as discussed earlier. For the small ligament tests, link-up occurred at 91 MPa and 126 MPa for the fatigue cracks and saw cuts, respectively. The failure stress was 209 MPa and 223 MPa for the fatigue cracks and saw cuts, respectively. For the large ligament tests, link-up occurred at 149 MPa and 181 MPa for the fatigue cracks and saw cuts, respectively. The failure stress was 195 MPa and 205 MPa for the fatigue cracks and saw cuts, respectively. Four ϵ_{yy} strain fields were generated for the tests with small ligaments: at 74% and 94% of the link-up stress for the LS test and 53% and 99% of the link-up stress for the SC test, as shown in Figures 6 and 7, respectively.

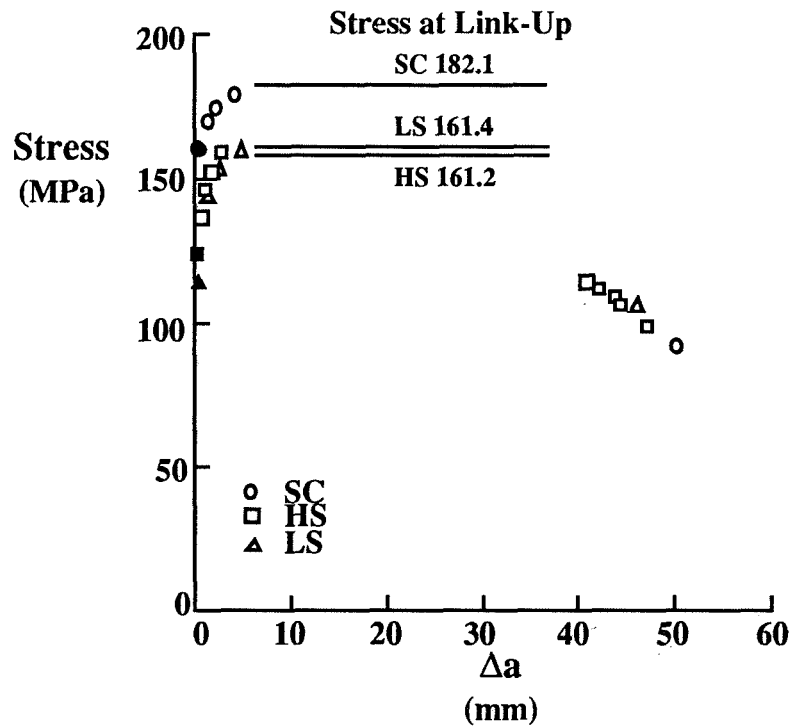
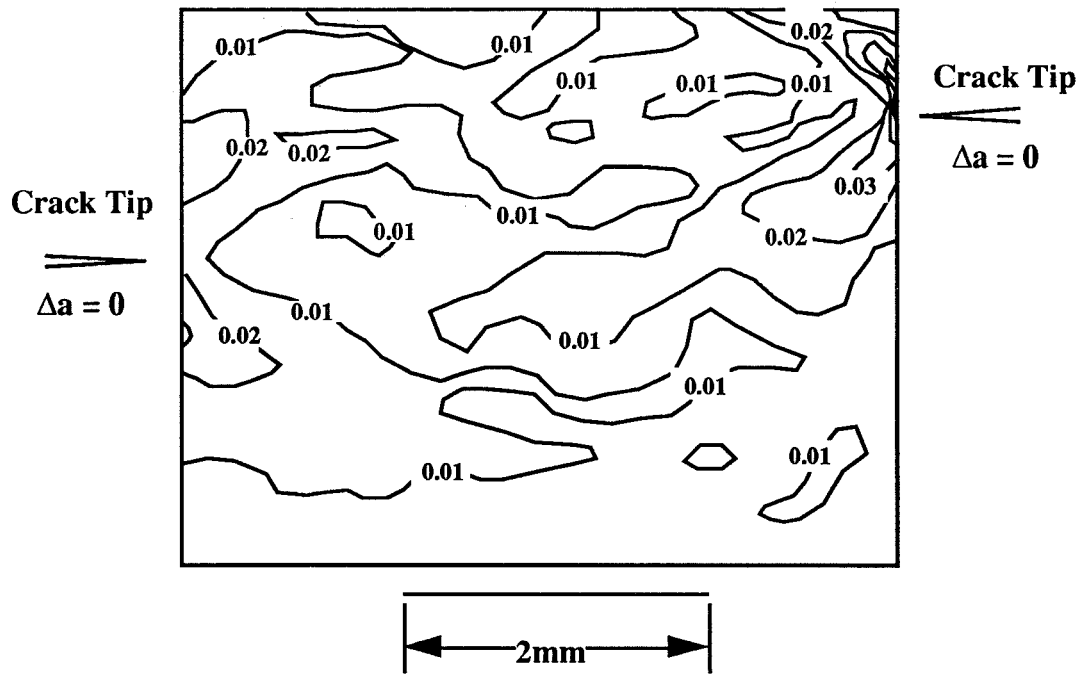
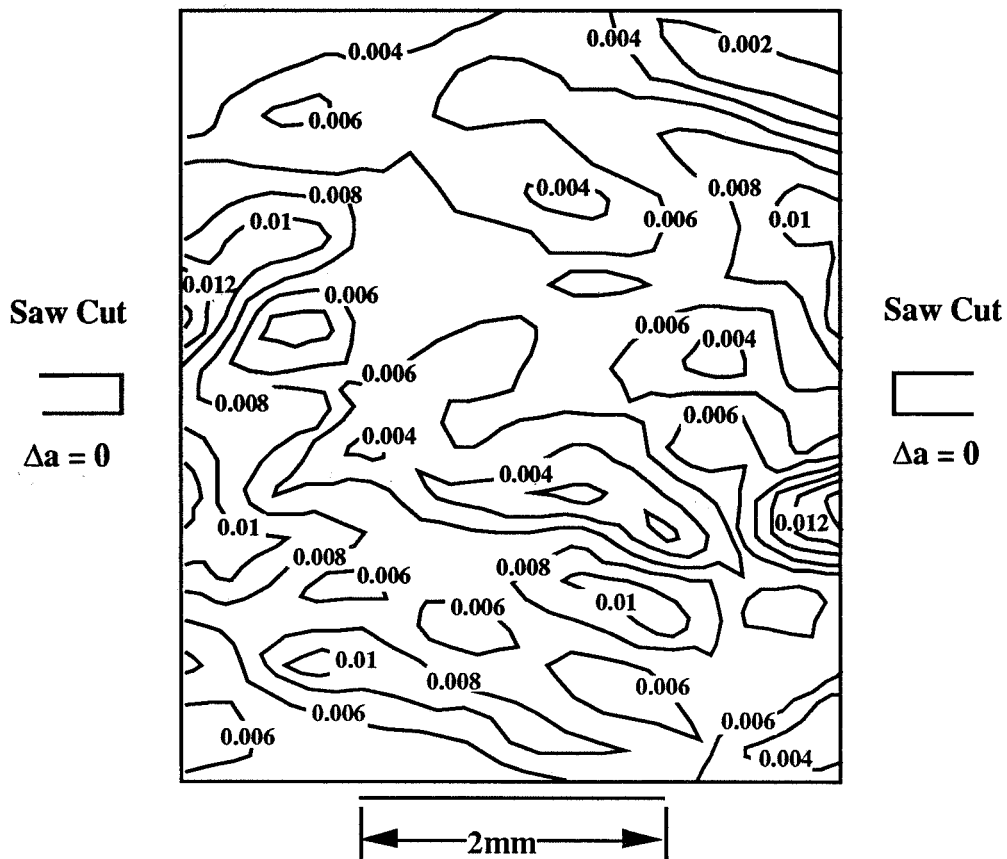


Figure 5 Applied stress against stable crack extension for the 5-crack fracture tests (solid symbols indicate the onset of crack growth).

The LS strain field at 74% of the link-up stress (Figure 6a) and the SC strain field at 53% of the link-up stress (Figure 6b) were at the same stress level ($S=67$ MPa). The strain in the direction of loading (ϵ_{yy}) throughout the LS ligament are clearly greater than those of the SC ligament and the strains in the LS ligament are above a yield strain of 0.007. The LS strain fields at 94% of the link-up stress (Figure 7a) and the SC strain fields at 99% of the link-up stress (Figure 7b) continue to exhibit this trend. Stable crack growth was observed at about 84% of the link-up stress (77 MPa) in the LS tests, but in the SC test stable crack growth did not begin until the link-up stress.

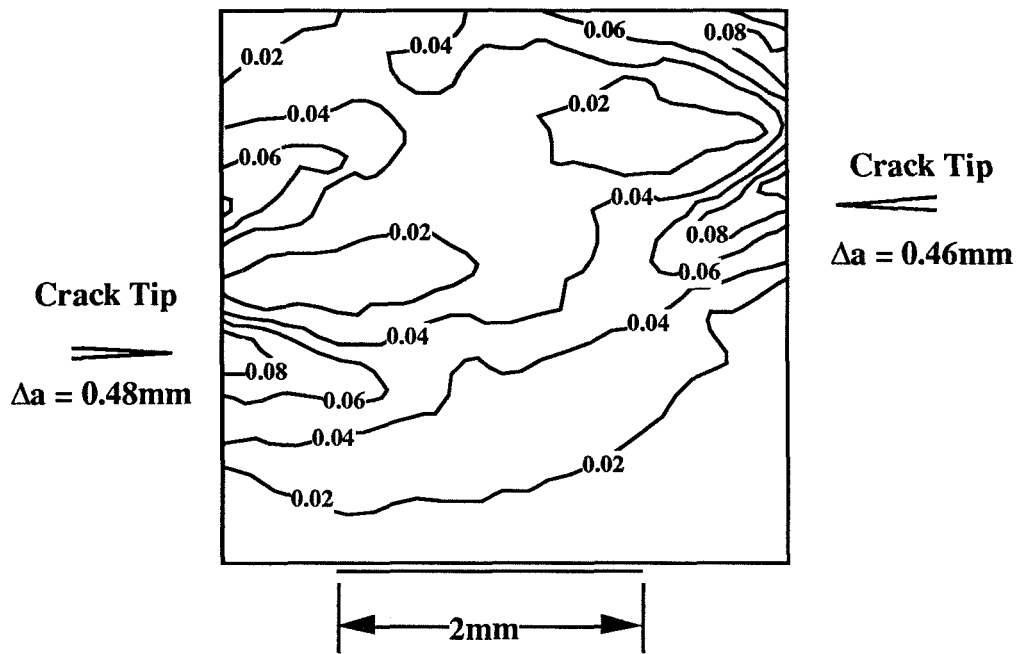


a. LS fracture tests ($S=67$ MPa, 74% of link-up stress)

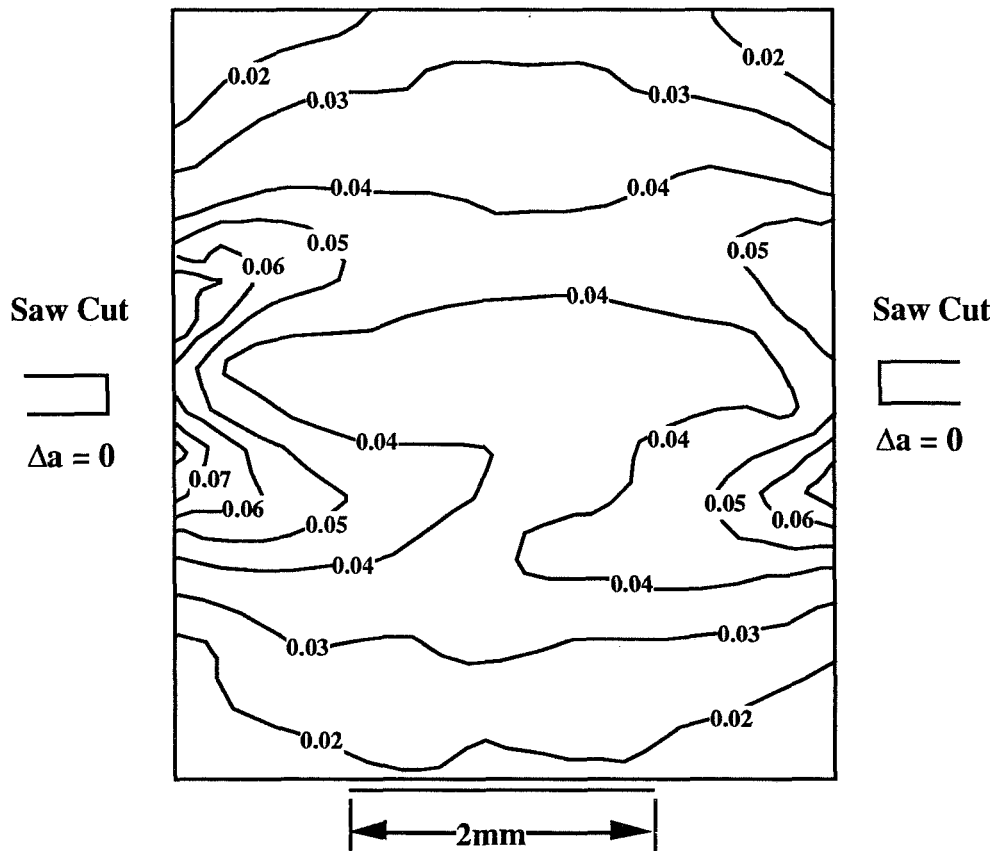


b. SC fracture test ($S=67$ MPa, 53% of link-up stress)

Figure 6 ϵ_{yy} strain fields for the ligament between two cracks 5.1mm apart.



a. LS fracture tests ($S=86$ MPa, 94% of link-up stress)



b. SC fracture test ($S=125$ MPa, 99% of link-up stress)

Figure 7 ϵ_{yy} strain fields for the ligament between two cracks 5.1mm apart.

CTOA Measurements

The measured critical CTOA values as a function of crack extension for the tests with low stress range (LS) fatigue precracking are shown in Figure 8. Also shown in Figure 8 is the scatter band from 76mm wide middle crack tension, M(T), tests conducted under LS conditions on the same material [8,9]. The measured CTOA values fall within the scatter band and have an average value of about 6° in the steady-state region beyond one thickness (2.3mm) of crack extension. The measured critical CTOA values for the tests with high stress range (HS) fatigue precracking and with saw cuts (SC) also fell within the scatter band for 76mm wide middle crack tension, M(T), tests conducted under HS conditions on the same material [8,9]. Again, the measured CTOA had an average value of about 6° in the steady-state region beyond about 2mm of crack extension. However, for shorter amounts of crack extension the CTOA angles, while higher than 6° , were less than observed in the LS tests.

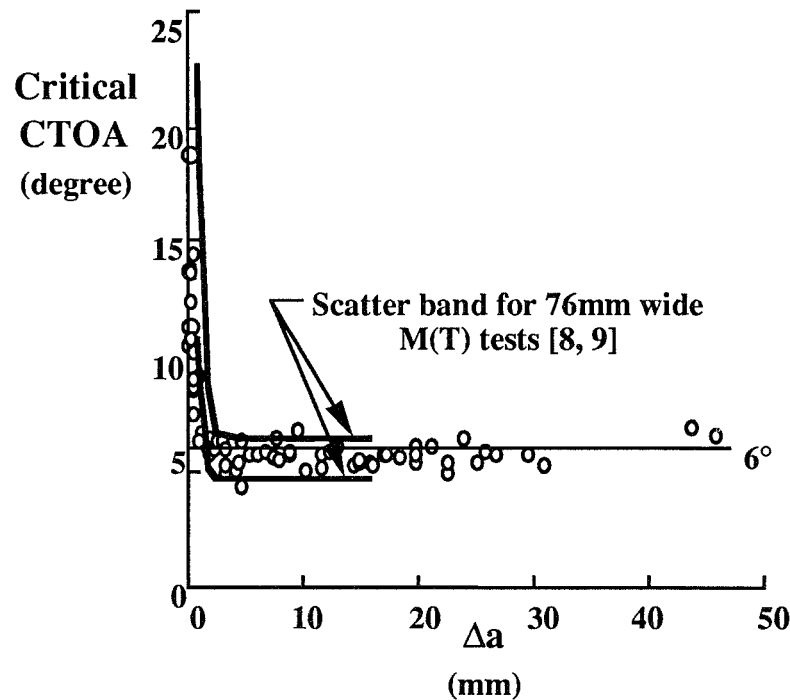


Figure 8 Critical crack-tip opening angles measured for the 305mm wide LS tests and the scatter band for the 76mm wide LS M(T) tests [8,9].

Finite Element Predictions

The fracture experiments were predicted using the elastic-plastic finite element code ZIP2D, the stress-strain relationship given in Table I, and the experimentally measured CTOA value of 6° . The critical displacement, δ_i , used to delay crack growth from the saw cuts, was determined by choosing a value that would best match the behavior of the

three SC tests. The finite element analysis was terminated after all link-ups had occurred and the stress dropped for 20 increments of crack extension.

All of the predictions of stress at link-up and failure stress were within 5% of the values obtained from the experiments. The stress against crack extension results from the single crack LS tests and predictions are shown in Figure 9. Initially, the finite-element analysis overpredicted the amount of crack growth for a given applied stress. However, severe tunneling has been observed in previous tests during this initial phase of stable tearing [8,9], resulting in more crack extension in the interior than measured on the surface. After about 4mm of stable crack growth, the predictions closely matched the experimental measurements for all three initial crack lengths.

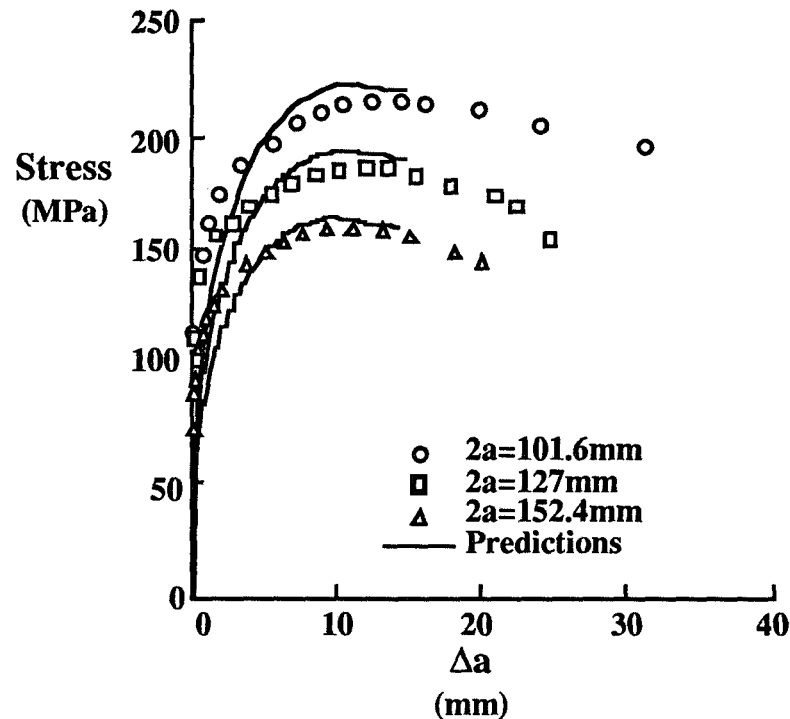


Figure 9 Stress against crack extension for the 305mm wide single crack LS tests.

The stress against crack extension results from the single crack HS tests and predictions are shown in Figure 10. Once again, the analysis overpredicted the initial amount of crack growth, but after about 4mm of stable crack growth, the predictions closely matched the experimental measurements for all three initial crack lengths. The simulated high fatigue stress range precracking caused the stress level required to initiate crack growth to be about 15% higher than required in the LS simulation. However, the failure stresses were not affected by the HS fatigue precracking.

The stress against crack extension results from the single crack SC tests and simulations are shown in Figure 11. These simulations were obtained by choosing a δ_i value that would result in the best match to the stress against crack extension behavior.

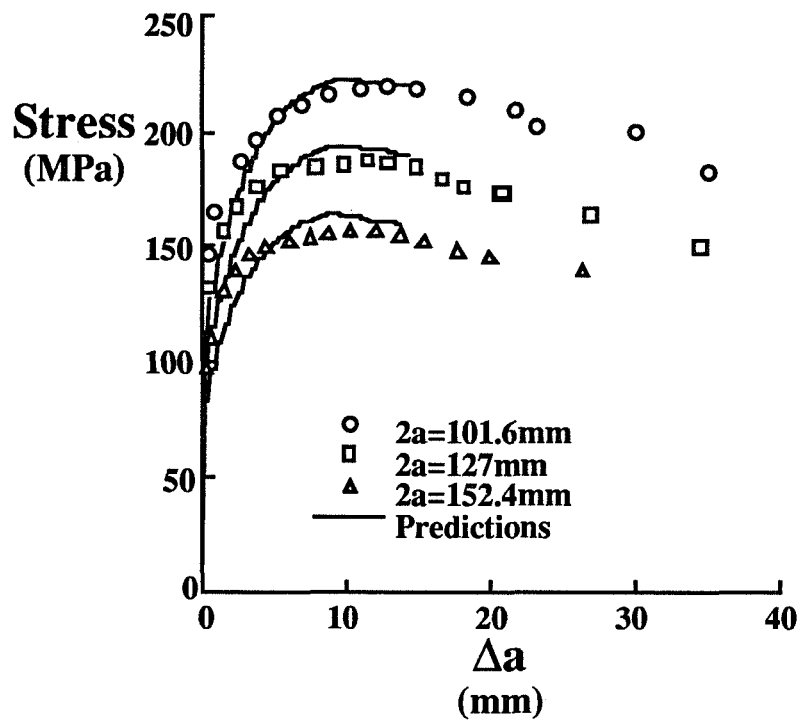


Figure 10 Stress against crack extension for the 305mm wide single crack HS tests.

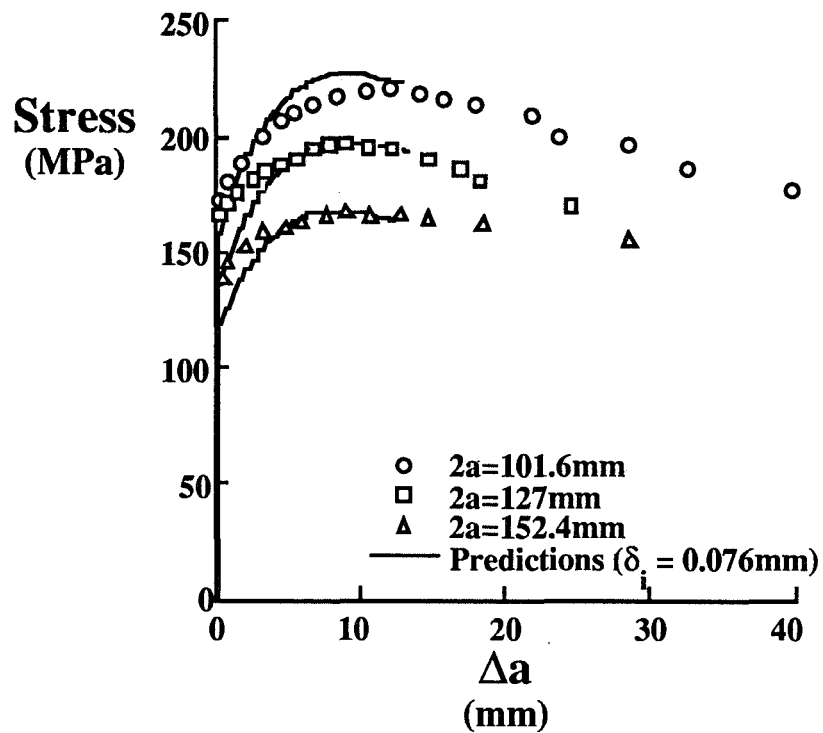


Figure 11 Stress against crack extension for the 305mm wide single crack SC tests.

The chosen value was $\delta_i = 0.076\text{mm}$ and this value was used in all subsequent SC predictions. The simulated saw cut behavior caused the stress level required to grow the crack to be about 50% higher than required in the LS simulation.

Predictions were made for the multiple crack fracture tests, the 3- and 5-crack configurations had a single long central crack and smaller collinear cracks, the 2-crack configurations had two roughly equal cracks with a ligament at the center of the specimen. The stress against crack extension results and predictions for the 3-crack (with small ligaments between cracks) fracture tests are shown in Figure 12. The predictions for all three crack histories (LS, HS, and SC) were in good agreement with the experimental measurements. Once again, the predicted initial crack growth was greater than observed experimentally, but the link-up and maximum stresses were within 2% of the experimental measurements. The stress against crack extension results and the predictions for the 3-crack (with large ligaments between cracks) fracture tests are shown in Figure 13. The predictions were in good agreement with the experimental results with the predicted link-up stresses (link-up occurred at maximum stress) were within 3% of the experimental measurements.

The stress against crack extension results and predictions for the 5-crack fracture tests are shown in Figure 14. The predictions for the LS and HS tests were in good agreement with the experimental measurements, but the SC predictions for stress at link-up (link-up occurred at the maximum stress) were about 5% greater than measured in the experiments.

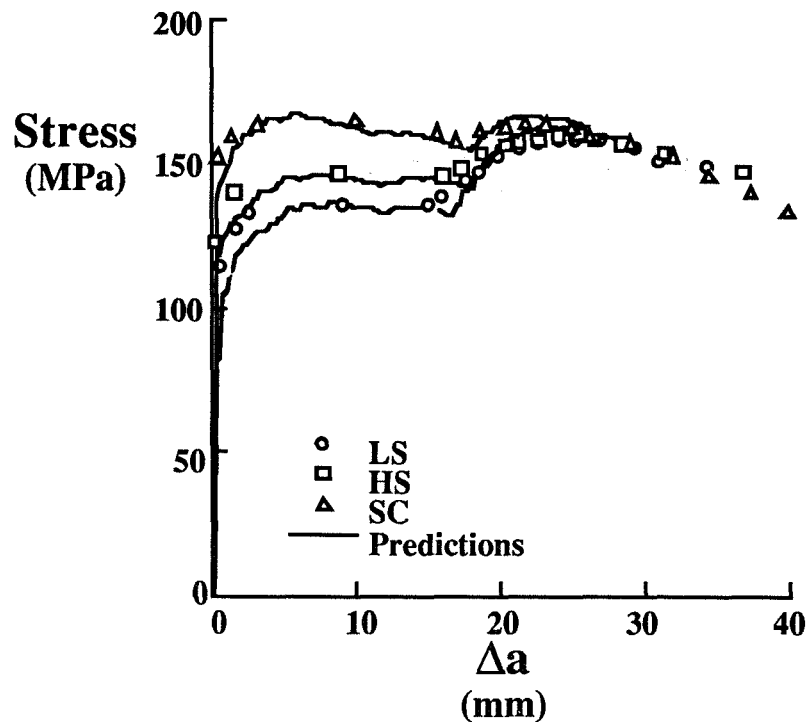


Figure 12 Stress against crack extension for three 305mm wide 3-crack (small ligaments between cracks) fracture tests.

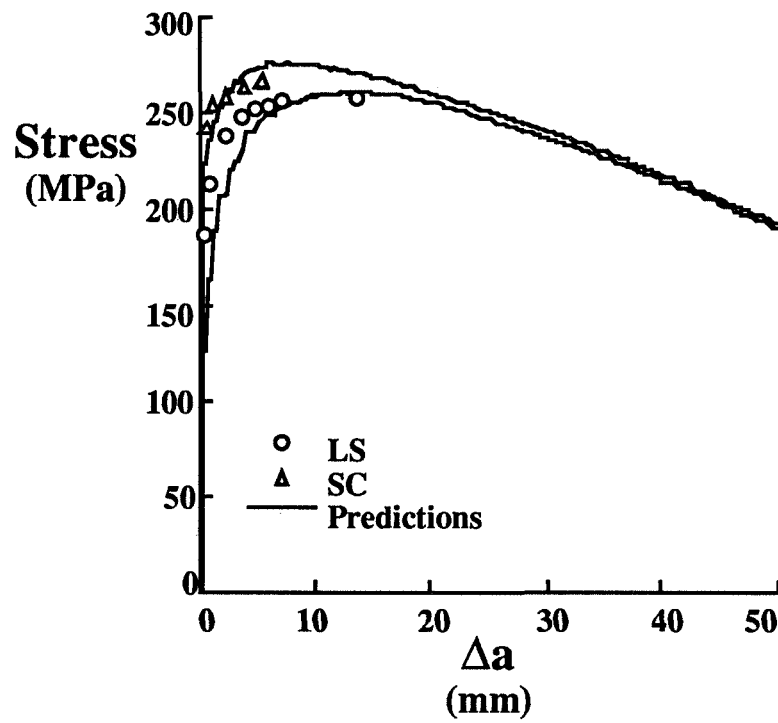


Figure 13 Stress against crack extension for two 305mm wide 3-crack (large ligaments between cracks) fracture tests.

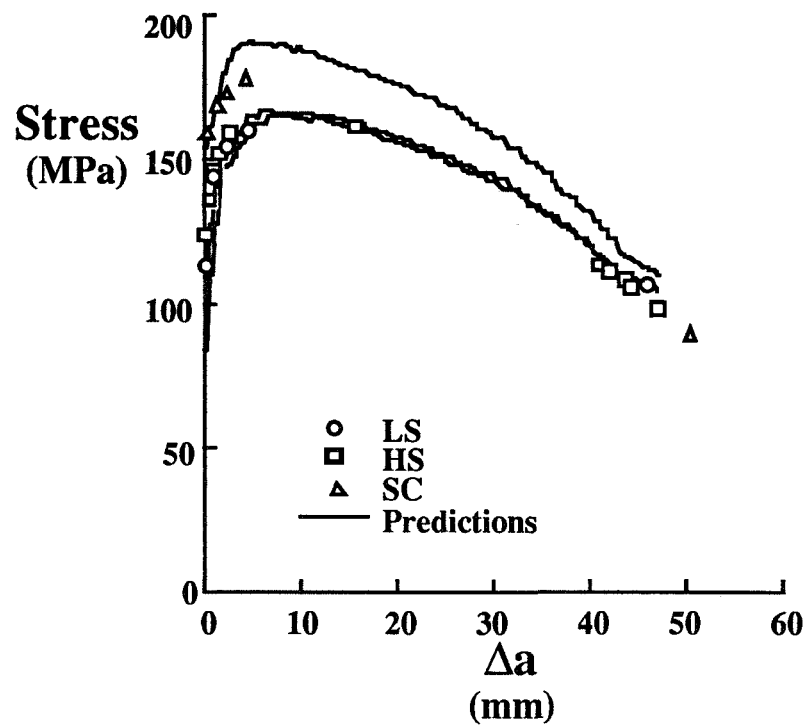


Figure 14 Stress against crack extension for three 305mm wide 5-crack fracture tests.

CONCLUDING REMARKS

A combination of experimental and analytical methods has demonstrated that the stable crack growth behavior and residual strength of thin sheet structures with multiple collinear cracks is influenced by the crack history and that this behavior can be accurately predicted (additional experimental results and numerical predictions are given in Reference 24). In particular, this research has shown that:

- (1) The initial crack history (saw cut, high stress level fatigue precracking, low stress level fatigue precracking) has a strong effect on the initial portion of stable crack growth.
 - (a) For a single crack, the influence of initial history (fatigue precracking stress level and saw cuts) is lost after about 10mm of crack growth. The effect on residual strength is about 4% or less.
 - (b) For multiple collinear cracks, the initial history (fatigue precracking stress level and saw cuts) was shown to cause differences of more than 20% in link-up stress and 13% in failure stress.
- (2) Saw cuts resulted in higher (unconservative) link-up and failure stresses than equivalent fatigue cracks. The behavior of saw cuts and cracks appears to be directly linked to experimentally observed differences in the local crack tip strain fields; the crack tip strains are highly concentrated, being much higher than the saw cut strains within 0.60mm of the tip (this corresponds to the large deformation region or fracture process zone).
- (3) The ZIP2D plane stress finite element model, coupled with the experimentally measured critical CTOA = 6° , accurately predict the behavior for single crack and multiple collinear crack configurations.
- (4) Accurate prediction of saw cut specimens requires both an initiation parameter, δ_i , as well as a critical CTOA.

REFERENCES

1. Harris, C. E., "NASA Aircraft Structural Integrity Program", NASA TM 102637, April 1990.
2. Anderson, H., "Finite Element Representation of Stable Crack Growth," *J. of Mech. and Phys. of Solids*, Vol. 21, 1973, pp. 337-356.
3. de Koning, A. U., "A Contribution to the Analysis of Quasi Static Crack Growth in Steel Materials," in *Fracture 1977, Proceedings of the 4th Int. Conf. on Fract.*, Vol. 3, pp. 25-31.
4. Wells, A. A., "Unstable Crack Propagation in Metals: Cleavage and Fast Fracture," in *Proceedings of the Cranfield Crack Propagation Symposium*, Vol. 1, 1961, pp. 210-230.
5. Wells, A. A., "Application of Fracture Mechanics at and Beyond General Yielding," *British Welding J.*, Vol. 11, pp. 563-570.

6. Wells, A. A., "Notched Bar Tests, Fracture Mechanics and Brittle Strengths of Welded Structures," *British Welding J.*, Vol. 12, pp. 2-13.
7. Newman, J. C., Jr., Dawicke, D. S., and Bigelow, C. A., "Finite-Element Analysis and Measurement of CTOA During Stable Tearing in a Thin-Sheet Aluminum Alloy," Proceedings from the Int. Workshop on Structural Integrity of Aging Airplanes, April 1992, pp. 167-186.
8. Dawicke, D. S. and Sutton, M. A., "Crack-Tip-Opening Angle Measurements and Crack Tunneling Under Stable Tearing in Thin Sheet 2024-T3 Aluminum Alloy", NASA-CR-191523, September 1993, also submitted to Exp. Mech.
9. Dawicke, D. S., Sutton, M. A., Newman, J. C., Jr., and Bigelow, C. A., "Measurement and analysis of Critical CTOA for an Aluminum Alloy Sheet", NASA-TM-109024, September 1993, also submitted to Fracture Mechanics: Twenty-Fifth National Symposium, ASTM STP 1220.
10. Newman, J. C., Jr., Dawicke, D. S., Sutton, M. A., and Bigelow, C. A., "A Fracture Criterion for Widespread Cracking in Thin-Sheet Aluminum Alloys", 17th International Committee on Aeronautical Fatigue, June 1993.
11. Swift, T., "Damage Tolerance in Pressurized Fuselages", 14th Int. Conf. on Aeronautical Fatigue, 1987.
12. Maclin, J., NASA CP-3160, Washington, DC, 1992, pp. 67-75.
13. Sutton, M. A., Bruck, H. A., Chae, T. L., and Turner, J. L., "Experimental Investigations of Three-Dimensional Effects Near a Crack Tip Using Computer Vision," *Int.J.of Fract.*, Vol. 53, 1991, pp. 201-228.
14. Sutton, M. A., Bruck, H. A., and McNeill, S. R., "Determination of Deformations Using Digital Correlation with the Newton Raphson Method for Partial Differential Correction," *Exp.Mech.*, Vol. 29 (3), 1989, pp. 261-267.
15. Sutton, M. A., Turner, J. L., Chae, T. L., and Bruck, H. A., "Development of a Computer Vision Methodology for the Analysis of Surface Deformation in Magnified Image," *ASTM STP 1094*, MICOM 90. 1990, pp. 109-132.
16. Sutton, M. A., Turner, J. L., Bruck, H. A., and Chae, T. L., "Full-Field Representation of the Discretely Sampled Surface Deformation for Displacement and Strain Analysis," *Exp.Mech.* Vol. 31 (2), 1991, pp. 168-177.
17. Sutton, M. A. and McNeill, S. R., "The Effects of Subpixel Image Restoration on Digital Correlation Error Estimates," *Optical Eng.* Vol. 27 (3), 1988, pp. 163-175.
18. Dohrmann, C. R. and Bushy, H. R., "Spline Function Smoothing and Differentiation of Noisy Data on a Rectangular Grid," Proceedings of the VI Int. Conf. on Exp. Mech., pp. 843-849, 1988.
19. Newman, J. C., Jr., "Finite-Element Analysis of Fatigue Crack Propagation--Including the Effects of Crack Closure," Ph.D. Thesis, VPI & State University, Blacksburg, VA, May 1974.
20. Zienkiewicz, O. C., Valliappan, S., and King, I. P., "Elasto-Plastic Solutions of Engineering Problems, Initial Stress, Finite Element Approach," *Int.J.of Numerical Methods in Eng.* Vol. 1, 1969, pp. 75-100.
21. Hom, C. L. and McMeeking, R. M., "Large Crack Tip Opening in thin, elastic-plastic sheets", *Int.J.of Fract.* Vol 45, 1990, pp 103-122.
22. McMeeking, R. M., "Finite Deformation Analysis of Crack Tip Opening in Elastic-Plastic Materials and Implications for Fracture", *J. of Mech. and Phys.of Solids*, Vol 35, 1977, pp 357-381.
23. McMeeking, R. M., "Recent Advances in Fracture Mechanics", *Fracture Mechanics: Microstructure and Mechanisms*, ASM Intl, 1987, pp. 1-30.
24. Dawicke, D. S., Newman, J. C., Jr., Sutton, M. A., and Amstutz, B. E., "Stable Tearing Behavior of a Thin-Sheet Material with Multiple Cracks", NASA TM-109131, June 1994.

1995108054

N95-14468

**STUDY OF MULTIPLE CRACKS IN AIRPLANE FUSELAGE
BY MICROMECHANICS AND COMPLEX VARIABLES**

348647

Sb-39

Mitsunori Denda and Y. F. Dong
FAA Center for Computational Modeling of Aircraft Structures
Rutgers University
P.O. Box 909, Piscataway, New Jersey 08855-0909, U.S.A.

23109

P-11

SUMMARY

Innovative numerical techniques for two dimensional elastic and elastic-plastic multiple crack problems are presented using micromechanics concepts and complex variables. The simplicity and the accuracy of the proposed method will enable us to carry out the multiple-site fatigue crack propagation analyses for airplane fuselage by incorporating such features as the curvilinear crack path, plastic deformation, coalescence of cracks, etc.

INTRODUCTION

Numerical techniques for plane elastic and elastic-plastic multiple crack problems are presented with the help of micromechanics concepts and complex variables. An amalgamation of the method of singular integral equations for cracks, the boundary element method, and the plastic source method for plastic deformation is achieved in a natural manner with the help of micromechanics tools such as dislocations, point forces, and their dipoles. The formulation is carried out in terms of complex variables to facilitate closed form integration of the boundary and the crack face (singular) integrals and the planar distribution of the plastic sources. For elastic problems, the crack opening displacements are modeled by the continuous distribution of dislocation dipoles such that, with the help of Chebyshev polynomials, the crack-face opening displacements and the crack-tip stress singularity contributions are automatically built in. There is no need to extrapolate the results to get the stress intensity factor. Further, by using complex variables, the crack-face singular integrals are evaluated in closed form. The approach is extended to elastic-plastic multiple crack problems such that the elastic singularity is canceled by the plastic deformation at the crack-tip. The techniques presented in this paper will serve as the key components in the planned FAA computer software for the residual life analysis of aging aircraft under widespread fatigue damage that takes into account such features as the curvilinear crack path, plastic deformation, coalescence of cracks, etc.

MICROMECHANICS TOOLS IN COMPLEX VARIABLES

Muskhelishvili's (ref. 1) complex variable formalism for plane isotropic elasticity uses two analytic functions or complex potential functions, $\phi(z)$ and $\psi(z)$, of a complex variable

$z = x + iy$ to express the solution. The displacement, stress, and strain components are given by

$$2\mu u(z) = \kappa\phi(z) - z\overline{\phi(z)'} - \overline{\psi(z)}, \quad (1)$$

and

$$\begin{aligned} \frac{\sigma_{xx} + \sigma_{yy}}{2} &= \phi(z)' + \overline{\phi(z)'}, \\ \frac{\sigma_{yy} - \sigma_{xx}}{2} + i\sigma_{xy} &= \overline{z}\phi(z)'' + \psi(z)', \end{aligned} \quad (2)$$

where μ is the shear modulus, κ is given by $\kappa = 3 - 4\nu$ in plane strain and $\kappa = (3 - \nu)/(1 + \nu)$ in plane stress in terms of Poisson's ratio ν . A prime attached to the analytic functions of z indicates differentiation with respect to z and a bar indicates the complex conjugate.

Fundamental Solutions

Consider a point force with the magnitude $f = f_x + if_y$ (per unit thickness) and an edge dislocation with the Burgers vector $b = b_x + ib_y$, independently located at ξ in the infinite isotropic medium. Their solutions are given in the same form (ref. 2)

$$\begin{aligned} \phi^{(s)}(z; \xi) &= -\gamma \log(z - \xi), \\ \psi^{(s)}(z; \xi) &= -k\overline{\gamma} \log(z - \xi) + \gamma \frac{\overline{\xi}}{z - \xi}, \end{aligned} \quad (3)$$

where $k = -\kappa$, $\gamma = f/2\pi(\kappa + 1)$ for the point force and $k = 1$, $\gamma = i\mu b/\pi(\kappa + 1)$ for the dislocation. The corresponding dipole solutions (i.e., the force and the dislocation dipoles) are given by

$$\begin{aligned} \phi^{(d)}(z; \xi) &= -\gamma d\{\log(z - \xi)\}, \\ \psi^{(d)}(z; \xi) &= -k\overline{\gamma} d\{\log(z - \xi)\} + \gamma d\left\{\frac{\overline{\xi}}{z - \xi}\right\}, \end{aligned} \quad (4)$$

where $d(\dots) = \frac{\partial}{\partial \xi}(\dots)d\xi + \frac{\partial}{\partial \overline{\xi}}(\dots)d\overline{\xi}$ is the total differentiation operator.

Continuous Distributions of the Singularities

The continuous distribution of point forces over an arc L (with arc parameter s) is given, from equation (3), by

$$\begin{aligned} \phi^{(s)}(z) &= -\int_L \Gamma(s) \log(z - \xi) ds, \\ \psi^{(s)}(z) &= \kappa \int_L \overline{\Gamma(s)} \log(z - \xi) ds + \int_L \Gamma(s) \frac{\overline{\xi}}{z - \xi} ds, \end{aligned} \quad (5)$$

with $\Gamma(s) = t/2\pi(\kappa + 1)$, where $t = t_x + it_y$ is the traction. The continuous distribution of dislocation dipoles is given, from Equation (4), by

$$\begin{aligned}\phi^{(d)}(z) &= - \int_L \gamma(s) d \{ \log(z - \xi) \}, \\ \psi^{(d)}(z) &= - \int_L \overline{\gamma(s)} d \{ \log(z - \xi) \} + \int_L \gamma(s) d \left\{ \frac{\bar{\xi}}{z - \xi} \right\},\end{aligned}\quad (6)$$

with $\gamma(s) = i\mu b/\pi(\kappa + 1)$, where $b = b_x + ib_y$ is the dislocation.

BOUNDARY ELEMENT METHOD IN COMPLEX VARIABLES

Consider a body R with its boundary ∂R subject to the traction $T = T_x + iT_y$ and the displacement $U = U_x + iU_y$. The displacement field in this body is obtained by assuming that the region R is embedded in an infinite medium and ∂R , which is simply a line marked out in the infinite domain, is covered by a continuous distribution of point forces with density T and by a continuous distribution of dislocation dipoles with the Burgers vector U . This is the physical interpretation of Somigliana's identity (ref. 3). We discretize and approximate the original boundary by a piecewise straight line, $L = \sum_{j=1}^M L_j$. The j -th boundary element $L_j = \xi_j \xi_{j+1}$ ($j = 1, 2, \dots, M$) has the slope ϕ_j . The boundary traction and the displacement are approximated by constant interpolation functions over an element. Let T_j and U_j be the traction and the displacement of the element, then the potential functions in (5) and (6) are integrated analytically with the result

$$\begin{aligned}\phi_j^{(s)}(z) &= \Gamma_j^{(T)} f_j(z), \\ \psi_j^{(s)}(z) &= -\Gamma_j^{(T)} \{ g_j(z) + e^{-2i\phi_j} f_j(z) \} - \overline{\Gamma_j^{(T)}} \kappa e^{-2i\phi_j} f_j(z), \\ \phi_j^{(d)}(z) &= -\gamma_j^{(U)} s_j(z), \quad \psi_j^{(d)}(z) = \gamma_j^{(U)} m_j(z) - \overline{\gamma_j^{(U)}} s_j(z),\end{aligned}$$

where

$$\begin{aligned}f_j(z) &= \left\{ (z - \xi) \log_j(z - \xi) + \xi \right\} \Big|_{\xi_j}^{\xi_{j+1}}, \quad g_j(z) = \bar{\xi} \log_j(z - \xi) \Big|_{\xi_j}^{\xi_{j+1}}, \\ s_j(z) &= \log_j(z - \xi) \Big|_{\xi_j}^{\xi_{j+1}}, \quad m_j(z) = \frac{\bar{\xi}}{(z - \xi)} \Big|_{\xi_j}^{\xi_{j+1}},\end{aligned}$$

and $\Gamma_j^{(T)} = T_j e^{-i\phi_j}/2\pi(\kappa + 1)$, $\gamma_j^{(U)} = i\mu U_j/\pi(\kappa + 1)$. For ξ on L_j , the branch line of the logarithm $\log_j(z - \xi)$ is given by a straight line connecting ξ , ξ_j , and ∞ ; thus the branch cut of the logarithm differs from element to element. The displacement and the traction contributions of the two layers are obtained by substituting these potential functions into (1) and (2). However, it is necessary to separate the real and imaginary parts of the displacement and the traction before establishing the boundary equations. The displacement boundary equations and the traction boundary equations are derived following the standard procedure of the BEM.

CRACK SOURCE METHOD

Define the Cauchy-type integrals

$$\begin{aligned} T^{(m)}(z) &= -\frac{1}{\pi} \int_{-1}^1 \frac{\sqrt{1-x^2} U_{m-1}(x) dx}{x-z} \quad (m \geq 0), \\ U^{(m-1)}(z) &= \frac{1}{\pi} \int_{-1}^1 \frac{T_m(x) dx}{\sqrt{1-x^2}(x-z)} \quad (m \geq 0), \end{aligned} \quad (7)$$

over the interval $-1 \leq x \leq +1$, where $T_m(x)$ and $U_{m-1}(x)$ are the Chebyshev polynomials of the first and second kind and $z = x + iy$ is a complex variable. The integrals in (7) can be evaluated analytically with the result

$$\begin{aligned} T^{(m)}(z) &= (z - \sqrt{z^2 - 1})^m \quad (m \geq 0), \\ U^{(m-1)}(z) &= -\frac{(z - \sqrt{z^2 - 1})^m}{\sqrt{z^2 - 1}} \quad (m \geq 0). \end{aligned} \quad (8)$$

Single Crack in the Infinite Body

A dislocation dipole over an infinitesimal segment $d\xi$ gives rise to a displacement discontinuity. We identify the displacement discontinuity as the crack opening displacement and call the dislocation dipole as the crack source. Further, the continuous distribution of the crack sources over an arc is called the crack element. Consider a straight center crack of length $2a$ subject to a self-equilibrated traction

$$\pm \tilde{\mathbf{t}} = \pm \begin{Bmatrix} \tilde{t}_x \\ \tilde{t}_y \end{Bmatrix}. \quad (9)$$

over its upper (+) and lower (−) surfaces. Select the local coordinate system xy with the coordinate origin at the center of the crack and the x -axis along the crack and introduce the non dimensional coordinates $X = x/a$ and $Z = z/a$, where $z = x + iy$ is a complex variable. The density function of the crack element is given by $\tilde{\gamma}(X) = \gamma(x) = i\mu\delta/\pi(\kappa + 1)$ in terms of the crack opening displacement $\delta = \delta_x + i\delta_y$. If we interpolate the density function by

$$\tilde{\gamma}(X) = \frac{i\mu}{\pi(\kappa + 1)} \sqrt{1-X^2} \sum_{m=1}^p \delta^{(m)} U_{m-1}(X),$$

then the complex potential functions, (4), for the crack element are integrated analytically, with the help of (8), with the result

$$\begin{aligned} \phi^{(d)}(Z) &= \pi \sum_{m=1}^p A^{(m)} T^{(m)}(Z), \\ \psi^{(d)}(Z) &= \pi \sum_{m=1}^p \left\{ \overline{A^{(m)}} T^{(m)}(Z) - mA^{(m)} Z U^{(m-1)}(Z) \right\}. \end{aligned}$$

The displacement and the traction contributions of the crack element can be evaluated by (1) and (2). Of interest is the traction

$$(t_x + it_y)^\pm(X) = \pm \frac{2\mu}{(\kappa + 1)a} \sum_{m=1}^p m \delta^{(m)} U_{m-1}(X) \quad (|X| \leq 1), \quad (10)$$

on the upper and the lower faces of the crack and the stress intensity factor

$$K(\pm 1) = K_I(\pm 1) + iK_{II}(\pm 1) = \frac{2\mu i}{\kappa + 1} \sqrt{\frac{\pi}{a}} \sum_{m=1}^p (\pm 1)^{m+1} m \delta^{(m)}.$$

The components $\delta^{(m)}$ of the crack opening displacement are determined from Equation (10) and the applied traction (9) by collocation.

Multiple Cracks in the Infinite Body

Consider the problem of N multiple straight cracks, L_j ($j = 1, \dots, N$), in the infinite body; the individual crack surface is loaded according to (9). First we formulate each crack in the respective local coordinate system and then assemble the contributions from all the cracks in the global coordinate system. The total traction $\mathbf{t}^{(k)+} = \{t_x^{(k)+}, t_y^{(k)+}\}^T$ on the upper surface of the crack L_k is given in the form

$$\mathbf{t}^{(k)+} = \sum_{j=1}^N \left\{ \sum_{m=1}^{p(j)} \Omega_{(kj)}^{*(m)} \delta_{(j)}^{(m)} \right\}, \quad (11)$$

where $\Omega_{(kj)}^{*(m)}$ is a coefficient matrix and $\delta_{(j)}^{(m)} = \{\delta_{(j)x}^{(m)}, \delta_{(j)y}^{(m)}\}^T$ ($j = 1, \dots, N$; $m = 1, \dots, p(j)$) are the unknown crack opening displacement coefficients, which will be determined, from Equations (11) and (9), by collocation.

Effect of the Finite Boundary

We now consider multiple center cracks in a finite body R whose boundary ∂R is subject to the traction $\mathbf{T} = \{T_x, T_y\}^T$ and displacement $\mathbf{U} = \{U_x, U_y\}^T$ and each crack surface is loaded according to (9). The total traction on the upper surface of crack L_k is given in the form

$$\mathbf{t}^{(k)+} = \sum_{j=1}^N \left\{ \sum_{m=1}^{p(j)} \Omega_{(kj)}^{*(m)} \delta_{(j)}^{(m)} \right\} + \sum_{n=1}^M \left\{ \mathbf{G}_n^{*(k)} \mathbf{T}_n - \mu \mathbf{H}_n^{*(k)} \mathbf{U}_n \right\}, \quad (12)$$

where the first term in the right hand side comes from (11) and the second and the third terms come from the traction BEM with constant interpolation functions. The quantities \mathbf{U}_n and \mathbf{T}_n are the boundary displacement and the traction vectors and $\mathbf{G}_n^{*(k)}$, $\mathbf{H}_n^{*(k)}$ are

coefficient matrices. The total displacement on the non-crack boundary ∂R is given in the form

$$2\mathbf{U}_k = \sum_{j=1}^N \left\{ \sum_{m=1}^{p(j)} \mathbf{II}_{(j)}^{(m)} \delta_{(j)}^{(m)} \right\} + \sum_{n=1}^M \left\{ \frac{1}{\mu} \mathbf{G}_n \mathbf{T}_n - \mathbf{H}_n \mathbf{U}_n \right\}, \quad (13)$$

where $\mathbf{II}_{(j)}^{(m)}$, \mathbf{G}_n , and \mathbf{H}_n are coefficient matrices. The solution is obtained by setting up traction equations on the upper surface of each crack from Equations (12) and (9) and displacement boundary equations on ∂R from Equation (13) and the boundary condition on ∂R .

Numerical Results

A single center crack in a plate in uniaxial tension was analyzed by the present method using one Chebyshev polynomial. The same problem, with identical mesh, was analyzed by the crack Green's function BEM, which uses the Green's function that satisfies the traction free crack surface boundary condition automatically. The stress intensity factor results agreed up to seven significant digits. Figures 1, 2, and 3 show two collinear cracks, two parallel cracks, and three parallel cracks, respectively, in the infinite body. The numerical results have been obtained for a large plate, compared to the cracks, using seven Chebyshev polynomials for each crack in each case. Comparison of the numerical results and the results from the stress intensity handbook (ref. 4) is listed in Tables 1, 2, and 3.

PLASTIC SOURCE METHIOD

In the presence of the plastic strain ϵ_{ij}^p the stress-strain relations for isotropic materials in two-dimensions are given by (ref. 2)

$$\sigma_{\alpha\beta} = 2\mu (\epsilon_{\alpha\beta} - \epsilon_{\alpha\beta}^p) + \lambda^* (\epsilon_{\gamma\gamma} - \epsilon_{\gamma\gamma}^p) \delta_{\alpha\beta},$$

and

$$\epsilon_{\alpha\beta} = \frac{1}{2\mu} (\sigma_{\alpha\beta} - \nu^* \sigma_{\gamma\gamma} \delta_{\alpha\beta}) + \epsilon_{\alpha\beta}^p,$$

where $\epsilon_{\alpha\beta}$ is the total strain, $\epsilon_{\alpha\beta}^*$ is the fictitious in-plane plastic strain, called the plane plastic strain, defined by

$$\epsilon_{\alpha\beta}^* = \begin{cases} \epsilon_{\alpha\beta}^p + \nu \epsilon_{33}^p \delta_{\alpha\beta} & \text{(plane strain)} \\ \epsilon_{\alpha\beta}^p & \text{(plane stress)} \end{cases}$$

The elastic moduli λ^* and ν^* are defined by

$$\lambda^* = \begin{cases} \lambda & \text{(plane strain)} \\ \frac{2\lambda\mu}{\lambda+2\mu} & \text{(plane stress)} \end{cases}, \quad \nu^* = \begin{cases} \nu & \text{(plane strain)} \\ \frac{\nu}{1+\nu} & \text{(plane stress)} \end{cases},$$

in terms of Lamé constants, λ and μ , and Poisson's ratio ν . The non-zero out of plane components are given by

$$\begin{aligned}\sigma_{33} &= \nu\sigma_{\gamma\gamma} - E\epsilon_{33}^p \quad (\text{plane strain}), \\ \epsilon_{33} &= -\frac{1}{2\mu} \frac{\nu}{1+\nu} \sigma_{\gamma\gamma} + \epsilon_{33}^p \quad (\text{plane stress}),\end{aligned}$$

where E is the Young's modulus.

Plastic Element

Consider a region D of plastic deformation where the plastic strain components ϵ_{11}^p , ϵ_{22}^p , ϵ_{12}^p , and $\epsilon_{33}^p = -\epsilon_{\gamma\gamma}^p$ are prescribed. In the numerical implementation the plastic region is discretized into a collection of plastic elements in each of which the plastic strain distribution is approximated by an interpolation function. We use the constant interpolation in this paper so that the problem can be treated as Eshelby's (ref. 5) stress-free transformation problem with constant transformation strain given by the plane plastic strain $\epsilon_{\alpha\beta}^*$. Then the displacement in the entire region is given by a continuous distribution of point forces over the boundary ∂D of the plastic region; the magnitude of the force over a segment $d\zeta$ of the boundary is given by

$$f = \frac{1}{2i} (\sigma_{11}^* + \sigma_{22}^*) d\zeta - \frac{1}{2i} (\sigma_{11}^* - \sigma_{22}^* + 2i\sigma_{12}^*) d\bar{\zeta}, \quad (14)$$

where

$$\sigma_{\alpha\beta}^* = 2\mu\epsilon_{\alpha\beta}^* + \lambda^*\epsilon_{\gamma\gamma}^*\delta_{\alpha\beta}$$

The solution is obtained by integrating the fundamental solution of the point force, (3) with (14), over the boundary ∂D with the result

$$\begin{aligned}\phi^*(z) &= -\int_{\partial D} \gamma^* \log(z - \zeta) d\zeta, \\ \psi^*(z) &= \kappa \int_{\partial D} \bar{\gamma}^* \log(z - \zeta) d\zeta + \int_{\partial D} \gamma^* \frac{\bar{\zeta}}{z - \zeta} d\zeta,\end{aligned} \quad (15)$$

where

$$\begin{aligned}\gamma^* &= \frac{1}{2i} (\sigma^* - \tau^* e^{-2i\psi}), \\ \sigma^* &= \frac{1}{2\pi(1+\kappa)} (\sigma_{11}^* + \sigma_{22}^*) = \frac{\mu + \lambda^*}{\pi(1+\kappa)} (\epsilon_{11}^* + \epsilon_{22}^*), \\ \tau^* &= \frac{1}{2\pi(1+\kappa)} (\sigma_{11}^* - \sigma_{22}^* + 2i\sigma_{12}^*) = \frac{\mu}{\pi(1+\kappa)} (\epsilon_{11}^* - \epsilon_{22}^* + 2i\epsilon_{12}^*),\end{aligned}$$

and ψ is the slope of the boundary ∂D .

Consider the polygonal plastic element of a constant plastic strain distribution bounded by N -lines $\Gamma = \sum_{j=1}^N \Gamma_j$, where $\Gamma_j = \zeta_j \zeta_{j+1}$ ($j = 1, 2, \dots, N$) is the j -th edge extending

from corners ζ_j to ζ_{j+1} with the slope ψ_j . The integrals in (15) are evaluated analytically with the result

$$\begin{aligned}\phi^*(z) &= -\sum_{j=1}^N \gamma_j^* f_j(z), \\ \psi^*(z) &= \sum_{j=1}^N \left\{ -(\kappa \overline{\gamma_j^*} + \gamma_j^*) e^{-2i\psi_j} f_j(z) - \gamma_j^* g_j(z) \right\},\end{aligned}\quad (16)$$

where

$$f_j(z) = [(z - \zeta) \log_j(z - \zeta) + \zeta]_{\zeta_j}^{\zeta_{j+1}}, \quad g_j(z) = [\overline{\zeta} \log_j(z - \zeta)]_{\zeta_j}^{\zeta_{j+1}},$$

and $\gamma_j^* = \frac{1}{2i} (\sigma^* - \tau^* e^{-2i\psi_j})$. The branch cut for the logarithm $\log_j(z - \zeta)$ for ζ located on the line Γ_j is specified as explained earlier for the BEM. The displacement and the stress are obtained by substituting the potential functions in (16) into (1) and (2) following the Eshelby's procedure of stress free transformation. This results in an additional term for the stress inside the plastic element (ref. 2).

Numerical Solution Procedure

The solution procedure whereby the unknown plastic strain distribution is determined was given by Denda and Lua (ref. 6) for standard elastoplastic problems. In order to use the crack source method it is convenient to break the problem into the elastic and the plastic solutions. The former is the elastic solution under the applied load and the latter the solution of the plastic elements. The crack source method is used for the determination of each solution, once for the elastic solution and several times, iteratively, for the plastic solution. Note that each solution gives rise to a $1/\sqrt{r}$ stress singularity. A singularity cancellation scheme, whereby the final solution is obtained by elimination of the total stress intensity factor, is used as a part of the convergence criterion of the procedure. The results will be reported elsewhere.

References

1. Muskhelishvili, N.I.: *Some Basic Problems of the Mathematical Theory of Elasticity*. Noordhoff, Groningen, 1958.
2. Denda, M.: Complex variable Green's function representation of plane inelastic deformation in isotropic solids. *Acta Mechanica*, vol. 72, 1988, pp. 205–221.
3. Denda, M.: A complex variable approach to inelastic boundary value problems. In Chung, H. et al., eds.: *Advances in Design and Analysis in Pressure Vessel Technology, ASME PVP - vol. 130, NE - vol. 2*, 1987, pp. 23–32.
4. Murakami, Y. et al.: *Stress Intensity Factor Handbook*. Pergamon Press, Oxford, 1987.

5. Eshelby, J. D.: The determination of the elastic field of an ellipsoidal inclusion and related problems. *Proc. Roy. Soc. London*, vol. 214A, 1957, pp. 376–396.
6. Denda, M.; and Lua, Y. J.: Formulation of the plastic source method for plane inelastic problems, Part 2. Numerical implementation for elastoplastic problems. *Acta Mechanica*, vol. 75, 1988, pp.111–132.

Table 1. Two Collinear Cracks ($F_{IA} = K_{IA}/\sigma\sqrt{\pi a}$ and $F_{IB} = K_{IB}/\sigma\sqrt{\pi a}$)

$2a/d$	F_{IA} (Handbook)	F_{IA} (Numerical)	F_{IB} (Handbook)	F_{IB} (Numerical)
0.05	1.00031	1.0018	1.00032	1.0018
0.1	1.0012	1.0027	1.0013	1.0028
0.2	1.0046	1.0061	1.0057	1.0071
0.3	1.0102	1.0117	1.0138	1.0153
0.4	1.0179	1.0194	1.0272	1.0287
0.5	1.0280	1.0295	1.0480	1.0495
0.6	1.0410	1.0426	1.0804	1.0821
0.7	1.0579	1.0596	1.1333	1.1351
0.8	1.0811	1.0827	1.2289	1.2314
0.9	1.1174	1.1187	1.4539	1.4639

Table 2. Two Parallel Cracks ($F_I = K_I/\sigma\sqrt{\pi a}$)

$2a/d$	F_I (Handbook)	F_I (Numerical)
0.0	1.0000	1.0011
0.2	0.9855	0.9870
0.4	0.9508	0.9517
0.8	0.8727	0.8732
1.0	0.8319	0.8440
2.0	0.7569	0.7746
5.0	0.6962	0.7129

Table 3. Three Parallel Cracks ($F_{IA} = K_{IA}/\sigma\sqrt{\pi a}$ and $F_{IB} = K_{IB}/\sigma\sqrt{\pi a}$)
(Handbook digital values for F_{IB} are not available.)

$2a/d$	F_{IA} (Handbook)	F_{IA} (Numerical)	F_{IB} (Handbook)	F_{IB} (Numerical)
0.1	0.99500	0.99687	—	0.99410
0.2	0.98198	0.98379	—	0.97306
0.3	0.96299	0.96430	—	0.94156
0.4	0.94010	0.94100	—	0.90361
0.5	0.91535	0.91650	—	0.86789
0.6	0.89080	0.89254	—	0.82333
0.7	0.86851	0.87041	—	0.78603
0.8	0.85052	0.85062	—	0.75234

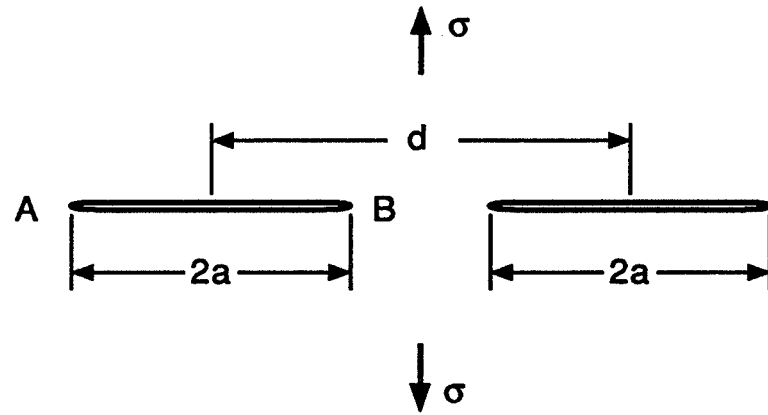


Figure 1: Two collinear cracks in the infinite body under uniaxial tension.

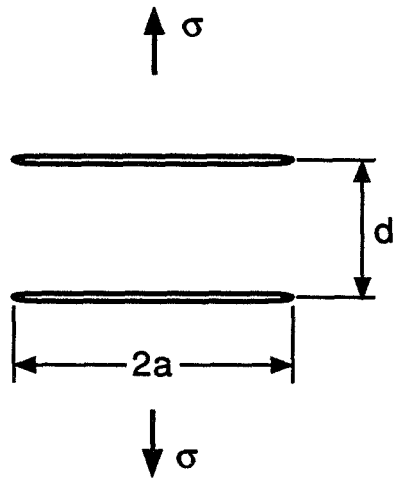


Figure 2: Two parallel cracks in the infinite body under uniaxial tension.

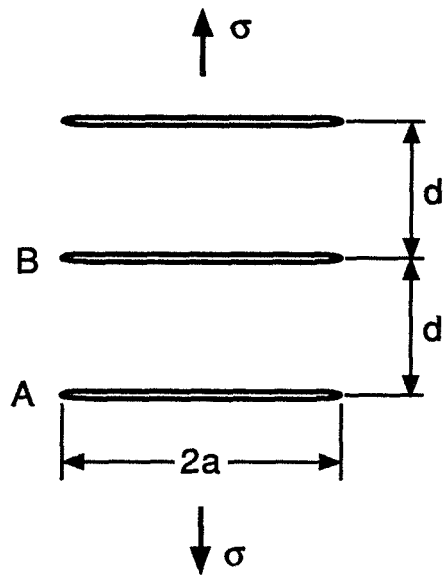


Figure 3: Three parallel cracks in the infinite body under uniaxial tension.

1995108055
EXTRACTING A REPRESENTATIVE LOADING SPECTRUM
FROM RECORDED FLIGHT DATA 348648
5/6-05
23.10
p. 16

Anthony G. Denyer
Principal Engineering Specialist
Rockwell International
El Segundo, CA

ABSTRACT

One of the more important ingredients when computing the life of a structure is the loading environment. This paper describes the development of an aircraft loading spectrum that closely matches the service experience, thus allowing a more accurate assessment of the structural life. The paper outlines the flight loads data collection system, the procedures developed to compile and interpret the service records and the techniques used to define a spectrum suitable for structural life analysis. The areas where the procedures were tailored to suit the special situation of the USAF B-1B bomber are also discussed. The results of the methodology verification, achieved by comparing the generated spectra with the results of strain gage monitoring during service operations, are also presented.

INTRODUCTION

The high cost of structural maintenance and the desire for a high rate of operational readiness place great emphasis on improving the analytic tools used to project the economic life of the structure and the inspection intervals necessary to ensure structural integrity. All the analytic models currently used for structural life assessment have a common ingredient, that of the loading environment. The importance of the load spectrum is evident when considering that a life variation of a factor of two (2) or more is not uncommon when the load magnitude varies by 10%.

Rockwell International has produced a spectrum generation procedure for the USAF B-1B Bomber. The B-1B, which entered service in 1984, is a variable swept wing aircraft designed to operate at low altitude and having terrain following capability in both automatic and manual modes. Each aircraft is equipped with a flight loads data recorder, built by Electrodynamics Inc., and designed to collect sufficient flight parameters to enable the construction of fatigue loads spectra representative of the service experience of the aircraft. By 1991 some 10,000 hours of data had been collected and compiled in a data base utilizing the specially written Loads / Environment Spectra Survey (L/ESS) program. This database was used in 1992 to provide stress spectra for a structural life assessment of the B-1B under service operations and to compare the service experience with the design criteria. The basis for representative spectrum generation was that the lifetime usage can be represented by a repeated application of a 100 flight spectrum in order to include all mission types that occur at least 1% of the time while eliminating very infrequent events. The spectrum was produced in terms of occurrences of aircraft center of gravity load factors (Nz) which were translated to local stresses in the structure utilizing the NASTRAN finite element program. The spectrum approach is based on the assumption that the external structural loads and the internal stresses are linear with respect to aircraft center of gravity load factor. Validation of the methodology was achieved by comparing the final stress spectrum at six structural locations with stress spectra compiled directly from the L/ESS strain gage records.

Spectra generated for the B-1B wing and fuselage included only symmetric flight maneuvers, vertical gusts and ground loads. Control of the B-1B in the roll axis is by means of differential movement of the horizontal stabilizers requiring the inclusion of both symmetric and roll maneuvers and vertical and lateral gusts in the empennage spectrum. For the purposes of simplicity and brevity the descriptions and tables in this paper reflect only the symmetric loads.

FLIGHT LOADS DATA RECORDER

On Aircraft Monitoring and Recording

The collecting of operational data is performed by a microprocessor based solid state data collection and storage device, known as the Structural Data Collector (SDC), linked to multiple dedicated L/ESS sensors and with connections to non L/ESS aircraft sub systems. The SDC accepts both analog and digital inputs, and performs parameter sampling, real time data validation, data compression and archival storage of time history data received from a variety of sensors. The SDC receives analog inputs from three linear accelerometers for aircraft acceleration data, structural strain data from six strain gages, and control surface position data. The majority of the signals received by the SDC are provided via the Central Integrated Test System (CITS) serial digital link. CITS monitors various aircraft systems, including the Central Air Data Computer, Fuel CG Management System, Stability and Control Augmentation System and the Engine Monitoring System, for parameters required by the SDC. TABLE 1 defines the list of parameters monitored and processed by the SDC. The CITS Control and Display Panel allows the manual entry of the necessary mission documentation to the SDC. This is also defined in TABLE 1.

Each parameter is sampled at rates appropriate to that parameter. Sample rates range from once (1) per second to forty (40) times per second. Analog parameters are initially digitized using an eight (8) bit analog to digital conversion. Each parameter is then validated to protect the SDC memory from erroneous information. Validation testing includes a maximum and minimum allowable value test, a maximum allowable rate of change test and an excessive activity test. After validation each parameter is processed through one of three data compression algorithms. These algorithms significantly increase the number of flight hours of data that can be stored in the SDC memory by systematically eliminating insignificant or redundant information.

The following is a general description of the three data compression algorithms:

- 1) Parameters that are cyclic in nature such as strain gages records are compressed using a peak valley search routine. The procedure locates and saves only local maxima and minima that represent cycles greater than a specified threshold criterion. All intermediate data points are discarded.
- 2) Smoothly varying parameters such as altitude are compressed by a moving window technique called time history compression. This procedure saves a value whenever its current value has changed by at least a predetermined amount from the last recorded value. Some parameters are time hacked to a time history parameter, that is they are recorded whenever the primary time history parameter is recorded. An example of this is the center of gravity position which is recorded when the gross weight is recorded.
- 3) Engine parameters are processed through a special compression algorithm which combines aspects of both peak valley and time history compression with special logic tailored to the unique inter-relationship of the engine parameters.

The data compression methods and the necessary numeric threshold constants are also shown in TABLE 1.

Validated, compressed data is stored in the SDC memory for later extraction and ground processing. Depending on the relative severity of flight activity, data compression allows the SDC to hold 40 to 80 flight hours of recording between data extractions.

Data Extraction Procedures

At scheduled intervals, or when the post flight CITS output indicates that the SDC memory is filled to capacity, the stored flight information is extracted from the SDC memory and transcribed to floppy disks at a ground transcribing station.

Parameter	Unit	Signal Type	Data Compression Method	Sample Rate /sec	Compression Constants	
					Threshold	Delta
Strain Gages						
Stabilizer Support Fitting Left Hand Side	ksi	Analog	PV	40	None	6.19
Stabilizer Support Fitting Right Hand Side	ksi	Analog	PV	40	None	6.19
Stabilizer Support Fitting Side Plate	ksi	Analog	PV	40	None	8.25
Wing Sweep Actuator	k lb	Analog	PV	40	None	42.70
Wing Lower Skin	ksi	Analog	PV	40	None	4.00
Forward Fuselage Dorsal Longeron	ksi	Analog	PV	40	None	8.29
Vertical Acceleration (Nz) (Air)	g	Analog	PV + A	40	0.77/1.2	0.14
Vertical Acceleration (Nz) (Ground)	g	Analog	PV + A	40	0.84/1.13	0.14
Lateral Acceleration (Ny) (Air)	g	Analog	PV + A	20	+/- 0.101	0.10
Lateral Acceleration (Ny) (Ground)	g	Analog	PV + A	20	+/- 0.047	0.05
Longitudinal Acceleration (Nx) (Air)	g	Analog	PV + A	20	+/- 0.094	0.09
Longitudinal Acceleration (Nx) (Ground)	g	Analog	PV + A	20	+/- 0.062	0.06
Pitch Rate	deg/sec	Digital	PV + A	8	+/- 2.10	2.10
Yaw Rate (Air)	deg/sec	Digital	PV + A	8	+/- 4.88	4.88
Yaw Rate (Ground)	deg/sec	Digital	PV + A	8	+/- 2.10	2.10
Roll Rate	deg/sec	Digital	PV + A	8	+/- 1.05	1.05
Pitch Acceleration	deg/sec^2	Digital	PV + A	8	+/- 25.2	5.60
Roll Acceleration	deg/sec^2	Digital	PV + A	8	+/- 46.8	15.62
Yaw Acceleration	deg/sec^2	Digital	PV + A	8	+/- 16.8	5.60
Wing Sweep Angle	degrees	Analog	TH + C	1	None	2.05
Flap Position	degrees	Digital	TH	1	None	4.03
Left Horizontal Stabilizer Position	degrees	Analog	THKA	20	None	None
Right Horizontal Stabilizer Position	degrees	Analog	THKA	20	None	None
Left Inboard Spoiler Position	degrees	Analog	THKA	20	None	None
Right Inboard Spoiler Position	degrees	Analog	THKA	20	None	None
Upper Rudder Position	degrees	Analog	THKA	20	None	None
Gross Weight	lbs	Analog	TH + C + D	1	None	4600.00
Center of Gravity	% MAC	Digital	THK C	1	None	None
Fuel Weight	lbs	Digital	THK D	1	None	None
Mach Number		Digital	TH	1	None	0.02
Airspeed	kts	Digital	TH	1	None	7.66
Altitude (Pressure)	ft	Digital	TH+E	1	None	237.00
Altitude (Radar)	ft	Digital	THKE	1	None	None
Wheel Speed (Main Gear)	kts	Digital	TH	1	None	None
Engine No. 2 Fan Speed	%	Digital	EPV	1	None	None
Engine No. 2 Core Speed	%	Digital	EPV	1	None	None
Engine No. 2 Power Lever Angle	degrees	Digital	EPV	1	None	4.80
Weight on Wheels (on/off)		Digital	disc	1	None	None
Main Gear Down		Digital	disc	1	None	None
Refuel Nozzle Latch (connect/unconnect)		Digital	disc	1	None	None
Structural Mode Control System (on/off)		Digital	disc	1	None	None
Terrain Following Status		Digital	disc	1	None	None
On/Off		Digital	disc	1	None	None
Manual/Auto		Digital	disc	1	None	None
Ride (soft/medium/hard)		Digital	disc	1	None	None
Engine Number 1 Stop		Digital	disc	1	None	None
Engine Number 2 Stop		Digital	disc	1	None	None
Engine Number 3 Stop		Digital	disc	1	None	None
Engine Number 4 Stop		Digital	disc	1	None	None

Disc - Discrete Signal
 PV - Peak-Valley Compression Algorithm
 EPV - Engine Compression
 TH - Time History Compression
 TH+C - Time History with group C time hack (typical)
 PV+A - Peak Valley with group A time hack (typical)
 THK A - Time Hack Parameter Group A (Typical)

DOCUMENTARY ITEMS

Aircraft Serial Number
 Mission Date
 Take Off Gross Weight
 Stores Weight
 Mission Type Code
 Base Code

TABLE 1 - SDC Parameter List

GROUND BASED PROCESSING PROGRAMS

A software package, shown in FIGURE 1 and consisting of three major programs, performs the task of accumulating the flight loads data received from the field and processing the data through validation programs and compiling the L/ESS database. The L/ESS database contains three major sections, namely USAGE STATISTICS containing the information necessary to reconstruct the B-1B mission profiles, LOAD FACTOR RECORDS compiled from accelerometer data and STRAIN GAGE RECORDS containing the data from the six strain gages.

Transcription Micro-computer Program

The first program in chain is the Transcription Micro-computer Program which provides the micro-computer to main frame interface. This program was developed by the USAF at the Aircraft Structural Integrity Management Information Systems (ASIMIS) facility and was specifically tailored to the USAF hardware/software environment. The floppy disks as received from the field are copied onto mainframe compatible storage media (disk files or magnetic tape). The data contained therein is copied, byte by byte, without reformatting onto a mainframe accessible storage device. The output file provides the input to the raw data reduction mainframe software.

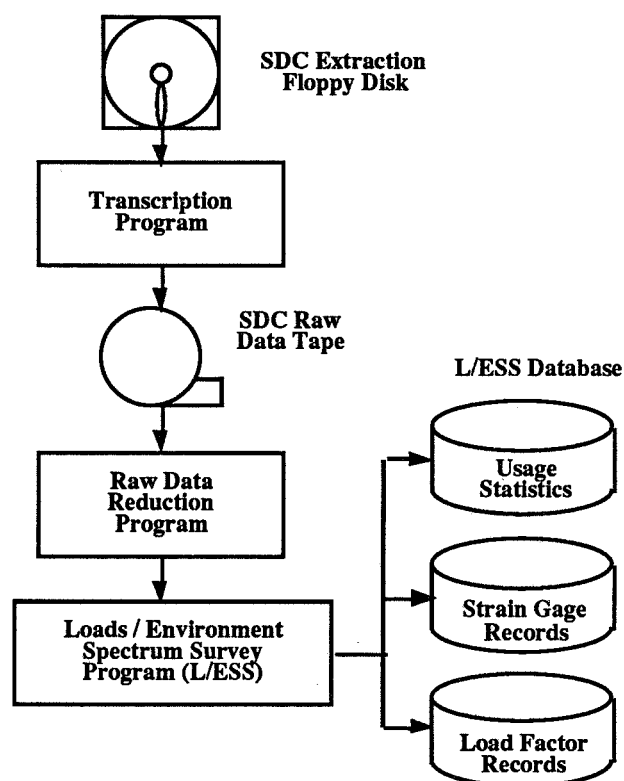


FIGURE 1 - Flow Chart for L/ESS Program

Raw Data Reduction (RADAR) Program

The RADAR program converts the recorded SDC information into sequenced time histories of each recorded parameter in engineering units. The program is equipped with sort routines to separate the data by aircraft and sort in date sequence, based on the dates provided in the SDC documentary data. The output of the program is passed to the L/ESS program.

A 'VALIDATION' module evaluates the SDC records for validity and suitability for further processing. If key aspects are missing, clearly invalid or inconsistent with other data, an entire flight may be declared invalid. Flights are declared invalid, for example, if the aircraft serial number identification has been omitted from all documentary records on a particular data extraction from the SDC. Another cause of invalid data is those flights for which the data is incomplete (flights appear to end in the air) due to saturation of the SDC memory or loss of communication between the SDC and CITS. Individual parameters are also evaluated and may be declared invalid. Validity checks include monitoring coincident values of various parameters such as Mach number and altitude for combinations outside the aircraft envelope. A not infrequent occurrence is 'drop out' where a parameter records an extreme value and returns to normal. These are detected and corrected. Extensive printed diagnostics allow the analyst to monitor automated validation decisions made by the program.

L/ESS Program and Compilation of the L/ESS Database

The L/ESS program performs additional validation analysis and interprets the raw recorded data into convenient statistical parameters that can be stored in the L/ESS database. The approach is to block the mission data into discrete periods or mission segments characteristic of a particular type of flying or ground taxi operation, and categorize the information into the three relational databases.

The time history records of aircraft weight, wing sweep, altitude and Mach number, simplified samples of which are shown in FIGURE 2, together with the documentary data, are used to classify each flight profile using a pattern recognition procedure.

A description of the current 34 mission type classifications is shown in TABLE 2. Once the mission profile has been classified, the mission data is broken down into discrete mission segments for which the selection criteria are shown in TABLE 3. Engineering review of plots of selected mission profile parameters ensures correct classification assignments and the addition of new profile or segment classes as necessary. Extensive statistics, shown in TABLE 4, are stored for each segment of each mission type. These statistics, which maintain the frequency of occurrence of the segment and running average values for each

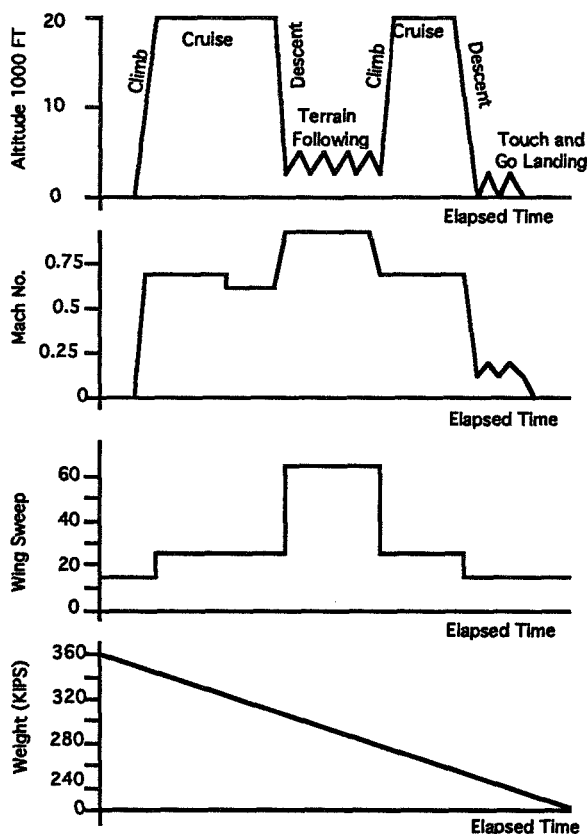


FIGURE 2 - Typical Profile Parameters

Mission Code		Mission Definition
Normal Weight	Heavy Weight	
1	1H	Training mission with at least 1 low altitude / high speed segment flown with terrain following system ON and with wings in aft position
2	2H	Training mission with at least 1 low altitude / high speed segment flown with terrain following system OFF and wing in aft position
3	3H	High altitude training mission with NO low altitude / high speed segment
4	4H	Ferry flight
5	5H	Functional check flight
6	6H	Ground alert - NO take off
7	7H	Airborne alert
8	8H	Operational mission similar to mission 1
9	9H	Operational mission similar to mission 2
10	10H	Operational mission similar to mission 3
11	11H	Pilot proficiency training
12	12H	Aircraft flight test mission
13	13H	General test support
14	14H	Training mission with at least 1 low altitude / high speed segment flown with terrain following system ON and at least 1 LHAS segment with wings less than 30 degrees
15	15H	Training mission with at least 1 low altitude / high speed segment flown with terrain following system OFF and at least 1 LHAS segment with wings less than 30 degrees
16	16H	Operational mission similar to mission 14
17	17H	Operational mission similar to mission 15

NOTE Normal weight missions have maximum in flight gross weight less than 375000 lbs
Heavy weight missions have maximum in flight gross weight greater than 375000 lbs

TABLE 2 - Mission Types

Segment Label	Definition
Take off run	Ground operations taken from 40 kt wheel speed to lift off
Touch and go taxi	Ground operations following a TAG touchdown and preceding a TAG liftoff
Landing runout	Ground operations taken from touch down to full stop
Miscellaneous taxi	Ground operations not otherwise defined
Full stop	Static ground time
Post take off climb	Rapid increase in altitude from lift off to flaps/gear retraction
Other climb	Any rapid significant increase in altitude not otherwise defined
Low cruise	Extended flight with no significant change in altitude. Average altitude less than 15000 ft and Mach/altitude combination that does not classify as LAHS segment
High cruise	Extended flight with no significant change in altitude. Average altitude greater than 15000 ft
Low refuel	In flight refuel operations with average altitude less than 15000 ft
High refuel	In flight refuel operations with average altitude greater than 15000 ft
Other descent	Any rapid significant decrease in altitude not otherwise defined
Pre Terrain following descent	Rapid decrease in altitude immediately preceding low altitude /high speed or terrain following segment
Post Terrain following climb	Rapid increase in altitude immediately following low altitude /high speed or terrain following segment
Low altitude/high speed	Low altitude / high speed flight performed with terrain following system off
Terrain Following (manual-soft)	Low altitude / high speed flight performed with terrain following system in manual mode and ride set to soft ride
Terrain following (manual-medium)	Low altitude / high speed flight performed with terrain following system in manual mode and ride set to medium ride
Terrain following (manual-hard)	Low altitude / high speed flight performed with terrain following system in manual mode and ride set to hard ride
Terrain following (auto-soft)	Low altitude / high speed flight performed with terrain following system in automatic mode and ride set to soft ride
Terrain following (auto-medium)	Low altitude / high speed flight performed with terrain following system in automatic mode and ride set to medium ride
Terrain following (auto-hard)	Low altitude / high speed flight performed with terrain following system in automatic mode and ride set to hard ride
Airwork - low altitude	Flight operations characterized by large numbers of maneuvers and changes in altitude with an average altitude less than 15000 ft
Airwork - high altitude	Flight operations characterized by large numbers of maneuvers and changes in altitude with an average altitude above 15000 ft
Go around (pattern flying)	Local landing pattern flight associated with touch and go landings and low approaches
Pre landing descent	Rapid decrease in altitude immediately preceding a TAG or full stop landing - from flaps/gear down to landing
Supersonic dash - low	Supersonic flight operations with average altitude below 15000 ft
Supersonic dash - high	Supersonic flight operations with average altitude above 15000 ft

TABLE 3 - Mission Segment Types

parameter, will be the basis for the compilation of the flight profiles for analysis. In addition, records are maintained for selected mission events, notably take offs, full stop and touch and go landings, landing gear extensions, flap and wing sweep operations and terrain following conditions.

The take off and landing statistics include the total number of the occurrences of the event, and the average condition defined by aircraft weight, c.g position, wing sweep and flap angles, velocity and thrust. The wing and flap movement events are defined in terms of the number of events and distributions of the degrees of movement. The terrain following statistics include distributions by time of aircraft weight, Mach number, altitude as well as the time operating in the manual or automatic modes and under various ride severity modes.

Number of times the segment recorded
 Total time
 Average Mach number
 Average altitude
 Average weight
 Average c.g. position
 Average fuel quantity
 Average wing sweep
 Average velocity
 Average thrust
 Average radar altitude
 Total Structural Mode Control System (SMCS) time
 Average segment start time (from mission start)
 Total gear down time
 Number of engine after burner operations
 Number of gear extensions
 Number of flap extensions (closed to partial)
 Number of flap extensions (closed to open)
 Total engine idle time
 Total engine intermediate power time
 Total engine MIL power time
 Total engine afterburner time

TABLE 4 - Data Stored for each Mission Type/Mission Segment/Wing Sweep Condition

important for the B-1B due to the variable wing sweep causing significant variation in mean load. Furthermore, the terrain following requirement results in the aircraft being subjected to gust loads while experiencing significant maneuver loads. Small cycles are accurately placed about elevated means and the collected data can be readily reconstructed.

The load parameters provided by the accelerometers and the strain gages are recorded by the SDC as load traces defined as a sequence of peaks and valleys with time tags. Each peak and valley from the strain gage trace is assigned to the mission classification and mission segment based on the time tag correlation with the flight profile records. Each load cycle is stored in a 'range/mean' matrix in a cell defined by the load range and mean value of the cycle as shown in FIGURE 3. The load factor data is dealt with in a similar manner except that each cycle is first designated as being due to a gust or a pilot induced maneuver. High frequency cycles are determined to be gusts and the remainder defined as maneuvers. The maneuver load cycles are classified by mission type, mission segment, wing sweep angle and flap position, while the gust load cycles are classified by wing sweep, altitude, Mach number and weight. TABLE 5 shows the list of eighty one (81) gust, maneuver or ground classifications extracted from more than 10000 classifications collected by the L/ESS program. Selection was based on those classes for which the maximum amount of data was recorded.

Range/mean tables provide a better definition of a random load spectrum than does the more commonly used cumulative occurrence data of peaks and valleys especially when the spectrum contains significant variation of mean loads. This is particularly

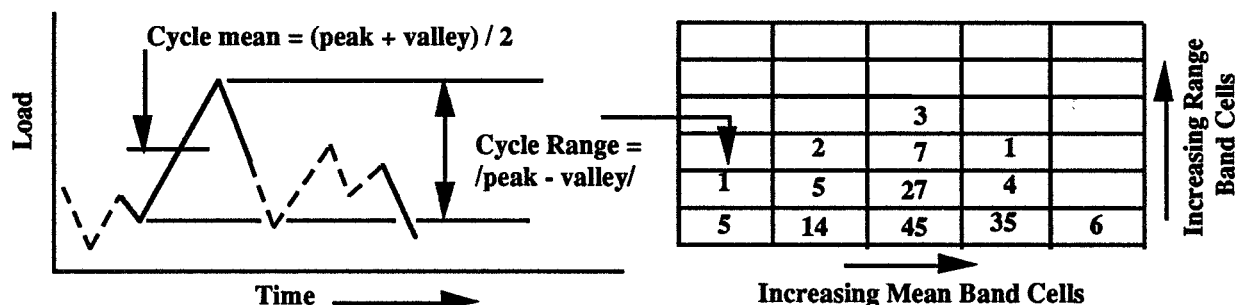


FIGURE 3 - Range/mean Table Definition

Load Type	Data ID	Mission Segment	Wing Angle	Flap Position	Altitude	Weight	Mach No.
Maneuver	1	Post Take Off Climb	< 22.5	Extend			
	2	Climb	< 22.5	Extend Up			
	3		< 22.5				
	4		22.5 - 30				
	5		> 60				
	6	Cruise	< 22.5	Extend Extend Up	< 15000		
	7		< 22.5		> 15000		
	8		< 22.5		< 15000		
	9		< 22.5		> 15000		
	10		22.5 - 30		< 15000		
	11		22.5 - 30		> 15000		
	12		50 - 60				
	13		> 60		< 15000		
	14		> 60		> 15000		
	15	Refuel	22.5 - 30				
	16	Descent	< 22.5	Extend Up			
	17		< 22.5				
	18		22.5 - 30				
	19		> 60				
	20	Pre Terrain Following Descent	22.5 - 30				
	21		> 60			< 315	
	22					> 315	
	23	Post Terrain Following Climb	22.5 - 30			< 310	
	24					> 310	
	25		> 60			< 310	
	26					> 310	
	27	Low Alt (Terrain Following System Off) Terrain Following Automatic- Hard Ride Terrain Following - Automatic - Med Ride Terrain Following - Automatic- Soft Ride				< 310	
	28					> 310	
	29					< 310	
	30					< 310	
	31					< 310	
	32					< 310	
	33					> 310	
	34	Airwork	22.5 - 30				
	35		> 60				
	36	Go Around & Pattern Flying	< 22.5	Extend Up			
	37		< 22.5				
	38	Pre-landing Descent	< 22.5	Extend Up			
	39		< 22.5				
Vertical Gust	40	All	< 22.5	Extend	< 1 AGL	200 - 250	< 0.4
	41				2.5 - 5		
	42				< 1 AGL	250 - 300	
	43				2.5 - 5		
	44				15 - 20		
	45				< 1 AGL	300 - 350	
	46				2.5 - 5		
	47	All	< 22.5	Up	2.5 - 5	200 - 250	0.4 - 0.6
	48				2.5 - 5	250 - 300	
	49				5 - 7.5		
	50				7.5 - 10		
	51				10 - 15		
	52	All	22.5 - 30		10 - 15	250 - 300	0.6 - 0.8
	53				15 - 20		
	54				20 - 30		
	55				10 - 15	300 - 350	
	56				15 - 20		
	57				20 - 30		
	58	Refuel	22.5 - 30		15 - 20	250 - 300	
	59				20 - 30		
	60	All	50 - 60		15 - 20	250 - 300	0.8 - 0.9
	61				20 - 30		
	62				15 - 20	300 - 350	
	63				20 - 30		
	64	All	> 60		< 1 AGL	250 - 300	0.8 - 0.9
	65				2.5 - 5		
	66				5 - 7.5		
	67				7.5 - 10		
	68				10 - 15		
	69				15 - 20		
	70	All	> 60		< 1 AGL	300 - 350	
	71				2.5 - 5		
	72				5 - 7.5		
	73				7.5 - 10		
	74				10 - 15		
	75				15 - 20		
Ground	76	Taxi				200 - 250	
	77					250 - 300	
	78					300 - 350	
	79					> 350	
	80	Pre-Flight Braking					
	81	Post Flight Braking					

TABLE 5 - Load Factor Data Records

COMPILING FLIGHT BY FLIGHT SPECTRA FROM THE L/ESS DATABASE

The spectrum generation procedure, shown diagrammatically in FIGURE 4, comprises the following tasks:

- Extract the mix of flight profiles that comprise the 100 flight representative usage, from the L/ESS database to become input to the spectrum generation program
- Reconstruct mission profiles from the L/ESS database to become input to the spectrum generation program. The flight profiles must be sufficiently detailed to describe the aircraft operational and loading environment.
- Generate local stress spectra at desired locations in the airframe structure using the flight profiles data, the mission mix statistics and accessing the L/ESS load factor database and the database of structural internal loads solutions from NASTRAN covering the required flight conditions.

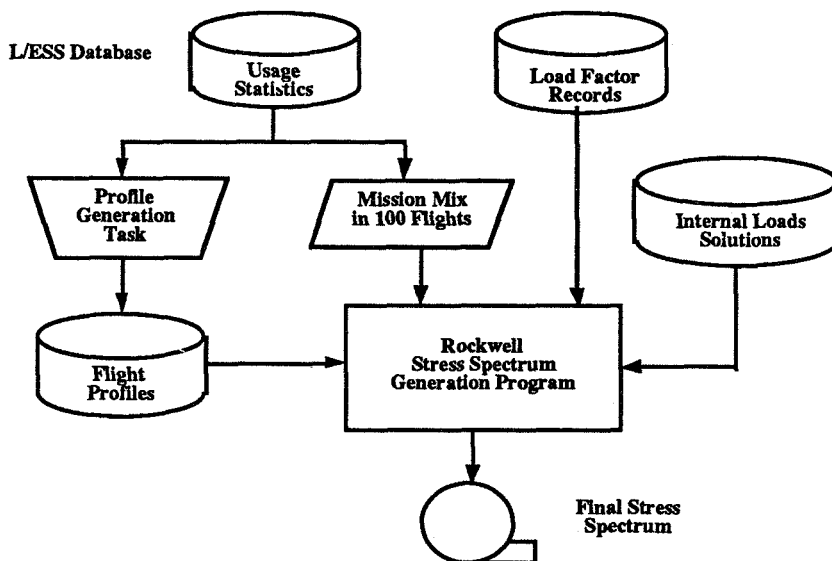


FIGURE 4 - Overview of Spectrum Generation Procedure

Mission Mix Representing Aircraft Service Usage

The first task is to establish the distribution of the available mission profiles that will represent the service experience of the B-1B. Interrogation of the L/ESS data base reflected that there were eight profiles that occurred at least once in 100 flights, the criteria chosen for a representative mission mix. That mix is shown in TABLE 6. It should be noted that mission type 1 is sub-divided into mission 1a and 1b. This was to accommodate the statistic that the number of terrain following segments approximated 1.5 per mission. Similarly mission types 2 and 3, where statistically air refueling occurs on every other flight, are subdivided.

Mission Code	Occurrences per 100 flts	Mission Definition	Mission Flt Hours
Training Missions			
1a	21	2 low altitude/high speed segments & terrain following ON	5.77
1b	21	1 low altitude/high speed segment & terrain following ON	3.91
2a	8	1 low altitude/high speed segment & terrain following OFF with air refuel	5
2b	7	1 low altitude high speed segment & terrain following OFF without refuel	5
3a	10	High Altitude with air refuel	3.65
3b	10	High Altitude without refuel	3.65
1H	2	Heavy weight mission 1	6.14
2H	2	Heavy weight mission 2	6.89
Other			
4	6	Ferry flight	4.02
5	1	Functional check flight	2.25
11	12	Pilot proficiency flight	0.99
Average for 100 flights			4.16

TABLE 6 - Mission Mix in 100 Flights

Detailed Mission Profiles

Considerable engineering judgment is applied to the task of reconstructing flight profiles from the L/ESS database statistics. The goal is to include all events that will cause changes in the structural loads and thus impact the computed fatigue life. The development of fracture mechanics analysis tools which account for loading sequence when computing crack growth rates has required attention to be paid to the sequence of mission segments and events as well as the magnitude of the loads. The detailed sequential flight profiles, a sample of which is presented in TABLE 7, are constructed with the following criteria to maintain consistency with the service records:

- a) All mission segments that occurred, on average, in every mission are included and sequenced appropriately. The sequence is defined by a combination of logical segment sequence for a mission from take off to landing and a survey of many collected profiles plots such as those in FIGURE 2.
- b) Mission segment times are consistent with the L/ESS statistical distribution adjusted to provide the recorded average flight length.
- c) Average flight parameters of wing sweep, gross weight, altitude, and Mach number are taken from the L/ESS statistics with adjustments, applied if necessary, to ensure consistency with the mission segment sequence. Typical adjustments include those to the gross weight to reflect declining weight as fuel is used. Parameters such as wing sweep and flap position are refined to the normal available operating positions.
- d) The spectrum profiles are then refined to match the number of significant events recorded in the L/ESS database. Among these are the number and degrees of wing sweep activities, the number of flap cycles, number of landings, distribution of terrain following situations such as automatic or manual flying, soft or hard ride setting and activation of the structural mode control system.

The profiles are stored on a database for convenient accessing by the spectrum generation program.

Segment Title	Time (mins.)	Weight (kips)	cg position % mac	Altitude (1000 ft.) ACL	Mach No.	Thrust (kips)	Wing (degrees)	No. of Touch and Go Landings	Flap (degrees)	No. of Flap Ops	Flaps Down Time (mins.)
Pre-flight	5.0	342.	20.7	0.0	0.00	28.7	15.0		25	0	5.0
Post Take Off	0.4	342.	20.2	0.5	0.33	30.9	15.0		25	1	0.4
Climb	11.7	323.	29.2	12.0	0.66	15.2	25.0		0	0	0.0
Cruise - High	53.0	323.	29.2	20.0	0.69	8.0	25.0		0	0	0.0
Descent	4.8	315.	28.9	16.0	0.66	1.7	25.0		0	0	0.0
Cruise - Low	9.2	315.	28.9	12.0	0.62	6.8	25.0		0	0	0.0
Pre T F Descent	3.6	307.	31.4	9.0	0.85	4.2	67.5		0	0	0.0
T F Hard Ride (Auto TF)	9.1	294.	30.0	0.9	0.85	7.6	67.5		0	0	0.0
TF System Off (Manual)	9.7	294.	30.0	1.2	0.85	7.7	67.5		0	0	0.0
T F Soft Ride (Auto TF)	12.9	294.	30.0	0.9	0.85	7.6	67.5		0	0	0.0
Post T F Climb	2.8	292.	31.2	9.0	0.85	10.9	67.5		0	0	0.0
Cruise - Low	6.5	292.	31.2	11.0	0.85	8.2	67.5		0	0	0.0
Pre T F Descent	3.0	292.	31.2	8.0	0.85	4.2	67.5		0	0	0.0
T F Hard Ride (Auto TF)	9.1	281.	30.0	0.9	0.85	7.6	67.5		0	0	0.0
TF System Off (Manual)	9.7	281.	30.0	1.2	0.85	7.7	67.5		0	0	0.0
T F Soft Ride (Auto TF)	12.9	281.	30.0	0.9	0.85	7.6	67.5		0	0	0.0
Post T F Climb	3.0	281.	30.0	9.0	0.85	10.9	67.5		0	0	0.0
Post T F Climb	5.5	262.	29.2	18.0	0.66	13.2	25.0		0	0	0.0
Refuel - High	26.9	291.	30.1	20.0	0.69	8.0	25.0		0	0	0.0
Cruise - High	97.0	262.	29.2	20.0	0.69	8.0	25.0		0	0	0.0
Descent	7.9	255.	24.1	14.0	0.51	0.8	15.0		0	0	0.0
Pre-land Descent	12.4	245.	18.2	1.3	0.33	5.9	15.0		25	0	12.4
Go Around	35.0	245.	18.2	1.7	0.41	7.1	15.0	5	25	2	29.2
Post Flight	5.0	238.	18.9	0.0	0.00	2.2	15.0		25	0	5.0

TABLE 7 - Typical Mission Profile

Database of Load Factor Occurrence Data

A summary of the available records selected from L/ESS database of load factor occurrence data are shown in TABLE 5. The load factor occurrence data are stored in "range/mean format" in a database for use by the spectrum generation program. The number of flight hours and missions represented by each range/mean table are also stored.

Database of Internal Loads Solutions

On the basis of the defined flight profiles, a series of external load conditions was developed to cover all mission segments within the flight profiles. In general, for each flight condition - defined by gross weight, cg position, Mach number, altitude and aircraft configuration (wing angle and flap position) - the following load conditions were generated:

- a) 1g conditions (42 conditions)
- b) Conditions representing a delta 1g maneuver (42 conditions)
- c) Conditions representing a delta 1g vertical gust (8 conditions)

In addition, ground loads were developed for a series of aircraft gross weights (6 conditions).

The basic approach that the external and internal loads are linear with respect to load factor allows the computation of loads for any load factor by combining the 1g loads with factors of the incremental gust and maneuver loads. The internal loads database was established to hold the internal forces and stresses for all members in B-1B complete airframe NASTRAN finite element model and to extract same by model member identification, type and load direction.

SPECTRUM GENERATION PROCEDURE

The stress spectrum generation task in FIGURE 4 is performed with a Rockwell written computer program, which incorporates the procedure shown in FIGURE 5. The spectrum program offers the following spectrum control options:

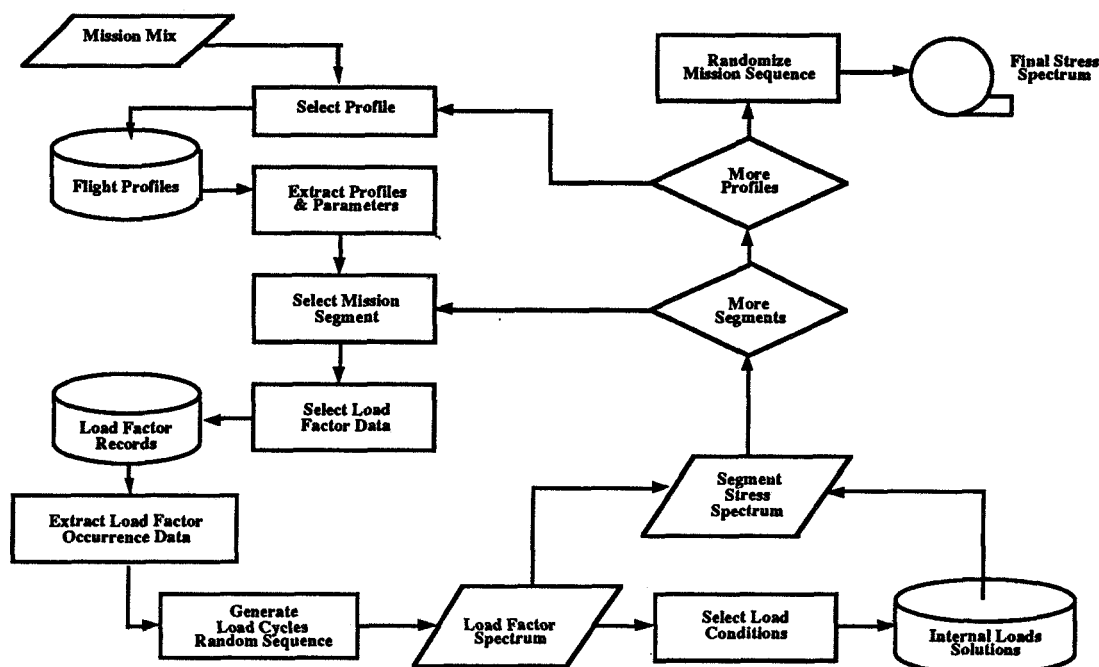


FIGURE 5 - Spectrum Generation Flow Chart

- a) Sequencing of loads within a mission segment (high/low, low/high or random). Random sequencing selected for the B-1B spectrum.
- b) Clipping of infrequent high loads - High loads that occurred less frequently than once in 100 flights were not included in the B-1B spectrum.
- c) Truncation of low loads - Load cycles for which the range (maximum load factor - minimum load factor) was less than 0.2g were removed from the B-1B spectrum.

The FIGURE 5 flowchart shows how the program loops through all required mission profiles, flight segment by flight segment. The primary tasks are to select the load factor data and create a load factor spectrum. The load factor spectrum is then related to the NASTRAN conditions by means of a code defining the appropriate internal loads conditions and the applied factors to obtain the structural stresses corresponding to the load factor.

Selection and Interpretation of Load Factor Data

The program selects appropriate data from the list of available range/mean records (TABLE 5) and converts the data to a number of randomly sequenced discrete load factor cycles representing the flight segment time. The range/mean data selection from TABLE 5 is based on the mission segment title, the flight profile parameters and aircraft geometry parameters for that segment. Typically both maneuver and gust data are selected for flight segments. Ground segments will typically select taxi and braking data.

The number of cycles extracted for each flight segment is defined by:

$$\text{Flight segment time} * \frac{\text{total number of cycles in the range/mean table}}{\text{total time represented by the range/mean table}} \quad (1)$$

Individual cycles are randomly selected using a select and not replace procedure to ensure the cyclic statistics are maintained. The range/mean file is re-supplied if the number of cycles in the table is less than the number required for the mission segment.

For range/mean data defined as maneuver data or taxi data the load cycle is defined as:

$$\text{The mean load factor } \pm 1/2 \text{ the range factor} \quad (2)$$

Range/mean data defined as gusts are interpreted as follows:

$$\begin{aligned} &\text{The magnitude of the gust is } \pm 1/2 \text{ the range load factor} \\ &\text{superimposed on a maneuver condition defined by the mean load factor.} \end{aligned} \quad (3)$$

Range/mean data defined as braking conditions are defined as a cycle with:

$$\begin{aligned} &\text{Maximum load of the braking force (Nx) combined with a 1g taxi condition} \\ &\text{Minimum load equal to the 1g taxi load.} \end{aligned} \quad (4)$$

Load Factor and Stress Spectrum Generation

Load cycles defined in terms of mean load factor and range are selected from within the statistics of the range/mean data to represent the mission time defined in the flight profile. The load cycles which occur less than once per flight are distributed statistically to the various missions using this range mean table. Peak and valley load factors are computed from the range and mean load factor. Each peak and valley in the load factor spectrum carries an identification code defining the mission segment, the flight parameters

such as weight, Mach number, altitude and geometry for which the load factor was derived. The code also reflects if the load factor was due to a gust, maneuver or ground condition.

Load factors are converted to stresses by relating the identification code to one or more of the NASTRAN solutions referred to above and applying the appropriate load factors. Stress spectra at any location in the airframe structure are available on demand by program operators by selecting the airframe component and the NASTRAN element numbers representing the structural location under consideration.

The forces or stresses from multiple NASTRAN elements can be combined using any arithmetic function to define the stress at the required structural detail.

SPECTRUM GENERATION METHODOLOGY VERIFICATION

The spectrum generation methodology was verified by comparing the stress spectra generated using the methodology outlined above with stress spectra compiled directly from strain gage records collected within the L/ESS program. Six strain gages are installed on every B-1B at the locations defined below.

- Strain gage 1 - Right hand arm of the stabilizer support fitting
- Strain gage 2 - Left hand arm of the stabilizer support fitting
- Strain gage 3 - Side plate of the stabilizer support fitting below the horizontal stabilizer
- Strain gage 4 - Wing sweep actuator rod end
- Strain gage 5 - Outboard wing lower skin
- Strain gage 6 - Forward fuselage dorsal longeron

The strain gage records were monitored and statistically compiled into range/mean tables according to mission classification, mission segment, wing angle and flap position. The cruise data was further defined by altitude range. The list of strain gage data segments with significant quantities of data is shown in TABLE 8. Stress spectra at the strain gage locations were recompiled from the L/ESS

Data ID	Description	Wing angle	Flap	Altitude	Weight
1	Post Take Off Climb	< 22.5	Extend		
2	Climb	< 22.5	Extend		
3		< 22.5	Up		
4		22.5 - 30			
5		> 60			
6	Cruise	< 22.5	Extend	< 15000	
7		< 22.5	Extend	> 15000	
8		< 22.5	Up	< 15000	
9		< 22.5		> 15000	
10		22.5 - 30		< 15000	
11		22.5 - 30		> 15000	
12		50 - 60			
13		> 60		< 15000	
14		> 60		> 15000	
15	Refuel	22.5 - 30			
16	Descent	< 22.5	Extend		
17		< 22.5	Up		
18		22.5 - 30			
19		> 60			
20	Pre TF Descent	22.5 - 30			< 315
21		> 60			> 315
22					
23	Post TF Climb	22.5 - 30			< 310
24					> 310
25		> 60			< 310
26					> 310
27	Low Alt (TFR off)	> 60			< 310
28					> 310
29	Terr. Foll - Hard Ride				< 310
30					< 310
31	Terr. Foll -Med Ride				< 310
32	Terr. Foll - Soft Ride				< 310
33					> 310
34	Airwork	22.5 - 30			
35		> 60			
36	Go Around	> 22.5	Extend		
37		> 22.5	Clean		
38	Pre-land	> 22.5	Extend		
39		> 22.5	Clean		
40	Ground				

TABLE 8 - Strain Gage Records (Typical)

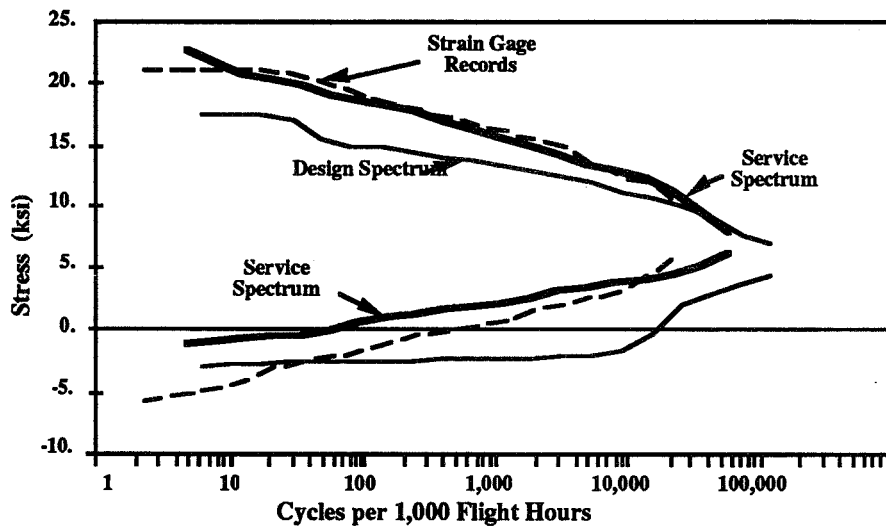


FIGURE 6 - Stress Spectra Comparison at Wing Strain Gage Location

database using the mission mix of TABLE 6. The spectra generated from strain gages were created in a similar manner to the load factor spectra but using the strain gage range/mean tables. The resulting spectra, representing 100 flights, are the stress spectra at each strain gage location. In order to provide a statistical representation of the 100 flight spectrum that could define the spectrum severity, an exceedance curve was generated for each strain gage location. Similar exceedance curves were generated from the analytic spectrum using the methods described previously to obtain the spectrum at the strain gage locations. This task was

completed for all the structural locations for which the strain gage records were available but only those pertaining to the wing and fuselage will be presented and discussed here. The compiled exceedance data are shown in FIGURES 6 and 7 for the wing and fuselage strain gage locations respectively. The curve defined as the "Service Spectrum" is based on the service recorded load factors and flight profiles and the analytically generated NASTRAN internal loads at the location of the strain gage. The curve defined as the "Strain Gage Records" was compiled from the L/ESS strain gage data while that defined as the "Design spectrum" was derived analytically from the original B-1B design criteria of expected usage and loads.

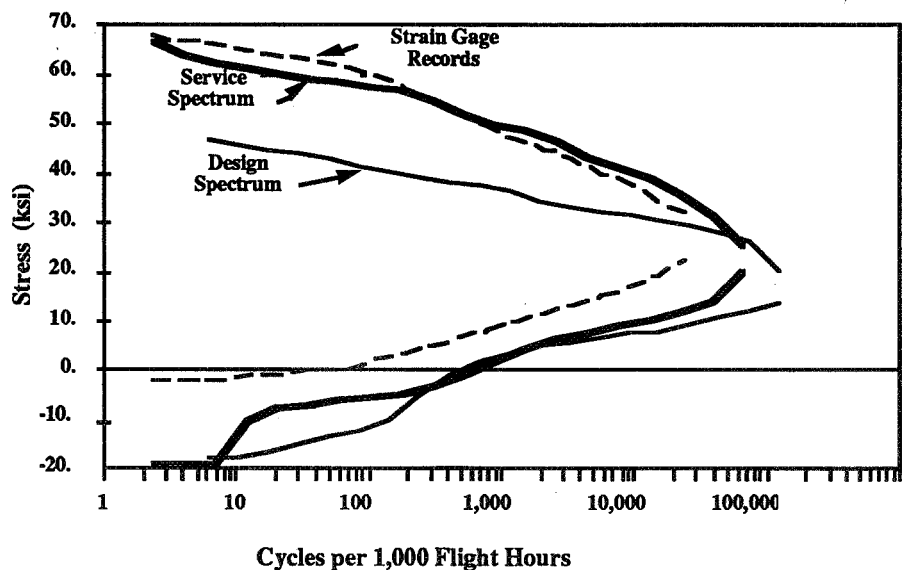


FIGURE 7 - Stress Spectra Comparison at Fuselage Strain Gage Location

The study showed good correlation between the load factor/analysis spectrum and the strain gage records for both wing and fuselage, providing confidence that the spectrum derived from the L/ESS load factors and profiles gives a good representation of the service structural environment throughout the wing and fuselage. The difference between the service exceedance curves and the design spectrum curves indicates a more severe usage experienced in service than was predicted by the design criteria.

TAILORING A SPECTRUM GENERATION PROCEDURE

Creation of an accurate fatigue spectrum requires that it include all operational and environmental events that cause significant changes in load. Spectra are therefore unique not only for aircraft types and models but also for various components within a structure. While many aspects of spectrum generation are common, a completely generic spectrum generation program is probably impractical. The spectrum generation procedure described in this paper was tailored to the product using extensive engineering knowledge of diverse subjects such as operational requirements, aerodynamics, performance, flight controls, aircraft response to the gust environment, external and internal loads, stress analysis and fatigue and fracture mechanics. One area of tailoring is the selection of recorded parameters where consideration must be given to the type of aircraft operations, aircraft design and performance, special aircraft geometry such as variable sweep wings and to the impact of flight control systems. Another area is in the setting up of the L/ESS database where the possible degrees of freedom of all recorded parameters leads to an unacceptably large database with many empty cells. The database for the B-1B, for example, has a much higher resolution for terrain following segments as a consequence of the high load cycle activity than it does for high altitude cruise. The final area specially written for the B-1B was the spectrum generation routines which selected range mean data and internal loads conditions from the available databases.

SUCCESS FACTORS

The success of the project, as measured by the comparison of the analytically derived spectrum with the strain gage records and by its ability to support structural life assessment analyses, was due to the following:

- 1) Developing a system that could be operated in a production mode with minimal user input while at the same time be adaptable in providing spectra for the evolving mission scenarios required by the USAF. The changing role of the B-1B within the USAF has resulted in the need to develop load spectra, in support of structural assessment, for a variety of missions. The L/ESS database and the spectrum generation programs have provided rapid response capability.
- 2) The L/ESS software that could efficiently handle enormous quantities of data, approximately 40,000 pieces of data per flight, and output a succinct graphical summary of each mission for timely engineering evaluation. The summaries provide weight, Mach Number, altitude and wing sweep plots as well as load factor and strain gage plots.
- 3) The many hundreds of hours spent reviewing the recorded data in order to understand the operational mission details and their relationship to the structural loads on the various structural components. This allowed the mission profiles to be accurately described and the programs refined as new types of missions were undertaken by the USAF.
- 4) The use of range/mean tables to statistically describe the random cyclic data. Unlike the normally used exceedance curves, which maintain only the overall frequency of peaks and valleys, range/mean tables keep the frequency of cycles completely defined by the load range and the mean load. The reconstitution of a load trace from a range/mean table more closely matches the original load trace than does one rebuilt from exceedance data due to the inclusion of cycles with small ranges of load about high and low mean load levels.
- 5) External and internal loads were generated for ninety two (92) conditions. These conditions covered the various flight segments and associated parameters, the aircraft geometry and types of loading encountered within the flight profiles.
- 6) An automated spectrum generation program linking the mission profiles, recorded load factor data and the internal structural loads from the NASTRAN finite element models. The automated program allows generation of stress spectra at any location within the structure with minimal user input.
- 7) Clipping the infrequent high loads to the level that occurred once in 100 flights. This ensured the inclusion of all load levels that may be statistically expected at least 20 times in a lifetime while eliminating the very infrequent high loads that may cause excessive crack growth retardation and an optimistic life assessment.

SUMMARY

As discussed in the introduction, the spectrum is an extremely important ingredient to the structural life assessment. The procedures defined in this paper provided a spectrum for the B-1B life assessment that closely matched the service experience. The benefit of a spectrum devised in this manner is a significantly improved estimate of the structural life over that computed from the design criteria usage. In addition this spectrum together with the large L/ESS database provides a reliable platform from which various mission scenarios can be assessed as to their impact on the airframe. The structural life computations based on these spectra provided an assessment of the economic life of the structure and the inspection requirements necessary to ensure safety.

The methodology was validated at six (6) discrete structural locations by comparing the results with strain gage records compiled from service records. This gave a high degree of confidence that the procedure was acceptable throughout the structure.

While most of the ideas discussed in the paper can be translated directly to other projects there are, as shown in the body of the paper, a number of aspects of the task of extracting load spectra from recorded flight data that must be tailored to the aircraft under consideration.

The primary lesson learned was that detailed engineering knowledge covering many disciplines in the fields of aerodynamics and structures was invaluable in establishing the validation criteria for recorded data and recognizing causes of significant load cycles. This knowledge was used to define those situations where more extensive analysis and review of service records were necessary in the interest of accuracy while spending less time on less important events. Another important lesson was that spectra generated by programs such as this are complex and long. The 100 flight spectrum for the B-1B wing for example contains 54000 cycles defined by 21000 peak/valley load steps. While efficient crack growth and fatigue programs operating on modern main frame and work station computers can handle spectra of this length it is necessary to prioritize the mission events and the loading parameters to prevent unacceptably long spectra.

1995108056

N95-14470

**THE ROLE OF FRETTING CORROSION AND FRETTING FATIGUE
IN AIRCRAFT RIVET HOLE CRACKING -
A STATUS REPORT ON TWO FAA GRANT PROGRAMS***

398649

517-39

23111

p. 6

Charles B. Elliott III

Mark Moesser

David W. Hoeppner

Quality and Integrity Design Engineering Center

University of Utah

Salt Lake City, Utah

SUMMARY

Personnel in the Quality and Integrity Design Engineering Center (QIDEC) at the University of Utah are working under a two year grant from the FAA to better understand the role of fretting corrosion and fretting fatigue in aircraft rivet hole cracking. The current program follows a one year grant program which was completed in 1993. This paper provides a status report on the results of these grant programs.

Recent effort has been focused on developing basic fretting fatigue models which consider variation in the coefficient of friction with time and location within the fretting interface. This is a very important characteristic of the QIDEC model because coefficient of friction varies significantly during the fretting fatigue process. Copies of QIDEC documents discussed in this paper can be obtained by contacting the authors.

INTRODUCTION

Fretting is a process in which two bodies in contact are subjected to relative motion of an amplitude small enough to allow resulting debris to be trapped between the contacting (faying) surfaces. Because the faying surfaces and debris are subject to corrosion as well as wear, the process is sometimes called fretting

* The FAA has supported this work through Grants No. 92-G-004 and No. 93-G-068. QIDEC is grateful for this support and the efforts of the FAA Grant Monitor, Dr. Thomas Flournoy.

corrosion. When one or both of the bodies also undergo cyclic tensile (fatigue) loading, the process is called fretting fatigue. The simultaneous action of wear, corrosion and fatigue mechanisms often results in a synergistic degradation of the components with a reduction in life which can be an order of magnitude more than would be expected based upon the operation of only one of the three mechanisms.

Fretting fatigue is increasingly being recognized in the aircraft industry as a major cause of failure. It is a failure mechanism which frequently leads to high maintenance and inspection costs and could potentially lead to catastrophic failure of aircraft components. Thus, it represents both a durability and a safety problem. Costs associated with fretting fatigue are significant. The 1988 Aloha Airlines disaster focused new attention on fretting in the aircraft industry as it was thought fretting could have played an important role in that failure.¹ Fretting can be present in any area of an aircraft structure (e.g. engines, aircraft primary and secondary structure, and landing gear components) in which small amplitude cyclic slip between adjacent contacting materials is possible. Rivets and mechanically fastened joints in general are particularly susceptible to fretting and fretting fatigue multiple-site damage. This damage can link up in aircraft structures and create catastrophic results. Thus, it is imperative to understand the role of fretting and fretting fatigue in producing multiple-site damage in riveted aircraft joints.

RESULTS FROM THE PREVIOUS GRANT PROGRAM

Based on a search of government and private literature from 1960 to 1992 a report was prepared. This report, "Literature Review and Preliminary Studies of Fretting and Fretting Fatigue Including Special Applications to Aircraft Joints" has been submitted to the FAA and is being considered for publication as an National Technical Information Service document.

The aircraft industry needs the ability to predict the role and influence of fretting on the fatigue life of riveted joints. For this reason, an extensive effort was started during the previous grant program and is continuing during the current program to improve quantitative prediction of fretting fatigue in aircraft joints. Due to the complex geometry of such joints, an accurate quantitative analysis could best be performed with the use of finite element methods.

QIDEC personnel presented four papers at the International Conference on Fretting Fatigue held in Sheffield, England in April 1993. These papers which will be published by the European Structural Integrity Society are as follows:

- Mechanisms of Fretting Fatigue (invited keynote paper) by Dr. Hoeppepner.
- The Role of Normal Pressure in Modeling Fretting Fatigue by Dr. Adibnazari and Dr. Hoeppepner.
- Finite Element Model of Fretting Fatigue With Variable Coefficient of Friction Over Time and Space by Mr. Moesser, Dr. Adibnazari and Dr. Hoeppepner.
- A Fretting Fatigue System Useable in a Scanning Electron Microscope by Dr. Elliott and Dr. Hoeppepner.

Additionally, Dr. Hoeppepner and Dr. Adibnazari co-authored a paper titled "Fretting Fatigue in Aircraft Joints" which Dr. Hoeppepner presented to the June 1993 International Committee of Aeronautical Fatigue in Sweden.

OVERVIEW OF THE CURRENT GRANT PROGRAM

QIDEC is currently working under FAA Grant 93-G-068 which was received in late September 1993 and will last two years. The objectives of the program are as follows:

- Construct, calibrate and verify a computer simulation model of a riveted joint.
- Perform a sensitivity study on some parameters which could influence fretting fatigue in riveted aircraft joints.
- Model the nucleation of fretting damage at riveted aircraft joints.
- Establish a design method that will allow an assessment of the likelihood that the fretting fatigue damage threshold will be exceeded.
- Conduct an assessment of the design approaches used by industry to alleviate fretting corrosion and fretting fatigue.
- Develop experimental techniques that allow assessment of fretting fatigue in riveted joints.
- Make all methods and findings applicable to a global aircraft reliability model.
- Maintain liaison with FAA technical personnel, other FAA programs, aircraft industry activities and ASTM activities with respect to fretting.

To accomplish these objectives, the program has been organized into the following major tasks:

- Develop and verify basic fretting fatigue models which consider variation in the coefficient of friction with time and location within the fretting interface. This is a very important (and to our knowledge a unique) characteristic of the QIDEC model because coefficient of friction varies significantly during the fretting fatigue process.

- Determine the coefficient of friction and faying surface sealant materials data necessary as input to the models.
- Plan and conduct a sensitivity study on some of the parameters which affect fretting fatigue in riveted aircraft joints.
- Plan and conduct an examination of riveted joints used in service.
- With knowledge gained from the basic fretting fatigue models, develop and verify a fretting fatigue model of a riveted joint.
- Use the results of this program to develop fretting fatigue design methods useful to the aviation community.
- Report results of this program to the aviation community through the FAA and the open literature.

This is one of several research programs being conducted by QIDEC that are leading to improved understanding throughout the aviation community of the adverse synergistic effects of wear, corrosion and fatigue mechanisms on aircraft structural integrity. Related research is being conducted for the Boeing Commercial Airplane Company and the Boeing Defense and Space Group in coordination with the U. S. Air Force. Non-aviation programs funding fretting-related research within QIDEC, which will indirectly benefit the aviation industry, include an orthopedic implant designer and a manufacturer of truck and trailer hubs.

STATUS OF THE PROGRAM

Major advances are being made in development of the basic fretting fatigue model. Recent activity included the transition from the ANSYS finite element program, used in preliminary work under FAA Grant No. 92-G-004, to the ADINA program. This switch was necessary to take advantage of the increased capability of the ADINA code available at the University of Utah. Two and three dimensional models were constructed using the ADINA code. These models were used to verify that the commercially available ADINA program can be used with the methods being developed by QIDEC. As part of this work, Fortran and C-shell codes were developed which proved the applicability of planned analytical methods for predicting changes in coefficient of friction as a function of time and location between the fretted surfaces. Basic fretting fatigue model development activities will continue with emphasis on incorporation of materials data when it is determined.

Development of the experimental methods and hardware to determine the coefficient of friction and faying surface sealant materials data necessary as input to the models is progressing on schedule. A rough

analysis of a riveted joint was conducted to determine the expected variability of normal surface tractions and relative displacements within a riveted joint. From this analysis it was determined that coefficient of friction data are desirable for relative slip an order of magnitude less than that reported in the literature. Collecting such data will present a challenge, but one which we are working to meet. Significant effort was expended developing and analyzing possible methods for determining coefficient of friction data at relative displacements as low as two microns. A preliminary test apparatus design was developed and is being refined. Methods and equipment for conducting faying surface sealant tests also will be developed.

QIDEC is in the process of developing a partnership with an industrial representative to help with planning the "sensitivity study on parameters important to fretting fatigue in riveted aircraft joints", and the "examination of riveted joints used in service" portions of the program. We are optimistic that such a partnership will be beneficial to both parties.

As part of the requirement to maintain liaison with the FAA and other aircraft industry activities, QIDEC personnel attended and made presentations at the FAA/NASA conferences in November 1993 at Lehigh University and March 1994, when QIDEC was the host organization. Additionally, QIDEC representatives attended the December 1993 USAF Structural Integrity Program Conference, where the Director of QIDEC made a presentation.

CONCLUDING REMARKS

The Quality and Integrity Design Engineering Center is pleased to have the opportunity to conduct this important research for the FAA and the aviation community in general. We will make every effort to disseminate our findings as they are developed.

REFERENCE

1. Brewer, John C.: Fretting Issues for the Aging Aircraft Program, U.S. DOT/FAATC, Oct. 1991.

BIBLIOGRAPHY OF QIDEC REPORTS AND PAPERS

Copies of the following reports and papers can be obtained by providing your name and address to Dr. Charles B. Elliott, III, University of Utah, Department of Mechanical Engineering, Merrill Engineering Building Room 3209, Salt Lake City, Utah 84112; phone: (801) 585-6429; FAX: (801) 581-8692; email: elliott@me.mech.utah.edu.

- Hoepfner, D. W., Adibnazari, S. and Moesser, M. W.: Literature Review and Preliminary Studies of Fretting and Fretting Fatigue Including Special Applications to Aircraft Joints. Submitted to the FAA in November 1993.
- Hoepfner, D. W.: Mechanisms of Fretting Fatigue. Invited keynote paper presented at the International Conference on Fretting Fatigue, Sheffield, England, April 1993.
- Adibnazari, S. and Hoepfner, D. W.: The Role of Normal Pressure in Modeling Fretting Fatigue. Presented at the International Conference on Fretting Fatigue, Sheffield, England, April 1993.
- Moesser, M. W., Adibnazari, S. and Hoepfner, D. W.: Finite Element Model of Fretting Fatigue With Variable Coefficient of Friction Over Time and Space. Presented at the International Conference on Fretting Fatigue, Sheffield, England, April 1993.
- Elliott, C. B. III and Hoepfner, D. W.: A Fretting Fatigue System Useable in a Scanning Electron Microscope. Presented at the International Conference on Fretting Fatigue, Sheffield, England, April 1993.
- Hoepfner, D. W. and Adibnazari, S.: Fretting Fatigue in Aircraft Joints. Presented to the International Committee of Aeronautical Fatigue in Stockholm, Sweden, June 1993.

INITIATION AND PROPAGATION OF SMALL CORNER CRACKS

Fernand Ellyin, Daniel Kujawski and David F. Craig

Department of Mechanical Engineering
University of Alberta
Edmonton, Alberta, Canada T6G 2G8

348650
5/8-39
23/12
p. 12

ABSTRACT

The behaviour of small corner cracks, inclined or perpendicular to loading direction, is presented. There are two aspects to this investigation: initiation of small cracks and monitoring their subsequent growth. An initial pre-cracking procedure under cyclic compression is adopted to minimize the residual damage at the tip of the growing and self-arresting crack under cyclic compression. A final fatigue specimen, cut from the larger pre-cracked specimen, has two corner flaws. The opening load of corner flaw is monitored using a novel strain gauge approach. The behaviour of small corner cracks is described in terms of growth rate relative to the size of the crack and its shape.

INTRODUCTION

Experimental observations indicate that initiated fatigue cracks first grow in a shear mode, which is termed Stage I after Forsyth [1]. After growing through a few surface grains at about 45 degrees, the actual macroscopic crack plane rotates to become normal to the far-field maximum principal stress. This is termed Stage II or Mode I in fracture mechanics terminology. The transition in crack direction from Stage I to II is generally of a crystallographic nature, and is associated with specific favourable slip systems in a polycrystalline solid. It has been also observed that during Stage I/II transition period the actual rate of propagation is highly variable. This erratic growth is usually ascribed to the grain boundary blocking mechanisms of the metallic microstructure [2-6].

In general, small cracks exhibit faster growth rate than that predicted based on the long-crack methodology, and they even grow below the threshold for long cracks [7-9]. These apparent "anomalies" of small crack behaviour may be influenced by a number of factors such as:

- (i) the lack of appreciable crack closure for small cracks due to the limited length of crack wake [eg. 9-11];
- (ii) the actual crack aspect ratio, a/c , i.e. the ratio of crack depth a to the half surface crack length c being small, and
- (iii) the crack plane orientation.

The effect of the latter two factors have not been investigated in a systematic manner. This is probably because most experimental studies are limited to small semi-elliptic surface cracks. In this type of investigation the crack depth behaviour is estimated from the surface crack measurement. Unfortunately, in such approaches, the crack aspect ratio, a/c , as well as the crack plane orientation, cannot be directly observed.

This paper presents a methodology, recently developed by the authors [12-14], which is used in investigating the behaviour of small corner cracks in a carbon steel. By employing this technique, the principal variables of corner cracks such as crack depth, crack aspect ratio as well as its plane of orientation can be measured. A pre-cracking procedure under cyclic compression [10] was adopted to minimize the residual damage left at the tip of a corner flaw. The opening load of the corner flaw is monitored using a novel strain gauge approach [14]. The behaviour of small corner cracks, inclined and perpendicular to loading direction, is presented in terms of growth rate relative to the size of the crack and its shape.

SPECIMENS AND EXPERIMENTAL PROCEDURES

The material investigated is the ASTM A-516 Gr. 70 carbon steel having tensile strength 540 MPa and 0.2% proof stress of 325 MPa. The mechanical properties of this ferritic/perlitic steel and the chemical composition are described in detail elsewhere [15].

Specimens

Final specimens with small corner flaws are manufactured in two stages as shown schematically in Fig. 1. First, a side-grooved compact-type (CT) specimen is pre-cracked in cyclic compression. The crack, which initiates from the notch, is permitted to grow until it self-arrests. A fatigue tension (FT) sample is subsequently cut from this pre-cracked specimen so as to include just the tip of the crack. This results in two small corner cracks because the fatigue crack front under cyclic compression has a concave shape. This shape can be influenced by the notch geometry as described in Ref. [16].

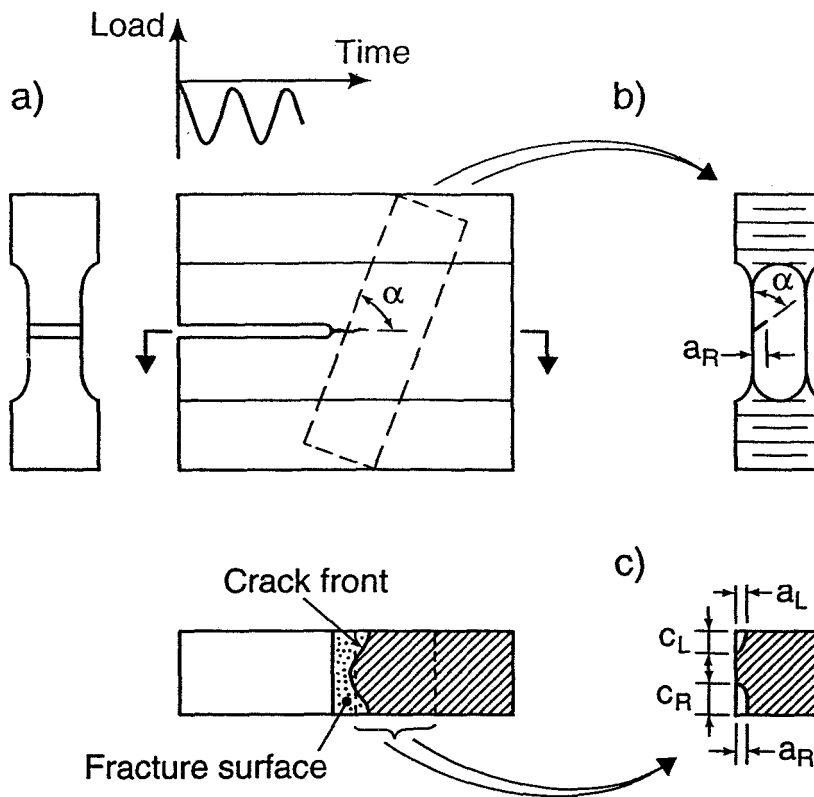


Fig. 1 Schematic of the test-specimen configuration
 (a) compact-type (CT) specimen, (b) fatigue tension (FT) specimens, (c) flawed cross-section with nomenclature: a - depth of crack, c - length of crack, L - left side, R - right side

Pre-Cracking and Fatigue Loading

Pre-cracking of the CT specimens was conducted on an AMSLER high-frequency vibrophore testing machine at about ~ 100 Hz sinusoidal compressive loading with a load ratio of $R = (P_{\min}/P_{\max}) = 10$. At the root of the notch, due to plastic outward flow of the material at P_{\min} , the local tensile stresses are induced upon unloading to P_{\max} . These tensile stresses are of sufficiently high magnitude to initiate a crack. As the crack advances from the notch-root, the rate of crack growth decreases progressively until a complete crack arrest occurs. Due to the self-arresting nature of the compressive pre-cracking, the extent of damage remaining at the tip of the crack is rather small and does not appreciably affect initial crack growth in the FT specimen. Furthermore, since closure loads during compressible pre-cracking are always negative, this therefore arrives at a naturally closure-free crack at $P = 0$ condition.

Fatigue tests of flawed FT specimens with small corner cracks (initiated in cyclic compression) are then conducted on an MTS servohydraulic machine at a frequency of 2-3 Hz with a maximum stress of 250 MPa. Load ratios, R , of 0.05 and -0.1 were used for inclined (45°) and perpendicular (90°) corner flaws, respectively.

Crack Monitoring

The technique adopted in this investigation for crack growth monitoring was a replica method. The specimen was first subjected to a load of half of P_{\max} , the surface wetted with acetone and the replica placed on the surface. The replica was then taped to a microscope slide for measurement and viewing under an optical microscope. A secant method was used to calculate the growth rate, da/dN , from the crack measurements,

$$\frac{da}{dN} = \frac{\Delta a}{\Delta N} = \frac{a_{i+1} - a_{i-1}}{N_{i+1} - N_{i-1}} \quad (1)$$

as a function of crack depth, a_i .

Determination of Crack Opening Load

The differential compliance method used in Ref. [17] was modified to measure the opening load. The technique utilized was to electronically difference two strain gauge readings ($\epsilon_1 - \epsilon_2$): ϵ_1 (the active gauge) situated over the mouth of the crack on the c-face and ϵ_2 located such that it was not significantly influenced by the crack, thus measuring the far field. The location of the gauges is shown in Fig. 2a. In Fig. 2a the relative sizes of the gauges and the corner cracks have been exaggerated.

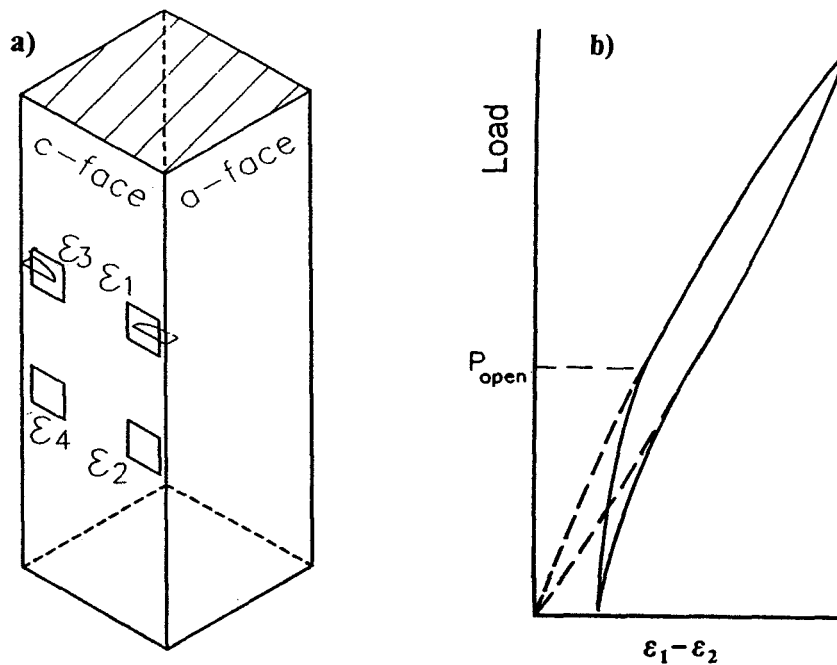


Fig. 2 Schematic illustration of (a) location of strain gauges, (b) differential compliance loop

A dedicated far field gauge, axially in line with the active gauge, was found to improve results from each active gauge compared to using a common far field gauge situated on the back of the specimen. The improved results can be attributed to eliminating the effect of the inevitable bending of the specimen during loading.

The interpretation of the opening load from the differential compliance loop was conducted using a curvilinear fit (illustrated in Fig. 2b) to a power-law (Ramberg-Osgood type) relation

$$\delta = (\epsilon_1 - \epsilon_2) = \frac{\Delta P}{M} + \left(\frac{\Delta P}{\bar{M}} \right)^{1/\bar{n}} \quad (2)$$

where δ is the differential displacement, $\Delta P = P_{\max} - P_{\min}$ is the load range, and M , \bar{M} and \bar{n} are fitted constants. When there is no crack closure, the two loops, i.e. experimental and fitted, will coincide.

The fitted curve is compared to the data to evaluate the opening load by following up the loading branch of the compliance curve to the point where the data curve and the fitted curve come close together. This curvilinear fit was found to be more sensitive than the traditional linear intercept approach, since the present approach takes into account the non-linearity of the applied load-differential displacement loop.

EXPERIMENTAL RESULTS

Typical results of the small corner cracks behaviour, both inclined (45°) and perpendicular to loading direction are presented below.

Inclined Corner Cracks

Figure 3 shows the growth rate, da/dN , versus crack depth, a , for corner cracks initially inclined at 45 degrees. The crack depth measurement was performed using three different microscopes. For each measurement the crack growth rate was computed and the results are plotted with different symbols. The crack extension rate in the through-the-width direction, dc/dN , is also depicted in Fig. 3 as a dashed line.

The da/dN and dc/dN curves generally follow a similar trend except that initially the corner flaws exhibit an erratic growth in the depth direction only. The through-the-thickness crack growth rate, da/dN , becomes continuous when the initially dormant through-the-width crack length, c , starts to propagate. This implies that during the erratic growth stage the orientation of the crack front as

well as the crack aspect ratio, a/c , changes. It is interesting to note that the change from the initial crack in Stage I to Stage II crack propagation is rather rapid with a blunt knee transition (see insets in Fig. 3).

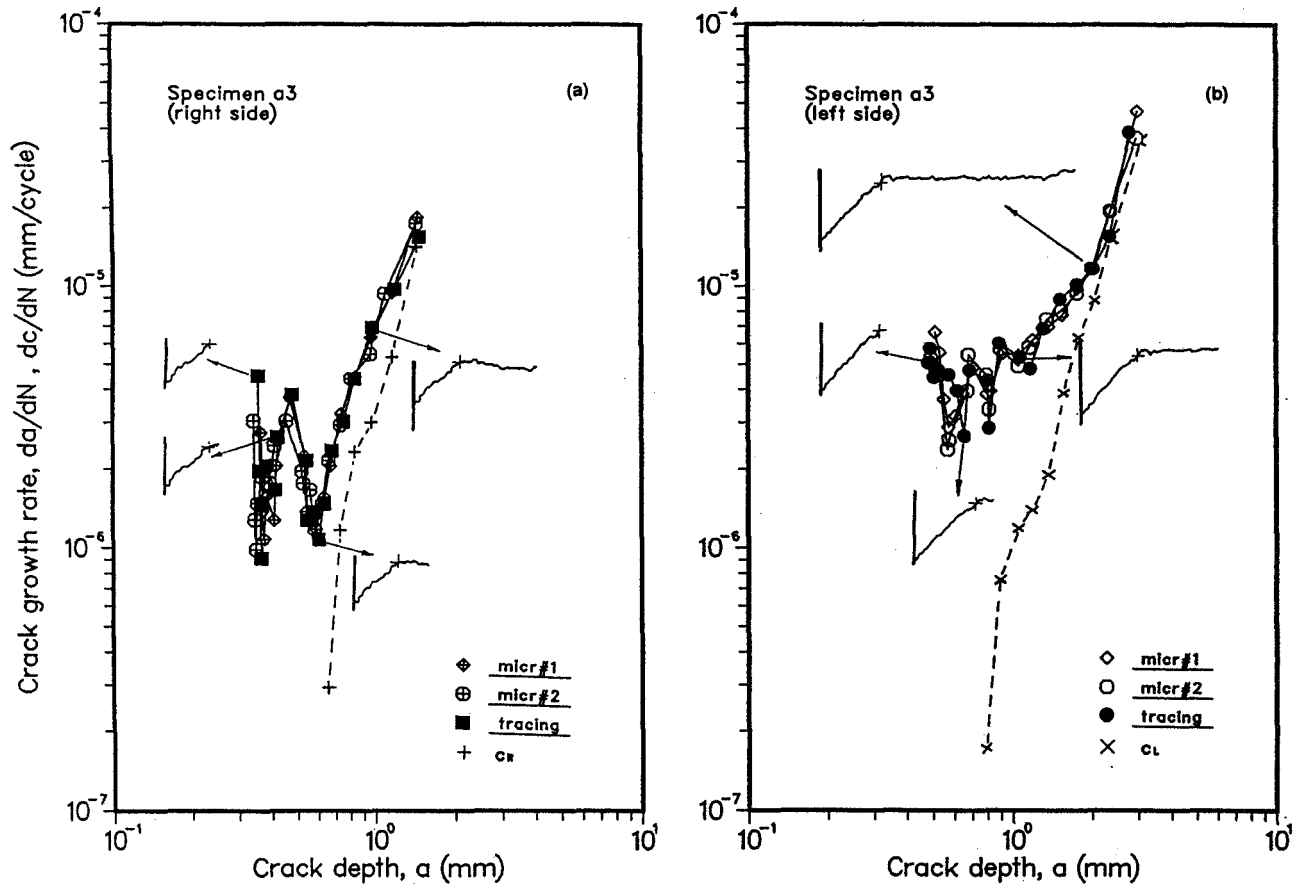


Fig. 3 Crack growth rate vs. crack depth for corner cracks initially inclined at 45°
(a) right side, (b) left side [13]

Figure 4 shows the corner crack aspect ratio, a/c , versus crack depth a . It is seen that the crack aspect ratio is not constant, but increases and the crack tends towards a quarter-circular shape. Similar observations were made in another test [13] with small corner flaws initially inclined at 45° and 60° .

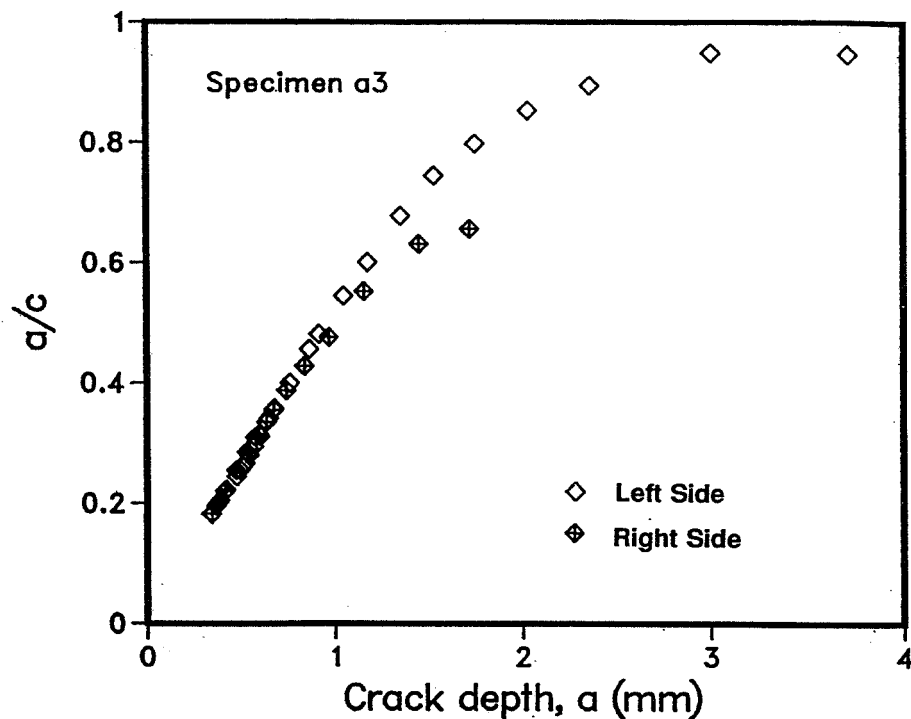


Fig. 4 Crack aspect ratio vs. crack depth for corner cracks initially inclined at 45° [13]

Perpendicular Corner Cracks

Growth rate da/dN and dc/dN versus the depth, a , of the corner cracks (perpendicular to loading direction) is presented in Fig. 5. When the calculated growth rate is less than the scale of the graph, a vertical downward arrow is placed at that data point. A vertical upward arrow is placed at the next point which does show growth and is connected with a dotted line.

Again, the early growth rate, da/dN , is erratic and the corner flaws grow initially in the depth direction only. The continuous crack growth seems to occur after the initially dormant crack length, c , starts to propagate. This is a typical behaviour of small corner cracks. The change in the aspect ratio, a/c , through the test is presented in Fig. 6. The aspect ratio is plotted versus the crack depth normalized with respect to the initial crack size, a/a_0 . The value of a_0 is included beside the corresponding curve. It is seen that the greater the initial aspect ratio (or larger the initial crack depth), the more quickly the aspect ratio will increase (steeper slope).

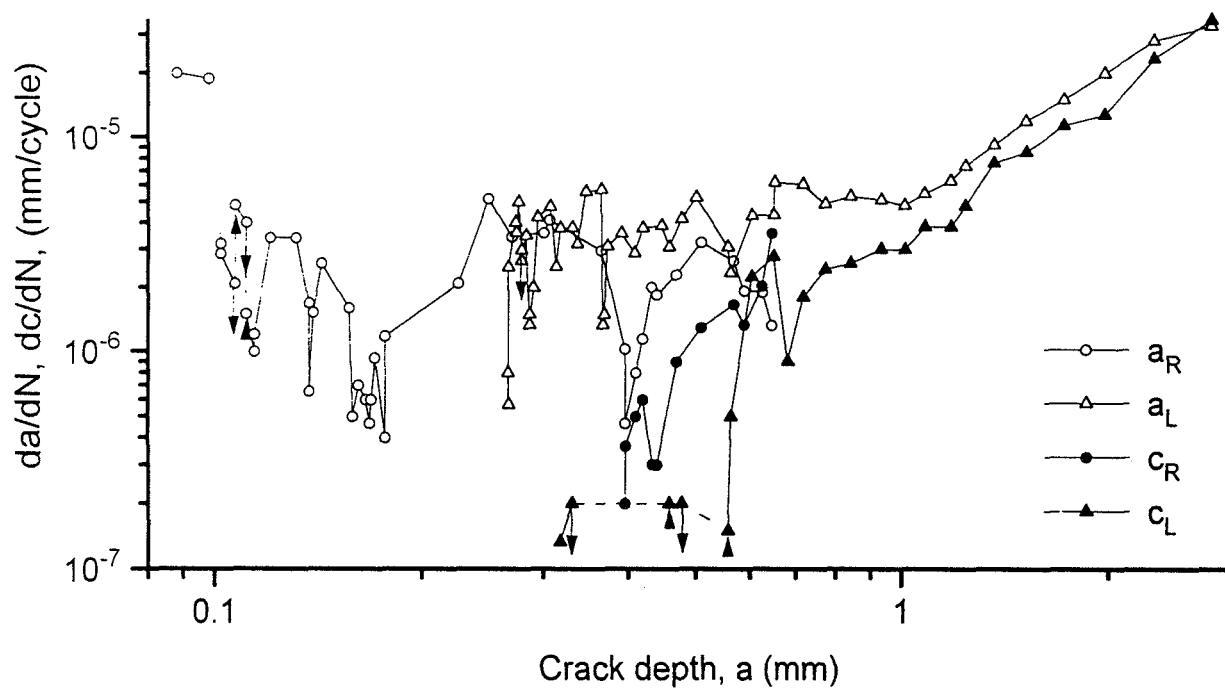


Fig. 5 Crack growth rate vs. crack depth for perpendicular corner cracks

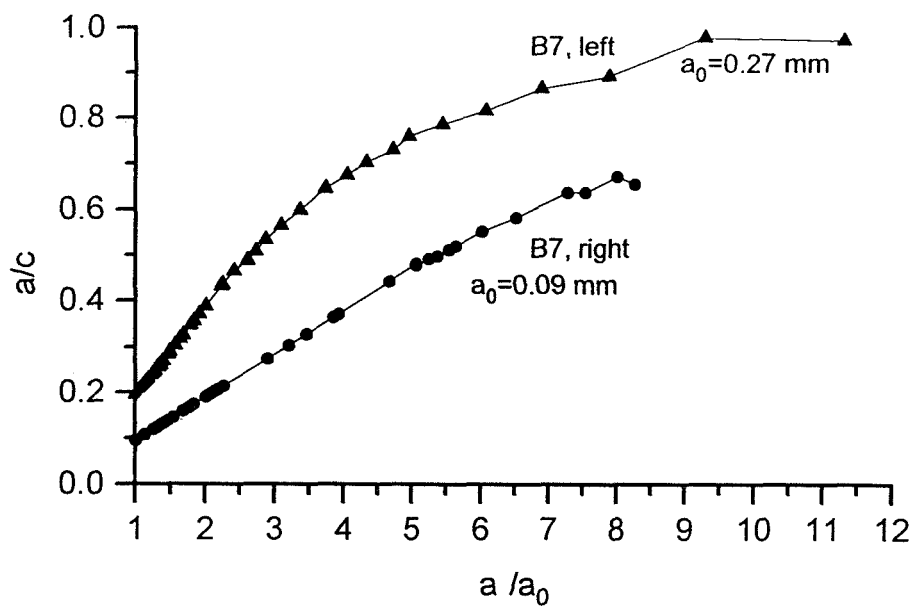


Fig. 6 Crack aspect ratio vs. normalized crack depth for perpendicular corner cracks

The opening load data, $P_{\text{open}}/P_{\text{max}}$ versus crack extension $\Delta a = a - a_0$, are shown in Fig. 7. The results from each corner crack are presented separately. The opening load decreases initially towards a minimum. This initial drop in crack opening load is probably associated with flattening of the fracture surfaces. As the length of crack wake increases with crack extension in depth, the opening load was found to build up gradually in an irregular manner towards a steady state value.

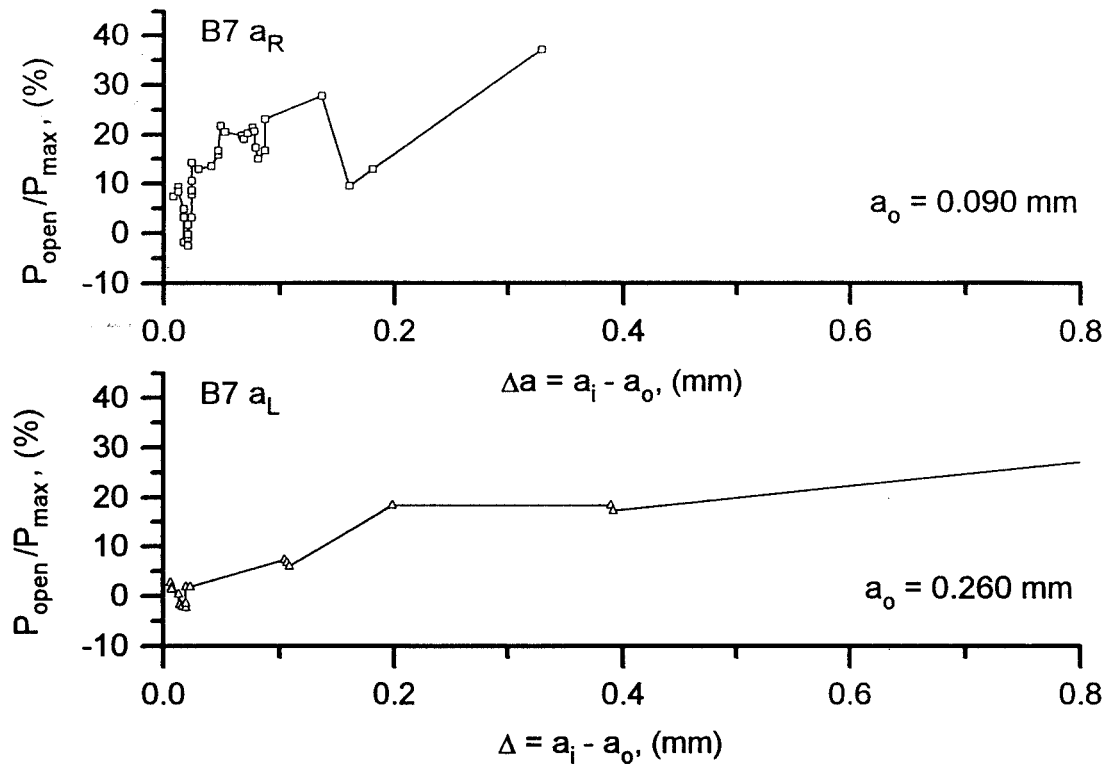


Fig. 7 Relative opening loads vs. crack extension for perpendicular corner cracks

CONCLUSIONS

The techniques presented here provide certain desirable features for the investigation of physically small corner cracks. The specimen preparation method produces a small pre-crack of controllable depth and plane orientation with minimal damage ahead of the tip. During the test this crack/specimen geometry permits one to monitor the development of the crack depth and utilize a strain gauge on the top of the c-face crack for sensitive measurement of the opening load.

These techniques were used to study the small crack behaviour in terms of growth rate and opening load relative to the depth of the crack and its shape.

ACKNOWLEDGEMENTS

This work was, in part, supported by the Natural Sciences and Engineering Research Council of Canada.

REFERENCES

1. Forsyth, P.J.E.: Fatigue Damage and Crack Growth in Aluminum Alloys. *Acta Metall.*, vol. 11, 1963, pp. 703-715.
2. Taylor, D. and Knott, J.F.: Fatigue Crack Propagation Behaviour of Short Cracks - The Effect of Microstructure. *Fatigue Engng. Mater. Struct.*, vol. 4, 1981, pp. 147-155.
3. Tanaka, K. and Akiniwa, Y.: Modelling of Small Fatigue Crack Growth Interacting with Grain Boundary. *Engng. Fract. Mech.*, vol. 24, 1983, pp. 803-819.
4. Miller, K.J.: Initiation and Growth Rates of Short Fatigue Cracks. In *Fundamentals of Deformation and Fracture (Proc. IUTAM Symposium Eshelby Memorial Conference)*, Cambridge University Press, Cambridge, 1984, pp. 477-500.
5. Lankford, J.: The Influence of Microstructure on the Growth of Small Fatigue Cracks. *Fatigue Fract. Engng. Mater. Struct.*, Vol. 8, 1985, pp. 161-175.
6. Navarro, A. and de los Rios, E.R.: Short and Long Fatigue Crack Growth, A Unified Model. *Phil. Mag.*, Vol. 57, 1988, pp. 15-36.
7. Suresh, S. and Ritchie, O.: Propagation of Short Fatigue Cracks. *Int. Metal. Rev.*, vol. 29, 1984, pp. 445-476.
8. Leis, N.B., Hopper, A.T. and Ahmad, J.: Critical Review of the Fatigue Growth of Short Cracks. *Engng. Fract. Mech.*, vol. 23, 1986, pp. 883-898.
9. McEvily, A.J.: On the Growth of Small/Short Cracks. *JSME Int. J.*, vol. 32, 1989, pp. 181-191.
10. Christman, T. and Suresh, S.: Crack Initiation under Far-Field Cyclic Compression and the Study of Short Fatigue Cracks. *Engng. Fract. Mech.*, vol. 23, 1986, pp. 953-964.

11. Lam, Y.C., Kujawski, D. and Ellyin, F.: The Development of the Crack Closure with Crack Extension. *Scripta Metallurgica and Materialia*, vol. 25, 1991, pp. 2313-2318.
12. Kujawski, D. and Ellyin, F.: Propagation of Small Corner Cracks Initiated in Cyclic Compression. *Engng. Fracture Mech.*, vol. 43, no. 4, 1991, pp. 657-662.
13. Kujawski, D. and Ellyin, F.: Fatigue Growth of Physically Small Inclined Cracks. *Fatigue Fract. Engng. Mater. Struct.*, vol. 16, no. 7, 1993, pp. 743-752.
14. Craig, D.: The Growth and Behaviour of Short Cracks in a Ferrite/Pearlitic Steel. M.Sc. Thesis, Department of Mechanical Engineering, University of Alberta, 1994.
15. Ellyin, F., Kujawski, D.: Plastic Strain Energy in Fatigue Failures. *ASME J. Pressure Vessel Tech.*, vol. 106, 1984, pp. 342-347.
16. Pippan, R.: The Length and the Shape of Cracks under Cyclic Compression: The Influence of Notch Geometry. *Engng. Fract. Mech.*, vol. 31, 1988, pp. 715-718.
17. DuQuesnay, D.L.: Fatigue Damage Accumulation in Metals Subjected to High Mean Stress and Overload Cycles. Ph.D. Thesis, University of Waterloo, 1991.

1995108058

N95-14472

**STATISTICAL INVESTIGATION OF FATIGUE CRACK INITIATION AND GROWTH
AROUND CHAMFERED RIVET HOLES IN ALCLAD 2024 T3
AS AFFECTED BY CORROSION***

M. I. Fadragas, M. E. Fine, B. Moran
Center for Quality Engineering and Failure Prevention
Northwestern University
Evanston, IL

34851
319-39
23/13
p. 17

SUMMARY

In panel specimens with rivet holes cracks initiate in the blunted knife edge of the chamfered rivet hole and propagate inward as well as along the hole. The fatigue lifetime to dominant crack formation was defined as the number of cycles, $N_{500\mu\text{m}}$, to formation of a 500 μm long crack. Statistical data on $N_{500\mu\text{m}}$ and on crack propagation after $N_{500\mu\text{m}}$ were obtained for a large number of uncorroded specimens and specimens corroded in an ASTM B 117 salt spray. Considerable variation in $N_{500\mu\text{m}}$ and crack propagation behavior was observed from specimen to specimen of the same nominal geometry and loading conditions. Statistical analysis of the data showed salt spray of Alclad 2024-T3 specimens with chamfered rivet holes increased the probability for both early formation and later formation of a propagating 500 μm fatigue crack. The growth of fatigue cracks after 500 μm size was little affected by prior salt spray.

INTRODUCTION

There is great variability in the fatigue behavior of any component even if the loading conditions are constant and this is due to many factors such as microstructure, surface finish, and environmental effects. The purpose of the present study was to assemble data sets on crack initiation, defined as the lifetime to a propagating 500 μm long crack, and the Paris equation constants for propagation after 500 μm crack length in samples of Alclad 2024-T3 aluminum alloy before and after exposure to ASTM B 117 salt spray with a 5% salt solution. The loading conditions were kept constant and the rivet holes were machined in a computer machine controlled tool. Statistical analysis of the data was performed. A small

* This work was supported by the Federal Aviation Administration through the Center for Aviation Systems Reliability

but definite effect of corrosion was observed mainly in the initiation stage. Considerable variation in cycles to fatigue crack initiation and in the Paris equation constants was observed in all of the data sets.

EXPERIMENTAL PROCEDURE

The material chosen for all the experiments was commercially available Alclad 2024-T3 aluminum alloy sheet. The sheet was 1.016 mm (0.040 in.) thick including an aluminum cladding thickness of 60 μm (0.00236 in.) on both sides. All the specimens were made from a single sheet of material. The specimens used in this study were small panel specimens with single rivet holes. Figure 1 shows the specimen dimensions, rivet hole dimensions, rolling direction, loading direction, and gripping configuration of the specimens. The specimens were gripped using friction grips and had a length of 108 mm (4.25 in.) between the grip edges. The specimens were 38.1 mm (1.5 in.) wide and were loaded normal to the rolling direction of the sheet. The width of the specimens corresponds to the inter-rivet spacing and the loading direction is consistent with the major stress axis of in-service airplane fuselages (refs. 1 and 2).

Flush head type rivet holes shown in figure 2 were drilled using a computer machine controlled tool to ensure repeatability of the hole dimensions and drilling conditions. The rivet holes were drilled to specifications used in the airplane industry (refs. 3, 4 and 5). The rivet holes were made with a chamfered region that makes a 100° angle centered on the vertical. The rivet hole chamfer was drilled so that it penetrated through 80% of the thickness of the material, 0.813 mm (0.032 in.). The rivet hole chamfer depth was measured using a ball bearing and the depth was controlled to within 5.0 μm (0.0002 in.). In actual industrial applications many of the rivet holes and chamfers are drilled by hand with a specialized tool. Considerably more variation in the rivet hole dimensions than that found in these experiments may be expected. Care was taken to accurately repeat the drilling process because the chamfered rivet holes tend to have a blunted knife edge (figure 2) that acts as a stress riser and a crack initiation site (refs. 1 and 6).

The tensile fatigue testing machine used was an MTS servo-hydraulic uniaxial fatigue apparatus System No. 821.74-01 which has a maximum capacity of 100 kN. All the tests were performed in ambient air at room temperature of 24 $^\circ\text{C}$. The loading was done at 5 Hz with a saw-tooth wave generated by a function generator and verified with the use of a digital recording oscilloscope. The specimens were attached to the testing machine using friction grips. The grips were aligned with the use of a Wood's metal pot.

The nominal stress reported in all the plots of the data was calculated by dividing the applied load by the cross-sectional area of the specimen neglecting the rivet hole. The fatigue testing was done in load control with an R ratio of 0.1 and a maximum load of 4.0 KN. This load corresponds to a nominal stress S of 100 MPa (14.5 ksi) in the cross-section of the specimen.

An optical microscope with a 4X objective and a 10X eyepiece equipped with a measuring micrometer X-Y stage was used to observe fatigue crack formation and measure fatigue crack growth quantitatively. The crack length measurements made with the X-Y stage were repeatable within 5 μm . The cracking that was observed around the rivet hole initially consisted of many small surface cracks. Later single cracks on each side of the hole became the dominant fatigue cracks. The fatigue crack lengths were measured on the blunted knife edge side of the specimen in-situ with the maximum load applied. The measurement was made from the edge of the rivet hole, where the fatigue crack initiated, to the crack tip.

In this study there were three batches of specimens. The three batches were cut from the same sheet of material but were fatigued and corroded in different ways from each other. The first batch was fatigued to fracture without any exposure to a corrosive atmosphere. The second batch was fatigued for 100,000 cycles, exposed to a corrosive atmosphere, and then fatigued to fracture. The third batch was exposed to a corrosive atmosphere prior to any cycling and then fatigued to fracture. The corrosive atmosphere used in this study was exposure to ASTM B 117 salt spray with a 5% salt solution for a period of 2 weeks. The specimens were then cleaned with deionized water and fatigued to fracture with intermittent crack length measurements.

Variability in the cycles to fatigue crack initiation is expected due to local variations in the surface finish of the hole caused by the drilling process as well as microstructural and chemical variations due to the processing of the material. The local variations in surface finish can be stress raisers such as burrs, machining marks, scratches, localized plastic deformation and particles in the material itself.

RESULTS

In previous studies (refs. 7 and 8) it was found useful to separate the fatigue process from a chamfered rivet hole into two distinct parts in order to compare the variations from specimen to specimen. For this purpose the fatigue cycles to fracture were broken down into a crack initiation segment and a crack growth segment. The initiation segment is defined as the cycles to the initiation of a propagating fatigue

crack 500 μm in length. The growth segment is defined as the cycles from the initiation of a propagating 500 μm long fatigue crack to fracture of the specimen.

Using in-situ optical microscopy it was observed that many small surface fatigue cracks initiated at the blunted knife edge (figure 2) of the rivet hole during the fatigue cycling of the specimens. These surface cracks varied in length but most did not appear to grow once they were initiated. It is thought that microscopically the small surface cracks link up to form through cracks which propagated on both the front and rear surfaces of the panel specimens. Two such through cracks, one on either side of the rivet hole normal to the loading direction, formed in all of the specimens. These cracks were the dominant fatigue cracks and grew to fracture. It was observed that once a through crack reached 500 μm in length it was identifiable as a dominant fatigue crack. Small cracks also formed ahead of the crack tip while the dominant fatigue cracks grew to fracture. The dominant fatigue cracks grow in part by joining up with the small cracks that form ahead of the crack tip.

The specimens that had been exposed to the salt spray formed a dominant fatigue crack on one side of the rivet hole many cycles before a dominant fatigue crack would form on the other side. This effect was observed to correlate with the fact that the fatigue specimens were placed upright on their sides while they were in the salt spray. The side that tended to first initiate a dominant fatigue crack coincided with the side that was lower in the salt spray and allowed more salt and water to collect on that side of the rivet hole.

The two cracks on each of the specimens were treated separately. Figures 3, 4 and 5 show the crack length (a) vs. number of cycles (N) curves for the three batches of specimens. The a vs. N data for each crack was curve fit to a least square exponential fit (eqn. 1) and the number of cycles to the initiation of a propagating 500 μm long fatigue crack were determined for each crack.

$$a = a_0 e^{vN} \quad (1)$$

Figure 6 is a plot of the fraction of rivet hole sides in which a propagating 500 μm long crack has not formed vs. the number of cycles (N) for the three batches of specimens. The distribution of the data is wider for the two batches of specimens that were exposed to the salt spray. For the batch that was exposed to the salt spray prior to any cycling, the probability for earlier initiation of a propagating 500 μm crack increased as well as the probability for later initiation as compared to the specimens that were not exposed to the salt spray. The same occurred for the batch exposed to salt spray after 100,000 cycles but to a lesser extent.

Empirical solutions for the stress intensity factor of a crack emanating from a chamfered rivet hole in a finite width specimen were not found in the literature. The ΔK values used were estimated using a combination of two finite element method (FEM) solutions found in Murikami (ref. 9). This compound method does not take into account the three dimensional effect caused by the rivet hole chamfer but is still useful for determining an approximate ΔK value for comparison purposes.

The first FEM solution for the stress intensity factor K was for two equal length cracks emanating from both sides of a circular hole in a finite width rectangular specimen. This solution was implemented to correct the ΔK values for the finite width specimen and to correct for the cracks emanating from a hole. The solution called for a radius R and a crack length C . The radius for the non-chamfer part of the rivet hole was used for R . The value used for C was the average of the measured crack lengths of the cracks emanating from both sides of the rivet hole. The stress σ used in the calculation was corrected for the loss of load bearing material due to the rivet hole and the crack length. The empirical formula for the solution was provided by H. Fühling (ref. 10).

The second FEM solution for the stress intensity factor K was for a single crack in a finite width rectangular specimen that is off center from the specimen centerline. This solution was implemented to correct the ΔK values for the difference in length of the two cracks emanating from the rivet hole. To avoid a double correction for a finite width specimen this solution was normalized so that only the relative magnitudes of the two K values were used. The solution called for a crack length C and the eccentricity E . The value used for C was the sum of the radius of the rivet hole and the average of the measured crack lengths of the cracks emanating from both sides of the rivet hole. The value used for E was calculated using the C value minus the radius R and the crack length on the opposite side of the specimen. The stress σ used in the calculation was corrected for the loss of load bearing material due to the rivet hole and the crack length. The empirical formula for the solution was provided by M. Isida (ref. 11).

The experiments were all performed with an R ratio of 0.1 thus the stress intensity range (ΔK) values were calculated using 90% of the maximum stress corrected for the loss of load bearing material due to the rivet hole and the crack length. Both the Fühling and Isida equations corrected for finite width specimens so the Isida equation was normalized to avoid a double correction for the finite width of the specimen. The final equation for ΔK is as follows:

$\Delta\sigma$ = stress range corrected for loss of load bearing material and R ratio

$F(\Phi, \Psi)$ = Fühling ΔK equation

$I_A(\alpha, \beta)$ = Isida ΔK equation for crack A

$I_B(\alpha, \beta)$ = Isida ΔK equation for crack B

$$\Delta K_A = \sqrt{\pi a} \Delta \sigma \cdot F(\Phi, \Psi) \cdot 2 I_A(\alpha, \beta) / (I_A(\alpha, \beta) + I_B(\alpha, \beta)) \quad (2)$$

(Fühling eqn.) (normalized Isida eqn.)

The previously obtained exponential curve fit data for the a vs. N curves was used to calculate the crack growth rate (da/dN) for each point on the a vs. N plots (eqn. 3).

$$da/dN = v a_0 e^{vN} \quad (3)$$

Figure 7, 8 and 9 are the da/dN vs. ΔK plots for the three batches of specimens. The data from all three batches of specimens fit into a scatter band bounded by $da/dN = 9.26 \times 10^{-11} (\Delta K)^{3.33}$ on the top and $da/dN = 6.45 \times 10^{-12} (\Delta K)^{3.31}$ on the bottom.

DISCUSSION

In deciding on inspection intervals the probability of early failure, of course, dominates. Salt spray prior to cycling has clearly increased the probability of early failure. It is not surprising that corrosion has increased the severity of defects responsible for crack initiation. The authors were surprised to find an increase in the long lifetime side of the distribution from the salt spray. There are specimens with relatively benign defects and perhaps minor cracks or flaws are filled with corrosion product and thus made less active. The effects of corrosion product in crack closure and in increasing the threshold stress intensity range for crack propagation is well known (ref. 12).

In order to more quantitatively compare corroded and non-corroded specimens the $N_{500\mu m}$ data for the three batches of specimens were fit by the Weibull equation (eqn. 4).

$$\text{Percentage without } 500 \mu m \text{ cracks} = \exp[-(N/N_0)^{m_w}] \quad (4)$$

Figure 10 is the same plot as figure 6 with the exception that the data was fit to the Weibull equation with the number of cycles of loading (N) as the variable and the Weibull exponent m_w and N_0 as the fitting parameters. The results of the curve fit are as follows for the three sets of specimens:

<u>Specimen Batch</u>	<u>N₀</u>	<u>m_w</u>
No Corrosion	145,944	4.776
Corrosion at 100,000 Cycles	144,692	5.842
Corrosion Prior to Cycling	133,908	4.234

The lower Weibull exponent is an indicator that the data for specimens which underwent corrosion prior to cycling has a more spread distribution of probabilities than that of specimens with no corrosion. The lower N₀ for pre-corroded compared to non-corroded specimens indicates that the 500 μm long dominant fatigue cracks initiated earlier in the pre-corroded batch of specimens in the low lifetime side of the distribution.

Salt spray after 100,000 fatigue cycles had much less of an effect than corrosion prior to any fatigue. Compared to the non-corroded specimens, the Weibull exponent is larger because the distribution was steeper in the mid-life regime; however, the Weibull coefficient is slightly smaller. The Weibull equation clearly fits these distributions only in the mid-range.

The cycles below which none of the specimens in a batch failed (i. e. the first data points in figures 6 and 10) are in the order corrosion at zero cycles, corrosion after 100,000 cycles, and no corrosion. This order is reversed in the plot regime where the probability of no 500 μm long dominant fatigue crack approaches zero.

Figure 11 is a plot of the Paris equation constant (C) vs. Paris equation exponent (m) that were derived from the da/dN vs. ΔK plots of figures 7, 8 and 9. The two parameters were derived by curve fitting the da/dN vs. ΔK data from each crack to the Paris equation (eqn. 5).

$$da/dN = C (\Delta K)^m \quad (5)$$

As discussed earlier the da/dN vs. ΔK data from all three batches of specimens fit into a relatively narrow scatter band bounded by $da/dN=9.26 \times 10^{-11} (\Delta K)^{3.33}$ on the top and $da/dN=6.45 \times 10^{-12} (\Delta K)^{3.31}$ on the bottom. As found in other metals there is a correlation of the C and m values. The data from each of the three batches of specimens were curve fit to an exponential equation (eqn. 6) and the results are as follows:

$$C = C_0 e^{\mu m} \quad (6)$$

<u>Specimen Batch</u>	<u>C₀</u>	<u>μ</u>
No Corrosion	1.8694e-08	-2.6843
Corrosion at 100,000 Cycles	2.4385e-08	-2.7748
Corrosion Prior to Cycling	1.6509e-08	-2.6635

These three curves are plotted in Figure 11 and there is little difference between them. The da/dN vs. ΔK curves were not significantly different for the three batches of specimens.

Figure 12 is a plot of the Paris equation exponent (m) vs. number of cycles to formation of a dominant 500 μm long crack (N_{500μm}). The data for the three batches of specimens were curve fit to a line (eqn. 7). The results are as follows:

$$m = m_0 + s \cdot N_{500\mu m} \quad (7)$$

<u>Specimen Batch</u>	<u>m₀</u>	<u>s</u>
No Corrosion	1.5770	1.7615e-05
Corrosion at 100,000 Cycles	1.5022	1.7561e-05
Corrosion Prior to Cycling	-0.8340	4.2212e-05

In this data there was a slight upward trend of increase in m with N_{500μm}, i.e. the cracks which initiated late in a number of cases grew more rapidly than the average.

In the three batches of specimens one crack would usually initiate earlier on one side of the specimen than on the other. On some occasions one crack would grow to several mm in length before a second dominant fatigue crack would appear on the other side of the specimen. This effect was more prevalent in the specimens that were exposed to salt spray either before cycling or after cycling for 100,000 cycles. The specimens were laid upright on their sides in the salt spray. This caused salt and water to deposit preferentially on the lower side of the rivet hole. In the salt sprayed specimens the side that tended to first initiate the dominant fatigue crack was the side where salt and water were deposited preferentially. This is further evidence that salt spray affects fatigue crack initiation.

1. Salt spray of Alclad 2024-T3 specimens with chamfered rivet holes increased the probability for early formation of a propagating 500 μm fatigue crack.

2. A plot of probability for initiation of a propagating 500 μm fatigue crack vs. cycles becomes more spread out from salt spray in both the high cycle and low cycle regimes.

3. The growth of fatigue cracks after 500 μm size was little affected by prior salt spray.

REFERENCES

1. Samavedam,G., Hoadley,D., Davin,J., "Test Facility for Evaluation of Structural Integrity of Stiffened & Jointed Aircraft Curved Panels", Springer Series in Computational Mechanics, Atluri, Sampath, Tong (Eds.), Structural Integrity of Aging Airplanes, Springer Verlag, Berlin Heidelberg, 1991, pp. 321-327.
2. Inventory of Foster-Miller Panels with attached Drawings, FAA, 29 NOV 91.
3. Installation, Inspection and Removal Methods for Aerolock 905, 906, 907 and 908 Rivets, H. D. Little Co., 10 SEPT 90.
4. Boeing 737 Structural Repair, Boeing Co., 1 FEB 69.
5. Boeing Part Standard, BACR15CE RIVET, 100⁰ Shear Head, Boeing Co., 22 JUL 87.
6. Pelloux,R., Warren,A., O'Grady,J., "Fractographic Analysis of Initiation and Growth of Fatigue Cracks at Rivet Holes", Springer Series in Computational Mechanics, Atluri, Sampath, Tong (Eds.), Structural Integrity of Aging Airplanes, Springer Verlag, Berlin Heidelberg, 1991, pp. 293-308.
7. M. I. Fadrakas, "Tensile Fatigue Crack Initiation And Growth Database For Chamfered Rivet Holes In Alclad 2024-T3 Aluminum Alloy", M. S. Thesis, Northwestern University, OCT 1993.

e-4.

8. "Tensile Fatigue Crack Initiation And Growth Database For Chamfered Rivet Holes In Alclad 2024-T3 Aluminum Alloy", Published as NAARP Report, Issue 3, JUL-OCT 1993, FAA Technical Center, Atlantic City International Airport, Atlantic City, NJ, 80405.
9. Murikami, Y., Stress Intensity Factors Handbook, Vol. 1, Pergamon Press, 1987, pp. 78-80, 291-297.
10. Fühling, H., "Approximation Functions for K-Factors of Cracks in Notches", *Int. J. Frac.*, Vol. 9 (1973), pp. 328-331.
11. Isida, M., "Stress-Intensity Factors for the Tension of an Eccentrically Cracked Strip", *Trans. ASME, Ser. E, J. Appl. Mech.*, Vol. 33 (1966), pp. 674-675.
12. S. Suresh, G. H. Zaminski and R. O. Ritchie, "Oxide-Induced Crack Closure: An Explanation for Near-Threshold Corrosion Fatigue Growth Behavior", Metallurgical Transactions, 12A (1981) pp. 1435-1443.

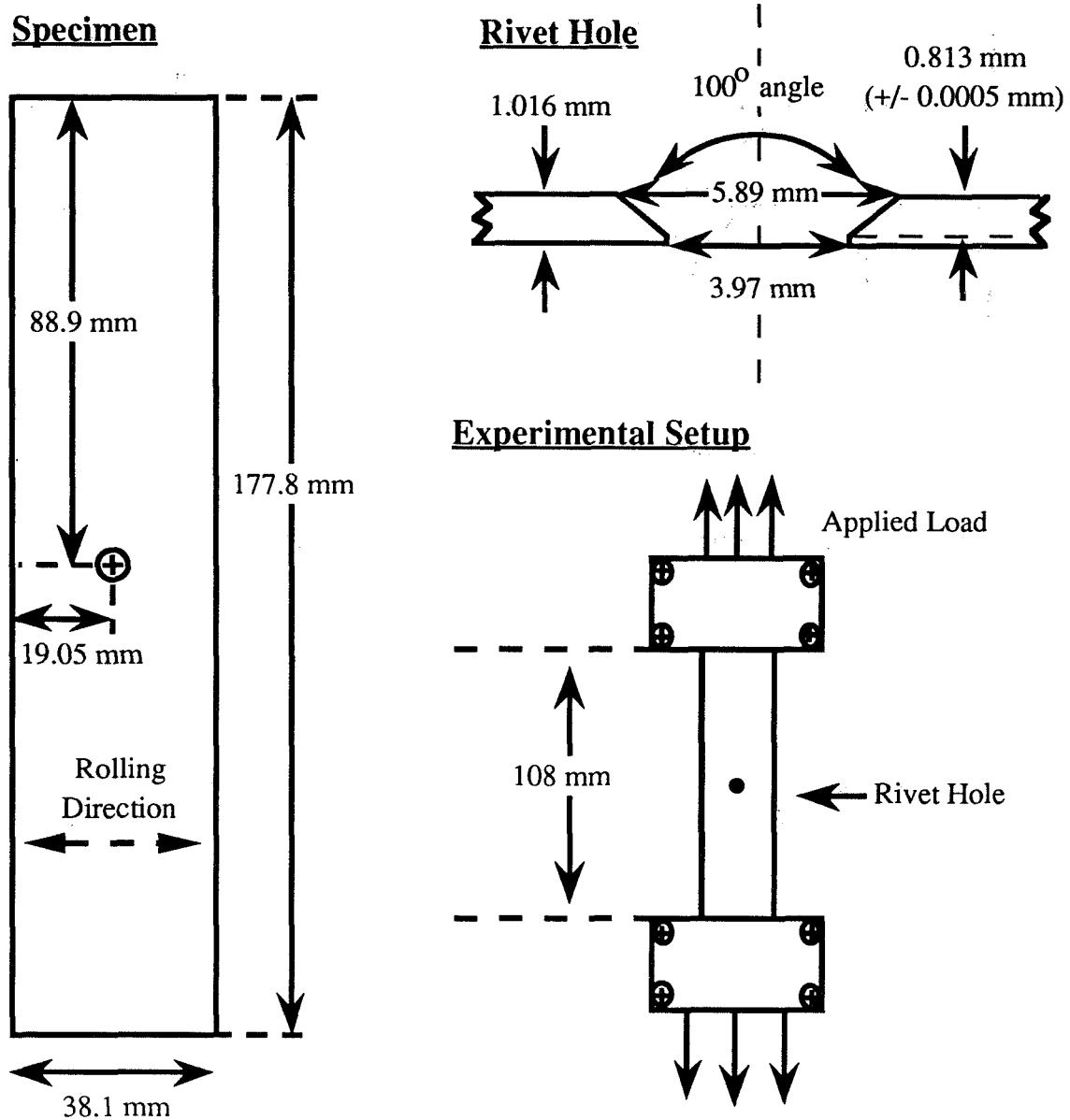


Figure 1. Specimen dimensions, rivet hole dimensions and experimental setup including loading and rolling directions.

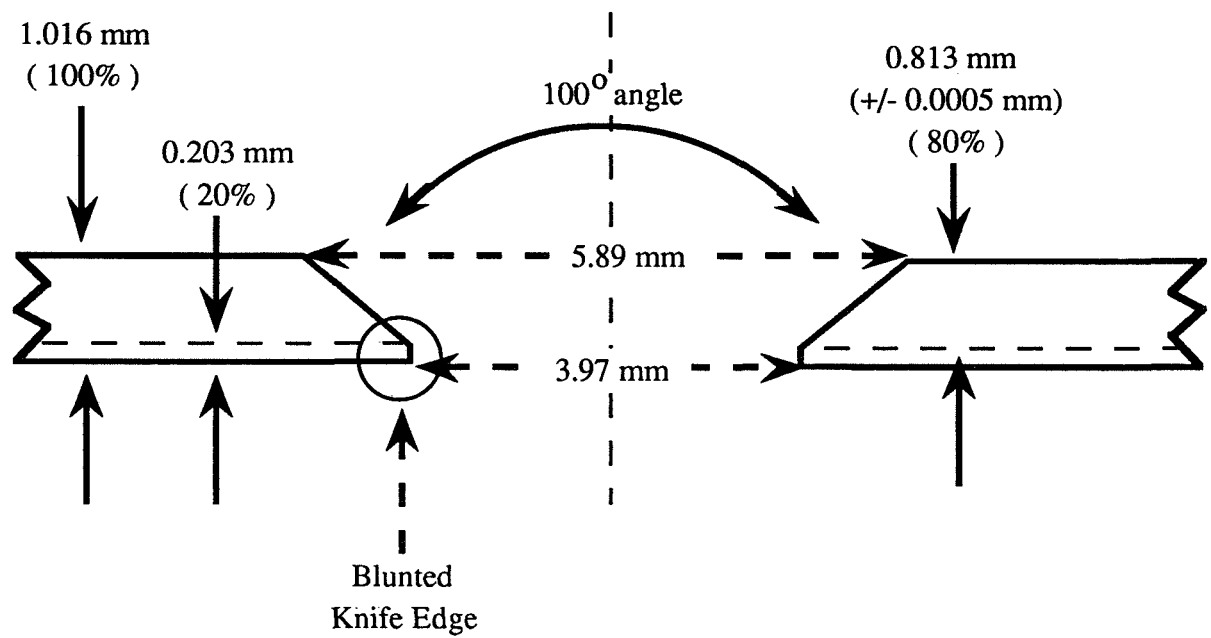


Figure 2. Rivet hole dimensions showing blunted knife edge.

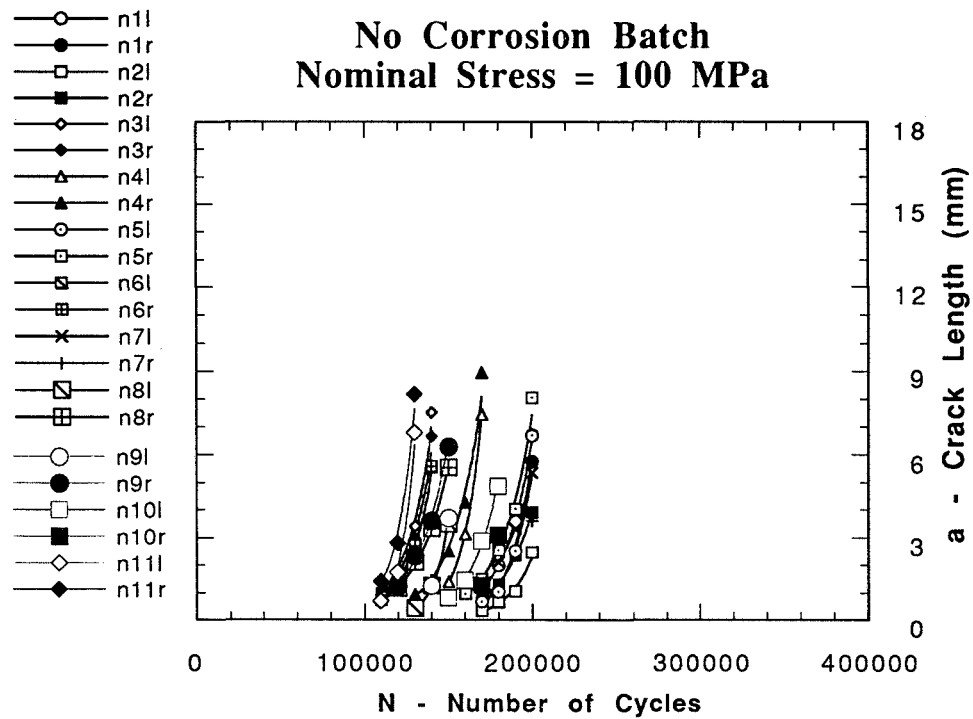


Figure 3. Crack length (a) vs. number of cycles (N) for specimens that were not exposed to salt spray.

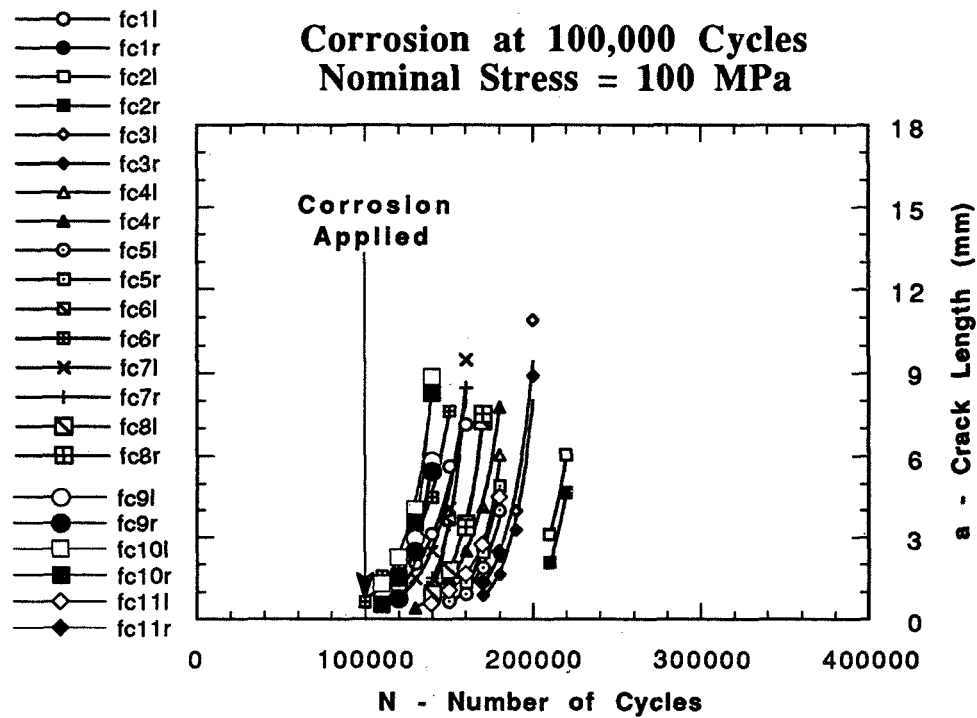


Figure 4. Crack length (a) vs. number of cycles (N) for specimens exposed to salt spray after 100,000 cycles.

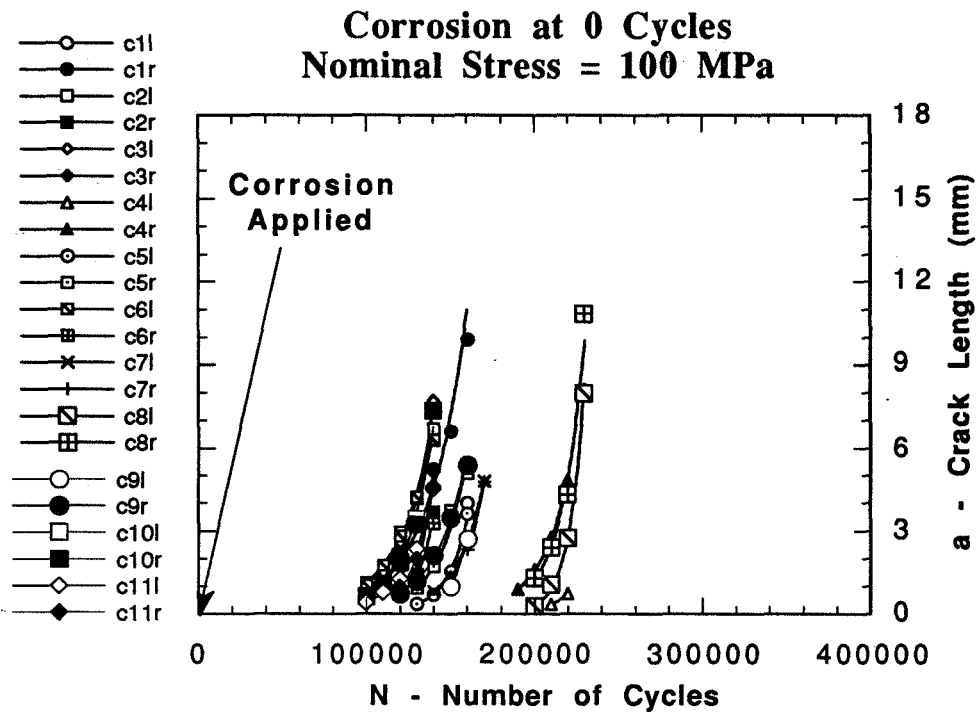


Figure 5. Crack length (a) vs. number of cycles (N) for specimens exposed to salt spray prior to cycling.

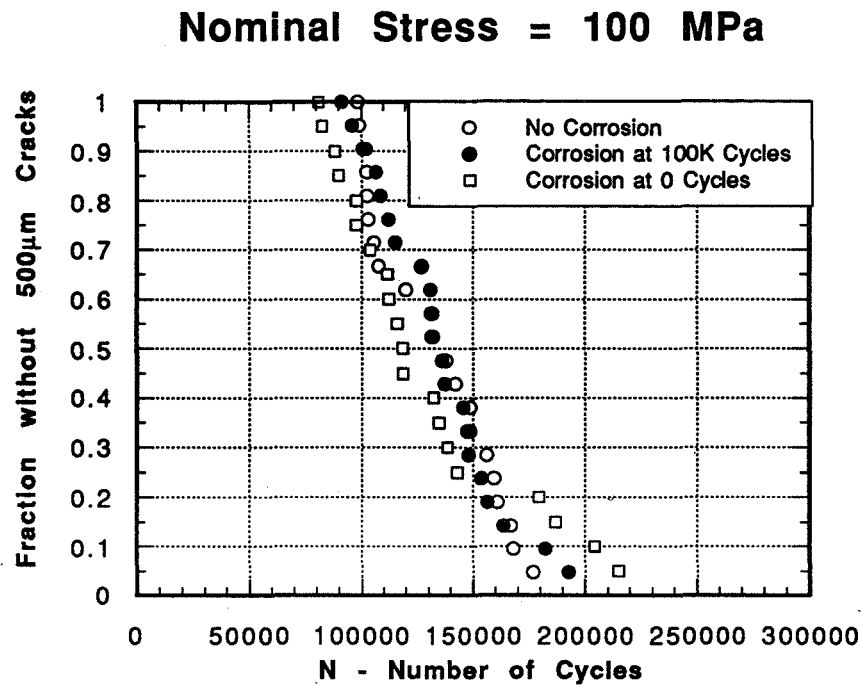


Figure 6. Fraction with no propagating 500 μ m cracks vs. number of cycles (N).

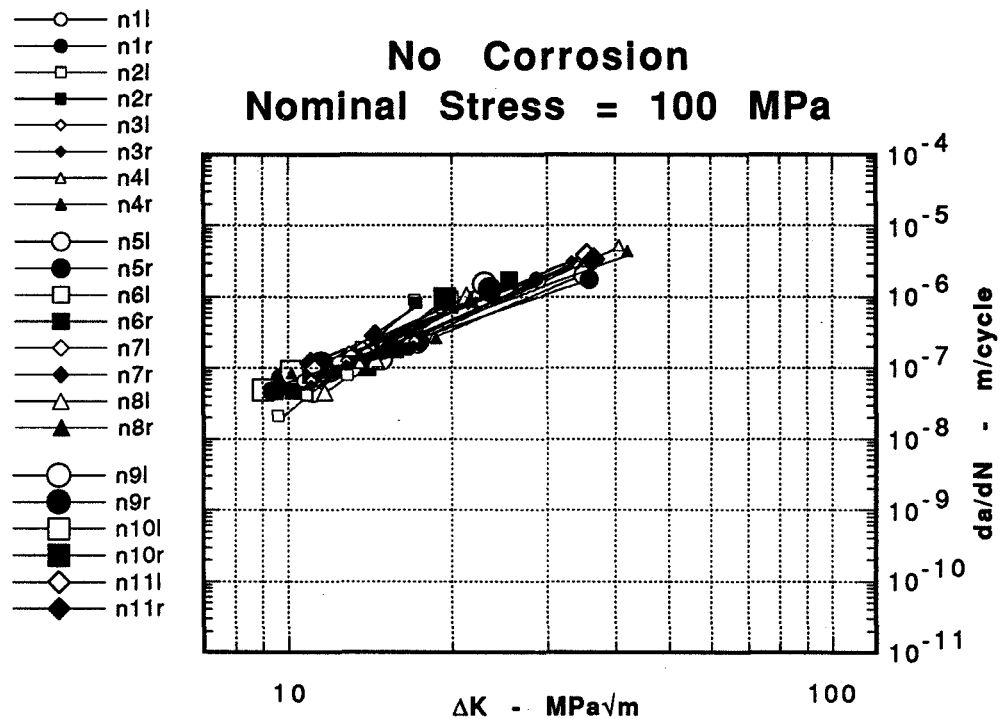


Figure 7. da/dN vs. ΔK for specimens not exposed to salt spray.

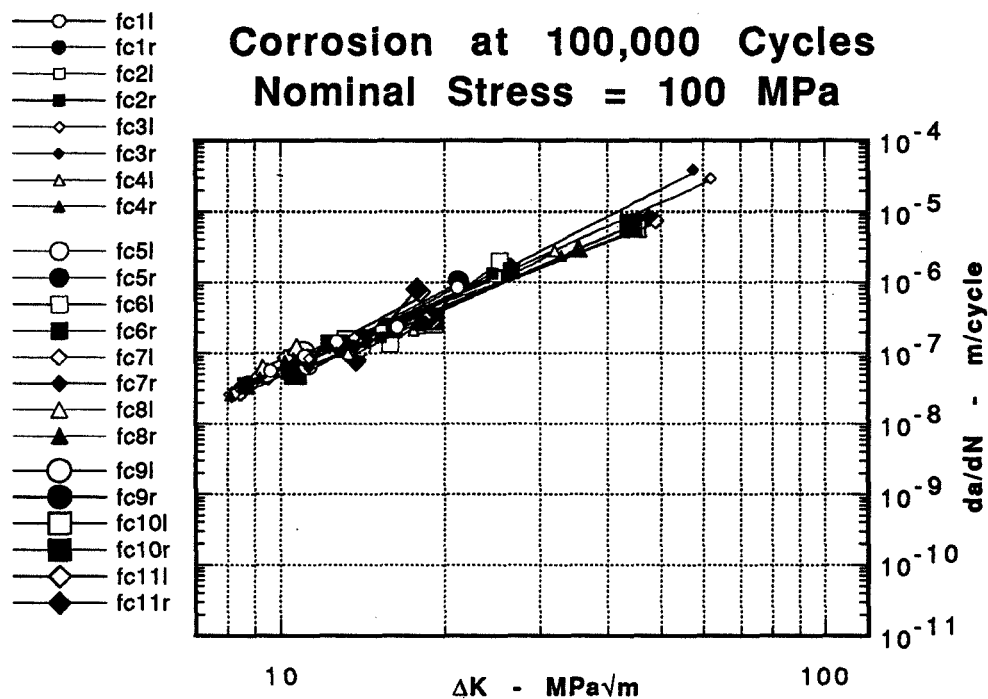


Figure 8. da/dN vs. ΔK for specimens exposed to salt spray after 100,000 cycles.

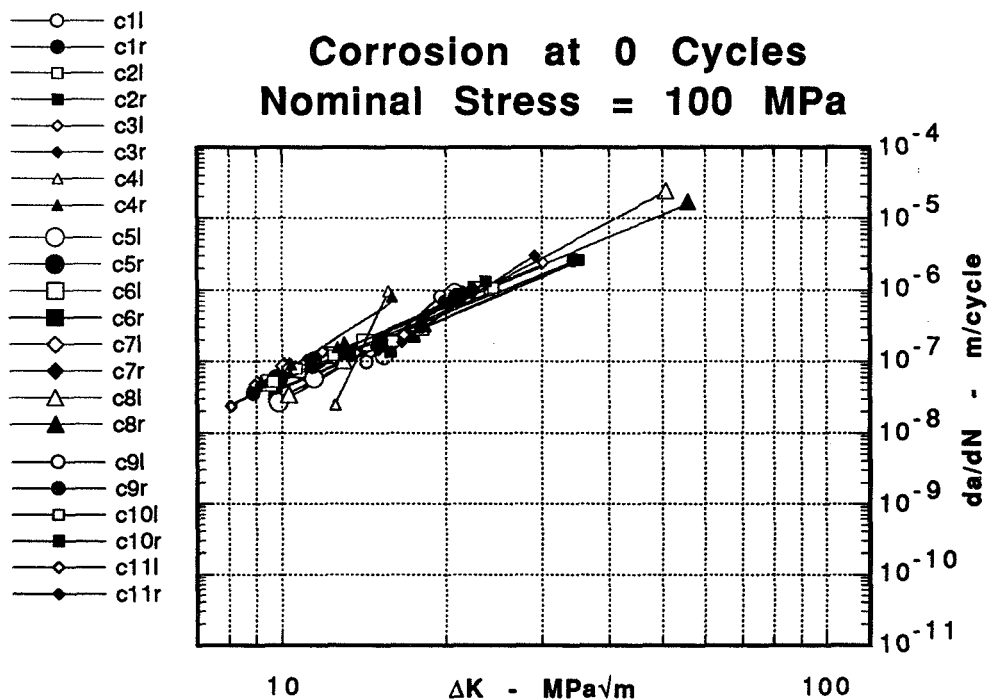


Figure 9. da/dN vs. ΔK for specimens exposed to salt spray prior to cycling.

Nominal Stress = 100 MPa

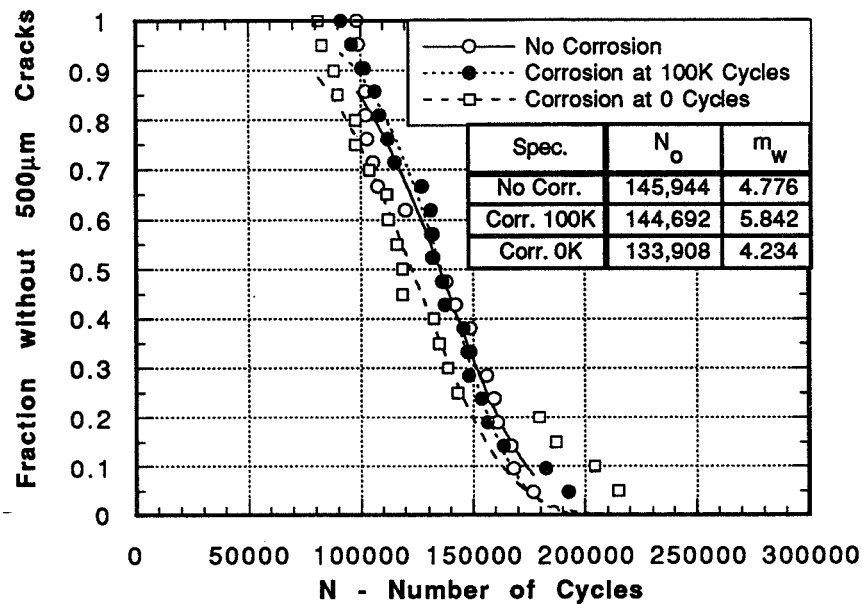


Figure 10. Fraction with no propagating 500 μm cracks vs. number of cycles (N) with curve fit to the Weibull equation.

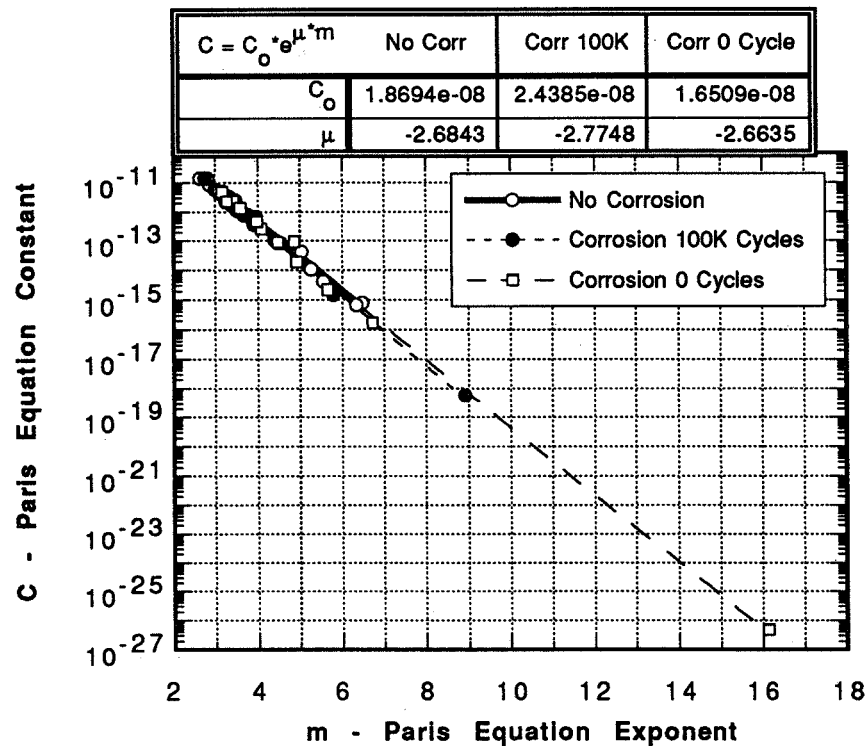


Figure 11. Paris equation constant (C) vs. Paris equation exponent (m).

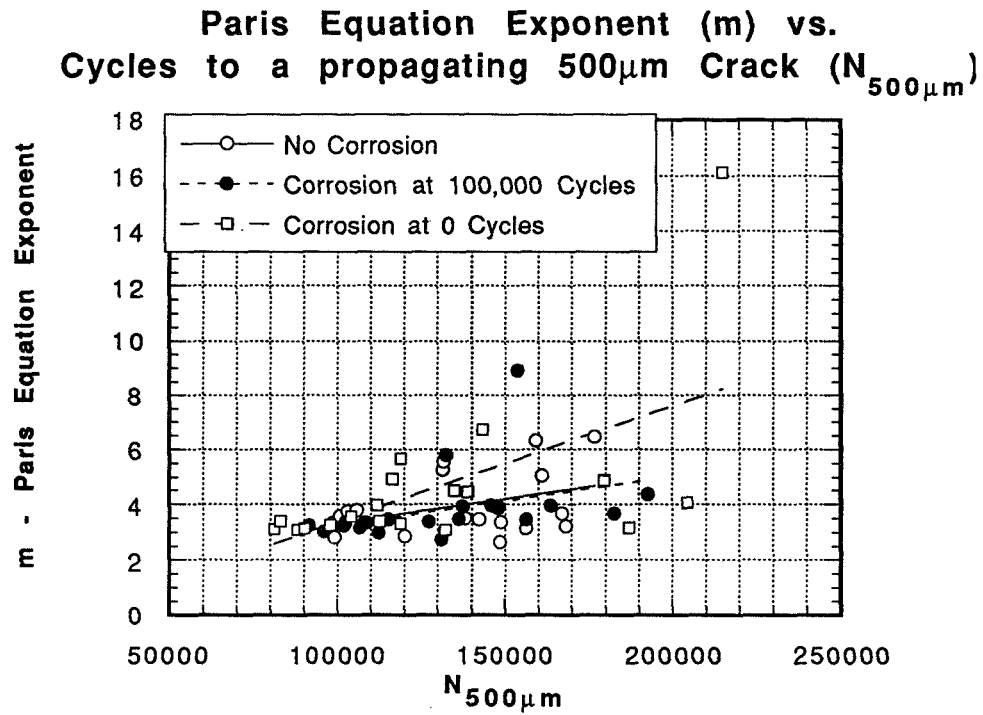


Figure 12. Paris equation exponent (m) vs. number of cycles to a propagating 500 μ m crack ($N_{500\mu m}$).

**DEVELOPMENT OF THE NASA/FLAGRO COMPUTER PROGRAM
FOR ANALYSIS OF AIRFRAME STRUCTURES**

R. G. Forman
National Aeronautics and Space Administration
Lyndon B. Johnson Space Center
Houston, Texas 77058

V. Shivakumar
Lockheed Engineering and Sciences Co.
2400 NASA Road 1
Houston, Texas 77058

J. C. Newman, Jr.
National Aeronautics and Space Administration
Langley Research Center
Hampton, Virginia 23665

SUMMARY

The NASA/FLAGRO (NASGRO) computer program was developed for fracture control analysis of space hardware and is currently the standard computer code in NASA, the U.S. Air Force, and the European Space Agency (ESA) for this purpose. The significant attributes of the NASGRO program are the numerous crack case solutions, the large materials file, the improved growth rate equation based on crack closure theory, and the user-friendly promptive input features.

In support of the National Aging Aircraft Research Program (NAARP), NASGRO is being further developed to provide advanced state-of-the-art capability for damage tolerance and crack growth analysis of aircraft structural problems, including mechanical systems and engines. The project currently involves a cooperative development effort by NASA, FAA, and ESA. The primary tasks underway are the incorporation of advanced methodology for crack growth rate retardation resulting from spectrum loading and improved analysis for determining crack instability. Also, the current weight function solutions in NASGRO for nonlinear stress gradient problems are being extended to more crack cases, and the 2-d boundary integral routine for stress analysis and stress-intensity factor solutions is being extended to 3-d problems. Lastly, effort is underway to enhance the program to operate on personal computers and work stations in a Windows environment. Because of the increasing and already wide usage of NASGRO, the code offers an excellent mechanism for technology transfer for new fatigue and fracture mechanics capabilities developed within NAARP.

INTRODUCTION

The NASGRO computer program was developed to provide an automated procedure for fracture control analysis of NASA space flight hardware and launch support facilities. In addition, it is applicable to analysis of non aerospace structures or hardware and may be used as a learning and research tool in fracture mechanics. The primary capability of the program is to calculate fatigue life and crack instability of cyclically or statically loaded structures which contain initial crack-like defects. The original version of NASGRO was completed in August 1986 and was revised in March 1989. General distribution of the program was initiated in 1990 by COSMIC*, the agency that distributes NASA-developed computer software.

Features of NASGRO that are new for the current version 2.0 include:

- 1) new and improved stress intensity factor solutions
- 2) an improved fatigue crack growth equation
- 3) expansion of the material properties file by over 300%
- 4) provisions for combining different blocks of a fatigue spectrum to form a load schedule
- 5) capacity for applying partial or fractional load cycles
- 6) option for plotting a vs. N during safe-life analysis
- 7) addition of sustained stress (da/dt) life analysis
- 8) capability for running the program by batch file as well as interactively
- 9) personal computer (PC) operating capability, including a Macintosh version
- 10) addition of boundary element method for performing stress analysis and obtaining stress intensity factor solutions
- 11) usage of weight function methods to analyze several crack cases with nonlinear stresses
- 12) improved user interface with ability to readily correct input errors

The program has been designed in a modular fashion, in order to allow for systematic revision and portability to various computer systems including main frame, personal computers, and work stations.

*COSMIC -(706)-542-3265
The University of Georgia
382 East Broad Street
Athens, Georgia 30602

VERSION 2.0 ADVANCED FEATURES

Crack Growth Relationship

Crack growth rate calculations in NASGRO 2.0 use a recently improved relationship* called the NASGRO 2.0 equation which is given by:

$$\frac{da}{dN} = \frac{C(1-f)^n \Delta K^n \left(1 - \frac{\Delta K_{th}}{\Delta K}\right)^p}{(1-R)^n \left(1 - \frac{\Delta K}{(1-R)K_c}\right)^q} \quad (1)$$

where N is the number of applied fatigue cycles, a is the crack length, R is the stress ratio, ΔK is the stress intensity factor range, and C , n , p , and q are empirically derived constants. Equation 1 produces da/dN - ΔK curves that are similar to those obtained from the equation used in earlier versions of NASGRO, but it provides a more direct formulation of the stress-ratio effect. Also, with Eq 1, variations in K_c and ΔK_{th} values have a reduced effect on the linear region of the curve, which produces a better fit to data. Figure 1 shows crack growth (da/dN - ΔK) data for aluminum-bronze CDA630, plotted together with a curve fit to Eq 1.

To analyze problems with combined loading, the stress intensity factor is expressed as:

$$K = [S_0 F_0 + S_1 F_1 + S_2 F_2 + S_3 F_3 + S_4 F_4] \sqrt{\pi a} \quad (2)$$

The stress quantities S_0 , S_1 , S_2 , and S_3 are the applied tension/compression, bending in the thickness and width directions, and pin bearing pressures. For the crack cases of biaxial tension/compression loading, the term S_4 is used for the stress in the lateral direction. The F values are geometric correction factors applicable to each type of applied stress and derived specifically for each crack case.

The program incorporates fatigue crack closure analysis for calculating the effect of the stress ratio on crack growth rate under constant amplitude loading. The crack opening function f , for plasticity-induced crack closure has been defined by Newman (ref. 1) as:

$$f = \frac{K_{op}}{K_{max}} = \begin{cases} \max(R, A_0 + A_1 R + A_2 R^2 + A_3 R^3) & R \geq 0 \\ A_0 + A_1 R & -2 \leq R < 0 \end{cases} \quad (3)$$

* Formulated for NASGRO 2.0 where different elements of the equation were obtained by Forman and Newman at NASA, de Koning at NLR, and Henriksen at ESA.

and the coefficients are given by:

$$A_0 = \left(0.825 - 0.34\alpha + 0.05\alpha^2\right) \left[\cos\left(\frac{\pi}{2} S_{\max}/\sigma_0\right) \right]^{\frac{1}{\alpha}} \quad (4)$$

$$A_1 = (0.415 - 0.071\alpha) S_{\max}/\sigma_0 \quad (5)$$

$$A_2 = 1 - A_0 - A_1 - A_3 \quad (6)$$

$$A_3 = 2A_0 + A_1 - 1 \quad (7)$$

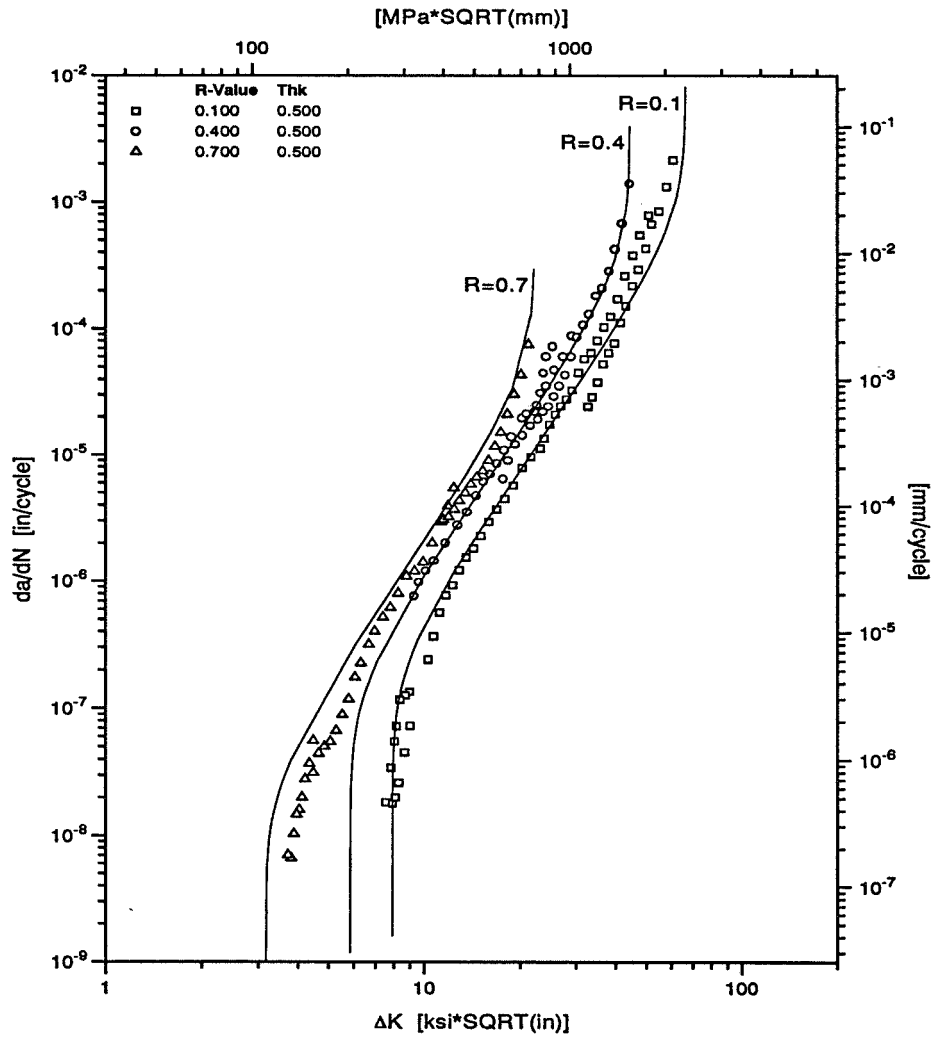


Figure 1 - Curve fit to Eq. 1 for aluminum-bronze CDA630

In these equations, α is a plane stress/strain constraint factor, and S_{\max}/σ_0 is the ratio of the maximum applied stress to the flow stress.

It should be noted that Eq. 1 may be reduced to the Paris equation with closure by setting $p=q=0$. The Paris equation with no closure can be further obtained by making $f=R$ which is the case when $S_{\max}/\sigma_0 = 1.0$ and $\alpha = 5.845$.

Threshold Stress Intensity Factor Range

The threshold stress intensity factor range in Eq 1, ΔK_{th} , is approximated as a function of the stress ratio, R , the threshold stress intensity factor range at $R = 0$, ΔK_0 , the crack length, a , and an intrinsic crack length a_0 , by the following empirical equation:

$$\Delta K_{th} = \Delta K_0 \left[\frac{4}{\pi} \tan^{-1}(1 - R) \right] \left(\frac{a}{a + a_0} \right)^{1/2} \quad (8)$$

This is a modification of a previous arctan rule (ref. 2) that takes into consideration the small crack effect demonstrated by Tanaka, et al. (ref. 3). The arctan form of the equation was chosen over the ΔK_{th} formulation included in the previous NASGRO version because it provides for a reduced nonlinear threshold behavior at negative stress ratios. Values of ΔK_0 are stored as constants in the NASGRO materials files, and a_0 has been assigned a fixed value of 0.004 in. (0.102 mm). This value agrees with an onset of short crack behavior at 0.025 in. (0.635 mm) which was coded into the previous NASGRO version and also agrees with the decrease in threshold with crack size shown by Tanaka for numerous steel alloys.

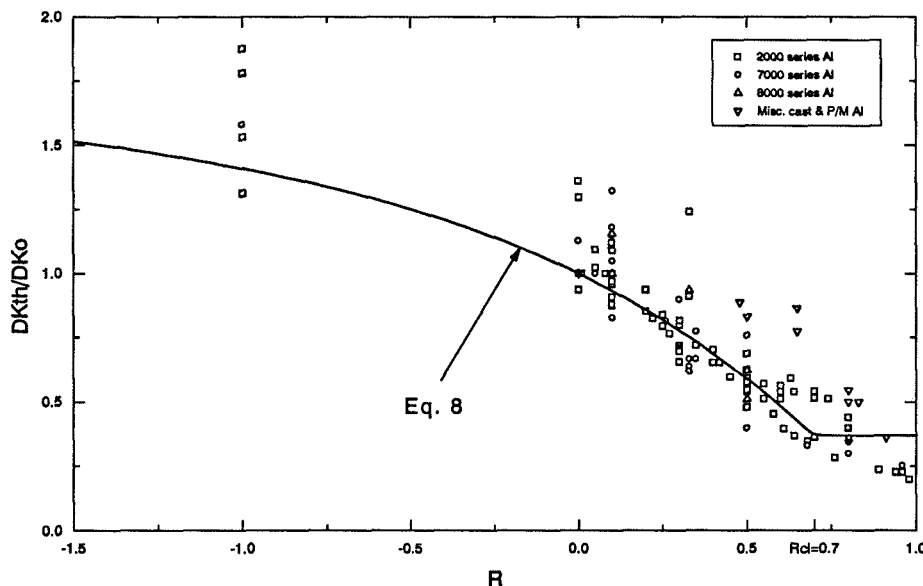


Figure 2 Crack growth threshold vs. R for aluminum

A comparison of ΔK_{th} vs. R data for several aluminum alloys with a curve fit according to Eq 8 indicates good agreement in Figure 2. As seen in this figure, ΔK_{th} approaches a constant value with increasing stress ratio. This effect is consistent with the decrease in crack closure observed at higher stress ratios, and thus R_{cl} has been defined as the stress ratio above which ΔK_{th} no longer changes (ref. 4). In most alloys, R_{cl} was determined to be about 0.7, so this value was used for materials when data at higher stress ratios were not available.

Stress Intensity Factor Solutions Using Weight Function Method

The weight function method was conceived by Bueckner (ref. 5) and Rice (ref. 6) and was used by several investigators to generalize the stress intensity factor solutions for cracks subjected to arbitrary loading. For one-dimensional variation of stresses acting across the potential crack plane, the basic relation between the stress intensity factor and the stress distribution is given by

$$K_I = \int_0^a \sigma_r(x) m(x, a) dx \quad (9)$$

where $\sigma_r(x)$ is the stress distribution on the crack face and $m(x, a)$ is the weight function which varies with the position coordinate x and the crack length a . Once the weight function is known, the stress intensity factor can be obtained by numerical quadrature. Variations in implementing the weight function scheme are essentially in the way the function $m(x, a)$ is obtained. It can be shown that

$$m(x, a) = \frac{H}{K} \frac{\delta u(x, a)}{\delta a} \quad (10)$$

where the stress intensity factor K and the crack face displacement $u(x, a)$ correspond to the same applied loading. H is a material constant and a is the crack length.

A new approach to computing the weight function was proposed by Shen and Glinka (ref.7, ref.8). In their approach, the weight function is assumed to be a four-term approximation in the form

$$m(x, a) = \frac{2}{\sqrt{2\pi(a-x)}} \left(1 + M_1 \left(1 - \frac{x}{a} \right)^{1/2} + M_2 \left(1 - \frac{x}{a} \right) + M_3 \left(1 - \frac{x}{a} \right)^{3/2} \right) \quad (11)$$

where the crack tip is at $x = a$. In principle, the three constants M_1 , M_2 , M_3 can be determined from three reference solutions for the stress intensity factors and there would be no need to obtain the displacement field. Thus, the inaccuracies resulting from numerical differentiation of the displacement field are avoided. The novelty of the present method introduced in NASGRO is in going another step forward by direct and accurate usage of numerical reference solutions in tabular form as opposed to using reference solutions in analytical form. Two important surface crack cases where reference solutions have been obtained by accurate finite element analysis, and the weight functions incorporated are shown in Figure 3. References 9 and 10 document the implementation of the weight function method for these two crack cases. In the solutions, the weight functions are given for the surface point or c -tip in our notation by

$$m_B(x, a) = \frac{2}{\sqrt{\pi x}} \left(1 + M_{1B} \left(\frac{x}{a} \right)^{\frac{1}{2}} + M_{2B} \left(\frac{x}{a} \right) + M_{3B} \left(\frac{x}{a} \right)^{\frac{3}{2}} \right) \quad (12)$$

and for the deepest point or a -tip, by

$$m_A(x, a) = \frac{2}{\sqrt{2\pi(a-x)}} \left(1 + M_{1A} \left(1 - \frac{x}{a} \right)^{\frac{1}{2}} + M_{2A} \left(1 - \frac{x}{a} \right) + M_{3A} \left(1 - \frac{x}{a} \right)^{\frac{3}{2}} \right) \quad (13)$$

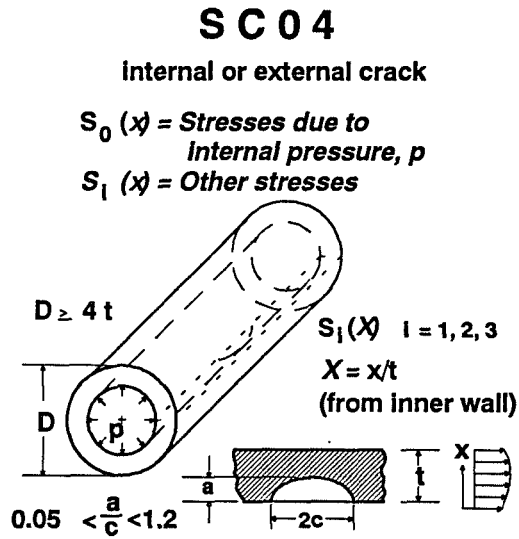
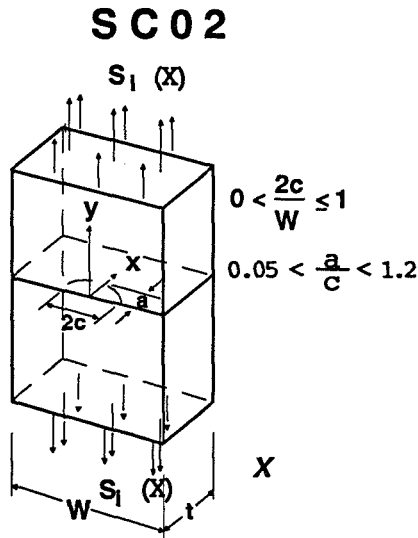
In order to solve for the three constants in each of the above two equations, two reference solutions and a third condition are used. The third condition for the c -tip is that the weight function vanishes at $x = a$ which gives

$$1 + M_{1B} + M_{2B} + M_{3B} = 0 \quad (14)$$

and the third condition for the a -tip is that the second derivative of the weight function be zero at $x = 0$ leading to

$$M_{2A} = 3 \quad (15)$$

For both crack cases, the two reference solutions used are the case of uniform tension and linearly decreasing stress as illustrated in Figure 4.



a. Surface crack in flat plate (SC02)

b. Axial surface crack in hollow cylinder (SC04)

Figure 3. Weight function crack case solutions

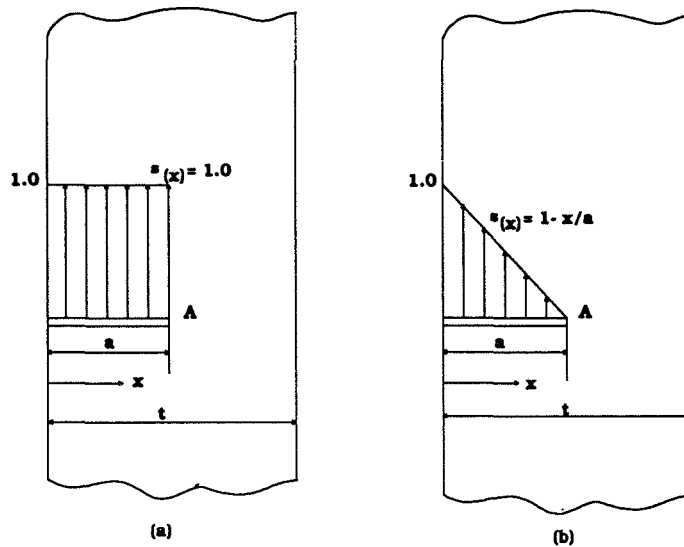


Figure 4 Two reference stresses used in the weight function method

As previously mentioned, more accurate weight function solutions were obtained by direct and accurate usage of numerical solutions in tabular form. Most surface and corner crack solutions in NASGRO 2.0 are in tabular form, both for weight function reference solutions and the other solutions, and were obtained by finite element analysis.

Unique nonlinear interpolation routines were developed for accurate and efficient table look-up of the tabular solutions. Since most tables are multi-dimensional (e.g., variables of a/c , a/t , $2c/w$ as in SC02 in Figure 3), preprocessing is performed after entry of geometry dimensions to derive a two dimensional table for a specific problem. Spline coefficients are calculated for this reduced table and reordered into a one-dimensional array for use in the crack growth analysis. This special preprocessing and reduction of array dimensions reduces the computer time to approximately a twentieth of that taken by a direct multi-dimensional and nonlinear interpolation procedure.

Boundary Element Method Analysis

The boundary element method (BEM) for solving complex geometry crack problems is particularly advantageous because only the interior and exterior boundaries must be discretized and no interior meshing is required such as for the finite element method. The BEM routine in NASGRO 2.0 is an advanced computational scheme for two-dimensional linear elastic analysis which overcomes the drawbacks of earlier developed BEM techniques. The analytical formulation and computer code for stress-intensity factor computations were developed by C. Chang (ref. 11) under a NASA grant from Langley Research Center. The user interface to the code and the formulation and coding for stress analysis capability were performed by V. Shivakumar and J. Beek, Lockheed Corporation, in support of the NASGRO development task at the Johnson Space Center.

For the crack analysis, the technique developed is essentially a modified boundary element scheme in which ordinary boundaries (i.e., boundaries other than crack surfaces) are modeled by conventional boundary integrals, while crack lines are modeled by integrals representing distributions of point dislocations and point loads. The formulation is similar to that given by Zang and Gudmundson (ref. 10), although the development and implementation differ in several important aspects which lead to a more complete and robust numerical strategy.

The advantage of the dislocation/BEM is that the solutions are highly accurate and efficient and the crack is only modeled by a single line of node points. The crack can be straight, curved, or even kinked. Quadratic type boundary elements are used which increase the accuracy of the results.

A summary of the BEM routine capabilities in NASGRO are as follows:

1. Arbitrary number of boundaries and cracks
2. Traction, displacement, and mixed boundary conditions
3. Internal and surface breaking cracks
4. Multiple material regions (e.g., sub structuring)
5. Simple modeling for multiple crack length solutions

Figure 5 shows the satisfactory accuracy for a very coarse mesh problem compared to a fine mesh modeled problem. The computer run time for the coarse mesh case was approximately 20 seconds for each crack length using an HP9000 work station.

Finally, Figure 6 illustrates the utility in NASGRO of applying the weight function analysis in conjunction with the BEM stress analysis. The problem illustrated is a stepped plate for which a solution is needed for a surface crack at the step radius location. The needed stress solution, $\sigma_z(x)$, on the crack plane without the crack is first calculated with the BEM 2-d routine; then the stress-intensity-factor solution is obtained using the weight function solution for a surface crack in a flat plate as shown earlier in Figure 3.

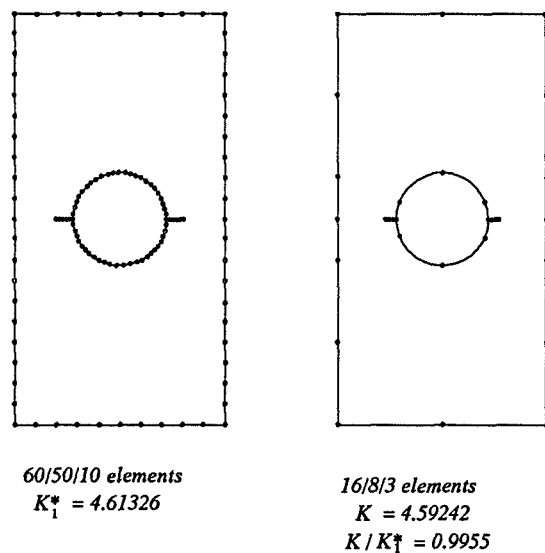


Figure 5 Comparison of fine versus coarse mesh solutions

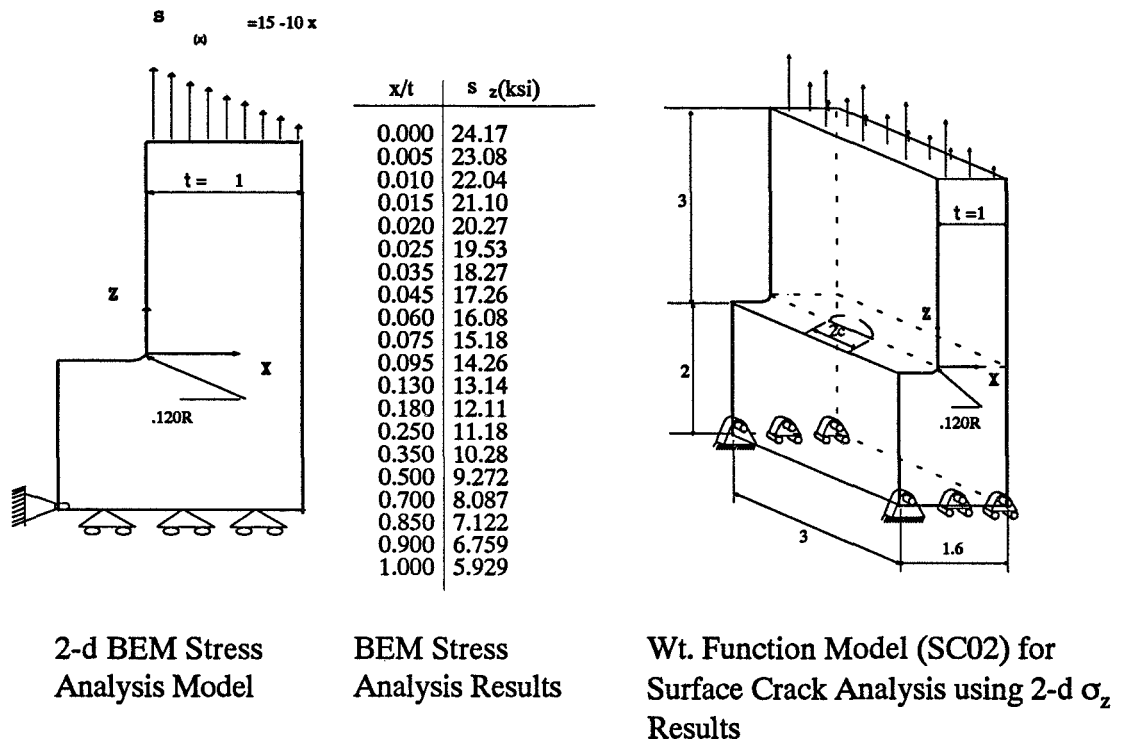


Figure 6 Application of BEM 2-d stress analysis in conjunction with 3-d weight function solutions

Future NASGRO Enhancements

Further development and improvements to NASGRO are covered by ongoing and scheduled long term task efforts. The future enhanced capabilities will be a function of improvements both in computer technology and in understanding and modeling fatigue crack growth and crack instability behavior.

Since analysis capabilities are strongly driven by computer power and speed, many improved features will be incorporated in NASGRO as computer capabilities increase. This is particularly applicable to 3-d BEM analysis, elastic-plastic analysis, and improved fatigue crack growth analysis which accurately accounts for variable amplitude loading. For instance, the current state-of-the-art in personal computer microprocessors is a speed of approximately 100 million instructions per second (MIPS). The expected capability for microprocessors in four more years is 2000 MIPS, or a 20 fold increase. In addition to this advancement, future development of NASGRO will be combined with improvements in computer operating systems, such as forthcoming advanced Windows type environments that will improve code portability and make NASGRO even more user-friendly.

The improvements in understanding crack growth behavior and development of appropriate modeling will be derived from research and development tasks now underway by NASA and other organizations, and these improvements will feed into future NASGRO versions. Both 3.0 and 4.0 versions are currently scheduled and will consist essentially of the following developments or enhancements:

3.0 VERSION - (1995)

- (1) Incorporate de Koning-Newman strip-yield & Willenborg retardation routines
- (2) Incorporate environmentally accelerated crack growth analysis capability
- (3) Expand weight function K solutions to many more crack cases
- (4) Expand materials properties file

4.0 VERSION - (1997):

- (1) Incorporate 3-d BEM routine
- (2) Enhance retardation & environmental da/dN routines
- (3) Crack instability analysis improvement (K-R curve or Newman 2-parameter)

On-Going Development Tasks/Studies

- (1) Small crack effects - constant amplitude & spectrum loading
- (2) ΔK_{th} behavior & modeling
- (3) New/more accurate crack case solutions
- (4) Code compatibility with different fatigue spectrum input formats
- (5) Compatibility with different computer systems & Windows environments

Conclusions

The NASGRO computer program offers an advanced state-of-the-art software package for aircraft damage tolerance and durability analysis. The code also offers an excellent mechanism for technology transfer for new fatigue and fracture mechanics capabilities developed within NAARP. The current 2.0 version offers numerous improvements over the previous 1989 version, and future improvements are planned for versions 3.0 and 4.0.

References

1. Newman, Jr., J. C.: A Crack Opening Stress Equation for Fatigue Crack Growth. *International Journal of Fracture*, Vol. 24, No. 3, March 1984, pp. R131-R135.
2. Forman, R. G.; and Mettu, S. R.: Behavior of Surface and Corner Cracks Subjected to Tensile and Bending Loads in Ti-6Al-4V Alloy. *Fracture Mechanics: Twenty-second Symposium*, Vol 1, ASTM STP 1131, H.A.H.A. Ernst, A. Saxena and D. L. McDowell, eds., American Society for Testing and Materials, Philadelphia, 1992, pp. 519-546.
3. Tanaka, K., Nakai, Y., and Yamashita, M.: Fatigue Growth Threshold of Small Cracks. *International Journal of Fracture*, Vol 17, No. 5, October 1981, pp. 519-533.

4. Schmidt, R. A. and Paris, P. C.: Threshold for Fatigue Crack Propagation and Effects of Load Ratio and Frequency. *Progress in Flaw Growth and Fracture Toughness Testing*, ASTM STP 536, American Society for Testing and Materials, Philadelphia, pp. 79-94.
5. Bueckner, H. F.: A Novel Principle for the Computation of Stress Intensity Factors. *Z. Angew. Math. Mech.*, 50, 1970, pp 129-146.
6. Rice, J. R.: Some Remarks on Elastic Crack-tip Stress Field. *Int. J. Solids Struct.*, 8, 1972, pp. 751-758.
7. Shen, G. and Glinka, G.: Determination of Weight Functions from Reference Stress Intensity Factors. *Theoretical and Applied Fracture Mechanics*, 15, 1991, pp. 237-245.
8. Shen, G. and Glinka, G.: Weight Functions for a Surface Semi-elliptical Crack in a Finite Thickness Plate. *Theoretical and Applied Fracture Mechanics*, 15, 1991, pp. 247-255.
9. Forman, R. G., Mettu, S. R., and Shivakumar, V.: Fracture Mechanics Evaluation of Pressure Vessels and Pipes in Aerospace Applications. *PVP - Vol. 241, Fatigue, Fracture and Risk*, Editors: W. H. Bamford, H. Mehta, B. A. Bishop, J. H. Phillips, and F. W. Brust, American Society of Mechanical Engineers, pp. 25-36, 1992.
10. Raju, I. S., Mettu, S. R., and Shivakumar, V.: Stress Intensity Factor Solutions for Surface Cracks in Flat Plates Subjected to Nonuniform Stresses. *Fracture Mechanics: Twenty Fourth Symposium*, ASTM STP 1207, American Society for Testing and Materials, Philadelphia, 1994.
11. Chang, C.: A Boundary Element Method for Two Dimensional Linear Elastic Fracture Analysis. *Ph.D Dissertation, The University of Texas at Austin*, December 1993.
12. Zang, W. and Gudmundson, P.: A Boundary Integral Method for Internal Piece-wise Smooth Crack Problems. *International Journal of Fracture*, 38, pp. 275-294, (1988).

Space Shuttle Fatigue Loads Spectra for Prelaunch and Liftoff Loads*

Judith Goldish
Rockwell Space Systems Division
Downey, CA

Raphael Ortasse **
Rockwell Space Systems Division
Downey, CA

SUMMARY

Fatigue loads spectra for the prelaunch and liftoff flight segments of the Space Shuttle were developed. A variety of methods were used to determine the distributions of several important parameters, such as time of exposure on the launch pad, month of launch, and wind speed. Also, some lessons learned that would be applicable to development of fatigue loads spectra for other reusable space vehicles are presented.

INTRODUCTION

Fatigue loads spectra for the shuttle.

The mission profiles for the Space Shuttle are unique because it is the only reusable space vehicle being flown today. This paper presents a discussion of the development of mission profiles for the prelaunch and liftoff flight segments of the space shuttle mission. The prelaunch and liftoff segments are not similar to anything experienced by a conventional aircraft. The methods developed for them may be useful examples for other programs.

* Work done on contract at Rockwell Space Systems Division, NAS9-18500

** Team lead engineer. Other team members included: Richard L. Stauf, Saroj Gupta, Brent A. Mann, Daniel D. Paul, Lawrence V. Purtle, William Harvey. Also Lawrence Tischner, Rudy Loera, Wendy W. Chang, Ramon C. Perez, Arthur Leong, Anne Armstrong, Scott Foust, Walter Miller, Lavant Wooten, and others.

For both prelaunch and liftoff, the starting point for the fatigue loads method was the methods already being used for development of design loads. In both cases, the tools for the design method were already in place, well designed, mature, and flexible. Even so, a considerable amount of effort was needed to adapt these tools for use in developing fatigue loads. Some reasons why this effort was needed are:

- Fatigue requires a time history of the loads where design requires only the single maximum load.
- In development of design loads generally every load case is desired to be a "worst" case. For fatigue, most cases should be "nominal" cases with only a certain number of occurrences of design type loads in the lifetime.
- The ground rules and assumptions for fatigue are different from those for design.

In the fatigue loads spectra process flow, Figure 1, the material covered in this paper falls within the first five steps.

The Space Shuttle

The Space Shuttle is designed to launch and retrieve a variety of payloads into and from earth orbit. The launch configuration consists of the Orbiter Vehicle, the External Tank (ET), and two solid rocket boosters (SRB). The Space Shuttle Vehicle is launched in a vertical attitude by means of the Space Shuttle Main Engines (SSME's) and two SRB's. The orbiter lands horizontally, similar to conventional aircraft. Figure 2 shows the configuration of the Space Shuttle. Figure 3 depicts a typical Shuttle mission. Prelaunch and liftoff, which are discussed in this paper, are shown in the lower left of the figure.

Fatigue generally requires looking at the entire vehicle mission including all flight segments because different components and parts are critically loaded in different flight segments.

PRELAUNCH

The Prelaunch Flight Segment

Prelaunch is the period from arrival of the Space Shuttle on the launch pad to main engine ignition. The main sources of loads are gravity, wind, and the Space Shuttle Main Engines (SSME's). Gravity itself is not cyclic in nature, but the movement of the structure

due to wind loads causes the center of gravity to shift and causes freeplay in the joints between the components, and these effects do cause cyclic type loading. However, both of these effects were already included in the computer program used for prelaunch analysis for design, so no additional effort was needed for fatigue.

The effect of wind loading on the Shuttle while on the launch pad is like a distributed load on a cantilever beam. On much of the structure the wind loads are not significant compared to loads during other flight segments. However, main engine thrust together with wind designs the aft skirt of the Solid Rocket Boosters (SRB's), the bolts that connect the SRB's to the Mobile Launch Platform (MLP), and the aft part of the SRB's.

For design loads, synthetic winds are used which are especially constructed to cause the greatest structural response. However, for fatigue, measured winds from Kennedy Space Center (KSC) were used. The issues that needed to be decided were: what winds to use, what the distribution should be (i.e. how many occurrences of the different wind speeds), and how long the total exposure time should be.

Time on the Launch Pad

The amount of time that the shuttle spends on the launch pad, exposed to wind, before launch affects the number of cycles of wind loading. The distribution of duration of stay on the launch pad is based on past experience. The past experience data do not fit any of the common distribution functions.

The time that the Shuttle has been exposed to the winds on the launch pad before a mission in the past has ranged from fourteen days to 161 days. The nominal time on the launch pad is 21 days currently, formerly 14 days. A launch delay and consequently longer stay may be caused by many types of weather problems, hardware problems, payload problems, conflicting launches from Cape Canaveral, etc. The maximum design case is a 180-day exposure, which by the ground rules was assumed to occur once in the fatigue lifetime. Inasmuch as neither the historic data for launch pad stay nor the factors that can affect it fit any of the common distribution functions, our approach to launch pad stay time was to use a probability of exceedance curve. The probability in the set of previous stays of exceeding each length of stay was plotted.

Table 1 shows the missions in the order that they were flown and the number of days the SSV was on the launch pad before the launch occurred. The average time on the launch pad for a mission was 42.0 days with a standard deviation of 31.2 days. Table 2 shows the months in which that stay occurred for each of the 41 launches.

Figure 4 shows the time on the launch pad for each mission in the order that they were flown. Neither a normal, polynomial, nor a Rayleigh distribution fits this data. A probability of exceedance method was used to derive the distribution of time on the launch pad. Figure 5

shows the probability of a stay on the launch pad exceeding a given length of time. This probability is derived from the 41 missions considered in the present analysis. In addition Figure 5 shows a line fitted through the measured data of the number of days stay on the launch pad. The line is the best fit to the log probability of exceedance that goes through the point giving 180 days a probability of 1 in 100 or 0.01, per a ground rule. Table 3 shows the probability of exceedance and the probability of a given stay on the launch pad from this curve, and Table 4 shows the number of missions in the 100-mission lifetime with each length of stay.

Month of Launch

The month of launch affects the winds encountered during liftoff and ascent. The missions are not evenly distributed among the months. Figure 6 presents the number and percent of all the 41 launches that occurred in each month of the year. We assumed, although no reason was known for the uneven distribution, that there were enough missions in the database that the distribution represented an actual bias, and therefore we distributed the month of launch according to the past missions rather than distributing them evenly between all the months. The distribution of month of launch that results from these numbers, though based on 41 actual missions and statistically projected to 100 missions, seemed biased for the months of April, September and November. At the direction of our customer, we revised the distribution on the following basis (see Figure 7):

1. The actual missions STS-1 through STS-40 as flown are used as the first 41 missions.
2. The three missions flown after STS-40 are used.
3. Forty-eight missions from the NASA flight manifest are used. (This manifest is a Flight Assignment Working Group's assessment of the NASA baseline for the future).
4. Eight missions are projected, based on (1) through (3).

The 180-day stay on the launch pad was placed to start in June, so that the stay on the launch pad will go through the months during which hurricanes are most likely to occur at Cape Canaveral. Furthermore, it was assumed that the Space Shuttle Vehicle is most likely to encounter a hurricane intensity wind during the 180-day stay on the launch pad.

After the length of stay on the launch pad and the month of launch for each mission were established, the 100 fatigue missions were sequenced in a random order.

Winds

For the fatigue loads spectra, measured winds were used. There was some difficulty in obtaining "nominal" wind data even though a large amount of wind data from Kennedy Space Center (KSC) is available. The distribution of the maximum hourly, daily, and monthly winds are available, but of course this cannot be converted into a forcing function. Also measured wind velocities and directions measured at 0.1-second intervals over time periods of about ten to twenty minutes in 1967-1968 were available for each month of the year, and these were used. These winds are somewhat conservative since the measuring instruments were especially likely to be turned on when a strong wind was expected. There is no way to know how the measured intervals differed from other intervals, or how typical the winds were in the years 1967-1968. Even if continuous long-term wind measurements had been available, they would probably have overstrained our computer resources at the time.

The computer program that calculates prelaunch loads, ASCENT, can handle forcing functions with up to 300 time points. Since the KSC winds were measured at a rate of one-tenth of a second, the winds were divided into segments of thirty seconds each. The segments were classified by the maximum wind speed in each segment. A Fast Fourier Transform was performed on each segment and the segment from each class with the most content at the first cantilever frequency of the Shuttle, 0.267 Hz, was selected. This resulted in the selection of a set of 30-second long wind segments. The ground rules called for one occurrence of a 47-knot wind and one occurrence of a 74-knot (hurricane speed) wind. A segment with a lower wind speed was scaled up to make these two segments.

The winds were taken from three directions, north, east, and south. (At that time it was believed that the launch tower effectively blocked winds from the west and therefore these could be ignored, so this was incorporated into the ground rules. Recent measurements during a storm showed that this may not be true in all cases.) The wind speed measurements in the segments were converted to Shuttle forcing functions.

The distribution of the wind segments versus wind speed was a Gumbel distribution with $\alpha=3.48$ and $\gamma=7.42$. This distribution was developed by NTI Corp. for NASA's Marshall Space Flight Center (MSFC). Note that the distribution is not dependent on the month in which the wind was originally measured or on the length of stay on the launch pad. Only the peak wind speed in the segment was considered in the distribution. The distribution of wind direction among the four cardinal directions was supplied by Marshall Space Flight Center as follows:

<u>Direction</u>	<u>North (0°)</u>	<u>South (90°)</u>	<u>East (180°)</u>	<u>West (270°)</u>
Wind speed:				(not used)
< 24 knots	24%	33%	25%	18%
≥ 24 knots	34%	22%	22%	22%

LIFTOFF

Liftoff Missions

Liftoff includes the ignition and buildup of the Space Shuttle Main Engines (SSME's), the ignition and buildup of the two Solid Rocket Boosters (SRB's), the breaking of the bolts that attach the SRB's to the Mobile Launch Platform (MLP), and the ascent of the Space Shuttle until it clears the launch tower.

The mission profiles for liftoff included:

- Nominal cases
- Design cases included in the ground rules:
 - Zero payload
 - Heavy payload (65,000 lb)
 - Engine out (one SSME shuts down after SRB ignition)(a design certification case)
- Design cases added to bring the set of fatigue loads close to the design certification set of 800 cases, identified by comparing body loads envelopes and attach loads:
 - Another engine-out on the other side of the Orbiter
 - Tuned gust winds instead of measured winds - one case for each cardinal direction, four altogether, to fill in SRB body loads envelopes. 34-knot tuned gust winds except South is 24-knots.
 - Seven cases to get design loads for the SRB and SRB/ET attach load indicators
- Non-flight conditions that are design certification conditions and hence were included in the ground rules:
 - One Flight Readiness Firing (FRF)
 - Two Pad Aborts (SSME's build up, then shut down)
(note: number of occurrences was established by the Loads and Dynamics Panel)

The system and method that were used for the design liftoff loads (DCR3) were also used for the fatigue loads. The existing cases could not be used because they were only run for ten seconds and we needed to run for fourteen seconds in order to get all the load cycles. Also, the fatigue loads used measured winds instead of synthetic winds, and measured SSME thrust instead of Main Propulsion Test Article (MPTA) thrust profiles.

Nominal Liftoff Fatigue Loads Cases

One hundred randomly nominally dispersed liftoff cases were created by using a "Monte Carlo" computer program to randomly assign values to the dispersions of those parameters that affect liftoff loads on the shuttle. Each parameter is taken as having either a normal or a random distribution. For each parameter, the mean and standard deviation (sigma) value are known. Then the computer program randomly assigns a value of from -4σ to $+4\sigma$ for each parameter with a probability distribution that is a normal distribution. (Note: very few values were over $\pm 3\sigma$.) Examples of these parameters are thrust mismatch between the right and left hand side boosters, SRB thrust misalignment, and time to 90% SSME thrust. The forcing functions representing SRB thrust are created from these parameters. Also the Monte Carlo program randomly selects from the available Orbiter models, SSME thrust measured profiles, and SSME measured sideloads for each mission.

Once the nominally dispersed cases are made, one design load case for each type of load is needed in the lifetime of one hundred missions. The design cases that are needed are identified by comparing the fatigue liftoff cases to the set of design liftoff cases, checking the body loads envelopes and the attach loads.

The body loads envelopes show the maximum and minimum load (three shears and three moments) at each node on the Orbiter fuselage and on the SRB. Where the fatigue body loads envelope fell significantly short of the design body loads envelope, additional fatigue cases were run to fill out the envelope. The attach loads were also compared for the component interfaces and the load indicators. Where the design certification load was 50% or more of the allowable load and the fatigue load was more than 20% below the design certification load, an additional fatigue case was considered necessary. Seven more cases were added by this criterion.

CONCLUSION

The result was that for both prelaunch and liftoff, a set of load cases with a good mix of nominal load cases, plus sufficient design load cases to ensure an occurrence of the design load for every component, were generated. This was achieved by:

- 1) Analysis of the program design certification requirements, as defined in Volume X.
- 2) Analysis of the shuttle missions to date
- 3) Checking of both the extrema and the distribution of the loads in the output loads cases and addition of cases to the database as needed.

LESSONS LEARNED

The experience of generating fatigue loads spectra for the space shuttle revealed a number of points which would be applicable to other programs and especially other reusable space vehicles.

1. Determine the analysis ground rules and assumptions as early as possible. (The tradeoff here is that it is often necessary to see some results before being able to decide whether assumptions are valid).
2. Plan to use tools and programs that are already in place for design loads analysis. But recognize that modifications will almost certainly be needed.
3. Plan for computer dataset storage. Fatigue files take up a great deal of space because
 - 1) For fatigue, essentially the entire loads analysis is repeated, so there will be a full set of files for each flight segment; and
 - 2) Fatigue files are often larger than their design counterparts; for example, fatigue liftoff datasets are larger than design liftoff datasets because they run for fourteen seconds instead of ten seconds.
 - 3a. Because of the enormous volume of data, it is vital to establish a consistent yet flexible naming convention for files before generating any data. Otherwise it may (will!) be impossible to find the data later.
 - 3b. Move files from on-line to tape storage continuously throughout the fatigue process as soon as they are not needed daily; don't wait until the end of the task. Waiting results in very high storage costs; a huge volume of dataset storage jobs at the end of the task; and a catalogue of files too large to navigate through.
4. Loads for the entire vehicle mission, including all flight segments, must be generated for fatigue. Generally for design there is a different system or tool for each flight segment because different forces are significant for each flight segment. Generally new loads cases must be generated for fatigue. The budget and schedule need to take account of the time to generate the cases of the cost of computer use and data storage, and of time to organize the information.
5. There are advantages to using a stress spectrum, rather than a loads spectrum, for fatigue/fracture analysis. A stress spectrum is less complicated than a loads spectrum because the loads spectrum must include time-consistent loads in all other degrees of freedom at the location, and sometimes at other locations as well, while a stress spectrum does not. Furthermore, in locations where the stress is strongly influenced by the loads in more than one of the principal directions, the peaks of the loads may not be peaks of stress.

In order to generate a stress spectrum, coefficients for converting load to stress must be provided by the stress group for each desired location. The coefficients are generated

either by unit-load runs of finite-element models, or by hand calculation. Loads must be converted to stresses *before peak counting*, and the schedule for provision of these coefficients must reflect this.

6. Close coordination between fatigue loads personnel and stress personnel is essential from the beginning of the program in order to ensure that:

- All the necessary locations and types of spectra are identified from the start
- The spectra generated are what the stress analysts need to do their work
- There is complete understanding and agreement about what each spectrum represents
- Unnecessary spectra are not generated, saving time and money.

7. A strategy of continuous evolutionary improvement is well suited to the task of fatigue loads spectra generation. Under Rockwell's Continuous Improvement (ci) program, there were four or five meetings of the Fatigue Product Improvement Team specifically to scrutinize the fatigue loads spectra process and to seek places in the process that were inefficient, inadequate, or offered potential for problems. The meetings gave the team members a chance to step back from the "trees" and see the "forest". Ideas developed in the meetings resulted in improvements that dramatically cut the cost and time for the analysis. Particularly significant were the concept of a single, compressed "Universal Database" output format and the automation of several steps of the fatigue spectra process.

Not only did significant ideas come from the meetings, but they gave team members a start in the habit of constantly looking for areas that needed improvement and developing improvements.

8. Last, but far from least, the fatigue loads spectra were very much a team effort. Team members checked each other's results, assisted each other with computer programming, "bounced" ideas off each other, and generally increased the morale of the whole team. It is not exaggeration to say that this task could not have been performed without a team approach.

Table 1. Mission and Time on Launch Pad

Flt Seq	Mission	Orbiter OV-	Days on Pad	Days on pad for:				Launch Date	On pad Date
				OV-102	OV-103	OV-104	OV-099		
1	STS-01	102	105	105				4/12/81	12/28/80
2	STS-02	102	74	74				11/12/81	8/30/81
3	STS-03	102	34	34				3/22/82	2/16/82
4	STS-04	102	33	33				7/27/82	6/24/82
5	STS-05	102	52	52				11/11/82	9/20/82
6	STS-06	099	126				126	4/4/83	11/29/82
7	STS-07	099	24				24	6/18/83	5/25/83
8	STS-08	099	29				29	8/30/83	8/1/83
9	STS-09	102	39	39				11/28/83	10/20/83
10	STS-11	099	22				22	2/3/84	1/12/84
11	STS-13	099	19				19	4/6/84	3/18/84
12	STS-14	103	78		78			8/30/84	6/13/84
13	STS-17	099	23				23	10/5/84	9/12/84
14	STS-19	103	17		17			11/8/84	10/22/84
15	STS-20	103	20		20			1/24/85	1/4/85
16	STS-23	103	14		14			4/12/85	3/29/85
17	STS-24	099	16				16	4/29/85	4/13/85
18	STS-25	103	15		15			6/17/85	6/2/85
19	STS-26	099	14				14	7/29/85	7/15/85
20	STS-27	103	31		31			8/27/85	7/27/85
21	STS-28	104	34			34		10/3/85	8/30/85
22	STS-30	099	15				15	10/30/85	10/15/85
23	STS-31	104	15			15		11/26/85	11/11/85
24	STS-32	102	42	42				1/12/86	12/1/85
25	STS-33	099	38				38	1/28/86	12/21/85
26	STS-26R	103	88		88			9/29/88	7/3/88
27	STS-27R	104	31			31		12/2/88	11/1/88
28	STS-29R	103	39		39			3/13/89	2/2/89
29	STS-30R	104	44			44		5/4/89	3/21/89
30	STS-28R	102	25	25				8/8/89	7/14/89
31	STS-34	104	51			51		10/18/89	8/28/89
32	STS-33R	103	27		27			11/22/89	10/26/89
33	STS-32R	102	43	43				1/9/90	11/27/89
34	STS-36	104	35			35		2/28/90	1/24/90
35	STS-31	103	39		39			4/24/90	3/16/90
36	STS-41	103	31		31			10/5/90	9/5/90
37	STS-38	104	75			75		11/15/90	2 TIMES
38	STS-35	102	161	161				12/2/90	2 TIMES
39	STS-39	103	49		49			4/28/91	2 TIMES
40	STS-37	104	22			22		4/5/91	3/15/91
41	STS-40	102	34	34				6/5/91	5/2/91
Total (days)			1723	642	448	307	326		
Average (days)			42.0	58.4	37.3	38.4	32.6		

Standard Dev 31.2

42.024 0

Total Time on Pad = 1723 days

42.024 18

Average Time on Pad = 42.0 days

Standard Deviation = 31.2 Days for 41 Missions STS-1 through STS-40

Table 2. Time on Launch Pad for Each Mission and the Month in which it Occurred

Flt	Orbiter OV-	31 Jan	28 Feb	31 Mar	30 Apr	31 May	30 Jun	31 July	31 Aug	30 Sept	31 Oct	30 Nov	31 Dec	STS-
1	102	31	28	31	12								3	1
2	102								1	30	31	12		2
3	102		12	22										3
4	102						6	27						4
5	102									10	31	11		5
6	099	31	28	31	4							1	31	6
7	099					6	18							7
8	099							29						8
9	102										11	28		41A
10	099	19	3											41B
11	099			13	6									41C
12	103						17	31	30					41D
13	099									18	5			41G
14	103										9	8		51A
15	103	20												51C
16	103			2	12									51D
17	099				16									51B
18	103						15							51G
19	099							14						51F
20	103							4	27					51I
21	104								1	30	3			51J
22	099										15			61A
23	104											15		61B
24	102	12											30	61C
25	099	28											10	51L
26	103							28	31	29				26
27	104											29	2	27
28	103		26	13										29
29	104			10	30	4								30
30	102							17	8					28
31	104								3	30	18			34
32	103										5	22		33
33	102	9										3	31	32
34	104	7	28											36
35	103			15	24									31
36	103									25	6			41
37	104						13	31	8		7	16		38
38	102				9	31	11		22	30	26	30	2	35
39	103		15	7	27									39
40	104			17	5									37
41	102					29	5							40
Total		157	140	161	145	70	85	152	160	202	167	175	109	1723
Percentage		9.1%	8.1%	9.3%	8.4%	4.1%	4.9%	8.8%	9.3%	11.7%	9.7%	10.2%	6.3%	
No. of flights on pad		8	7	10	10	4	7	7	10	8	12	11	7	101
		8%	7%	10%	10%	4%	7%	7%	10%	8%	12%	11%	7%	

Table 3. Probability of a Given Stay on the Launch Pad

Days	Probability of Exceedance of Stay	Midpoint (days)	Probability of Stay
12	1.00	21*	0.453
30	0.550	45	0.303
60	0.247	75	0.136
90	0.111	105	0.0613
120	0.0497	135	0.0274
150	0.0223	165	0.0123
180	0.0100	180 and up	0.0100

Table 4. Distribution of Length of Stay on Launch Pad for 100 Missions

<u>Days on Pad</u>	<u>Number of missions</u>
21	45
45	30
75	14
105	6
135	3
165	1
180	1

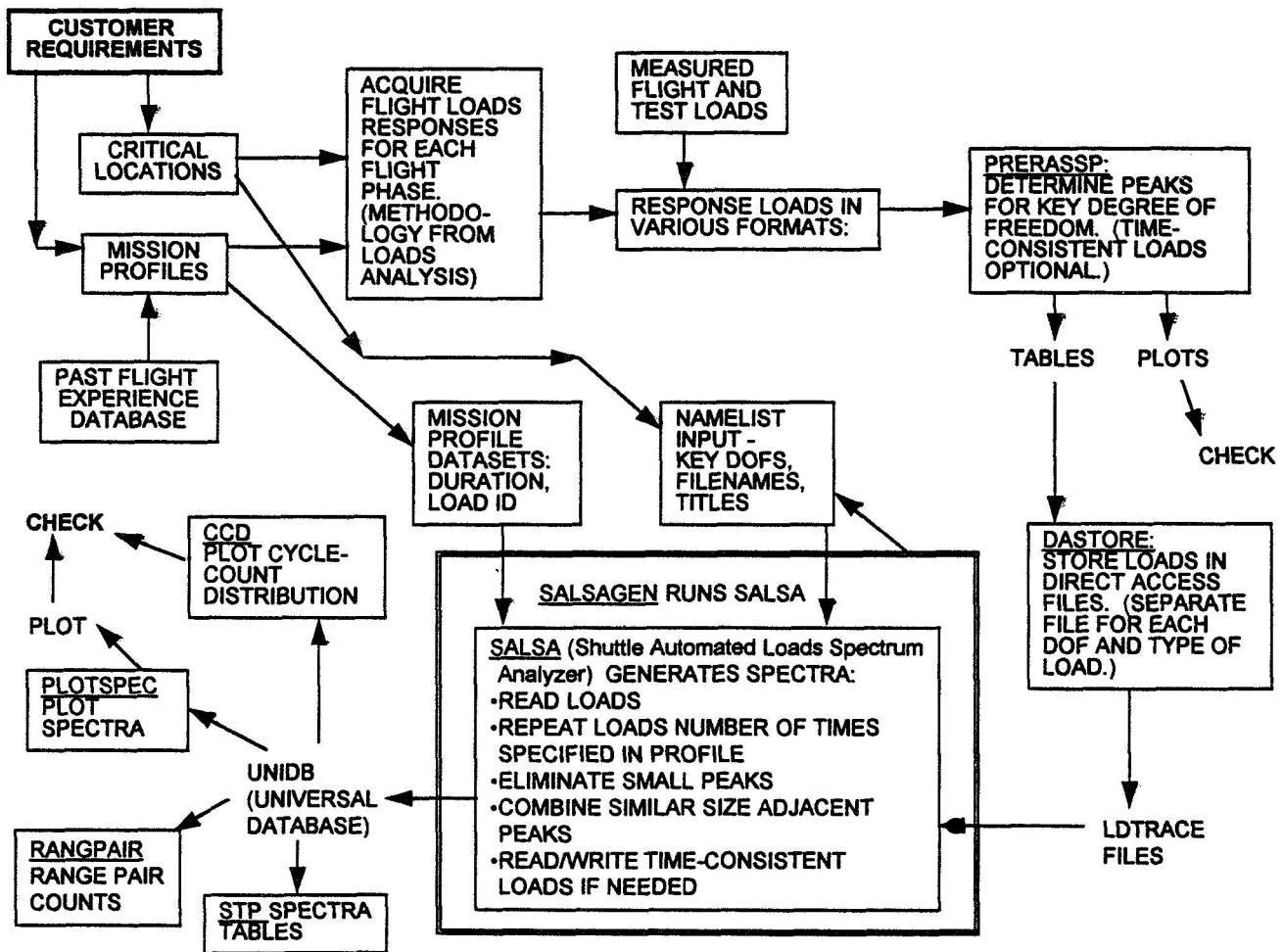


Figure 1. Fatigue Loads Spectra Process Flow

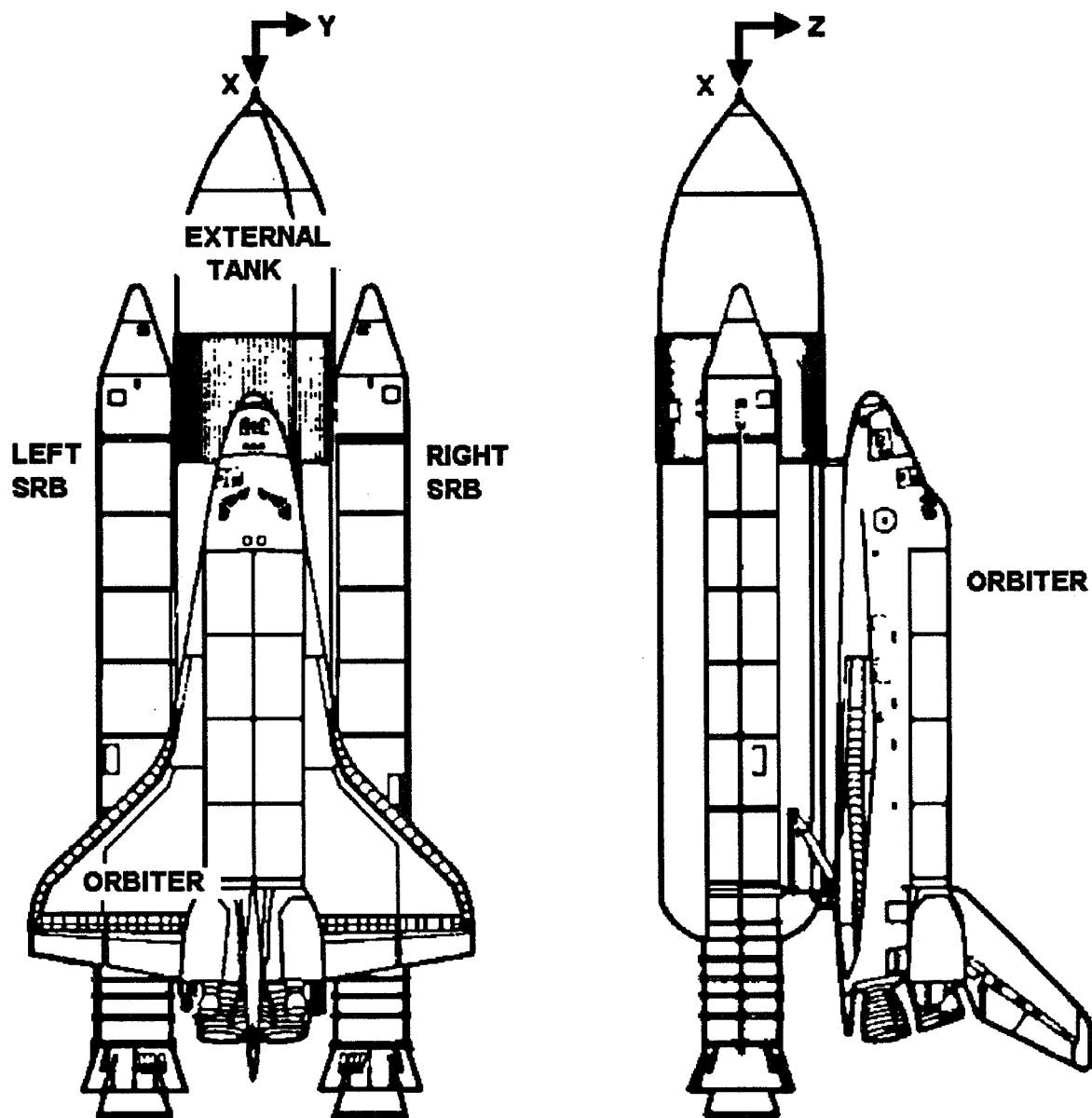


Figure 2. Launch Vehicle Geometry

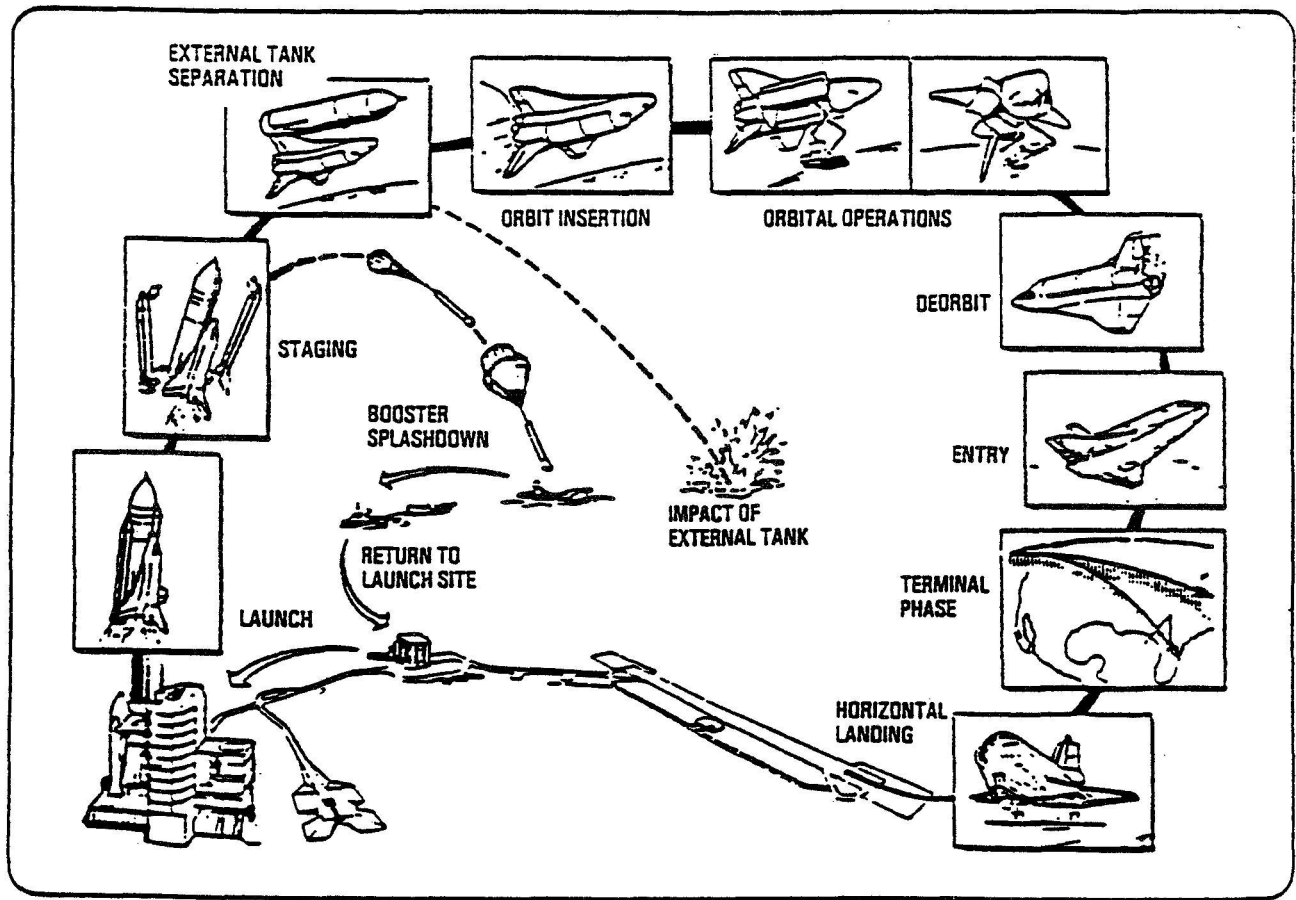


Figure 3. Space Shuttle Mission

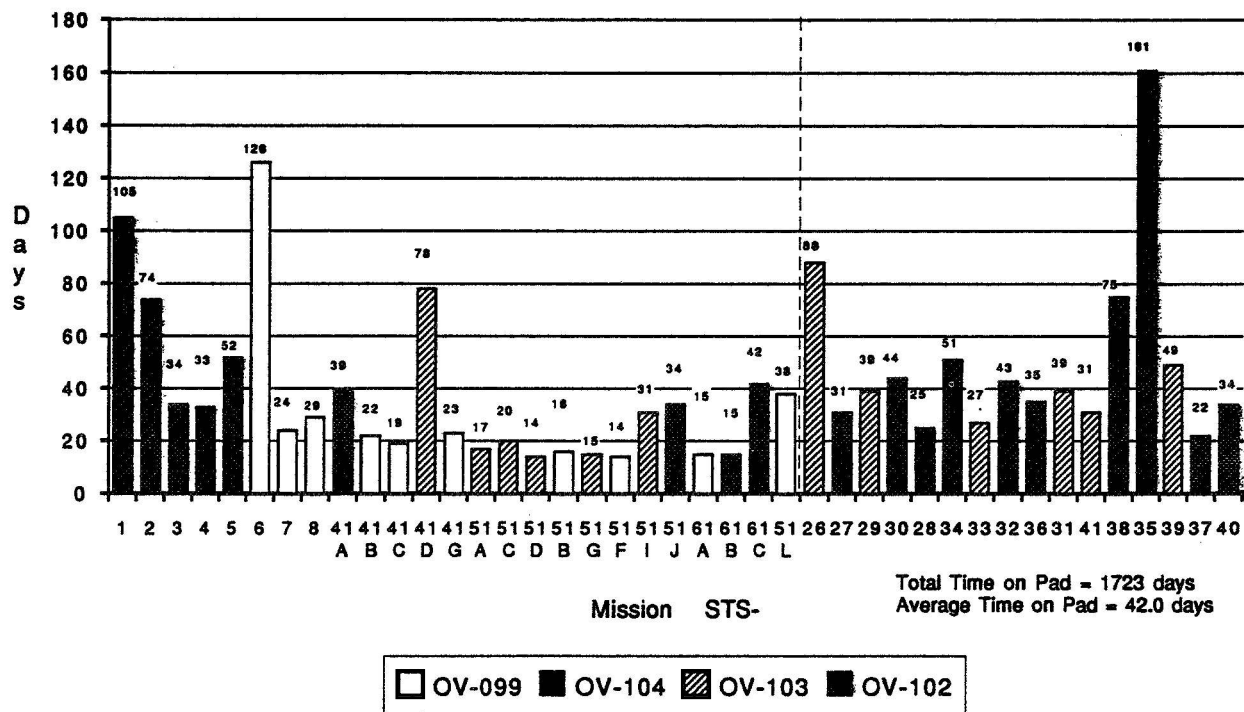


Figure 4. Time on Launch Pad for Each Mission

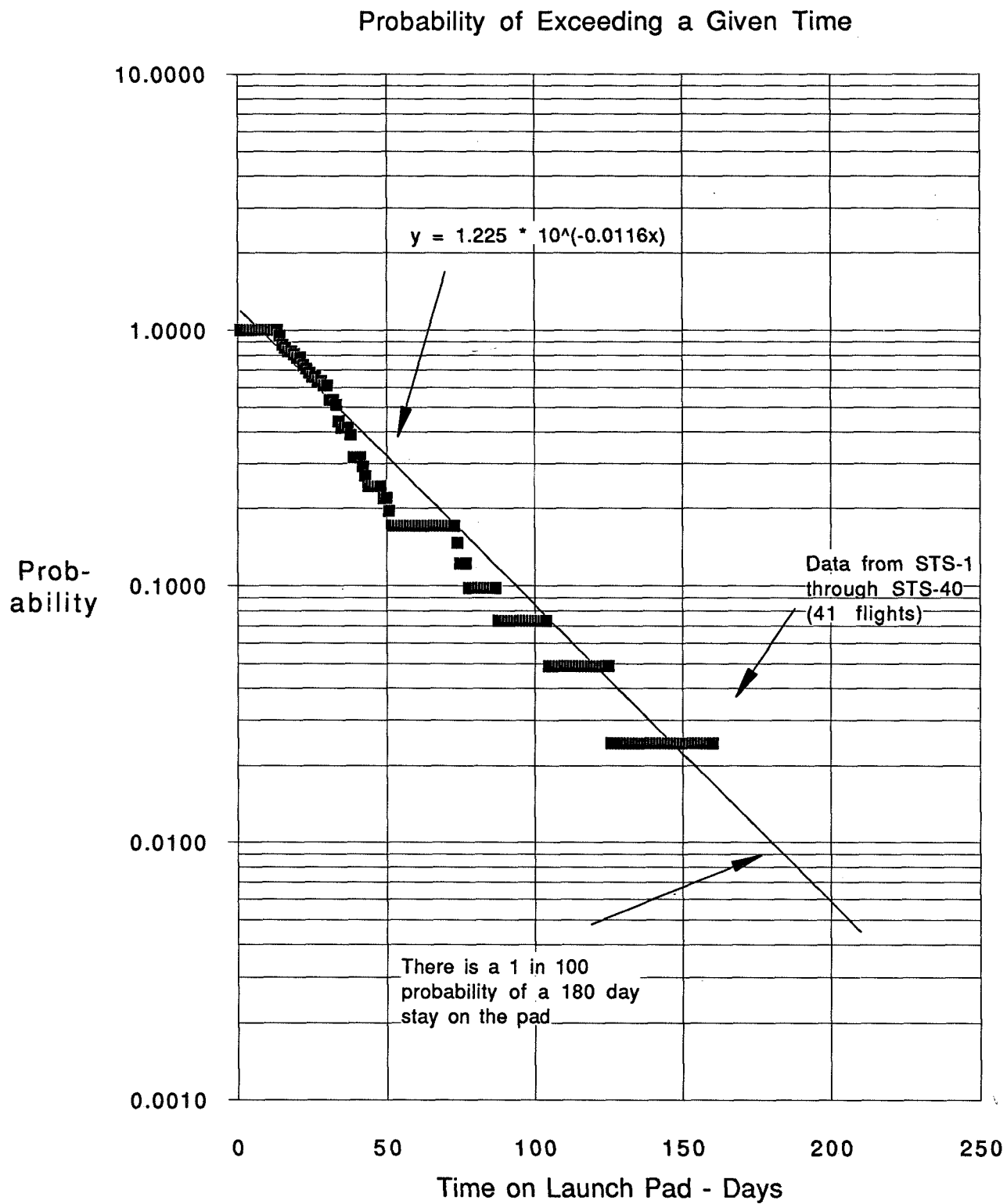


Figure 5. Time on Launch Pad

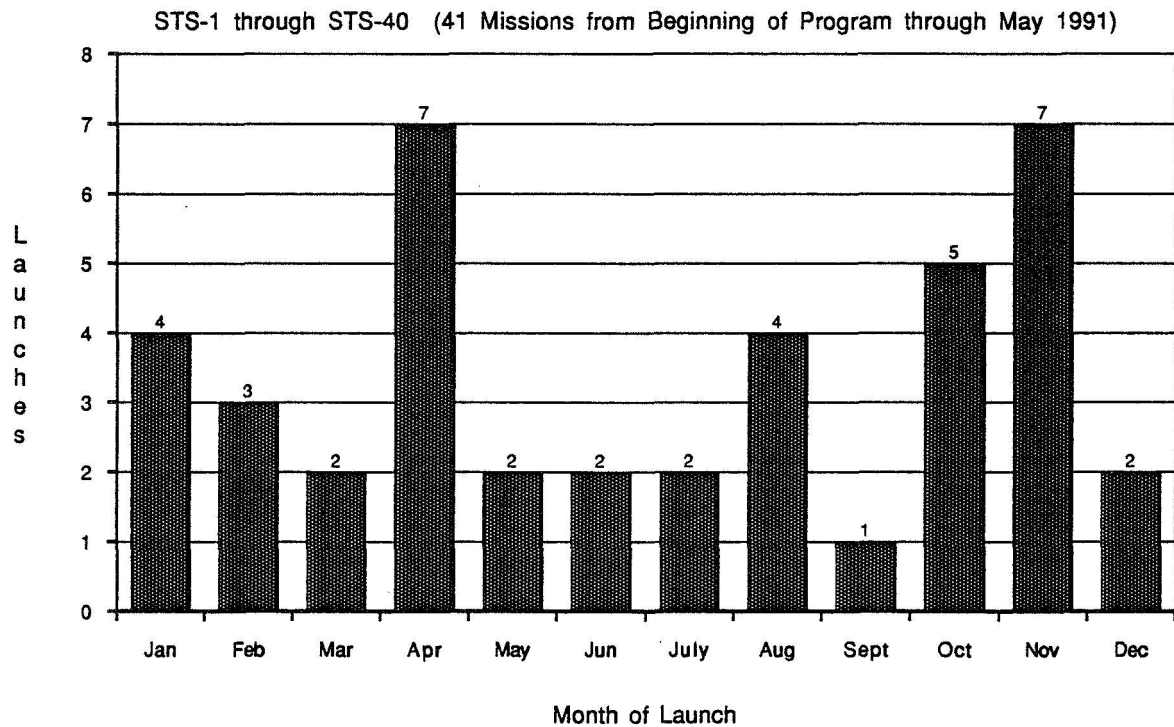
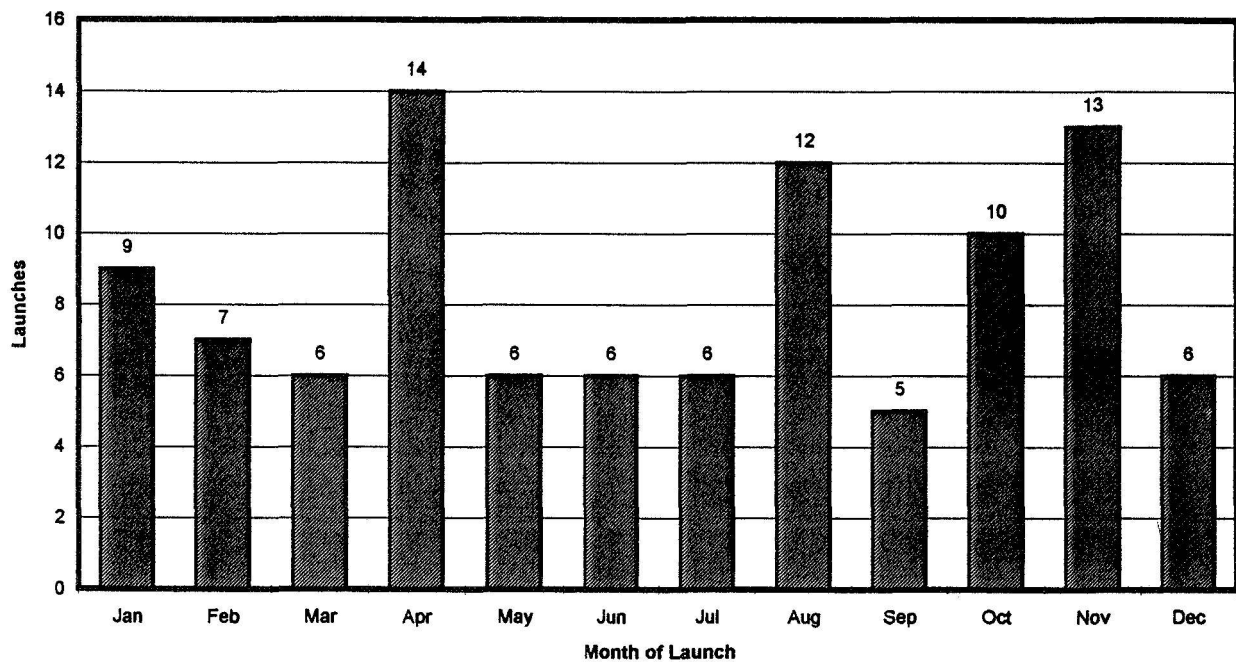


Figure 6. Number of Shuttle Launches in Each Month



Reference: (1) 41 Missions (STS-1 to STS-40)
 (2) 3 Missions after (1) and 48 missions from flight manifest (1992-1997)
 (3) 8 Missions projected based on (1) and (2)

Figure 7. Distribution of 100 Missions from KSC

FATIGUE RELIABILITY METHOD WITH IN-SERVICE INSPECTIONS

H.H. Harkness¹, M. Fleming, B. Moran and T. Belytschko
Robert R. McCormick School of Engineering and Applied Science
Northwestern University, Evanston, Illinois 60208-3109

348660

522-38

23116

p. 20

ABSTRACT

The first order reliability method (FORM) has traditionally been applied in a fatigue reliability setting to one inspection interval at a time, so that the random distribution of crack lengths must be recharacterized following each inspection. The FORM presented here allows each analysis to span several inspection periods without explicit characterization of the crack length distribution upon each inspection. The method thereby preserves the attractive feature of FORM in that relatively few realizations in the random variable space need to be considered. Examples are given which show that the present methodology gives estimates which are in good agreement with Monte Carlo simulations and is efficient even for complex components.

1. Introduction

Probabilistic fatigue methods are often applied in a setting where critical structural components are subjected to crack inspections by non-destructive evaluation (NDE) techniques, so that cracked components can be identified and repaired or replaced. These inspections can significantly reduce the probability of fatigue failure of structures, as well as increase the useful service lives. Quantified measures of reliability (provided by probabilistic methods) allow maximization of these inspection effects through optimization of the inspection schedule. These measures of reliability also allow comparisons of various inspection methods.

A risk analysis methodology for the assessment of structural integrity of aircraft structures has been outlined by Berens et. al. (1991). This methodology which is based on direct integration of probability of failure integrals works extremely well when the number of random variables is relatively small and a single parameter characterization of crack size is adequate. For complicated geometries (involving characterization of three-dimensional crack growth, for example), other modeling techniques such as Monte Carlo simulations (MCS) and the first order reliability method (FORM) are useful for calculating probabilities of failure (see Harkness et. al.(1992) and references therein). Traditionally, these latter techniques have been applied to one inspection interval at a time. However, that approach requires characterization of the crack

¹Current address; Hibbitt, Karlsson, Sorenson and Associates, Pawtucket, Rhode Island

size distribution (i.e., crack size probability density function) following each inspection, which is costly and difficult. Techniques for recharacterizing crack size distributions at each inspection with FORM are discussed in Rahman and Rice (1992).

An alternative approach is given here which does not require recharacterization of the crack size distribution. The first order reliability method is augmented to account for the effects of the inspections so that the crack size distribution need only be characterized at an initial state. This is of considerable advantage since recharacterizations of the crack length distribution are often tedious or impractical to obtain. In the present work, it is assumed that components with detected cracks are repaired such that their subsequent likelihood of failure is negligible.

In Section 2, the standard FORM and its application to fatigue reliability are reviewed. The introduction of non-destructive evaluation (NDE) into the fatigue reliability problem is discussed in Section 3 along with a description of the augmentation of FORM to efficiently treat multiple inspections. The first part of section 3 is devoted to identifying the quantities of interest in a fatigue reliability analysis with in-service inspections; techniques to evaluate these quantities are given in the remainder of the section. An important aspect of FORM is finding the so-called design points. An algorithm for this task which is applicable to both the standard FORM and the augmented FORM is provided in the Appendix.

Two numerical examples are presented in Section 4. The first example investigates the accuracy of augmented FORM by comparison to MCS results. A more complex fatigue problem is studied in the second example where the MCS approach is not computationally feasible, yet the augmented FORM requires only minutes of CPU time on a workstation. In these examples, the inspection schedule is adjusted so that inspections occur when the probability of failure reaches a specified value. Further discussion and concluding remarks are given in Section 5.

2. FIRST ORDER RELIABILITY METHOD

2.1. Standard Reliability Statement

We begin by defining a performance function, $G(\mathbf{x})$, which distinguishes between safe and unsafe realizations of the random variables \mathbf{x} (see Fig. 1a). Performance functions are typically defined so that positive outcomes indicate safe realizations and negative outcomes indicate unsafe realizations (the limit case of $G(\mathbf{x})=0$ is often included in the failure domain). The objective of a reliability analysis is to determine the probability of failure

$$P_f = P[G(\mathbf{x}) \leq 0], \quad (2.1)$$

which is given by

$$P_f = \int_{\Omega_f^x} f_X(\mathbf{x}) d\mathbf{x}, \quad (2.2)$$

where Ω_f^x is the failure space ($G(\mathbf{x}) \leq 0$), and $f_X(\mathbf{x})$ is the joint probability density function for realizations in the space of random variables \mathbf{x} .

The random variables \mathbf{x} are often non-normally distributed, making the integral in Eq. (2.2) difficult to evaluate. The random variables \mathbf{x} can be mapped to standardized equivalent normal random variables \mathbf{r} , where each component r_i is an independent Gaussian variable with zero mean and unit variance. This mapping can be achieved via the Rosenblatt transformation (see Rosenblatt 1952; Ang and Tang 1984)

$$r_i = \Phi^{-1} \left[F_i(x_i | x_1, x_2, \dots, x_{i-1}) \right], \quad (2.3)$$

where F_i is the conditional cumulative probability at x_i given x_1, x_2, \dots, x_{i-1} . In standardized space, the performance function is transformed to $g(\mathbf{r}) = G(\mathbf{x}(\mathbf{r}))$ and Eq. (2.2) becomes

$$P_f = \int_{\Omega_f^r} f_R(\mathbf{r}) d\mathbf{r}, \quad (2.4)$$

where Ω_f^r is the failure space ($g(\mathbf{r}) \leq 0$) as in Fig. 1b, and $f_R(\mathbf{r})$ is the joint probability density function for realizations of random variables \mathbf{r} . The joint probability density function, $f_R(\mathbf{r})$, is simply the product of the probability density functions for all random variables r_i and is given by

$$f_R(\mathbf{r}) = \prod_{i=1}^n \frac{1}{\sqrt{2\pi}} \exp\left(-\frac{1}{2} r_i^2\right). \quad (2.5)$$

The essence of FORM is to approximate the limit surface $g(\mathbf{r})=0$ by a tangent hyperplane at the most likely point of failure, \mathbf{r}_d . In standard FORM the most likely failure point is the point which minimizes the distance $\|\mathbf{r}\|$ to the failure surface. The resulting “first order” estimate of the probability of failure is then given by

$$P_f^1 = \Phi(-\beta), \quad (2.6)$$

where $\beta = |\mathbf{r}_d|$ and Φ is the standard normal cumulative distribution function. Because the random variables \mathbf{r} are Gaussian, the decay of $f_R(\mathbf{r})$ is exponential and therefore using the closest point provides a good estimate for calculating probability of failure using standard FORM. It will be shown in Section 3.3 that the closest point may not be the most likely failure point when in-service inspections are accounted for.

2.2. Fatigue Reliability

In a fatigue setting, the failure set contains all realizations that result in fatigue lives less than a desired service life, so an appropriate performance function is

$$G(\mathbf{x}) = N_f(\mathbf{x}) - N, \quad (2.7)$$

or in standard Gaussian space

$$g(\mathbf{r}) = N_f(\mathbf{x}(\mathbf{r})) - N, \quad (2.8)$$

where N_f is the fatigue life (which is influenced by several uncertainties) and N is the desired service life. Note that the fatigue life may be defined as the number of cycles for a crack to reach some specified critical size - which may not necessarily correspond to catastrophic failure of the component. Failure is deemed to occur when the fatigue life is shorter than the desired service life ($g < 0$). Standard FORM described above is often effective for estimating failure probability versus service life in the absence of inspections or for estimating the probability of failure with inspections when the crack length distribution following an inspection is known. In the latter, a standard FORM analysis is performed for each inspection interval of interest, and the probability of failure is determined in each analysis. This approach requires knowledge of the crack size distribution following each inspection. A more efficient method for treating inspections is introduced in the following Section.

3. FATIGUE RELIABILITY AND IN-SERVICE NDE INSPECTIONS

Consider a fatigue reliability setting where the component is subjected to in-service NDE inspections according to some schedule. The inspection schedule may be prescribed and the failure probabilities sought or conversely, the aim of the analysis may be to determine an inspection schedule which will keep failure probabilities below a specified level. Let N denote the service life (in cycles) and N_f denote the number of

cycles to the inspection prior to N . We seek a method to determine the fatigue reliability (or alternatively failure probability) over the service life, N . As mentioned previously, standard FORM techniques require a complete characterization of the probability density function for the crack size following each inspection. However, an exact determination of the crack size probability density function may be extremely tedious or impractical to obtain especially for cracks in complicated geometries. Rahman and Rice (1992) discuss a method based on the standard FORM itself to recharacterize the crack size distribution at each inspection, but this method may require extensive computations. In the following subsection, we introduce a straightforward and efficient method based on the initial crack size distribution for determining fatigue reliability with NDE inspections, i.e., explicit knowledge of the crack size distribution at each inspection is not required.

3.1. Statement of Reliability Problem with NDE Inspections

The probability of failure is defined here as the probability that the service life of the component exceeds the fatigue life as a result of undetected cracks. Thus the probability of failure, P_f , after N fatigue cycles, can be written as

$$P_f(N) = P[N_f \leq N \mid O_i = 0, i = 1, 2, \dots, I] \quad (3.1)$$

where I is the number of previous inspections at N cycles ($N > N_f$), O_i indicates the outcome of the i -th inspection which is given by:

$$O_i = \begin{cases} 0 & \text{no crack detected } i^{\text{th}} \text{ inspection} \\ 1 & \text{crack detected } i^{\text{th}} \text{ inspection} \end{cases} \quad (3.2)$$

and N_f is the fatigue life. The outcome of each inspection is random due to uncertainties in the inspection technique and the crack length at the time of the inspection.

Other functions which may be of particular interest can be derived from P_f . The hazard function (or failure rate) $h(N)$ is given by

$$h(N) = \frac{1}{[1 - P_f(N)]} \frac{\partial P_f(N)}{\partial N} \quad (3.3)$$

The factor $[1-P_f]$ in Eq. 3.3 is typically very close to unity in a reliability analysis, so the hazard function is effectively equal to the derivative of the probability of failure. Another useful failure probability is the probability of failure since the last inspection (due to an undetected crack), i.e.,

$$P_{fI}(N_s) = P[N_I < N_f \leq N | O_i = 0, i=1,2,\dots,I] \quad (3.4)$$

where I is the number of previous inspections at N cycles, and N_I and O_i are as previously defined.

As in the standard FORM the random variable space can be transformed to standardized Gaussian variable space. The probability density function for realizations of \mathbf{r} in this space is $f_R(\mathbf{r})$ (see Eq. 2.5). To derive an expression for the probability of failure, P_f , at cycle N allowing for NDE inspections, we require the probability density function associated with realizations, \mathbf{r} , for which the associated cracks are undetected. The probability density function for realizations with undetected cracks after the first I inspections is given by

$$f_U(\mathbf{r}) = f_R(\mathbf{r})P_{nd}(\mathbf{r}, N). \quad (3.5)$$

Here, $P_{nd}(\mathbf{r}, N)$ is the probability that cracks associated with the realization \mathbf{r} are not detected in all of the inspections prior to the current cycle, N , i.e., $P_{nd}(\mathbf{r}, N) = P[O_i = 0 \text{ for } i=1,2,\dots,I | \mathbf{r}]$, and is given by

$$P_{nd}(\mathbf{r}, N) = \prod_{i=1}^I \{1 - \text{POD}[a(\mathbf{r}, N_i)]\} \quad (3.6)$$

where $\text{POD}[a(\mathbf{r}, N_i)]$ is the given probability of detection for the inspection method, and $a(\mathbf{r}, N_i)$ is the crack length upon the i^{th} inspection for the realization \mathbf{r} .

The probability of failure is therefore given by

$$P_f(N) = \int_{\Omega_f^r} f_R(\mathbf{r})P_{nd}(\mathbf{r}, N) d\mathbf{r} \quad (3.7)$$

where Ω_f^r includes all \mathbf{r} such that $g \leq 0$ (i.e. $N_f \leq N$). The probability of failure since the last inspection is given by

$$P_{fI}(N) = \int_{\Omega_{fI}^r} f_R(\mathbf{r})P_{nd}(\mathbf{r}, N) d\mathbf{r} \quad (3.8)$$

where Ω_f includes all \mathbf{r} such that $N_I < N_f \leq N$. Note that the computation of N_f is not influenced by the inspections, i.e. the failure surface $g(\mathbf{r})=0$ is not influenced by in-service inspections. Rather, it is the integrands in Eqs. (3.7) and (3.8) which incorporate the effect of inspections on failure probability.

3.2. Evaluation of the Integral for Failure Probability

The integrals in Eqs. (3.7) and (3.8) differ from that which arises in standard FORM in that the integrands have been multiplied by the non-Gaussian function $P_{nd}(\mathbf{r}, N)$ and, therefore, the integration technique must be modified to accurately integrate the functions. A simple modification of the standard FORM integration procedure is introduced here for the evaluation of the integral in Eq. (3.7). As in standard FORM, the failure surface is approximated by a tangent hyperplane at the most likely failure point, \mathbf{r}_d (the so-called design point). The sharp variation of $P_{nd}(\mathbf{r}, N)$ in the direction of the gradient of g prevents the direct evaluation of the integral via the standard normal cumulative distribution function, as in Eq. (2.6). Nevertheless, we wish to maintain the essential structure of the FORM integration procedure and thus it is convenient to discretize the domain Ω_f into subdomains as shown in Fig. 2. By approximating $P_{nd}(\mathbf{r}, N)$ as constant over each subdomain we obtain

$$P_f(N) \approx \sum_{j=1}^{n_s} \left[\bar{P}_{nd}^j \int_{\Omega_j} f_R(\mathbf{r}) d\Omega \right], \quad (3.9)$$

where n_s is the number of subdomains and \bar{P}_{nd}^j is the approximation of $P_{nd}(\mathbf{r}, N)$ in the subdomain Ω_j . The remaining integrands $f_R(\mathbf{r})$ are Gaussian, so the standard cumulative normal function Φ is useful for “first order” approximations of these integrals. Thus, Eq. (3.9) leads to approximations of the form

$$P_f^l(N) = \sum_{j=1}^{n_s} \left\{ \bar{P}_{nd}^j [\Phi(-|\mathbf{r}|_j) - \Phi(-|\mathbf{r}|_{j+1})] \right\} + \bar{P}_{nd}^{n_s} \Phi(-|\mathbf{r}|_{n_s}), \quad (3.10)$$

where \mathbf{r}_j is the integration point on the surface of the subdomain Ω_j as shown in Fig. 2. In this numerical integration scheme, the design point is taken as the first integration point, i.e., $\mathbf{r}_1 = \mathbf{r}_d$. Subsequent integration points are found by

$$\mathbf{r}_j = [1 + (j-1)\delta] \mathbf{r}_d, \quad (3.11)$$

where \mathbf{r}_j is the position of the j^{th} integration point and δ is the desired step size for the integration. The number of subdomains, the magnitude of δ , and the location, \mathbf{r}_{n_s} of the last integration point depend on the

accuracy desired and can be deduced through numerical experimentation and comparison with known solutions. A non-uniform subdomain discretization can be used in place of Eq. (3.11) if desired.

3.3 Location of Design Points

In standard applications of FORM, the most likely failure point can be shown to be the closest point to the origin on the surface $g=0$ through the use of Lagrange multipliers (Ang and Tang 1984). The approximation of the failure surface as a tangent hyperplane at the design point leads to the first order approximation in Eq. (2.6). In the present application of FORM with in-service inspections, the integrand in Eq. (3.7) contains the non-Gaussian variable $P_{nd}(\mathbf{r}, N)$ and the most likely failure point is not in general the closest point to the origin on $g=0$. The question then arises as to which point provides the most appropriate first order approximation to the failure surface, i.e. where to locate the design point. One possibility is to take the closest point to the origin on $g=0$ as in standard FORM. However, due to variations in $P_{nd}(\mathbf{r}, N)$ along the surface $g=0$, an alternative point is suggested which will maximize the integrand in Eq. (3.7).

A procedure for locating the design point at the most likely failure point on $g=0$ is introduced here. By suitable choice of parameters, the algorithm can also be used to locate the design point at the closest point to the origin. Consider β such that

$$\Phi(-\beta) = P_{nd}(\mathbf{r}, N) \Phi(-|\mathbf{r}|). \quad (3.12)$$

The design point is the point on the surface of constant g which will minimize β (or maximize the product $P_{nd}(\mathbf{r}, N) \Phi(-|\mathbf{r}|)$). Typically, the variation in $P_{nd}(\mathbf{r}, N)$ is small in the direction of constant g and the design point and the closest point are nearly coincidental. However, some problems do show a significant difference. The Rackwitz algorithm (Rackwitz and Fiessler, 1978) can be used to find the design point for standard FORM, but this algorithm can be non-convergent for high values of β if the failure surface is not relatively flat. A variation of the Rackwitz algorithm which corrects for this problem and has been generalized for use with both standard and augmented FORM is presented in the Appendix.

4. NUMERICAL EXAMPLES

4.1. Edge Crack

We first consider the fatigue of an edge crack in a semi-infinite plate to investigate the accuracy of the augmented FORM based on comparisons with Monte Carlo simulations (MCS). It is assumed that the cracks propagate according to the Paris model (Paris and Erdogan, 1963)

$$\frac{da}{dN} = D(\Delta K)^m \quad (4.1)$$

where da/dN is the rate of crack growth, D and m are material parameters, and ΔK is the amplitude of the stress intensity factor. The stress intensity factor range for an edge crack of length a , is given by $\Delta K = 1.12\sigma(\pi a)^{1/2}$ where σ is the amplitude of the applied stress. Using this relation, Eq. 4.1 can be integrated to obtain the number of cycles for a crack of initial length a_i to grow to a crack of length a_f

$$N_f = \frac{a_f^{1-\frac{m}{2}} - a_i^{1-\frac{m}{2}}}{D(1-\frac{m}{2})(1.12\sigma\sqrt{\pi})^m}, \quad (m \neq 2) \quad (4.2)$$

$$N_f = \frac{\ln(a_f/a_i)}{\pi D(1.12\sigma)^2}, \quad (m=2). \quad (4.3)$$

The material is taken to be ingot 304 stainless steel with fracture toughness $K_{Ic} = 48 \text{ MPa} \sqrt{\text{m}}$. The crack is cyclically loaded in tension-tension fatigue with an R -ratio of 0 and remote applied stress amplitude of $\sigma = 250 \text{ MPa}$. Motivated by the experimental findings of McGuire (1993)*, the initial crack size distribution is taken to be lognormal with mean 0.1mm and standard deviation 0.033mm. The quantity $m-1$ is also taken to be lognormal with mean 2.67 and standard deviation 0.75. The coefficient D and the exponent m are also found to be functionally related as $\log D = -1.50m - 7.29$ - the units of D are $\text{m/cycle}/(\text{MPa}\sqrt{\text{m}})^m$.

It is assumed that the probability of detecting an existing crack of length a upon inspection is (Palmberg et al., 1987)

$$POD(a) = \frac{\alpha a^\beta}{1 + \alpha a^\beta}, \quad (4.4)$$

* The experimental data collected by McGuire (1993) are for fatigue crack growth from a hole in a tension-loaded bar. The statistical data obtained for this configuration are not directly transferable to the edge crack configuration, but do provide a reasonable representation of fatigue crack growth in this material.

where the parameters α and β depend on the inspection technique.

Figure 3 shows a comparison of augmented FORM and MCS results with evenly-spaced inspections modeled at 2.25×10^5 , 2.75×10^5 , 3.25×10^5 , and 3.75×10^5 cycles. Monte Carlo results obtained using 10 million realizations are not very dependable for $P_f(N)$ below about 2×10^{-6} . To obtain dependable MCS results, the POD curve A in Fig. 4 is used ($\alpha=0.0032 \text{ mm}^{-\beta}$, $\beta=3.5$) to yield probabilities of failure greater than 2×10^{-6} . The integration over the failure space is performed using the integration technique presented in Section 3.2 with $n_s=100$ and $\delta=0.01$. As can be seen from the figure, excellent agreement is obtained between the two methods.

In a fatigue reliability setting, it is generally desirable to have failure probabilities much lower than those in Fig. 3. The probability of failure can be kept below a desired level by scheduling inspections at uneven intervals as well as improving the probability of detection through better NDE inspection techniques. Fig. 5 shows results for inspections modeled at 2.25×10^5 , 2.55×10^5 , 3.15×10^5 , and 2.75×10^5 cycles and using the POD curve B in Fig. 4 ($\alpha=1.0 \text{ mm}^{-\beta}$, $\beta=3.0$) and using the same integration parameters for Eq. (3.11) as before ($n_s=100$, $\delta=0.01$). Using this inspection schedule and POD relation, the peak probability of failure is kept below 10^{-5} . The augmented FORM and MCS estimates are in close agreement; however, as previously stated, MCS results are not very dependable for $P_f(N)$ below about 2×10^{-6} .

4.2. Semi-Elliptical Surface-Breaking Crack

For complicated component geometries and crack shapes, a closed form expression for fatigue life is generally not available. This requires that the fatigue life for each realization of random variables \mathbf{r} be determined by numerical integration, with the stress intensity factors updated as crack growth is simulated. This makes MCS infeasible for studies of extreme reliabilities. The augmented FORM requires the consideration of relatively few realizations, so these analyses are feasible when parameterizations or interpolation schemes for the stress intensity factors are available (see Newman and Raju 1986, for example).

A semi-elliptical surface-breaking crack in a plate as shown in Fig. 6 is considered, with the dimensions (in mm) $h=b=5.0$, $t=2.5$. It is assumed that there are no initial cracks in the component. Instead, a random distribution of the cycles to initiation, N_{init} , of a crack of depth $80 \mu\text{m}$ is considered. It is assumed the crack remains planar and semi-elliptical as it propagates. Post-initiation crack growth is modeled by applying the Paris law to the crack depth, a , and half crack width, c

$$\frac{da}{dN} = D(\Delta K_A)^m \quad (4.5a)$$

$$\frac{dc}{dN} = D(\Delta K_C)^m \quad (4.5b)$$

Failure is assumed to correspond to the crack reaching a critical depth, a_f .

The stress intensity factors at points A and C, parameterized according to Newman and Raju (1986), are given by

$$K_A = S_t(\pi a / Q)^{1/2} F_s^A \quad (4.6a)$$

$$K_C = S_t(\pi a / Q)^{1/2} F_s^C, \quad (4.6b)$$

where S_t is the applied tensile stress, Q is the shape factor for an ellipse, and F_s is a boundary correction factor.

For this example, the initial crack length (a_i) is taken to be a deterministic variable at $a_i=80 \mu\text{m}$ and the initial half crack width (c_i) is taken as $c_i=1.1a_i$. The maximum allowable crack length, a_f , is taken as $a_f=1.25 \text{ mm}$, which is 50% of the plate thickness.

The time required for a crack to reach the initiation depth, N_{init} , is taken to be a lognormally-distributed random variable with mean 10^6 and standard deviation 0.5×10^6 . The stress amplitude (S_t) is taken to be a normally distributed random variable with mean 250 MPa and standard deviation 7.5 MPa. The distributions for m and D are the same as in the previous example. The POD for the inspection technique considered in this example is shown in curve C in Fig. 4 ($\alpha=100 \text{ mm}^{-\beta}$ and $\beta=5$).

Augmented FORM results are shown in Figs. 7 and 8 for probability of failure and probability of failure since the last inspection, respectively. Note that the entire set of data points shown was obtained with less than two minutes of CPU on an HP 9000 series 750 computer. Inspections were simulated at 4.2×10^5 , 5.1×10^5 , 5.8×10^5 , and 6.5×10^5 . As in the last example, the inspections times have been adjusted so the probability of failure peaks at about 10^{-5} before an inspection is performed.

Note that the reliability results are given over a range of fatigue lives considerably below the mean value of N_{init} . This shows that even though the initiation times are usually great, it is the few relatively short initiation times which are important to the reliability and to the scheduling of inspections.

5. SUMMARY AND DISCUSSION

A technique to incorporate periodic in-service inspections in a FORM analysis of fatigue life has been presented. The attractive feature of FORM is preserved in that relatively few realizations in the random variable space need to be considered. This is especially important when fatigue reliability of complex components is studied, since closed form expressions for the fatigue life are not available and numerical integration is required to determine the fatigue life corresponding to a combination of random variables.

Previous applications of FORM to multiple inspection intervals have required that the probability density function for the crack length be determined at an initial state as well as after each inspection. The augmented FORM only requires knowledge of the initial distribution of crack lengths (or the distribution of cycles to crack initiation), which is a significant advantage. Recharacterizing the crack length distribution after each inspection requires the consideration of a great deal of realizations. Therefore, the advantage of FORM is greatly diminished, if not lost, if the crack length distribution must be recharacterized at various stages of the fatigue life.

Demonstrations of the augmented FORM were given for two components to show the accuracy and versatility of the method. The first component had a simple configuration which allowed comparisons with Monte Carlo simulations. These comparisons showed that the augmented FORM yields accurate probability of failure estimates. In the second component, the augmented FORM was shown to be efficient for even complex components when other methods, such as MCS and standard FORM, were computationally infeasible.

The method has also been shown to be an effective tool for scheduling inspection times based on a maximum probability of failure. The probability of failure was kept below a specified level by performing non-uniform inspections, rather than evenly spaced inspections. This and related aspects of the method are subjects of our ongoing research in this area.

ACKNOWLEDGMENTS

This work was partially supported by the National Institute for Standards and Technology through a subcontract with Iowa State University and partially supported by the Federal Aviation Administration. Helpful discussions with Dr. Al Berens, University of Dayton Research Institute, are gratefully acknowledged.

REFERENCES

- Ang, A.H., and W.H. Tang. *Probability Concepts in Engineering Planning and Design*, 1st Edit., Vol. II. Wiley and Sons, New York (1984).
- Berens, A.P., J.G. Burns, and J.L. Rudd. Risk Analysis for Aging Aircraft Fleets. In *Structural Integrity of Aging Airplanes*. ed. S.N. Atluri, S.G. Sampath, and P. Tong. Springer-Verlag, New York (1991).
- Harkness, H.H., T.B. Belytschko, and W.K. Liu. Finite element reliability analysis of fatigue life. *Nucl.Engng Des.* **133**, 209-224 (1992).
- Harkness, H.H. Computational Methods for Fracture Mechanics and Probabilistic Fatigue. Ph.D. diss., Northwestern University (1993).
- McGuire, S.M. Quantitative Measurement of Fatigue Crack Initiation and Propagation in 304 Stainless Steel as Related to Design and Nondestructive Evaluation. Ph.D. diss., Northwestern University (1993).
- Newman, J.C. Jr., and I.S. Raju. Stress intensity factor equations for cracks in three dimensional finite bodies subjected to tension and bending loads. In *Computational Methods in the Mechanics of Fracture*, ed. S.N. Atluri, 312-334. North-Holland, New York (1986).
- Palmberg, B., A.F. Blom, and S. Eggwertz. Probabilistic damage tolerance analysis of aircraft structures. In *Probabilistic Fracture Mechanics and Reliability*. ed. J.W. Provan. Martinus Nijhoff, Boston (1987).
- Paris, P.C., and F. Erdogan. A critical analysis of crack propagation laws. *J. Bas Engng*, **85**, 528-534 (1963).
- Rackwitz, R., and B. Fiessler. Structural reliability under combined random load sequences. *Computers and Structures*. **9**, 489-494 (1978).
- Rahman, S., and R. Rice. Assessment of the reliability of the commercial aircraft fleet considering the potential adverse effects of multiple repairs and multiple site damage, preliminary technical interchange report for U.S. DOT/FAATC Aging Aircraft Program (1992).
- Rosenblatt, M. Remarks on a Multivariate Transformation. *Annals of Mathematical Statistics*. **23**, 470-472 (1952).

APPENDIX: ALGORITHM TO LOCATE DESIGN POINTS

A variation on the Rackwitz algorithm (Rackwitz and Fiessler, 1978) is presented in the following four steps (Harkness, 1993):

- 1) define failure function $G(x)$, initialize iteration count: $v=0$; estimate design point coordinates r_i^0 ; transform r_i^0 to x_i^0 .

2) evaluate g , $\frac{\partial \beta}{\partial r_i}$ and $\frac{\partial G}{\partial r_i}$ at x_i^v , r_i^v and compute:

$$I_i = -\lambda \frac{\partial G}{\partial r_i} / \frac{\partial \beta}{\partial r_i}, \text{ where } \lambda = |\nabla_r \beta| / |\nabla_r g|$$

3) increment iteration count: $v=v+1$; update r_i values in two steps:

$$\text{a) } r_i^{\text{temp}} = r_i^{v-1} - (G - G^*) \frac{\partial G}{\partial r_i} / (\nabla_r G)^2; \text{ adjusts magnitude of } \mathbf{r}$$

$$\text{b) } r_i^v = r_i^{\text{temp}} (\xi + (1 - \xi) I_i), \quad 0 < \xi < 1; \text{ adjusts direction of } \mathbf{r}$$

4) transform r_i^v to x_i^v ; check for convergence:

If not converged, go to step 2.

If converged, design point found; reliability index $\beta_d = |\mathbf{r}^v|$.

This algorithm minimizes β on any surface of constant g (equal to g^*). Other distinctions between this algorithm and the Rackwitz algorithm are:

1) $G=G^*$ is not enforced on each iteration. Instead, step 3a just brings \mathbf{r}^v toward the limit surface. In practice, $G \approx G^*$ after several iterations (i.e., after $v > 4$) with the algorithm presented above.

2) The iteration parameter ξ is introduced to avoid the large angular corrections in \mathbf{r}^v which lead to non-convergence.

An intermediate value of the iteration parameter, such as $\xi=0.7$, is recommended. For practical purposes, convergence can be assumed to have occurred when each of the standardized variables changes by less than 0.01 in an iteration. Convergence is typically achieved within ten to twenty iterations with this algorithm, and lack of convergence is uncommon.

The algorithm can be used to find design points for standard or augmented FORM. The algorithm calls for partial derivatives of $\beta=|\mathbf{r}|$ and G with respect to r_i . For standard FORM, these derivatives are given by

$$\frac{\partial \beta}{\partial r_i} = \frac{r_i}{\beta} \quad (\text{A.1})$$

$$\frac{\partial G}{\partial r_i} = \frac{\partial G}{\partial x_i} \frac{\partial x_i}{\partial r_i} \quad (\text{A.2})$$

If $G = N_f - N$ and the desired service life is deterministic, then

$$\frac{\partial G}{\partial x_i} = \frac{\partial N_f}{\partial x_i} \quad (\text{A.3})$$

and

$$\frac{\partial x_i}{\partial r_i} = \sigma_i^N, \quad (\text{A.4})$$

where σ_i^N are the equivalent normal standard deviations in the Rosenblatt transformation (see Ang and Tang, 1984). With these substitutions,

$$\frac{\partial G}{\partial r_i} = \frac{\partial N_f}{\partial x_i} \sigma_i^N. \quad (\text{A.5})$$

For augmented FORM, the derivatives of β with respect to r_i are modified to account for the affect of the $P_{nd}(\mathbf{r}, N)$ function on the design points (see Section 3.3). The derivatives can now be calculated as

$$\frac{\partial \beta}{\partial r_i} = \frac{r_i}{\beta} + \frac{R}{\beta} \frac{\partial R}{\partial r_i} \quad (\text{A.6})$$

where $R = \sqrt{\beta^2 - |\mathbf{r}|^2}$. The derivatives of the “augmented component” R can be calculated using finite differences.

For both standard and augmented FORM, $|\nabla_r \beta| = 1$.

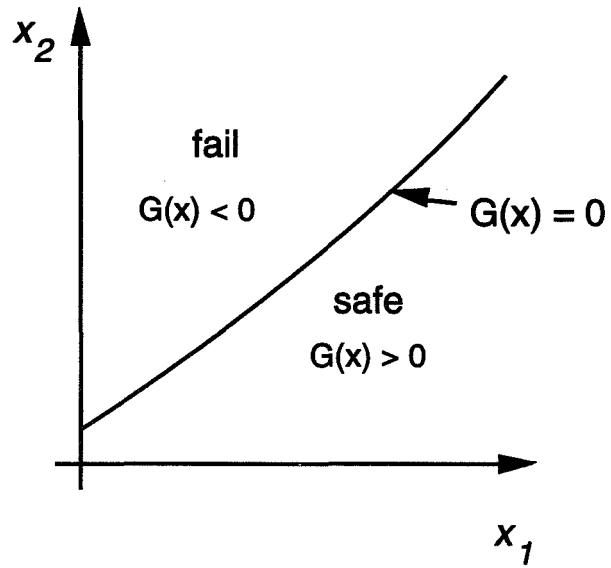


Figure 1a. Failure surface in original space

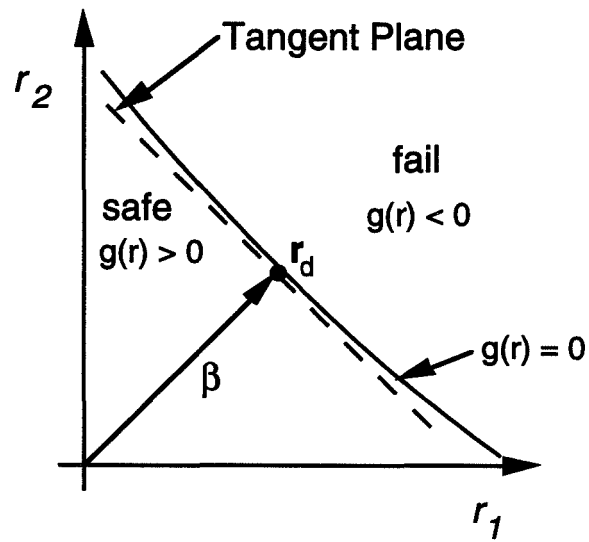


Figure 1b. Failure surface in standardized space

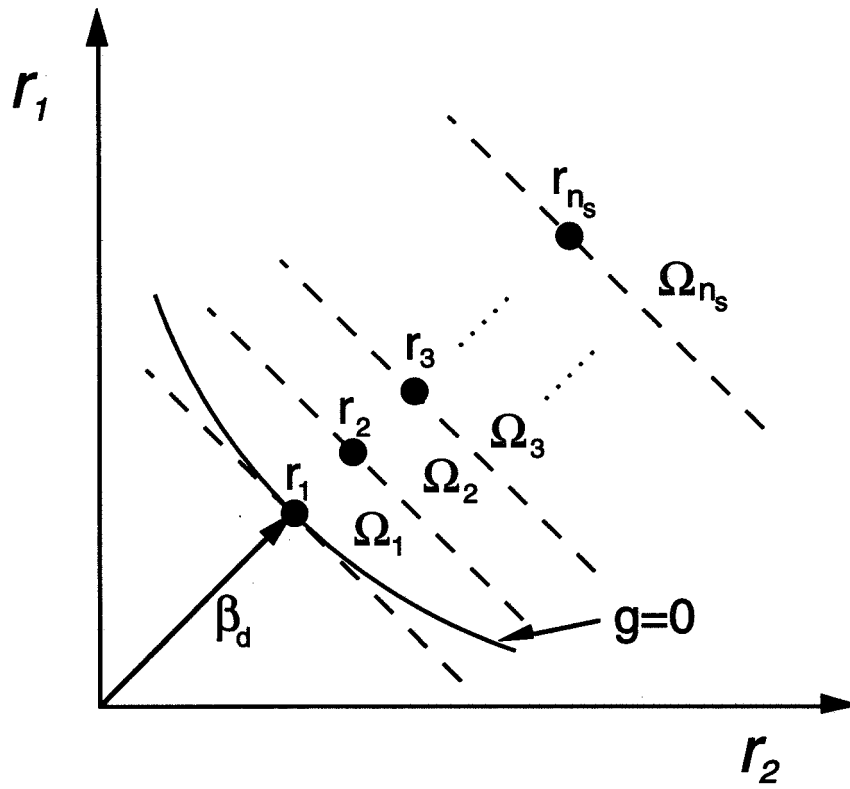


Figure 2. FORM integration scheme

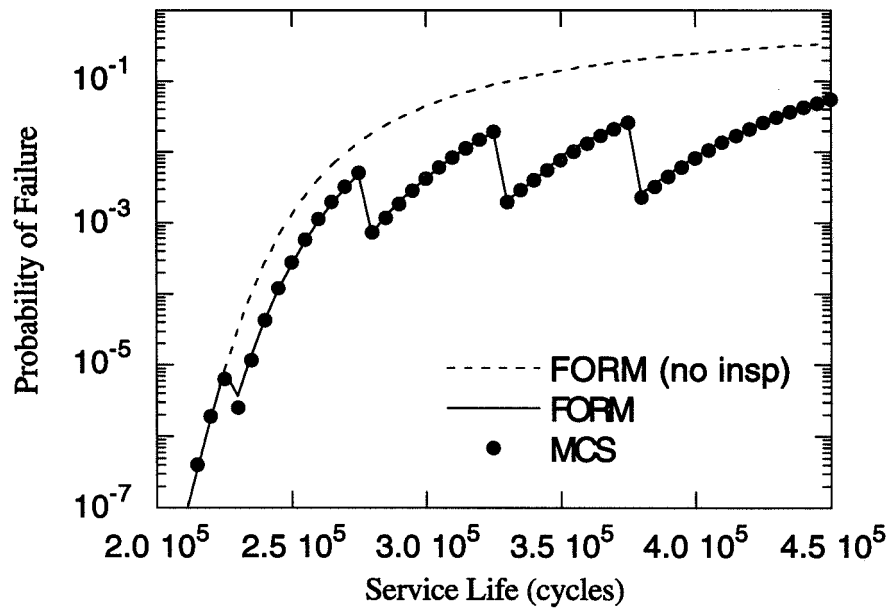


Figure 3. Probability of Failure for test case with and without inspections.

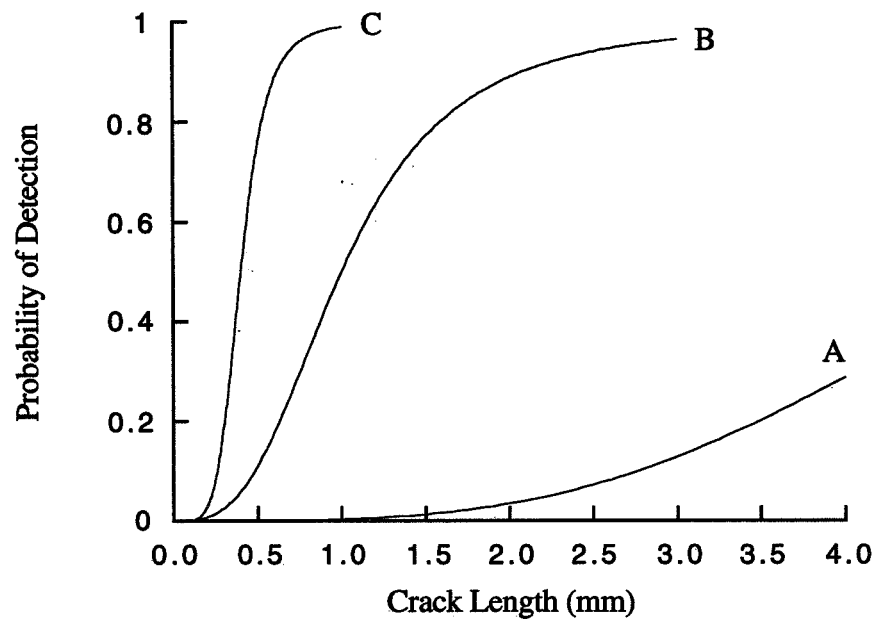


Figure 4. Probability of detection curves (A: $\alpha=0.0032 \text{ mm}^{-\beta}$, $\beta=3.5$; B: $\alpha=1 \text{ mm}^{-\beta}$, $\beta=3$; C: $\alpha=100 \text{ mm}^{-\beta}$, $\beta=5$)

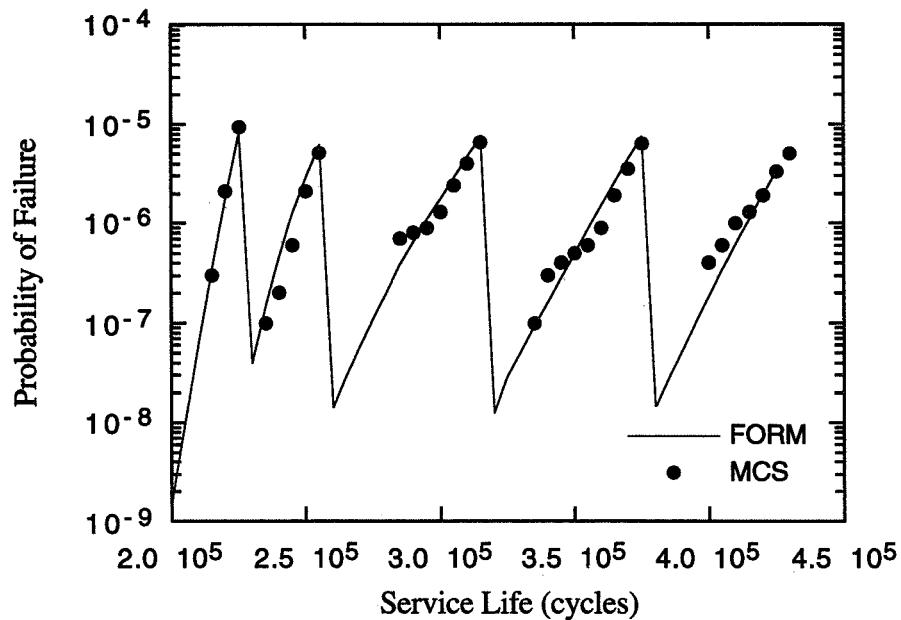


Figure 5. Results for edge crack using augmented FORM and uneven inspection intervals.

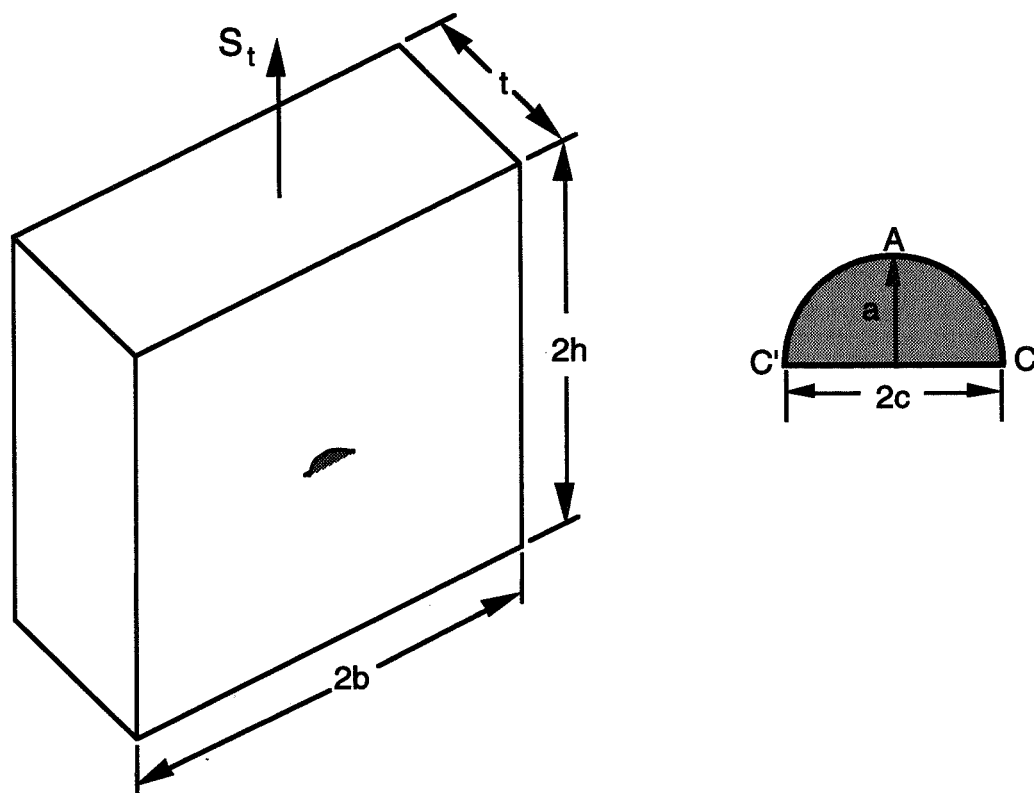


Figure 6. Rectangular plate with surface-breaking semi-elliptical crack.

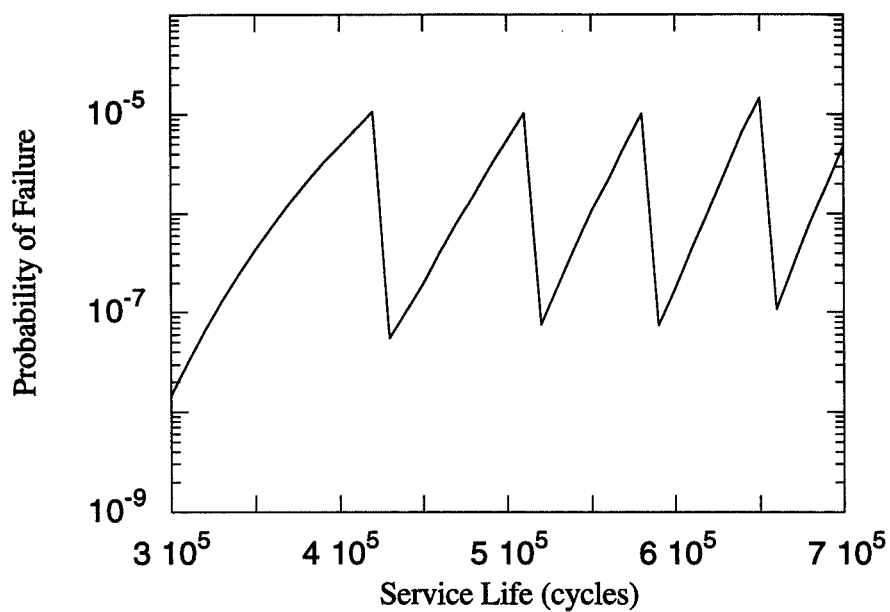


Figure 7. Probability of failure for surface-breaking crack in a plate.

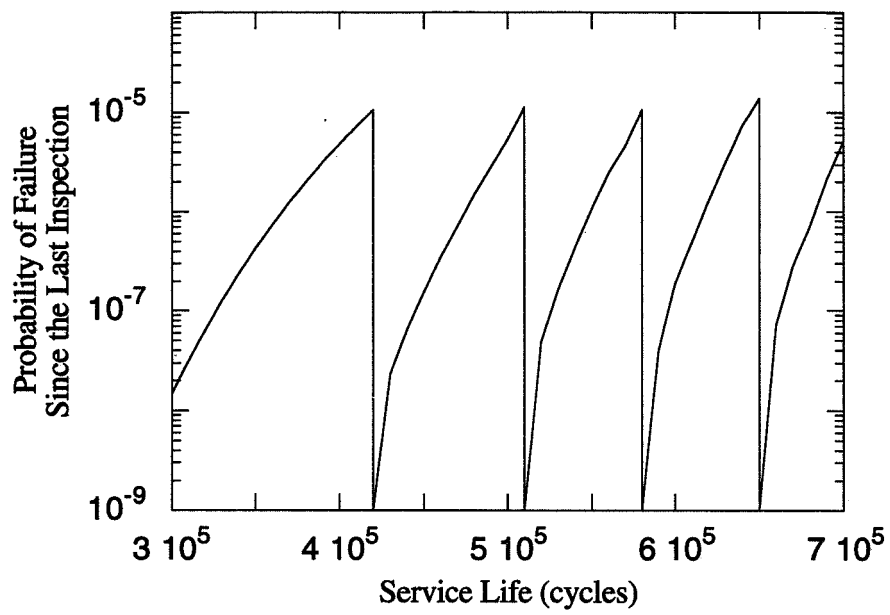


Figure 8. Probability of failure since the last inspection for surface-breaking crack in a plate

NONLINEAR BULGING FACTOR BASED ON R-CURVE DATA

David Y. Jeong and Pin Tong¹
U.S. Department of Transportation
Research and Special Programs Administration
Volpe National Transportation Systems Center
Cambridge, MA 02142-1093 USA

348661
523-39
23117
p 12

SUMMARY

In this paper, a nonlinear bulging factor is derived using a strain energy approach combined with dimensional analysis. The functional form of the bulging factor contains an empirical constant that is determined using R-curve data from unstiffened flat and curved panel tests. The determination of this empirical constant is based on the assumption that the R-curve is the same for both flat and curved panels.

INTRODUCTION

Bulging refers to the rotation and deflection of the edges of a longitudinal crack in a pressurized fuselage. Physically, the bulging phenomenon causes local bending at the crack tips which increases the effective stress intensity factor. The conventional engineering approach to account for this effect is to apply a bulging factor to the stress intensity factor.

Bulging factors have been developed both analytically and empirically. For example, one of the most commonly used bulging factors is an empirical formula derived by Kuhn [1]:

$$\beta_B = 1 + 10 \left(\frac{a}{R} \right), \quad \frac{R}{t} > 100 \quad . \quad (1)$$

¹ Also, Hong Kong University of Science and Technology, Kowloon, Hong Kong.

The obvious shortcoming of this bulging factor is the apparent independence of bulging on skin thickness. Analytical bulging factors have been derived by Folias [2,3] and by Erdogan and Kibler [4]. For example, Folias [3] derived the following bulging factor

$$\beta_B = \sqrt{1 + 0.317\lambda^2} \quad , \quad \lambda = \frac{\alpha}{\sqrt{Rt}} \sqrt[4]{12(1-\nu^2)} \quad (2)$$

where α is the half crack length, E is the modulus of elasticity, ν is Poisson's ratio, R is the radius of curvature, and t is the skin thickness. Folias [3] states that equation (2) is applicable for all values of λ . However, the analytical bulging factors [2-4] tend to overestimate the bulging effect in most practical cases. This conclusion has been supported by research performed by Ansell [5] who showed that more realistic deformation behavior in the vicinity of the crack tip can be achieved using a geometrically nonlinear analysis rather than a linear analysis. The nonlinear character of crack bulging has been taken into account by Chen [6] who derived a bulging factor that depends on the applied stress. Furthermore, Broek [7] has noted that bulging causes membrane tension which, in turn, produces the main resistance to bulge formation rather than bending stiffness. Consequently, the bulging factor becomes nonlinear because the membrane stress depends on the depth of the bulge.

In this paper, a nonlinear bulging factor is derived using a strain energy approach similar to that used by Chen [6], but combined with dimensional analysis. The resulting bulging formula contains an empirical constant which is determined using R-curve data from unstiffened flat and curved panel tests. The numerical value of this empirical constant is found by assuming that the R-curve or crack resistance curve is the same for both flat and curved panels.

DERIVATION OF NONLINEAR BULGING FACTOR

A strain energy approach is used to derive the mathematical form of the nonlinear bulging factor. The following derivation initially resembles that used by Chen [6].

The energy release rate is related to the derivative of the strain energy with respect to half-crack length, and can be written as

$$\mathcal{G} = \frac{d}{d\alpha}(F - U) \quad (3)$$

where F is the work done by external forces and U is the elastic strain energy of the system associated with crack extension. For a pressurized cylinder, the quantity $F - U$ is assumed to be comprised of two components; one due to crack bulging and another due to the applied pressure², or

$$\mathcal{G} = \frac{d}{d\alpha}(F_{bulge} - U_{bulge} + F_{flat} - U_{flat}) \quad (4)$$

The component due to the crack face deformation or bulging is derived by assuming that the out-of-plane deformation field in the neighborhood of the crack can be characterized by the pyramidal shape shown schematically in Figure 1. Denoting s_1 and s_2 as characteristic lengths, and w_o as the maximum out-of-plane displacement, Chen [6] found that

$$\frac{d}{d\alpha}(F - U)_{bulge} \approx \frac{1}{3} p s_1 s_2 \frac{dw_o}{d\alpha} \quad (5)$$

where p is the applied pressure.

The component due to the applied pressure or hoop stress is

$$\frac{d}{d\alpha}(F - U)_{flat} = p^2 R^2 \frac{\pi \alpha}{E t} = \mathcal{G}_{flat} \quad (6)$$

² The present derivation uses this decomposition as a simplifying assumption. However, this assumption implicitly decouples the effects of applied loading and bulging. Strictly speaking, these effects should be coupled.

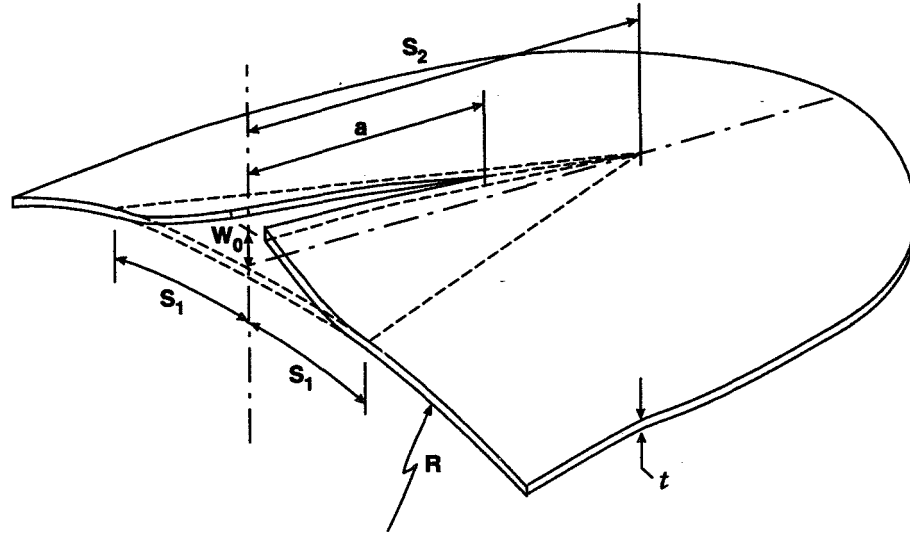


Figure 1. Deformation of crack faces due to bulging.

Combining equations (5) and (6), the energy release rate for a panel with bulging becomes

$$\mathcal{G}_{curve} = \frac{1}{3} p s_1 s_2 \frac{dw_o}{da} + p^2 R^2 \frac{\pi a}{Et} . \quad (7)$$

The bulging factor is defined as the ratio of stress intensity factors for curved to flat panels, or

$$\beta_B = \frac{K_{I_{curve}}}{K_{I_{flat}}} . \quad (8)$$

The bulging factor is assumed to be related to the energy release rates for panels with and without bulging by

$$\beta_B = \sqrt{\frac{\mathcal{G}_{curve}}{\mathcal{G}_{flat}}} . \quad (9)$$

Thus, the bulging factor has the following mathematical form:

$$\beta_B = \sqrt{1 + \frac{E t s_1 s_2}{3 \pi \alpha p R^2} \left(\frac{dw_o}{d\alpha} \right)} \quad (10)$$

At this point, the derivation of the functional form of the bulging factor deviates from Chen's approach [6], and dimensional analysis is employed. That is, dimensionless constants are used to simplify the mathematical representation of the bulging factor. For example, the characteristic lengths, s_1 and s_2 , can be expressed in terms of a proportion to half crack length, α ; or

$$s_1 = \alpha_1 \alpha, \quad s_2 = \alpha_2 \alpha \quad (11)$$

In addition, an expression for the out-of-plane deformation, which has its basis in large displacement theory of elasticity [8], can be written as

$$w_o = \alpha_3 \alpha \sqrt[3]{\frac{p \alpha}{E t}} \quad (12)$$

where α_3 is a constant. Therefore, the increment of out-of-plane deformation with respect to crack length can be written as

$$\frac{dw_o}{d\alpha} = \alpha_4 \sqrt[3]{\frac{p \alpha}{E t}} = \alpha_4 \sqrt[3]{\frac{\sigma_o \alpha}{E R}} \quad (13)$$

since the hoop stress is

$$\sigma_o = \frac{p R}{t} \quad (14)$$

Thus, a general nonlinear bulging factor may be found by combining equations (10), (11), (13) and (14):

$$\beta_B = \sqrt{1 + \alpha \left[\left(\frac{E}{\sigma_o} \right) \left(\frac{\alpha}{R} \right)^2 \right]^{2/3}} \quad (15)$$

where α is an empirical constant. The determination of the numerical value for this empirical constant is described in the following section.

DATA ON STABLE TEARING

A series of flat and curved panel tests has been conducted by Foster-Miller, Inc. (FMI) to provide a database from which analytical models can be verified [7,9]. R-curve data were collected during these tests in terms of stable crack extension versus applied pressure. For flat panels, crack resistance in terms of the stress intensity factor can be calculated as

$$K_R = \sigma_o \sqrt{\pi(a_o + \Delta a)} \sqrt{\sec\left(\frac{\pi(a_o + \Delta a)}{W}\right)} \quad (16)$$

where W is the width of the panel. A regression analysis was performed to fit the FMI flat panel data to the following two-parameter R-curve equation:

$$K_R = K_o \Delta a^b \quad (17)$$

The results of the regression analysis were: $K_o = 106.1 \text{ ksi-in}^{1/2}$ and $b = 0.212$.

For curved panels, crack resistance in terms of stress intensity factor depends on the bulging factor³:

$$K_R = \sigma_o \beta_B \sqrt{\pi(a_o + \Delta a)} \sqrt{\sec\left(\frac{\pi(a_o + \Delta a)}{W}\right)} \quad (18)$$

³ This equation is an approximation to the actual stress intensity factor for fracture resistance because the curved test panels are biaxially loaded which has not been taken into account.

In principle, if the assumption is made that the R-curve is the same for both flat and curved panels, then the constant, α , can be determined by combining equations (17) and (18), and equating the result with the nonlinear bulging factor described by equation (15), or

$$\frac{K_o \Delta \alpha^b}{\sigma_o \sqrt{\pi(\alpha_o + \Delta \alpha)} \sqrt{\sec\left(\frac{\pi(\alpha_o + \Delta \alpha)}{w}\right)}} = \sqrt{1 + \alpha \left[\left(\frac{E}{\sigma_o} \right) \left(\frac{\alpha_o + \Delta \alpha}{R} \right)^2 \right]^{2/3}} \quad (19)$$

Using this equation, a different numerical value for the empirical constant can be calculated for each collected data point where the amount of stable crack extension was measured at a given level of applied stress. A total of 251 data points were collected during the unstiffened curved panel test. Each point was used to calculate the numerical value of the empirical constant. The average or mean value of α was found to be 0.671⁴.

Figure 2 compares the flat and curved panel data, as derived by this method, with the regression curve. Good agreement between the test data and the two-parameter R-curve equation is evident between 0 to 0.6 inches of stable crack extension. After $\Delta \alpha = 0.6$ inches, the curved panel test data are approximately 10% higher than the regression curve in terms of stress intensity factor.

DISCUSSION

Figure 3 compares the nonlinear bulging factor or equation (15) where $\alpha = 0.671$ with other bulging factors, namely, equations (1) and (2). The nonlinear bulging factor is approximately equal to equation (1) at extremely small values of crack length. As the crack length increases, however, the nonlinear bulging factor deviates from the Folias bulging factor which is based on the assumptions of linear elastic material behavior and small displacements. Residual strength tests were conducted on curved panels with ratios of half crack length to radius of curvature between 0.06 to 0.10. Figure 3 shows that over the range of test values that the difference between the empirical and the nonlinear bulging factors is not as significant as that between the empirical and Folias solution.

⁴ For the FMI curved panels, E was assumed to be 10 msi and R is 75 inches.

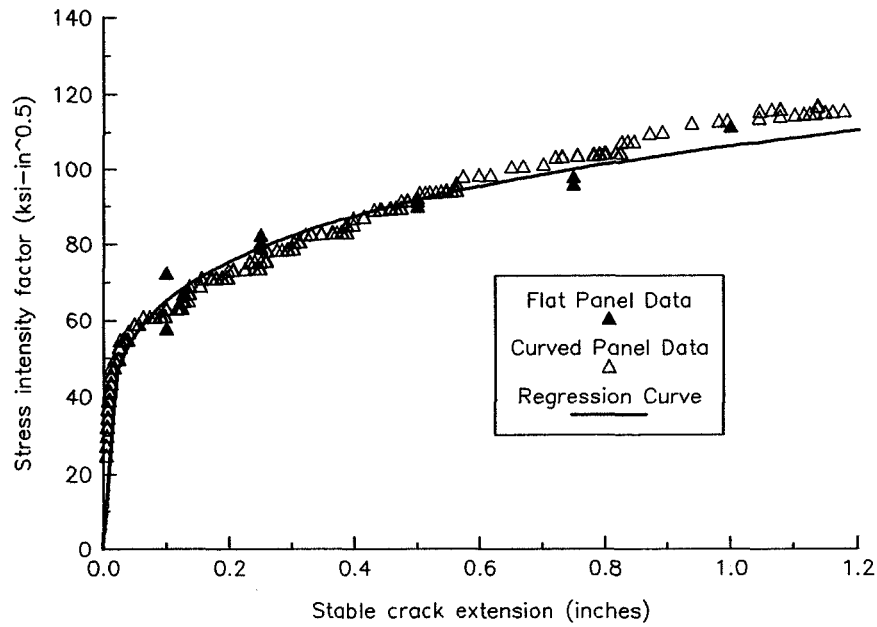


Figure 2. R-Curve for flat and curved panels.

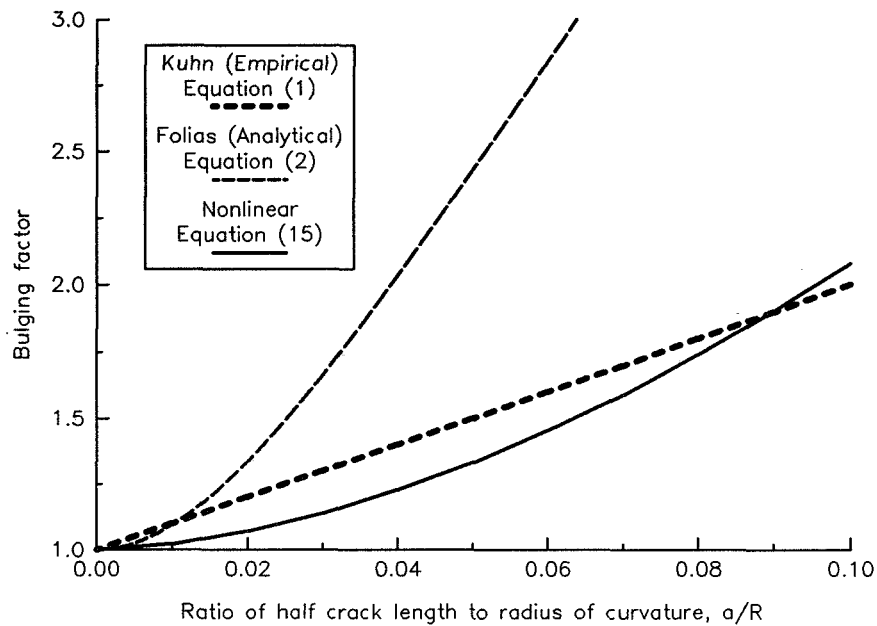


Figure 3. Comparison of bulging factors ($R = 75$ inches and $t = 0.040$ inch).

As mentioned previously, the numerical value of the empirical constant was determined by calculating the constant at each data point on the R-curve from the FMI curved panel tests, and taking the average or mean value. Figure 4 shows the frequency distribution of the calculated values for the empirical constant. A normal distribution curve is also shown for comparison. The mean value was found to be 0.671, and the standard deviation was 0.095. The frequency plot indicates that 242 of 251 data points resulted in a value between 0.5 and 0.7. Thus, the mean value of 0.671 appears to be reasonable.

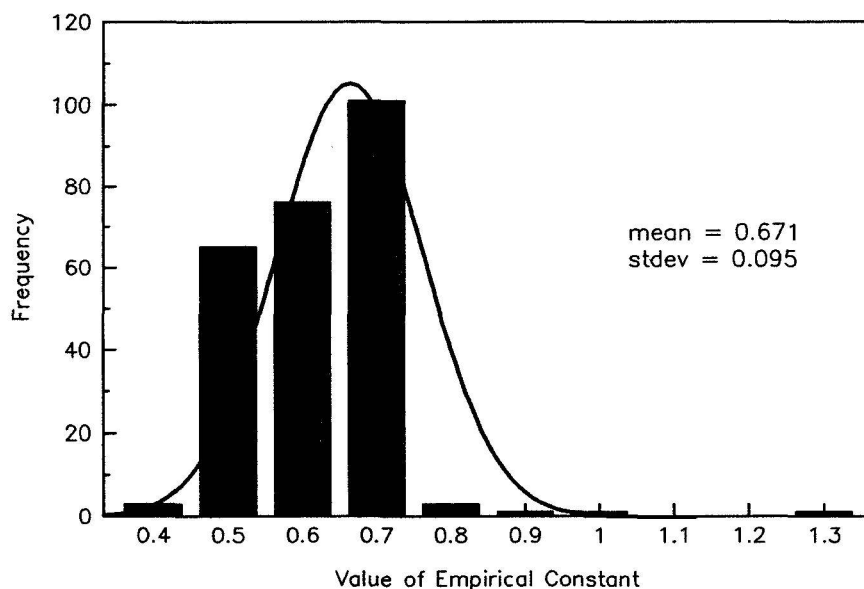


Figure 4. *Distribution of numerical values for empirical constant in nonlinear bulging factor.*

Predictions of failure were made for the Foster-Miller curved panels using the two-parameter R-curve equation and the nonlinear bulging factor. Two tests were conducted at the FMI full-scale test facility with unstiffened curved panels [9]. Table 1 lists the results of these tests which used two different values of initial crack length. The table compares the test results with the failure predictions based on the R-curve analysis. Predictions of failure stress are shown to be within 10% of the experimental data, which is within reasonable engineering agreement. Figure 5 shows a plot comparing the R-curve predictions with the experimental results.

Table 1. Failure Stresses for Foster-Miller Unstiffened Curved Panels

Initial half-crack length (inches)	Failure stress (ksi)		% difference
	Prediction	Experiment	
5.5	13.4	12.2	+9.8%
8.0	8.8	9.2	-4.3%

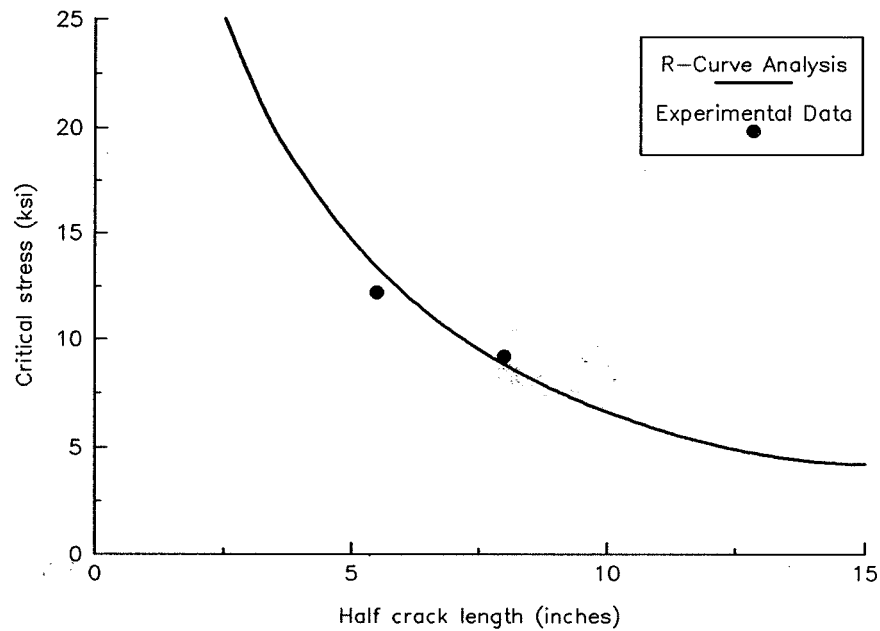


Figure 5. Failure predictions for FMI curved panels using R-curve data and nonlinear bulging factor.

The effect of biaxial loading has not been explicitly taken into account in the present methodology. Bulging is affected by the ratio of hoop-to-longitudinal stress. Chen [6] found that the bulge factor of a biaxially loaded specimen is significantly lower than that of a uniaxially loaded specimen.

Since the results presented in this paper were generated on the basis of two unstiffened curved panels, the results are considered to be developmental. While additional research is recommended in the determination of appropriate bulging factors, the approach presented in this paper appears to give encouraging results.

CONCLUSIONS

The mathematical or functional form of a nonlinear bulging is derived using a strain energy approach similar to that used by Chen [6]. The derivation is complemented with dimensional analysis which leads to an unknown or empirical constant in the nonlinear bulging factor.

A methodology to determine the numerical value of the unknown constant is proposed in this paper. The methodology is based upon the assumption that the R-curve is the same for both flat and curved panels. Experimental data from unstiffened flat and curved panel tests were used to demonstrate the application of this approach. Different values for the empirical constant are calculated for each data point where stable crack extension is measured at a given level of applied load. The average of all these values is taken as the numerical value of the empirical constant.

Failure predictions of two unstiffened curved panels were made using the measured R-curve data and the nonlinear bulging factor as determined by the present technique. Analytical predictions of panel failure were found to be within 10% of the experimental values.

Acknowledgement - The research described in this paper was performed in the support of the Federal Aviation Administration Technical Center's Aging Aircraft Research Program. The support and interest from Dr. Michael L. Basehore at FAATC is gratefully appreciated.

REFERENCES

- [1] Kuhn, P.: Notch Effects on Fatigue and Static Strength, Symposium of the International Committee on Aeronautical Fatigue (ICAF), Rome, Italy, 1963.
- [2] Folias, E.S.: An Axial Crack in a Pressurized Cylindrical Shell, *International Journal of Fracture Mechanics* 1, 104-113, 1965.
- [3] Folias, E.S.: On the Prediction of Catastrophic Failures in Pressurized Vessels, *Prospects of Fracture*, Noordhoff International, Leyden, The Netherlands, 405-418, 1974.
- [4] Erdogan, F.; and Kibler, J.J.: Cylindrical and Spherical Shells with Cracks, *International Journal of Fracture Mechanics* 5, 229-236, 1969.
- [5] Ansell, H.: Bulging of Cracked Pressurized Aircraft Structure, Ph.D. Thesis, Linköping Institute of Technology, Sweden, 1988.
- [6] Chen, D.: Bulging of Fatigue Cracks in a Pressurized Aircraft Fuselage, Ph.D. Thesis, Delft University of Technology, 1991.
- [7] Broek, D.: The Effects of Multi-Site Damage on the Arrest Capability of Aircraft Fuselage Structures, FractuREsearch Report TR 9302, June 1993.
- [8] Timoshenko, S.; and Woinowsky-Krieger, S.: *Theory of Plates and Shells*, Second Edition, McGraw-Hill, New York, NY, 1959.
- [9] Thomson, D.; Hoadley, D.; and McHatton, J.; Load Tests of Flat and Curved Panels with Multiple Cracks, Foster-Miller, Inc. Draft Final Report to Volpe Center, September 1993.

DEVELOPMENT OF A COMPOSITE REPAIR AND THE ASSOCIATED INSPECTION
INTERVALS FOR THE F111C STIFFENER RUNOUT REGION

R. Jones
Professor of Mechanical Engineering,
Monash University, Clayton,
Victoria 3168, Australia.

L. Molent, J. Paul
Airframes and Engines Division,
Aeronautical Research Laboratory, DSTO,
506 Lorimer St, Pt Melbourne,
Victoria 3207, Australia.

T. Saunders
Aircraft Structural Integrity,
HQ Logistics Command, Royal Australian AirForce,
350 St. Kilda Road, Melbourne,
Victoria, 3004, Australia.

W. K. Chiu
Mechanical Engineering, Monash University,
Caulfield, Victoria 3168, Australia.

SUMMARY

This paper presents an overview of the structural aspects of the design and development of a local reinforcement designed to lower the stresses in a region of the F-111C wing pivot fitting which is prone to cracking. The stress analysis, with particular emphasis on the use of a unified constitutive model for the cyclic inelastic response of the structure, representative specimen testing, thermal analysis and full scale static testing of this design are summarised.

INTRODUCTION

F-111C aircraft in service with the Royal Australian Airforce (RAAF) are known to experience cracking in the Wing Pivot Fitting (WPF), and this has resulted in failure during Cold Proof Load Testing (CPLT) [1]. CPLT was originally introduced to ensure the continued airworthiness of the structure and involves the application of loads to the aircraft, at -40°C , where the load cycle is defined by the current Structural Integrity Program (SIP). Currently SIP III requires in a -2.4g , 7.33g -3.0g , 7.33g load applied to the aircraft. In the F-111C aircraft in service with the RAAF the critical area is Stiffener Runout No. 2 (SRO #2) on the upper surface of the WPF. The cause of these cracks and subsequent failure in the CPLT is discussed in [2]. In summary, local bending of the stiffener results in compressive yielding in the stiffener runout under high positive g loads. As a result, subsequent negative g loads, and to a limited extent positive g loads, produce very high tensile strains. The structure of the wing is comprised of a 2024-T856 wing skin spliced onto a D6AC steel WPF by an array of flush stainless steel fasteners. Cracking is occurring inboard from the splice in the runout region of the top surface integral stiffeners. The general geometry of the critical region is shown in Figure 1.

This paper presents an overview of the design and development of a boron epoxy reinforcement (doubler) designed to lower the stresses in the critical region [3,4]. This design is currently being installed progressively on RAAF fleet aircraft prior to them undergoing their next CPLT.

In order to determine the associated inspection intervals it was necessary to obtain the residual stress, after CPLT, and the stress "per g " both with and without doubler and with various grind out configurations. Since during CPLT SRO #2 undergoes gross plastic yielding, to obtain this information requires a detailed elastic-plastic analysis. However, classical techniques for modelling this cyclic behaviour have inherent difficulties in representing the response to large cyclic inelastic strain excursions. Indeed, the use of classical analysis techniques resulted in an inspection interval, for the modified structure, of under 500 hours. This contrasts with service experience which has shown that there is little further cracking. Indeed, for modified aircraft there has been no further cracking since 1985. To overcome this shortcoming the use of a "unified constitutive" model, see [5,6], was investigated.

REPAIR PROCEDURES

The reinforcement (doubler) consists of two discrete boron/epoxy doublers bonded, using an elevated temperature cure cycle, to the upper surface of the F-111 WPF. The doublers are located over those stiffeners known to be subject to the highest strains, see Figure 2. One large doubler covers stiffeners number 4 and 5, and a smaller doubler covers stiffener number 2. The doublers were fabricated from uni-directional boron/epoxy composite and are co-cured with an adhesive at elevated temperatures. Each doubler consists of two segments. The lower segment is bonded to the D6AC steel to provide a bridge level with the aluminium skin step, and the upper segment is bonded to the aluminium skin and over the lower segment. Each segment of the preferred design consists of approximately 60 plies of boron in the

middle, suitably tailored to achieve single plies at the extremities of the doubler. The lower segment contains a cutout region adjacent to the aluminium skin step, designed to reduce the stress concentration produced by the discontinuity of the load path, see Figure 3.

FINITE ELEMENT MODELS

Two Dimensional Models

Initially a series of two and three dimensional finite element models were created to represent the unreinforced critical region, see [3,4], and the models were calibrated using strain data from a survey conducted in the US [7] in support of the failure investigation of a WPF. For the reinforced model, the left hand wing was deemed to be the design case, as from all available data at the time, this wing recorded the highest strain levels and thus the most severe problem. In order for the model to adequately represent the local detail of the structure in the wings, spring elements (or equivalent plate elements) were used to account for the restraint provided by the remainder of the structure. One spring was attached to the extreme left hand side of the model and the other to the vertical web. Both springs only possessed stiffness along their major axes. The bolts which join the WPF to the upper and lower aluminium splice were included and were modelled as described in [3].

MATERIAL PROPERTIES AND FAILURE CRITERION

The material properties used for the boron/epoxy system were $E_{11}=208.1$ GPa, $E_{11}/E_{22}=8.18$, $G_{12}=G_{13}=7.24$ GPa, $G_{23}=4.94$ GPa, $E_{33}=E_{22}$, $\nu_{12}=\nu_{13}=0.1677$, $\nu_{13}=0.035$ and the adhesive has $G=750$ MPa and $\nu=0.35$. The Young's modulus and Poisson's ratio for the aluminium were taken to be 71×10^3 MPa and 0.33, respectively. Young's modulus, Poisson's ratio and yield stress (compressive) for the steel were taken to be 207 GPa, 0.3 and 1600 MPa respectively. The doubler design criteria were to achieve a stress reduction sufficient to prevent yielding of the steel, and to withstand an applied loading of 7.3g or -2.4g*. The design allowables for the adhesive shear stress $\tau < 40$ MPa, peel stress $\sigma_p < 40$ MPa, and fibre stress $\sigma_f < 1000$ MPa for the boron/epoxy system were assumed. The interlaminar stresses in the doubler must also be below their critical values. The manufacturer's value for the boron/resin system used are : $\tau_{xy} < 90$ MPa and $\sigma_y < 70$ MPa

ELASTIC-PLASTIC ANALYSIS

Unified Constitutive Model

Classical techniques of modelling plasticity have a high degree of accuracy provided the inelastic strains are kept small. However, they become increasingly inaccurate when the material exhibits high inelastic strains and undergoes cyclic loading that causes gross plastic yielding. The current problem in the F-111 SRO #2 undergoes the two previously mentioned phenomena and the use of classical techniques was found to lead to large errors. To overcome this shortcoming the Unified Constitutive model, originally developed by Ramaswamy [5], was used. (This model is an extension of the generic back stress and drag stress model proposed by Bodner and Stouffer [6].) Indeed, the authors have extensively used, and developed [8,9], these constitutive equations to model non-linear material behaviour in aluminium, adhesives and steels. In order to represent the material D6ac steel correctly in the high strain, cyclic loading regime, experimental stress/strain data was obtained from coupon tests [10], at room temperature. The experimental stress/strain curve under a loading of III SIP was compared with one generated using the Unified Constitutive model (see Figure 4) and one generated using classical plasticity finite element (see Figure 5). From these two Figures it is clear that classical plasticity does not adequately represent the material behaviour under cyclic loading and as the strain level is increased so too is the error.

Finite Element Configuration

Considerable wing-to-wing geometry variation exists in the fleet. Consequently, although the basic finite element models used in this analysis were as described in [3,4], it was necessary to perform a parametric study to quantify the effect of this variation on structural integrity. A total of 36 models, incorporating the various geometric configurations including plate thickness variation for each of the 7 main configurations, grind out depths and kink angles, i.e. the angle between the upper plate and the aluminium wing skin, were examined. The parameters in the analysis matrix analysed were directly based on the fleet inspection data collected by the RAAF.

Model Calibration

The unreinforced models were calibrated from the USAF strain survey data [7]. The finite element mesh used and gauge locations 6L and 9L used in the calibration process are shown in Figure 6. The reinforced models were calibrated from the recent CPLT of the A8-113 aircraft [16] and the 'kink' angle, i.e. the angle between the upper plate and the aluminium skin, was obtained from the RAAF doubler application reports for the A8-113 wing. In general good agreement, i.e. to within 7%, was obtained

with the experimental strain gauge data. The unreinforced finite element analysis was calibrated with the USAF strain survey. The plastic analysis results are shown in Figure 7.

Residual Stresses

This analysis revealed that, for the nominal wing geometry, the peak residual stress following CPLT was approximately 1000 MPa; this contrasts with a value of approximately 1950 MPa obtained using classical plasticity, and that following reworking of the stiffener, see below, and doubler installation this reduces to less than 50 MPa. It was also found that following doubler installation the stress per g, at the critical location, is reduced by approximately 30%.

REDESIGN OF THE STIFFENER RUNOUT REGION

Finite Element Analyses

When bonded to the upper surface of the WPF the doubler reinforcement was found to considerably decrease the stress magnitude in the stiffener runout, approximately 30%, see [3]. Even so if the geometry of the SRO is left unmodified the stress level may be sufficient to cause yielding. This is a direct result of the stress concentration produced by the sharp re-entrant corner at the runout. To suppress local yielding various grind radius configurations (4mm, 11mm, and 22mm) at the corner as well as complete removal of the stiffener runout were investigated [3]. From the results of the stress analyses, using Von Mises' criterion, for the 4mm, 11mm, 22mm and the total grind out cases, the 22mm case was chosen as the optimum rework. Indeed, it was found that the combination of a 120 ply doubler and a grind out radius of approximately 22mm will achieve the desired stress reduction and prevent yield under CPLT loading. This prediction was confirmed via a thermal emission experiment [12].

In the case of the "complete" stiffener grindout (see [3]), the maximum value of the stress in the critical region is less than for the basic reinforced structure. However in this case the problem of crack initiation in the plate is a major concern.

DOUBLER STRESSES

The locations of the most critical points in the doubler were also investigated [3]. The design of the reinforcement was developed to minimise the stresses at these locations. These 'design points' are shown in Figure 8 and are labelled A to I. (The adhesive filler is present in the doubler cut out to provide it with

stability.) For the adhesive the combined stress state elevates the permissible shear stress, such that the computed values are below critical (see [3]). The combined stress state in the boron/epoxy is also beneath critical values. This can be evaluated either using the critical energy or using a stress polynomial failure criteria, see [12]. The fibre stresses are below the critical design value. The adhesive filler has the effect of slightly reducing the peak values of the stress at points 'C' and 'F'. It also decreases the peak bending at point 'H' on the doubler.

For extreme kink angles in conjunction with geometric imperfections the interlaminar stresses (strain energy) in the upper doubler exceeded allowables. This was reflected by early failures in CPLT. To overcome this the local matrix material thickness was increased in the critical region of the doubler. This also has the effect of increasing the local load transfer region. As such interlaminar failure considerations, rather than the adhesive allowables, drove the final design concept. This is in marked contrast to the PABST design philosophy, see [13], whereby joints and composite repairs are designed on the basis of the maximum load transfer capability of the adhesive. In this case adopting the PABST design approach would have resulted in an unconservative design and catastrophic failure of the repair. Indeed, this is illustrated by the early failures in CPLT for doublers which were initially designed on the basis of adhesive allowables.

FULL SCALE STRUCTURAL TESTS

In the final stages of the proof-of-concept phase, a detailed strain survey was conducted on an F-111C wing both with and without doublers [14]. The results of the reinforced case survey were compared to those for the unreinforced case [15]. A damaged and subsequently repaired wing and wing carry through box (WCTB) were made available for use in the ARL strain survey program. A rig was fabricated to support the wing and WCTB, which was capable of applying the proof load conditions of 7.3g and -2.4g. Load was applied to the wing by hydraulic jacks located at the four pylon points, the number 2 flap track attachment point on the rear spar, and at the rib nearest the wing tip.

The wing loading arrangement reproduced the loads experienced by the wing during certification testing of the F-111 in the CPLT, at a sweep angle of 26°.

Cold Proof Load Test

The final test in the 'proof of concept' phase of this design was under CPLT conditions at -40°C [16]. Due to the scale and economical restraints it was decided that, for the purposes of ascertaining the reinforcement integrity, only the area in the immediate vicinity of the reinforcement needed to be cooled. For this to be achieved an insulated chamber constructed from polystyrene foam was erected around the

WPF. The construction extended two metres outboard from the wing root, two metres chordwise and was one and a half metres deep.

With the temperature of the upper wing surface approximately steady at -40°C , the wing was successfully loaded to -100% proof load. Following this the load jacks were reconfigured, whilst holding the temperature steady, and uploading was commenced. A strain reading was taken at +95%, but then the wing suddenly failed approaching +100% proof load.

The test article wing had been salvaged from a crashed aircraft, and was repaired to a state capable of withstanding 'significant' test loads. The repairs to this wing, as described in [16], were extensive and of 'boiler plate' construction as distinct from aircraft quality. Thus, from the inception of the strain survey program, higher loads were approached cautiously.

During loading of the wing at high levels, the deflected shape of the wing revealed a sharp change in slope at the outboard end of this mechanically repaired region. It was in this region that failure occurred during this CPLT. The areas of failure, in this vicinity (see [16]) were the rear and forward spars, lower wing skin, a section of the upper wing skin and all internal spars. Note, the failure occurred through the aluminium wing structure and thus was not affected by the applied temperature. No structural damage was detectable on the WPF.

Whilst there was a concern over the non-linear behaviour of a few doubler gauges (see [16]), sufficient data were available to demonstrate that the doublers behaved satisfactorily during CPLT. The delamination and debond of the small doubler was considered to have been caused by the 'shock' loading experienced immediately upon failure of the wing. This load was significant as can be deduced from the resultant damage to the test rig in the immediate vicinity below the doubler. In view of the observed non-linearity in a few strain gauge readings the corners of the production doublers were 'softened' to reduce their stiffness. This modification results in the corner of the doublers having a chordwise, as well as a spanwise, taper thus reducing the load concentration at these locations.

IN-SERVICE PERFORMANCE

Currently fourteen aircraft have been reinforced and there were problems associated with three aircraft reinforced early in the program. A brief description of the early prototype doublers and the current production doubler system is given. The early prototypes of the doublers were installed on Aircraft A8-148, followed by aircraft A8-144. In summary, failures, at high load levels during CPLT, occurred in both doubler sets. Both sets of wings were considered to vary significantly (geometrically) from the specification drawings. Post-failure investigations revealed some deficiencies in the doubler application process, and these were subsequently addressed.

Following the early doubler failures modifications were made to the application process resulting in the current production models. Specifically, as the failures occurred in the boron/adhesive interface, the

changes mainly addressed this area. In summary, (a) The matrix thickness near the top of the lower doubler was increased to increase the damage tolerance of this region, (b) Micro-cracking induced into the boron matrix due to the grit-blasting procedure was eliminated, (c) All adhesive thicknesses were doubled.

All these changes were certified through laboratory coupon testing and Aircraft A8-142 was the first to receive these changes. In addition, an attempt was made to apply higher preloads during the application process. Unfortunately, due to a problem with the system used to preload the wing, the doubler was formed on the aircraft wing at a preload of 98 kN (22,000 lbs), but was cured to the wing at 129 kN (29,000 lbs). This resulted in non-conformity of shape at the higher preload. Following the doubler application process on unloading the wing, at RAAF Base Amberly, doubler failure was experienced, at zero load, during a 10 minute pause to collect strain data. This failure did not occur on commencement of the strain survey but took a considerable time to occur.

Two doublers on A8-142 that also failed during CPLT Post-failure investigation revealed large void areas. This failure, which also occurred during a 10 minute pause to collect strain data, was also attributed to the non-conformity of the doublers to the wing curvature during the higher preload curing procedure.

Subsequent to this failure the preload was fixed at 89 kN (20,000 lbs), for both the forming and application of the doublers. A final change to the application procedure was the incorporation of a humidity control system, used to minimise the environmental humidity during the curing of the doublers. Aircraft A8-126 was the first to undergo CPLT, with the doublers incorporating all the above changes, and did so successfully. To date a further nine aircraft have successfully completed CPLT.

These two failure events highlighted the time dependent nature of the failure process for composite bonded repairs and illustrated the need to account for load and strain holds in the design process. Failure was often interlaminar failure in the composite doubler. As such interlaminar failure considerations, rather than the adhesive allowables, drove the final design concept. This is in marked contrast to the PABST design philosophy, see [13], whereby joints and composite repairs are designed on the basis of the maximum load transfer capability of the adhesive. In this case adopting the PABST design approach would have resulted in an unconservative design and catastrophic failure of the repair. Consequently, for composite doublers attention must be paid to assuring that the interlaminar stresses are beneath the (rate dependent) design allowables. To this end an extensive study of the effects of rate dependency, strain holds, creep and time on the mechanical performance of adhesives and composite joints was performed. This study has resulted in a detailed understanding of these processes together with an experimentally validated design philosophy for designing damage tolerant repairs, see [9,18].

CPLT of A8-113

Finally, as part of a wider data gathering program, aircraft A8-113 was strain surveyed during routine CPLT at Sacramento Air Logistics Command, USA, during April 1990. Prior to this survey, a preliminary strain survey was conducted on this aircraft at Amberley, Australia, to certify the strain gauges and acquisition system, and to gather baseline data [19].

This aircraft was extensively strain gauged, including the doublers and the critical stiffener areas. The results of the survey [20] indicated that no permanent set was evident in the stiffener runouts, as predicted in [3], indicating that the boron/epoxy doublers were effective in preventing further yielding at these locations. All data gathered from gauges on the doublers were linear, indicating no deterioration of the adhesive bond.

CONCLUSIONS

From the results of this analysis and the testing program summarised in this work, an all boron/epoxy doubler reinforcement should achieve the initial design requirements, that is WPF survival in the CPLT, when applied to a fleet aircraft. This was confirmed during routine CPLT testing of an F-111 aircraft. From the results of numerous strain surveys of a boron/epoxy reinforced WPF, it has been shown that substantial strain reductions were achieved. In the critical region, the relative strain reductions were approximately 40% and 20% for the positive and negative load cases respectively.

The reinforcement was loaded to $\pm 100\%$ proof load under ambient and -40°C conditions with no visible signs of deterioration. Further yielding of the WPF had not occurred at these load levels. The measured strain reductions were in good agreement with those predicted by finite element analysis. Good agreement was also shown between finite element analysis and test specimens designed to reproduce the adhesive stresses in the doublers.

The parametric study on the F111C Stiffener Run Out Number 2 has shown that the local geometry, i.e. plate thickness, kink angle, etc, has a significant effect on the stress and the residual stress distribution through the stiffener. The most significant parameter affecting the stress and residual stress is the radius of the grind, with the plate thickness also having a lesser effect. The analysis performed on the doubled aircraft show that the local angle of the plate to the skin has a significant effect on the bending of the local section. This was confirmed in the calibration of aircraft A8-113.

The results of the elastic/plastic analysis, and the residual stresses, obtained in the parametric study on the F111C Stiffener Run Out Number 2 have subsequently been used as the stress input to the RAAF DADTA analysis. Here one of the main objectives of the DADTA analysis was to determine the inspection intervals for RAAF F111C aircraft fitted with the boron doubler applied. Using this stressing information for a aircraft with no doubler, and worst case scenario of geometry, the inspection interval

predicted was 87 hours. However, for the same configuration, but with a doubler, the inspection interval was calculated as 2,000 hours. At the other extreme, the inspection interval has been predicted to be 446 hours with no doubler and 6,000 hours with a doubler. This result now enables the RAAF to reconsider the current maintenance schedules with a potential dramatic cost saving and increased aircraft availability.

From the technical point of view two major points were highlighted; viz:

- (i) Interlaminar failure considerations, rather than the adhesive allowables, drove the final design concept. This is in marked contrast to the PABST design philosophy, see [13], whereby joints and composite repairs are designed on the basis of the maximum load transfer capability of the adhesive. In this case adopting the PABST design approach would have resulted in an unconservative design and catastrophic failure of the repair. Consequently, for composite doublers attention must be paid to assuring that the interlaminar stresses are beneath the (rate dependent) design allowables.
- (ii) Classical techniques for modelling the cyclic behaviour had inherent difficulties in representing the response to large cyclic inelastic strain excursions. Indeed, the use of classical analysis techniques resulted in an inspection interval, for the modified structure, of under 500 hours. To overcome this shortcoming the use of a unified constitutive model was necessary.

ACKNOWLEDGEMENT

This paper summarizes the structural work performed as part of the RAAF Sponsored F111 Doubler Development Task, performed at ARL, and to a limited extent at Monash, under Professor Rhys Jones as Task Manager. The authors wish to acknowledge the contributions of Wing Commander Eric Wilson, Wing Commander Phil Campbell and Sqn. Ldr. Greg McDougall, to the overall direction of the Task; of Dr. A. A. Baker, Mr. M. J. Davis, T. Hill and J. D. Roberts for materials development and application technologies; and of Mr I. Anderson, P. Ferrarotto, D. Smith and C. Rey for their participation.

The analysis was performed using the PAFEC finite element program in conjunction with the PUPPIES (PAFEC), alpha release, suite of interactive programs, and the non-linear adhesive joint analysis was performed using the BJ4C (Bonded Joints For Composites) program marketed by MONSAFE at Monash University.

REFERENCES

1. Buntin, W.D., "Concept and conduct of proof test of F-111 production aircraft", Paper presented to R. Aero. Society, 27 October 1971, London, England.

2. Bland, L., "Final engineering report: A8-112 wing pivot fitting failure investigation,(Manufacturing processes)", FZM-12-5130A, General Dynamics, Fort Worth, USA, June 1982.
3. Molent L., Callinan R. J. and Jones R., "Design of an all boron epoxy doubler for the F-111C wing pivot fitting: Structural aspects", Journal of Composite Structures, 11, 1, pp. 57-83, 1989.
4. Molent, L. and Jones, R., "Stress analysis of a boron/epoxy reinforcement for the F-111C wing pivot fitting", Aero. Res. Labs., ARL-STRUC-Rep-426, DSTO, Melbourne, Aust., March 1987.
5. Ramaswamy V.G., "A constitutive model for the inelastic multiaxial cyclic response for a nickel base superalloy Rene 80", NASA Contract Report 3998, July 1986.
6. Stouffer D.C. and Bodner S.R., "A relationship between theory and experiment for a state variable constitutive equation", American Society for Testing and Materials STP, 765, 239-250, 1982.
7. Susans, G.R., Patching, C.A., and Beckett, R.C., "Visit by an Australian team to the US to discuss the failure of A8-112 during CPLT", Dept. of Defence, AF1511/912/100 Pt.3, Canberra, Australia.
8. Kuruppu M. D., Williams J. F., Bridgford N., Jones R. and Stouffer D. C., "Constitutive Modelling of the elastic-plastic behaviour of 7050-T7451 Aluminium Alloy", J. of Strain Analysis, 27, 2, 85-92, 1992.
9. Jones R., Chiu W. K. and Paul J., "Designing for damage tolerant bonded joints", Composite Structures 25 (1993) 201-207.
10. Molent, L. and Swanton G., "F-111 fuel hole #13 strain surveys", ARL-TN-33, Aeronautical Research Laboratory, D.S.T.O. Melbourne, Australia, June 1993.
11. Bland, L., "A8-112 wing pivot fitting failure investigation, final crack growth rates and crack growth intervals", FZ-12-465, General Dynamics, Fort Worth, USA, June 1982.
12. Molent, L. and Lombardo, D., "An Investigation into Various Reworks of a F-111 Stiffener Replica Specimen Using the Thermoelastic Effect", Aero. Res. Labs., ARL-STRUC-TM-500, DSTO, Melbourne, Aust., Nov 1988.
13. Hart-Smith, L.J., "Adhesively bonded double lap joints", NASA CR 112235, January 1973.
14. Molent, L. and Ferrarotto, P., "Strain survey of a boron/epoxy reinforced F-111C wing pivot fitting", Aero. Res. Labs., ARL-STRUC-TM-460, DSTO, Melbourne, Aust., April 1987.

15. Anderson, I., Ferrarotto, P. and Smith, D., "Strain survey of an F-111C Wing Pivot Fitting", Aero. Res. Labs., ARL-STRUC-TM-523, DSTO, Melbourne, Aust., 1990.
16. Molent, L., "Cold Proof Load Test of a Boron/Epoxy Reinforced F-111c Wing Pivot Fitting", Aero. Res. Lab., ARL-STRUC-TM-497, DSTO, Melbourne, Aust. Aug 1988.
17. Molent, L., "Ambient Proof Load Test of a Boron/Epoxy Reinforced F-111C Wing Pivot Fitting", Aero. Res. Lab., ARL-STRUC-TM-486, DSTO, Melbourne, Aust. Jun 1988.
18. W.K. Chiu, D. Rees, P. Chalkley and R. Jones, "Designing for damage tolerant repairs", ARL Aircraft Structures Report 450, August 1992, also published in J. of Composite Structures, 1994 (in press).
19. Lombardo, D.C., Piperias, P., Patterson, A.K., Ferrarotto, P. and Smith, D., "Preliminary Strain Survey on F-111C Aircraft A8-113", Aero. Res. Lab., ARL-STRUC-TM-566, DSTO, Melbourne, Aust., Oct. 1990.
20. Molent, L. and Patterson, A.K., "Strain Survey of F-111 Aircraft A8-113", Aero. Res. Lab., ARL-STRUC-TM-585, DSTO, Melbourne, Aust., July 1992.

RECENT ADVANCES IN THE MODELLING OF CRACK GROWTH UNDER FATIGUE
LOADING CONDITIONS

A.U. de Koning and H.J. ten Hoeve
National Aerospace Laboratory NLR
The Netherlands

T.K. Henriksen
European Space Agency, ESTEC
The Netherlands

SUMMARY

Fatigue crack growth associated with cyclic (secondary) plastic flow near a crack front is modelled using an incremental formulation. A new description of threshold behaviour under small load cycles is included. Quasi-static crack extension under high load excursions is described using an incremental formulation of the R-(crack growth resistance)- curve concept.

The integration of the equations is discussed. For constant amplitude load cycles the results will be compared with existing crack growth laws. It will be shown that the model also properly describes interaction effects of fatigue crack growth and quasi-static crack extension.

To evaluate the more general applicability the model is included in the NASGRO computer code for damage tolerance analysis. For this purpose the NASGRO programme was provided with the CORPUS and the STRIP-YIELD models for computation of the crack opening load levels. The implementation is discussed and recent results of the verification are presented.

INTRODUCTION

For over two decades models of fatigue crack growth have been based on empirical laws that relate the amount of crack growth in a load cycle to the stress intensity factor range $\Delta K = K_{\max} - K_{\min}$ or the effective [1] range $\Delta K_{\text{eff}} = K_{\max} - K_{\text{op}}$. Correction factors were included for near threshold behaviour and accelerated growth in the high K regime.

From a physical point of view such crack growth laws are speculative because crack growth and plastic deformation are irreversible processes that depend on the loading history. By nature, such processes must be described in an incremental way and properly integrated to obtain the amount of crack growth for a load cycle or the part of a load cycle for which the incremental description is valid [2, 3]. Clearly, such a new description allows that a distinction is made between the part of a load range where secondary (cyclic) plastic flow is observed and the part where primary plastic flow develops under monotonic increasing loads. For each of these domains an incremental crack growth law can be formulated. Then after integration over the appropriate load ranges the contributions to the crack growth rate for the load cycle under consideration are obtained. In a

similar way "range pair" (or "rain flow") principles may be used to select the appropriate crack growth equations and associated ranges of applicability. In addition, the incremental formulation allows the introduction of other terms representing time and/or environment dependent crack growth. In these applications the integration of the incremental equations becomes more complicated, however, with the increased capabilities of both the numerical techniques and the new generation of computer systems numerical integration appears to be feasible.

In this paper the formulation of two incremental crack growth laws, one describing fatigue crack growth and a second one for static crack extension, is discussed. For constant amplitude loading the equations are integrated analytically to obtain the crack growth rate per load cycle. The result can be compared with the common crack growth laws and allows the material parameters to be determined from the results of simple fatigue crack growth tests. For more complicated load sequences like block programme loading and arbitrary, cycle by cycle defined sequences, a method for integration of the crack growth rate is discussed. The models and methods were implemented into the NASGRO (ESACRACK) software [4] and thoroughly tested. In view of uncertainties about the values of constraint factors a preliminary verification was executed using some new test results obtained for three materials: a titanium alloy Ti-6Al-4V, the aluminium alloy 7075-T73 and the "COLUMBUS" skin material 2219-T851 for the European space station manned module. Two material thicknesses were involved: 2 or 4 mm sheet and, 10 mm, plate material. The initial precracks were edge cracks, surface cracks and through the thickness cracks. After preliminary verification the models were readjusted and the constraint factors specified in more detail. Some of the proposed modifications are discussed. The final verification also includes a large number of test cases collected from the open literature in addition to in-house test results [5]. This paper describes the status of the study after completion of the preliminary verification and the model evaluation.

THE LOADING AND CRACK GROWTH REGIMES DISTINGUISHED IN THE UPWARD PART OF A LOAD CYCLE

In the upward part of a load cycle different regimes can be distinguished, depending on the characteristics of the plastic deformation behaviour and the state of opening of the crack. To illustrate these domains in figure 1 the loading path is shown in a K versus c plot, where c is the crack length. The different loading regimes are indicated and discussed one after another.

Closed crack regime 1, $K_{min} \leq K < K_{op}$

Starting at the minimum stress intensity factor K_{min} the load is increased until the crack opening level K_{op} is obtained. In this first regime 1, characterized by $K_{min} \leq K < K_{op}$, the crack is at least partly closed and the contact areas on the crack surfaces decrease when the applied load is increased. Although the stress intensity factors in this regime are calculated assuming the presence of the crack, it is clear that the effective loading of the crack tip region is very small and no crack growth is assumed in this regime.

Opened crack but no growth regime 2, $K_{op} \leq K < K_{op} + \delta K_{th}$

At level K_{op} the crack is fully opened, but, it takes another increase by δK_{th} to initiate crack growth. Obviously, some crack tip blunting occurs in this regime 2. Models and empirical equations

for computation of values for K_{op} and δK_{th} are discussed later on.

Fatigue crack growth in regime 3, $K_{op} + \delta K_{th} \leq K < K_$*

Upon a further increase of the applied load crack growth is initiated when the stress intensity factor K exceeds the level $K_{op} + \delta K_{th}$. In this regime 3 alternating secondary plastic flow is observed in a relatively small plastic zone. At level $K = K_*$, however, the cyclic plastic flow is assumed to change to primary plastic flow. This transition is characterized by a discrete jump in plastic zone size and a loss of load history effects on the state of deformation. To describe the crack growth behaviour in regime 3, corresponding to $K_{op} + \delta K_{th} < K \leq K_*$, the following incremental crack growth law is adopted

$$dc = \left[C_1(K - K_{op})^n + C_2\delta K_{th}^p(K - K_{op})^{n-p} \right] dK \quad (1)$$

In this expression the first term on the right hand side is an incremental form of Elber's law. The second one is added to describe threshold effects, if present. The power $n-p$ follows from the requirement that the units of both terms must be the same.

At initiation of crack growth, when, $K = K_{op} + \delta K_{th}$, it follows that

$$\left(\frac{dc}{dK} \right)_{th} = \delta K_{th}^n (C_1 + C_2) \quad (2)$$

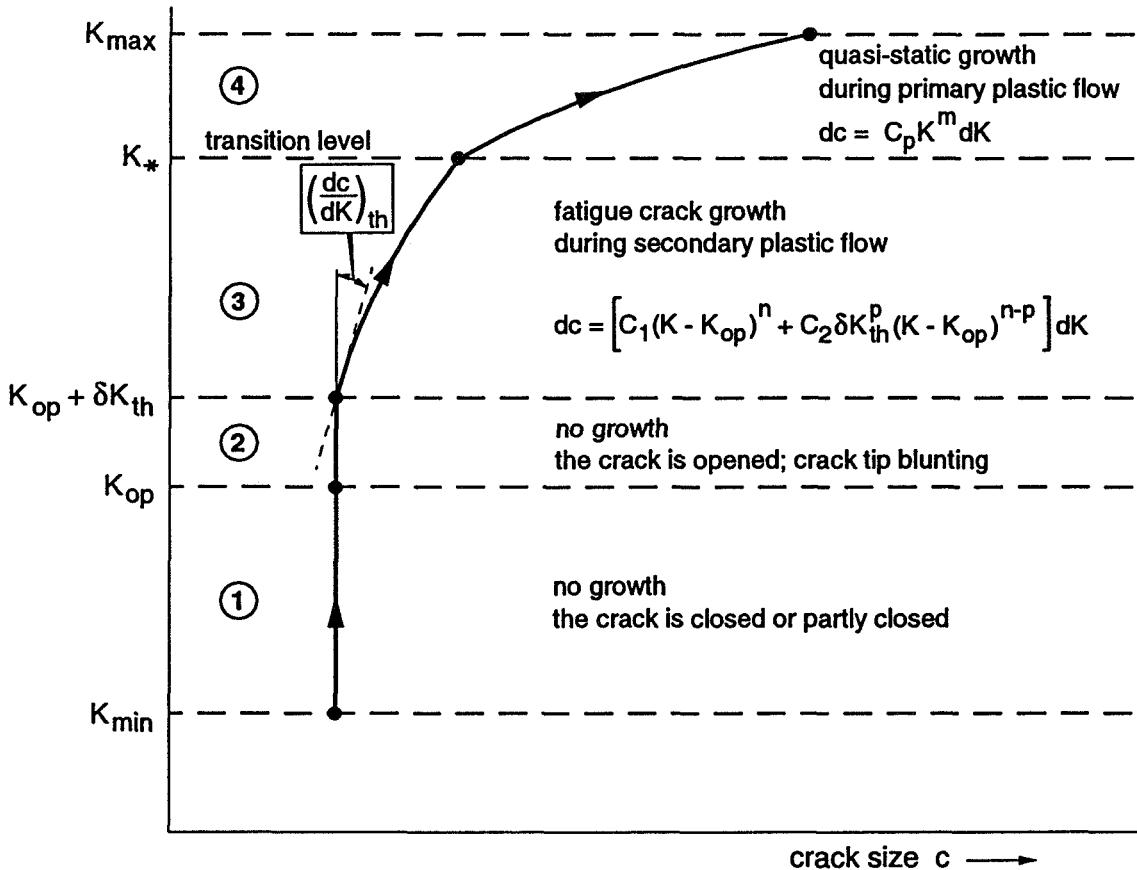


Fig. 1 Different loading and crack growth regimes in one (half) load cycle

Obviously, there exists a relation between the material parameters C_1 and C_2 , the threshold level δK_{th} and the slope of the crack growth curve (see Fig. 1). At the present time knowledge about this slope is lacking. Therefore, a convenient value for the slope is selected to simplify the equations. This value is

$$\left(\frac{dc}{dK} \right)_{th} = p C_1 \delta K_{th}^n / (n+1) \quad (3)$$

To obtain the amount of crack growth Δc_s created under regime 3 the crack growth law (1) must be integrated over the range $K_{op} + \delta K_{th} < K \leq K_*$. There results

$$\Delta c_s = \frac{C_1}{n+1} (K_* - K_{op})^{n+1} \left[1 - \left(\frac{\delta K_{th}}{K_* - K_{op}} \right)^p \right] \quad (4)$$

In the next section this equation is used to derive an equation for computation of the transition level K_* . If the transition level is above K_{max} then the upper bound in the integration of eq. (1) is K_{max} and in eq. (4) K_* is substituted by K_{max} .

Quasi-static crack extension regime 4, $K_ \leq K \leq K_{max}$*

Loading above the transition level K_* is assumed to induce quasi-static crack extension. In this regime the plastic deformation behaviour takes place under monotonic increasing loads. This implies that the effects of secondary cyclic loading on the actual material behaviour are lost. Thus, the crack opening load and threshold behaviour become insignificant [2, 3]. Moreover, the plastic zone sizes are much greater. To describe crack growth in this domain we will adopt the incremental formulation of the R (or J) curve approach. Assuming small scale plastic behaviour and small amounts of static crack extension the crack growth law adopted is written as

$$dc = C_p K^m dK \quad (5)$$

In addition, for cases where wide scale plastic deformation occurs or the amount of static crack extension becomes large we may choose to introduce new -or sub- regimes and formulate the applicable crack growth law in such a way that it describes these processes properly. The incremental crack growth law must be integrated over the applicable range to obtain the contribution Δc_p to the crack growth increment for a load cycle. There results

$$\Delta c_p = \frac{C_p}{m+1} \left[K_{max}^{m+1} - K_*^{m+1} \right] \quad (6)$$

DETERMINATION OF THE TRANSITION LEVELS K_{op} , $K_{op} + \delta K_{th}$, AND, K_*

The crack opening level, K_{op}

In this study the following crack opening models are used: The mechanical STRIP-YIELD (= modified discretized Barenblatt/Dugdale) model [6, 7, 8, 9] and the empirical CORPUS

(Computation Of Retarded crack Propagation Under Spectrum loading) model [10, 11, 12]. Both models were included in the NASGRO software [4, 5]. In both crack opening models constraint factors are introduced to account for 3D effects on the yield stresses of material in front of the crack tip (in tension and in compression) and the yield stress for loading of material in compression in the wake of the crack. These effects are thought to be determined by the state of stress, the uniaxial yield limit $\bar{\sigma}$ and the sheet or plate thickness T . Only two parameters are considered to be material parameters, namely: the ratio α_{NEW} of the cyclic yield limit in tension over its value in compression, and, the uniaxial yield limit $\bar{\sigma}$. The modelling of the constraint effects will be discussed later on. The STRIP-YIELD model included in NASGRO was derived from the NLR model [7]. Newman's method [13] for computation of the crack opening load from the contact stress solution at the minimum load in the cycle was adopted.

Since in some of the applications the static crack extension plays an important role its effect on the crack opening level K_{op} must be accounted for. In the STRIP-YIELD model this is simulated by unzipping elements in front of the crack tip one after another. In this study unzipping takes place at the minimum load in the cycle (no additional plastic deformation is added to the wake). In the next version of the model, currently under development, the elements are unzipped at the proper stress intensity level. Then, the effect of the additional stretch resulting from static growth of the crack is automatically included.

In an application of the CORPUS model [10] the crack opening level is calculated using the crack opening function $f(R, \alpha_{NEW}, S_{max}/\bar{\sigma})$. This function is chosen in such a way that the STRIP-YIELD analyses results of constant amplitude data are described accurately. The CORPUS model defines a set of rules for selection of the representative load ratio R and the stress level S_{max} from the loading history. In the next version of CORPUS implemented in the NASGRO software the crack opening function will be corrected for the effects of static growth and other improvements of the STRIP-YIELD model. Then, the model can be used to determine the material parameters also for the STRIP-YIELD model in an efficient way.

To illustrate such corrections on the crack opening function the correction accounting for the effect of static crack extension is discussed in a similar way as in reference [8] where a first order approximation was used. Thus, the crack opening level is written as

$$K_{op}/K_{max} = f(R, \alpha_{NEW}, S_{max}/\bar{\sigma}) \quad (7)$$

From the result of eq. (7) we can calculate the crack opening load level S_{op} and estimate the fictitious, STRIP-YIELD based, contact area Δc_w near the crack tip at the minimum load level

$$\Delta c_w = c \left[1 - \sin \left[\frac{\pi}{2} \left(1 - \frac{S_{op} - S_{min}}{\sigma_y^c} \right) \right] \right] \quad (8)$$

where σ_y^c is the yield stress of the material in the wake of the crack. Assuming that the contact area is extended by the amount of growth Δc_p it follows for the correction on the crack opening stress that

$$\Delta S_{op} = \frac{2\sigma_y^c}{\pi} \left[\arcsin \left(\frac{c - \Delta c_w}{c} \right) - \arcsin \left(\frac{c - \Delta c_w}{c - \Delta c_p} \right) \right] \quad (9)$$

in eq. (9) c denotes the crack size.

The effective threshold level, $K_{op} + \delta K_{th}$

The effective threshold range δK_{th} is derived from the empirical relation used in the NASGRO software. There results

$$\delta K_{th} = \frac{1 - f(R, \alpha_{NEW}, S_{max}/\bar{\sigma})}{1 - R} (K_{th} - K_{min}) \quad (10)$$

where $K_{th} - K_{min}$ represents the NASGRO threshold stress intensity range and $f(R, \alpha_{NEW}, S_{max}/\bar{\sigma})$ is the opening function. The threshold value δK_{th} applies to constant amplitude loading of through the thickness cracks. In the applications to part through cracks and to variable amplitude loading the value of δK_{th} is reduced.

*The stress intensity factor at transition from cyclic (secondary) plastic flow to primary flow, K_**

To derive an expression for computation of the level K_* at which the transition from secondary plastic flow to primary plastic flow occurs a loading sequence as given in figure 2 is used. The first spike load 1 has created an overload plastic zone and at the time the second spike is applied the crack tip is assumed to be still situated inside this overload plastic zone. In terms of K versus crack length the situation is sketched in figure 3. Then, from a geometrical consideration and the assumption that the transition occurs when the actual primary plastic zone D_* touches the end of the overload plastic zone D_{SP} the following expression can be written

$$c - c_{SP} + \Delta c_s + D_* - D_{SP} = 0 \quad (11)$$

where c is the crack length at initiation of crack growth in the actual overload cycle 2. The secondary crack growth increment Δc_s , given by eq. (4), is a function of K_* .

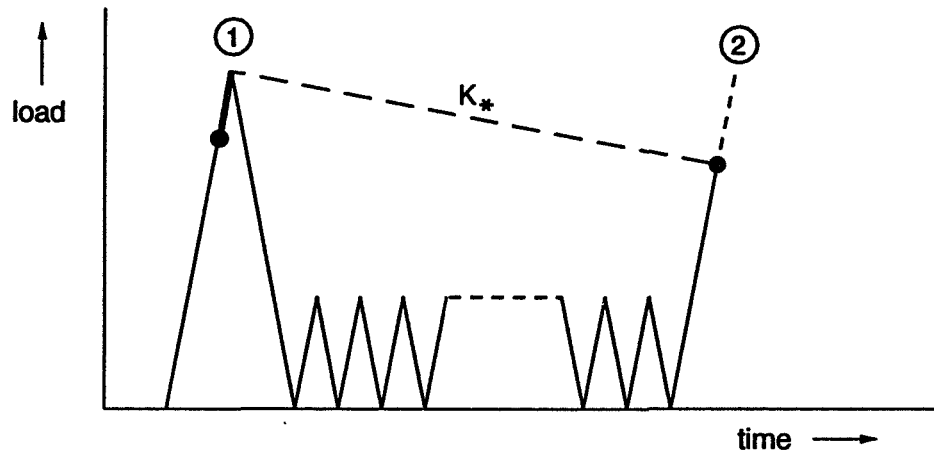


Fig. 2 The loading schedule used to derive an equation for computation of the transition level from secondary to primary plastic flow

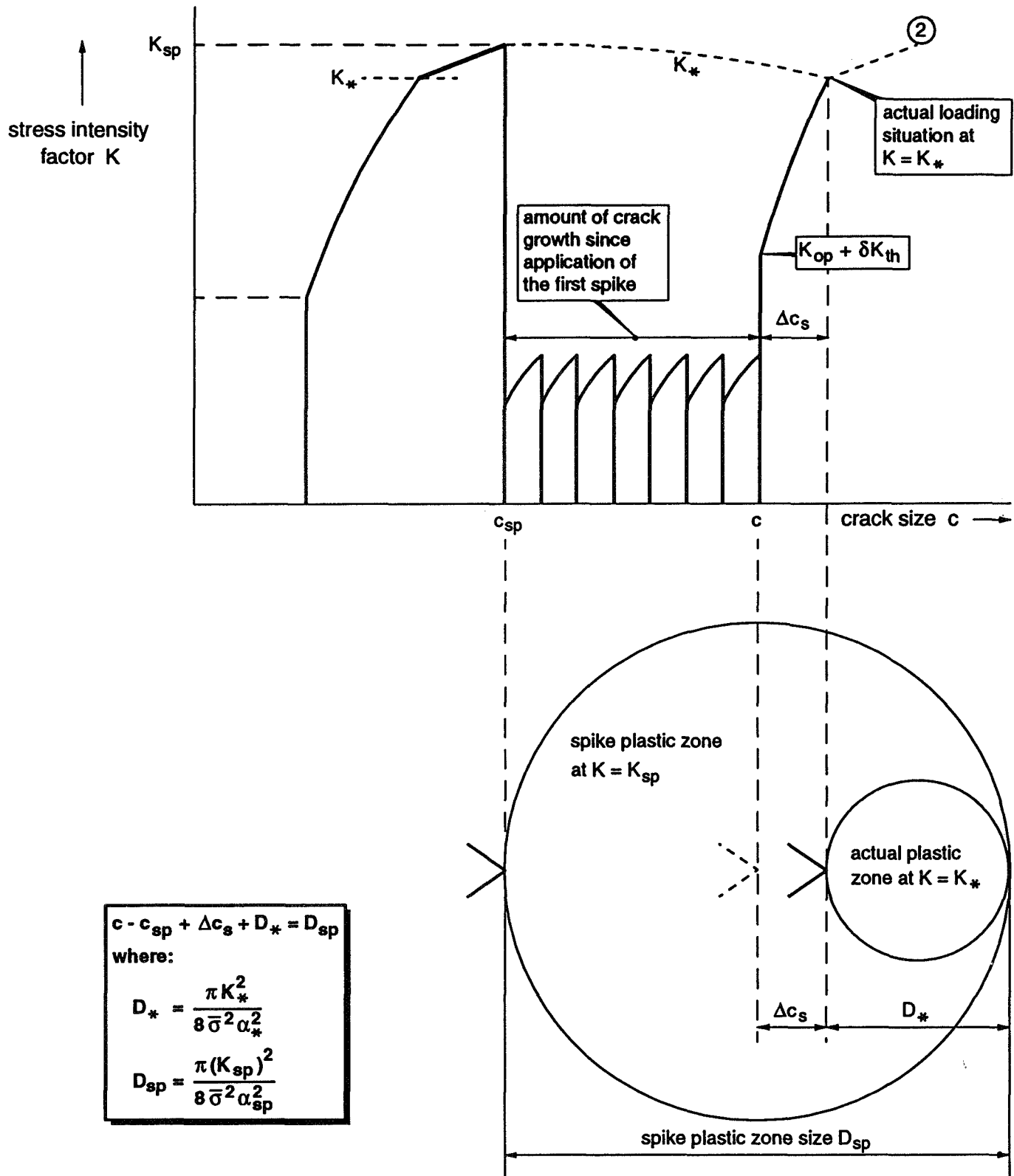


Fig. 3 Geometrical consideration used for determination of the transition level K_*

Further, the plastic zone sizes will be approximated using a first order estimate, that is

$$D_* = \frac{\pi}{8} \frac{K_*^2}{(\alpha_* \bar{\sigma})^2} \quad (12)$$

and

$$D_{SP} = \frac{\pi}{8} \frac{(K_{SP})^2}{(\alpha_{SP} \bar{\sigma})^2} \quad (13)$$

where α_* and α_{SP} are constraint factors introduced to account for 3D effects on the yield stress for primary plastic flow. In the preliminary verification the values α_* and α_{SP} are set equal to the material parameter α_{NEW} . In the next version of the model a more correct description of the constraint behaviour will be introduced. From eqs. (11) to (13), and eq. (4), the value of K_* can be solved in an iterative way. Finally, the value calculated for K_* must be compared with K_{max} in order to establish the presence of primary plastic flow and associated quasi-static crack extension. Primary flow is absent, if $K_* > K_{max}$.

APPLICATION OF THE INCREMENTAL CRACK GROWTH LAWS

Constant amplitude loading

From the foregoing considerations it is concluded that the crack growth rate per load cycle $\Delta c/\Delta N$ can be written as

$$\Delta c/\Delta N = \Delta c_s + \Delta c_p \quad (14)$$

where Δc_s and Δc_p denote respectively the amounts of crack growth associated with secondary plastic flow and with primary plastic flow. After substitution of eqs. (4) and (6) and using the knowledge that in constant amplitude loading $K_{min} \leq K_{op} + \delta K_{th} < K_* \leq K_{max}$ we can calculate $\Delta c/\Delta N$.

In constant amplitude loading K_* is slightly lower than K_{max} in the major part of the crack growth curve. Using this result and recognizing that, in figure 3, c_{SP} can be identified with c eq. (14) can be approximated by

$$\Delta c/\Delta N = C(K_{max} - K_{op})^{n+1} \left[1 - \left(\frac{\delta K_{th}}{K_{max} - K_{op}} \right)^p \right] \left[1 + \left(\frac{K_{max}}{K_{ref}} \right)^{m-2} \right] \quad (15)$$

where $C = C_1/(n+1)$ and the parameter K_{ref} is a combination of the constraint factor α_* and a number of material parameters according to

$$(1/K_{ref})^{m-2} = C_p m \pi (\alpha_* \bar{\sigma})^2 / 2. \quad (16)$$

In eq. (15) the first part on the right hand side is equal to Elber's crack growth law. The second factor accounts for threshold behaviour in a common way and the third, non-singular, part accounts for static crack extension at higher crack growth rates. Eq. (15) is very similar to common crack growth laws like the NASGRO modified Forman law. This allows the conversion of parameter values by requiring that the different multipliers in eq. (15) have approximately the same effect on $\Delta c/\Delta N$ as the corresponding factors in the crack growth law under consideration. It is concluded here that the incremental description of crack growth has given a physical interpretation of the increased crack growth rate at high K_{\max} levels. Further, it is noted that, for any other initial slope of the crack growth curve an expression similar to eq. (15) can be derived.

Constant amplitude loading interrupted at regular intervals for application of a spike load excursion

Relatively large amounts of static crack extension are observed during spike loading excursions applied at regular intervals in an otherwise constant amplitude load sequence, as indicated in figure 4a. Such sequences can be used to determine the material parameter values involved in static crack extension by fitting the integrated crack growth equation to measured data points. In general, an overload ratio OL is chosen of the order 1.5 to 1.7. The number of constant amplitude cycles in one block is in the order of 500 to 2000.

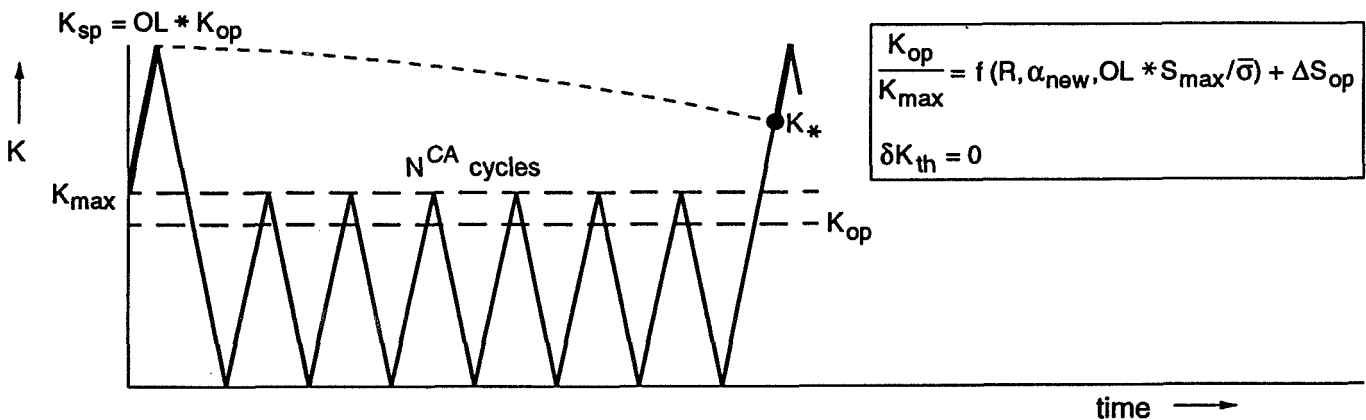


Fig. 4a The spike load sequence for the case, $K_{\max} < K_* \leq OL * K_{\max}$. (Small N^{CA})

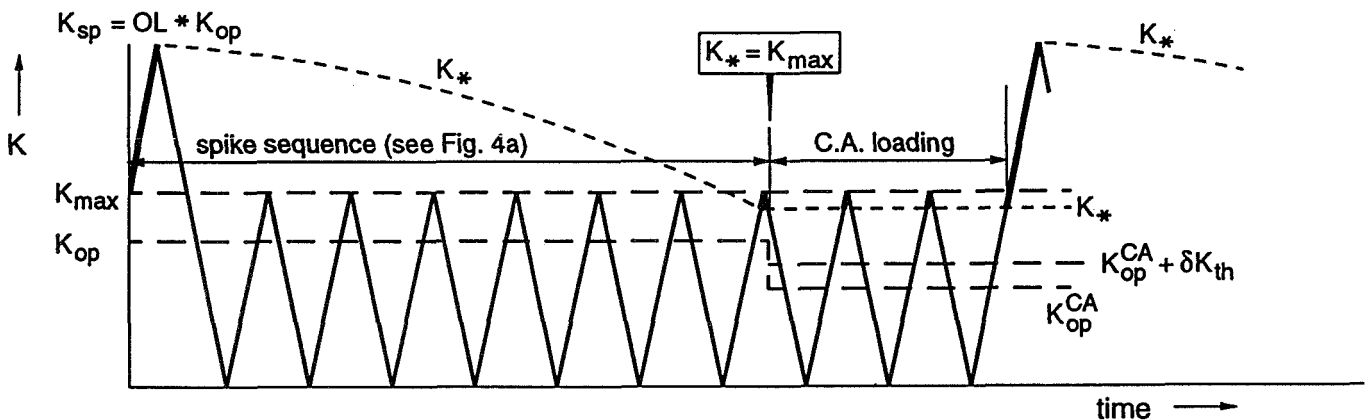


Fig. 4b The spike load sequence for the case of non-interacting spike loads. (Large N^{CA})

C-5.

In such sequences static growth is absent in the constant amplitude cycles provided that $K_{\max} < K_* \leq OL * K_{\max}$. Thus, the crack growth equation (4) for secondary (cyclic) plastic flow applies to the constant amplitude cycles. For the spike load exclusion K_* must be solved iteratively from eq. (11) and it must be verified that $K_* \geq K_{\max}$. Then, it can be derived that the average crack growth rate resulting from application of one block of N^{CA} constant amplitude cycles plus one spike load excursion can be written as

$$\Delta c / \Delta N = \frac{\left[C \left[(K_{\max} - K_{op})^{n+1} * N^{CA} + (K_* - K_{op})^{n+1} \right] + \frac{C_p}{m+1} \left[K_{sp}^{m+1} - K_*^{m+1} \right] \right]}{(N^{CA} + 1)} \quad (17)$$

where it is assumed that K_{op} is independent on the crack size and can be calculated using the simple crack opening function (7) when S_{\max} , α_{NEW} , and R are associated with the spike load cycle. In the case $K_* \leq K_{\max}$ the contribution of static growth of the crack must be calculated. This situation is shown in figure 4b. To calculate the crack growth rate for this part of the constant amplitude cycles eq. (15) can be used. The result can be added to eq. (17) as a weighted average to obtain crack growth rate for one block.

In the applications discussed in this paper the Overload Level OL is chosen to be so high that threshold behaviour is absent, and, $K_* > K_{\max}$.

Block programme loading and randomized or cycle by cycle defined load sequences

In the aerospace industry load spectra are often defined as blocks consisting of a number of different load steps each of which containing a distinct number of constant amplitude cycles of a given amplitude and mean load level. In the analysis the load steps can be applied one after another and, using some additional assumptions about the transition from one load step to the next one, we can analyze this specific load sequence derived from the load spectrum (see Fig. 5). Alternatively,

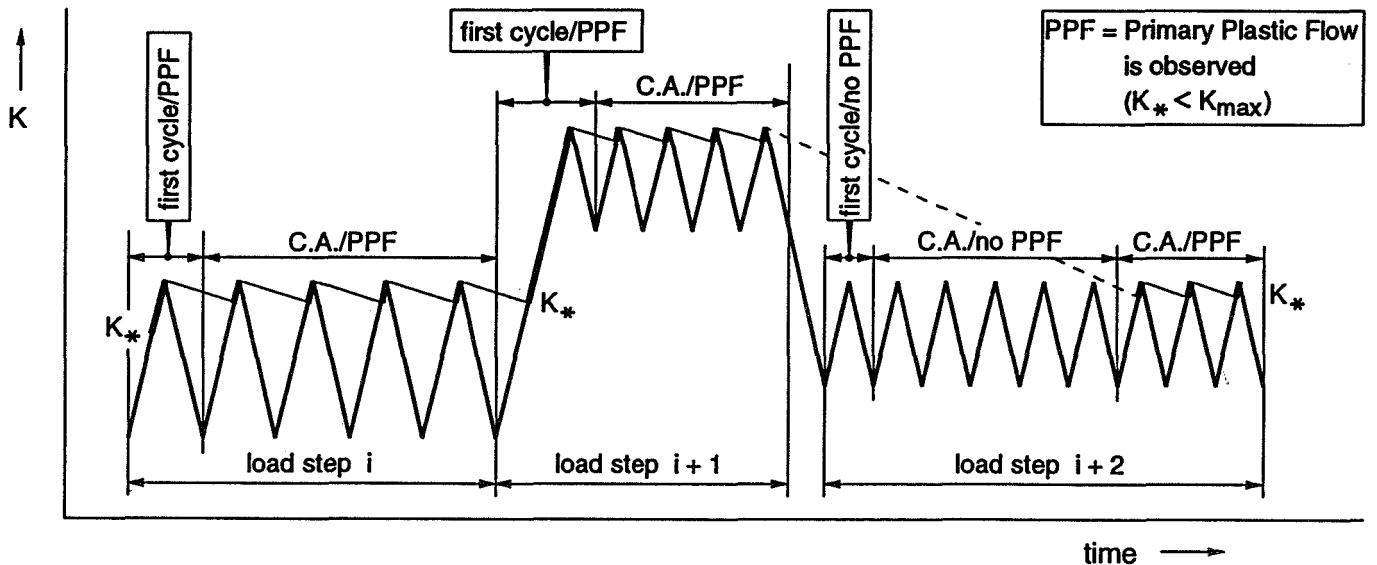


Fig. 5 Three load steps from a block programme load sequence. Parts where crack growth during primary plastic flow (PPF) occurs are indicated. Note the different behaviour in the first cycle of a load step compared to the remaining part of the constant amplitude cycles.

we can randomize the cycles in such a way that, after verification by application of counting methods, the sequence properly represents the load spectrum. In this way different sequences can be constructed all representing the same load spectrum. It is noted, however, that the load sequences do not inevitably represent the same fatigue loading experience.

Characteristic for the aircraft wing and tail load sequences is the presence of air-ground-air load cycles that are included in the load sequence at the proper intervals. In general, these sequences contain many (short) periods of constant amplitude loading that can be described as load steps.

Other cycles can also be described as load steps by defining them as single (half) cycles.

In the NASGRO software such a definition of load steps was applied. Each first cycle in a load step is analysed using a separate crack growth prediction module that calculates the crack growth increments Δc_p and Δc_s for that particular cycle.

The remaining constant amplitude cycles are analysed by taking discrete steps Δc and (using mid point integration at $c + \frac{1}{2}\Delta c$) the number of cycles corresponding to the stepsize Δc is calculated and subtracted from the number of cycles left in the load-step. In this way each of the load steps is analysed one after another.

PRELIMINARY VERIFICATION AND MODEL EVALUATION

Model definition

In an application of the crack growth and crack opening models additional assumptions must be made to quantify constraint effects on the yielding and crack opening behaviour.

In an early stage of this study it was decided to execute the preliminary predictions using a highly simplified system of constraint factors. The yield stresses adopted are illustrated in figure 6. The material yield parameter α_{NEW} is accounting for different yielding behaviour of material loaded in tension compared to material yielding in compression. In compression the yield stress for the wake of the crack is assumed to be the same as the yield stress of material in front of the crack tip. All

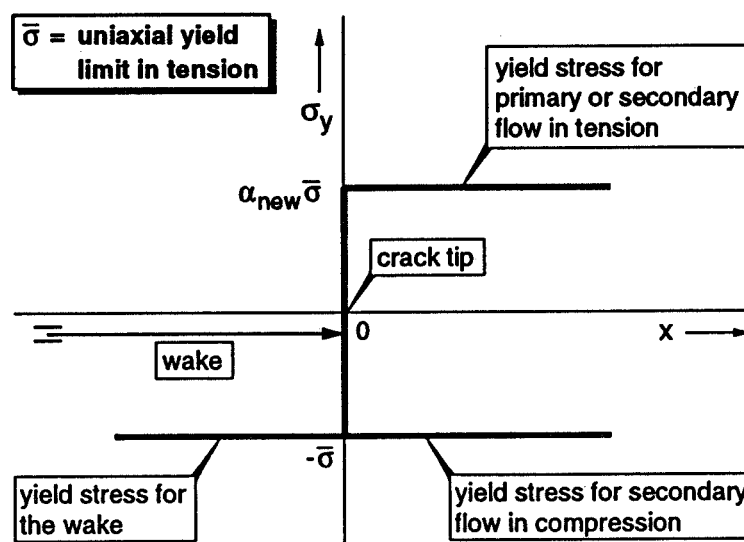


Fig. 6 Yield stresses used for the preliminary predictions

other constraint or Bauschinger effects are assumed to be absent. Later on, after completion and evaluation of the preliminary predictions a more correct definition of constraint factors will be introduced. In the conclusions and discussion some directives are given for such a system. In the application of the CORPUS model the NLR crack opening function is used. The function is given in appendix A.

Test programme

An experimental programme was defined and executed to collect crack growth data for determination of the material parameters in the crack growth law and to verify the models as implemented in the NASGRO software.

The materials involved are Ti-6Al-4V, Al-7075-T73(51) and Al-2219-T851. Both sheet and plate materials are used. The sheet specimens were centrally precracked (through the thickness crack $2c_0 \approx 6$ mm). The specimen width is 120 mm in all cases. The 10 mm thick plate specimens contained a corner crack or a surface crack. The crack size was 1 mm ($a_0/c_0 = 1$). The load sequences applied in the test are constant amplitude loading at $R = 0.05$ and $R = 0.70$, repeated and single spike load sequences and a Space Transportation System STS (pay load) spectrum. The STS spectrum is applied in blocks of constant amplitude loads (full cycles). For the Al-7075-T73(51) material the test programme is given in tables 1a and 1b. For the other two materials a similar test program was executed. As the conclusions drawn from the results of the preliminary verification are the same for all three materials, in this paper the discussions are concentrated on the 7075-T73(51) material. In reference [5] the results obtained for the other materials are discussed in detail.

Table 1a Test programme for 2 mm thick 7075-T73 sheet material. Specimen width is 120 mm

Group	Spec.	Fatigue loading programme	
		Basic loading	Spikes
I	S017075	C.A., $R = 0.05$, $S_{\max} = 89.2$ MPa	-
	S027075	C.A., $R = 0.05$, $S_{\max} = 89.2$ MPa	-
II	S037075	C.A., $R = 0.7$, $S_{\max} = 282.5$ MPa	-
	S047075	C.A., $R = 0.7$, $S_{\max} = 282.5$ MPa	-
III	S057075	C.A., $R = 0.05$, $S_{\max} = 89.2$ MPa	$S_{sp} = 151.6$ MPa, $\Delta N = 500$ cycles
	S067075	C.A., $R = 0.05$, $S_{\max} = 89.2$ MPa	$S_{sp} = 151.6$ MPa, $\Delta N = 1000$ cycles
	S077075	C.A., $R = 0.05$, $S_{\max} = 89.2$ MPa	$S_{sp} = 151.6$ MPa, $\Delta N = 2000$ cycles
	S087075	C.A., $R = 0.05$, $S_{\max} = 89.2$ MPa	$S_{sp} = 151.6$ MPa at $c = 5, 7, 10$ mm
IV	S117075	C.A., $R = 0.05$, $S_{\max} = 101.1$ MPa	$S_{sp} = 151.6$ MPa at $c = 5, 7, 10$ mm
	S147075	C.A., $R = 0.05$, $S_{\max} = 101.1$ MPa	$S_{sp} = 151.6$ MPa, $\Delta N = 2000$ cycles
V	S127075	STS spectrum, $S_{\max} = 151.6$ MPa	-
	S137075	STS spectrum, $S_{\max} = 282.1$ MPa	-

Table 1b Test programme for 10 mm thick 7075-T7351 sheet material. Specimen width is 50 mm

Group	Spec.	Type of notch	Fatigue loading programme	
			Basic loading	Marker loading or spikes
A	P017075	SC	C.A., $R = 0.05$, $S_{\max} = 135$ MPa	Marker loading: C.A., $R = 0.6$ $S_{\max} = 66.8$ Mpa at $c = 5, 7.5, 10, 13$ mm
B	P027075	SC	C.A., $R = 0.05$, $S_{\max} = 135$ MPa	$S_{sp} = 229.5$ MPa, $\Delta N = 2000$ cycles
	P077075	SC	C.A., $R = 0.05$, $S_{\max} = 135$ MPa	$S_{sp} = 229.5$ MPa at $c = 5, 7, 10$ mm
	P047075	CC	C.A., $R = 0.05$, $S_{\max} = 135$ MPa	$S_{sp} = 229.5$ MPa, $\Delta N = 2000$ cycles
C	P057075	SC	C.A., $R = 0.05$, $S_{\max} = 153$ MPa	$S_{sp} = 229.5$ MPa at $c = 5, 7, 10$ mm
	P087075	CC	C.A., $R = 0.05$, $S_{\max} = 153$ MPa	$S_{sp} = 229.5$ MPa, $\Delta N = 2000$ cycles
D	P067075	SC	STS spectrum, $S_{\max} = 340$ MPa	-

c = half crack length along specimen surface

SC = Surface Crack

CC = Corner Crack

Determination of the material parameters

The material parameters appearing in the crack growth laws (4) and (15) can be determined by minimizing the distances of the measured data points to the plotted graph of the crack growth equation in the $\log \Delta K = K_{\max} - K_{\min}$ versus $\log (da/dN)$ domain. From the test matrix defined for centrally cracked sheet specimens the following tests were chosen for determination of the material parameters:

S017075 Constant amplitude loading at $R = 0.05$.

S037075 Constant amplitude loading at $R = 0.70$.

S067075 Constant amplitude loading, interrupted each 1000 cycles for application of a spike load. The spike load ratio $S_{sp}/S_{\max} = 1.7$. The load ratio $R = 0.03$ (for the spike).

The test results obtained for these 3 tests are collected in one series of $dc/dN(i)$ - $\Delta K(i)$ data sets. Then, using a standard routine the parameter values in the crack growth law are determined in an iterative way such that

$$\text{sum} = \sum_i \left[\ln(dc/dN(i)) - \ln F(\Delta K(i), K_{op}(i), S_{\max}, R) \right]^2 \quad (18)$$

is a minimum. Thus, the least squares fit is applied on a log scale. In eq. (18) function $F(\Delta K(i), K_{op}(i), S_{\max}, R)$ represents the right hand side of the crack growth law eq. (15) for S017075 and S037075. In the evaluation of test S067075, eq. (17) is used to calculate the average crack growth rate.

The crack opening loads $K_{op}(i)$ and, therefore, the values of the material parameters in F depend on the crack opening model that is chosen. In the determination of the material parameters the CORPUS model is applied in combination with the NLR opening function. A complicated iterative scheme based on a STRIP-YIELD analysis of $K_{op}(i)$ was thought to be impractical. The "fit" results are indicated in figure 7b. For comparison the fit results obtained for Ti-6Al-4V and Al-2219-T851 are given in figures 7a and 7c. From figure 7 it is concluded that the data of the constant amplitude load sequences (S01 and S03) are described properly. The spike load sequence (S06) is more difficult. In the lower ΔK regime the crack growth rate is underestimated by the CORPUS model. At higher ΔK Levels the contribution of the primary plastic flow component to the crack growth rate is described in a correct way [14] and the value for the yield parameter α_{NEW} in this study can be determined.

Clearly, the addition of the spike load sequence to the constant amplitude sequences helps to determine a useful value for α_{NEW} . Further, it is noted that the more common non-retardation models for crack growth prediction can not predict a lower crack growth rate for case S06 compared to S01. The contribution of the spikes will slightly increase the crack growth rate in these models. From figure 7, however, it can be seen that the crack opening models predict a crack growth rate that is one order of magnitude lower (case S06) compared to case S01. This agrees with the test results.

The values obtained for the material parameters are shown in table 2. Other material properties are given in reference [5]. The corresponding values of parameters in the NASGRO crack growth law [4] were determined by fitting the same data points. In this case the parameters q and K_c are thought to represent the static crack growth properties; values for these two parameters are calculated directly from m and K_{ref} in the incremental crack growth model discussed here. Further, the threshold parameter is kept at the same value, so, in this case the fit parameters are C , n , p and α_{NEW} . In sequence S06 the contribution of static growth due to the spikes is accounted for in the same way as described for the incremental crack growth law. The parameter values obtained are shown in table 3.

Table 2 Material parameter values determined for the incremental crack growth law discussed in this study (in MPa, mm)

	7075-T73	Ti-Al-4V	2219-T851
Elber coefficient C	0.276E-10	0.294E-10	0.32527E-10
Elber exponent $n+1$	2.999	2.656	2.895
Threshold exponent p	1.36	5.955	5.948
Threshold level ΔK_{th}	87.49	506.28	249.20
Static growth exponent m	17.64	10.06	12.99
Static growth parameter K_{ref}	1945.2	4427.2	1889.4
Yield parameter α_{NEW}	1.053	1.197	1.24

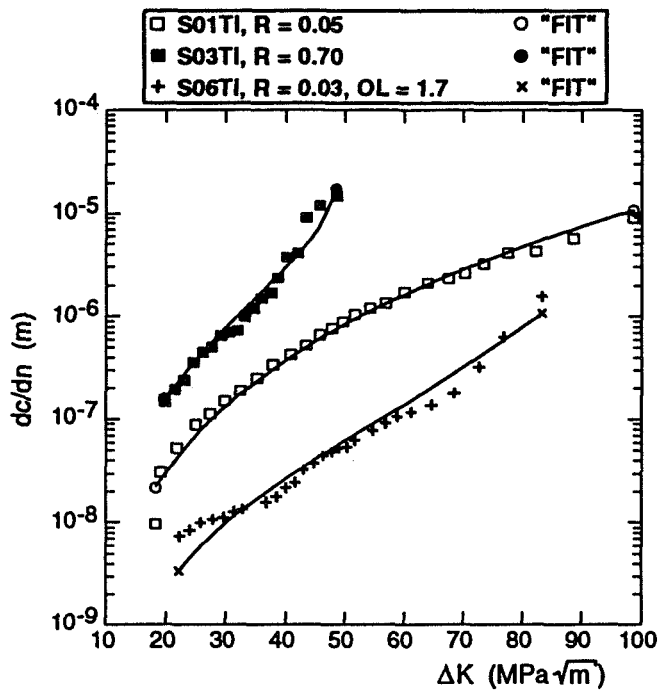


Fig. 7a Plot of the crack growth equation fitted to the measured data points. The material is Ti-6Al-4V. The thickness is 2 mm.

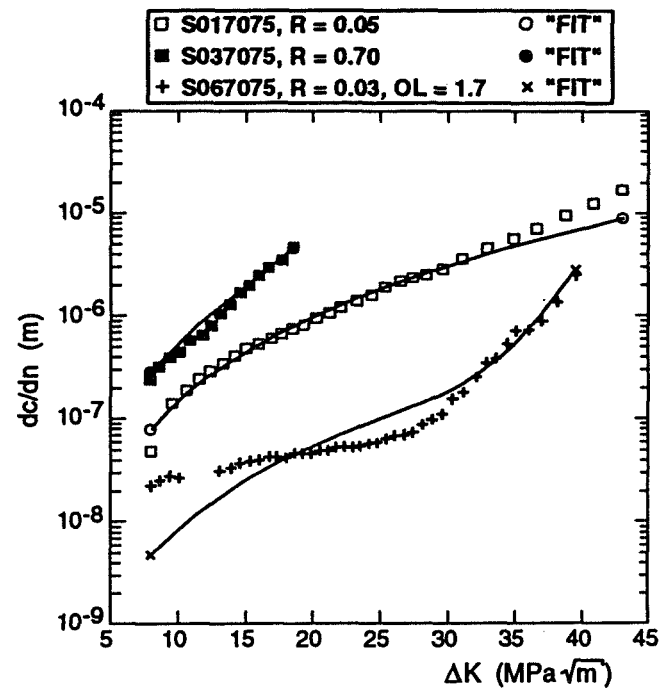


Fig. 7b Plot of the crack growth equation fitted to the measured data points. The material is 7075-T7351. The thickness is 2 mm.

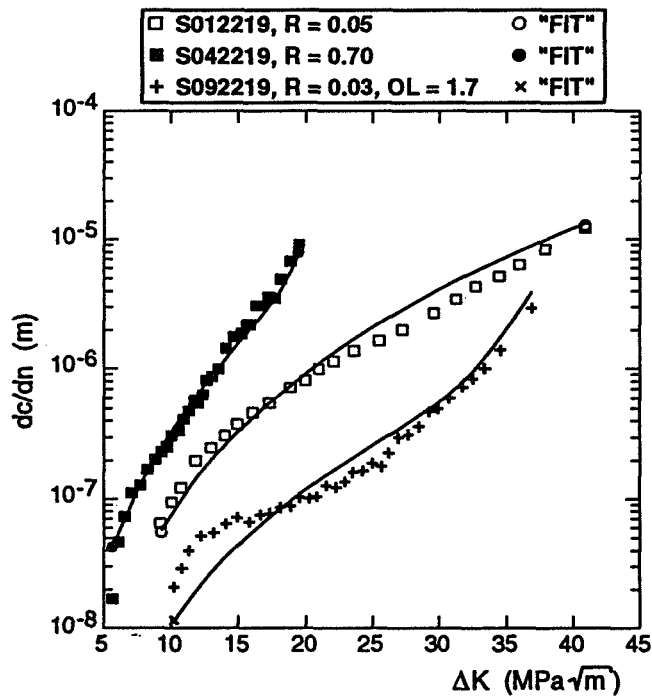


Fig. 7c Plot of the crack growth law fitted to the measured data points. The material is 2219T851. The thickness is 2 mm.

Table 3 Material parameter values determined for the NASGRO modified Forman crack growth law (MPa, mm)

	7075-T73	Ti-Al-4V	2219-T851
Elber coefficient C	0.1745E-9	0.2621E-10	0.135E-10
Elber exponent n	2.657	2.656	3.399
Threshold exponent p	1.150	0.113	0.100
Threshold level ΔK_{th}	87.49	506.28	249.20
Static growth exponent q	0.208	0.382	0.213
Critical K_c	2063.30	5254.92	2040.89
Yield parameter α_{NEW}	1.049	1.199	1.358

Results obtained for the sheet specimens

Using the NAGRO programme and the values of the material parameters from table 3 the crack growth rates and crack size were predicted. The results are collected in figures 8 and 9. Each plot represents one test case that includes the experimental result and the result predicted by the CORPUS and the STRIP-YIELD models. The first symbol in the identification indicates the type of material (Sheet or Plate). The next digits give, the sequence number of the test and the rest identifies the material.

Comparison of dc/dN versus c data (Figs. 8a and 8b)

The data sets used for the determination of the material parameter values were S017075, S037075 and S067075. From the corresponding plots it is seen that the "fit" results are reproduced properly by the CORPUS and by the STRIP-YIELD modules in NASGRO. This justifies the use of the CORPUS crack opening model for determination of the material parameters. The rather strong deviations observed for smaller crack sizes in the S05, S06 and S07 spike load tests are probably due to the simple definition of the constraint parameters. The same applies to all crack sizes for the relatively low spike level in test S14. It appears that too much plastic deformation is predicted by

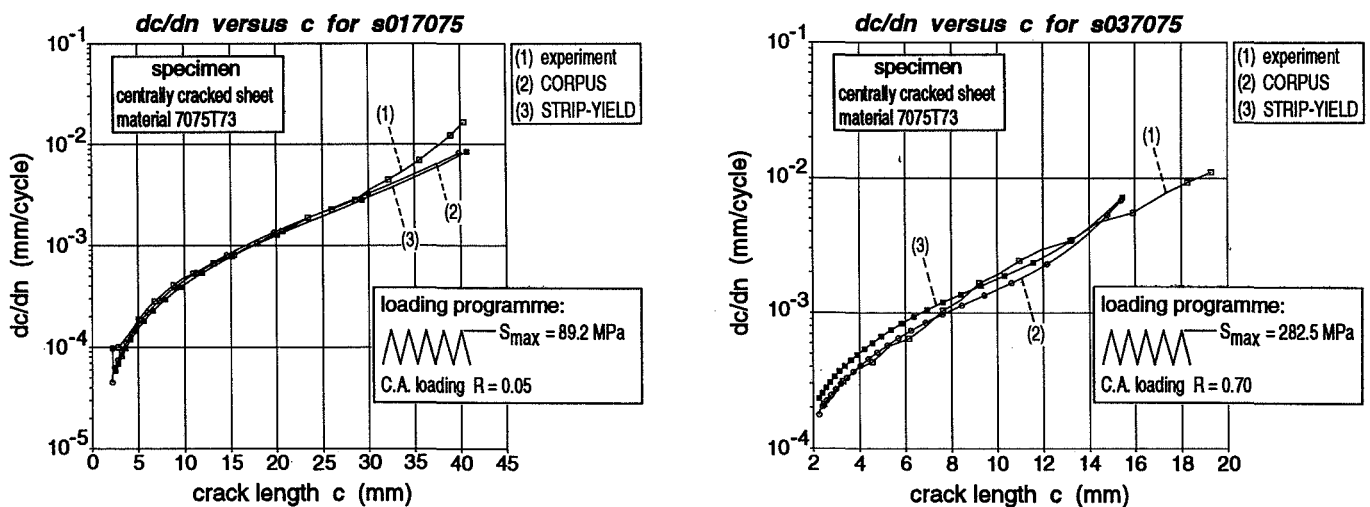


Fig. 8a Comparison of measured and predicted crack growth rates, SHEET specimens

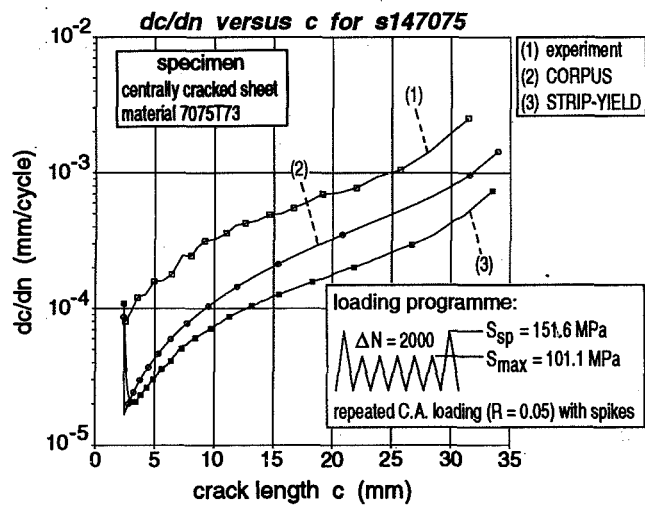
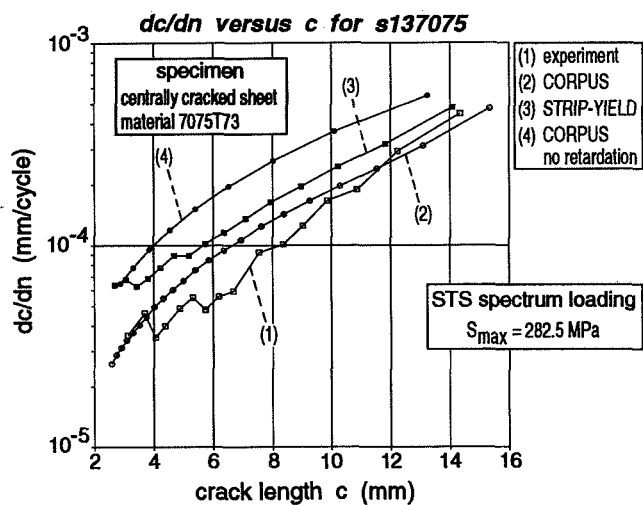
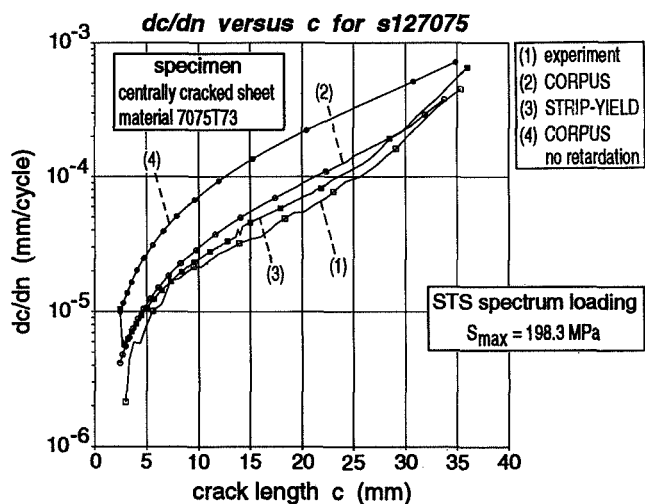
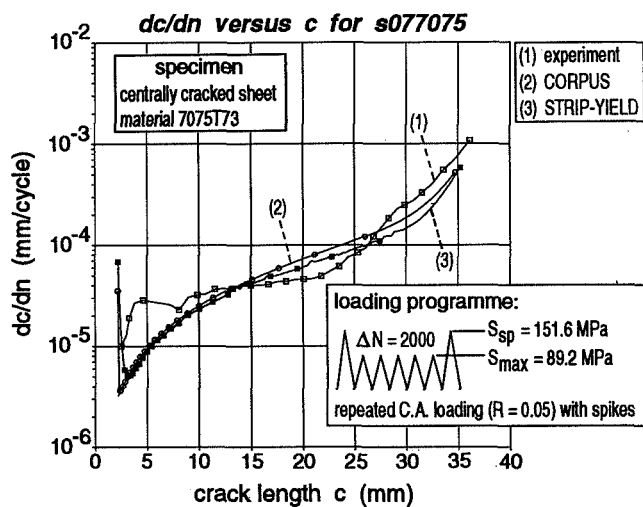
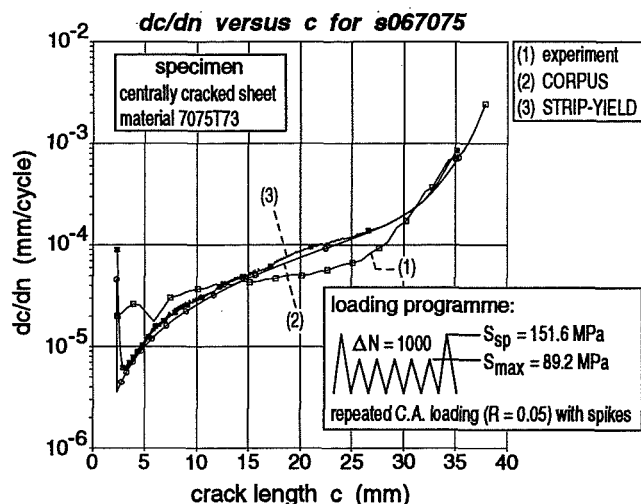
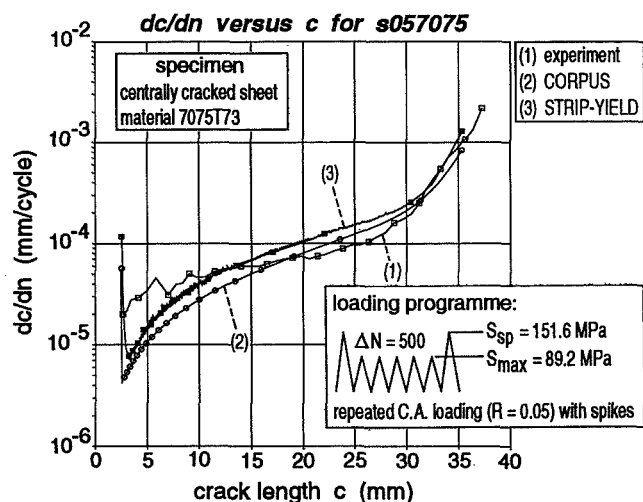


Fig. 8b Comparison of measured and predicted crack growth rates, SHEET specimens (continued)

the STRIP-YIELD model. So, the constraint effect on yielding in secondary flow in tension is underestimated. In constant amplitude loading without spikes this effect is absent. The data predicted by the STRIP-YIELD model for constant amplitude loading at $R = 0.70$ are based on a cycle by cycle analysis. This guarantees that the contact area at the minimum load is properly modelled (this area is of the same order of magnitude as the element size applied in front of the crack tip).

In general, the first cycle of the load sequences shows a different crack growth rate. This is caused by the model used to predict growth during primary plastic flow. The deviations disappear if the average values for the crack growth rate are plotted in stead of the values per load cycle. It is also observed that the STRIP-YIELD results show some transient behaviour at the beginning of the curves. The CORPUS model does not account for such effects. The interval between two measured data points was too large to see a similar behaviour in the tests.

The three times repeated single spike sequences, S08 and S11, were included in the test program to verify the effect of constraint on the retardation region. As this should be judged in a c versus N plot these results are discussed in the next section.

The behaviour of the specimens subjected to the STS load spectrum (S13) are also shown. The differences are fairly large. The origin of the differences is unknown. For comparison the results obtained for a non-retardation model are also presented.

From the results discussed so far it is concluded that the definition of the constraint factors needs improvement. Further, an increased value of the constraint factor for secondary plastic flow in tension must be used. This will certainly improve the accuracy of the spike load cases as for smaller crack sizes the predicted crack growth rates will increase. For larger crack sizes the effect will diminish compared to the contribution of static crack extension to the crack growth rate. In view of these observations a judgement on the basis of crack size versus number of cycles would be cripple as the deviations observed for the smaller crack sizes will govern the whole picture. For this reason this judgement is postponed until the constraint problems are solved in a satisfactory way.

Comparison of c versus N data (Fig. 9)

The results obtained for the sheet specimen subjected to three single spikes are given in

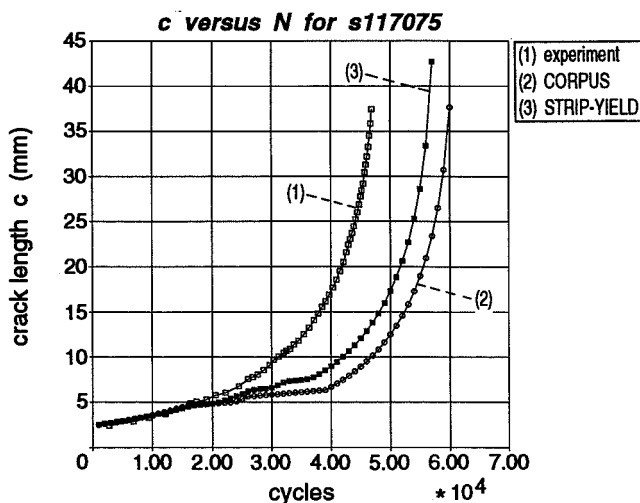


Fig. 9 Comparison of measured and predicted crack growth curves. SHEET specimen subjected to C.A. loading and three single spike loads

figure 9. It is seen that the predicted effects of overloads on the crack growth rate is overestimated. The 1.5 overload level (S11) gives less retardation and, as a result, all curves are more close to the case of constant amplitude loading. The spike loads are applied at approximately the same number of load cycles as used in the experiment. This implies that the crack sizes (and K factors) are smaller and so the plastic zone size and retardation region. As most of the spikes are applied at crack sizes smaller than 10 mm (pure plane stress conditions not yet present) it must be concluded that under plane strain conditions the constraint factor α is higher than assumed in the models. The results obtained for specimen S08 were out of range. These results are left out of the discussion. It is noted that predictions based on linear models do not show any retardation.

Results obtained for the plate materials

Comparison of dc/dN versus c data (Fig. 10a and 10b)

The predictions for the plate material are based on the same material parameter values as used for the sheet specimens. By nature, the influence of bending stresses induced by clamping the thick specimens is more pronounced than for the case of sheet specimens. This may explain part of the larger differences in results obtained for the plate specimens.

For the spike load sequences the conclusion can be drawn that the crack opening load is too high. As mentioned previously this indicates that too much plastic deformation occurs in the constant amplitude cycles and gives support to the introduction of an increased value for the constraint factor for secondary cyclic plastic flow in tension.

The prediction of the specimen under STS spectrum loading is conservative. Further, the deviations between the CORPUS and the STRIPY predictions are relatively large. The source is unknown. Again, it is concluded that the definition of the constraint factor α needs reconsideration.

Comparison of c versus N data (Fig. 11)

The behaviour observed for the single spikes applied three time on the plate specimens is shown in figure 11. The following conclusions can be drawn. The agreement between measured data points and predictions is good for the 1.5 overload cases (P05). For the 1.7 spike load case the predicted delay is far to large for the case (P05), indicating that the constraint factor α must have a higher value to reduce the plastic zone size and the retardation region.

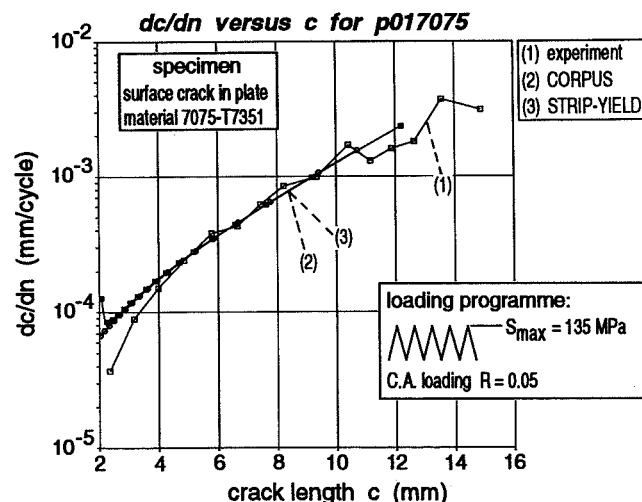


Fig. 10a Comparison of measured and predicted crack growth rates. PLATE specimen

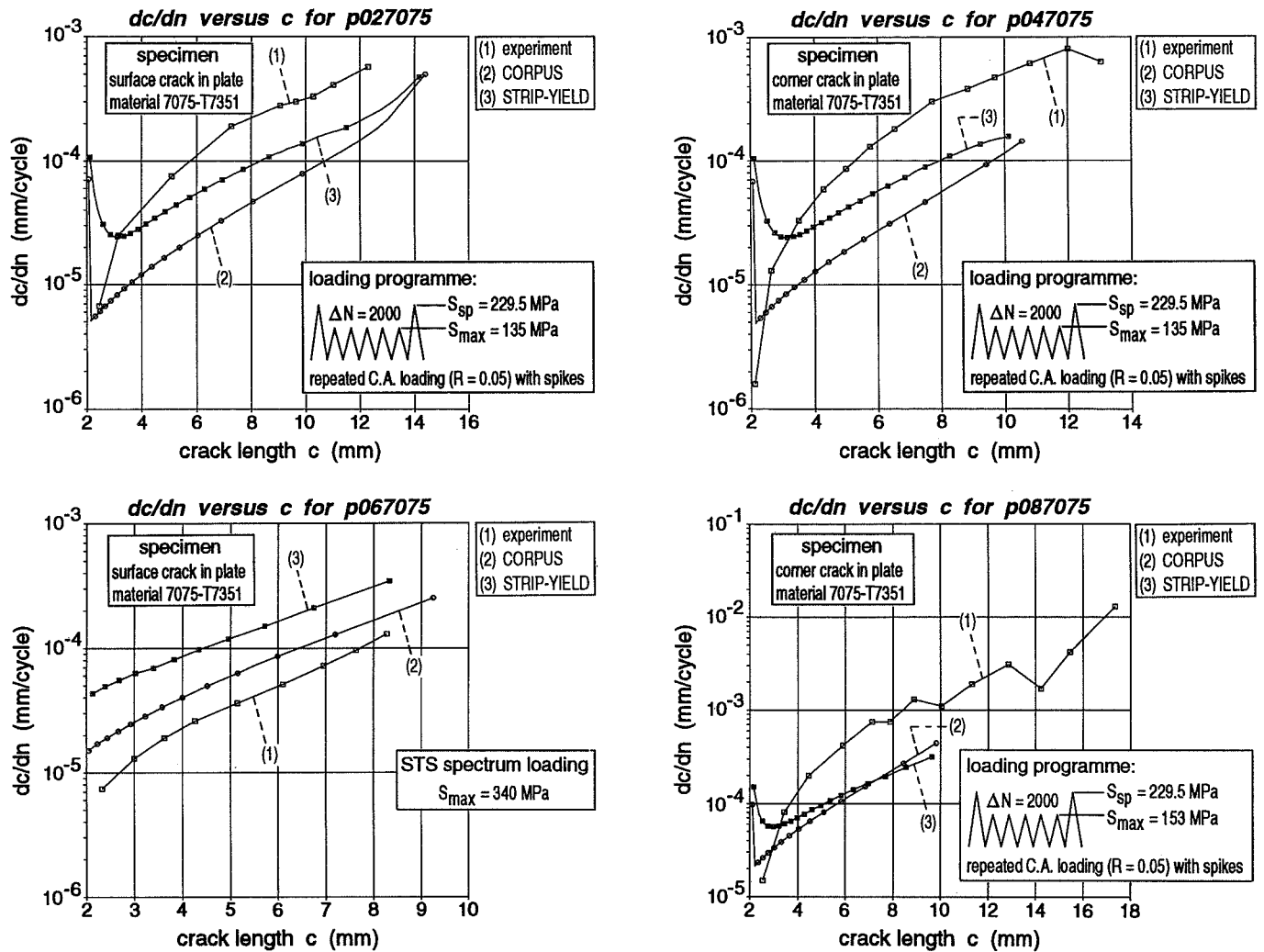


Fig. 10b Comparison of measured and predicted crack growth rates, PLATE specimens (continued)

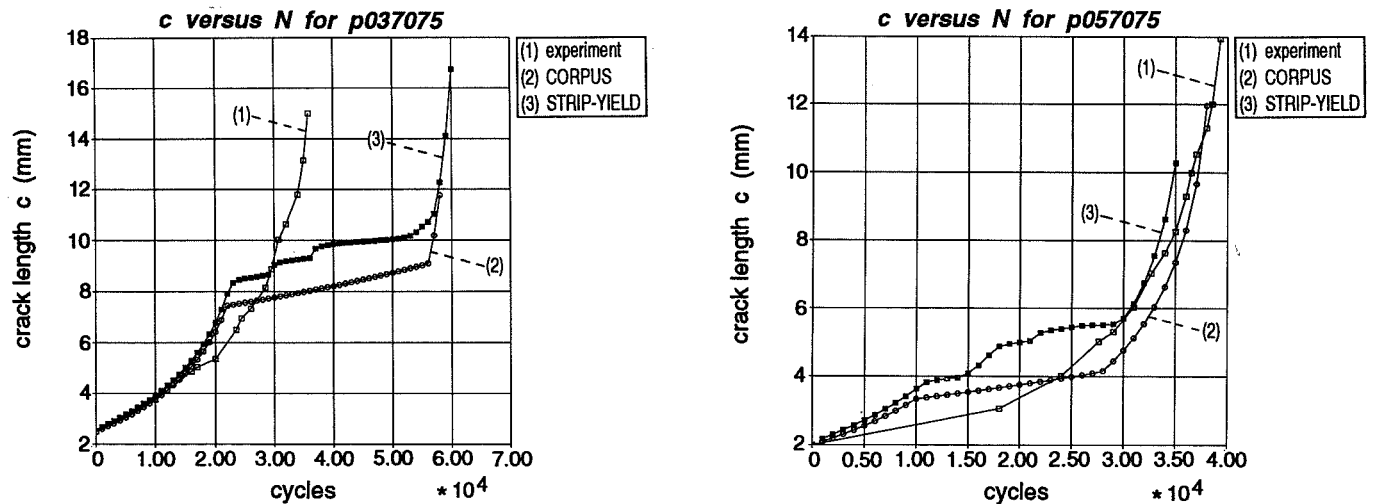


Fig. 11 Comparison of measured and predicted crack growth curves, PLATE specimens

CONCLUSIONS AND RECOMMENDATIONS FOR FURTHER STUDY

1. The empirical CORPUS model and the mechanical STRIP-YIELD model for prediction of the crack opening load level were designed and implemented in the NASGRO software to yield the NASGRO-STRIPY-93 software. This software was tested successfully.
2. Material parameter values were determined successfully using two constant amplitude load sequences executed respectively at R values of 0.70 and 0.05. In addition a repeated spike load sequence was introduced to determine the value of the yield parameter α_{NEW} and the parameters involved in static crack extension during primary plastic flow. For all three materials, Ti-6Al-4V ($t = 2$ mm), 7075-T73(51) ($t = 2$ mm) and 2219T851 ($t = 4$ mm) the material parameters were determined.
3. The model used to describe threshold behaviour under variable amplitude loading is sufficiently accurate. In eq. (1) the threshold parameter C_2 is still to be determined. Further research is recommended.
4. The model introduced to describe accelerated crack growth during primary plastic deformation in virgin material describes the high crack growth rates observed at high K_{max} levels in a satisfactory way. The iterative scheme for computation of the transition levels K_* appears to be functioning properly.
5. It is important to note that constraint effects primarily depend on the state of stress and, therefore, on the loading history, as such a discussion in terms of material parameters is not very useful.
6. The definition and quantification of constraint factors need further improvement. The best way to proceed is to collect and evaluate full 3D Finite Element analyses results of the elastic-plastic deformation and crack growth problem. These are not yet available in sufficient detail. For the time being we need engineering judgement and empirical methods to proceed.
7. The results obtained for constant amplitude loading (cases S01, S03 and P01) are covering states of stress ranging from plane strain to plane stress conditions. This indicates that in constant amplitude loading the crack opening level primarily depends on the yield ratio parameter α_{NEW} . The results obtained for constant amplitude loading interrupted for application of single spikes indicate that under plane strain conditions the yield stresses in tension are much higher than assumed in this study (the value of α_{NEW} appears to be independent of the state of stress). Thus, the constraint system depends on the state of stress. In addition the transition from plane strain to plane stress must be modelled. This can be done in a way as described in references [9] and [11].
8. It is not likely that the constraint effects at different locations in the wake of the crack (resulting from residual stresses) are the same as the constraint effects active in yielding in compression in front of the (closed) crack. Measurement of the residual stresses on the fracture surface is strongly recommended to quantify these constraint effects.

9. The results of this verification indicate that the accuracy of the CORPUS model is close to the accuracy of the STRIP-Yield model in its current formulation. However, the possibility to improve the description of constraint effects gives the STRIP-YIELD model the potential to be superior compared to the empirical CORPUS model. Further, compared to the common non-retardation models for crack growth prediction a better description of the behaviour observed for spike load sequences is demonstrated for both the CORPUS and the STRIP-YIELD models.

ACKNOWLEDGEMENTS

The authors gratefully acknowledge M. Richmond (ARL) for the software development support during the period he worked at NLR, and L. Schra for his efforts to obtain and evaluate the experimental results. The incremental crack growth model was developed under contract no. 1823 with the Netherlands Agency for Aerospace Programs (NIVR). The other work reported in this paper was performed under contract no. 9691 with the European Space Agency (ESA).

REFERENCES

1. Elber, W., The significance of fatigue crack closure. ASTM STP486, 1971, pp. 230-242.
2. Koning, A.U. de, Dougherty, D.J., Prediction of low and high crack growth under constant and variable amplitude loading. Proc. of the spring meeting on "Fatigue crack growth under variable amplitude loading", ed. J. Petit, Paris, 1988.
3. Dougherty, D.J., Koning, A.U. de, and Hillberry, B.H., Modelling high crack growth rates under variable amplitude loading, *Advances in Fatigue Lifetime Predictive Techniques* ASTM STP 1122, 1992, pp. 214-233.
4. Fatigue crack growth computer program "NASA/FLAGRO" version 2.0. JSC-22267 A, Jan 1993, Draft.
5. Koning, A.U. de., Advanced Tools for life prediction and damage tolerance analyses, Contract Report NLR CR 93523 L, 1993.
6. Newman, J.C. Jr., A crack closure model for predicting fatigue crack growth under aircraft spectrum loading, ASTM STP 748, 1981, pp. 53-84.
7. Koning, A.U. de, Liefing, G., Analysis of crack opening behaviour by application of a discretised STRIP-YIELD model, ASTM STP 982, 1988, pp. 437-458.
8. Newman, J.C., Poe, C.C., Dawicke, D.S., Proof test and fatigue crack growth modeling on 2024T3 aluminium alloy, Proc. of Fatigue 90, July 1990.

9. Wang, G.S., Blom, A.F., A modified Dwydale-Barenblatt model for fatigue crack growth predictions under general load conditions FFA TN 1987-79, Stockholm, 1987.
10. Koning, A.U. de., A simple crack closure model for prediction of fatigue crack growth rates under variable-amplitude loading. ASTM STP 743, 1981, pp. 63-85.
11. Koning, A.U. de, Linden, H.H. van der., Prediction of fatigue crack growth rates under variable loading using a simple closure model, Proc. of the 11th ICAF Symposium in the Netherlands, 1981 (also NLR MP 81023).
12. Padmadinata, A.H., Investigation of crack-closure prediction models for fatigue in Aluminium Alloy sheet under flight-simulation loading. Thesis, March 27th 1990, Technical University Delft.
13. Newman, J.C., FASTRAN-II- A fatigue crack growth structural analysis program. NASA TM 104159, Febr. 1992.
14. Schijve, J., Fundamental aspects of predictions on fatigue crack growth under variable-amplitude loading. Proc. of "Theoretical concepts and numerical analyses of fatigue". ed. A.F. Blom and C.J. Beevers, EMAS, Birmingham, 1992, pp. 111-130.

APPENDIX A The NLR/CORPUS crack opening function

The crack opening function $f(\alpha_{NEW}, R, S_{max}/\bar{\sigma}) = \frac{S_{op}}{S_{max}}$ is defined in the following way:

$$f = 1 - \alpha_{NEW} + \alpha_{NEW} * CF1 \quad 0 < \alpha_{NEW} < 1$$

$$f = \frac{1}{2} \left[\frac{3}{\alpha_{NEW}} - 1 \right] CF1 + \frac{3}{2} \left[1 - \frac{1}{\alpha_{NEW}} \right] CF2 \quad 1 \leq \alpha_{NEW} \leq 3$$

$$f = \frac{3}{\alpha_{NEW}} CF2 + \left[1 - \frac{3}{\alpha_{NEW}} \right] CF3 \quad \alpha_{NEW} > 3$$

In the current CORPUS module the functions CF are assumed to be the following form:

$$\begin{aligned} CF1 &= (.505 + .18R - .135R^2 + .81R^3 - .36R^4) * Hr & 0 \leq R < 1 \\ CF1 &= (.505 + .18R) * Hr & R < 0 \end{aligned}$$

$$\begin{aligned} CF2 &= .25 + .06R + 1.13R^2 - .44R^3 & 0 \leq R < 1 \\ CF2 &= .25 + .06R & R < 0 \end{aligned}$$

$$\begin{aligned} CF3 &= R & 0 \leq R < 1 \\ CF3 &= 0 & R < 0 \end{aligned}$$

where:

$$Hr = 1 - 0.2(1 - R)^3 \left[\frac{S_{max}}{\bar{\sigma}} \right]^3$$

AXIAL CRACK PROPAGATION AND ARREST IN PRESSURIZED FUSELAGE¹

M. Kosai, A. Shimamoto², C.-T. Yu, S.I. Walker, A.S. Kobayashi and P. Tan³

University of Washington
Department of Mechanical Engineering
Seattle, WA

348684
526-39
23120
p. 18

SUMMARY

The crack arrest capability of a tear strap in a pressurized precracked fuselage was studied through instrumented axial rupture tests of small scale models of an idealized fuselage. Upon pressurization, rapid crack propagation initiated at an axial through crack along the stringer and immediately kinked due to the mixed modes I and II state caused by the one-sided opening of the crack flap. The diagonally running crack further turned at the tear straps. Dynamic finite element analysis of the rupturing cylinder showed that the crack kinked and also ran straight in the presence of a mixed mode state according to a modified two-parameter crack kinking criterion .

INTRODUCTION

The role of a tear strap in an airplane fuselage is to arrest an axial crack which is propagating either subcritically under fatigue loading or dynamically after reaching criticality. Such crack arrest can occur at lower stress due to the reinforcing effect of the tear strap or by crack kinking due to the complex crack tip stress field generated by the crack flap and the tear strap. The latter provides controlled damage and depressurization of the fuselage. Although the tear strap is the last defense of an axially rupturing fuselage, little is known about its effectiveness in arresting the crack. Thus, much of the tear strap design is based on empirical rules derived from sub- and full-scale testing of pressurized fuselages. Literature is abundant with analytical and experimental papers dealing with axial fatigue crack extension and possible arrest in idealized and actual fuselages but few consider crack kinking and flapping as an arrest criterion. The first theoretical paper dealing crack kinking and flapping as an arrest criterion appears to be that of Kosai and Kobayashi (1991).

¹ This research was supported by the Federal Aviation Administration Grant No. 92-G-0005.

² On leave from Saitama Institute of Technology, Okabe, Saitama, Japan at the time of this investigation.

³ Federal Aviation Administration, Technical Center, Atlantic City International Airport, NJ.

In the above mentioned paper, the axial crack was assumed to open symmetrically, i.e. mode I crack tip deformation, in a fuselage reinforced by longitudinal stringers, frames and tear straps. The crack-tip plastic zone associated with this symmetric axial crack exceeded 102 mm (4 in.) with the axial stress ahead of the crack tip exceeding 345 MPa (50 ksi). This large axial stress was generated through axial stretching of two crack flaps and was the cause of crack kinking as described by Kobayashi et. al. (1988). If, however, failure were to occur along the multiple site damages (MSD's) in a lap joint, evidences [Sampath and Broek (1991); NTSB (1989)] show that fracture occurs in the upper skin with the lower skin still attached to the stringer. The axial stretching due to the resultant one-sided crack flap would then generate axial tensile stresses along the cracked upper skin and imposed a mode II state at the crack tip. The importance of mode II deformation and the attendant mode II stress intensity factor, K_{II} , were also observed in a recent fatigue crack growth study of an idealized model of a stringer reinforced fuselage by Fyfe and Sethi (1991). Kosai and Kobayashi (1993) then postulated a crack propagation and kinking criteria in the presence of K_{II} and reanalyzed the crack arrest capability of a tear strap in a pressurized fuselage.

THEORETICAL BACKGROUND

As mentioned previously, the function of a tear strap is not so much as to arrest a propagating axial crack by reducing the circumferential stress in the crack path, but to deflect the crack in the circumferential direction. The large opening due to crack flapping would then reduce the crack driving force through controlled depressurization of the cabin and thus arrest the crack. Such crack deflection is accomplished by the presence of mode II stress intensity factor, K_{II} , which is generated by the flap of the upper skin. The large crack flap also generates a large axial stress ahead of the propagating crack tip [Kobayashi, et. al. (1988); Kobayashi, et. al. (1988a)], and together with the reduced circumferential stress due to the presence of the tear strap, augments the propensity for crack kinking under a mixed mode crack tip deformation.

In a previous analysis [Kosai and Kobayashi (1991)], an elastic crack kinking criterion for a stationary mode I crack [Streit and Finnie (1980)] with plasticity correction was used to assess the effectiveness of the tear strap for a symmetric crack flap. The unsymmetric crack flap considered in this study, however, will generate a combined mode I and II crack tip deformation field [Fyfe and Sethi (1991)] and thus crack kinking is inherent in such crack tip deformation.

On the other hand, if the apparent mode I stress intensity factor, K_I , is elevated by the presence of a row of MSD's along the axis of the crack, then the crack will continue to propagate in the axial direction despite the presence of an inevitable crack tip bulging and the resultant K_{II} in a pressurized fuselage [NTSB (1989)]. The physical evidence of such self similar crack extension along a row of MSD's in the presence of K_{II} thus requires a new crack propagation and kinking criteria.

Previous experimental results [Arakawa (1991)] involving crack propagation in thin aluminum fracture specimens recorded maximum crack velocities of the order of 40 meters per second for the brittle 7075-T6 aluminum alloys. For the more ductile 2024-T3, the corresponding maximum crack velocity is estimated to be lower than 20 meters per second. At this low crack velocity, the *crack tip state of stress* can be approximated by its static counterpart despite the fact that the entire structural deformation must be treated dynamically. This greatly simplifies the theoretical analysis in this investigation.

Using the maximum stress criterion which is also identical with the maximum circumferential stress criterion in this case, and the crack tip stress field, the angle of crack kinking, θ_c in the presence of K_{II} was derived by Erdogan and Sih (1963). This maximizing condition yields a crack kinking criterion which predicts a positive θ_c for a negative K_{II} and a negative θ_c for a positive K_{II} . In the absence of K_{II} , however, the Erdogan-Sih criterion predicts a self-similar crack propagation or $\theta_c = 0$ and fails to explain the physically observed crack instability where crack kinking takes place in a K_I field. The static elastic crack kinking criterion, which incorporates the second order term in the crack tip stress field, of Streit and Finnie (1980) or the dynamic counterpart of Ramulu and Kobayashi (1983) predicts such crack kinking and was found to agree well with available experimental data. This mixed mode fracture criterion can be represented as

$$K_{Ic} = K_I \cos^3 \frac{\theta_c}{2} - 3K_{II} \cos^2 \frac{\theta_c}{2} \sin \frac{\theta_c}{2} + \frac{\sqrt{2\pi r_c}}{2} \sigma_{ox} (1 - \cos 2\theta_c) \quad (1)$$

where r_c is a material property.

Equation (1) incorporates the second order effect into the Erdogan-Sih criterion and follows a similar trend where a positive θ_c is predicted for a positive K_I and a negative K_{II} . The crack kinking angle, θ_c , increases with increasing σ_{ox} where negative σ_{ox} tends to stabilize the crack path. Equation (1) shows that for the same K_I and K_{II} and positive σ_{ox} , $\theta_c = 0$ and the crack will propagate straight ahead.

The crack kinking angle can be obtained by maximizing the crack tip circumferential stress and results in the following transcendental equation:

$$\frac{K_{II}}{K_I} = \frac{-\sin \frac{\theta_c}{2}}{(3 \cos \theta_c - 1)} \left[2 \cos \frac{\theta_c}{2} - \frac{16\sqrt{2\pi}}{3} A^* \cos \theta_c \right] \quad (2)$$

$$A = \sqrt{r_c} \frac{\sigma_{ox}}{K_I} \quad (3)$$

The term, A , is related to the critical distance, r_c , from the crack tip and is proportional to the nonsingular stress, σ_{ox} . For a pure mode I crack tip stress field, Ramulu and Kobayashi

(1983) have shown that r_c is a material dependent parameter which must be determined experimentally. Thus, Equation (1) incorporates the second order term and represents a mixed-mode extension of the crack kinking criterion by Streit and Finnie (1980) and Ramulu and Kobayashi (1983).

The crack extension criterion represented by Equation (1) and the crack kinking criterion represented by Equation (2) do not account for the elevation in stress intensity factors, K_I and possible K_{II} , due to the presence of MSD. The effect of MSD obviously is to promote self-similar crack extension, as seen in the NTSB report (1989), and can be incorporated into this analysis by artificially increasing K_I by a magnification factor which represents the interaction effect between the axial crack and the small crack emanating from adjacent fastener holes.

After kinking under the presence of mixed mode, i.e. K_I and K_{II} crack tip loading, the crack could propagate under a pure mode I crack tip loading due to the lack of a constraining stringer. Continuous crack curving under such condition will require that

$$r_o = \frac{9}{128\pi} \left(\frac{K_I}{\sigma_{ox}} \right)^2 < r_c \quad (4)$$

and the crack curving angle, θ_c , is

$$\theta_c = \cos^{-1} \left[\frac{1 \pm \sqrt{1 + \frac{1024\pi}{9} r_c \left(\frac{\sigma_{ox}}{K_I} \right)^2}}{\frac{512\pi}{9} r_c \left(\frac{\sigma_{ox}}{K_I} \right)^2} \right] \quad (5)$$

The development of a flap and the constraints due to the tear strap and the frame most likely will reduce the dominant K_I during the crack curving process and will result in crack arrest.

To reiterate, the proposed crack propagation and kinking criteria in the presence of mixed mode, K_I and K_{II} , crack tip deformation provide the necessary analytical tools for assessing the possibility of crack flapping in the event of rapid axial propagation in a pressurized fuselage.

EXPERIMENTAL PROCEDURE

The crack arrest capability of a tear strap in a pressurized fuselage was studied through instrumented, axial rupture tests of a small scale model of an idealized fuselage. Some of the details of the experimental procedure are described in the following.

Specimen

The test specimen consisted of a pressurized thin 2024-T3 aluminum cylinder of 360 mm diameter x 914 mm length x 0.3 mm thickness with one or two riveted and bonded lap or butt joint(s). Simulated tear straps were riveted and bonded to this scale model fuselage which was clamped between two steel cylinders of 406 mm diameter x 1219 mm length. This assembly represents the diameter-to-length ratio of a typical passenger plane. An axial through crack, 100 mm in length, was machined as a starter crack adjacent to a stringer and sealed with a cork gasket and silicon rubber sealant. The fuselage segment was instrumented with three to five strain gages along the anticipated crack path and a pressure transducer under the starter crack. A schematic layout of the fuselage model and the test fixture are shown in Figures 1 and 2, respectively.

Test Procedure

The test fixture was shielded to contain the flying debris which was generated by the explosive nature of the test. The strain gage and pressure transducer data was recorded on a magnetic tape recorder. To insure air tightness, the model was pre-pressurized at low pressure and checked for leaks which were then sealed with silicon rubber. Increasing pressure was applied to the scale model fuselage until a rapidly propagating axial crack initiated from the precrack.

High speed photographs of the rupturing scale model of the fuselage were taken by an IMACON 790 camera which was triggered by a crack wire in the crack path. Since the minimum framing rate of 10,000 frames/sec of this camera was too fast to record the entire rupture event, high speed photographs of four identical specimens were recorded at different time delays. The composite picture obtained by assembling these four series of photographs provided a visual display of the large deformation associated with the one sided flap opening.

NUMERICAL ANALYSIS

The unsymmetric crack tip deformation along the stringer required that at least one quarter of the scale model fuselage be considered as shown in Figure 3. The longitudinal stringers and the tear straps were modelled by beam elements. Implicit in this one-quarter segment modeling is an assumption, which was made to reduce the computational time, that an identical axial crack was also propagating in the other symmetric quarters of the fuselage. Because of the inevitable coupling effect between the two symmetrically propagating cracks, this modeling will not model correctly a very large crack flap opening of the single crack in the scale model fuselage.

One of the unknown quantities is the actual pressure distribution on the flap as the crack continues to open up. Previous numerical study on a rupturing full scale fuselage (Kosai and Kobayashi, 1993) showed that minor variation in the prescribed flap pressure yielded less than two percent variation in the crack tip stress intensity factor and thus the measured full pressure was prescribed on the opening flap.

The fracture parameters, K_I , K_{II} and σ_{ox} were determined through an elasto-dynamic finite element code (FEM), which was executed in its generation mode by prescribing the measured crack velocity together with the time-varying applied loads, using shell elements. The stress intensity factors were computed through a calibrated crack tip stress [Kosai and Kobayashi (1993)]. The remote stress component, σ_{ox} , was computed by subtracting the singular stress component from the axial stress component ahead of the crack tip.

The numerically determined K_I , K_{II} and σ_{ox} are then used to assess the potential of self similar crack propagation or crack kinking as described in the section of Theoretical Background.

RESULTS

Ten cylinders, without the simulated tear straps, and eleven cylinders, with the tear strap of various configurations, as shown in Table 1, or a total of twenty-one rupture tests were conducted. Specimens of Type a-1 (Table 1-1), without the lap joint or stringer along the precrack, were tested to check in the absence of K_{II} , for crack curving due to the axial tensile stress generated by large crack flaps after Kobayashi et al (1988). The rapidly propagating crack did not bifurcate but turned abruptly and ran circumferentially along the two steel end-cylinders. Likewise, the crack in Type e-1 specimen (Table 3) ran axially until it hit the tear straps and then ran circumferentially along the tear straps. These results indicate that the flap was not large enough to develop sufficiently large axial tension to kink the running crack prior to reaching the two steel end-cylinders.

For Type a-2 (Table 1), b-1, b-2 (Table 2) and d-1 (Table 3) specimens, the crack kinked immediately upon propagation and ran diagonally until it hit the steel end-cylinder. In this case, the crack kinked due to the presence of K_{II} which was generated by the one-sided flap away from the lap joint and/or stringer.

For Type c-1, c-2 (Table 2) and c-3 (Table 3) specimens, the crack kinked immediately upon extension but then propagated in an off-axis direction until it approached the tear straps where it turned circumferentially and propagated along the tear straps. Figure 4 shows photographs, which are a composite of two tests, of a rupturing Type c-3 specimen. This sequential photograph shows the development of the crack flap after it kinked immediately upon extension,

Figure 5 shows typical strain gage results obtained during a rupture test. The strain gage results were used to estimate the crack velocities which ranged from 30 to 120 meters per second in all of the tests. This low crack velocity justified the use of the static crack tip equations of Equations 1 through 4 to extract the variation in the mixed mode stress intensity factors, K_I and K_{II} , and the remote stress components, σ_{ox} , with crack extension.

Figures 6 and 7 show the variations in K_I , K_{II} and σ_{ox} with crack extension for Specimen No. 11 (Type e c-3) and Specimen No. 13 (Type b-2). Since Figure 7 shows that $K_{dynI} > K_{IC}$ in Specimen No. 13, the crack will not kink despite the fact that the computed $r_o > r_c$ according to the crack kinking criterion set forth in the Theoretical Background. On the other hand, crack kinking will occur at the onset of rapid crack propagation in Specimen No. 11 due to the presence of K_{II} and $r_o > r_c$. The good agreement between the predicted and the measured crack kinking angles and the subsequent self similar crack extension demonstrated the effectiveness of the crack kinking criterion as applied to a rupturing fuselage. The legend in Figure 6 shows that the crack kinking angle estimated without the σ_{ox} term is 1/2 of that measured.

Five of the twenty-one small-scale fuselage test results were analyzed using the procedure describe above. In all cases, the modified crack kinking criterion of Kosai et al correctly predicted the experimentally crack kinking angles.

CONCLUSIONS

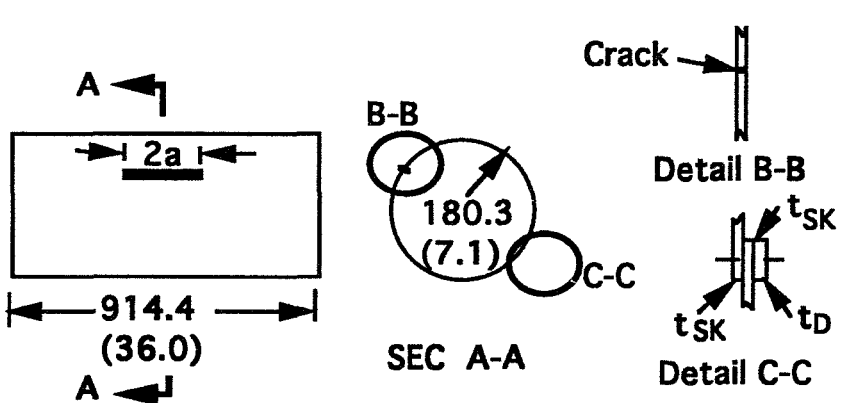
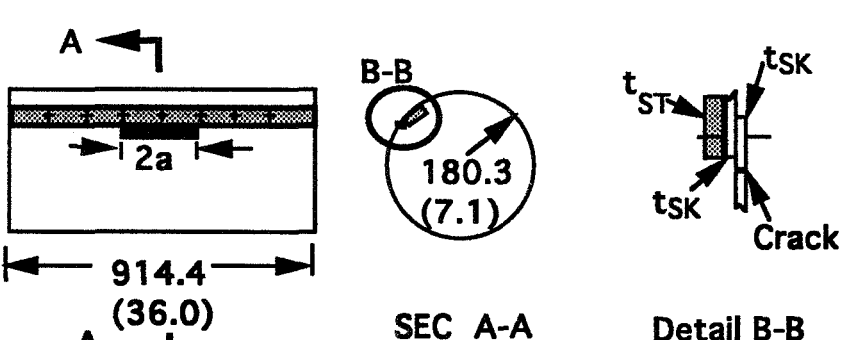
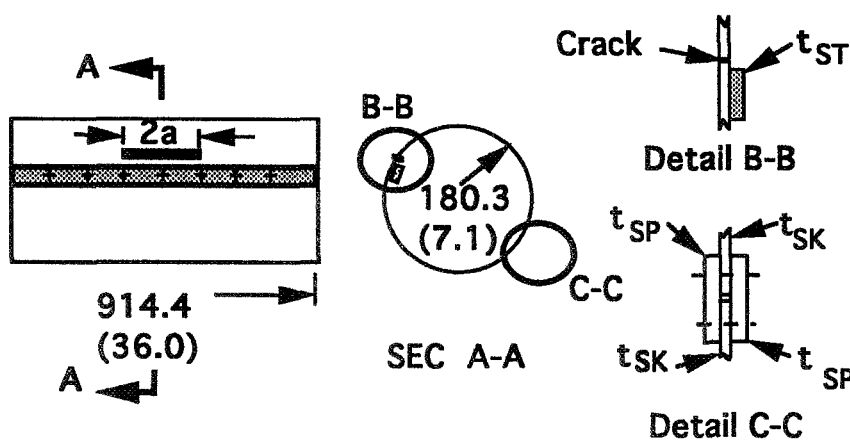
A hybrid analysis, which utilizes the test results of a rupturing small-scale fuselage model to drive a large deformation, elastodynamic finite element code, was effectively used to study the mechanics of the crack arrest at a tear strap in a pressurized fuselage.

The modified crack kinking criterion of Kosai et al (1993) will predict the crack kinking angle in the small-scale fuselage test specimens.

BIBLIOGRAPHY

- Arakawa, K., Drinnon, R.H., Jr., Kosai, M. and Kobayashi, A.S. (1991). "Dynamic Fracture Analysis by Moire Interferometry," *Experimental Mechanics*, 31 306-309.
- Erdogan, F. and Sih, G.C. (1963). "On the Crack Extension in Plates Under Plane Loading and Transverse Shear," *Journal of Basic Engineering*, 85 519-527.
- Fyfe, I.M. and Sethi, V. (1991). "The Role of Thin Cylinder Bulging on Crack Curvature," *AIAA Paper 914086*, 32nd Structures, Structural Dynamics and Materials Conference, Baltimore, MD.
- Kobayashi, A.S., Emery, A.F., Love, W.J. and Chao, Y.H. (1988). "Subsize Experimental and Numerical Modeling of Axial Rupture of Gas Transmission Lines," *ASME Journal of Pressure Vessel Technology*, 110, 155-160.
- Kobayashi, A.S., Emery, A.F., Love, W.J., Chao, Y.H. and Johannsen, O. (1988a). "Crack Bifurcation and Arrest in Pressurized Pipe," *Fracture Mechanics: Nineteenth Symposium*, ASTM STP 609, ed. T.A. Cruse, ASTM, 441-465.
- Kosai, M. and Kobayashi, A.S. (1991). "Axial Crack Propagation and Arrest in Pressurized Fuselage," *Structural Integrity of Aging Airplanes*, eds. S.N. Atluri, S.G. Sampath and P. Tong, Springer-Verlag, 225-239.
- Kosai, M., Kobayashi, A.S. and Ramulu, M. (1993). "Tear Straps in Airplane Fuselage," to be published in *Structural Integrity of Aging Airplanes*, eds. S.N. Atluri, S.G. Sampath and P. Tong, Technological Publications, Atlanta, GA.
- Maclin, J.R. (1991). A paper presented at the 1991 International Conference on Aging Aircraft and Structural Airworthiness, Washington, D.C.
- National Transportation Safety Board Aircraft Accident Report. (1989). "Aloha Airlines Flight 243, Boeing 737-200, N73711, Near Maui, Hawaii, April 28, 1988," NTSB/AAR-89/03.
- Ramulu, M. and Kobayashi, A.S. (1983). "Dynamic Crack Curving — A Photoelastic Evaluation," *Experimental Mechanics*, 23, 1-9.
- Sampath, S. and Broek, D. (1991) "Estimation of Requirements of Inspection Intervals for Panels Susceptible to Multiple Site Damage," *Structural Integrity of Aging Airplanes*, eds. S.N. Atluri, S.G. Sampath and P. Tong, Springer-Verlag, 339-389.
- Streit, R. and Finnie, I. (1980). "An Experimental Investigation of Crack Path Directional Stability," *Experimental Mechanics*, 20, 17-23.

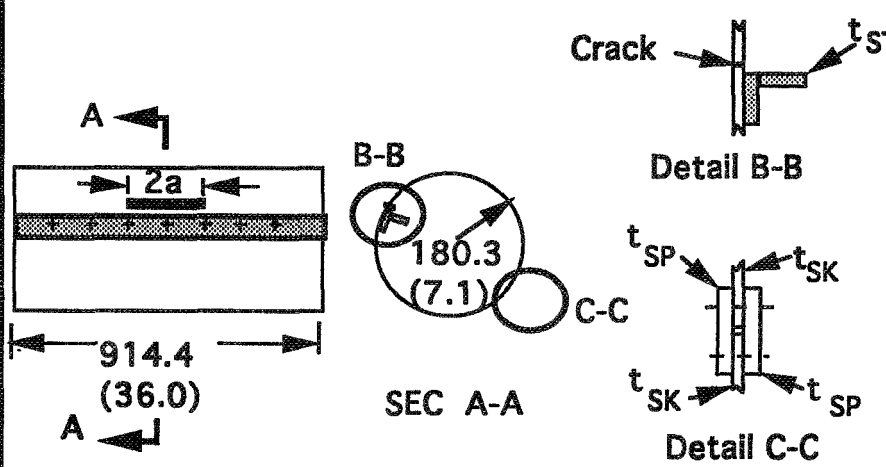
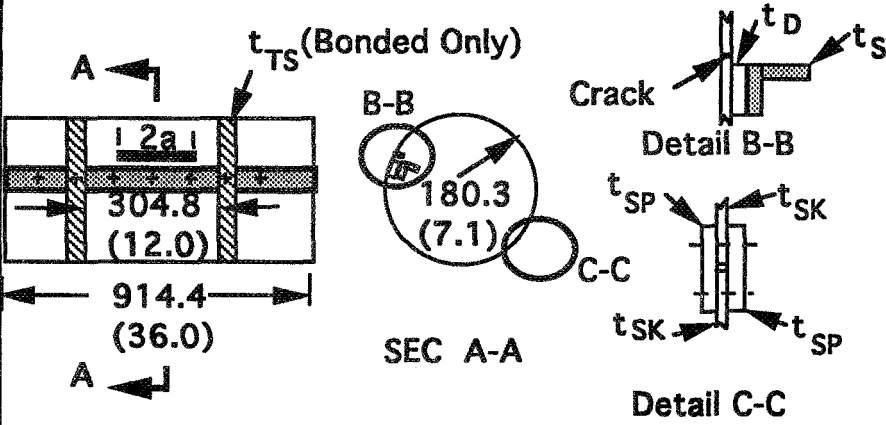
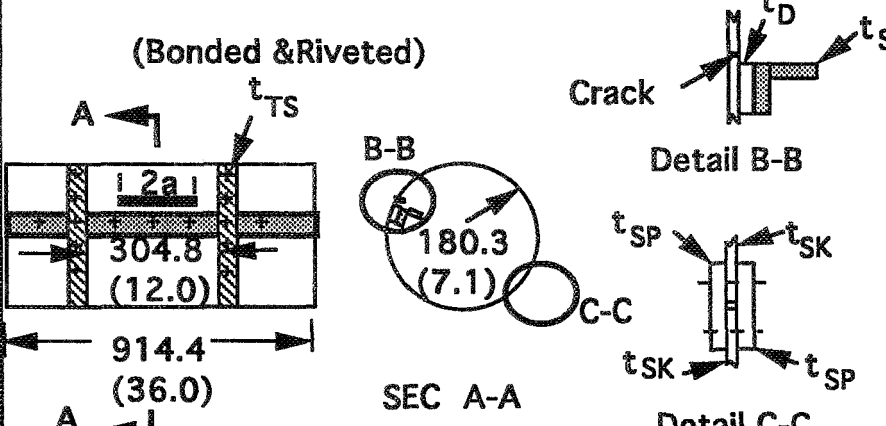
Table 1. Small-Scale Fuselage Specimens

Type	Configuration	Spec. No.
a-1	 <p> $2a = 127.0$ (5.0) $t_{SK} = 0.3$ (0.012) $t_D = 0.6$ (0.025) Lap Splice </p>	1
a-2	 <p> $2a = 101.6$ (4.0) $t_{SK} = 0.3$ (0.012) $t_{ST} = 0.6$ (0.025) Lap Splice 1" Width Flat Stringer </p>	2
b-1	 <p> $2a = 101.6$ (4.0) $t_{SK} = 0.3$ (0.012) $t_{ST} = 0.6$ (0.025) $t_{SP} = 0.6$ (0.025) Butt Splice 1" Width Flat Stringer </p>	3 4

SK : Skin ST : Stringer SP : Splice Plate D : Doubler

Unit : mm
(Inch)

Table 2. Small-Scale Fuselage Specimens

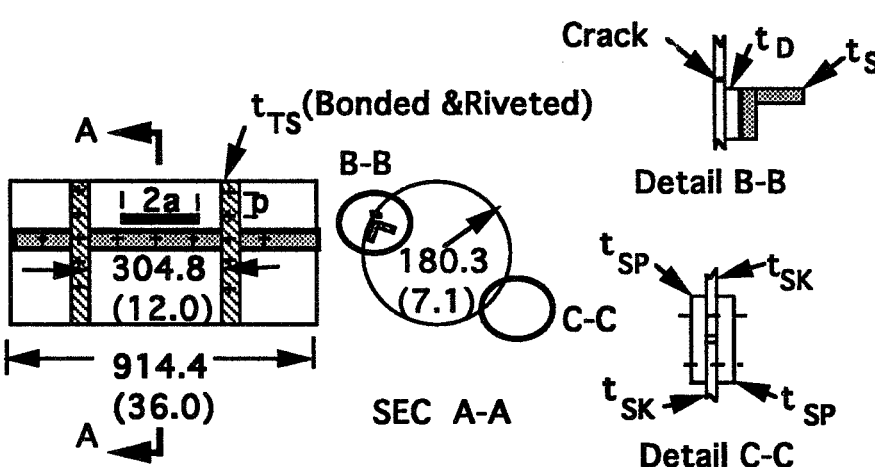
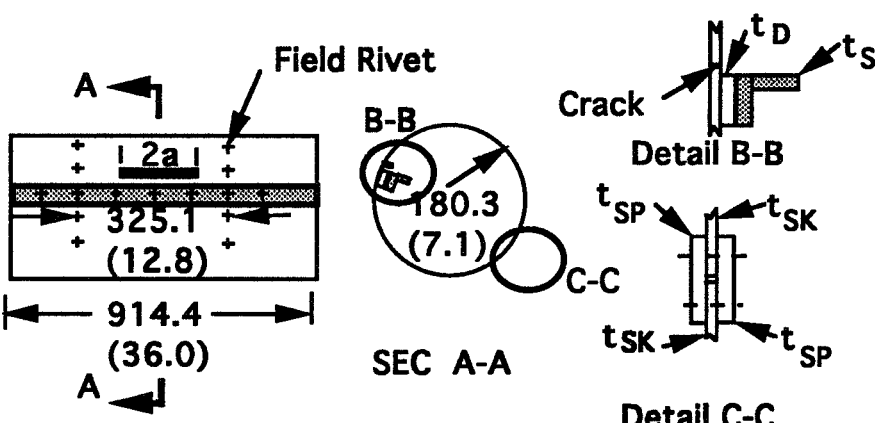
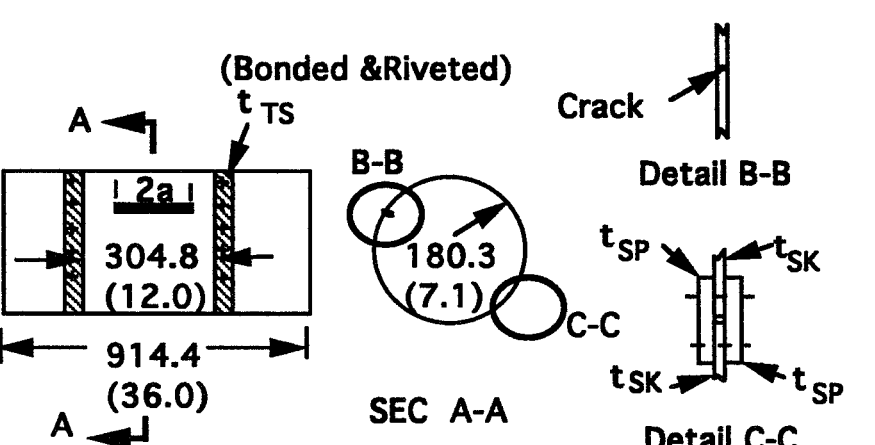
Type	Configuration	Spec. No.
b-2	 <p>2a = 101.6 (4.0) t_{SK} = 0.3 (0.012) t_{ST} = 0.8 (0.032) t_{SP} = 0.6 (0.025) Butt Splice 1"×1" L-Stringer</p>	5 6 14* 15* 16*
c-1	 <p>2a = 101.6 (4.0) t_{SK} = 0.3 (0.012) t_{ST} = 0.6 (0.025) t_{TS} = t_{SP} = t_D = 0.6 (0.025) Butt Splice 1"×1" L-Stringer Bonded Tear Strap (w=0.8")</p>	7
c-2	 <p>2a = 101.6 (4.0) t_{SK} = 0.3 (0.012) t_{ST} = 0.6 (0.025) t_{TS} = t_{SP} = t_D = 0.6 (0.025) Butt Splice 1"×1" L-Stringer Bonded & Riveted Tear Strap (w=0.8")</p>	8 9

SK : Skin ST : Stringer TS : Tear Strap SP : Splice Plate
* : Driven by the pneumatic riveter.

D : Doubler

Unit : mm
(Inch)

Table 3. Small-Scale Fuselage Specimens

Type	Configuration	Spec. No.
c-3	 <p>Crack</p> <p>Detail B-B</p> <p>Detail C-C</p> <p>SEC A-A</p> <p>Butt Splice 1"*1" L-Stringer Bonded & Riveted Tear Strap(w=0.8")</p>	10 11 17* 18* 19* 20* 21*
d-1	 <p>Field Rivet</p> <p>Crack</p> <p>Detail B-B</p> <p>Detail C-C</p> <p>SEC A-A</p> <p>Butt Splice 1"*1" L-Stringer No Tear Strap</p>	12
e-1	 <p>Crack</p> <p>Detail B-B</p> <p>Detail C-C</p> <p>SEC A-A</p> <p>Butt Splice No Stringer Bonded & Riveted Tear Strap(w=0.8")</p>	13

SK : Skin ST : Stringer TS : Tear Strap SP : Splice Plate D : Doubler Unit : mm

* : Driven by the pneumatic riveter.

(Inch)

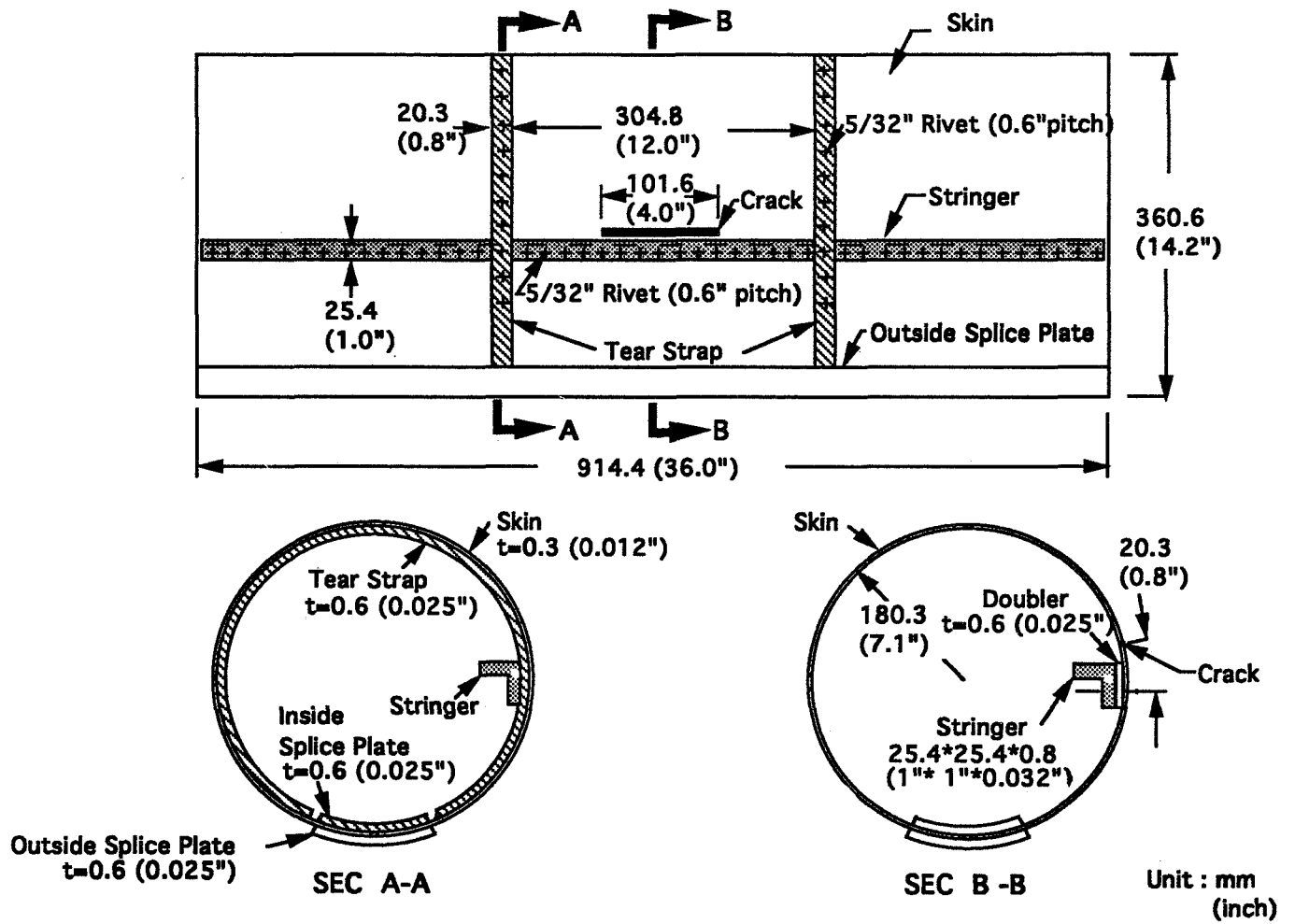


Figure 1. Scale model fuselage specimen.

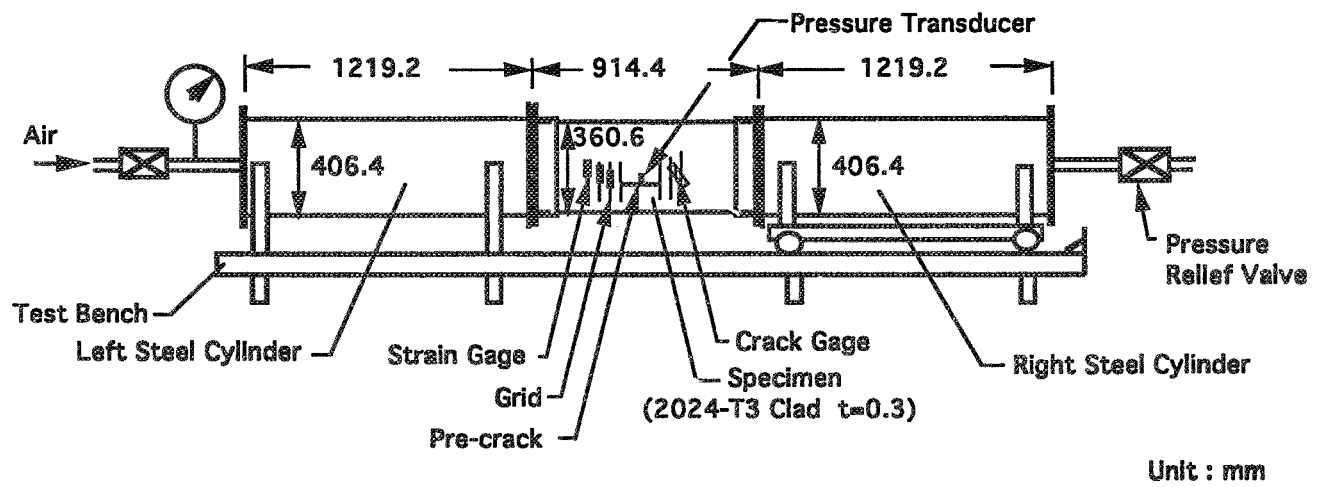
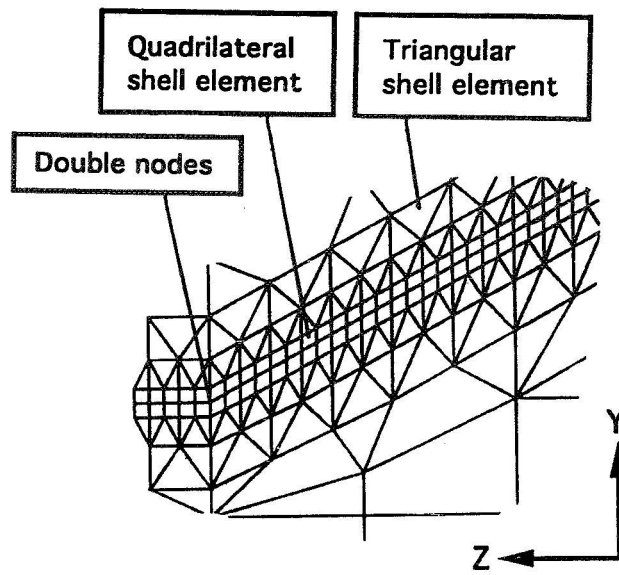


Figure 2. Test setup.



Detail of mesh along the crack path

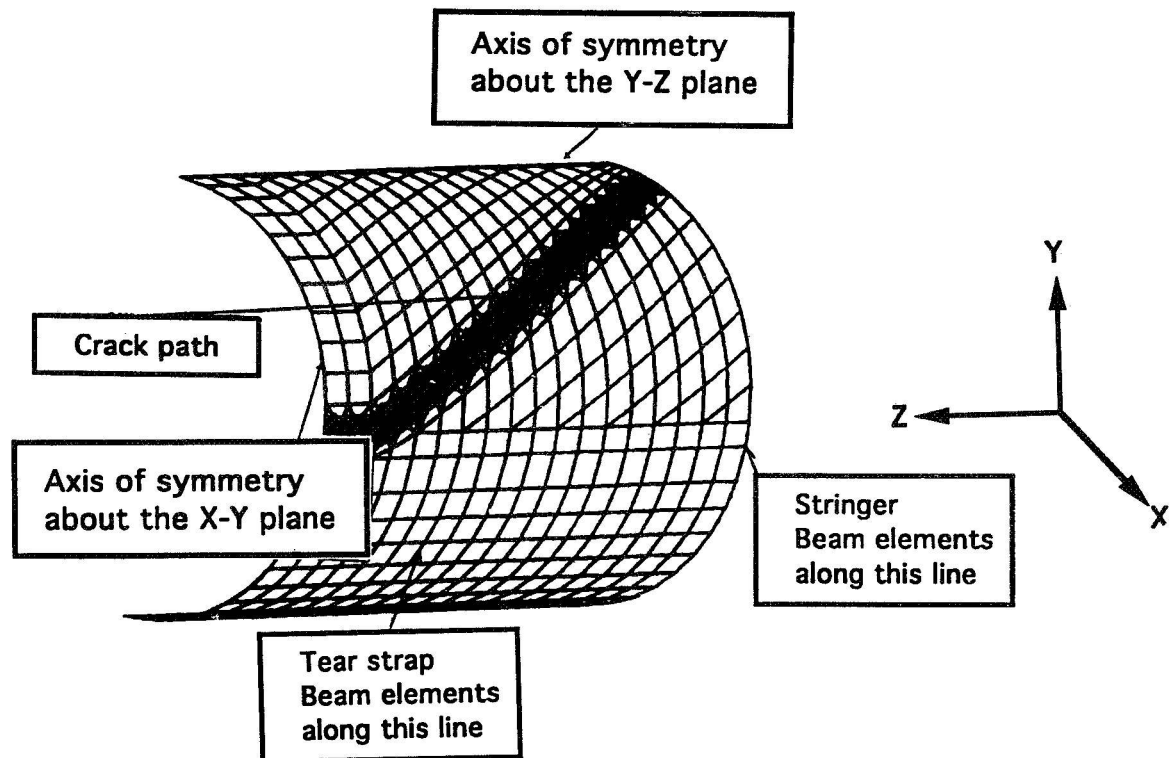
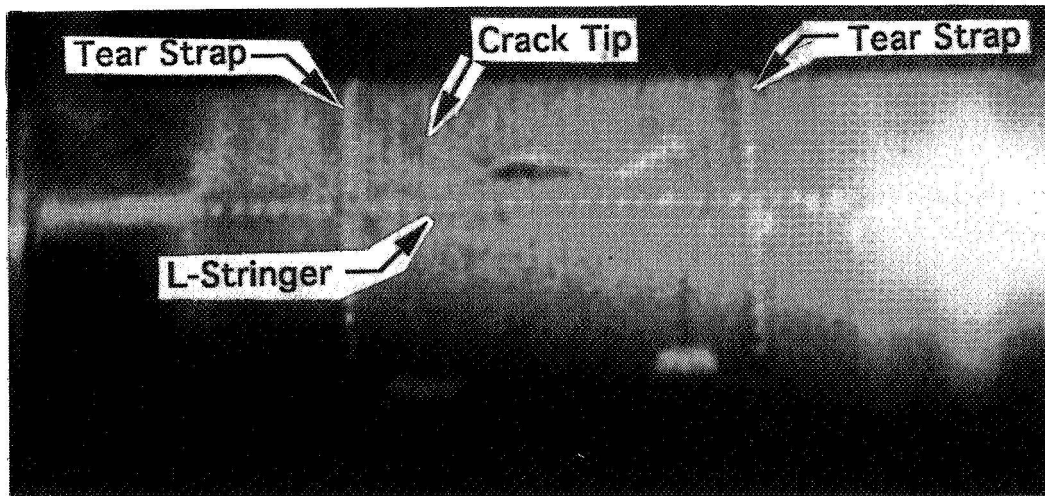
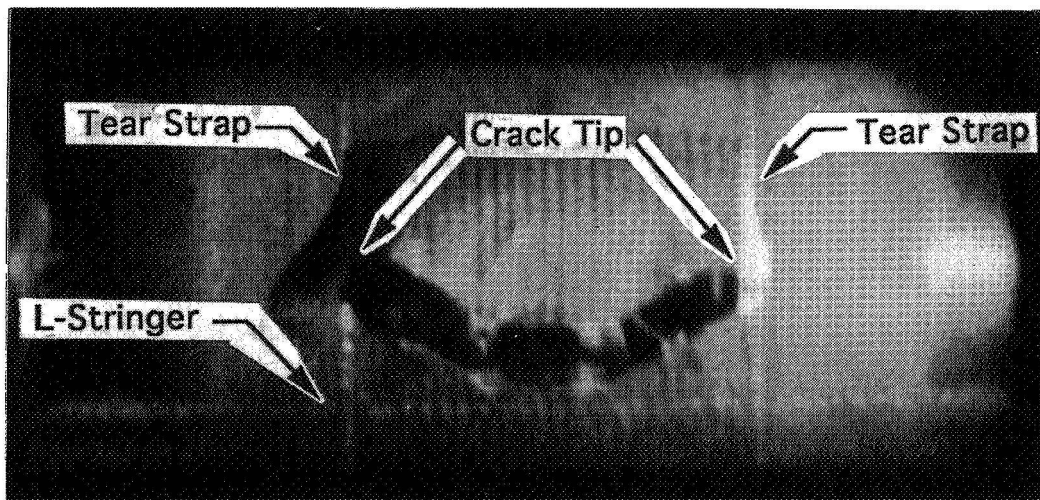


Figure 3. Finite element mesh.



$\Delta t = 0.4 \text{ msec}$



$\Delta t = 1.3 \text{ msec}$

Δt : Delay time after the crack passed through the crack gage.

Figure 4. High speed photographs of a rupturing small-scale fuselage. Type c-3.

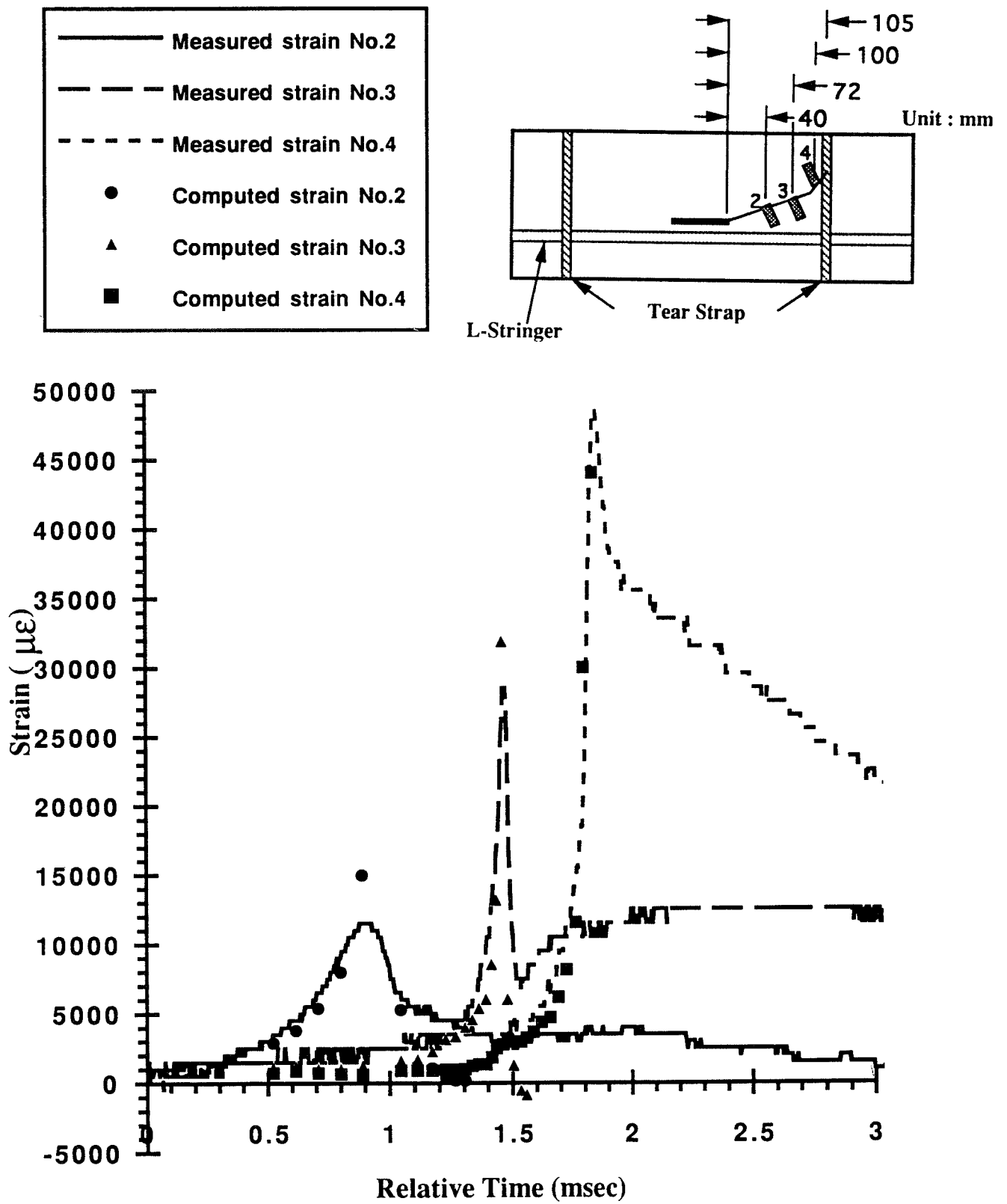


Figure 5. Strain gage response in Specimen No.11. Type c-3.

θ_m : Measured kinking angle (degrees)

θ_c : Computed kinking angle (degrees)

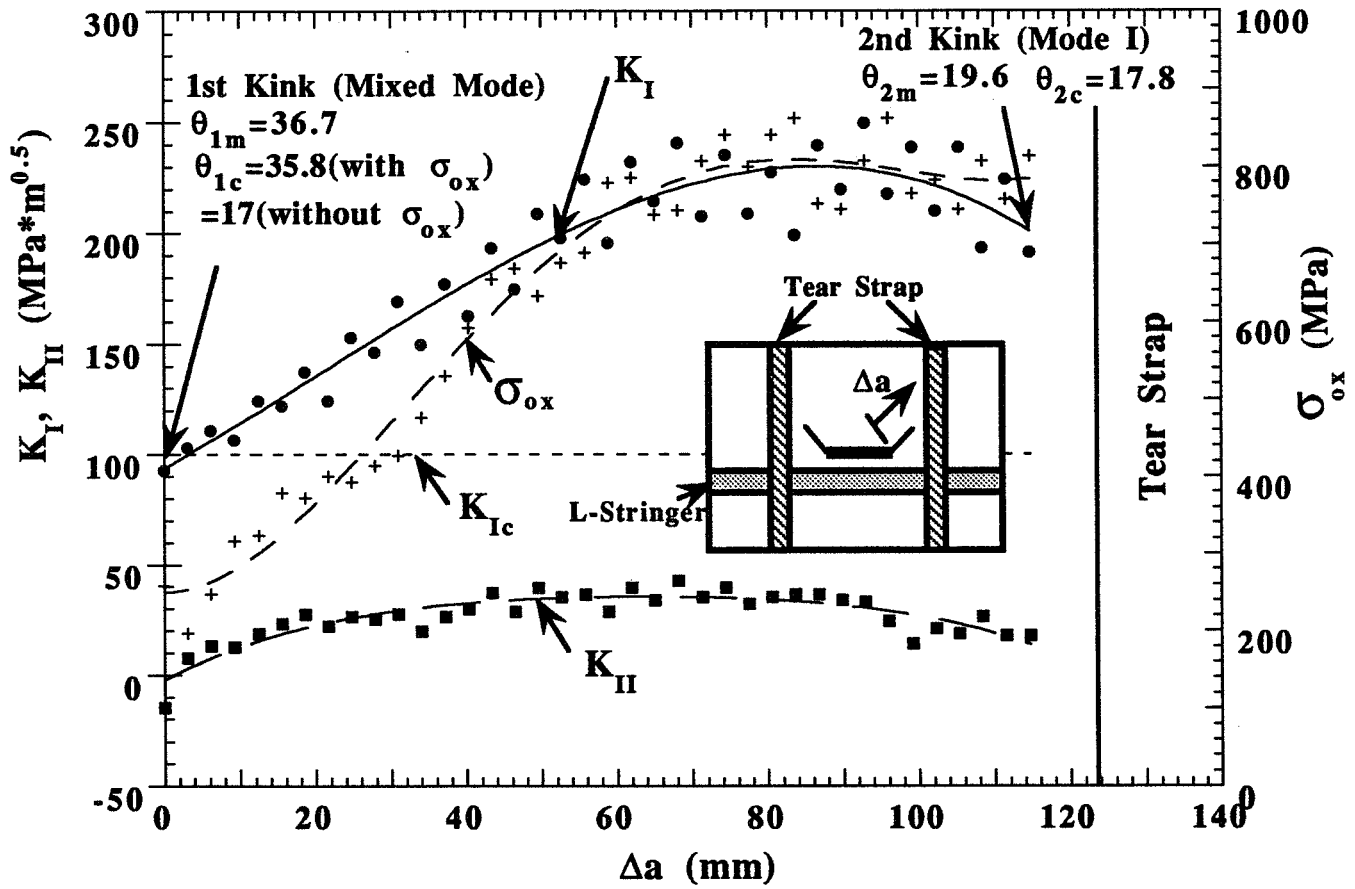


Figure 6. Variations in K_I , K_{II} and σ_{ox} with crack extension. Specimen No.11 (Type c-3).

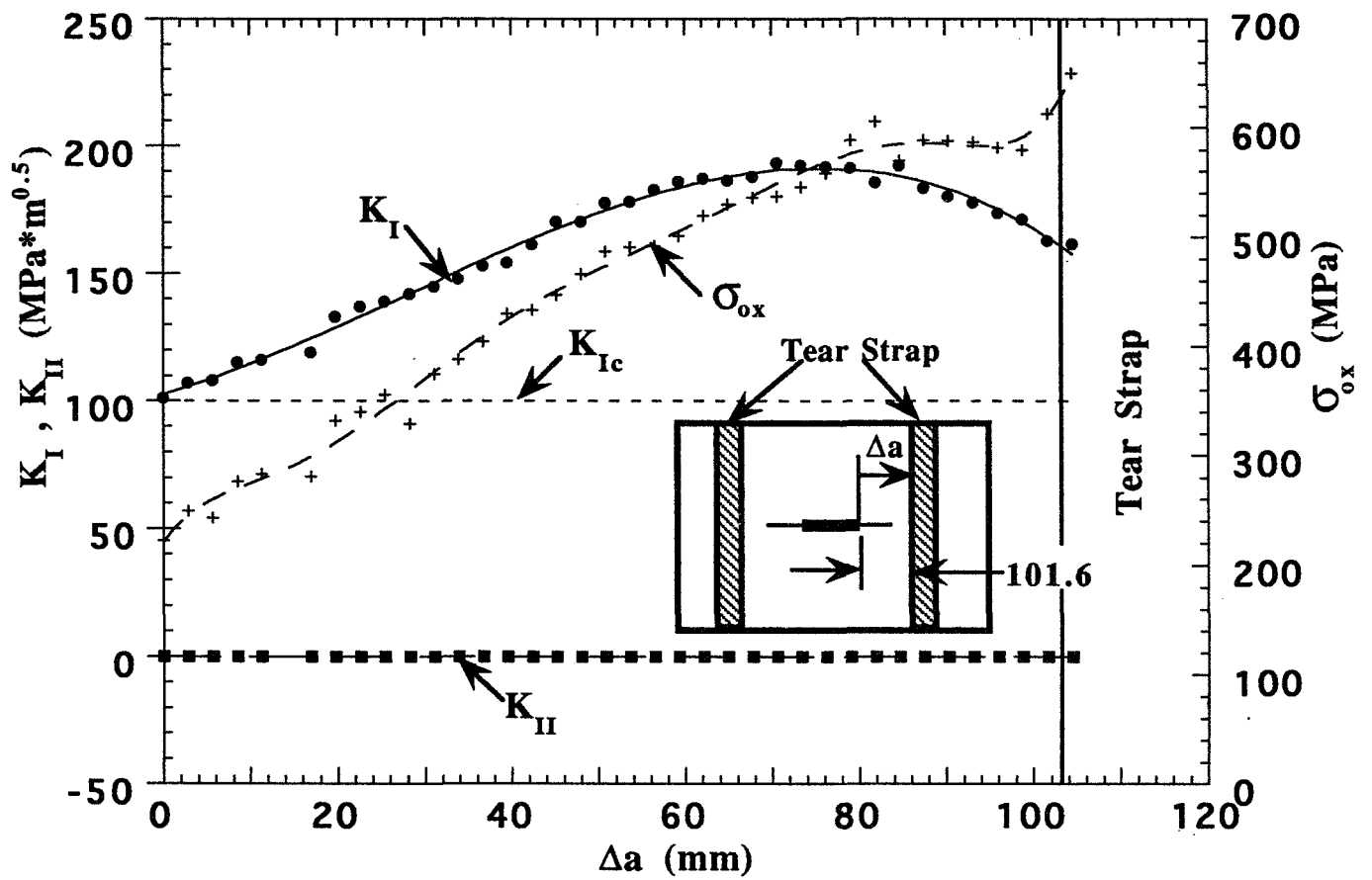


Figure 7. Variations in K_I , K_{II} and σ_{ox} with crack extension. Specimen No.13 (Type e-1).

FRACTURE MECHANICS VALIDITY LIMITS

Dennis M. Lambert and Hugo A. Ernst
GW Woodruff School of Mechanical Engineering
The Georgia Institute of Technology

348665
527-39
23121
P 15

SUMMARY

The consideration of fracture behavior in design is of vital concern to the aerospace industry. Fracture behavior is characteristic of a dramatic loss of strength compared to elastic plastic deformation behavior. Fracture parameters such as K , G , J , and J_M have been developed and exhibit a range within which each is valid for predicting growth. Each is limited by the assumptions made in their development: all are defined within a specific context. For example, the stress intensity parameter, K , and the crack driving force, G , are derived using an assumption of linear elasticity. To use K or G , the zone of plasticity must be small as compared to the physical dimensions of the object being loaded. This insures an elastic response, and in this context, K and G will work well. Rice's J -integral [1] has been used beyond the limits imposed on K and G . J requires an assumption of nonlinear elasticity, which is not characteristic of real material behavior, but is thought to be a reasonable approximation if unloading is kept to a minimum. As well, the constraint cannot change dramatically (typically, the crack extension is limited to ten-percent of the initial remaining ligament length). Rice, et al [2] investigated the properties required of J -type parameters, J_x , and showed that the time rate, dJ_x/dt , must not be a function of the crack extension rate, da/dt . Ernst [3] devised the modified- J parameter, J_M , that meets this criterion. J_M correlates fracture data to much higher crack growth than does J . Ultimately, a limit of the validity of J_M is anticipated, and this has been estimated to be at a crack extension of about 40-percent of the initial remaining ligament length.

None of the various parameters can be expected to describe fracture in an environment of gross plasticity, in which case the process is better described by deformation parameters, e.g., stress and strain. In the current study, various schemes to identify the onset of the plasticity-dominated behavior, i.e., the end of fracture mechanics validity, are presented. Each validity limit parameter is developed in detail, and then data is presented and the various schemes for establishing a limit of the validity are compared. The selected limiting parameter is applied to a set of fracture data showing the improvement of correlation gained.

INTRODUCTION

The safety and reliability of structures has always been a matter of vital concern to the aerospace industry. In this respect, fracture mechanics is especially useful, since it can provide a quantitative description of the capability of structural parts to tolerate flaws. The initial conditions considered for fracture mechanics were quasi-linear elastic conditions (LEFM). The methods were eventually developed further to include cases where yielding was not confined to a small region.

The parameters developed for use in the LEFM technology, G and K , are efficient as fracture predicting tools as long as the material responds in a linear-elastic manner. This occurs when the plastic

zone present at the tip of the crack is found to be much smaller than the ligament dimensions. To consider a more realistic class of problems, where the plasticity was not limited to a very small region, Elastic-Plastic Fracture Mechanics [EPFM] Methods were developed. The J-Integral was developed by Rice [1] by assuming non-linear elasticity, and was thereby limited in the range of applicability. The requirements for J-control are small crack tip displacement (CTOD), proportional loading, and small crack extension. Hutchinson and Paris [4] defined ω which evaluates the degree of nonproportionality, with the significance that some unloading can be tolerated without invalidating J, as long as the ω -criterion holds. The last requirement was established to avoid crack growth to an extent that the constraint environment controlling fracture changes. Constraint as used here is the degree of triaxiality of the stress field.

TESTING RESULTS

Tests were conducted according to ASTM E1152-87 [5] with intermediate crack lengths determined by using unloading compliance data. Crack fronts had considerable curvature and a linear averaging was used to produce a single length dimension. The curvature can affect the crack length-versus-compliance relationship and the intermediate crack lengths were adjusted using the curvature correction discussed in ASTM E647-91 [6].

Figure 1 shows collections of the J_M -resistance ($J_M R$) data for the aluminum and the nickel alloys. The $J_M R$ -curve format was selected because $J_M R$ -curves correlated data to a higher level of crack extension while the JR-curves progressed towards constant J. Two observations can be made of the resistance curves presented in these graphs: (1) the resistance data shows a broad range of behavior, and (2) three separate trends of behavior appear for the aluminum, while two emerge for the nickel.

After some degree of crack growth, many of the $J_M R$ -curves exhibit an inflection point and become concave-upwards. This is thought to be the signalling of a change of behavior from a regime controlled by fracture mechanics into one dominated by plasticity. To properly evaluate the effect of constraint in fracture requires that the data be qualified as representative of fracture mechanics behavior, such that the only variation is the constraint and not a change in the behavioral mode.

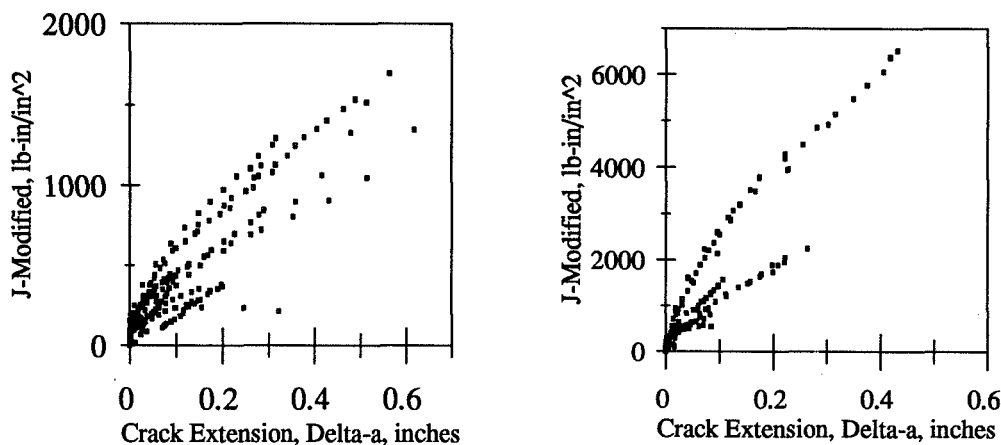


Figure 1: $J_M R$ behavior of Task I Al6061-T651 and IN718-STA1 fracture specimens: (a) $J_M R$ curves for aluminum CT specimens, (b) $J_M R$ curves for nickel CT specimens.

FRACTURE MECHANICS VALIDITY LIMITS PARAMETERS

The matter for current consideration is an assessment of the limits within which fracture mechanics parameters must operate and to ultimately apply those limits to the data set. In the process of loading, structures made of ductile materials may respond to the loading with fracture mechanics behavior, and with sufficient crack extension, the behavior will become plasticity-dominated. A method must be established to properly separate the region of fracture-dominated behavior from that of plasticity-dominated material behavior. This segregation of behavior would be necessary even if a parameter were found to describe crack growth behavior throughout the whole fracture mechanics regime: a limit to the fracture mechanics regime exists. This qualification of fracture behavior will be essential to an investigation of the three-dimensional aspects of fracture for two reasons: (1) the resulting material fracture resistance data collected for planar specimens might be applied to the general, three-dimensional case, and (2) the fracture mechanics validity limits analysis in two-dimensions might produce some insight applicable to three-dimensional fracture.

Several commonly used fracture parameters are subject to very confining limits. For example, for the stress intensity parameter, K , the plastic zone must be small with respect to relevant dimensions of the structure. This has been expressed as follows [7]:

$$\rho \equiv \frac{\pi}{8} \left(\frac{K}{\sigma_o} \right)^2 \ll B, b, a \quad (1)$$

Equation 1 gives an estimate of the plastic zone size, ρ , while σ_o is the flow stress. The parameter, ρ , must be small versus the specimen dimensions for K to be valid.

A second fracture parameter used is the J-integral [1]. The development of J requires an assumption of nonlinear elasticity to establish the path-independent nature of the integral. Nonlinear elasticity does not faithfully represent actual structural material behavior, where energy is dissipated and permanent deformation occurs. The elasticity assumption may still suffice as long as unloading is avoided. The first limit of J, required to assure the assumptions, is that the crack tip opening displacement (CTOD) must be small compared to ligament dimensions. This is necessary to ensure small deformation theory and is expressed in a ratio with the ligament length:

$$\rho_J \approx \frac{b_o}{CTOD} \equiv \frac{b_o \sigma_o}{J} \gg 1 \quad (2)$$

A minimum value of $\rho_J \geq 20$ to 25 is generally accepted to be the limit of J-controlled behavior. Other limits of J exist. Though crack growth causes unloading and pronounces the permanent deformation behavior, the inaccuracy due to the deviation from nonlinear elasticity can be kept to an acceptable level if certain limits are held. For J, the additional validity limits are expressed [4,8,9] as:

$$\omega = \frac{b}{D} = \frac{b}{J_{Ic}} \frac{dJ}{da} \gg 1 \quad (3)$$

$$\Delta a \leq 0.1 \times b_o \quad (4)$$

In equation 3, D defines the area associated with nonproportional loading. Equation 4 limits the crack growth to small enough that the constraint does not change. As long as the limits expressed in equations 3 and 4 are obeyed, J is considered valid for predicting fracture behavior.

Ernst [10,11] developed the modified J-integral, or J_M , that relaxed the tight limits imposed on J . The J-integral was developed assuming nonlinear elasticity, i.e., the deformation process was considered to be reversible. This assumption was acceptable within the limits of ω . With J , the load versus displacement (P-v) and crack length-versus-displacement (a-v) records were assumed to be path-independent.

Rice, Drugan, and Sham [2] determined that in the presence of a growing crack, any J-type parameter, say J_X , must have a rate, dJ_X/dt , that is independent of the crack growth rate, da/dt . Ernst [10,11] introduced the modified J-integral (J_M) which complies with this requirement:

$$J_M = G + \int_0^{v_{\phi}} \left. \frac{\partial J_{pl}}{\partial v_{\phi}} \right|_a dv_{\phi} \quad (5)$$

J_M assumes real plasticity, and follows the actual, irreversible process, with the change in plastic displacement always greater than or equal to zero, i.e., $dv_{\phi} \geq 0$ [11]. Whereas J_{pl} is the area between two "calibration" (i.e., non-growing crack) curves (load-versus-plastic displacement) of like specimens of infinitesimally different crack length, $J_{M,pl}$ was defined as the change in area between the load-versus-plastic displacement curves of two specimens with growing cracks where an infinitesimal difference in the crack length is always maintained. J_M meets the Rice-criterion, and includes some of the irreversibility of the fracture event. This allows fracture characterization to a much greater extent of crack growth. To compare J and J_M a typical J-resistance curve, or *JR curve*, has been enclosed (figure 2a). This graph plots the crack extension on the abscissa versus J and J_M on the ordinate. The "ASTM box" [5] has been drawn showing the limits of J that appear in equations 2 and 4, using a value of $\rho_f = 20$ to predict a value of J_{max} . Note that the location where the J limit is reached, J and J_M begin to diverge noticeably. This behavior is common to all data produced in this investigation.

Limits for J_M were estimated to be a crack extension of 40-percent of the original remaining ligament for the different specimen sizes and configurations tested [11]. Later works by Ernst and Pollitz [12,13] and Ernst [14,15] have further considered the limit of validity of J_M and have suggested it to be the inflection point of the J_M R-curve.

It has been observed that with sufficient crack growth, the J_M R-curve will pass from a concave-downwards shape to one that is concave-upwards. The upwards inflection is thought to be due to a change in the deformation character. Specifically, the specimen has passed into a regime where deformation and crack growth are better described using stress-strain relationships and considering the full-field problem instead of local fracture mechanics parameters. The point at which fracture mechanics methods are no longer effective in describing the fracture event is termed herein as the *fracture mechanics validity limit* (symbolized VL). Because of this change of dominant behavior, the two regimes should be separated for evaluation. This is not a new concept. Ernst and Pollitz [12] discussed ways of extrapolating J_M in order to allow estimation of the behavior of large, thick structures from the behavior of small test specimens. The extrapolation makes use of an apparent improvement of correlation derived from using J_M instead of the J-integral parameter. They considered two options for establishing the limit of the J_M data to be used in the extrapolation: (1) the inflection point of the J_M R curve or (2) the inflection point of a plot of the plastic displacement-versus-crack extension. An assortment of schemes were then used to extend the truncated resistance curve to estimate much greater crack extension.

The inflection point observed in the J_M R-curve is often subtle and can be difficult to determine. This suggests that other parameters might be devised to better identify the validity limit of fracture mechanics. Six candidates were considered in this investigation, although only the ones showing the most promise will be discussed in detail. Along with these, the location on the JR-curves corresponding to the maximum load during the test was determined and certain comments will be made at an appropriate time regarding the observations.

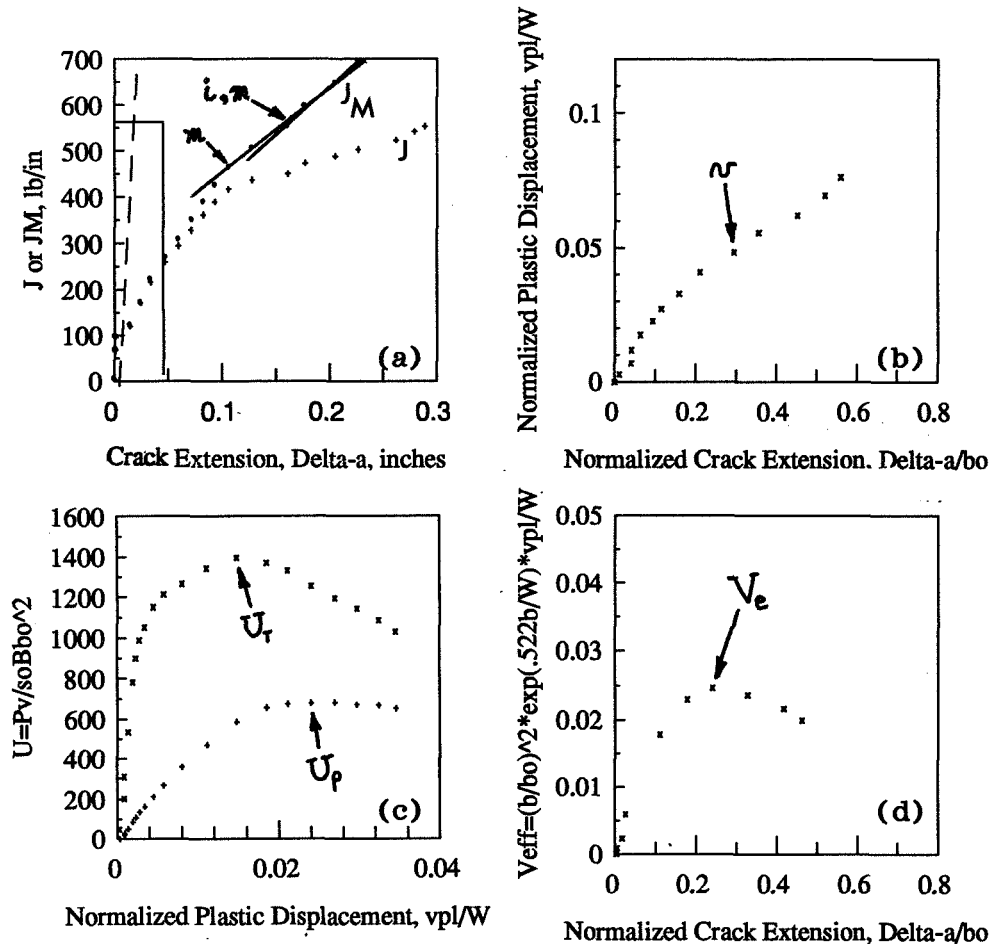


Figure 2: Various validity limit parameter definitions: (a) typical J_M R curve showing inflection point and constant slope points, (b) inflection point of plastic-displacement-versus-crack extension, (c) product of load times plastic or total displacement, and (d) effective volume.

The first candidate VL parameter is the inflection point of the J_M R-curve. This has been discussed as an indication in the R-curve of the onset of a new behavior, and the location is labelled "i", as in the inflection point of the J_M R-curve, in figure 2a. One parameter which has been discarded as a candidate is the point at which the J_M R-curve becomes straight (symbol "m"). Two such possibilities for the initiation point of constant slope are indicated in the figure. The first possibility is thought to be due to the approach of the inflection point. The second possibility is synonymous with the inflection point, i. Earlier work by Ernst [15] suggests that if fracture parameters can be scaled in the same way as plastic deformation processes, then the behavior has become plasticity-dominated, and fracture mechanics treatments are invalid. Ernst further showed that this case would be manifested as a straight line in the JR-curve format. A third candidate is the inflection point of the curve of plastic displacement-versus-crack extension (symbol "y" in figure 2b). Again, the phenomenological change is thought to be a transition from fracture-driven processes to plasticity. As with the i-criterion, this point is often subtle and not easily established. The

fourth and fifth candidates (symbolized by " U_p " and " U_t ", respectively) were discussed by Ernst [15] and are the product of load-times-plastic displacement or load-times-total displacement (figure 2c). The last candidate for a fracture mechanics regime limit is the onset of constant effective volume (symbol " V_o ", figure 2d). Constant volume deformation is commonly assumed for plastic deformation, and the onset of plasticity would be expected to exhibit this behavior.

The following sub-sections are devoted to the development of any formulae and theory for use in the evaluation of the various candidate VL parameters and discussions of the relevance of each.

INFLECTION POINT OF $J_M R$ CURVE, SYMBOL "i"

The inflection of the $J_M R$ -curve has been discussed earlier (figure 2a) as an indication of the onset of a new behavior mode. This is thought to be the result of the saturation of the ligament. This is documented by Rice, Drugan, and Sham [2], and the slope of the $J_M R$ -curve is given by the following equation:

$$\frac{dJ_{(x)}}{da} = A_o + R_o \ln \left(\frac{R}{R_o} \right) \quad (6)$$

$$R_o = R(A_o) \quad (7)$$

In this discussion, $J_{(x)}$ is J-modified, and R estimates the plastic zone size. The small scale yielding (SSY) behavior is given by

$$R = R_{ssy} \approx .25 \times E / \sigma_o^2 \quad (8)$$

In equation 8, E is Young's modulus. The behavior for large scale yielding (LSY) is a linear function of the ligament length:

$$R \Rightarrow R_{LSY} = \alpha b \quad (9)$$

When R increases to a point that $R \approx R_o$, then the $J_M R$ curve behavior begins to change. When the slope is characterized by equation 9, the inflection point has been reached. In the process of fracture, the ligament length b will be decreased, and this would produce an increasing slope after the point of saturation.

POINT OF CONSTANT $J_M R$ CURVE SLOPE, SYMBOL "m"

The proper scaling associated with fracture mechanics is thought to be $\Delta a_1 = \Delta a_2$ at $J_1 = J_2$. Ernst [15] has discussed the circumstances where the fracture behavior of two different specimens (proportionally sized but with different absolute dimensions) can be scaled otherwise. For example, if the behavior has become proportional crack growth (PCG), then is characterized by

$$\left(\frac{J}{W}\right)_1 = \left(\frac{J}{W}\right)_2 \quad \text{at} \quad \left(\frac{\Delta a}{W}\right)_1 = \left(\frac{\Delta a}{W}\right)_2 \quad (10)$$

This behavior is represented by a constant slope of the JR curve (figure 2a) and is not scaled properly for fracture mechanics. The current validity limit analysis has considered the constant slope of $J_M R$. Some evidence was seen in the data of the presence of a constant $J_M R$ curve slope. As was seen in figure 2a, a linear region seemed to occur either before or after the inflection point. The earlier indication may be due to the approach of the inflection point.

INFLECTION POINT OF PLASTIC DISPLACEMENT-VS.-CRACK EXTENSION, SYMBOL "v"

In the course of fracture tests, the load, total displacement, and the unloading compliance are recorded (P , v , and C , respectively). From these, and the assumption that the displacement can be decomposed into linear (v_{el}) and nonlinear (v_{pl}) parts, the nonlinear displacement can be calculated, as follows:

$$v = v_{el} + v_{pl} \quad (11)$$

$$v_{el} = P \cdot C \quad (12)$$

$$v_{pl} = v - v_{el} = v - P \cdot C \quad (13)$$

Graphs of nondimensionalized plastic displacement versus crack extension were produced (figure 2b). The use of the inflection point of the v_{pl} -versus- Δa curve as a VL parameter was discussed by Ernst and Pollitz [15]. They used a point where v_{pl}/W had grown to five-percent above the amount inferred by linearly extrapolating from the inflection point using the slope at the inflection point.

MAXIMUM OF THE PRODUCT OF LOAD TIMES DISPLACEMENT, SYMBOLS "U_p" AND "U_T"

In general, an increment of external work comes from crack growth plus a change in strain energy:

$$Pdv = Jda + \Delta U \quad (14)$$

The terms in equation 14 can be decomposed into elastic and plastic components, and the plastic portion of the expression will be considered further. This plastic portion is written from equation 14 as:

$$Pdv_{pl} = dU_{nl} + BJ_{pl}da, \text{ with } dU_{nl} \geq 0 \quad (15)$$

If $dU_{nl} = 0$, the end of validity has been reached. This can be developed further to give a simple expression for U_{nl} by using a Ramberg-Osgood constitutive form:

$$J_{pl} = \frac{\eta}{bB} U_{nl} \Rightarrow U_{nl} = \frac{J_{pl} bB}{\eta} \quad (16)$$

$$U_{nl} = \int P dv_{pl} \propto \int v_{pl}^N dv_{pl} = \frac{v_{pl}^{N+1}}{N+1} \quad (17)$$

$$U_{nl} \propto \frac{P v_{pl}}{N+1} \quad (18)$$

Equation 17 comes by using $P \propto v_{pl}^N$. Looking at equations 15 and 18, a peak in load times plastic displacement is expected to signal a limit to fracture mechanics validity., i.e.,

$$\text{as } dU_{nl} \Rightarrow 0, \quad P \times v_{pl} \Rightarrow \text{constant} \quad (19)$$

As an alternative, the use of U_{tot} was substituted for U_{nl} . This was evaluated similarly:

$$\text{as } dU_{tot} \Rightarrow 0, \quad P \times v \Rightarrow \text{constant} \quad (20)$$

Since the theory was developed based on plasticity concepts, the use of U_{tot} may be debatable, but it has been considered, and some results discussed. The criterion shown in equation 19 is symbolized " U_p " while that in equation 20 is symbolized as " U_t ". The curves in figure 2c have been normalized to produce a stress-like quantity.

CONSTANT EFFECTIVE VOLUME, V_e

Plastic deformation is often assumed to occur at constant volume. This behavior might be applicable, given an appropriate volume, to indicate when the fracture processes have evolved to the point where fracture mechanics is no longer valid: if the change of volume goes to zero, then the fracture mechanics validity limit has been reached. An effective volume must be determined, and using the work functions or η -factors, an effective area can be defined, noting first that the η -factor arises from the assumption that the load can be separated into one function of crack length and one of plastic displacement:

$$P = g(a) \times F(v_{pl}) \quad (21)$$

$$\eta \equiv \frac{\partial P}{\partial b} \frac{b}{P} \quad (22)$$

In the case of CT specimens,

$$\eta = 2 + 0.522 \frac{b}{W} = \frac{\partial P}{\partial b} \frac{b}{P} \quad (23)$$

$$\frac{\partial P}{P} = \left(2 + 0.522 \frac{b}{W} \right) \frac{\partial b}{b} = \left(\frac{2}{b} + \frac{0.522}{W} \right) \partial b \quad (24)$$

Integrating the last equation produces a logarithmic form which can be rewritten as

$$P = C \times b^2 \exp\left(0.522 \frac{b}{W}\right) \quad (25)$$

Here, C is a constant of the integration with respect to b and can be a function of plastic displacement. Thus, C contains $F(v_{pl})$. By using the definition of stress, an effective area can be suggested:

$$A_{eff} = \frac{P}{\sigma} = \frac{C}{\sigma} \times b^2 \exp\left(0.522 \frac{b}{W}\right) \quad (26)$$

The quotient C/σ is associated with plasticity and the remaining part of equation 26 will provide the sole contribution to any changes in the effective area. From this, an effective volume for a CT specimen is written:

$$V_{eff,CT} = l_{eff} \times A_{eff} = v_{pl} \times b^2 \exp\left(0.522 \frac{b}{W}\right) \quad (27)$$

Since the effective area is written in association with the plastic portion of the load-line displacement, the appropriate length is assumed to be the plastic displacement. The effective volume criterion has been labelled " V_e " in figure 2d.

For a center-cracked tension specimen, the limit load is assumed to be the net cross-sectional area times the flow stress. This gives rise to a formula for the effective volume of a CCT specimen:

$$V_{eff,CCT} = v_{pl} \times Bb \quad (28)$$

RESULTS

If no clear evaluation of the VL parameter was obvious, then the questionable data were not included. Because of this the methods using inflection points, i.e., candidates i and v , provided fewer data. Two point and five point, unequal spacing formulae were used to estimate the derivative, dJ_M/da and $dv_{pl}/d\Delta a$, but the resulting plots possessed too much scatter and did not indicate the location of the inflection points as clearly as careful visual inspection.

Three methods, U_p , U_v , and V_e , were easily evaluated, since the maxima of the relatively smooth curves were obvious. Two means of comparing results were available: (1) crack extension at VL, and (2) J -modified at VL. In both cases, the values were normalized:

$$J_M: \Rightarrow \rho \equiv \frac{b_0 \sigma_0}{J_M} \quad (29)$$

$$\Delta a: \Rightarrow \frac{\Delta a}{b_o} \quad (30)$$

The first expression can be associated with the crack opening displacement. The second equation is the fraction of the initial ligament cracked to reach the limit. Both are similar to criteria used to define the J-integral validity limits. The results were more consistent with the $\Delta a/b_o$ -form, and the ρ -form results have been excluded, because they were redundant with those of the $\Delta a/b_o$ results. Certain trends were observed in either case. These trends differed somewhat between the two materials, AL6061-T651 and IN718-STA1. It is suggested that these differences were due to the different hardening characteristics of the two materials. The nickel exhibits some hardening behavior, while the aluminum acts rather like an elastic perfectly-plastic material, exhibiting little hardening.

LOCATION OF MAXIMUM LOAD ON JR- AND J_M R-CURVES

The datum at which the maximum load was reached in each test was recorded and this location appears to be associated with the imminent divergence of J and J_M , at a crack extension of approximately five-percent of the ligament length for both materials ($\Delta a/b_o = .05 \pm .018$).

DEPENDENCE OF VARIOUS CANDIDATES ON LIGAMENT DIMENSIONS

The values of $\Delta a/b_o$ associated with each of the parameters were plotted against ligament dimensions, B, b_o and B/b_o , and the following discussion presents these results. As new parameters are brought into the discussion, they are also compared to those introduced earlier.

For the aluminum and the nickel, the inflection point of the J_M R curve is approximately constant in the $\Delta a/b_o$ form. This is especially good for $b_o > 0.4$. It should be mentioned here that, though no dependence of the i-criterion upon ligament length is stated, $\Delta a/b_o$ implicitly includes a functionality with respect to b_o . Specimen #E0 (aluminum, CT, W = 1-inch, B = 1/2-inch, $a/W = 0.75$) has been shown as an exception to the well-defined trend. An alternate formulation for the aluminum i-criterion results arises and includes specimen #E0, suggesting that a linear relationship exists for $\Delta a/b_o$ -versus- B/b_o . This would provide a " $\Delta a/B = \text{constant}$ " functionality of the i-criterion for aluminum. Specimen #E0 is different than other CT specimens, being the only one with a ligament proportion ratio, B/b_o , greater than unity. Compact tension and center cracked tension specimens produce a different constant. No data were available to suggest the value for nickel CCT specimens. The results for the nickel appear constant. If the results from specimen #E0 are omitted, the suggested values for the i-criterion validity limits are:

$$\text{CT Specimens: } \left(\frac{\Delta a}{b_o} \right)_{AL,CT}^i \approx .35, \text{ and } \left(\frac{\Delta a}{b_o} \right)_{IN,CT}^i \approx .34 \quad (31)$$

$$\text{CCT Specimens: } \left(\frac{\Delta a}{b_o} \right)_{\text{AL,CCT}}^i \approx .11 \quad (32)$$

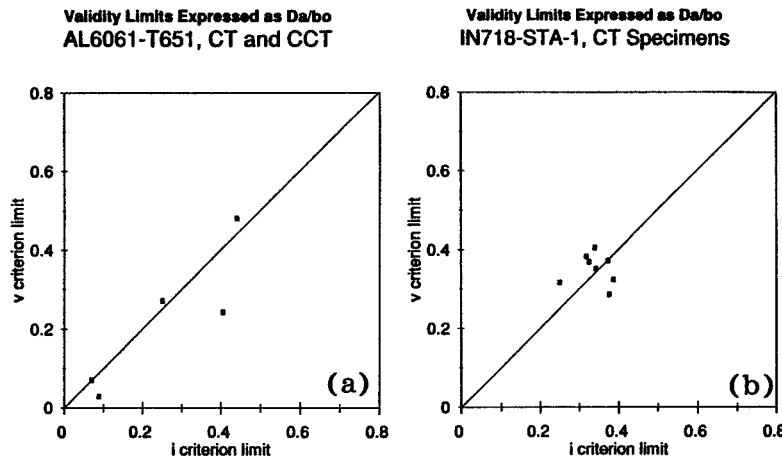


Figure 3: Comparison of inflection points of $J_M R$ curves and plastic displacement-versus-crack extension for (a) aluminum alloy and (b) nickel alloy.

The next parameter is the v -criterion, the inflection point of v_{pl} -versus- Δa . Parameter v appears to be constant. However, the results in the aluminum suggested that v *may* be a function of ligament length, b_o . Judging from a comparison of i and v in figure 3, i and v seem to give a one-to-one correspondence, and for the IN718-STA1, the results have a smaller range. The difference in range is suggested to be due to the different material properties and perhaps the selected range of the ligament dimensions in the nickel test matrix. The equivalence of i and v does seem reasonable.

The third and fourth criteria are U_p and U_t . U_p is not related to ligament length, b_o , but is a function of ligament thickness, B . Considering this functionality, and looking at figures 4a and 4b, no correspondence is obvious between U_p and i . A comparison between U_p and U_t appears in figures 4c and 4d. For AL6061-T651, U_t precedes U_p uniformly, and for IN718-STA1, U_t appears to be constant. Again, the lack of comparable results between the two materials must arise from differences in the material properties. No further conclusion will be drawn here, nor is one thought necessary, since U_t was included somewhat arbitrarily, as discussed earlier.

The last criterion is constant volume. V_c appears to be relatively constant for both aluminum and for nickel throughout the range of ligament dimensions and proportions investigated. None of the CCT specimens were tested to a point where a constant volume point was exhibited. For both materials,

$$\text{CT Specimens: } \left(\frac{\Delta a}{b_o} \right)_{\text{CT}}^{V_c} \approx .30 \quad (33)$$

Figures 5a and 5b show a comparison of V_c and i . For both materials, V_c and i seemed similar, although i ranges more widely for AL6061-T651. Two specimens, #E0 and #C8, possessing a ligament ratio of $B/b_o = 2$ are the notable exceptions to this. The exceptions associated with these two might be some early loss

of in-plane constraint not present with the other specimens or more simply due to ambiguity in determining i. Consideration of the Δa -shifting, mentioned earlier, will not substantially affect these findings.

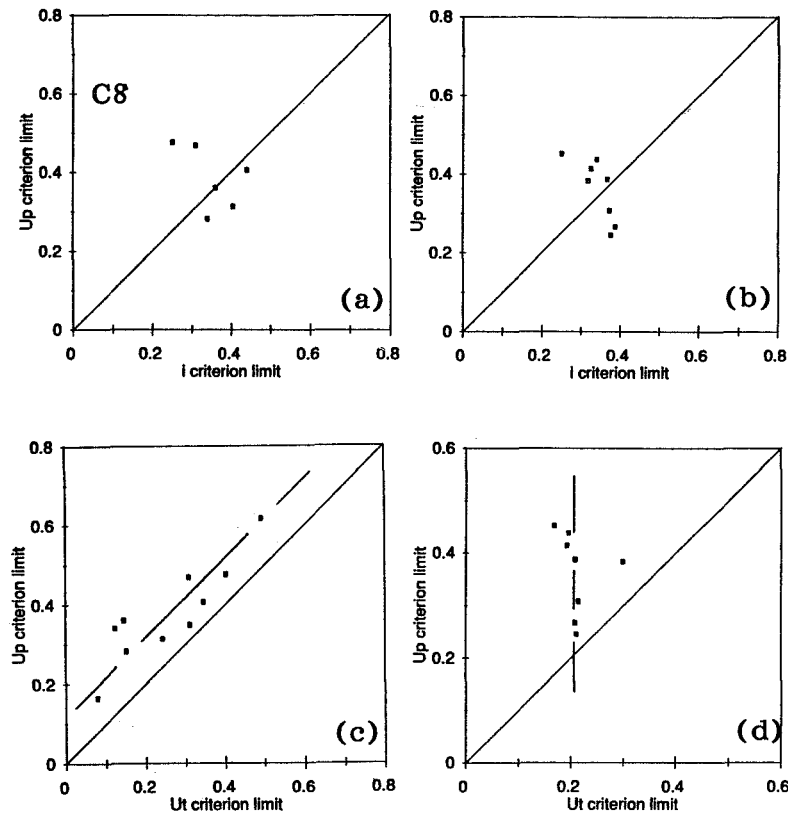


Figure 4: Comparison of load times plastic displacement criterion with inflection point of $J_M R$ curve for (a) aluminum alloy, and (b) nickel alloy, and comparison of load times plastic displacement with load times total displacement for (c) aluminum alloy, and (d) nickel alloy.

Looking at figures 5c and 5d, U_p and V_e are compared. These two criteria are very similar, but V_e precedes U_p by a significant amount. In figure 5c, one datum falls below the $U_p = V_e$ line (specimen #D6, aluminum, CCT, $2W = 2$ -inches, $B = 1/2$ -inch, $a/W = 0.5$).

DISCUSSION

The first observation to be made regarding all of the candidate validity limit parameters is that those parameters that pass through a maximum are the easiest to evaluate. These include U_p , U_t , V_e . The parameters that exhibit an inflection point are much harder to evaluate with confidence, and by taking derivatives that might provide an alternative formulation with a maximum, it was found that the experimental error was exaggerated to the point where the parameter was, again, difficult to evaluate with confidence. These parameters included i and v .

The effective volume, V_e , and the inflection point of the $J_M R$ curve, i , seem to be associated primarily with the ligament length. These criteria probably represent the saturation of the ligament: when V_e and i occur, the plasticity has grown enough to reach the back face of the specimen. The problems associated

with specimen #E0 seem to conflict with this conclusion; however, the inflection point of the $J_M R$ curve for specimen #E0 was difficult to determine positively. A second possible inflection point, in the vicinity of V_e , was identifiable in the figure. The lowest value was used in the analysis. The second, higher, value of $\Delta a/b_0$ was much better, but was still low compared to the other data.

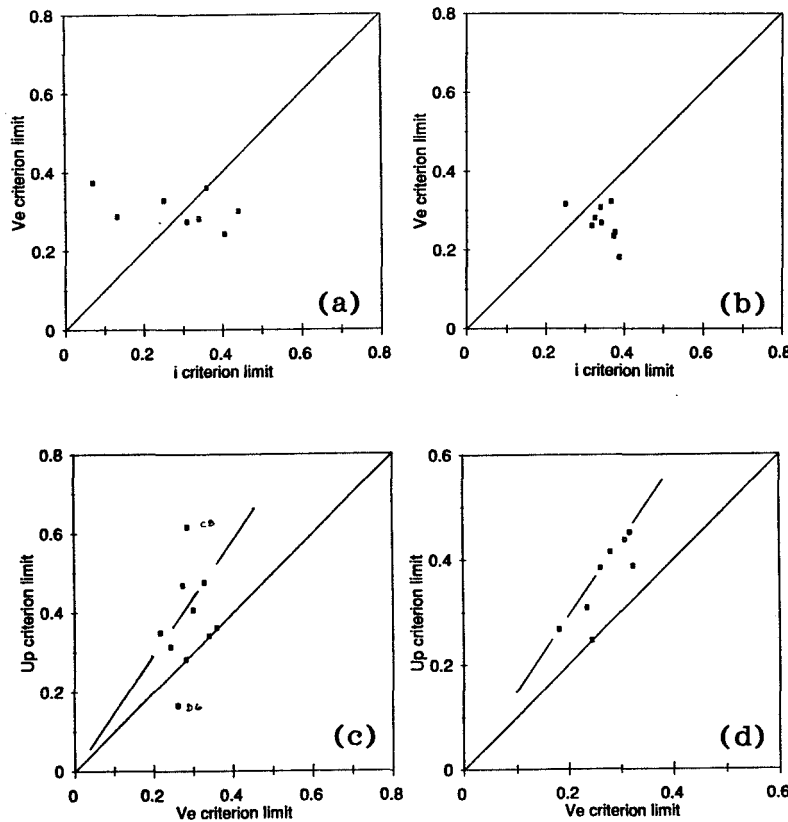


Figure 5: Comparison of effective volume criterion with inflection point of $J_M R$ curve for (a) aluminum alloy and (b) nickel alloy, and with load-times-plastic displacement for (c) aluminum alloy and (d) nickel alloy.

The observed maximum of the product of load-times-total displacement is a precursor to load-times-plastic displacement, and U_t is a conservative estimate of U_p . U_p appears to arise from both b_0 and B . The functional form of U_p is not clear from the data presented here, although one suggestion is that U_p signals some overall loss of constraint. Since the crack front shape is expected to develop up to some stable shape, U_p may represent the onset of that stable crack front shape for these low-hardening materials. V_e signals a loss of in-plane constraint, only.

The lack of conclusive data for the CCT specimens is unfortunate. Where available for the aluminum CCT specimens, the results *are* considered to be consistent with the discussion, above.

Looking at i , the inflection point of the $J_M R$ curve is manifested by almost all specimens in the matrix, and although the CCT specimens do not exhibit V_e , the loss of in-plane constraint is still evident in the $J_M R$ inflection. The difficulty of establishing i in all cases is a weakness, but the earlier development and discussion suggests that the inflection point of the $J_M R$ curve is an appropriate limit to use when employing fracture mechanics methodologies. It is suggested that for compact tension specimens, subjected to tensile loading plus a bending component, V_e be used to infer i . It appears to be equivalent when B/b_0 is no larger than unity, and it is much easier to evaluate.

As a result of these findings, the $J_M R$ curves were qualified by limiting the curve to that portion preceding the upwards inflection point. For a given bending-to-tension characteristic associated with a specific specimen configuration, this might be simplified to a maximum crack extension which is some percentage of the initial length of the ligament. This is expected to vary for materials of different hardening characteristics, but for the two materials used in this evaluation, the crack extension associated with V_e or i is, as follows:

$$\left(\frac{\Delta a}{b_o} \right)_{CT} \approx .30 \quad (34)$$

$$\left(\frac{\Delta a}{b_o} \right)_{CCT} \approx .10 \quad (35)$$

The $J_M R$ curves have been qualified, and the results appear in figures 6a and 6b.

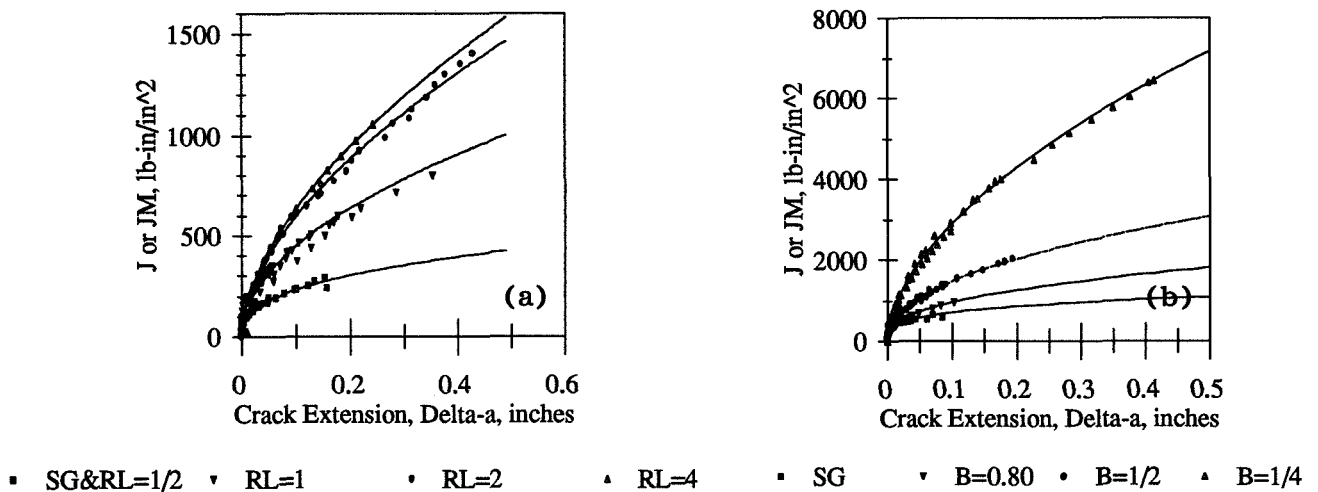


Figure 6: Results of application of inflection point of $J_M R$ curve as a validity limiting criterion, also showing results of the regression analysis of the qualified data (a) aluminum alloy, and (b) nickel alloy.

REFERENCES

1. Rice, J.R., "A Path Independent Integral and the Approximate Analysis of Strain Concentration by Notches and Cracks", *Journal of Applied Mechanics*, June 1968, pp. 379 - 86.
2. Rice, J.R., Drugan, W. J., and Sham, T.-L., "Elastic-Plastic Analysis of Growing Cracks", *Fracture Mechanics, 12th Conference, ASTM STP 700*, ASTM (1980), pp. 189 - 221.
3. Ernst, H.A., "Material Resistance and Instability Beyond J-Controlled Crack Growth", *ASTM STP 803*, Vol. 1 (1984), pp. I-191 - I-213.
4. Hutchinson, J.W., and Paris, P.C., "Stability Analysis of J-Controlled Crack Growth", *ASTM E803*, Vol.1 (1984), pp. 191-213.

5. ASTM E1152-87, "Standard Test Method for Determining JR-Curves", *1989 Annual Book of ASTM Standards*, Vol. 03.01 (1989), pp. 814-24.
6. ASTM E647-91, "Standard Test Method for Measurement of Fatigue Crack Growth Rates", *1992 Annual Book of ASTM Standards* (1992) Vol. 03.01.
7. Dugdale, D.S., "Yielding of Steel Sheets Containing Slits", *J. of Mechs. and Phys. of Solids*, Vol. 8 (1960), pp. 100-4.
8. McMeeking, R.M., and Parks, D.M., in *Elastic Plastic Fracture*, ASTM STP 668 (1979), pp. 175-94.
9. Shih, C.F., DeLorenzi, H.G., and Andrews, W.R., in *Elastic Plastic Fracture*, ASTM STP 668 (1979), pp. 65-120.
10. Ernst, H. A., "Material Resistance and Instability beyond J-Controlled Crack Growth", *ASTM STP 803*, American Society for Testing and Materials, 1983.
11. Ernst, H.A., "Further Developments on the Modified J-Integral", ASTM STP 995, (1989), pp. 306-19.
12. Ernst, H. A. and Pollitz, E. T., "Fracture Toughness from Surveillance Data", EPRI RP-2975-10, Final Report, March 1989.
13. Ernst, H. A. and Pollitz, E. T., "Methods to Characterize Crack Growth Under Elastic Plastic Conditions".
14. Ernst, H. A., "Study on the Deformation and Modified J-Integrals for Fracture Toughness Characterization" Final Report, ORNL RP-SB670-17, September 1988.
15. Ernst, H. A., "Recent Developments in Elastic Plastic Crack Growth Characterization", *Fracture Mechanics: 22nd Symposium*, ASTM 1131, Vol. I (1992), H.A. Ernst, A. Saxena, and D.L. McDowell, eds., pp. 136-157.

1995108057

N95-14481

CHALLENGES FOR THE AIRCRAFT STRUCTURAL INTEGRITY PROGRAM

John W. Lincoln
Aeronautical Systems Center
Wright-Patterson Air Force Base, Ohio

348666
528-05
28122
p-15

Thirty-six years ago the United States Air Force established the USAF Aircraft Structural Integrity Program (ASIP) because flight safety had been degraded by fatigue failures of operational aircraft. This initial program evolved, but has been stable since the issuance of MIL-STD-1530A in 1975. Today, the program faces new challenges because of a need to maintain aircraft longer in an environment of reduced funding levels. Also, there is increased pressure to reduce cost of the acquisition of new aircraft. It is the purpose of this paper to discuss the challenges for the ASIP and identify the changes in the program that will meet these challenges in the future.

INTRODUCTION

The modern era began for military aircraft in 1958 with the adoption of the USAF Aircraft Structural Integrity Program (ASIP). The ASIP defines all of the structurally related activities on an aircraft from initial development until retirement. Therefore, it is a program that is used in aircraft acquisition as well as for aging aircraft. The original objectives of the structural integrity program were to control structural failure of operational aircraft, determine methods of accurately predicting aircraft service life, and provide a design and test approach that will avoid structural fatigue problems in future weapon systems. These objectives still constitute the basis of the present ASIP. This program, however, was significantly changed as a result of the failure of an F-111 in 1969. This event ushered in the era of damage tolerance in the USAF. This change in approach prompted considerable research and development in area of fracture mechanics. In addition, since the damage tolerance approach forced the designer to better understand the stresses in the structure, emphasis was placed on the emerging finite element methods. These capabilities permitted the USAF to perform a damage tolerance assessment of all the major weapon systems in the inventory. This effort required over one million man-hours and every major manufacturer was involved with this activity. As a result of this activity, industry was able to develop the technology required for this type of analysis. This technology is also suitable for application to new aircraft developments. As a result, the USAF was able to include damage tolerance requirements in the specification for new aircraft procurement.

The original damage tolerance requirements for the USAF were derived during the assessments performed on the C-5A and the B-1A in 1971 and 1972. These requirements were derived for monolithic (i.e., slow crack growth) structures. The failure of an F-4 wing on 23 January 1973 in a structural location that was believed to be fail-safe demonstrated to the USAF that a structure could not be fail-safe without an inspection program. This failure strongly influenced the damage tolerance requirements as formally established first in MIL-A-83444 and subsequently in AFGS-87221A. The technology for the analysis of fail-safe designs has evolved slowly, primarily because of the need for extensive finite element programs supported by expensive test programs.

PAGE 408 INTENTIONALLY BLANK

PRECEDING PAGE BLANK NOT FILMED

ACQUISITION OF NEW AIRCRAFT

System acquisition programs in the U.S. Air Force typically go through a total of five phases. These are:

- Concept Exploration and Definition
- Demonstration/Validation
- Engineering and Manufacturing Development
- Production and Deployment
- Operations and Support

To be successful in the development of a new aircraft, the structural integrity effort must begin before the Engineering and Manufacturing Development phase of the program. In the USAF, the structural activity starts in earnest in the Wright Laboratories even before the Demonstration/Validation phase. However, it is normally the Demonstration/Validation phase that is particularly critical for the transition of structural technology from the laboratory to the aircraft. There are many examples of successful transitions of technology from the laboratory to full-scale development. Many of these successes were derived from a well-conceived plan or "road map" that formed the basis or criteria for technology transition. In general, these road maps have included programs directed at several levels of technology maturity. These levels are referred to as basic research, exploratory development, advanced development and manufacturing technology development. Most of the advanced development and manufacturing technology development program effort is directed towards the demonstration of the technology by means of the manufacture and testing of a specific piece of hardware.

A key element in the development of the road maps was a knowledge of the threats to structural integrity from the environment in which the structure must be able to perform its function. The understanding of these threats typically is derived from experiences with other materials. There are situations, however, where a new material may be sensitive to a threat that in the past has not been a major factor.

A study of those successful road maps for transition of technology to full-scale development reveals that they had certain factors in common. These factors may be combined to form a criterion for the transition process to be successful.

From a study of the successful transitions of structural technologies from the laboratory to full-scale development it was found that five factors constituted a common thread among these successes. Also, it was found that these five factors were essential to the successful completion of the tasks of the United States Air Force Structural Integrity Program (ASIP). These five factors are:

- Stabilized material and/or material processes
- Producibility
- Characterized mechanical properties

Predictability of structural performance

Supportability

In this listing there was no attempt to establish a ranking of importance of these factors. A deficiency in any one of the factors could constitute a fatal defect. A description of each of these five factors involved in the transition of structural technologies to full-scale development is given in Reference 1.

The current version of the ASIP includes five separate tasks that cover all aspects of the development and support of an aircraft structure. These tasks, some of which are shown in Figure 1, are identified as follows:

- I. Design Information**
- II. Design Analyses and Development Tests**
- III. Full-Scale Testing**
- IV. Force Management Data Package**
- V. Force Management**

Within Task I (Design Information), there is an element called "Damage Tolerance and Durability Control Plans." The damage tolerance control plans have proved to be effective for inspection, tracking, and control of fracture critical parts. However, it has been found that emphasis is needed to ensure that process controls are developed to enhance the durability of the structure. Further, emphasis is needed to ensure that strength critical structure (that is, buckling critical) has the proper controls to maintain dimensional requirements.

It is planned to enlarge the scope of the durability control plans to require trade studies on the use of process controls to determine the economic benefits of their use. This should identify what parts over which it is important to exercise process controls. Further, there will be an emphasis on the identification of acceptable tolerances on structure that is strength critical. This will be based on analyses and the results of component tests to ensure that the processes (including drawings, etc.) are able to produce the structure to the desired tolerances.

Another important element of Task I is "Selection of Materials, Processes, and Joining Systems." A key aspect of this element is selection of the corrosion protection system. The corrosion problem is now becoming more acute in that the environmental protection laws have eliminated the use of some of the standard corrosion inhibitors. Current and proposed regulations eliminate volatile organic compounds, chromates, and carcinogens. New environmentally safe methods are needed for corrosion inhibitors, paints, and paint stripping processes.

The "Design Service Life and Design Usage" element of Task I is heavily influenced by weight changes of the aircraft. Weight control and reduction are almost guaranteed to be a major part of any acquisition program. History has shown that contractor weight estimates are typically optimistic. Also, for new aircraft the weight is not predictable from existing

parametrics. There have been major errors in the prediction of the weight of propulsion and some other subsystem weights. Another problem is that the weight used for the design of the aircraft is the proposal weight rather than the weight that is expected when the aircraft has reached the point of initial operational capability (IOC). It has been determined that weight growth has typically been eight percent through the EMD phase of development. It has also been found that prototyping does not reduce the weight growth in EMD. The weight savings associated with contractor weight reduction programs are typically excessively optimistic. Also, new technology and specification changes have only had a moderated impact on weight growth. Further, the center of gravity control has been historically inconsistent.

The use of IOC weight for the design process would eliminate many of the problems with weight growth. Further, early involvement of weight engineers would also provide the oversight necessary to perform realistic estimates. Another initiative is to emphasize to program managers that weight control is expensive and appropriate funding should be established.

In Task II there is an element called "Loads Analysis" and an element called "Stress Analysis," both of which have caused considerable problems because of the tremendous leverage they have in influencing the outcome of the damage tolerance analysis. It has been found, in fact, that errors in the external loads have significantly impacted the life of aircraft structures. In addition, the load and control system gain changes during EMD have led to cost and schedule problems. In spite of all the buffet problems experienced on the F-15 and F-18, the technology to accurately predict buffet loads is not available. With regard to internal loads, it has been found that there have been significant differences in the quality of finite element analyses. The complex internal load distributions found in the F-16 were extremely difficult to simulate with current technology. Also, the state of the art for the determination of the thermal environment and the induced loads from that environment are far from adequate.

It will likely remain difficult to attain the desired level of accuracy of the external loads. The use of computational fluid mechanics should be emphasized for both steady state and buffet loads in an attempt to improve accuracy and reduce the cost of wind tunnel testing programs. There should be a program management initiative to develop a strategy for obtaining an early freeze on both the configuration and control laws in EMD. The use of flight load surveys that are more comprehensive should be a program goal. A deficient flight loads survey was conducted on the A-7D. This led to ignorance about buffet loads on the wings being a factor in the degradation of its life until the aircraft were nearing retirement. The guidance in AFGS-87221A will be expanded for the purpose of using an experimental approach for validation of the internal loads in major component tests.

The "Design Service Loads Spectra" is another difficult area of Task III. Historically, the usage for a new aircraft has been derived from usage data collected from existing operational aircraft. In many cases, such as the F-16, this approach has been found to be very unconservative. For this aircraft, the air-to-ground operation was considerably different than that derived from an aircraft such as the F-4, for example. The maneuver freedom that is

given the pilot by the angle of attack limiter on the F-16 was believed to be a major factor in this radical change.

Simulators have matured to the point that they are able to augment our understanding of the usage for a new aircraft. The use of these devices should be included in the demonstration/validation phase of acquisition for this purpose. Load limiters should be installed on low g aircraft such as bombers and transport aircraft. The B-1 operational experience indicates that there are frequent exceedances of limit load factor. Also, on the B-1, it was found that the design fuel reserves were considerably higher than that being experienced in operational flying. Efforts should be made to work with the using command early in the design program to establish realistic fuel reserves. As indicated above, a significant benefit would be derived if aircraft were designed to IOC weights. The eight percent weight increase that has been observed up to IOC translates into approximately a forty percent loss in structural life. As part of the design process, trade studies will be performed to assess the cost and schedule impact of incorporating a life margin in the design. Certainly, the past experience of the Air Force indicates that an additional life margin is warranted.

In Task III of ASIP the major full-scale testing is accomplished. In static testing, it has been found that stability failures are, by far, the most predominant mode of failure. Current design practice and the pressure for weight savings have introduced unacceptable risk of failure in full-scale testing. Further design development testing, which is one of the most important elements of Task II, has been inadequate because of funding constraints. The ideal analytical method for assessment of stability critical structure would be the nonlinear finite element analysis. However, the state of the art of these analyses is not adequate at this time. In many cases there is still an uncertainty of ten to fifteen percent in the ability to calculate the true failure load. Clearly, the economic consequences of premature failure in static test are unacceptable.

There will be an increased emphasis on design development testing to help eliminate premature failures in full-scale static testing. The guidance for this will be placed in AFGS-87221A. There will be developed a set of "best practice" rules for each type of aircraft (i.e., fighters, bombers, transports). There will need to be trade studies performed for structure that is expected to buckle below limit load to ensure that there is an economic benefit from the use of such practice. The structure should be sized by analysis to withstand 160 percent of design limit load to enhance the ability of reaching 150 percent of design limit load in test.

It has long been recognized that early testing of the full-scale structure was important. Although the early airframes are generally not completely representative of the final configurations, it is essential to get early information on deficiencies so they can be corrected in production. The C-5A program is an example where both the static and fatigue tests were performed after a significant number of production aircraft had been produced. Both of these tests resulted in serious failures that occurred significantly short of the design requirements. Because of the lateness of the tests, no changes were incorporated in any of the production aircraft. As a result, the aircraft had to operate under severe restriction until

the entire fleet could be retrofitted with new wings. This, of course, was a major expense to the government.

As indicated in Reference 2, a precept of the damage tolerance approach is the safety of the aircraft and its economic operation should be independently proven. The damage tolerance analysis, supported by testing, was the basis for safe operations and the full-scale durability test was the basis for establishing the economic burden associated with service usage. The damage tolerance analysis, supported by testing, has been effective in identifying areas of the aircraft that could potentially cause a safety problem. It is desirable, however, to ensure they have been identified through the full-scale durability test. The spectrum used by the USAF for both the damage tolerance and durability analyses and testing is the expected average usage. MIL-A-8867B(USAF) (Reference 3), which was released 22 August 1975, stated the full scale durability test should be run for a minimum of two lifetimes unless the economic life was reached prior to two lifetimes. The economic life of a structural component is reached when that component is more economic to replace than repair. The economic life of a component is extremely difficult to determine analytically. It may be, however, demonstrated in durability testing. The same guidance that was given in MIL-A-8867B(USAF) was given later in AFGS-87221A (Reference 4). There was no guidance given, however, on the rationale for a need for testing for more than two lifetimes. Consequently, it has been a program decision to test every aircraft for two lifetimes since 1975. All the known service experience demonstrates that an aircraft, after successfully passing a two lifetime flight-by-flight durability test, will not reach its economic life in one lifetime of service usage representative of the test spectrum. There is a question, however, whether a full-scale durability test that simulates two lifetimes of planned operational usage will adequately interrogate the structure to determine all the areas in all aircraft that could potentially cause a safety problem.

A procedure is described in Reference 5 that is believed to be useful for establishing the duration and/or the severity of testing that should be performed in a full-scale durability test to ensure that all of the significant regions of the structure have been identified. It is based primarily on data that could be derived from the existing analyses and development testing. An example problem discussed in Reference 5 indicates that the length of testing required using an average spectrum may be uneconomical. However, it appears practical to increase the severity of the spectrum to provide for an adequate test and to complete the test in a timely manner.

The procedure also provides a basis for the success of the test. During or at the end of the full-scale durability test, a crack may be found that initially appears to be significant. This would not automatically indicate that the structure has failed to pass the test. It would, however, indicate additional investigation should be undertaken. A fractographic examination should be conducted to determine if the crack growth was faster than predicted. If it was found to be faster than predicted based on the earlier analyses and tests, then an investigation should be conducted to determine the local stresses and the fracture data (crack growth rate) for the material used in the full-scale test article. An assessment should also be made to determine the implication on the damage tolerance derived inspection program.

After a study of all available information, a judgment is then made on the need for aircraft modification or additional inspections to maintain economic and safe operational aircraft.

It is often found that a region or part of the aircraft needs to be redesigned based on failure in the durability test. There may be occasions where the redesigned part is obviously robust enough such that additional testing is not required. However, in general, the redesign should be subjected to the same rigors of testing as the original airframe. This can often be accomplished with a component test. However, there are some cases where this is not practical. This retesting generally results in significant costs that were not part of the original funding. The prospect of retesting the aircraft should be adequate motivation to take the necessary precautions to ensure that the risk is low at the start of testing.

One of the critical elements of Task IV is the development of the Force Structural Maintenance Plan (FSMP). This plan tells the maintainer of the aircraft how, when and where the aircraft are to be inspected and/or modified as they proceed through their operational lives. For new aircraft, the guidance in Reference 4 is to establish the stresses such that no inspections are mandatory to provide flight safety. This means that the stresses are established such that there are two lifetimes of slow crack growth capability from the damage tolerance initial flaw to critical crack length. However, an inspection should be developed that could be used in the case of usage severity or mass increases. For most military aircraft, experience has shown that there is a considerable difference in usage severity among the individual aircraft. The accounting for the actual usage of the aircraft is determined by the individual aircraft tracking program and the loads/environment spectra survey. These two elements work together to obtain an estimate of the stress spectra for a number of control points in the structure. For aircraft that are designed according to the damage tolerance philosophy, the generated stress spectrum is used to determine the time at which the damage tolerance initial flaws would grow to critical. This time is divided by a factor of two to determine the number of flight hours that the inspection should be performed. For aircraft that are operated under a safe life approach, the tracking program is used to determine, for the various tracking control points, the life expended relative to the fatigue test demonstrated life. Another important element of Task IV is the "Strength Summary." It is this report that provides the important structural characteristics, limitations, and capabilities in terms of operational parameters. The durability, damage tolerance, and static test results coupled with the results of instrumented ground and flight testing provide the basis for this document.

It is noted that the contractor typically performs the elements of Task IV of ASIP and the Air Force normally performs the elements of Task V. However, there is a growing trend to obtain contractor assistance in the performance of Task V. It is Task V, which continues until the aircraft is retired where the effects of aging of the aircraft can emerge and incur a significant additional maintenance burden.

AGING AIRCRAFT

As indicated above, two of the main products of the ASIP process are to develop strength summary and operating restrictions report and to develop the force structural maintenance

plan. If there is a need to change either of these documents because of flight beyond design usage that could introduce new critical areas, corrosion, widespread fatigue damage, or repairs, then the aircraft is said to be aging.

Experience with operational aircraft has revealed they are typically not flown to the loading spectrum for which they were designed. Data from flight load recorders have shown, in general, that there are considerable differences in usage severity among aircraft with the same designation. Further, it is often found the average aircraft usage is more severe than originally perceived early in the design process. This problem is aggravated by the fact the damage tolerance analysis may have not identified an area that would be a concern if the aircraft usage was more severe than that assumed for design. Also, experience has shown the mass of an aircraft increases as a result of additional equipment or modification after an aircraft enters operational service. In addition, there are differences because (1) pilot technique changes as they become more familiar with the aircraft, and (2) mission changes because of new weapons and tactics. The aircraft-to-aircraft variability comes from several sources such as base to base variations in distance to test ranges and training. These experiences tend to degrade the capability of the full-scale durability test that consisted of two lifetimes of average usage to identify all the areas of the aircraft that could potentially cause a safety problem. Consequently, the structural engineer should, based on historical evidence, make some allowances for increased usage severity occurring as a result of mission severity changes and aircraft to aircraft variations in operational usage. To ensure aircraft durability, this should be done both in the design of the aircraft and in the test. The historical evidence of usage differences derived from changes in pilot technique and mission changes is generally not easily translatable to new designs.

The study reported in Reference 6 found that corrosion damage to USAF aging aircraft causes the most significant cost burden of any structurally related item. In this study, funded by Warner Robins Air Logistics Center, the researchers found that the costs of corrosion to the Air Force could be conservatively estimated at \$700 million per year. This is the largest maintenance cost of any structurally related item. In many cases the materials that were used in these aircraft were driven by the need for improved performance and little attention was given to the potential for corrosion and stress corrosion cracking damage. Further, when many of these aircraft were built, the focus on corrosion protection was not what it is today. Many of these early corrosion protection systems have broken down. In the open areas these can be readily renewed. There is, however, no easy way to renew the corrosion protection system in the joints. Experience with remanufacturing of aging aircraft has revealed that joints that were not properly protected experience significant damage that results in costly modifications.

It was indicated above that the corrosion problem is now becoming more acute in that the environmental protection laws have eliminated the use of some of the standard corrosion inhibitors. Another issue is that the nondestructive evaluation techniques are marginal. The standards for corrosion damage are, at best, poorly defined such that characterization of damage found is not well understood. Further, the predictive capability for corrosion is basically nonexistent. This deficiency creates a real problem in the future years cost prediction for structural maintenance.

One initiative that is believed to be needed is the establishment of an advisory council from the Army, Navy, Air Force, FAA, and NASA to provide guidance on programs relating to corrosion. This could provide the impetus to perform the necessary research and development and develop the standards needed. Emphasis must be placed on providing the tools for nondestructive evaluation for corrosion in hidden areas of the structure. There is a need to enforce the policy in the Air Force that corrosion damage will be fixed and not allowed to jeopardize safe and economical operation. In addition, there is a need to emphasize the need for the development of new corrosion protection systems that are environmentally safe.

The USAF has undertaken a teardown of a KC-135 taken from service for the purpose of assessing the extent of corrosion on these aircraft. The USAF owns approximately 700 of these tanker aircraft and they are considered a national asset. It is essential that they remain in the inventory well into the next century. Another goal of the program is to evaluate the potential of nondestructive evaluation to detect hidden corrosion in the joints of the aircraft. However, the main virtue of the program is that it has established the areas where corrosion is a problem. If these areas are not given the proper maintenance action to correct these problems, then the situation will only get worse and incur additional cost. It is essential that a program be initiated now to correct this problem rather than waiting for the crisis that is sure to occur.

For some of the older USAF aircraft that were not designed to the modern damage tolerance requirements as detailed in Reference 7, there is a potential for cracking to be so widespread in the structure that the application of the deterministic damage tolerance process may not protect the safety of these aircraft. This situation could exist in monolithic structures. This, in fact, did happen on the T-38 trainer aircraft. The analysis associated with the T-38 risk assessment that was made to treat this problem is described in Reference 8. However, the primary concern is with structures that were initially designed to be fail safe. For these structures, the occurrence of widespread fatigue damage can significantly degrade the fail safety of the structure. This has been experienced on the KC-135, C-5A and the C-141 aircraft. The KC-135 and C-5A experiences are discussed in Reference 7. These aircraft were subjected to teardown inspections and the results of these inspections were incorporated in a risk assessment to quantify the time when the probability of failure, conditioned by the fact there had been discrete source damage, become unacceptable.

In the case of the C-5A, it was judged that fail safety had been compromised if the conditional failure probability on a single flight was greater than 10^{-4} . For that aircraft, the critical area of the wing was the inner wing surface that was constructed with individual panels that incorporated integral stringers. For this location, it was believed that the threat was a loss of a wing panel from engine disintegration or from battle damage. For a given aircraft, it is necessary that the conditional failure probability and the threat be determined for each area. For example, for areas that are in the path of failed engine parts, the penetrations of these parts would be the threat. The likelihood of occurrence may be determined from the available statistics on in-flight engine failures. In other parts of the aircraft, an evaluation must be made for the possibility of other threats, such as accidental

damage from manufacturing, maintenance, or ground handling. The threat assessments must be made to ensure that the probability of catastrophic failure is maintained within an acceptable bound. For the USAF, the acceptable bound is a catastrophic failure probability of 10^{-7} . In the case of the C-5A, the time at which the joint probability of discrete source damage and fatigue cracking exceeded 10^{-7} was less than the time at which fatigue cracking alone of the intact structure exceeded 10^{-7} . However, in some cases, the threat of fatigue cracking may be the dominant threat. This was found to be the case for the C-141 inner to outer wing splice as demonstrated by Lockheed in their work documented in Reference 9. In this case, the problem was the progressive failure of the structure because of fatigue cracking. For any structure, both the external source damage case and the intact structure case should be examined.

The USAF recognized the need for additional work in the area of risk assessment technology for maintaining safety of operational aircraft. Consequently, the Wright Laboratories sponsored a program in this area. The results of this program are documented in Reference 10. In this effort, the University of Dayton Research Institute developed the computer program PROF (PRObability Of Fracture). The program may be used to evaluate maintenance costs in addition to safety.

One of the primary inputs to the risk assessment approach to determine the onset of the time to widespread fatigue damage is the distribution of cracks in the structure. Teardown inspection of full-scale fatigue test articles or operational aircraft is believed to be the best method currently available to obtain the data required to derive the probability distribution function for equivalent initial cracks in each of the critical areas of the structure. The word "critical" here refers to an area that could significantly contribute to the probability of failure.

The Wright Laboratories has sponsored considerable research effort in the determination of initial crack distributions in aircraft structures. Much of this effort was concentrated on the interpretation of the cracks found in the teardown inspection of the F-16 wing after the durability test had been performed. This program is reported in Reference 11.

The probabilistic approach also requires the stress density function for each critical area be determined. The data from which the stress density function can be derived are available through the usage information that is generated by the individual aircraft tracking programs that is part of ASIP for USAF aircraft. The desired stress density function is the one for a single flight of an aircraft selected at random. This may be easily derived from the stress exceedance function that is developed as a part of the deterministic damage tolerance analysis. The joint probability distribution of cracks and stress is computed and integrated over the point set where the crack size has reached critical length. The result of this calculation is the single flight probability of failure. The time at which the probability of failure is unacceptable is the onset of widespread fatigue damage.

The damage scenarios in an airplane that could constitute widespread fatigue damage differ depending on location in the aircraft. However, typically, they fall into two categories. The first of these is multiple site damage that is characterized by cracks in multiple details in the

same structural element. The second is multiple element damage where there are cracks in multiple structural elements. For the case of fail safe structures, the emphasis must be placed on the influence of elevated stresses as a result of discrete source damage. These elevated stresses have been shown by test data and analyses to significantly lower the crack size at which the structure will fail by rapid fracture. If these failures cannot be arrested, then the aircraft will fail catastrophically. Each of the potential failure scenarios must be evaluated to ensure that they will not lead to total structural failure.

The previous efforts on this type of analysis have shown that it can readily be applied to the structures where the concern is multiple element damage. This was the case, for example, for the KC-135 and the C-5A. The application of the risk assessment technology to the case of multiple site damage is very much the same as it is for the case of multiple element damage. In the case of multiple site damage there will typically be a "boundary" that will determine if the cracking has the potential to become catastrophic. For example in the case of the fuselage lap splice, the boundary would be the crack stopper built into the structure at the frame or between the frames and its surrounding structure. This crack arrest feature protects the integrity of the structure. The condition of the crack stopper and its surrounding structure (i.e., the boundary) will determine if the damage could propagate to catastrophic failure. Therefore, the interest is primarily in the degradation of the boundary with time and not the growth of the holes in the lap splice to link-up. When the problem is thought of in this manner, it may be treated similarly to the multiple element damage problem. An example of this was demonstrated by Lockheed in their work documented in Reference 9 on the risk assessment of the inner to outer wing joint of the C-141 aircraft.

There must be an emphasis placed on the detection, through nondestructive evaluation, of cracks that could be significant for determination of the onset of widespread fatigue damage. As indicated above, there is a need to make an estimate of this onset based on probabilistic assessment of cracking data derived from the teardown inspection of fatigue test articles or operational aircraft. It must be recognized, however, that this is only an estimate. It is not realistic to expect that this time could be determined with great accuracy even with the most sophisticated fracture mechanics programs. The actual time may be either somewhat earlier or later than this estimate. It is important, therefore, to be able to validate this prediction with nondestructive evaluation. This task is made difficult by the fact that the size of defect to be found is quite small. The experimental evidence to date indicates that cracks of the order of two millimeters can significantly lower the fail safety capability of certain structural configurations.

Traditionally, the repairs placed on aircraft have been designed based only on static strength considerations. On some of the aging aircraft, however, the USAF has funded the effort for the original equipment manufacturer to design the standard repairs to be damage tolerant. This effort was a logical activity subsequent to the damage tolerance assessments that were made for the intact structure. There is a need to reevaluate these repairs in light of the emerging capability for composite repairs of metallic structure. There are numerous applications currently of composite repairs in the USAF, in addition to the applications in Australia and Canada. The applications made by the original equipment manufacturer include the C-130, C-141, KC-135, and the B-1. The success of these applications has

motivated the USAF to spend the resources to fully exploit this technology. A significant program in composite repair technology has been completed by the Wright Laboratories Materials Directorate. This program provides the technology for routine repairs using composite materials. The procedures have been established for successfully preparing the surface for the bonding operation. It has been found that the additional technician training required for making the patches is very little. Also, the technology requirements for the design of the patch are not demanding. This technology is being used in a specific application on the F-16. However, by far, the most significant accomplishment in the application of the composite patches has been the patching of the weep hole cracks in the lower surface of the C-141 lower inner wing surface. This problem forced the grounding of almost all of the aircraft. This effort was able to restore the structural integrity of that wing with minimum interference to the using command. The weep hole cracking problem on the C-141 is discussed in some depth in Reference 12.

Another problem is the constraints placed on the ASIP managers by program management. Program management faces pressures of schedule and cost that does not always permit adequate attention to integrity concerns such as corrosion control. Also, these ASIP managers are so burdened with detail maintenance problems they have little time to devote to the consideration of broader issues for their aircraft. An example of a broader issue is the determination of when to expect the onset of widespread fatigue damage such as that revealed in the inner to outer wing joint of the C-141. Another example is the unanticipated cracking in the A-7D wings that led to a structural failure in December of 1988. Still another example is the identification of nondestructive inspection capability that will enable them to inspect more accurately and economically in the future.

A particularly difficult problem for the ASIP is the procurement of aging off-the-shelf aircraft. In the marketplace there are many used aircraft that could be purchased far below the price of a new off-the-shelf aircraft. The reasons for the low price on these aircraft are that they have overflown their design service life, they have corrosion problems, they have widespread fatigue problems, and they have numerous repairs, many of which are not damage tolerant. That is, they generally possess all of the ingredients, identified and discussed above, to be classified as an aging aircraft. Unfortunately, many of these problems can be hidden from view and the aircraft appear to be airworthy. Experience has shown that significant problems do exist and the cost of refurbishing these aircraft is considerably above original expectations.

Another problem with off-the-shelf aircraft is the lack of external and internal loads information. This has, of course, been a chronic problem in the commercial world because of the need to have an understanding of the loads to make repairs that are damage tolerant. Since, in most cases, the original equipment manufacturer has not seen the benefit of releasing loads information, a loads research program is needed to establish the methodology to accomplish the task of providing this information.

Many of the aging military aircraft problems find an exact parallel in aging commercial aircraft. It is prudent, therefore, that these problems be worked through the combined talents

and resources of the Air Force, FAA and NASA. Efforts to date indicate that this approach will be successful and most efficient in solving these complex problems.

CONCLUSIONS

The ASIP is a process that has enabled the safe and economic operation of military aircraft. As an indicator of this success, the failure rate for all systems designed to and/or maintained to the current policy is one aircraft lost due to structural reasons in more than ten million flight hours. This is significantly less than the overall aircraft loss rate from all causes by two orders of magnitude. This success, however, should not be used to indicate that there is no need for continued vigilance in the treatment of aircraft structural problems. The success of the program has, in fact, made it more difficult to obtain funding for research and development in the structural area. It has also, at times, given program managers a false sense about the remoteness of structural failures.

One of the major problems found in operations with aging aircraft is the cost associated with corrosion damage. Unfortunately, the progress made in the recent past in the control of this problem does not bode well for the future. This is especially true when one considers the impact of new environmental laws that remove many of the corrosion fighting chemicals that are currently used. Continued emphasis in research in the area of corrosion control is certainly one area that could have significant benefit.

Another major problem is widespread fatigue damage in primary structural elements. There will be costs incurred to establish an estimate of the time of onset of this problem. This will need to be done through the analysis of data derived from teardown inspections of fatigue test articles and/or of operational aircraft. These estimates will need to be corroborated through the use of detail inspections of suspect structural elements. Once this onset time has been reached, then there will be costs incurred by the modification of the aircraft to remove this problem.

The severity of both of these problems is made worse today because of a lack of adequate nondestructive evaluation techniques to look for corrosion damage in structural joints and to find the small cracks that would be the indicator of the onset of widespread fatigue damage. It appears that the current efforts in research in nondestructive evaluation will produce the technology for these problems. It remains to be seen if there is an economic motivation to transition this technology from the laboratory to inspections of operational aircraft.

The Air Force will have increasing pressure to buy aircraft that have been certified by an agency outside of the Air Force. It is the intent to judge these aircraft based on the content of the ASIP. As has been done in the past, aircraft procured in this manner will be assessed based on requirements under which they were certified, how well their design missions meet the Air Force requirements and the extent of their service experience. Additional structural testing and analysis will only be done where needed.

REFERENCES

1. Lincoln, J.W., "Structural Technology Transition to New Aircraft," Proceeding of the 14th Symposium of the International Committee on Aeronautical Fatigue," Ottawa, Ontario, Canada, 1987.
2. Lincoln, J.W., "Damage Tolerance - USAF Experience," Proceeding of the 13th Symposium of the International Committee on Aeronautical Fatigue," Pisa, Italy, 1985.
3. Department of the Air Force, "Airplane Strength and Rigidity Ground Tests," Military Specification MIL-A-008867B(USAF), 1975.
4. Department of the Air Force, "Air Force Guide Specification, Aircraft Structures, General Specification for," AFGS-87221A, 1990.
5. Lincoln, J.W., "Assessment of Structural Reliability Derived from Durability Testing," Proceeding of the 17th Symposium of the International Committee on Aeronautical Fatigue," Stockholm, Sweden, 1993.
6. Cooke, Garth E., et al, "A Study to Determine the Annual Direct Cost of Corrosion Maintenance for Weapon Systems and Equipment in the United States Air Force," Final Report on Contract #F09603-89-C-3016, WR-ALC/CNC, Robins AFB, GA.
7. Lincoln, J.W., "Risk Assessments-USAF Experience," Proceeding of the International Workshop on Structural Integrity of Aging Airplanes, Atlanta, GA, March 31 - 2 April 1992.
8. Lincoln, J.W., "Risk Assessment of an Aging Military Aircraft," *Journal of Aircraft*, Volume 22, Number 8, 1985.
9. Alford, R.E., Bell, R.P., Cochran, J.B., and Hammond, D.O., "C-141 W.S. 405 Risk Assessment," Proceedings of the 1991 U.S. Air Force Structural Integrity Conference, WL-TR-92-4045, July 1992.
10. Berens, A.P., Hovey, P.W., and Skinn, D.A., "Risk Analysis for Aging Aircraft Fleets," WL-TR-91-3066, Wright Laboratory, Wright-Patterson AFB, OH, October 1991.
11. Manning, S.D., and Yang, J.N., "Advanced Durability Analysis," Vol 1-5, AFWAL-TR-86-3017, Flight Dynamics Laboratory, Wright-Patterson AFB, OH July 1988.
12. Lincoln, J.W., "Considerations in the Service Life Extension Program for the C-141 Aircraft," Presented at the International Pacific Air & Space Technology Conference, Singapore, 14-18 February 1994.

TASK I	TASK II	TASK III	TASK IV	TASK V
DESIGN INFORMATION	DESIGN ANALYSES AND DEVELOPMENT TESTS	FULL SCALE TESTING	FORCE MANAGEMENT DATA PACKAGE	FORCE MANAGEMENT
ASIP MASTER PLAN — STRUCTURAL DESIGN CRITERIA — DAMAGE TOLERANCE & DURABILITY CONTROL PLANS — SELECTION OF MAT'L'S, PROCESSES & JOINING METHODS — DESIGN SERVICE LIFE AND DESIGN USAGE	MATERIALS AND JOINT ALLOWABLES — LOADS ANALYSIS — DESIGN SERVICE LOADS SPECTRA — DESIGN CHEMICAL/ THERMAL ENVIRONMENT SPECTRA — STRESS ANALYSIS — DAMAGE TOLERANCE ANALYSIS — DURABILITY ANALYSIS — SONIC ANALYSIS — VIBRATION ANALYSIS — FLUTTER ANALYSIS — NUCLEAR WEAPONS EFFECTS ANALYSIS — NON-NUCLEAR WEAPONS EFFECTS ANALYSIS — DESIGN DEVELOPMENT TESTS	STATIC TESTS — DURABILITY TESTS — DAMAGE TOLERANCE TESTS — FLIGHT & GROUND OPERATIONS TESTS — SONIC TESTS — FLIGHT VIBRATION TESTS — FLUTTER TESTS — INTERPRETATION & EVALUATION OF TEST RESULTS	FINAL ANALYSES — STRENGTH SUMMARY — FORCE STRUCTURAL MAINTENANCE PLAN — LOADS/ENVIRONMENT SPECTRA SURVEY — INDIVIDUAL AIRPLANE TRACKING PROGRAM	LOADS/ENVIRONMENT SPECTRA SURVEY — INDIVIDUAL AIRPLANE TRACKING DATA — INDIVIDUAL AIRPLANE MAINTENANCE TIMES — STRUCTURAL MAINTENANCE RECORDS

Figure 1. The Tasks of the Structural Integrity Program

1995108068

N95- 14482

THE EFFECTS OF PITTING ON FATIGUE CRACK NUCLEATION IN 7075-T6 ALUMINUM ALLOY

Li Ma and David W. Hoepfner *
University of Utah
Salt Lake City, UT

SUMMARY

A high-strength aluminum alloy, 7075-T6, was studied to quantitatively evaluate chemical pitting effects on its corrosion fatigue life. The study focused on pit nucleation, pit growth, and fatigue crack nucleation. Pitting corrosion fatigue experiments were conducted in 3.5% NaCl aqueous solution under constant amplitude sinusoidal loading at two frequencies, 5 and 20 Hz. Smooth and unnotched specimens were used in this investigation. A video recording system was developed to allow in situ observation of the surface changes of the specimens during testing. The results indicated that pitting corrosion considerably reduces the fatigue strength by accelerating fatigue crack nucleation.

A metallographic examination was conducted on the specimens to evaluate the nature of corrosion pits. First, the actual shapes of the corrosion pits were evaluated by cross-sectioning the pits. Secondly, the relation between corrosion pits and microstructure was also investigated. Finally, the possibility of another corrosion mechanism that might be involved in pitting was explored in this investigation.

The fractography of the tested specimens showed that corner corrosion pits were responsible for fatigue crack nucleation in the material due to the associated stress concentration. The pits exhibited variance of morphology. Fatigue life for the experimental conditions appeared to be strongly dependent on pitting kinetics and the crack nucleation stage.

INTRODUCTION

Pitting corrosion is a form of serious damage in aircraft structures, because aluminum alloys, particularly high-strength aluminum alloys used in aircraft structures, are susceptible to pitting when exposed to an aggressive environment. This is of importance, as aircraft often operate in aggressive environments. Many studies have been done on aluminum alloys dealing with this localized form of corrosion attack, such as determining the conditions that lead to pitting, how the basic mechanisms of pitting works, and developing effective methods of protection; however, little has been reported on the effects of pitting on the fatigue life of these alloys. Studies by Hoepfner [1,2] showed that pitting did have a significant effect on corrosion fatigue life. This study is an extension of this earlier work focusing on the pitting and crack nucleation stages of the work.

In recent years issues concerning the structural integrity and continued safe operation of aging aircraft have focused much attention on the effects of corrosion on the fatigue behavior of aircraft structural materials. Since high-strength aluminum alloy 7075-T6 is widely used in aircraft structures included in the aging fleet, it was believed important to study 7075-T6. Also, the conjoint action of corrosion pitting with fatigue loading lowers the overall structural integrity of those aircraft made of 7075-T6. This is oftentimes an extremely dangerous situation, as rapid failure without warning may occur under certain conditions. Thus, an extensive study on pitting corrosion fatigue behavior of this material is necessary.

In order to investigate the effects of pitting on the fatigue life of 7075-T6 aluminum alloy, the present work was mainly concerned with stages of pit nucleation and growth, and nucleation of fatigue cracks at

*This paper is based, in part, on the Ph.D. dissertation of the first author.

corrosion pit sites, because pitting corrosion was considered to have a more pronounced influence on the stage of crack nucleation in the overall fatigue process.

The primary objectives of this investigation were to develop a method for better understanding the role of pits in corrosion fatigue, and quantitatively assess pitting corrosion fatigue behavior of 7075-T6 aluminum alloy exposed to an aggressive environment.

EXPERIMENTS AND RESULTS

Experimental Procedures

Tests were conducted on 7075-T6 aluminum alloy. Typical mechanical properties and nominal composition (%wt) of the material are given in Tables 1 and 2 respectively.

The specimen used in this study was smooth and unnotched, and is shown in Fig. 1. The observed surface, which was the midsection of the upper surface of the specimen when mounted in the grips, was ground flat with 600-grit emery paper and cleaned with acetone before testing. The other surfaces including sides and bottom which could not be observed during testing, were coated with epoxy resin to isolate them from the corrosive solution.

The testing was conducted in a fretting fatigue machine which was modified for pitting corrosion fatigue tests. An environmental system was built to provide a flowing corrosive environment around the midsection of the specimen. A video recording system was developed to allow in situ observation of the specimen surface and real-time video recording. The use of this system permitted direct observation of transient surface changes without disturbing the reacting surface during the pitting corrosion fatigue testing. A schematic diagram of the system is shown in Fig. 2. Video images were produced using a microscope with a zoom lens fitted to a video camera. The microscope, which has two degrees of freedom, was positioned parallel to the specimen surface. Surface changes on the specimen during testing were monitored and recorded in real time by using the microscope, camera, VCR and monitor. A video micrometer was used for pit size and crack length measurement. A character generator was allowed to add titles or captions in the video images recorded and a video printer was used to produce permanent records of the images.

Seventeen unnotched specimens were tested in a 3.5% NaCl solution having pH values between 5 and 6. One specimen was tested in laboratory air for comparison. All tests were conducted at room temperature. In order to obtain fatigue lives of 10^6 to 10^7 cycles, the maximum stress levels used were varied between 79 MPa and 89 MPa. All specimens were tested under sinusoidal loading with a load ratio, $R=0.1$, at frequencies 5 and 20 Hz.

The fatigue load was applied after the specimen had been immersed in the 3.5% NaCl solution for a few minutes. The exposed areas of each specimen were the upper midsurface having areas of approximately 46 to 65 mm². The solution was circulated through the environmental chamber at a rate about 125mL/h. The solution was renewed for each test. Tests were not interrupted except for checking and cleaning the exposed surface, and taking photos.

Results and Discussion

Pit Nucleation

The pit size life in terms of number of cycles, plotted against the maximum stress level is shown in Fig. 3. Here, the pit detection life is defined as the number of cycles to the "first observed" pit at the length of about 0.02 mm on the exposed surface. Thus, the pit detection life includes the nucleation phase as well as some pit growth. It should be noted that fairly large scatter (between 9,52,800 and 2,621,300 cycles) in the pit detection life data was observed at both frequencies (5 and 20 Hz). This scatter is believed to be related to the distribution of constituent particles, inclusions, as well as grain shape, size, and orientation.

The data shown in Fig. 3 indicate that pitting generally was detected after approximately one million cycles. The reason for the delay in pit formation is that pitting corrosion is a time (or cycles) dependent process. It takes time for aggressive anions (Cl^-) contained in the solution to penetrate the passive film and locally destroy it. It was observed that, in 3.5% NaCl solution, the exposed surfaces of the specimens were corroded over whole areas in the very early stages of the test. Then corrosion pits were generated within the heavily corroded region. A typical series of video photographs showing the change in surface state of a specimen exposed to 3.5% NaCl solution are shown in Fig. 4. Within 68,900 cycles of exposure, the surface was obscured. The formation of a continuous corrosion product layer formed with progressive cycling, and the pits nucleated at localized attack sites. This observation is consistent with previous observation of Hoeppner[2] and Cox.[3]

One characteristic feature observed during the testing was the formation of blisters. These blisters occurred on the surface and burst after remaining on the surface for a while. This observation supports the view regarding pit nucleation in aluminum offered by Barger and Givens.[4] They found that blistering occurred along the oxide/metal interface and resulted in breaking of the film because of high hydrogen gas pressure created in blisters, which therefore acted as precursors of pits.

The data shown in Fig. 3 also indicated that no appreciable frequency effect was identified at frequencies between 5 and 20 Hz. However, it is probable that lower frequencies would have a significant effect. This aspect is under further study. In addition, the life to detection of a corrosion pit is hardly affected by stress levels between 79 and 89 MPa. The average pit detection life was about 35% of total corrosion fatigue life.

Final Failure

An S/N plot of maximum fatigue stress versus cycles to failure is shown in Fig. 5. Only the results of the specimens tested in 3.5% NaCl solution are shown in this plot. The specimen tested in laboratory air at a stress level of 80 MPa ran out at 7,811,500 cycles, which is the highest number of cycles of survival for all tested specimens. For comparison, some of the results presented by Antolovich and Saxena [5] are also shown in Fig. 5. These results are from specimens of 7075-T6 aluminum alloy that were tested in laboratory air. Cracks nucleated at the corners of the specimen in all cases and the detectable crack size for the nucleation was about 0.4 mm. Since the period between crack detection and final failure was only several thousand cycles, it was difficult to observe crack propagation during testing. Therefore, the effect of environment is considered to contribute mainly to the fatigue crack nucleation and early propagation processes. Additional studies of this aspect also are underway. It should be mentioned here that the life spent to detect the fatigue crack means the life from the beginning of the experiment until the detection of a 0.4 mm crack. The detection of the crack at a length of 0.4 mm includes the pit nucleation and growth stages as well as crack formation at the pits plus some growth. Clearly, to completely model this process additional detailed studies are needed. Indeed, portions of these studies are underway.

As shown in Fig. 5, a 3.5% NaCl environment lowers about 60% the fatigue strength of aluminum 7075-T6 specimens. For these conditions, since corrosion pits were found on the exposed surfaces of

almost all specimens tested in 3.5% NaCl solution and the specimen tested in laboratory air did not fail at the same stress level, it is believed that the pits provide local stress concentrations that accelerate fatigue crack nucleation and reduce fatigue life of 7075-T6 material. In addition, we observed intergranular cracks in the pits. These also may play a significant role in nucleating the fatigue cracks. As expected, the lower frequency (5 Hz) reduces the fatigue life a slight amount compared to the higher frequency (20 Hz). The reason is because low frequency allows more time for corrosion reactions to occur. Additional studies of the effect of frequency and variable amplitude loading cycles are underway within Quality and Integrity Design Engineering Center in the Mechanical Engineering Department at the University of Utah.

METALLOGRAPHIC INVESTIGATION

In order to evaluate the effect of the microstructure on pitting corrosion fatigue behavior of 7075-T6 aluminum alloy, a metallographic examination was conducted on specimens tested in 3.5% NaCl solution using an optical stereo microscope.

Profiles of adjacent cross sections of a tested specimen are shown in Fig. 6. To produce these adjacent cross sections, a vertical section was made through preselected pits and they were photographed. Then more material was removed from the specimen and the corrosion pits again were photographed. This process was repeated a third time. It is evident that the three pits shown in Fig. 6 (a) have coalesced. After removing a layer of metal from the pit cross section, it can be seen that the same pits were separate and had varied shapes and sizes, Fig. 6 (b). It is obvious that discrete pits nucleated at first, but that with increasing exposure time, pit coalescence took place to cause more extensive local attack. The same phenomenon was observed by Baker [6] when he studied the corrosion resistance of aluminum-magnesium-silicon alloy under a salt-spray condition.

According to ASTM standard G 46-76 (Standard practice for Examination and Evaluation of Pitting Corrosion), the pits shown in Fig. 6 (a) and (b) appear in the elliptical shape except for the smaller one in Fig. 6 which shows the narrow and deep shape. To evaluate the cross-sectional shapes of the same pits in more detail, another layer of the pit cross section was removed and the resulting pit shapes are shown in Fig. 6 (c). It is interesting to note that two pits joined together under the surface showing the undercutting shape with different depths, and other pits exhibited intergranular attack which originated from the base of the pit. Therefore, it can be concluded that a pit shape may vary irregularly when growing and it is difficult to determine the true maximum pit depth by the method of cross-sectioning the pit because the deepest pit may not have been selected and the pit may not be sectioned at the deepest point of the penetration. This observation provides evidence that modeling the pits will be an extremely complex process. Perchance on equivalent initial flaw size approach will be the best we can do. Modeling studies have been underway [1,2] by the first author and they are continuing under this program.

Further evidence of intergranular corrosion occurring along with the pit, in which case intergranular fissures advance into the metal laterally from the pit cavity, was identified on the exposed surface of another specimen after polishing and etching. Fig. 7 shows that the cracks which nucleated from the pit on the exposed surface of the specimen were caused by intergranular corrosion attack. In both cases (Figs. 6 (c) and 7) intergranular cracking originated from the pit. The reason for this might be that the electrochemical conditions in the pit readily lead to the occurrence of intergranular attack. According to Lifka,[7] in high-strength aluminum alloys the susceptibility to intergranular attack results from a localized decomposition of a solid solution at the grain boundaries and the formation of a precipitation in the vicinity of the grain boundaries. In the case of 7075-T6 aluminum, intergranular corrosion is probably related to the precipitation of the grain boundary phases, such as $MgZn_2$, which may themselves behave anodically with respect to the adjacent alloy. Hence, it is reasonable to believe that intergranular corrosion is another corrosion mechanism involved in crack nucleation in this research. Additionally, since the intergranular corrosion was found to penetrate deeply into the metal leaving behind little visible evidence of damage (Fig. 8), it is possible that intergranular corrosion may cause failure with extreme suddenness, especially when the materials are subjected to a lower fatigue stress level and a longer exposure time than in the present testing.

This observation provides evidence for the great concern that pit formation and growth, accompanied by intergranular attack may lead to degradation of integrity. In this case, based on the metallographic examination and the observation during testing, pitting seems the predominant corrosion attack mechanism. This observation has potential significance in relation to modeling the corrosion pitting fatigue process.

It also is noted that pit growth was strongly dependent on the orientation with respect to the rolling direction of the material as shown in Fig. 6. The same phenomenon was found in the other specimens. Fig. 8 presents the pits on the exposed surface of a different specimen. The picture shows that severe attack occurred along the fibrous grain orientation in the rolling direction.

FRACTOGRAPHIC INVESTIGATION

A fractographic examination of the specimen fracture surfaces was conducted using scanning electron microscopy. This was done to confirm the notion, based on this and other experimental work, that has demonstrated that pits have been considered to be the cause of accelerated fatigue crack nucleation with a concomitant reduction in fatigue life. As well, the fractography was done to provide additional insight into the mechanisms involved in the pitting corrosion fatigue phenomenon. This investigation included two steps. First, the fracture surfaces were examined to study the origin of fracture and fracture modes involved in the fracture processes. Second, the exposed surfaces, which were related to the fracture, were examined to deal with the corrosion damage.

Fracture Surface Examination

By tracing the radial track surface features shown in Fig. 9 it is evident that the fatigue cracks originated at the sites of corner corrosion pits. This observation confirms the assumption that the corrosion pits acted as stress concentration sites which resulted in nucleation of fatigue cracks. Careful examination around the crack nucleation areas showed that corner pits at the origin sites nucleated in the areas close to the corner of the edge surfaces which were covered with coating broken by solution penetrating during testing. The observations for the other specimens also indicated that the corner pits and pits close to the corners were preferential sites for fatigue crack nucleation. The reason for the evident preference for the crack to start at the corner pits or the pits close to the corners could be explained by the fact that the curved edges of the specimens were the most highly stressed areas compared to the other areas in the specimens. Finite element analysis confirmed this and is to be reported elsewhere. Some small pits also were found on the fracture surface, Fig. 9. However, it is obvious that crack nucleation was dominated by the large corner corrosion pit. It is recognized that in other cases the multiple damage sites (pits) away from the corners nucleate cracks that link up. This has been reported in other work by Hoeppner.[2]

One interesting phenomenon noticed was that the fatigue cracks seem to nucleate from the bottoms of the pits, Fig. 9. Some research [8] showed that a growing pit is a local electrochemical cell. The bottom of the pit is the anode and the surrounding walls of the pit and surface of the metal are the cathode. The fatigue crack nucleation occurred at the bottom of the corrosion pit, probably because this place is electrochemically active and the stress concentration is large enough to lead to the crack. Therefore, it is natural to conclude that corrosion fatigue nucleation is controlled by the rate at which pits nucleate and grow to a critical depth and shape. This interpretation must be tempered by the observation of intergranular cracking as discussed above.

Most of the fracture surface was the fatigue crack propagation region where transgranular fracture was found to be the primary fracture path. Fig. 10 shows cleavage-like fracture, with river patterns emanating from the origin in the area adjacent to the fracture origin (see also Fig. 11). A small corrosion pit appeared on the surface, but no indication of the intergranular decohesion which would be the result of the intergranular corrosion was observed during the metallographic examination. Similar features were seen in

specimens tested in air from the literature.[9] Observation of the fracture surface also shows little ductility in that the cleavage facets with a few dimples appeared in the crack propagation region, Fig. 11. This phenomenon was observed repeatedly. Although crack propagation did involve other mechanisms, "quasi-cleavage" was found to be the primary mechanism for 7075-T6 aluminum tested in 3.5% solution under cyclic loading.

Away from the fatigue crack nucleation sites, well-defined fatigue striations were found in the crack propagation region, Fig. 12. This feature was observed in most specimens examined. No evidence of environmental influence was identified after the crack became long enough. This corresponds to the observation from the experimental work, in which crack propagation was too fast (only several thousand cycles taken in the crack propagation stage) to allow the chemical reaction to occur. Also, this is consistent with many observations in this field. Separate studies of the role of environments on fatigue crack propagation have been done by the second author and others and also are currently underway as part of this overall program.

Exposed Surface Examination

Numerous small and shallow cavities were observed on the exposed surface as shown in Fig. 13. These cavities were the result of the local breakdown of protective films and presumably attack at constituent particles and act as precursors of pits. Relatively large and deep corrosion pits also were found on the exposed surfaces of the specimens. These pits were distributed randomly on the exposed surfaces and appeared in different shapes and sizes. Figs. 14 and 15 show the appearance of pits observed in one specimen. It was interesting to notice that these pits had different shapes on the same exposed surface. Fig. 14 shows a typical hemispherical pit located at near center of the exposed surface. A group of pits was found on the same exposed surface as shown in Fig. 15, which exhibits multi-site damage (MSD) related to corrosion pitting. This group of the pits showed coalescence of pits giving rise to more local attack, and these pits appeared in irregular shapes. Numerous pits in a group also were observed in the other specimen as shown in Fig. 16. Pits in this group grew along the orientation with respect to the rolling direction of the material. All the pits were three dimensional in nature. The shapes of the corrosion pits might influence the fatigue life in different degrees, since the magnitude of the stress concentrations depends on the pit shape and geometry dimensions.

Pits created on the exposed surfaces generally showed the sharp edges that are believed to be caused by crystallographic corrosion tunneling, Fig. 17. A micro-crack also was observed at the pit edge in this figure. Furthermore, the walls of pits were found to be rough. The crack-like sharp corners and the rough sites inside a pit should increase the local stress concentration and play an important role in the fatigue life of the material.

CONCLUSIONS

The following conclusions are drawn from this study:

1. Corrosion pits, especially corner corrosion pits, were responsible for fatigue crack nucleation of 7075-T6 aluminum specimens tested in 3.5% NaCl solution. The fatigue life was found to be strongly dependent on pit formation and growth.
2. The fatigue strength of 7075-T6 aluminum tested in 3.5% NaCl solution was reduced by about 60% compared with that tested in laboratory air. The latter data were obtained from the literature. It is believed that the reason is the corrosion pits act as the sites of stress concentration to accelerate fatigue crack nucleation and also produce intergranular cracks.

3. No appreciable frequency effect was observed in the pit nucleation process for the frequencies tested in this work. However, this parameter was found to have an effect on total corrosion fatigue life. It is believed that reduction of fatigue life at low frequency was associated with a greater corrosion effect on promoting the pit growth rate than at high frequency.

4. Pits appeared in various morphologies and were three-dimensional in nature. It was found that pits had rough internal walls and crack-like sharp edges. These crack-like sharp edges and rough pit walls were considered to cause higher stress concentrations and to readily nucleate the fatigue crack, leading to the reduction of the fatigue life.

5. The growth of the pits depends strongly on the orientation of the grain with respect to the microstructure and crystallographic orientation of the material.

6. Intergranular corrosion cracks were found along with pitting, suggesting that intergranular attack might lead to fatigue cracking.

7. The mechanism governing the propagation of the fatigue cracks originating at corrosion pits was "quasi-cleavage".

FUTURE STUDIES

This research is a small part of an extensive activity on pitting corrosion fatigue dating back to 1965. Additional detailed studies are underway and planned related to those reported herein as follows:

- (1) Fracture mechanics based modeling activities.
- (2) Frequency and load spectrum effects.
- (3) Effect of aircraft environments. This activity involves sampling aircraft environments at aircraft maintenance and overhaul activities.
- (4) Additional studies of pit characterization.
- (5) Statistically planned experiments for more reliable evaluation of some of the early observations.
- (6) Corrosion pitting studies with other aluminum and titanium alloys.

REFERENCES

1. Hoepfner, D.W.: Corrosion Fatigue Considerations in Materials Selections and Engineering Design. *Corrosion Fatigue: Chemistry Mechanics and Microstructure*, O. Devereux, A.J. McEvily, R.W. Staehle, Ed., NACE-2, National Association of Corrosion Engineers, 1972.
2. Hoepfner, D.W.: Model for Prediction of Fatigue Lives Based Upon a Pitting Corrosion Fatigue Process. *Fatigue Mechanisms*, Proceedings of an ASTM-NBS-NSF Symposium, J.T. Fong, Ed., ASTM STP 675, American Society for Testing and Materials, 1979.
3. Cox, J.M.: Pitting and Fatigue-Crack Initiation of 2124-T851 Aluminum in 3.5% NaCl Solution. *M.S. Thesis*, University of Missouri-Columbia, 1979.

4. Bargeron, C.B.; and Givens, R.B.: Source of Oscillations in the Anode Current during the Potentionatatic Pitting of Aluminum. *Electrochemical Society Journal*, Vol.124, 1977, pp.1230-1232.
5. Antolovich, S.D.; and Saxena, A.: Fatigue Testing. *Metals Handbook*, 9th Edition, Vol.8, ASM International, Metals Park, Ohio, 1985, p.364.
6. Baker, S.V.; Lyon, S.B.; Thompson, G.E.; Wood, G.C.; and Lewis, K.G.: A Comparison of Potentiodynamic Polarization Tests with Wet-dry Mixed Salt-Spray Testing of Aluminum-Magnesium-Silicon Alloy. *New Methods for Corrosion Testing of Aluminum Alloys*, ASTM STP 1134, Philadelphia, 1992, pp.32-49.
7. Lifka, B.W.; and Sprowls, D.O.: Significance of Intergranular Corrosion in High-Strength Aluminum Alloy Products. *Localized Corrosion - Cause of Metal Failure*, ASTM STP 516, 1972, pp.120-144.
8. Payer, J.H.; and Staehle, R.W.: Localized Attack on Metal Surface. *Corrosion fatigue: Chemistry, Mechanics and Microstructure*, National Association of Corrosion Engineers, 1972, pp. 211-218.
9. Kerlins, V.: Modes of Fracture. *Metals Handbook*, 9th Edition, Vol.12, ASM International, Metals Park, Ohio, 1987, p.54.

ACKNOWLEDGMENTS

The authors would like to thank the Boeing Commercial Airplane Company for providing financial support for this study. The authors also are grateful to the staff at the Quality and Integrity Design Engineering Center in the Department of Mechanical Engineering at the University of Utah for assistance with experimental work. This effort is part of an effort on studies on environmental effects on fatigue behavior of aircraft structural materials.

Table 1. Mechanical properties of 7075-T6 aluminum alloy

Yield strength (MPa)	Ultimate strength (MPa)	Elongation (%)	Modulus of elasticity (MPa x 10 ³)
503	572	11	72

Table 2. Chemical composition of 7075-T6 aluminum alloy, wt%

Cu	Mg	Zn	Cr	Al
1.6	2.5	5.6	0.3	Balance

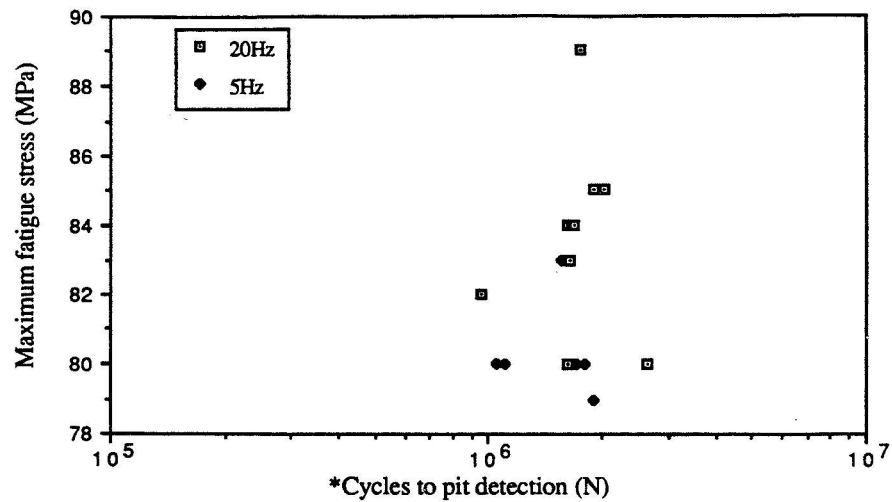


Fig. 3. Stress Vs. life plot of pit detection data.

* Cycles to pit detection means the cycles at which the "first pit" was observed at the length of about 0.02 mm. Thus, this length includes pit nucleation plus some growth.

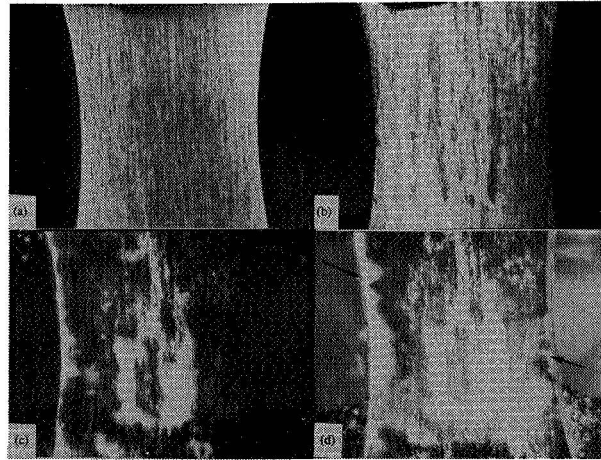


Fig. 4. Video images of changes in surface states of the specimen in 3.5% NaCl, magnification 10.5X, (a) cycle, N=0, (b) cycles, N=68,900, (c) cycles, N=828,000, (d) cycles, N=3,082,000. Arrows indicate pits.

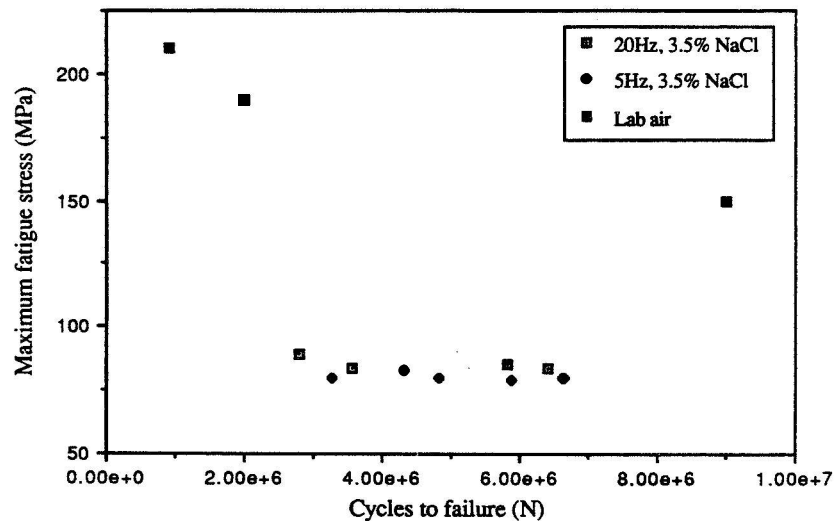


Fig. 5. Plot of maximum stress vs. number of cycles to failure for pitting corrosion fatigue tests. Lab air data[2] is used for comparison.

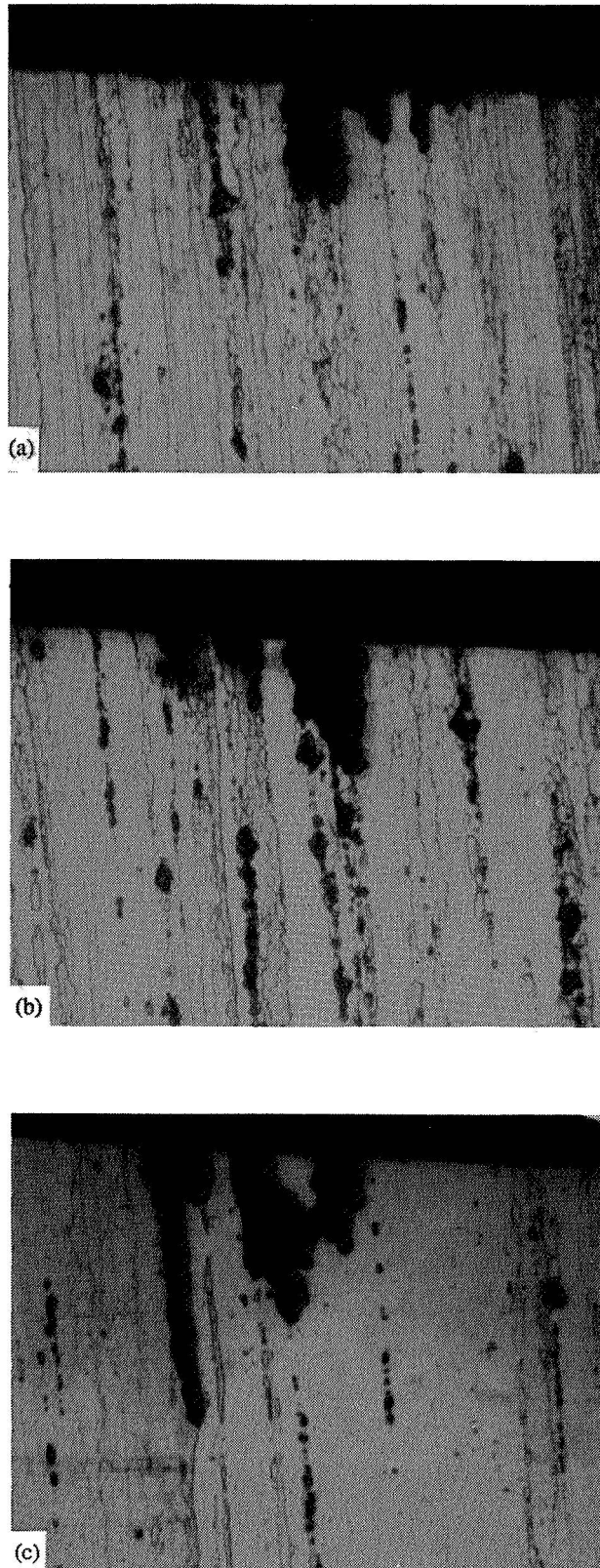


Fig. 6. Cross section of pits in the specimen tested in 3.5% NaCl solution, magnification 400X (reproduced by 320 magnification), (a) after cross-sectioning, (b) after removing a layer of metal, (c) after removing the second layer of metal.

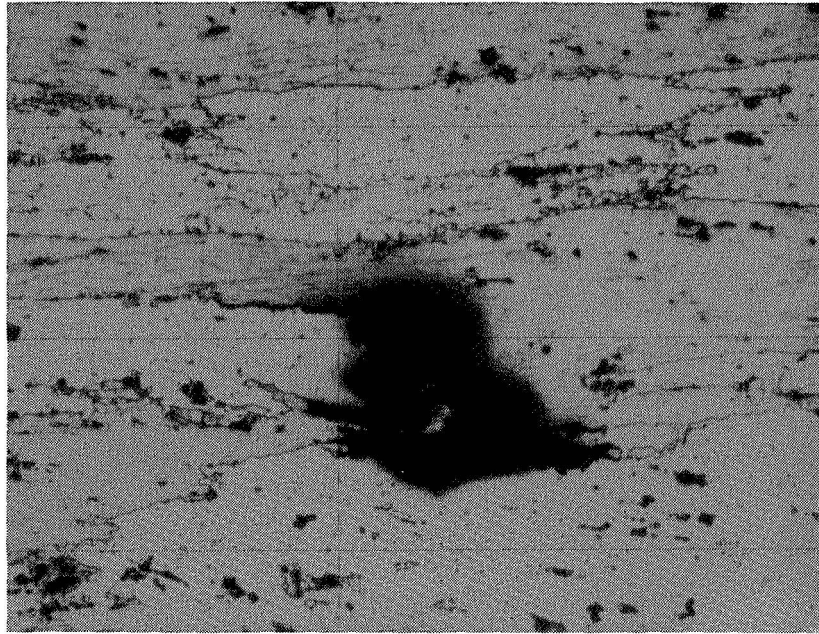


Fig. 7. Corrosion pit along with the intergranular corrosion cracks on the exposed surface of the specimen tested in 3.5% NaCl solution, magnification 200X. Arrows indicate the loading directions.

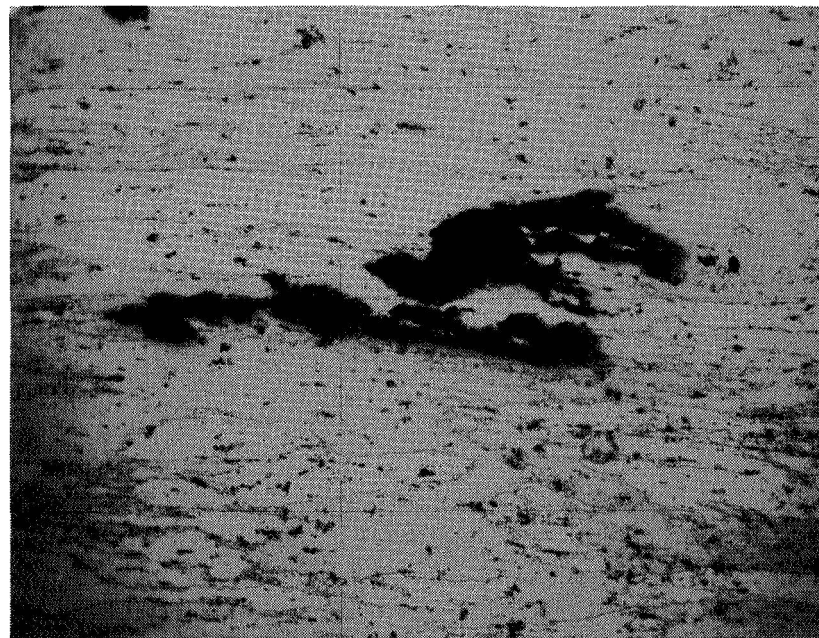


Fig. 8. Corrosion pits on the exposed surface of the specimen showing pit growth in the rolling direction, magnification 100X.

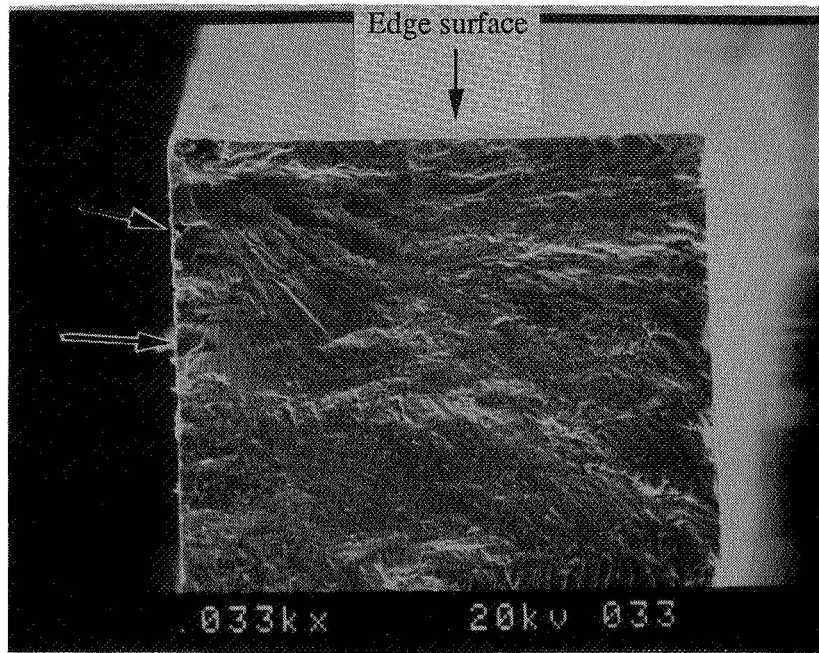


Fig. 9. The crack nucleation area of the specimen tested in 3.5% NaCl solution showing the fracture origin at a corrosion pit. Arrows indicate the exposed surface and a small pit.

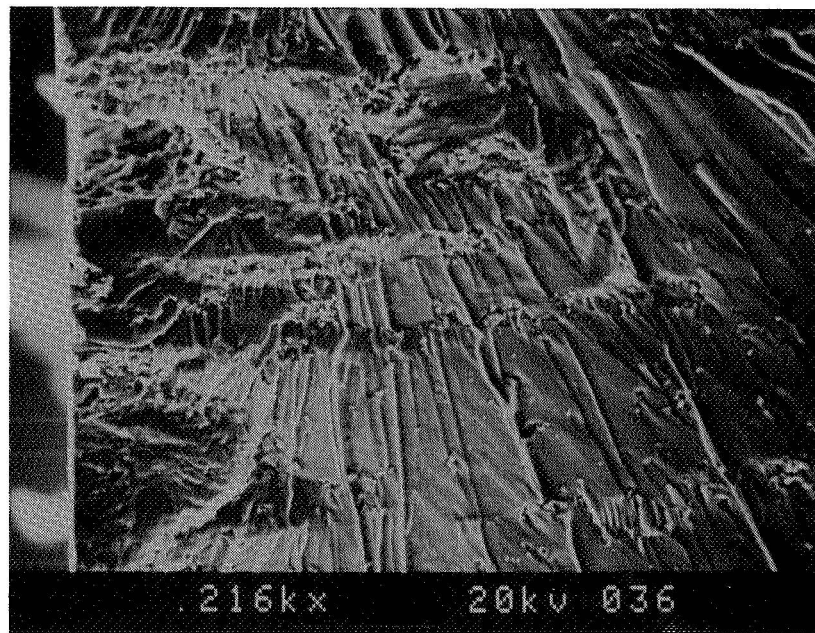


Fig. 10. Cleavage-like fracture near the crack origin of the same specimen showing in Fig. 9.

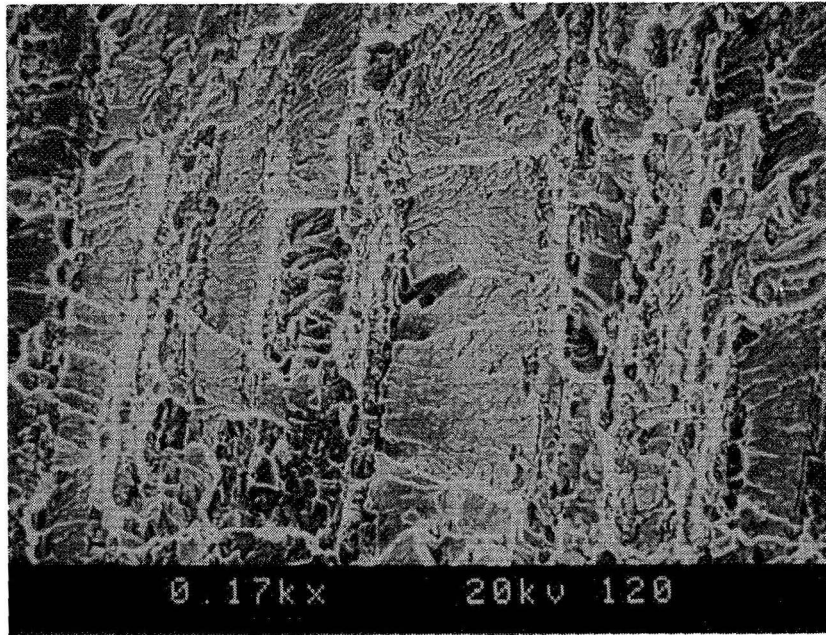


Fig. 11. Cleavage facets with a few dimples in the crack propagation area of the specimen tested in 3.5% NaCl solution.

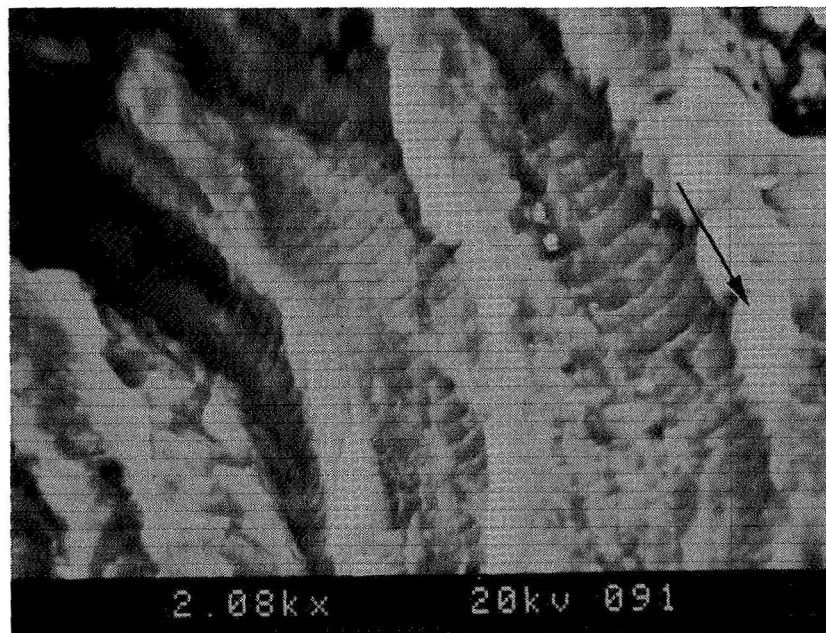


Fig. 12. Fatigue striations in the crack propagation area of the specimen tested in 3.5% NaCl solution. Arrow indicates the crack propagation direction.

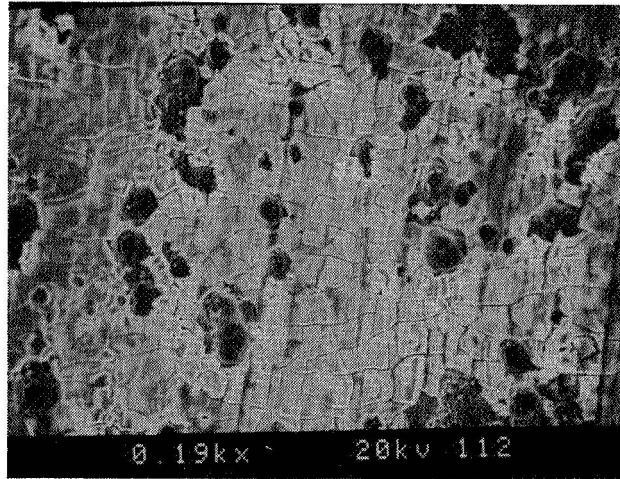


Fig. 13. Small cavities on the exposed surface of the specimen tested in 3.5% NaCl solution (cycles to failure are 4,822,200).

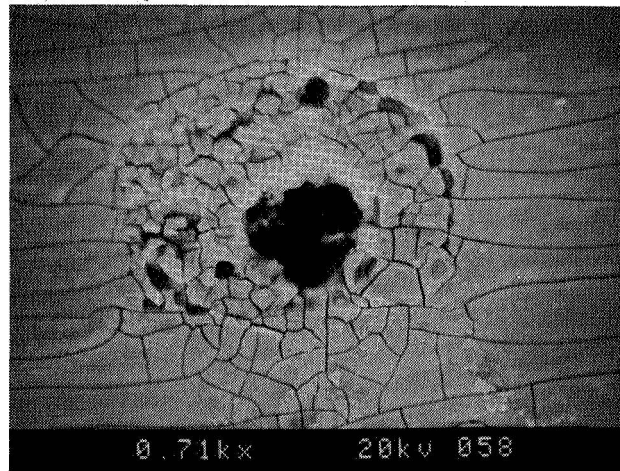


Fig. 14. Hemispherical shape of pit on the exposed surface of the specimen tested in 3.5% NaCl solution (cycles to failure are 3,279,300).

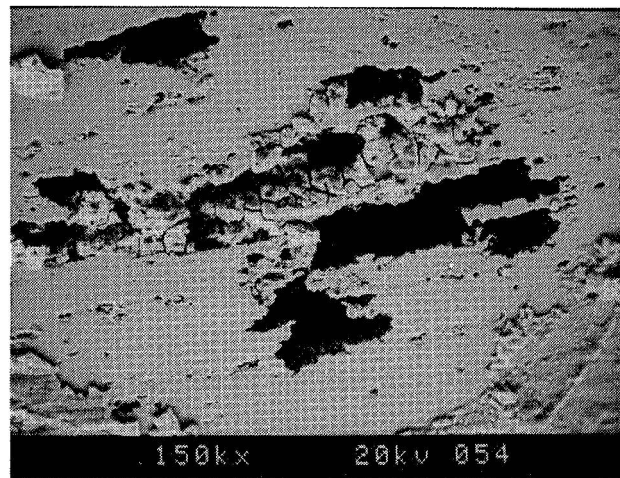


Fig. 15. Group of pits on the same specimen showing in Fig. 14.

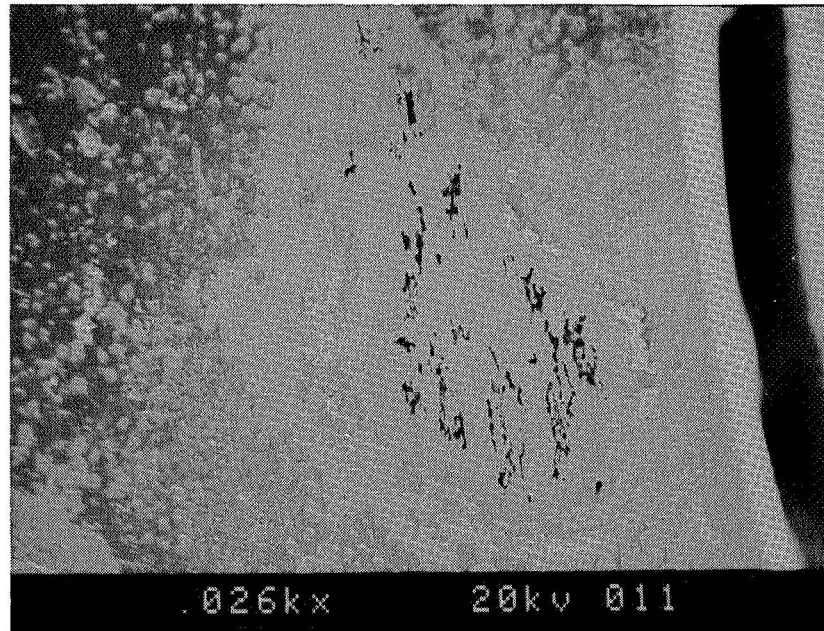


Fig. 16. Pits appear in a group in the specimen tested in 3.5% NaCl solution.

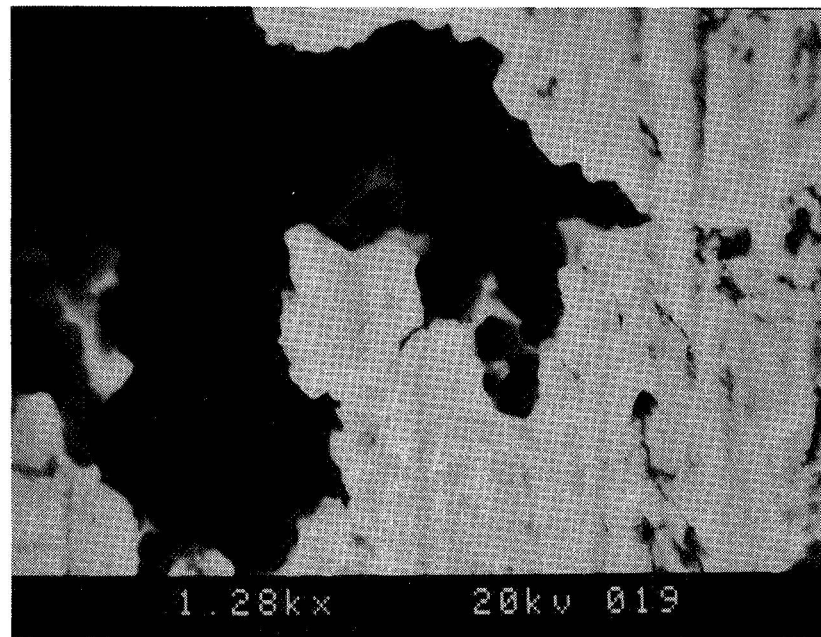


Fig. 17. Part of the pit showing the sharp edges of the pit and the microcrack at the pit in the specimen tested in 3.5% NaCl solution.

Modeling Time-Dependent Corrosion Fatigue Crack Propagation in 7000 Series Aluminum Alloys

Mark E. Mason and Richard P. Gangloff

Center for Electrochemical Science and Engineering
Department of Materials Science and Engineering
University of Virginia
Charlottesville, VA 22903

44866
S30-26
23/24
p. 22

ABSTRACT

Stress corrosion cracking and corrosion fatigue experiments were conducted with the susceptible S-L orientation of AA7075-T651, immersed in acidified and inhibited NaCl solution, to provide a basis for incorporating environmental effects into fatigue crack propagation life prediction codes such as NASA FLAGRO. This environment enhances da/dN by five to ten-fold compared to fatigue in moist air. Time-based crack growth rates from quasi-static load experiments are an order of magnitude too small for accurate linear superposition prediction of da/dN for loading frequencies above 0.001 Hz. Alternate methods of establishing da/dt , based on rising-load or ripple-load-enhanced crack tip strain rate, do not increase da/dt and do not improve linear superposition. Corrosion fatigue is characterized by two regimes of frequency dependence; da/dN is proportional to f^{-1} below 0.001 Hz and to f^0 to $f^{-0.1}$ for higher frequencies. Da/dN increases mildly with both increasing hold-time at K_{MAX} and with increasing rise-time for a range of loading waveforms. The mild time-dependence is due to cycle-time-dependent corrosion fatigue growth. This behavior is identical for S-L and L-T crack orientations. The frequency response of environmental fatigue in several 7000 series alloys is variable and depends on undefined compositional or microstructural variables. Speculative explanations are based on the effect of Mg on occluded crack chemistry and embrittling hydrogen uptake, or on variable hydrogen diffusion in the crack tip process zone. Cracking in the 7075/NaCl system is adequately described for life prediction by linear superposition for prolonged load-cycle periods, and by a time-independent upper bound relationship between da/dN and ΔK for moderate loading times.

INTRODUCTION

A variety of chemical and electrochemical environments enhance rates of fatigue crack propagation (FCP) in aluminum and titanium alloys,^{1,2} however, such behavior is not described sufficiently in fracture mechanics-based life prediction codes such as NASA FLAGRO.^{3,4} Two issues are particularly important: the complex dependence of environmental fatigue crack propagation (EFCP) rate (da/dN) on stress intensity range (ΔK) and stress ratio (R), including both intrinsic damage and crack closure contributions, as well as the time and crack tip strain rate dependencies of

da/dN. This paper considers the latter issue for aqueous chloride EFCP in precipitation hardened 7000-series aluminum alloys.

Work to date demonstrated that loading frequency (f),⁵⁻¹¹ waveform^{9,10,12,13} and hold-time (τ_H)^{9,10,13} affect EFCP rates for aluminum alloys such as 7075-T6 in full immersion chloride solutions at 25°C. Da/dN vs f data are summarized in Fig. 1, and demonstrate this strong and time-dependent environmental effect for several alloys.^{5-7,11} While da/dN is always frequency-independent for FCP in either vacuum or moist air at frequencies below 50 Hz, three frequency dependencies are observed

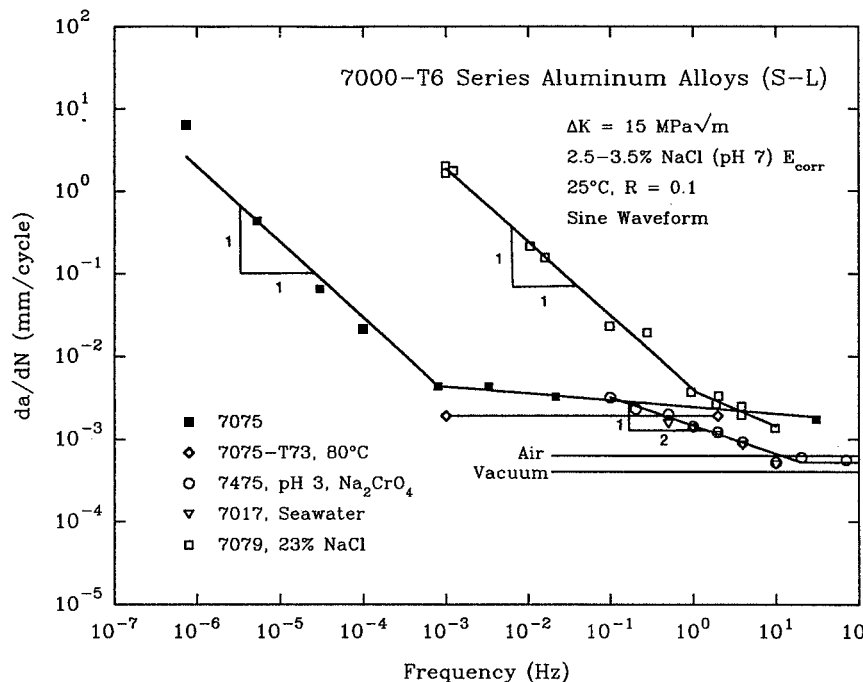


Figure 1 - Effect of frequency on corrosion fatigue crack propagation in 7000 series aluminum alloys in aqueous chloride.^{5-7,11}

for the chloride cases. So-called true corrosion fatigue involves frequency-independent cracking at rates well above the benign environment values, as shown approximately for 7075 at frequencies above about 10^{-3} Hz.^{1,5} Purely time-dependent FCP is indicated by da/dN data that are proportional to $1/f$ for 7079 and 7075 at frequencies below 1 and 10^{-3} Hz, respectively.^{5,11} Cycle-time dependent corrosion fatigue is characterized by $da/dN \propto f^{-\beta}$, where β is on the order of 1/2, as observed for 7017 and 7475.^{6,7} The underlying causes for the varied EFCP resistances and frequency dependencies shown for similar 7000 alloys in Fig. 1 are not understood.

The EFCP frequency dependencies shown in Fig. 1 can be modeled based on empirical curve-fitting¹⁴, linear superposition¹⁵, or mass transport and chemical reaction kinetics.^{1,16} The simple linear superposition approach may be applicable to EFCP in 7000-series aluminum alloys because of the low threshold stress intensity (K_{ISCC} or K_{TH}) of about 5 MPa√m for such alloys, particularly in the S-L orientation.^{5,17} This method equates the total environmental da/dN to the sum of the crack growth rate per load cycle due to fatigue damage in an inert environment (da/dN_{Mech}) and the contribution from time and K -dependent monotonic-load environmental cracking ($da/dt_{SCC}(K)$), integrated over a portion of each fatigue cycle (τ) where $K(t)$ exceeds K_{ISCC} :

- 1 The data in Fig. 1 were obtained for constant applied ΔK , R , a sinusoidal loading waveform, and S-L crack orientation (loading is parallel to the plate thickness (S) direction and the crack growth direction is parallel to the rolling (longitudinal-L) direction). Modest variations from the constant solution chemistry of 2.5 to 3.5 wt% NaCl, pH 7, aerated free corrosion potential, and 25°C are noted. All data were obtained for an applied ΔK of 15 MPa√m with the exception of the results for 7075-T6¹¹. These data were measured for a single ΔK of 9.5 MPa√m ($R=0.3$) and extrapolated to 15 MPa√m ($R=0.1$) by the Forman crack growth rate relationship.³

$$\frac{da}{dN} = \frac{da}{dN_{Mech}} + \int_{\tau} \left[\frac{da}{dt_{SCC}}(K) \right] K(t) dt \quad (1)$$

τ often defines the loading-only portion of the fatigue cycle where process zone stresses are tensile. Traditionally, da/dt_{SCC} has been determined by either constant load or constant crack mouth opening displacement experiments, and is K -independent for aluminum alloys in chloride above K_{ISCC} .¹⁷ For this case, and when da/dN_{Mech} is a small fraction of da/dN , Eq. 1 leads to the prediction that da/dN depends on $1/f$, as observed for 7079 in NaCl (at frequencies less than 1 Hz) and for 7075 (at $f < 0.001$ Hz, Fig. 1). For these two cases, linear superposition effectively predicts the effects of ΔK , R , f , hold time, and wave form on environmental da/dN .

Holroyd and Hardie demonstrated that linear superposition was incapable of describing the magnitude of da/dN and the frequency dependence of FCP for 7017 in seawater (Fig. 1).⁶ Although K_{ISCC} was low, da/dt_{SCC} from quasi-static load testing was too small to account for the necessary time-dependent enhancement over da/dN_{Mech} through Eq. 1. For this case, the time-dependence is considered based on:

$$\frac{da}{dN} = \frac{da}{dt} \frac{1}{\alpha f} \quad (2)$$

where da/dt is the average time-based crack growth rate during a fraction ($1/\alpha$) of the load cycle and may be frequency-dependent. If da/dt increases with increasing frequency, raised to a power (n) on the order of one-half¹⁸, then da/dN will vary with $f^{(n-1)}$ or $f^{-0.5}$, as indicated in Fig. 1. The implication of this argument is that da/dt should be measured for crack tip strain rates typical of FCP; quasi-static load experiments may not yield relevant time-based crack growth rates for modeling EFCP da/dN . For example, da/dt could be determined from EFCP experiments conducted with several hold times and analyzed with Eq. 1.¹³ Alternately, da/dt could be measured by a rising load or rising displacement method that systematically varies crack tip strain rate and stress intensity;¹⁹ the issue is whether such growth rates exceed da/dt_{SCC} determined from quasi-static load or displacement experiments. Strain rate-dependent da/dt is understandable from the film rupture and transient dissolution/ repassivation perspective.¹⁸ Both this mechanism and hydrogen environment embrittlement must be considered to predict time-cycle-dependent EFCP.^{1,16,18}

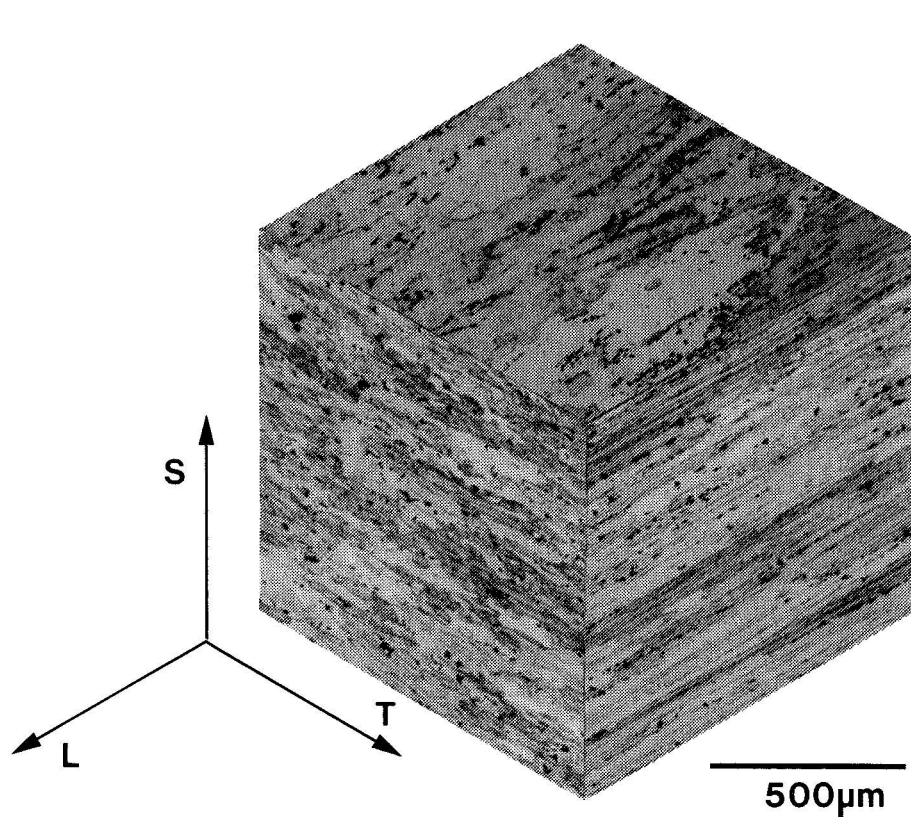
OBJECTIVE AND APPROACH

The objectives of this research on an SCC-susceptible 7000-series aluminum alloy in aqueous chloride are four-fold: (1) to test static load or displacement-based linear superposition predictions of da/dN vs ΔK and f , (2) to determine if da/dt_{SCC} is affected sufficiently by crack tip strain rate to enable improved linear superposition predictions of da/dN , (3) to measure the frequency, load waveform and hold-time dependencies of da/dN , and (4) to speculate on the metallurgical and electrochemical origin(s) of the important variability shown in Fig. 1. The output of this work will be improved data and understanding on time-cycle-dependent EFCP kinetics for use in NASA-FLAGRO.

Constant load/displacement, monotonically rising load, and ripple load experiments are conducted with a cracked fracture mechanics specimen to determine the stress intensity and crack tip strain rate dependencies of da/dt_{SCC} . Computer-automated constant ΔK and ΔK -decreasing experiments are employed to determine da/dN as a function of loading frequency, waveform and hold-time.

EXPERIMENTAL PROCEDURE

Material



Al-Zn-Mg-Cu alloy 7075 (52 mm-thick rolled plate) was studied in the peak-aged, T651 condition (24 hrs at 120 to 124°C). Chemical composition and mechanical properties are given in Table I. The optical micrographs shown in Fig. 2 reveal large flattened grains elongated in the rolling direction. Average grain dimensions in the L, transverse (T), and S directions are 1 mm, 200 μm , and 10 to 20 μm , respectively. This lot of material was previously studied in an ASTM interlaboratory test program on stress corrosion cracking.²⁰

Figure 2 - Representative microstructure of 7075-T651 aluminum alloy. Magnification 52X.

Table I. Nominal Chemical Composition and Mechanical Properties of 7075-T651

Chemical Composition (wt pct)

Zn	Mg	Cu	Cr	Mn	Ti	Fe	Si	Al
5.1-6.1	2.1-2.9	1.2-2.0	0.18-0.4	0.3 max	0.2 max	0.7 max	0.5 max	bal.

Mechanical Properties

Yield Strength MPa (ksi) *	Tensile Strength MPa (ksi) *	Elongation Pct *	K _{IC} , MPa√m (ksi√in) **
472 (68.4)	540 (78.2)	4.0	22.2 (19.3)

* Loading axis parallel to L.

** S-L orientation.

Crack Growth Measurement

The wedge-opening-load (WOL) specimen (thickness, B = 7.6 mm; width, W = 52.3 mm; and half-height to width ratio, H/W = 0.486), machined from the plate in the S-L orientation was used throughout. Specimens were mounted in the load train via clevises with roller bearings at the load pins to provide free rotation. Established stress intensity and compliance solutions were utilized for the WOL specimen.²¹ Experiments were performed using a closed-loop servo-hydraulic test machine interfaced to a personal computer for automated stress intensity control during both monotonic and fatigue loading. Crack mouth opening displacement (CMOD), load, and crack length from direct current electrical potential (DCPD) were continuously measured and variously used as the

active control signal. The DCPD solution for the compact tension specimen was successfully employed for the similar WOL geometry.^{22,23}

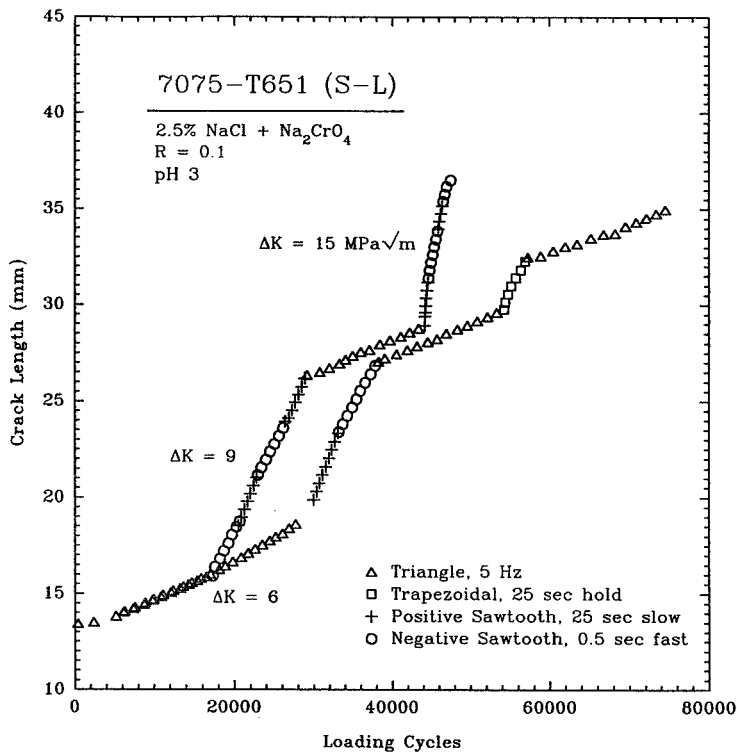


Figure 3 - Fatigue crack length vs loading cycles at constant ΔK (6, 9, 15 MPa√m; R=0.1) for peak-aged 7075 (S-L orientation) in NaCl.

CMOD, measured by an extensometer, controlled the rising load and constant displacement experiments; additional experiments were conducted at constant load. Crack length was measured by DCPD for each case. Both constant ΔK and ΔK -decreasing experiments were conducted in load control, were based on DCPD crack lengths, and followed standardized procedures.²² The machine control software provided a variety of cyclic loading frequencies, hold-times and waveforms. Fig. 3 shows cyclic crack length data from two typical constant stress intensity range EFCP experiments aimed at determining da/dN (from linear regression of crack length, a , vs loading cycles, N) for positive and negative

sawtooth, trapezoidal and triangular waveforms at three constant ΔK levels. This procedure provides steady-state EFCP growth rates at fixed ΔK and R , distinguishes small differences in da/dN , and provides a qualitative indication of the effect of crack closure (which could change with increasing crack length and specimen immersion time). Changing loading conditions often marked the fracture surface for post-test visual observations to improve DCPD crack length accuracy by linear error correction.²³ Such measurements verified less than a 10% difference between crack lengths from DCPD and actual values. Corrected crack lengths were employed for all calculations of da/dN and ΔK . Fatigue crack closure stress intensities were not measured.

Environment

The polymethyl methacrylate (PMMA) environmental cell shown in Fig. 4 was used to fully immerse the crack tip in an aerated solution of deionized water, 2.5 wt pct NaCl, 0.5 wt pct Na_2CrO_4 , and dropwise added HCl to decrease the bulk solution pH to 3. Chromate inhibitor, added to facilitate electron microscopy of fracture surfaces, reduces passive current density slightly (0.1 to 0.02 A/m²) with a negligible decrease in da/dt .¹¹ Solution was circulated continuously at 1 ml/sec, through the cell and specimen notch parallel to the crack front from a 1 liter reservoir. All experiments were conducted at the open circuit condition, without galvanic coupling of the grounded WOL specimen and test machine. Throughout each experiment, a chloridized silver reference electrode, located within the notch at the specimen midplane, monitored electrode potential which varied by less than ± 50 mV about 770 mV_{SCE}.

RESULTS AND ANALYSIS

Monotonic Load Environmental Cracking

Stress Corrosion Cracking

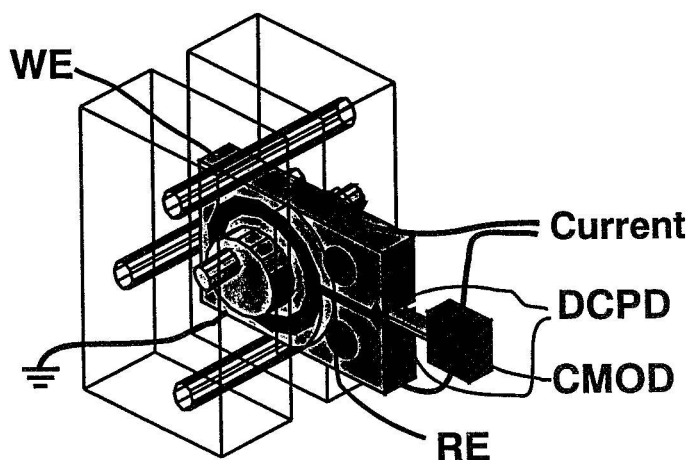


Figure 4 - Schematic of environmental cell and mechanical testing set-up.

The quasi-static load/displacement stress corrosion cracking behavior of 7075, in the susceptible S-L orientation and T651 temper, is summarized by the literature results in Fig. 5.^{5,24-26} For full immersion (FI) in neutral NaCl at free corrosion electrode potentials, SCC is characterized by K -independent cracking at a rate of about 10^{-8} m/sec, transitioning to a threshold K_{ISCC} below 4 to 5 MPa $\sqrt{\text{m}}$. Extensive, long-term results from multiple-laboratory testing of 7075-T651 (S-L) in 3.5 wt pct NaCl (FI) compare favorably with the data in Fig. 5.²⁷

Given these extensive data, only limited experiments were conducted for the heat of 7075-

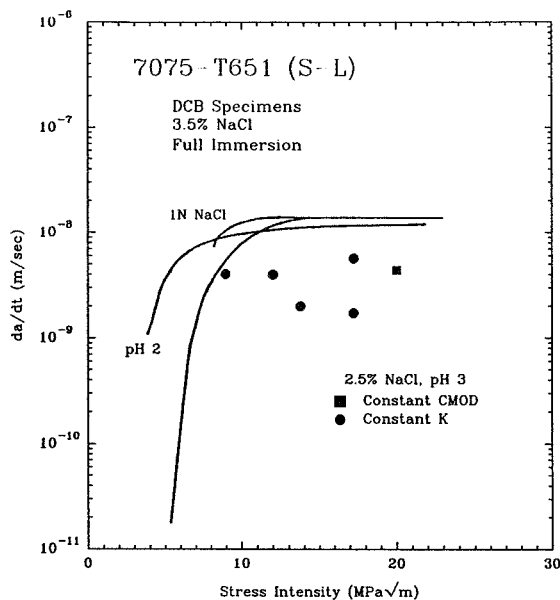


Figure 5 - Effect of stress intensity on da/dt showing K-independent da/dt_{II} above K_{ISCC} for 7075 in chloride.^{5,24-26}

Linear Superposition

For linear superposition modeling, $da/dt_{SCC}(K)$ was equated to the highest measured Stage II velocity of 4.4×10^{-9} m/sec for 7075-T651 (S-L), and assuming no crack growth below a K_{ISCC} of 5 MPa√m. FCP rates for L-T 7075-T651 in helium or vacuum comprised the mechanical component.²⁸ Equation 1 was integrated numerically to yield the predicted EFCP rates that are shown in Fig. 6 for fixed frequencies between 0.01 and 20 Hz, with K varying sinusoidally as a function of time.²⁹ These predictions are compared with corrosion fatigue data generated with sinusoidal loading at 5 Hz.

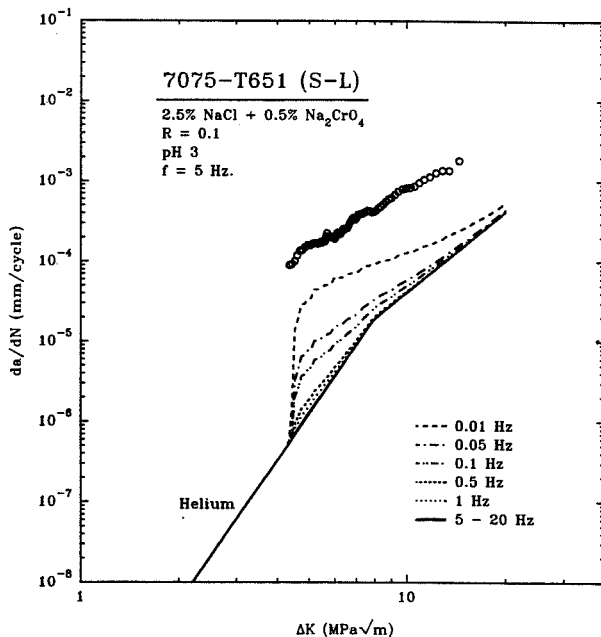


Figure 6 - Linear superposition model predictions of EFCP for the S-L 7075-T651/NaCl (FI) system compared with measured da/dN vs ΔK at $f=5$ Hz and $R=0.1$.

T651 (S-L) used in the current study. Measured values of da/dt_{SCC} are plotted as points (● for constant stress intensity and ■ for constant CMOD) in Fig. 5 with constant K applied utilizing DCPD crack length and load as the active feedback. Growth rates averaged over at least 2 mm of crack extension are consistent with K-independent cracking; however, measured da/dt_{SCC} values vary from 2.0 to 4.4×10^{-9} m/sec and are slower than the literature results.

Colvin et al. reported an approximate da/dt_{SCC} of 5×10^{-9} m/sec based on alternate immersion (AI) exposure of this same heat of 7075 in the T651 temper and for constant displacement.²⁰ Rechberger reported that da/dt_{SCC} equaled 2×10^{-9} m/sec at a K of 10 MPa√m and increased to 1.5×10^{-8} m/sec at 18 MPa√m for 7075-T651 (S-L) in neutral NaCl (FI) and at constant load; SCC was not K-independent.¹¹

Linear superposition underpredicts substantially the 5 Hz EFCP rate for 7075-T651 in NaCl, as reported for 7017 and 7475.^{6,7} This error is attributed to the slow da/dt_{SCC} compared to the order of magnitude increase in actual aqueous da/dN values over inert helium. Due to the low value of da/dN_{SCC} relative to da/dN_{Mech} , predicted EFCP rates do not show an inverse frequency dependence for the range above 0.01 Hz.

At ΔK of 15 MPa√m, the measured EFCP rate is 2×10^{-3} mm/cycle. Applying Eq. 2 and a

frequency independent da/dt_{SCC} of 4×10^{-6} mm/sec, da/dN_{SCC} becomes a dominant factor below frequencies of 0.001 Hz. Fig. 1 confirms that da/dN depends on f^{-1} for 7075, but only for frequencies less than 0.001 Hz.²

Crack Tip Strain Rate Effects

The crack tip strain rate ($d\epsilon_{CT}/dt$) during constant load or displacement measurements of K_{ISCC} and da/dt is low for 7075/NaCl due to low levels of the three factors that control $d\epsilon_{CT}/dt$; crack tip creep deformation, dK/dt and da/dt ^{1,18}. Strain rate, and perhaps da/dt , are increased if the precracked specimen is subjected to a monotonically increasing K at a fixed CMOD rate.

No such effect was detected for 7075-T651 (S-L) in chloride, loaded at a fixed CMOD rate of 2×10^{-5} mm/sec. The results in Fig. 7, plotted as the K level where crack extension was first easily detected by DCPD (K_{TH}) versus CMOD rate, show that K_{TH} equals K_{IC} (\square) for mechanical failure in moist air. This single result agrees with extensive data from similar rising-load SCC experiments with 2024-T351 (S-L) in NaCl (FI) plotted as the line in Fig. 7.¹⁹ K_{ISCC} for this system equaled 5 to 7 MPa \sqrt{m} and the quasi-static da/dt_{SCC} was 6×10^{-9} m/sec. A sharp transition, from K_{TH} equalling K_{ISCC} at low loading rates to K_{TH} equalling K_{IC} at faster rates, was observed at the applied load-line

displacement rate of 3×10^{-7} mm/sec. (Load-line displacement and CMOD rates are proportional and similar.)

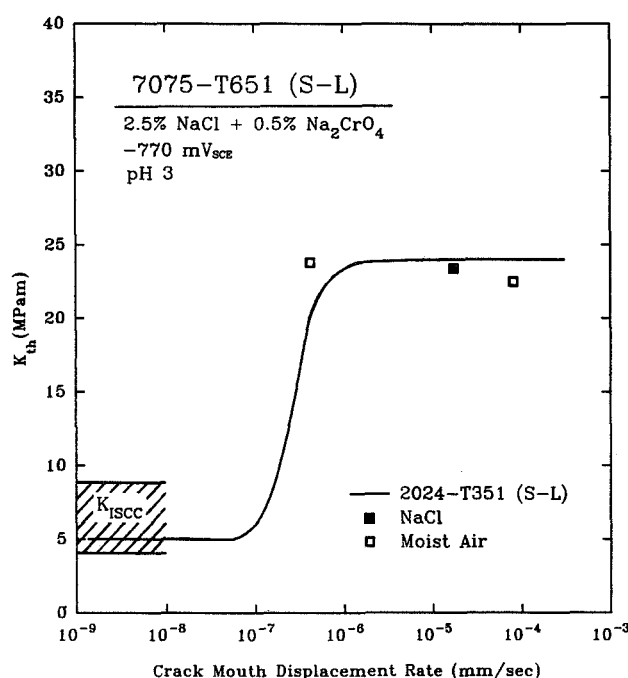


Figure 7 - K_{th} vs CMOD rate showing no decrease in K_{th} for increased CMOD rate for the 7075-T651/NaCl system.¹⁹

Da/dt , measured during the rising load NaCl experiment represented in Fig. 7, equalled 2 to 6×10^{-9} m/sec. Similar-rate rising load experiments in moist air produced an apparent da/dt of 1 to 2×10^{-9} m/sec at higher K . This result is probably due to temperature and plasticity enhanced resistivity and not subcritical crack growth. Accordingly, da/dt from the NaCl rising load experiment is essentially equal to the quasi-static load da/dt_{SCC} values presented in Fig. 5.³ Rechberger reported that da/dt varied by 3-fold compared to da/dt_{SCC} as dK/dt increased from 10^{-6} to 10^{-4} MPa \sqrt{m}/sec ; however, the precise dependence of da/dt on dK/dt was complex.¹¹ (At the highest displacement rate for chloride in Fig. 7, dK/dt equals 9×10^{-4} MPa \sqrt{m}/sec .) There is no evidence that the

- 2 The EFCP behavior of 7079 shown in Fig. 1 is modeled similarly by linear superposition;⁵ however, the reason for the several order of magnitude increase in da/dt_{SCC} is not known.²⁶
- 3 Considering the displacement rate of 2×10^{-5} mm/sec, K_{IC} is achieved in 6.5 hours. If da/dt were enhanced by 5 to 10 times above da/dt_{SCC} , sufficient to predict da/dN in Fig. 6, then between 0.4 and 0.8 mm of environmental crack growth would be produced. The complex effects of temperature and plasticity on DCPD measurements are small compared to these crack growth increments, and enhanced da/dt should be measurable.

rising load method provides crack tip strain rate-dependent da/dt values that improve superposition predictions of EFCP kinetics.

A strain rate calculation based on McMeeking's crack tip strain field indicates that the transition CMOD rate in Fig. 7 produces a $d\epsilon_{CT}/dt$ value of $3 \times 10^{-6} \text{ sec}^{-1}$ at a distance of one blunted crack tip opening ahead of the tip and at a K level of $8 \text{ MPa}\sqrt{\text{m}}$ achieved by loading over 100 hours.³⁰ If the crack surface passive film failure strain is on the order of 1%,¹⁸ then a film rupture event should occur every 3000 seconds at this strain rate and every 15 seconds at the fastest CMOD rate shown in Fig. 7. Since a clean aluminum surface is likely to fully repassivate in less than 10 seconds, the fastest displacement rate is required to begin to electrochemically destabilize the crack tip surface by repeated rupture before full repassivation. Similar lowered electrochemical activity is expected at all CMOD rates below about 10^{-4} mm/sec , equivalent to the quasi-static conditions. If repassivation is more rapid, then even faster strain rates are required to alter da/dt_{SCC} . Environmental cracking did not occur at displacement rates above about $2 \times 10^{-5} \text{ mm/sec}$ (and perhaps 10^{-7} mm/sec) because some other step in the damage sequence was presumably rate limiting, and unstable fracture dominated.³¹

Ripple Load Testing

The superposition of a small amplitude cyclic stress intensity, on a constant or slowly rising K , could destabilize mechanically the crack tip surface to enhance electrochemical activity and hence increase da/dt above da/dt_{SCC} . While Bayles and coworkers reported that 7075-T651 is susceptible to enhanced chloride cracking under high frequency, low ΔK "ripple" loading, the stress intensity amplitude employed was sufficiently large to produce process zone volume fatigue damage.³²

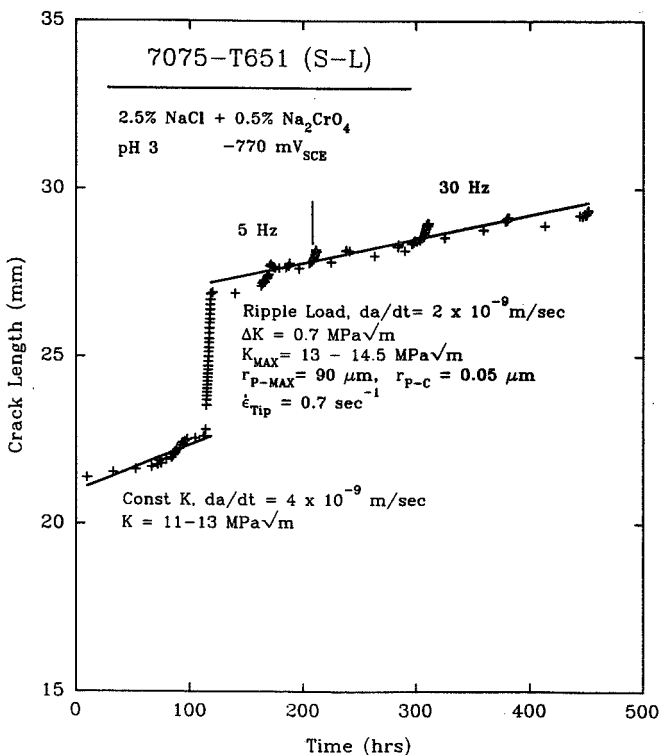


Figure 8 - Crack length vs time showing the results of a constant K (11 to 13 $\text{MPa}\sqrt{\text{m}}$) with and without applied ripple loading ($\Delta K = 0.7 \text{ MPa}\sqrt{\text{m}}$)

In an effort to separate the hypothesized surface-strain enhanced SCC from near-threshold corrosion fatigue, experiments were conducted with a very low amplitude cyclic load, with ΔK equalling $0.7 \text{ MPa}\sqrt{\text{m}}$, at a frequency of first 5 then 30 Hz. The data plotted in Fig 8 show a negligible difference between the constant stress intensity case and the addition of the low ΔK . For each case, da/dt equalled between 2 and $4 \times 10^{-9} \text{ m/sec}$. (The high rate cracking between the constant K and ripple load segments was produced by EFCP at a K_{MAX} of $13 \text{ MPa}\sqrt{\text{m}}$ and a high ΔK of $11 \text{ MPa}\sqrt{\text{m}}$.)

The average crack tip near-surface strain rate produced by the ripple load is presumed to be orders of magnitude higher than that for the constant load condition. This conclusion is based on a calculation that equates average $d\epsilon_{CT}/dt$ to the product of frequency, ΔK raised to the fourth power, and a constant defined from a continuum fracture mechanics strain field.^{1,30} Average

$d\epsilon_{CT}/dt$ equals between 0.2 sec^{-1} (5 Hz) and 1.2 sec^{-1} (30 Hz), where the critical distance over which this strain rate is calculated was assumed to equal 20% of the cyclic plastic zone diameter (calculated from $0.026 (\Delta K/\sigma_{YS})^2$). At these rapid strain rates, the crack tip passive film should rupture every 0.01 seconds, resulting in both enhanced anodic dissolution and cathodic atomic hydrogen production. This strain rate is similar to the values relevant to the lower frequency-higher ΔK EFCP conditions that are the target of linear superposition modeling.

Since the measured da/dt in Fig. 8 did not indicate an effect of the ripple load, it is likely that the continuum estimates of strain rate are low. That is, the very small scale of the crack tip cyclic deformation at ΔK of $0.7 \text{ MPa}\sqrt{\text{m}}$ precluded homogeneous dislocation plasticity sufficient to destabilize the crack tip surface. Since higher ΔK levels could produce process zone fatigue damage, in addition to surface destabilization, ripple load testing does not provide a simple means of defining da/dt for superposition modeling.

Environmental Fatigue Crack Propagation

Since simple linear superposition does not describe EFCP for an important range of frequencies, even for the SCC-susceptible 7075/NaCl system²⁰, it is necessary to predict time, ΔK and R effects on da/dN based on chemical and mechanical damage within the crack tip process zone.^{1,16,18} An element of this approach is to carefully characterize the time and loading waveform dependencies of EFCP rates, and to compare the results, particularly the variability shown in Fig. 1, to crack tip film rupture and hydrogen embrittlement damage mechanisms.

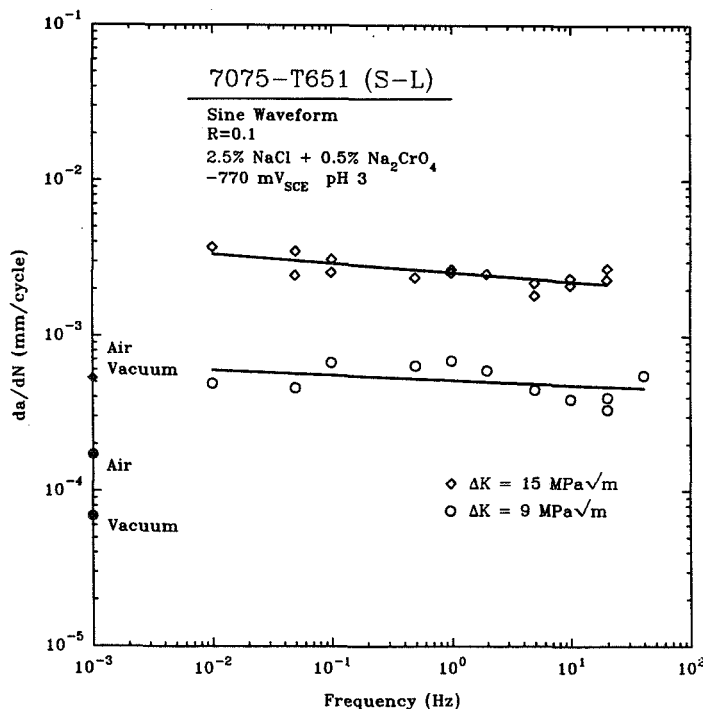


Figure 9 - Da/dN vs frequency showing results of constant ΔK (16.8 and $8.5 \text{ MPa}\sqrt{\text{m}}$) sinusoidal loading for 7075-T651/NaCl.

Effect of Sinusoidal Loading Frequency

Corrosion fatigue crack propagation rates were measured for 7075-T651 (S-L) in NaCl (FI) with sinusoidal loading at frequencies from 20 to 0.01 Hz and a constant R of 0.1. Load was computer-controlled to produce constant ΔK , with the frequency changed after each 2.5 mm of crack growth as monitored by DCPD. A single WOL specimen provided as many as eight constant ΔK segments, as illustrated by the cyclic crack length data in Fig. 3. Da/dN from least squares fits of a vs N data are plotted as a function of frequency in Fig. 9 for high (15 $\text{MPa}\sqrt{\text{m}}$) and intermediate (9 $\text{MPa}\sqrt{\text{m}}$) ΔK levels. A parallel Paris law relationship (see Fig. 12) accounted for small (less than 20%) differences in applied ΔK to obtain da/dN for comparison at a single ΔK . FCP rates for this alloy in moist air and vacuum or He²⁸ are shown to indicate the magnitude of the NaCl effect on da/dN .

EFCP rate decreases mildly with increasing frequency for both ΔK levels, with a very weak frequency dependence ($f^{-0.080}$ for $\Delta K = 15 \text{ MPa}\sqrt{\text{m}}$, $f^{-0.074}$ for $\Delta K = 9 \text{ MPa}\sqrt{\text{m}}$) observed. This result is consistent with the literature findings for 7075-T6 in Fig. 1, but is in contrast to the $f^{-1/2}$ relationship reported for 7017 and 7475.^{6,7}

Effect of Load-Hold-Time

Trapezoidal loading, with varying hold-time at constant K_{MAX} , was employed to define da/dt vs K data that were useful in predicting EFCP rates in high strength steels and nickel-based superalloys.¹³ The average time-based crack growth rate was calculated from the difference in measured da/dN at two τ_H values that differed by 100 times, coupled with linear superposition analysis of this load-time history. The implication is that the crack tip strain rates associated with cyclic loading and unloading enhance da/dt over the quasi-static da/dt_{SCC} . In this same study, 7075-T6 (L-T) in chloride exhibited no measurable enhancement of da/dN for hold-times of 0.1 sec and 10 sec.¹³

For 7075-T6 in the S-L orientation, results from corrosion fatigue experiments at two constant stress intensity ranges indicate no strong hold-time-dependence for the loading and unloading rates and times tested. Measured da/dN (e.g., Fig. 3) are plotted vs hold-time at K_{MAX} in Fig 10. Da/dN is essentially constant for relatively rapid rise/fall (t_{Rise} and $t_{\text{Fall}} = 0.025 \text{ sec}$) trapezoidal waveforms with hold times of 0.1, 5, and 50 seconds. Although mild corrosion-induced closure may account for the small fall in da/dN with increasing τ_H at the higher ΔK , this is more likely due to experimental error and the limited data. In contrast da/dN increases mildly with increasing τ_H for the lower ΔK case, consistent with the results for EFCP under sinusoidal loading (Fig. 9).

Effect of Load-Rise-Time on EFCP

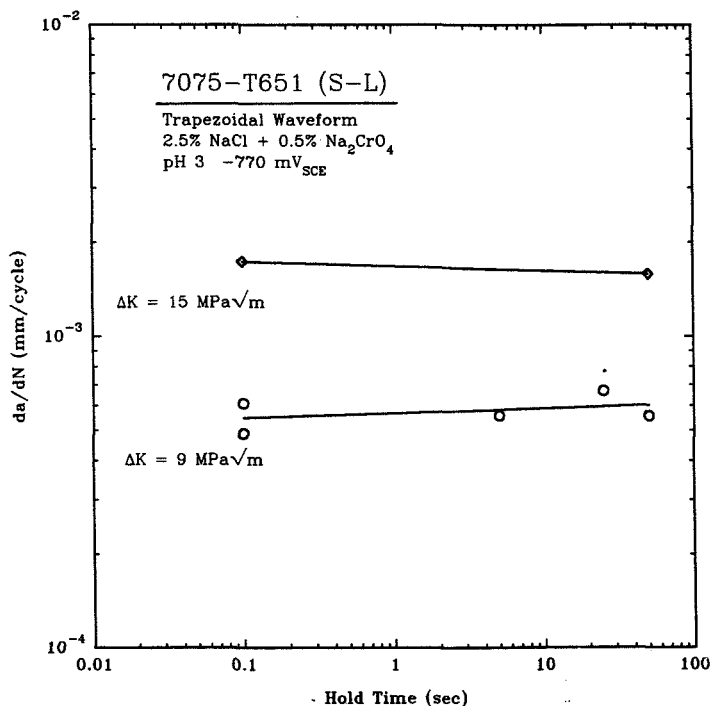


Figure 10 - Da/dN vs cycle hold time at K_{MAX} for constant applied ΔK (15, 9 $\text{MPa}\sqrt{\text{m}}$) for 7075-T651/NaCl, $R=0.1$.

Constant ΔK and R EFCP experiments were conducted with 7075-T651 (S-L) in NaCl to further examine the effect of loading rise-time (t_R) on da/dN . The results are plotted in Fig. 11 in terms of da/dN vs the rise-time to K_{MAX} for constant ΔK segments including triangular, asymmetric triangular with either a slow/fast or a fast/slow rise/fall sequence, trapezoidal (Fig. 10) and sinusoidal (Fig. 9) $K(t)$ loading functions. Small differences in applied ΔK were accounted for by the wide-range EFCP rate relationship (see Fig. 12). Least squares analyses of these data show that da/dN is proportional to t_R^λ , where λ is 0.074 (± 0.018) for ΔK of 9 $\text{MPa}\sqrt{\text{m}}$ and 0.080 (± 0.021) for ΔK of 15 $\text{MPa}\sqrt{\text{m}}$.

Since the time-dependence in Fig. 11 is weak, the constant ΔK method is well-suited to resolve the effect of increasing load rise-time. For example, the data in Fig 3 show a vs N for constant ΔK segments and two specimens. Rise-

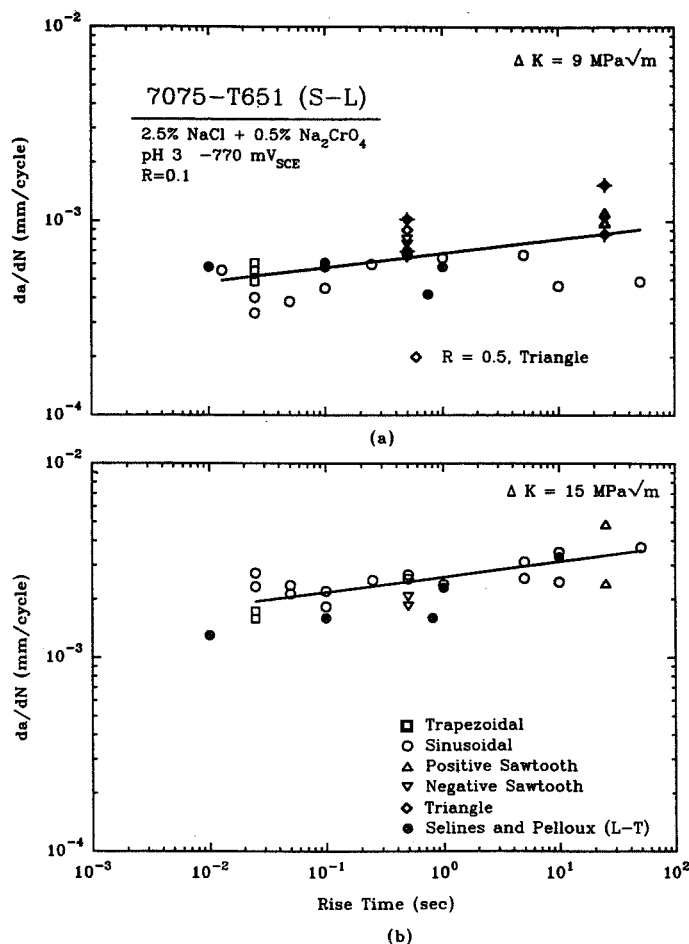


Figure 11 - EFCP da/dN vs rise time for 7075-T651: (a) $\Delta K=9$ MPa \sqrt{m} . and (b) $\Delta K=15$ MPa \sqrt{m} . L-T 7075-T6 data are from Selines and Pelloux.⁹

intrinsic effect of stress ratio on EFCP. The R of 0.5 results show the same rise time-dependence as the findings for the lower stress ratio. In all cases examined at the lower R , da/dN values were essentially equal when determined at constant ΔK , but at varying crack length and hence total solution exposure time during the experimental sequence (e.g., Fig. 3). 7075-T6 in uninhibited 3.5 wt pct NaCl solution does not show strong corrosion product induced closure effects.¹¹ Scaling da/dN data obtained at $R=0.3$ ¹¹ to $R=0.1$, using a Forman relation fit to chloride data to account for plasticity-induced crack closure, yields growth rates that are equal to the current values for inhibited acidified chloride. For this case, the Forman-predicted increase in da/dN at R of 0.3 is less than 200% because the lower slope of the chloride data compared to that for moist air produces a weaker dependency of da/dN on the crack closure function (f) and R . There is no evidence to suggest that the time-dependencies shown in Figs. 9 through 11 are influenced by time-dependent crack closure.

time is varied in the slow/fast to fast/slow sequence, while maintaining total cycle period (see + to \circ), and a decrease is noted in the crack growth rate. The results in Fig. 11 are in excellent agreement with data (\bullet) for peak-aged 7075 (L-T) orientation; da/dN is proportional to t_R raised to the 0.10 power.⁹ Ouchi et al. showed a similar dependence of da/dN on t_R , with λ equalling 0.3 for a moderate tensile strength alloy steel in NaCl.³³

Fatigue Crack Closure

The role of fatigue crack closure, specific to corrosion debris produced in the chromate inhibited chloride environment, was investigated by conducting a constant ΔK triangle waveform experiment at a load ratio of 0.5. The resulting EFCP rates are plotted (\diamond) in Fig. 11. Da/dN is increased at each rise-time by 30% in response to the increase in R from 0.1 to 0.5. Calculations using a Forman relation, fit to the moist air da/dN vs ΔK data in Fig. 12 to account for plasticity induced closure, predict a 200% increase in da/dN from R of 0.1 to 0.5 at ΔK of 9 MPa \sqrt{m} .⁴ If the lesser 30% increase in da/dN is indicative of crack closure, it is not likely due to corrosion debris. Since a substantial amount of plasticity induced closure is predicted, the result in Fig. 11 can not be interpreted based on an

4 Forman equation fit constants: $C = 5.148 \times 10^{-19}$, $n = 5.773$, $P = -21.56$, $Q = -0.2167$.

Summary

The results of all EFCP experiments with S-L 7075-T651 in aqueous chloride are summarized in Fig. 12, compared to the results of the continuous ΔK -decreasing experiment with this alloy in moist air and peak aged 7075 in inert environments.²⁸ Constant stress ratio ΔK -decreasing NaCl results at 5 Hz (Fig. 6) are represented by the smaller solid diamonds (\blacklozenge) in Fig 12 and are described by a Paris power-law relation with an exponent of 2.4, as shown by the solid line. The large symbols (\blacklozenge) for sinusoidal loading represent results from constant ΔK , variable frequency experiments (Fig. 9). The 5 Hz ΔK -decreasing results are in good agreement with the data from the various constant ΔK experiments with sinusoidal loading, as well as with the data for trapezoidal (Fig. 9) and triangular (Fig. 10) K(t) functions.

DISCUSSION

Implications for Life Prediction Modeling

The experimental results for 7075-T651 (S-L) in aqueous NaCl illustrate the complexities of describing EFCP in a fatigue life prediction code such as NASA FLAGRO. While K_{ISCC} is low, da/dt_{SCC} is slow and the simple linear superposition of this quasi-static cracking rate with da/dN_{Mech} only describes frequency, ΔK , waveform and R-value effects on da/dN for slow loading frequencies below about 0.001 Hz and rise times above 500 seconds. Strong environmental effects on da/dN are none-the-less observed for higher frequencies, as illustrated by the data in Fig. 12. From an engineering perspective, EFCP rates in this regime are frequency, waveform and rise-time

independent and are well described by the upper bound da/dN - ΔK relationship shown in Fig. 12. This bound, plus linear superposition (Fig. 6) for slow loading cycle periods could be incorporated in FLAGRO to describe the EFCP enhancement.

Various loading methods, aimed at increasing the crack tip strain rate above the static load/displacement value, and thus increasing da/dt above da/dt_{SCC} were unsuccessful. This approach does not provide improved superposition predictions of da/dN .

Comparisons between literature data and the new results in Figs. 9 through 12 show that crack orientation has no resolvable effect on EFCP in 7075-T651 for the frequency regime above 0.001 Hz. This is in contrast to the well-known effect of crack orientation on $da/dt_{SCC}(K)$.^{17,26} Specifically, the S-L results in Fig. 9 are identical to limited da/dN values

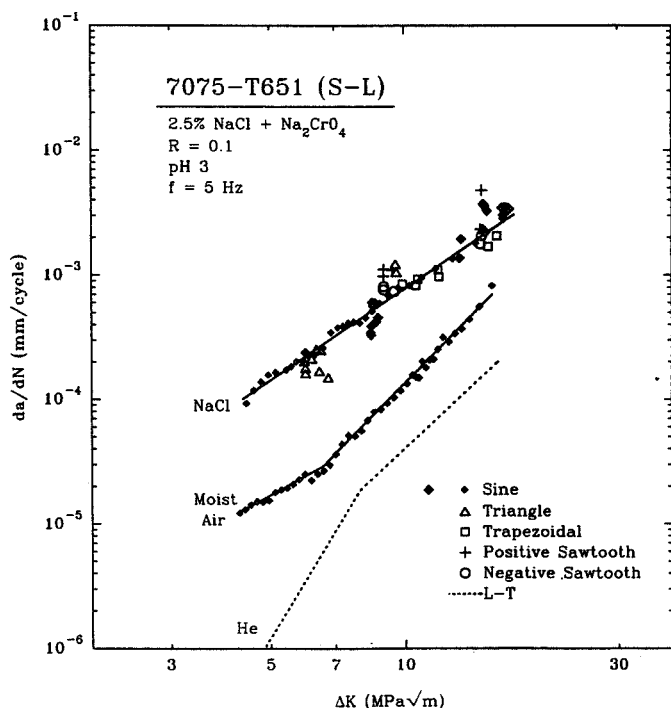


Figure 12 - EFCP data for 7075-T651/NaCl under several loading frequencies, waveforms, and ΔK control formats.

C-6

reported for 7075-T651 in the L-T orientation.^{9,13} EFCP rates for trapezoidal loading of the S-L orientation (Fig. 10) are similar to literature data on trapezoidal loading of L-T 7075-T6.¹³ The environmental effect on fatigue crack growth is identical for the S-L and T-L orientations with asymmetric triangular loading (Fig. 11).⁹ The S-T and T-L orientations of peak aged 7075 exhibit identical FCP rates at a higher stress ratio ($R=0.5$) for both inert nitrogen and aggressive chloride environments.³⁴ Since these corrosion fatigue crack growth rates are orientation-independent, it is reasonable to conclude that mildly time-cycle-(in)dependent EFCP does not occur along high angle grain boundaries which are arrayed anisotropically in 7000 series aluminum alloy microstructures. Rather, EFCP may involve more isotropic intersubgranular or brittle transgranular damage processes.

The variability in the time-dependence of da/dN shown in Fig. 1 presents an additional problem to fatigue life prediction because the factors that govern the difference in the behavior of the similar 7000 series alloys are not understood.

Implications for Mechanism-Modeling

Effect of Rising Load and Hold Time on EFCP Rate

To improve linear superposition, Wei and Gao proposed that EFCP rate is composed of three terms according to:³⁵

$$\frac{da}{dN} = \frac{da}{dN_{Mech}} + \frac{da}{dN_{CF}} + \int_{\tau} \left[\frac{da}{dt_{SCC}}(K) \right] K(t) dt \quad (3)$$

The first and third terms are analogous to the elements of linear superposition (Eq. 1), while da/dN_{CF} is the rate of time-cycle-dependent EFCP that reflects the synergism between cyclic deformation and chemical reaction. Da/dN_{Mech} and da/dN_{CF} are assumed to proceed in parallel (concurrently), with each occupying a fraction of the crack surface by an identifiable damage process, and can be more precisely stated in terms of such fractional areas.³⁵ Da/dN_{SCC} occurs in series (consecutively) by an intergranular process for 7000 aluminum alloys. The contribution of da/dN_{SCC} to the sum of the first two terms must be first defined, then the time-cycle-dependence of da/dN_{CF} must be considered based on mass transport and reaction kinetics.¹⁶

The time dependencies shown in Figs. 9 through 11 (mildly increasing da/dN with decreasing f and increasing t_{Rise}) are not explained sufficiently by superposition of da/dN_{SCC} upon time-independent environment-enhanced da/dN_{CF} . Consider the case of sinusoidal loading represented in Fig. 9 and amplified in Fig. 13. The rising portion of a 0.005 Hz load cycle should produce 1.5×10^{-4} mm of quasi-static load environmental crack advance for ΔK of 15 MPa \sqrt{m} and 2×10^{-4} mm for ΔK of 15 MPa \sqrt{m} .⁵ For the low ΔK case, da/dN equals 4.2×10^{-4} mm/cycle at 100 Hz and 6.2×10^{-4} mm/cycle at 0.005 Hz, from the trend line. Da/dN_{SCC} accounts for 75% of this EFCP rate increase. For the high ΔK , da/dN increases from 20 to 35×10^{-4} mm/cycle for this same f -range. Da/dN_{SCC} of 2×10^{-4} mm/cycle is clearly small compared to this difference. An identical conclusion is established

5 This calculation assumes that $da/dt_{SCC} = 3 \times 10^{-9}$ m/sec and $K_{ISCC} = 5$ MPa \sqrt{m} , Fig. 5.

by this analysis applied to the rise-time dependencies shown in Fig. 11. (Increasing t_R from 10^{-2} to 10^2 seconds results in da/dN increases from 5 to 9.5×10^{-4} mm/cycle and from 20 to 30×10^{-4} mm/cycle for the ΔK levels in Fig. 11.)

Interpretation of the hold-time results in Fig. 10 is complicated by limited data and experimental variability. The observed mild decrease in da/dN with increasing τ_H at the higher ΔK is consistent with the nil effect of da/dN_{SCC} . At lower ΔK , da/dN increases from 5.3 to 6.0×10^{-4} mm/cycle with increasing τ_H from 0.1 to 50 seconds. This difference is smaller than the predicted contribution from da/dN_{SCC} (1.5×10^{-4} mm/cycle). Additional experiments are required to examine the hypothesis that is suggested by these results; da/dN_{CF} is time-independent for fast-rise trapezoidal loading, and is only governed by rise time and the associated active loading rate.

The linear superposition argument also suffers from the presumption that there is some portion of intergranular SCC operating in series with EFCP. This has not been documented here or elsewhere. If the fatigue crack grows along an isotropic intersubgranular or transgranular path, then it is difficult to envision how the crack tip could involve the series operation of a high angle grain boundary path that is tens-of-microns removed from the transgranular tip. The more likely interpretation is that da/dN_{CF} is mildly frequency and rise-time dependent for 7075 in NaCl (FI) for the portion of the time-dependence in Fig. 13 where da/dN is not proportional to reciprocal f . This dependence may be understood based on the kinetics of mass transport and electrochemical reaction.¹⁶

Variability in Time-Cycle-Dependent Corrosion Fatigue of 7000 Series Aluminum Alloys

Considering time-cycle-dependent EFCP in the three 7000 series alloys represented in Fig. 13, the mild frequency dependence for 7075 is an upper bound on more strongly f -dependent growth in 7017 and 7475. This behavior is amplified in Fig. 14, a plot of the trend line from Fig. 12 with literature data for peak aged 7017 (S-L)⁶. Comparison with EFCP results for 7475 in chloride at 0.1

Hz (the lowest f reported for 7475/NaCl) gives an identical result.⁷ The behavior shown in Figs. 13 and 14 can be rationalized based on a critical EFCP rate (da/dN_{Crit}), above which growth is mass transport or reaction rate limited at a specific frequency and compared to single slope power-law behavior at lower rates (and lower ΔK). This transition is shifted to higher da/dN_{Crit} values with decreasing loading frequency and increasing exposure time. EFCP is f -independent, with da/dN equalling da/dN_{Crit} , for all frequencies below the critical value (f_{Crit})

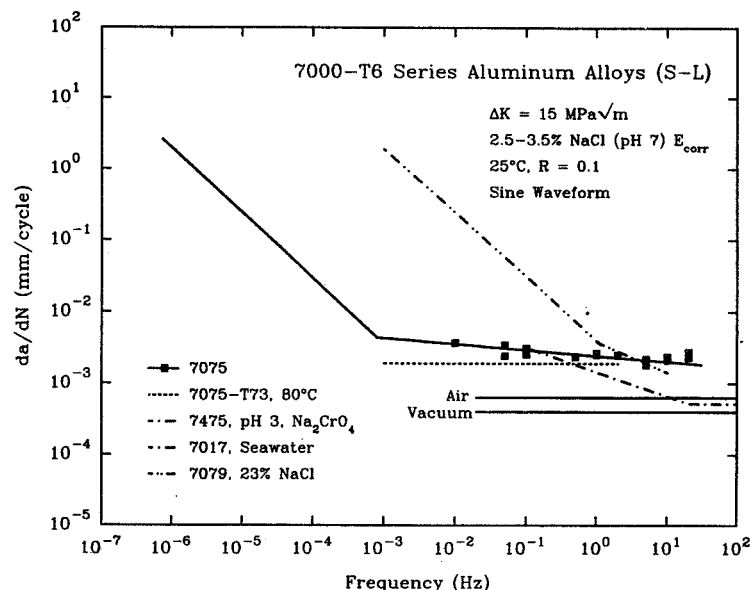


Figure 13 - Comparison of EFCP da/dN vs frequency at a constant ΔK ($15 \text{ MPa}\sqrt{\text{m}}$) for the S-L orientation of several 7000 series aluminum alloys with results for 7075-T651.

corresponding to da/dN_{Crit} .⁶ EFCP is f -dependent for faster frequencies. This interpretation is supported by fractographic observations that demonstrate a transition from brittle transgranular cracking to ductile-striated cracking, with increasing da/dN through the transition level, for both 7017 and 7475.^{6,7}

The behavior of 7075 compared to 7475 and 7017 is understood if it can be shown that da/dN_{Crit} is higher for the former alloy, at a given frequency, or that f_{Crit} for a given da/dN_{Crit} is higher relative to the fastest frequencies examined for 7075 in the current and previous studies.^{5,11} At the single ΔK level and frequencies represented in Fig. 13, 7075 is cracking in the " $below da/dN_{Crit} - f_{Crit}$ " regime, while 7017 and 7475 are in the " $above da/dN_{Crit} - f_{Crit}$ " regime. At faster frequencies, da/dN would be time-cycle-dependent for 7075. The former case involves essentially time-cycle-independent cracking ($da/dN \propto f^0$ to $f^{-0.1}$), while the latter obeys a stronger time-dependence ($da/dN \propto f^{-0.5}$).

It is difficult to develop this hypothesis because the environmental cracking mechanism is controversial, be it hydrogen environment embrittlement, film rupture/transient repassivation, or a coupling of each. Additionally, the transport plus reaction sequence that feeds these mechanisms is multi-featured.^{1,16}

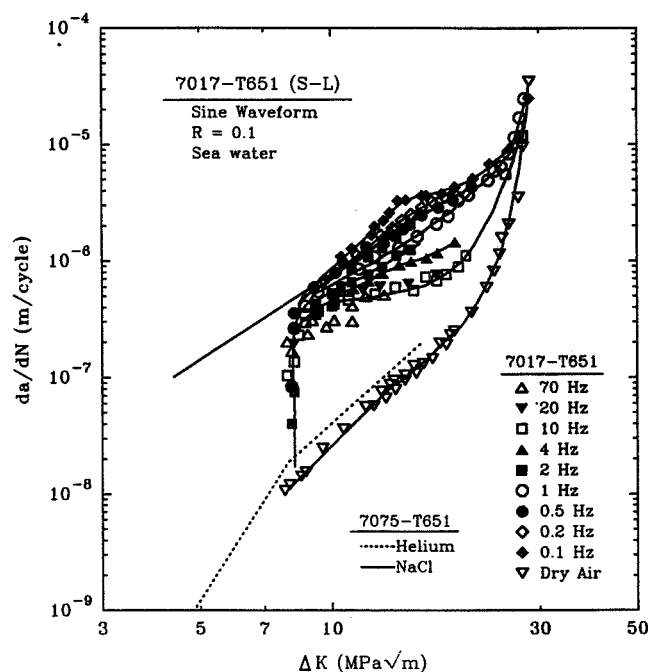


Figure 14 - Effect of ΔK on da/dN for peak aged 7075 and 7017⁶ in chloride showing upper bound, f -independent EFCP.

mechanics of process zone fatigue damage. Da/dN_{Crit} then corresponds to the growth rate at which hydrogen diffusion is just sufficient to penetrate to a critical concentration, over Δx in Δt . This relationship was formalized to predict the frequency dependence of da/dN_{Crit} .^{6,7}

$$\frac{da}{dN_{crit}} = \frac{2}{\sqrt{fN}} \sqrt{D_H} \operatorname{erf}^{-1} \left(1 - \frac{C_{Crit}}{C_s} \right) \quad (4)$$

D_H is the diffusivity of hydrogen in aluminum, be it grain boundary, lattice or dislocation transport.

6 Below f_{Crit} and da/dN_{Crit} , the results in Figs. 9 through 11 and 13 demonstrate that da/dN is mildly time-cycle-dependent.

C_{crit} is the amount of hydrogen that must be provided for cracking at the deepest point of the fatigue damage distribution within the process zone, and C_s is the concentration of the atomic hydrogen on the crack tip surface in equilibrium with the occluded crack tip solution electrochemistry. This equation predicts that da/dN_{crit} varies as $f^{-0.5}$, as would all da/dN - ΔK values above this level if simple parallel slope behavior is operative, as illustrated schematically in Fig. 15.

Green and Knott compared Eq. 4 to EFCP rates for 7475 in acidified and inhibited NaCl.⁷ Da/dN_{crit} varied with $f^{-0.5}$; these data yielded D_H of 5×10^{-9} cm²/sec and C_{crit}/C_s of 0.14, assuming per-cycle crack advance. A similar result was reported by Holroyd and Hardie for 7017 in seawater with an inferred D_H of 3×10^{-9} cm²/sec and C_{crit}/C_s of 0.3.⁶ These diffusivities are an order of magnitude faster than lattice D_H for aluminum alloys, suggesting that grain boundary or subgrain/dislocation pipeline hydrogen diffusion is important even for transgranular EFCP in these alloys.

Considering the alloy-dependence of da/dN_{crit} , higher values of this rate at fixed f are favored by increased D_H and C_s , and by decreased C_{crit} and N (Eq. 4). Speculatively, dislocation transport could increase D_H to a value as high as 5×10^{-7} cm²/sec;³⁶ da/dN_{crit} would be raised by 10-fold, or the bounding f required for rate-limited EFCP would be increased by two orders of magnitude. Frequencies on the order of 200 Hz would be required for time-cycle-dependent da/dN at moderate ΔK levels. There is no reason to implicate dislocation transport in 7075, but not in 7475 or 7017, and the notion of dislocation transport of H in aluminum alloys has been challenged.³⁷ Dislocation transport may be by enhanced pipe diffusion of hydrogen through the crack tip dislocation structure

produced by cyclic plastic deformation. This structure could be deformation mode and alloy-dependent.

Alternately, C_s could be alloy-dependent. For example, Zn or Mg could be present in varying amounts in precipitates, lattice solid solution, or segregated to grain boundaries. These elements could preferentially dissolve to enrich the crack solution in cations which in turn could increase C_s by affecting the ratio between the absorption and desorption rate constants involved in H production on the crack surface.⁷ A surface film enriched in a segregant could also affect such a change. Mg segregation to grain boundaries in 7000 series aluminum alloys has been documented.³⁸⁻⁴⁰ Cation effects on electrochemistry, and surface film effects on H entry, have not been substantiated by either crack chemistry measurements or permeation experiments with aluminum alloys. Alternately, Anyalebechi demonstrated that C_s in aluminum is enhanced by solid solution elements such as Li;⁴¹

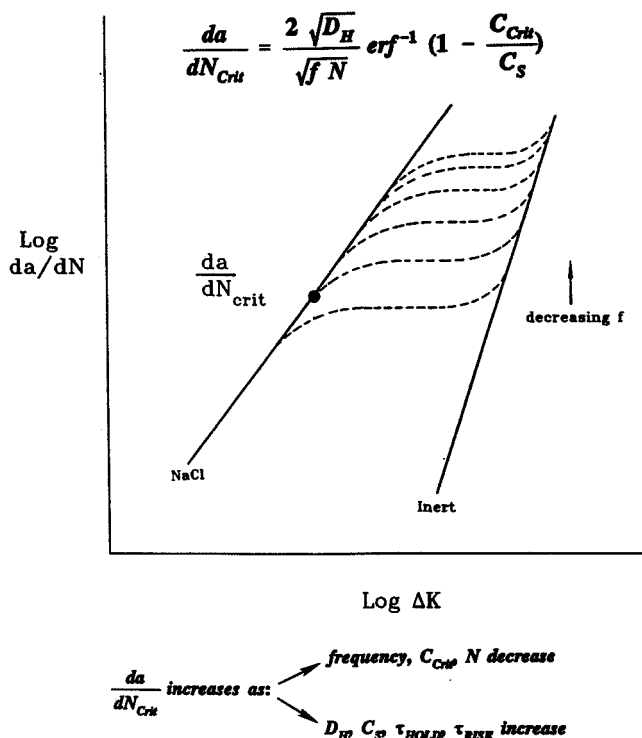


Figure 15 - Schematic EFCP da/dN vs ΔK showing the f dependence of da/dN and da/dN_{crit} .

the role of Mg in this regard is unclear. C_{crit} depends on the structure and local strength of the sites of hydrogen-enhanced fatigue damage. It is unknown how this concentration varies with alloy microstructure and cyclic deformation processes.

Similar arguments for the variability in the frequency dependence of EFCP rates in 7000 series aluminum alloys could be suggested based on alloy effects on surface reaction kinetics,^{16,38,42} particularly if the crack tip surface is filmed and competitively bared by strain. Explanations based on crack solution mass transport control are not apparent because of uncertainties in the molecules and ions that rate limit surface reactions. The problem is complex and any explanation is speculative. Measurements of crack chemistry, hydrogen production and passivation kinetics are required to define the composition and microstructural features of 7000 series alloys that determine whether EFCP rate is time-independent, time-cycle dependent, or time-dependent.

CONCLUSIONS

1. Fatigue crack propagation rates for 7075-T651 (S-L orientation) in chromate inhibited, acidified NaCl solution are enhanced five to ten-fold over rates in moist air and are over an order of magnitude faster compared to cracking in helium.
2. Measured time-based crack growth rates for 7075-T651 (S-L), subjected to quasi-static load or displacement, are an order of magnitude too small to predict the effect of NaCl on FCP rates for loading frequencies above 0.001 Hz and by linear superposition.
3. Alternate methods of establishing da/dt , based on enhanced crack tip strain rate, do not provide a means of enabling linear superposition modeling of EFCP in peak-aged 7075/NaCl. Imposed constant crack mouth opening displacement rate does not accelerate da/dt . Da/dt is not enhanced by high frequency-low amplitude cyclic loading, designed to increase crack tip surface strain rate, in conjunction with a high sustained stress intensity.
4. Crack propagation rates for corrosion fatigue of 7075-T651 (S-L) in NaCl show two regimes of frequency dependence; da/dN is proportional to f^{-1} below 0.001 Hz and proportional to $f^{-\lambda}$, where λ is between 0 and 0.1, for f above 0.001 Hz. Da/dN and da/dN_{CF} increase mildly with increasing rise-time for a range of loading waveforms but may not depend on hold-time at K_{MAX} . The strong frequency dependence is modeled based on simple linear superposition, while the mild time-dependence is due to cycle-time-dependent corrosion fatigue.
5. The NaCl environmental effect on time-cycle-dependent fatigue crack growth is identical for the S-L and L-T orientations of peak aged 7075, suggesting a minimal involvement of anisotropic high angle grain boundaries.
6. The frequency response of EFCP in 7000 series alloys is variable and depends on an undefined compositional or microstructural variable. Crack solution cations, from segregant or a second phase in the alloy, could alter hydrogen production kinetics, or H diffusion within the crack tip process zone could vary based on dislocation and grain boundary

processes. High hydrogen production/uptake and rapid hydrogen diffusion favor f-independent cracking persisting to higher frequencies and crack growth rates.

7. EFCP in the 7075/NaCl system is adequately described for computer life prediction by linear superposition for long load-cycle periods, and by a time-independent upper bound relationship between da/dN and ΔK for moderate frequencies and load rise-times.

ACKNOWLEDGEMENTS

This research was supported by the Mechanics of Materials Branch at the NASA Langley Research Center, under Grant No. NAG-745-1, with R.S. Piascik and J.C. Newman, Jr. as technical monitors. AA7075 was provided by E.A. Colvin of the Alcoa Technical Center. E. Richey contributed experimental results. This support is gratefully acknowledged. The need to incorporate environmental effects into NASA FLAGRO was suggested by R.G. Forman at the NASA-Johnson Space Flight Center.

REFERENCES

1. Gangloff, R. P.: Corrosion Fatigue Crack Propagation in Metals. in *Environment-Induced Cracking of Metals Proceedings*, Gangloff, R. P. and Ives, M. B., eds, NACE, Houston, TX, 1990, pp. 55-109.
2. Feeney, J. A.; McMillan, J. C.; and Wei, R. P.: Environmental Fatigue Crack Propagation of Aluminum Alloys at Low Stress Intensity Levels. *Metall. Trans. A*, vol. 1, 1970, pp. 1741-1757.
3. Forman, R. G.; Shivakumar, V.; Newman, J. C.; and Piotrowski, S. M.; and Williams, L. C.: Development of the NASA/FLAGRO Computer Program in *Fracture Mechanics: 18th Symposium, ASTM STP 945*, ASTM, Philadelphia, PA, 1988, pp. 781-803.
4. Gangloff, R. P.; Piascik, R. S.; Dicus, D. L.; and Newman, J. C.: Fatigue Crack Propagation in Aerospace Aluminum Alloys. *Journal of Aircraft*, vol. 31, 1994, pp. 720-729.
5. Speidel, M. O.: Stress Corrosion and Corrosion Fatigue Crack Growth in Aluminum Alloys. in *Stress Corrosion Research*, Arup, H.; and Parkins, R. N., eds., Sijthoff & Noordhoff, Alphen aan den Rijn, Netherlands, 1979, pp. 117-176.
6. Holroyd, N. J. H.; and Hardie, D.: Factors Controlling Crack Velocity in 7000 Series Aluminum Alloys During Fatigue in an Aggressive Environment. *Corrosion Science*, vol. 23, 1983, pp. 527-546.

7. Green, A. M.; and Knott, J. F.: Effects of Environment and Frequency on the Long Fatigue Crack Growth of Aluminum Alloy 7475. in *Advances in Fracture Research*, Salama, K.; Ravi-Chandar, K.; Taplin, D. M. R.; and Rao, R. P., eds., Pergamon Press, Oxford, UK, 1989, pp. 1747-1756.
8. Baldantoni, A.; Wallace, W.; Raizenne, M. D.; and Dickson, J. Y.: The NRC Contribution to the FACT Programme. in *The Fatigue in Aircraft Corrosion Testing (FACT) Programme*, Wanhill, R. J. H.; De Luccia, J. J.; and Russo, M. T., eds., AGARD Report No. 713, NATO, 1985, pp. 162-173.
9. Selines, R. J.; and Pelloux, R. M.: Effect of Cyclic Stress Wave Form on Corrosion Fatigue Crack Propagation in Al-Zn-Mg Alloys. *Metall. Trans. A*, vol. 3, 1972, pp. 2525-2531.
10. Kim, Y. H.; and Manning, S. D.: A Superposition Model for Corrosion-Fatigue Crack Propagation in Aluminum Alloys. in *Fracture Mechanics: Fourteenth Symposium - Volume 1: Theory and Analysis, ASTM STP 791*, Lewis, J. C.; and Sines, G., eds., American Society for Testing and Materials, Philadelphia, PA, 1983, pp. 446-462.
11. Rechberger, J.: *The Transition from Stress Corrosion Cracking to Corrosion Fatigue in AA-7075 and AA-8090*. Ph.D. Dissertation, University of British Columbia, Vancouver, Canada, 1989.
12. Barsom, J. M.: Effect of Cyclic Stress Form on Corrosion Fatigue Crack Propagation Below K_{ISCC} In a High Yield Strength Steel. in *Corrosion Fatigue, Chemistry, Mechanics, and Microstructure*, Devereaux, O.; McEvily, A. J.; and Staehle, R. W., eds., NACE, Houston, TX, 1972, pp. 424-436.
13. Dill, H. D.; and Saff, C. R.: *Environment-Load Interaction Effects on Crack Growth*. AFFDL-TR-78-137, McDonnell Douglas Corp., St. Louis, MO, 1978.
14. Larsen, J. M.; and Nicholas, Theodore: Cumulative Damage Modeling of Fatigue Crack Growth. in *AGARD Advisory Group for Aerospace Research and Development, Conference Proceedings No. 368*, NATO, 1987.
15. Wei, R. P.; and Landes, J. D.: Correlation Between Sustained-Load and Fatigue Crack Growth in High-Strength Steels. *Materials Research and Standards*, vol. 9, 1969, pp. 25-27, 44-48.
16. Wei, R. P.; and Gangloff, R. P.: Environmentally Assisted Crack Growth in Structural Alloys: Perspectives and New Directions. in *Fracture Mechanics: Perspectives and Directions, ASTM STP 1020*, Wei, R. P.; and Gangloff, R. P., eds., ASTM, Philadelphia, PA, 1989, pp. 233-264.
17. Speidel, M. O.: Stress Corrosion Cracking of Aluminum Alloys. *Metall. Trans. A*, vol. 6A, 1975, pp. 631-651.

18. Ford, F. P.: The Crack-Tip System and Its Relevance to the Prediction of Cracking in Aqueous Environments. in *Environment-Induced Cracking of Metals*, Gangloff, R. P.; and Ives, M. B., eds., NACE, Houston, TX, 1988, pp. 139-165.
19. Dietzel, W.; Schwalbe, K. H.; and Wu, D.: Application of Fracture Mechanics Techniques to the Environmentally Assisted Cracking of Aluminum 2024. in *Fatigue and Fracture of Engineering Materials and Structures*, vol. 12, 1989, pp. 495-510.
20. Colvin, E. L.; and Emptage, M. R. (1991), The Breaking Load Method. in *New Methods for Corrosion Testing of Aluminum Alloys*, ASTM STP 1134, Agarwala, V. S.; and Ugiansky, G. M., eds., ASTM, Philadelphia, PA, 1992, pp. 82-100.
21. Saxena, A.; and Hudak, S. J., Jr.: Review and Extension of Compliance Information for Common Crack Growth Specimens. *Int. J. of Frac.*, vol. 14, No. 5, 1978, pp. 453-468.
22. Standard Test Method for Measurement of Fatigue Crack Growth Rates. Designation E647-91 in *1991 Annual Book of ASTM Standards*, ASTM, Philadelphia, PA, pp. 674-701, 1991.
23. Donald, J. K.; and Ruschau, J.: Direct Current Potential Difference Fatigue Crack Measurement Techniques. in *Fatigue Crack Measurement: Techniques and Applications*, Marsh, K. J.; Smith, R. A.; and Ritchie, R. O., eds., EMAS, Ltd., West Midlands, UK, 1991, pp. 11-37.
24. Thompson, J. J.; Tankins, E. S.; and Agarwala, V. S.: A Heat Treatment for Reducing Corrosion and Stress Corrosion Cracking Susceptibilities in 7XXX Aluminum Alloys. *Materials Performance*, vol. 26, No. 6, 1987, pp. 45-52.
25. Le, A. H.; and Foley, R. T.: Stress Corrosion Cracking of 7075-T651 in Various Electrolytes - Statistical Treatment of Data Obtained Using DCB Precracked Specimens. *Corrosion Science*, vol. 39, No. 10, 1983, pp. 379-383.
26. Holroyd, N. J. H.: Environment-Induced Cracking of High-Strength Aluminum Alloys. in *Environment-Induced Cracking of Metals*, Gangloff, R. P.; and Ives, M. B., eds., NACE, Houston, TX, 1988, pp. 311-345.
27. Domack, M. S.: Evaluation of K_{ISCC} and da/dt Measurements for Aluminum Alloys Using Precracked Specimens. in *Environmentally Assisted Cracking: Science and Engineering ASTM STP 1049*, Lisagor, W. B.; Crooker, T. W.; and Leis, B. N., eds., ASTM, Philadelphia, PA, 1990, pp. 391-409.
28. Piascik, R. S.; and Gangloff, R. P.: Environmental Fatigue of an Al-Li-Cu Alloy: Part I. Intrinsic Crack Propagation Kinetics in Hydrogenous Environments. *Metall. Trans. A*, vol. 22A, 1991, pp. 2415-2428.
29. Richey, E., III; Wilson, A. W.; Pope, J. M.; and Gangloff, R. P., *Computer Modeling the Fatigue Crack Growth Rate Behavior of Metals in Corrosive Environments*, University of Virginia Report, Charlottesville, VA, in press, 1994.

30. Young, L. M.: *Environment Assisted Cracking in Beta-Titanium Alloys*. MS Thesis, University of Virginia, Charlottesville, VA, 1993.
31. Holroyd, N. J. H.; and Hardie, D.: Strain-Rate Effects in the Environmentally Assisted Fracture of a Commercial High-Strength Aluminum Alloy (7049). *Corrosion Science*, vol. 21, 1981, pp. 129-144.
32. Bayles, B. A.; Pao, P. S.; Gill, S. J.; and Yoder, G. R.: Ripple-Load Cracking in Three Alloys Systems. in *Systems Engineering Approach to Mechanical Failure Prevention*, Pusey, H. C.; and Pusey, S. C., eds., Vibration Institute, Willowbrook, IL, 1993, pp. 167-176.
33. Ouchi, H.; Kobayashi, J.; and Soya, I.: Formulation of Stress Waveform and Frequency Effects on Fatigue Crack Growth Rates in Steel Immersed in Seawater. Nippon Steel Corporation, Kanagawa, Japan, Unpublished Report, 1988.
34. Santner, J. S.; and Kumar, M.: Corrosion-Fatigue Crack Propagation Rates in Commercial 7075 and P/M X7091 Aluminum Alloys. in *Corrosion Fatigue: Mechanics, Metallurgy, Electrochemistry, and Engineering ASTM STP 801*, Crooker, T. W.; and Leis, B. N., eds., ASTM, Philadelphia, PA, 1983, pp. pp. 229-255.
35. Wei, R. P.; and Gao, M.: Reconsideration of the Superposition Model for Environmentally Assisted Fatigue Crack Growth. *Scripta Metall.*, vol. 17, 1983, pp. 959-962.
36. Albrecht, J.; Bernstein, I. M.; and Thompson, A. W.: Evidence for Dislocation Transport of Hydrogen in Aluminum. *Metall. Trans. A*, vol. 13A, 1982, pp. 811-819.
37. Watson, James W.; and Meshii, M.: Hydrogen Transported by Dislocations in Aluminum Alloys. in *Hydrogen Effects on Material Behavior*, Moody, N. R.; and Thompson, A. W., eds., TMS-AIME, Warrendale, PA, 1990, pp. 241-248.
38. Wei, R. P.; Gao, Ming; and Pao, P. S.: The Role of Magnesium in CF and SCC of 7000 Series Aluminum Alloys. *Scripta Metall.*, vol. 18, 1984, pp. 1195-1198.
39. Holroyd, N. J. H.; and Scamans, G. M.: The Role of Magnesium During Environment-Sensitive Fracture of Aluminum Alloys. *Scripta Metall.*, vol. 19, 1985, pp. 915-916.
40. Shastry, C. R.; Levy, M.; and Joshi, A.: The Effect of Solution Treatment Temperature on Stress Corrosion Susceptibility of 7075 Aluminum Alloy. *Corrosion Science*, vol. 21, 1981, pp. 673-688.
41. Anyalebechi, P. N.; Talbot, D. E. J.; and Granger, D. A.: Hydrogen Solution in Al-Li Alloys. in *Light-Weight Alloys for Aerospace Applications*, Lee, E. W.; Chia, E. H.; and Kim, N. J., eds., TMS-AIME, Warrendale, PA, 1989, pp. 249-270.
42. Gao, M.; Pao, P. S.; and Wei, R. P.: Chemical and Metallurgical Aspects of Environmentally Assisted Fatigue Crack Growth in 7075-T651 Aluminum Alloy. *Metall. Trans. A*, vol. 19A, 1988, pp. 1739-1750.

ANALYSIS OF SMALL CRACK BEHAVIOR FOR AIRFRAME APPLICATIONS

R. C. McClung, K. S. Chan, S. J. Hudak, Jr., and D. L. Davidson
Southwest Research Institute
San Antonio, Texas

348669
531-39
23125
P-19

ABSTRACT

The small fatigue crack problem is critically reviewed from the perspective of airframe applications. Different types of small cracks—microstructural, mechanical, and chemical—are carefully defined and relevant mechanisms identified. Appropriate analysis techniques, including both rigorous scientific and practical engineering treatments, are briefly described. Important materials data issues are addressed, including increased scatter in small crack data and recommended small crack test methods. Key problems requiring further study are highlighted.

INTRODUCTION

"Small" fatigue cracks are sometimes observed to grow faster than traditional "large" cracks at the same nominal value of the cyclic crack driving force, ΔK . Small cracks have also been observed to grow at non-negligible rates when the nominal applied ΔK is less than the threshold value, ΔK_{th} , determined from traditional large crack test methods. These phenomena imply that a structural life assessment based on large crack analysis methods can be nonconservative if the life is dominated by small crack growth.

Although the earliest documentation of the small crack effect was motivated by aircraft applications [1], small cracks have historically not been an important issue for most airframe structures. Classic damage tolerance analysis (DTA) typically mandates an initial flaw size beyond the small flaw regime, and other structural integrity assessments based on safe-life logic neglect explicit fatigue crack growth (FCG) arguments altogether.

However, ongoing developments in the airframe industry appear to be increasing the significance of small cracks for fracture control of aircraft structures. It is now recognized that multiple small flaws associated with multiple-site damage (MSD) can degrade residual strength capability in aging aircraft [2, 3]. In response to this observation, the Industry Committee on Widespread Fatigue Damage (WFD) of the Airworthiness Assurance Working Group (AAWG) has recently identified small cracks as a critical issue requiring further focused research [4]. In applications where durability analyses are employed, the equivalent initial flaw size (EIFS) which is back-calculated from some economic total life is often well within the small flaw regime [5]. Ongoing improvements in non-destructive evaluation (NDE) capabilities may lead to the re-definition of initial flaw sizes for traditional DTA which are down in the small flaw regime. And in some applications, structural integrity assessments formerly based on safe-life calculations now must be performed with DTA logic. The relevant crack sizes for these applications, however, are often much smaller than those historically associated with the DTA method.

The purpose of this paper is to provide a critical overview of the small crack problem in the context of airframe applications. Different types of small cracks are carefully defined and relevant mechanisms identified. Appropriate analysis techniques, including both rigorous scientific and practical engineering treatments, are briefly described. Important materials data issues are addressed,

including increased scatter in small crack data and recommended small crack test methods. Key problems requiring further study are highlighted. Although this paper does provide an expert review of the small crack problem, it is not intended to be an exhaustively complete summary of all important research in the field. Many researchers have contributed to the level of understanding outlined in this paper, and it is not possible or attempted to acknowledge all of them individually.

DIFFERENT TYPES OF SMALL CRACKS

All small cracks are not the same. Different mechanisms are responsible for different types of "small crack" effects in different settings. Criteria which properly characterize small crack behavior in one situation may be entirely inappropriate in another situation. It is critical, therefore, to understand the different types of small cracks before selecting suitable analytical treatments. This review will consider three different types of small cracks: microstructurally-small, mechanically-small, and chemically-small.

Before beginning, one note on nomenclature is needed. The terms "small crack" and "short crack" both appear in the literature, and sometimes the two appear to be used interchangeably. In recent years, however, the two terms have acquired distinct meanings among many researchers. In the US research community, the currently accepted definition for a "small" crack requires that all physical dimensions (in particular, both the length and depth of a surface crack) are small in comparison to the relevant length scale. In contrast, a crack is defined as being "short" when only one physical dimension (typically, the length of a through-crack) is small in comparison to the length scale. These definitions are illustrated in Figure 1. However, it should be noted that this distinction has not always been observed in the literature, and that some current authors (esp. in Europe) choose to employ the terms with nearly reverse meanings. Whatever the usage, the reader should carefully observe which type of "little" crack is present in a given application. Some of the different implications of short vs. small cracks are discussed later in the paper.

Microstructurally-Small Cracks

A crack is generally considered to be microstructurally-small when all crack dimensions are small in comparison to characteristic microstructural dimensions. The relevant microstructural feature which defines this scaling may change from material to material, but the most common microstructural scale is the grain size. The small crack and its crack tip plastic zone may be embedded completely within a single grain, or the crack size may be on the order of a few grain diameters.

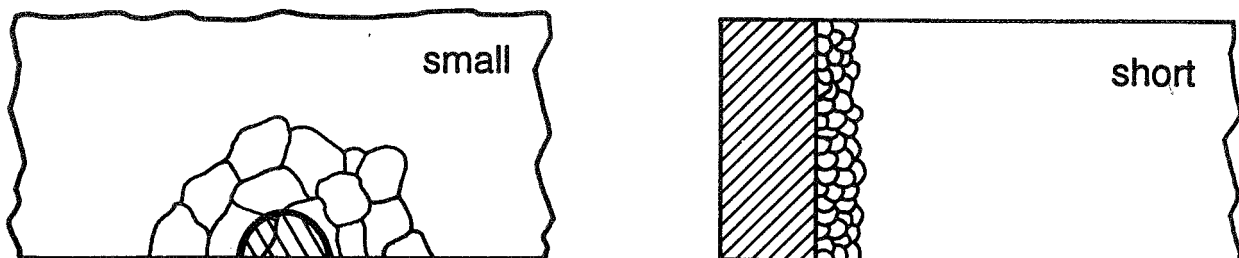


Figure 1. Schematic of "small" and "short" cracks, including relationship to microstructure.

Typical crack growth data for microstructurally-small cracks are shown for a 7075 aluminum alloy in Figure 2, along with traditional large crack data for the same material [6]. Note that small crack growth can occur at nominal ΔK values below the large crack threshold. Small crack growth rates are often faster than would be predicted by the large crack Paris equation (the dashed line in Figure 2), and the apparent Paris slope for the small crack data can be smaller than for the large crack data. Crack arrest (momentary or permanent) can occur at these low ΔK values, and this arrest is often observed to occur when the crack size, a , is on the order of the grain size, GS (i.e., when the crack tip encounters a grain boundary). However, not all small cracks arrest or even slow down at these microstructural barriers. As the crack continues to grow, the small crack da/dN data often merge with large crack data.

Why do microstructurally-small cracks behave this way? Several factors are involved, all related to the loss of microstructural and mechanical similitude. When the crack-tip cyclic plastic zone size, r_p^c , (and sometimes the crack itself) is embedded within the predominant microstructural unit (e.g., a single grain), the crack-tip plastic strain range is determined by the properties of individual grains and not by the continuum aggregate. The growth rate acceleration of small cracks embedded within a single surface grain is primarily due to enhancement of the local plastic strain range resulting from a lower yield stress for optimum slip in the surface grains [7, 8, 9]. This microplastic behavior also causes (and, in turn, is affected by) changes in crack closure behavior [10].

As a small crack approaches a grain boundary, the fatigue crack may accelerate, decelerate, or even arrest, depending on whether or not slip propagates into the contiguous grain [7]. The transmission of slip across a grain boundary in turn depends on the grain orientation, the activities of secondary and cross slip, and the planarity of slip. The transition of the small crack from one grain to another may require a change in the crack path, which may also influence crack closure. The resulting crack growth behavior is therefore very sensitive to the crystallographic orientation and properties of individual grains located within the cyclic plastic zone. As the crack grows, the number of grains interrogated by the crack-tip plastic zone increases and the statistically-averaged material properties become smoother.

However, it is important to note that the fundamental mechanism of crack growth is the same for small and large cracks in the near-threshold regime. In both cases, FCG occurs as an intermittent process involving strain range accumulation and incremental crack extension, followed by a waiting period during which plastic strain range reaccumulates at the crack tip [11]. Fatigue striations of equivalent spacing have been observed on the fracture surfaces of both large and small fatigue cracks tested under equivalent nominal ΔK ranges, as shown in Figure 2 for 7075 Al [11]. The essential difference between large and small cracks is that the number of fatigue cycles per identical striation is less for small cracks, due to differences in the local crack driving force.

How can the behavior of microstructurally-small cracks be modeled/predicted analytically? Several different approaches have been developed, ranging from detailed scientific models to simplified engineering treatments. At one extreme, complex micromechanical models attempt to address directly the changes in the local crack driving force. For example, a model derived by Chan and illustrated in Figure 3 incorporates microplastic grains ahead of a Barenblatt-Dugdale crack [7]. The nominal ΔK is modified by influence functions which explicitly describe the effects of microplastic/macroplastic yield strength, large scale yielding at the crack tip, and crack closure.

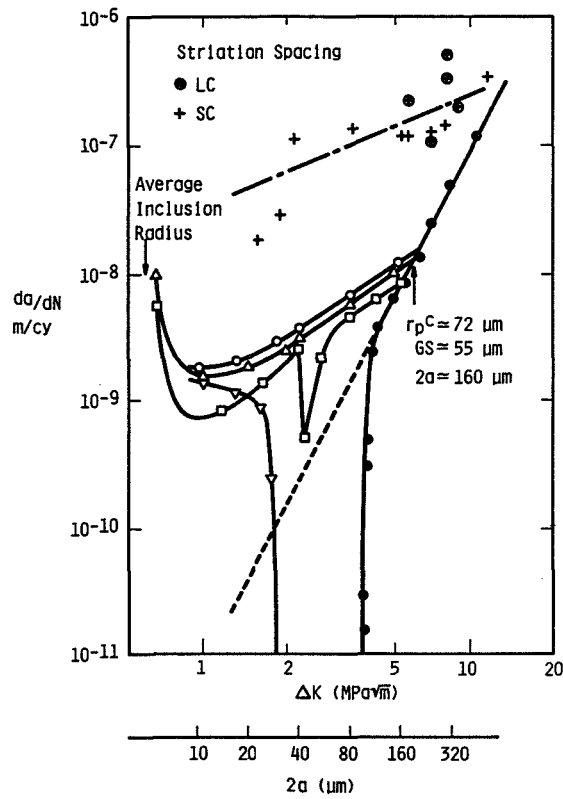


Figure 2. FCG data for 7075 Al, comparing crack growth rates and striation spacings for large cracks and microstructurally-small cracks.

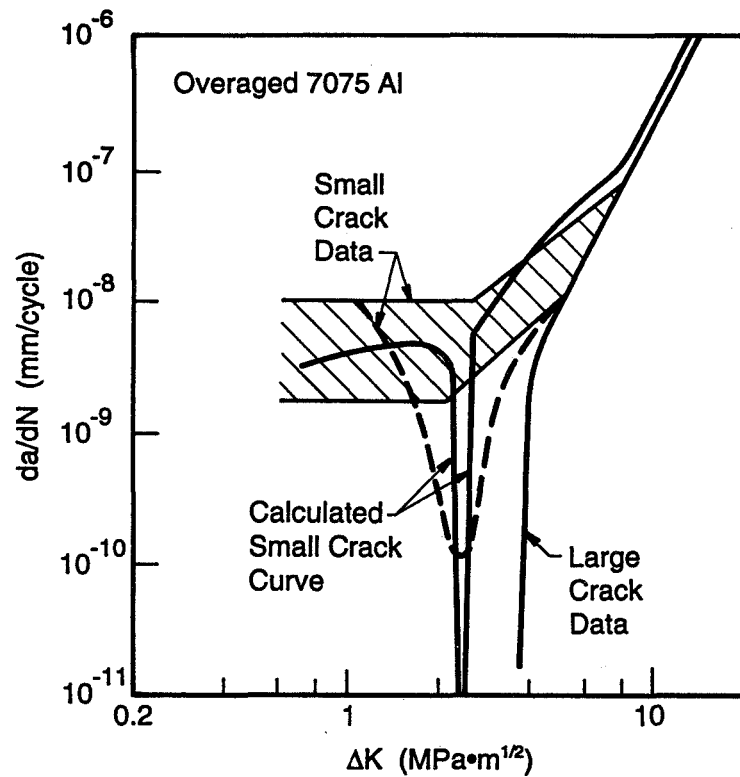


Figure 3. Predictions of a micromechanical model for microstructurally-small cracks.

Detailed experimental measurements of near-tip strains and displacements have suggested a general phenomenological model for microstructurally-small cracks which has been successfully applied to both engine disc and airframe alloys [12, 13]. Small crack growth rates were satisfactorily correlated with large crack data using a parameter $\Delta K_{eq} = (E \Delta J)^{1/2} = (E \Delta \sigma \delta_r)^{1/2}$, where the crack tip stress range $\Delta \sigma$ was calculated from the measured crack-tip strain range and δ_r is the cyclic crack-tip opening displacement. The parameter ΔK_{eq} was found to be simply related to the applied ΔK according to the expression $\Delta K_{eq} = \Delta K_p + U \Delta K$, where ΔK_p characterizes the plastic contribution to the crack driving force for small cracks and U is the effective stress range ratio which characterizes crack closure: $U = \Delta K_{eff} / \Delta K$. See Figure 4. Note that crack closure alone was not able to correlate the small crack data.

Simpler mechanical treatments have also been proposed to address FCG behavior in the microstructurally-small crack regime. The attractive simplicity of these models is that they avoid dealing directly with complex microstructural issues. Small crack acceleration effects are incorporated through simple modifications to mechanical parameters in the expression for the crack driving force. One such approach is that of El Haddad et al. [14], who replaced the actual crack length a by an effective length $a + a_0$ in order to calculate ΔK . This enhances the predicted crack growth rate when a is very small. A much more sophisticated approach has been developed by Newman [15]. The Newman model is based on computed changes in plasticity-induced crack closure for small cracks growing out of initiation sites simulated as micronotches. Newman has shown reasonably good success in predicting small crack growth rates and total fatigue lives for several different materials, including airframe alloys. These practical successes are encouraging, but it should be remembered that the simple mechanical treatments do not address the most fundamental causes of the microstructurally-small crack effect. Hence, the generality of the models cannot be assured.

Two other types of approaches, summarized in Figure 5, may be useful for some engineering applications in which it is not possible or practical to address changes in the driving force explicitly. *Stochastic treatments* which acknowledge the inherent uncertainties associated with microstructurally-small crack growth could address this uncertainty through appropriate statistical techniques. Formulation and calibration of these techniques would require extensive analysis of statistical-quality small crack data, which is a limitation. Variability of small-crack data is discussed further below. *Empirical engineering treatments* may be conservative bounding approaches which simply draw some upper bound to the crack growth data in the defined small-crack regime and use that bound as part of a total life computation, or fitting approaches which perform regression on small-crack data to generate a new set of Paris equation constants. These engineering treatments may be a useful means of avoiding detailed analysis, especially when small-crack data are available for materials and load histories representative of service conditions.

Based on these observations and models, several practical suggestions can be offered to predict growth rates for microstructurally-small cracks. In general, it appears that the large-crack Paris equation can be extrapolated downward at least to some microstructural limit. This limit is often estimated as about 5-10 grain diameters [16, 17, 18], or as the point at which the cyclic plastic zone size equals the grain size [16], although the actual limit is probably a more complex function of microplasticity and closure behavior [12]. The large-crack threshold should be neglected in this extrapolation. Some treatment of nominal plasticity and crack closure effects on the crack driving force (discussed at more length in the next section) is often useful to improve agreement with large crack data. However, it must be emphasized that some nonconservatism may remain if the true local microstructural effects have not been addressed. Guidance for addressing these effects can be obtained from various scientific approaches, although practical considerations may dictate the use of more general engineering approaches.

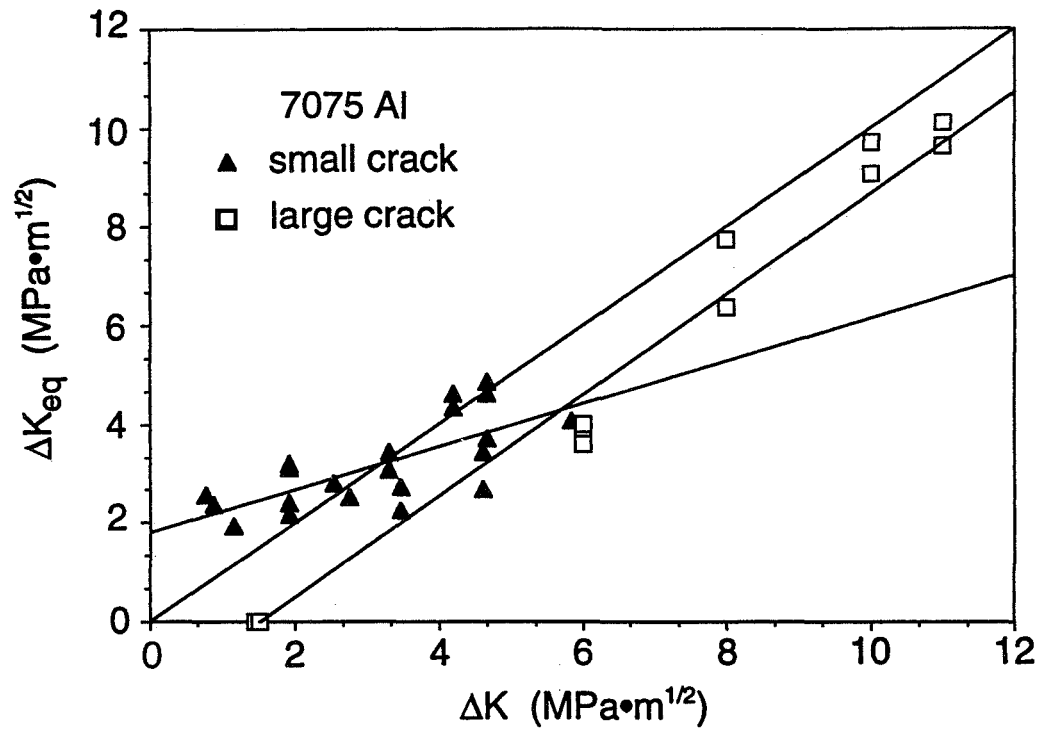


Figure 4. Comparison of ΔK_{eq} and nominal ΔK for large and small fatigue cracks in 7075 Al.

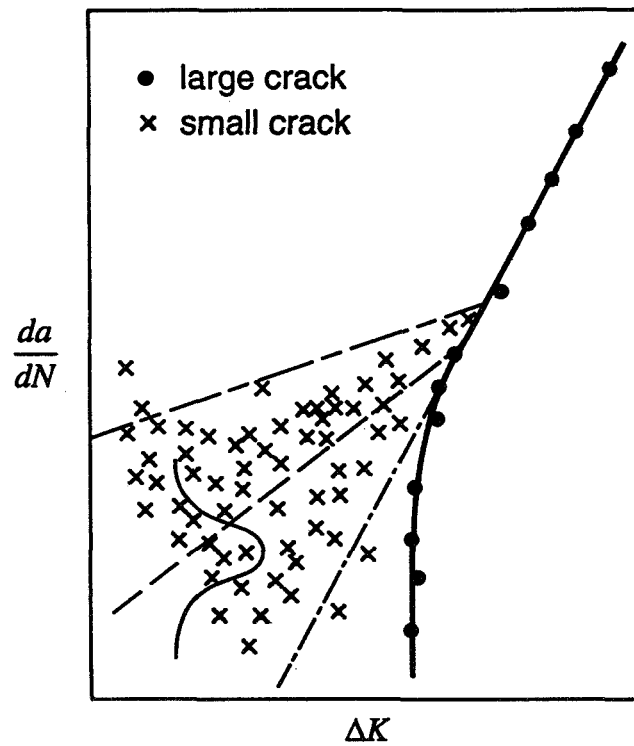


Figure 5. Schematic of potential stochastic and empirical engineering models for microstructurally-small crack growth.

Mechanically-Small Cracks

A crack is generally considered to be mechanically-small when all crack dimensions are small compared to characteristic mechanical dimensions. The relevant mechanical feature is typically a zone of plastic deformation, such as the crack tip plastic zone or a region of plasticity at the root of some mechanical discontinuity (e.g., a notch). The crack may be fully embedded in the plastic zone, or the plastic zone size may simply be a large fraction of the crack size, as illustrated by Figure 6. As discussed below, many microstructurally-small cracks are also mechanically-small, but our focus in this section is on mechanically-small cracks which are microstructurally-large. The "short" crack, as defined earlier, also behaves in the same manner as the mechanically-small crack. The crack front of a short crack interrogates many different grains and hence is not subject to strong microstructural effects.

Typical crack growth data for mechanically-small cracks are shown in Figure 7 for an HSLA steel [19]. Similar data are available for common airframe alloys [20]. Note again that small crack growth can occur below the large crack threshold. The slope of the Paris equation often appears to be roughly the same for small and large crack data, but the small crack data often fall above the large crack trend line when expressed in terms of nominal ΔK . Small or short cracks growing in notch fields often exhibit much faster growth than large cracks at comparable ΔK values, as shown in Figure 8 [21]. These small crack growth rates can actually decrease with increasing crack growth until they eventually merge with large crack data.

Why do mechanically-small cracks grow in this manner? The primary motivation appears to be that local stresses are significantly larger than those encountered under typical small-scale yielding (SSY) conditions, especially at near-threshold values of ΔK . These local stresses may have been elevated by the presence of a stress concentration, or they may simply be large nominal stresses in uniform geometries. These large local stresses significantly enhance crack-tip plasticity, which in turn enhances the crack driving force, either directly through violations of K -dominance, or indirectly through changes in plasticity-induced crack closure. The appropriate analytical treatment of the mechanically-small crack, then, primarily involves appropriate treatments of the elastic-plastic crack driving force and crack closure.

The nominal elastic formulation of ΔK , gradually becomes less accurate as a measure of the crack driving force as the applied stresses become a larger fraction of the yield stress. When $\sigma_{\max}/\sigma_{ys}$ exceeds about 0.7, a first-order plastic correction to ΔK may be useful. This correction may be based on the complete Dugdale formulation for the J -integral, expressed in terms of K [22, 23]. Alternatively, the correction can be based on an effective crack size defined as the sum of the actual crack size and the plastic zone radius [23, 24]. However, in most cases this first-order correction will change the magnitude of ΔK by no more than 10 to 20 percent. When the nominal plastic strain range becomes non-negligible (typically, when the total stress range approaches twice the cyclic yield strength), it will generally be necessary to replace ΔK entirely with some alternative parameter, such as a complete ΔJ formulation [24]. A comprehensive practical methodology for elastic-plastic FCG based on ΔJ is currently under development [25].

Plasticity-induced crack closure also becomes increasingly significant outside the small-scale yielding regime [24]. Normalized crack opening stresses are a function of normalized maximum stress, stress ratio, and stress state, and changes in closure behavior are most pronounced for large stresses, low stress ratios (R), and plane stress: typical conditions for mechanically-small cracks. Newman [26] has developed a simple closed-form equation based on a modified-Dugdale closure model of an infinite center-cracked plate which predicts normalized crack opening stress ($\sigma_{\text{open}}/\sigma_{\max}$) as a function of $\sigma_{\max}/\sigma_{\text{flow}}$, R , and constraint factor α . Recent finite element studies [27] have sug-

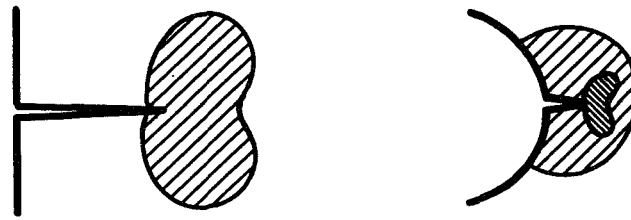


Figure 6. Schematic of relationship between mechanically-small cracks and plastic zones.

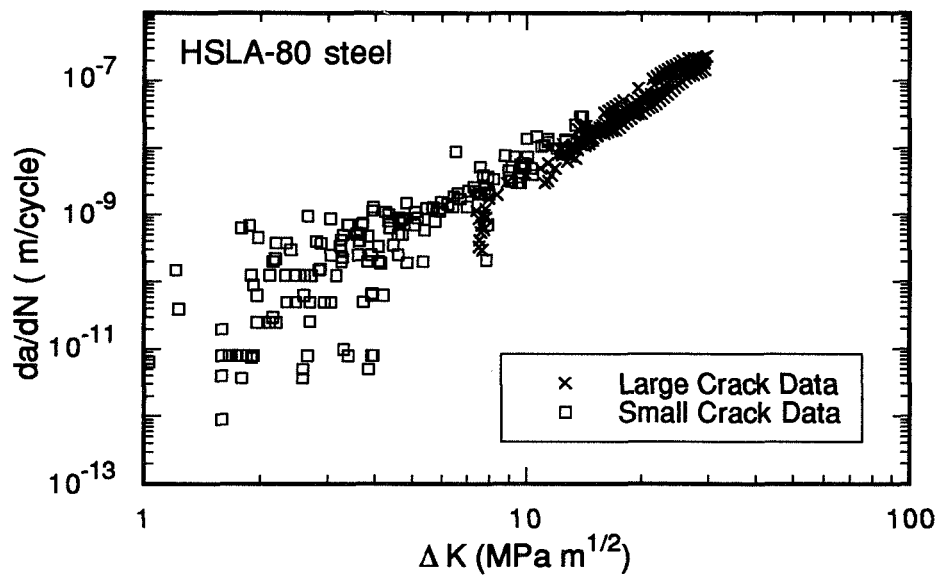


Figure 7. FCG data for large cracks and mechanically-small cracks in HSLA-80 steel.

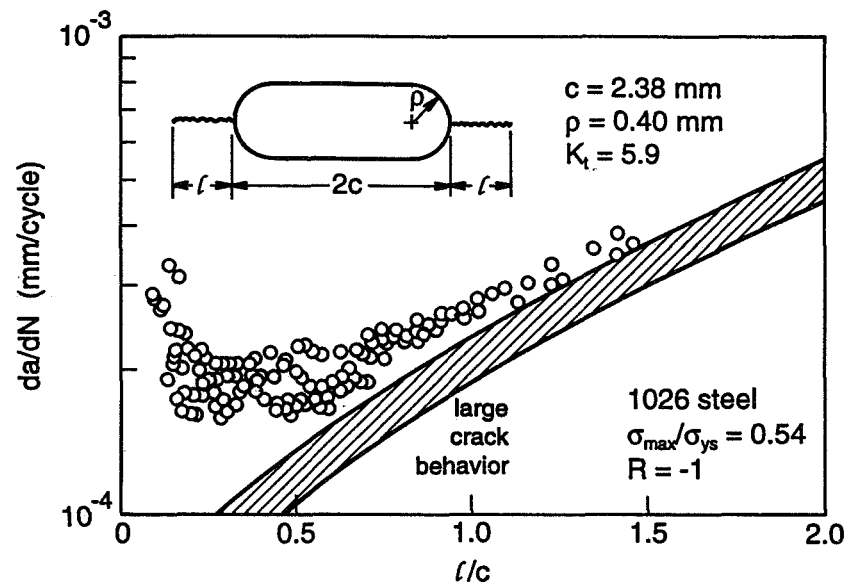


Figure 8. Typical FCG data for short cracks at notches.

gested that the Newman model may be extended satisfactorily to other geometries if $\sigma_{\max}/\sigma_{\text{flow}}$ is replaced by K_{\max}/K_0 , where $K_0 = \sigma_{\text{flow}} (\pi a)^{1/2}$. The Newman equation and the finite element results are illustrated in Figure 9 for plane stress, $R = -1$. Changes in closure behavior are also significant for crack growth at notches, and simple models are available to predict these changes [21].

If appropriate revisions to the crack driving force based on plasticity and crack closure considerations are carried out, the growth rates of mechanically-small cracks can usually be predicted successfully by extrapolating the large-crack Paris equation and neglecting the large-crack threshold. This implies that if plastic corrections to ΔK are relatively minor, and if the closure behavior of the small crack does not differ significantly from the large cracks used to derive the Paris equation, that the small crack growth rates may be essentially the same as for the large cracks at the same nominal ΔK . It is not entirely clear under what conditions the large crack threshold will be observed by the small cracks, and in the absence of contradicting data, it is probably prudent to neglect the threshold for all mechanically-small cracks. If a complete crack closure analysis is not possible or practical, it may be sufficient to predict the growth rates of mechanically-small cracks using closure-free (high stress ratio) large crack data [28].

As noted earlier, the regimes of mechanically-small and microstructurally-small cracks can overlap. A more complete organizational scheme for large and small cracks from both microstructural and mechanical perspectives is given in Table 1 [29]. The "microstructurally-small" crack discussed earlier in this paper is often both microstructurally- and mechanically-small, although it is also possible to have a crack which is microstructurally-small and mechanically-large (cracks in single crystals, or cracks in very large grained materials). The traditional "mechanically-small" (or "short") crack discussed in this paper is typically microstructurally-large. Traditional large cracks are both microstructurally and mechanically large. The table also includes some suggestions for approximate size criteria based on comparisons of the crack size with either the crack-tip plastic zone size, r_p , or the microstructural unit size, M .

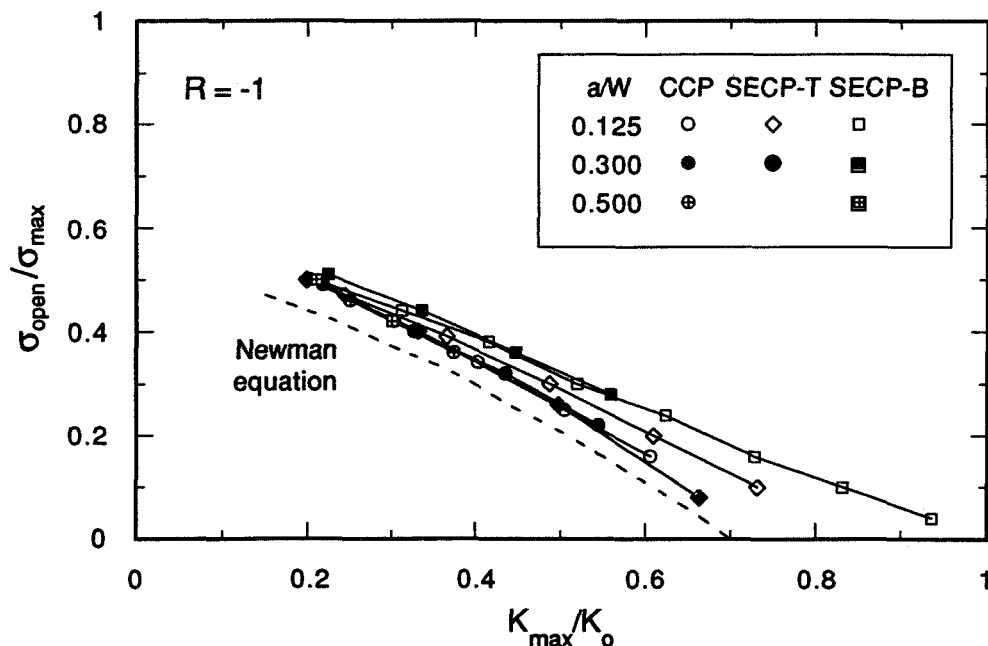


Figure 9. Normalized crack opening levels as a function of K_{\max}/K_0 , as predicted by FEM analyses and the Newman modified-Dugdale model.

Table 1. Classification of Crack Size According to Mechanical and Microstructural Influences

Micro- Structural Size \ Mechanical Size	Large $a/r_p > 4-20$ (SSY)	Small $a/r_p > 4-20$ (ISY and LSY)
Large $a/M > 5-10$ ($r_p/M \gg 1$)	Mechanically and Microstructurally Large (LEFM valid)	Mechanically Small/ Microstructurally Large (may need EPFM)
Small $a/M < 5-10$ ($r_p/M \sim 1$)	Mechanically Large/ Microstructurally Small (single crystal)	Mechanically and Microstructurally Small (inelastic, anisotropic, stochastic)

Chemically-Small Cracks

Experiments on a variety of ferritic and martensitic steels in aqueous chloride environments have shown that under corrosion-fatigue conditions, small cracks can also grow significantly faster than large cracks at comparable ΔK values [30, 31, 32]. This phenomenon is believed to result from the influence of crack size on the occluded chemistry which develops at the tip of fatigue cracks. The specific mechanism responsible for this "chemical crack size effect" is believed to be the enhanced production of embrittling hydrogen within small cracks resulting from a crack size dependence of one or more factors which control the evolution of the crack-tip environment—specifically, convective mixing, ionic diffusion, or surface electrochemical reactions [33, 34]. This mechanism is distinctly different from that responsible for the enhanced rate of crack growth in microstructurally- or mechanically-small fatigue cracks.

The chemical crack size effect is clearly illustrated by the data of Gangloff [31] for 4130 steel in an aqueous NaCl environment (see Figure 10). Note that corrosion-fatigue crack growth rates from small surface cracks (0.1 to 1 mm deep), as well as short through-thickness edge cracks (0.1 - 3 mm), are appreciably faster than corrosion-fatigue crack growth rates from large through-thickness cracks (25 - 40 mm) in standard compact tension specimens. It is also interesting to note that the corrosion-fatigue crack growth rates for small surface cracks decrease with increasing applied stress (at a given ΔK), and this trend is opposite to the dependence of applied stress on crack growth rates in small fatigue cracks. Moreover, all of the corrosion-fatigue crack growth rates in NaCl are enhanced compared to those in a moist laboratory air environment, even though the latter were generated with both small and large cracks. Thus, in relation to the fatigue small crack effect, the chemical small crack effect is of potentially greater importance since it can occur over a much larger range of crack sizes (up to 3 mm).

The chemical crack size effect in high strength steels is relevant to aircraft structural components such as landing gear. Do similar effects occur in high strength aluminum alloys used in airframes?

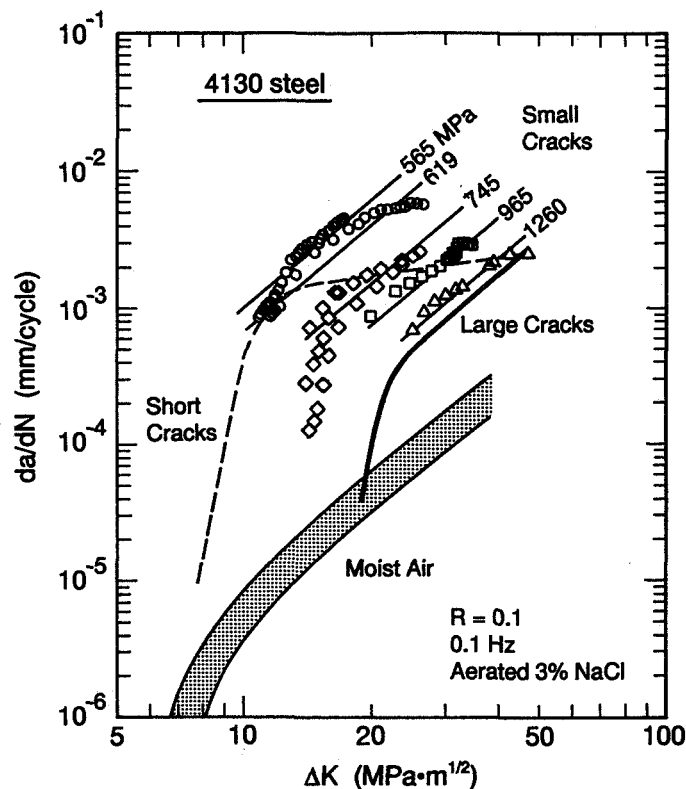


Figure 10. Corrosion-fatigue crack growth data for large and chemically-small cracks in 4130 steel [31].

Although data on the aluminum alloys is sparse at this point, preliminary data are available which enable an initial assessment of the problem. Data of Piascik and Gangloff [35] suggest the lack of a chemical crack size effect in both 2090 and 7075 aluminum alloys exposed to an aqueous chloride environment. Recent data from NASA-Langley [36] on 2024-T3 in a similar environment also support the lack of a chemical crack size effect, as shown in Figure 11. Thus, in contrast to steels, aluminum alloys may be immune from chemical crack size effects. Further studies are currently underway to address this question.

Several possible reasons for the apparent difference in the small crack behavior of steel and aluminum alloys can be hypothesized. First, it should be recognized that the data on steels and aluminum alloys have been generated under different environment and loading conditions. Specifically, the aluminum small crack data have been obtained under deaerated conditions and an electrode potential of -700 mV (versus the saturated calomel electrode, SCE), while the steel small crack data have generally been conducted under aerated conditions and, in the case of Ref. [31], an electrode potential of -550 mV SCE. In addition, most of the aluminum small crack data were obtained at high load ratios (R), particularly in the important low ΔK regime, while the steel small cracks were obtained at low load ratios. This difference in load ratios may be significant since it causes differences in the crack opening displacement. Analytical models for the evolution of the environment within cracks indicate that the ratio of crack surface area to occluded solution volume is a fundamental variable affecting the crack-tip environment [34].

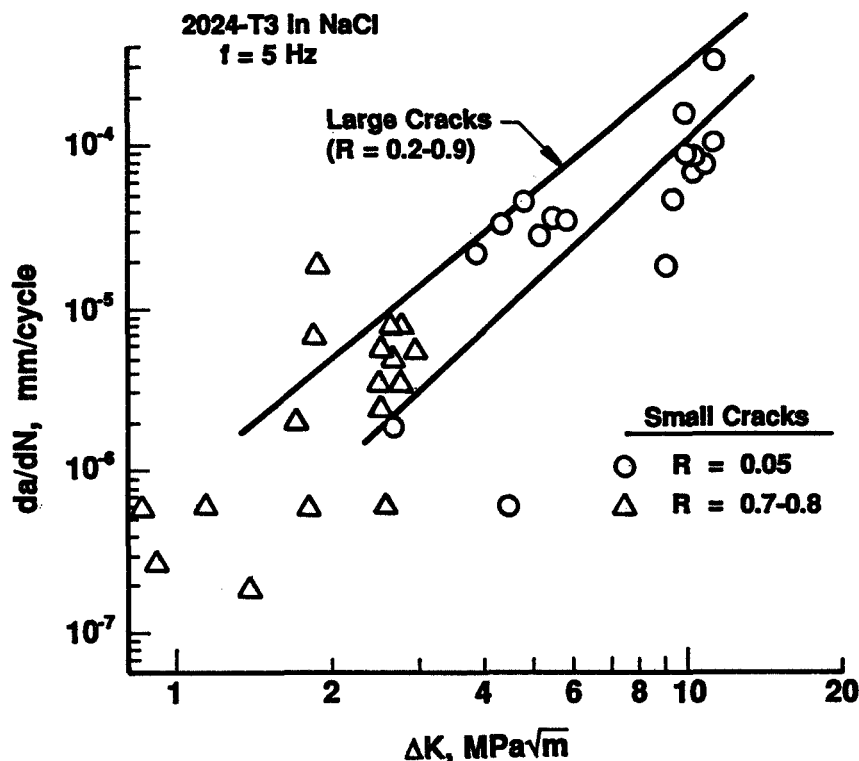


Figure 11. Corrosion-fatigue crack growth data for large and small cracks in 2024-T3 Al [36].

Second, the rate controlling process for environment-enhanced FCG may differ in steel and aluminum alloys. Crack growth rates in steels are controlled by electrochemical reactions on the freshly created metal at the crack tip [37]. Studies of aluminum alloys exposed to water vapor suggest that the surface reaction in the aluminum-water system is relatively fast, so that transport of water to the crack tip is the rate controlling process [38]. Unfortunately, specific results on the rate controlling process for aluminum alloys in liquid water are not yet available. Thus, an assessment of whether or not these fundamental differences in rate controlling processes account for the observed differences in chemical crack size effect in these two alloy systems must await further elucidation of the underlying kinetic mechanism(s).

MATERIALS DATA ISSUES

Scatter in Small Crack Data

Even when suitable analysis techniques are able to predict the central tendencies of small crack data, the life prediction task may still be difficult. The remaining problem is the large amount of scatter (sometimes several orders of magnitude) often observed in small crack growth rate data. This leads to greater uncertainty in life calculations, especially when the small crack regime dominates the total life. Analytical approaches based on simple upper bounds to the small crack regime, as suggested earlier, may be unacceptably overconservative in some applications.

At least three major sources of this apparent variability have been identified [19]. Some true variability is due to stochastic microstructural effects: local differences in grain orientation, micro-plastic yield strength, and grain boundary effects, which may become especially significant when the crack driving force is small. On the other hand, some apparent variability is actually only an artifact of measurement error. These errors become significant when the crack growth increment becomes small relative to the measurement resolution. Finally, some apparent variability can be attributed to mathematical averaging effects. The normal point-to-point variability is effectively averaged out for most large cracks, when the crack travels a long distance during the measurement interval. Since the small crack travels only a short distance during the measurement interval, this normal variability becomes more evident (as it would be if large cracks were measured at much shorter intervals).

The appropriate treatment for small crack scatter depends, at least in part, on the origin of the scatter. Some scatter which is only apparent can be effectively reduced with improvements in the analytical schemes used to process the raw crack growth data, including data filtering and modified incremental polynomial techniques [39]. However, other forms of scatter may require a formal stochastic treatment of the data. Many stochastic FCG models are available in the literature. Unfortunately, many of these models require extensive data of high statistical quality, which is often difficult (expensive) to obtain for small cracks. Other stochastic FCG models designed for practical engineering applications, such as the lognormal random variable (LRV) model, require fewer data and simpler calculations. However, these models are often not able to address the unique scatter associated with small cracks on a consistent basis with the reduced scatter associated with large cracks. New stochastic FCG models are currently being investigated to address these issues. Figure 12 compares a modified LRV model [19] with the standard LRV approach for the HSLA-80 steel data presented earlier.

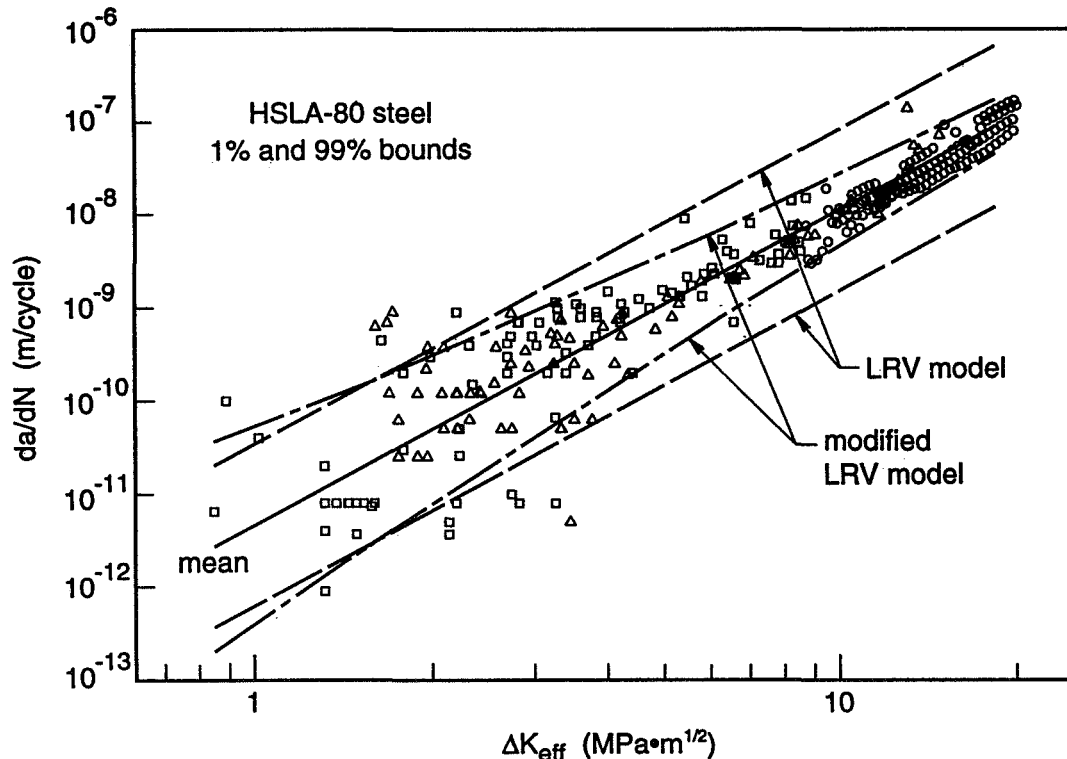


Figure 12. Stochastic treatments of large and small crack data for HSLA-80 steel, based on conventional and modified lognormal random variable models.

Small Crack Test Methods

Previous suggestions about practical engineering treatments of small cracks have usually attempted to derive predictions of small crack growth rates from commonly available large crack data. In some applications, however, this approach will not be adequate (e.g., for some microstructurally-small cracks), and in other applications the need may arise to obtain further experimental evidence for small crack behavior. Unfortunately, small crack growth rates cannot usually be measured with the standard procedures developed for large cracks, such as the current ASTM Test Method E 647 [40].

To address this dilemma, the Task Group on Small Fatigue Cracks within ASTM Committee E 8 on Fatigue and Fracture is currently attempting to develop an appendix to Test Method E 647 to provide guidelines for measuring the growth rates of small fatigue cracks. Since that document is currently undergoing the balloting process required to become an official ASTM standard and has not yet been formally approved, it is not prudent to provide specific details at this time. However, a few general remarks are appropriate.

Complete, detailed test procedures are not prescribed. Instead, the appendix provides general guidance on the selection of appropriate experimental and analytical techniques and identifies aspects of the testing process that are of particular importance when fatigue cracks are small. Several different crack length measurement techniques are permitted, and detailed descriptions of each are available in a recent ASTM STP [41]. Several different specimen geometries are suggested, including rectangular or cylindrical surface crack specimens, corner-crack specimens, and part-through cracks in edge-notched specimens. Special attention is given to issues such as surface preparation, crack initiation sites, and calculation of ΔK and da/dN .

DISCUSSION

The small crack problem is certainly a complex and multidimensional subject. Occasional confusion on the part of researchers about different types of small cracks and their appropriate experimental or analytical treatment has added further to the complexity of the literature. This short review paper, while attempting to better organize the complexity and point towards practical analytical solutions, has inevitably oversimplified some of the intricate details. But that is the inevitable limitation of nearly any practical engineering treatment of a complex technical problem. The goal is not to create universally precise theories, but rather to construct working engineering models which predict, to a first order, the key characteristics of the phenomena under consideration, based on fundamental understandings of the relevant scientific mechanisms.

Additional work is needed to develop further the analytical methods identified or proposed here. Some of these needs have been highlighted in the text: practical engineering methods to describe microstructurally-small crack growth at the subgrain size, clarification of the chemically-small crack effect (or lack thereof) in aluminum alloys, statistical treatments of small crack behavior, etc. Further verification testing and analysis is also required to confirm the applicability of these methods to common airframe alloys for characteristic geometries and load histories.

Some other unsolved problems have not yet been mentioned in this paper. One challenge of particular importance is variable amplitude loading. The great majority of previous small crack studies, including most of those referenced herein, have been limited to constant amplitude loading. Variable loading effects on small cracks are not well understood as a result, but available studies have suggested that variable amplitude loading can exacerbate the small crack effect [20, 42]. This may be

due, at least in part, to changes in crack closure behavior for variable load histories outside the small-scale yielding regime [43], but other microstructural effects may also be significant. Other outstanding small crack issues include the proper treatment of crack dwell or crack arrest as an intrinsic feature of microstructurally-small crack growth, and the characterization of crack closure in practical airframe geometries such as fastener holes with residual stresses.

The practical relevance of small crack phenomena for engineering analysis of airframe structures has not yet been fully established. Further study of problems such as MSD in aging aircraft should provide helpful guidance. In those applications where the growth of small cracks must be considered, however, reliable analytical and experimental techniques are now available to perform many of the required computations of damage growth with reasonable confidence.

CONCLUSIONS

1. A proper identification of the *type* of small crack encountered is essential to choosing an appropriate analytical treatment.
2. Satisfactory scientific explanations for small crack behavior are now available, but some additional work is needed to develop satisfactory engineering treatments for all applications.
3. A practical engineering methodology for mechanically-small cracks includes extrapolation of the large-crack Paris equation, with appropriate attention to changes in crack closure and plasticity modifications to the crack driving force.
4. Practical engineering methodologies for microstructurally-small cracks are less complete. Available simple mechanics approaches may be useful, but will be inadequate in some applications. Micromechanics and phenomenological approaches provide valuable guidance, but ultimately statistical or simple bounding approaches may be required.
5. It is not entirely clear if aluminum alloys commonly used in airframe applications exhibit a significant chemically-small crack effect.
6. Small cracks often exhibit significantly greater scatter in growth rates than large cracks due to stochastic variations in the local microstructure, measurement error, and decreased mathematical averaging. Alternative analytical techniques may be required to address this variability.
7. Guidelines for small crack test methods are becoming available.

ACKNOWLEDGMENTS

The substantial support of research on small cracks and related topics at SwRI over the past fifteen years by AFOSR, AFWAL, NASA, ARO, ONR, and others is gratefully acknowledged. Dr. Tony Torng is thanked for his contributions to the discussion of probabilistic modeling.

REFERENCES

1. Pearson, S.: Initiation of Fatigue Cracks in Commercial Aluminum Alloys and the Subsequent Propagation of Very Short Cracks. *Engng Fract. Mech.*, Vol. 7, 1975, pp. 235-247.
2. Goranson, U. G.: Elements of Structural Integrity Assurance. *Int. J. Fatigue*, Vol. 16, 1994, pp. 43-65.

3. Swift, T.: Widespread Fatigue Damage Monitoring—Issues and Concerns. Proc. 5th Int. Conf. Structural Airworthiness of New and Aging Aircraft, Hamburg, Germany, June 1993.
4. Final Report, Industry Committee on Widespread Fatigue Damage, Airworthiness Assurance Working Group, July 1993.
5. Wanhill, R. J. H.: Short Cracks in Aerospace Structures. *The Behaviour of Short Fatigue Cracks, EGF 1*, Mechanical Engineering Publications, London, 1986, pp. 27-36.
6. Lankford, J.: The Growth of Small Fatigue Cracks in 7075-T6 Aluminum. *Fatigue Engng Mater. Struct.*, Vol. 5, 1982, pp. 233-248.
7. Chan, K. S., and Lankford, J.: The Role of Microstructural Dissimilitude in Fatigue and Fracture of Small Cracks. *Acta Metall.*, Vol. 36, 1988, pp. 193-206.
8. Morris, W. L., Cox, B. N., and James, M. R.: Microplastic Surface Deformation of Al 2219-T851. *Acta Metall.*, Vol. 35, 1987, pp. 1055-1066.
9. Davidson, D. L., and Chan, K. S.: The Crystallography of Fatigue Crack Initiation in Course Grained Astroloy at 20°C. *Acta Metall.*, Vol. 37, 1989, pp. 1089-1097.
10. Suresh, S.: Crack Deflection: Implications for the Growth of Long and Short Fatigue Cracks. *Met. Trans. A*, Vol. 14A, 1983, pp. 2375-2385.
11. Lankford, J., and Davidson, D. L.: The Micromechanisms of Small Fatigue Crack Growth and the Influence of Metallurgical Factors. *Small Fatigue Cracks*, TMS, 1986, pp. 51-71.
12. Hudak, S. J., Jr., Davidson, D. L., Chan, K. S., Howland, A. C., and Walsch, M. J.: Growth of Small Cracks in Aeroengine Disc Materials. AFWAL-TR-88-4090, June 1988.
13. Davidson, D. L.: Small and Large Fatigue Cracks in Aluminum Alloys. *Acta Metall.*, Vol. 36, 1988, pp. 2275-2282.
14. El Haddad, M. H., Smith, K. N., and Topper, T. H.: Fatigue Crack Propagation of Short Cracks. *ASME J. Engng Mater. Technol.*, Vol. 101, 1979, pp. 42-46.
15. Newman, J. C., Jr.: A Review of Modelling Small-Crack Behavior and Fatigue-Life Predictions for Aluminum Alloys. *Fatigue Fract. Engng Mater. Struct.*, Vol. 17, 1994, pp. 429-439.
16. Chan, K. S., Lankford, J., and Davidson, D. L.: A Comparison of Crack-Tip Field Parameters for Large and Small Fatigue Cracks. *ASME J. Engng Mater. Technol.*, Vol. 108, 1986, pp. 206-213.
17. Lankford, J.: The Influence of Microstructure on the Growth of Small Fatigue Cracks. *Fatigue Fract. Engng Mater. Struct.*, Vol. 8, 1985, pp. 161-175.
18. Taylor, D., and Knott, J. F.: Fatigue Crack Propagation of Short Cracks; The Effect of Microstructure. *Fatigue Engng Mater. Struct.*, Vol. 4, 1981, pp. 147-155.
19. Torng, T. Y., and McClung, R. C.: Probabilistic Fatigue Life Prediction Methods for Small and Large Fatigue Cracks. Proc. 35th Structures, Structural Dynamics, and Materials Conf., April 1994, pp. 1514-1524.
20. Newman, J. C., Jr., and Edwards, P. R.: Short-Crack Growth Behaviour in an Aluminum Alloy—An AGARD Cooperative Test Programme. AGARD Report No. 732, 1988.
21. McClung, R. C., and Sehitoglu, H.: Closure and Growth of Fatigue Cracks at Notches. *ASME J. Engng Mater. Technol.*, Vol. 114, 1992, pp. 1-7.
22. Chan, K. S.: Local Crack-Tip Field Parameters for Large and Small Cracks: Theory and Experiment. *Small Fatigue Cracks*, TMS, 1986, pp. 407-425.
23. Newman, J. C., Jr.: Fracture Mechanics Parameters for Small Fatigue Cracks. *Small-Crack Test Methods*, ASTM STP 1149, 1992, pp. 6-33.
24. McClung, R. C., and Sehitoglu, H.: Characterization of Fatigue Crack Growth in Intermediate and Large Scale Yielding. *ASME J. Engng Mater. Technol.*, Vol. 113, 1991, pp. 15-22.

25. McClung, R. C., Chell, G. G., Russell, D. A., and Orient, G. E.: Development of a Practical Methodology for Elastic-Plastic Fatigue Crack Growth. Proc. Conf. Advanced Earth-to-Orbit Propulsion Technology, NASA Marshall Space Flight Center, May 1994.
26. Newman, J. C., Jr.: A Crack Opening Stress Equation for Fatigue Crack Growth. *Int. J. Fract.*, Vol. 24, 1984, pp. R131-R135.
27. McClung, R. C.: Finite Element Analysis of Specimen Geometry Effects on Fatigue Crack Closure. *Fatigue Fract. Engng Mater. Struct.*, Vol. 17, No. 6, 1994.
28. Hertzberg, R., Herman, W. A., Clark, T., and Jaccard, R.: Simulation of Short Crack and Other Low Closure Loading Conditions Utilizing Constant K_{\max} ΔK -Decreasing Fatigue Crack Growth Procedures. *Small-Crack Test Methods, ASTM STP 1149*, 1992, pp. 197-220.
29. Hudak, S. J., Jr., and Chan, K. S.: In Search of a Driving Force to Characterize the Kinetics of Small Crack Growth. *Small Fatigue Cracks*, TMS, 1986, pp. 379-405.
30. Gangloff, R. P.: The Criticality of Crack Size in Aqueous Corrosion Fatigue. *Research Mechanical Letters*, Vol. 1, 1981, pp. 299-306.
31. Gangloff, R. P.: Crack Size Effects on the Chemical Driving Force for Aqueous Corrosion Fatigue. *Met. Trans. A*, Vol. 16A, 1985, pp. 953-969.
32. Gangloff, R. P., and Wei, R. P.: Small Crack-Environment Interactions: The Hydrogen Embrittlement Perspective. *Small Fatigue Cracks*, TMS, 1986, pp. 239-264.
33. Gangloff, R. P.: Oxygen Inhibition Model of the Chemical Crack Size Effect in Corrosion Fatigue. *Embrittlement by the Localized Crack Environment*, TMS, 1984, pp. 265-290.
34. Turnbull, A., and Ferriss, D. H.: Mathematical Modelling of the Electrochemistry in Corrosion-Fatigue Cracks. *Proc. Conf. Corrosion Chemistry within Pits, Crevices, and Cracks*, HMSO, 1987, pp. 357-396.
35. Piascik, R. S., and Gangloff, R. P.: Environmental Fatigue in Al-Li-Cu Alloy: Part 1. Intrinsic Crack Propagation Kinetics in Hydrogenous Environments. *Met. Trans. A*, Vol. 22A, 1991, pp. 2415-2427.
36. Piascik, R. S., and Willard, S. A.: The Growth of Small Corrosion Fatigue Cracks in Alloy 2024. NASA TM 107755, April 1993.
37. Shih, T.-H., and Wei, R. P.: The Effects of Load Ratio on Environmentally Assisted Fatigue Crack Growth. *Engng Fract. Mech.*, Vol. 18, 1983, pp. 827-837.
38. Gao, M., Pao, P. S., and Wei, R. P.: Chemical and Metallurgical Aspects of Environmentally Assisted Fatigue Crack Growth in 7075-T651 Aluminum Alloy. *Met. Trans. A*, Vol. 19A, 1988, pp. 1739-1750.
39. Larsen, J. M., Jira, J. R., and Ravichandran, K. S.: Measurement of Small Cracks by Photomicroscopy: Experiments and Analysis. *Small-Crack Test Methods, ASTM STP 1149*, 1992, pp. 57-80.
40. Standard Test Method for Measurement of Fatigue Crack Growth Rates. ASTM E 647-93, *Annual Book of ASTM Standards*, Vol. 03.01, 1993.
41. Larsen, J. M., and Allison, J. E., Eds.: *Small-Crack Test Methods, ASTM STP 1149*, American Society for Testing and Materials, Philadelphia, PA, 1992.
42. Blom, A. F.: Relevance of Short Fatigue Crack Growth Data for Durability and Damage Tolerance of Aircraft. *Small Fatigue Cracks*, TMS, 1986, pp. 623-638.
43. McClung, R. C.: Finite Element Modeling of Fatigue Crack Growth. *Theoretical Concepts and Numerical Analysis of Fatigue*, EMAS, 1992, pp. 153-172.

1995108071

N95- 14485

FULL-SCALE TESTING AND ANALYSIS OF FUSELAGE STRUCTURE

M. Miller, M. L. Gruber, K. E. Wilkins, R. E. Worden
The Boeing Company, Seattle, Washington 98124

348670

532-39

23/26

p. 16

SUMMARY

This paper presents recent results from a program in the Boeing Commercial Airplane Group to study the behavior of cracks in fuselage structures. The goal of this program is to improve methods for analyzing crack growth and residual strength in pressurized fuselages, thus improving new airplane designs and optimizing the required structural inspections for current models. The program consists of full-scale experimental testing of pressurized fuselage panels in both wide-body and narrow-body fixtures and finite element analyses to predict the results. The finite element analyses are geometrically nonlinear with material and fastener nonlinearity included on a case-by-case basis. The analysis results are compared with the strain gage, crack growth, and residual strength data from the experimental program. Most of the studies reported in this paper concern the behavior of single or multiple cracks in the lap joints of narrow-body airplanes (such as 727 and 737 commercial jets). The phenomenon where the crack trajectory is curved creating a "flap" and resulting in a controlled decompression is discussed.

INTRODUCTION

The Boeing Commercial Airplane Group has a continuing program to investigate the durability and damage tolerance of airplane structures. In the mid-1980s, the opportunity arose to build two test fixtures to study the behavior of typical fuselage structure. To complement this test program, a parallel activity to conduct finite element analyses of typical fuselage configurations was initiated. The objective is to improve our damage tolerance methods for the design and evaluation of fuselage pressure structure. This should result in safer designs and a reduced inspection burden on the operators. In recent times, the scope of the research has been extended to include assessments of the effects of multiple site damage on the residual strength of fuselage lap joints.

PRESSURE TEST FACILITY

The test facility, illustrated in Figure 1, consists of two cylindrical fixtures.

The first fixture has a radius of 74 inches (1.88 m) to match Boeing's typical narrow-body airplanes, and the second has a radius of 127 inches (3.23 m) to match the wide-body airplanes. Both fixtures are 20 feet (6.1 m) in length as shown in Figure 2. The overall geometry of the fixtures is consistent with typical fuselage design: 7075-T6 frames at a 20 inch (508 mm) pitch and 2024-T3 clad stringers at a 9.25 inch (235 mm) pitch. The frames are attached to the stringers by means of stringer clips, but are otherwise not connected directly to the skin. The skin, frame and stringer gages are thicker than typical minimum gage fuselage structure but have been selected to maintain realistic fixture stiffness. All fastener holes in the skin are cold-worked and protruding head fasteners are used to provide maximum fixture longevity. External 2.8 inch (71 mm) wide circumferential tear straps of 2024-T3 clad sheet are riveted to the skin at a 20 inch (508 mm) spacing. The end bulkheads are steel, one of which is fixed and the other on rollers to permit axial expansion during pressurization.

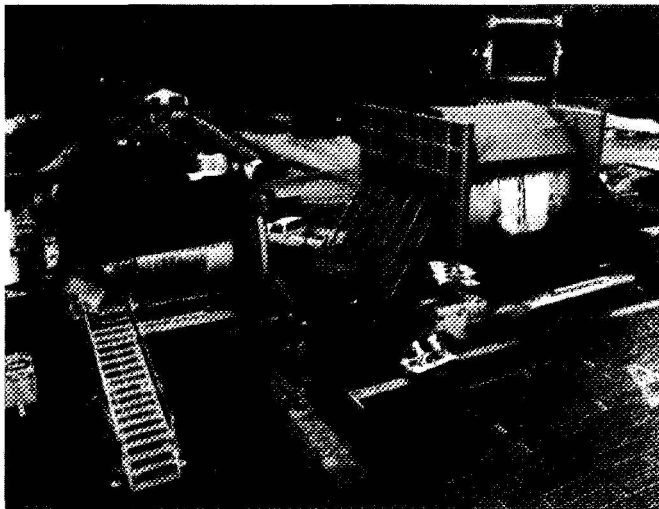


Figure 1. Pressure test site.

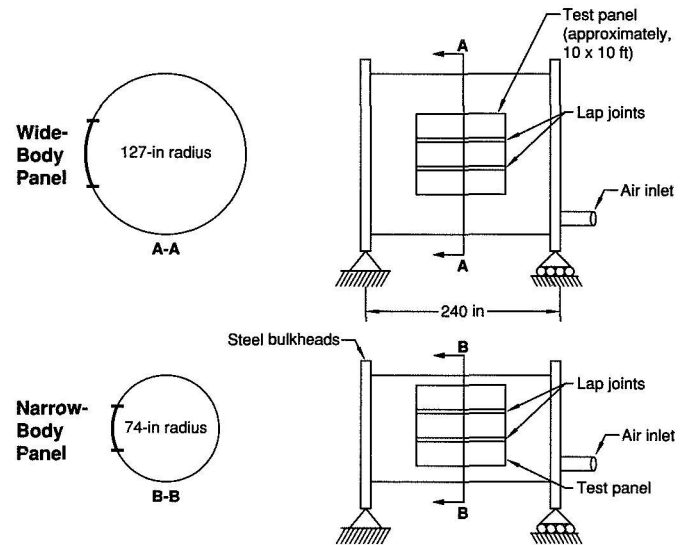


Figure 2. Schematic of pressure test fixtures.

The narrow-body fixture has a single rectangular cutout 10 feet x 10 feet (3.05 m x 3.05 m), designed to accept the test panels. Similarly, the wide-body fixture has two diametrically opposed cutouts also 10 feet x 10 feet (3.05 m x 3.05 m). The test panels are attached to the fixture at the skin, frames, and stringers by a fusing arrangement that allows the panel to fail at loads below the elastic limit of the fixture components. The stringer and frame splices are designed to allow attachment fasteners to shear during a dynamic panel failure. The test panel skin is allowed to tear circumferentially along the perimeter fasteners with the help of a sharp notch introduced into the panel prior to its installation in the fixture. With these features, it is possible to conduct residual strength tests which result in test panel failure without extensive damage to the test fixture.

Compressed air is used as the pressurizing medium. Five electric compressors are capable of producing a differential pressure of 90 psi (0.62 MPa) resulting in delivery of a nominal 1600 cubic feet (45.3 cubic meters) of air per minute. The flow of air is regulated into the fixtures by means of a digitally controlled valve. Cyclic rates are 1 minute per cycle in the narrow-body fixture and two minutes per cycle in the wide-body fixture. Polystyrene blocks are placed within the fixtures to reduce the required air volume.

To reduce air leakage during testing, 0.1 inch (2.5 mm) thick rubber air bladders are placed against the inner skin of the test panel in the vicinity of the crack. Some testing has been conducted with insulation blankets used on a commercial airplane. These have inadequate strength and durability however for long-term testing. Thin aluminum sheet, loosely attached to the interior of the skin panel, was found to affect crack growth behavior and is no longer used.

The data acquisition system consists of up to 300 channels for recording test information, principally from strain gages. Typically, rosettes are used on the skins and axial gages on the stringers, tear straps, and frame chords. Most tests are remotely monitored using video cameras. The test differential pressures are superimposed on the video image in real time. The resulting film is available for subsequent review and analysis.

TEST RESULTS

The discussion of test results is divided into two sections dealing with narrow-body and wide-body panels respectively. Experience has indicated that the behavior of each can be significantly different; there is a tendency toward controlled decompression in narrow-body panels. This results when a longitudinal crack in the skin turns to grow in the circumferential direction. A segment of the skin peels back creating an opening that prevents further pressurization. This phenomenon, often described as “flapping,” is rarely encountered in wide-body panels. It is believed to be primarily a function of skin gage, but is also influenced by initial crack location, tear strap dimensions, the presence of shear-ties and other detail design features.

Narrow-Body Tests

Four tests were conducted on narrow-body panel 74-A shown in Figure 3. In general, the test procedure consisted of inserting a 5 inch (127 mm) sawcut at the selected test location and pressure cycling until either test termination or the crack reached a length at which a residual strength test was performed. Each crack was repaired before inserting the next sawcut. The test panel is divided into two halves by a single longitudinal lap joint. All frames are “floating,” connected to the stringers only by means of stringer clips. In the upper half of the panel the skin is 0.040 inch (1.02 mm) thick, and in the lower half of the panel the skin is 0.056 inch (1.32 mm) thick. All longitudinal cracks are parallel to the longitudinal grain direction of the 2024-T3 clad skin. Internal bonded tear straps are installed at each frame location. The tear strap dimensions are defined in terms of a strap stiffening ratio:

$$R_s = A_{\text{strap}} / (B \cdot t_{\text{skin}})$$

where A_{strap} is the tear strap cross-sectional area, B is the frame spacing, and t_{skin} is the skin gage. The frame cross-sectional area is not included in the evaluation of the strap stiffening ratio.

Test 1 on this panel consisted of a longitudinal 5 inch (127 mm) sawcut adjacent to stringer 4L in the 0.056 inch (1.32 mm) skin. The strap stiffness ratio R_s was 0.14. The panel was subjected to a cyclic differential pressure of 8.6 psi (.059 MPa) with a stress ratio of zero. As is typical with sawcuts at such a location, the direction of fatigue crack growth gradually diverged from longitudinal. In this case, failure consisted of a controlled decompression as shown in Figure 4. Figure 5 shows that 5400 pressure cycles were required to grow the crack to its final length.

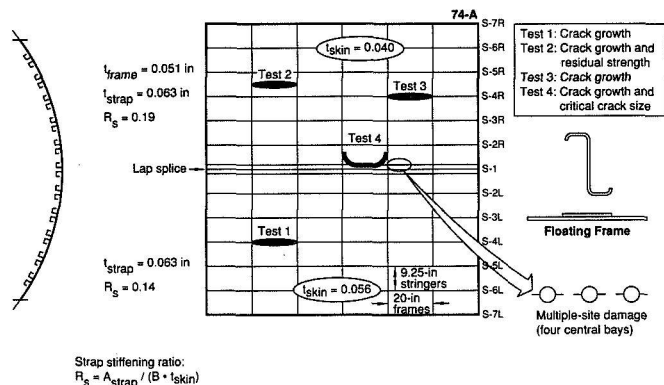


Figure 3. Initial damage locations on narrow-body panel 74-A.

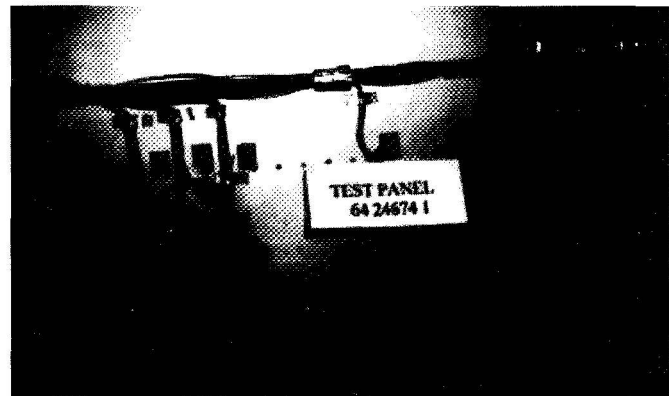


Figure 4. Final failure of Test 1 on panel 74-A.

Test 3 consisted of a longitudinal five inch (127 mm) sawcut adjacent to stringer 4R in the 0.04 inch (1.02 mm) gage skin. The direction of crack growth was similar to test 1 and resulted in a controlled decompression after 950 cycles. Comparison of the data in Figure 5 shows that the midbay crack of test 2 has a shorter crack growth life than the crack in test 3. This is consistent with data presented in Reference 1. The crack length at instability for Test 3 of 14.8 inches (380 mm) can be compared with a crack length at instability of 18 inches (460 mm) in Test 1, attributable in part to the stresses associated with the different skin gages.

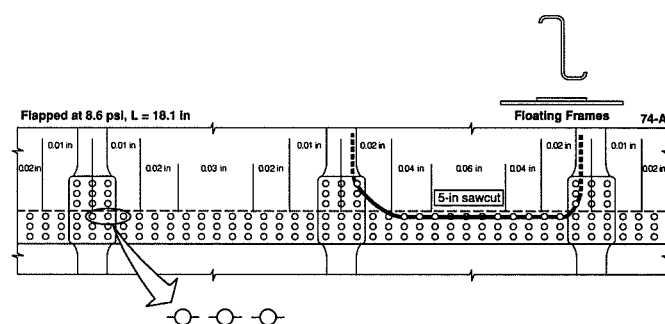


Figure 6. Multiple site damage test on panel 74-A lap joint.

A single test was conducted on Panel 74-B. This panel differed from panel 74-A by the use of shear-ties to attach the frame directly to the skin and bonded tear strap as shown in Figure 9. In this test, the tear strap stiffening ratio R_s was 0.12. The initial condition consisted of a five inch (127 mm) sawcut along the upper fastener row of the lap joint. Again, each fastener hole ahead of the initial sawcut had two small diametrically opposed longitudinal sawcuts introduced during the original panel assembly. The secondary sawcut lengths were varied in a manner similar to those in panel 74-A. However, the panel had not been subjected to prior fatigue cycling before introduction of the 5 inch sawcut. Review of the lap joint following final failure

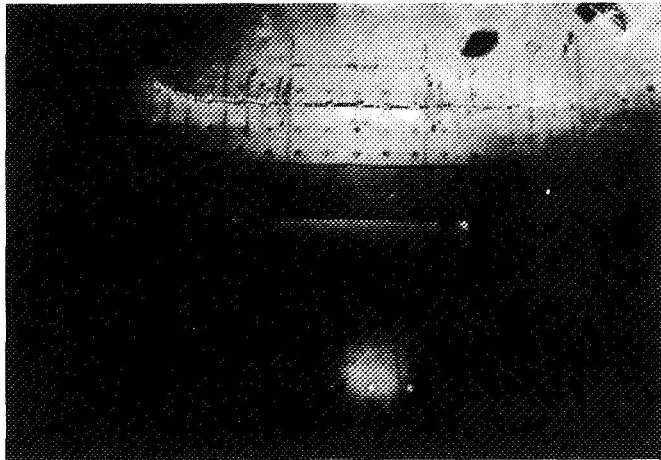


Figure 7. Crack progression during multiple site damage test on panel 74-A lap joint.

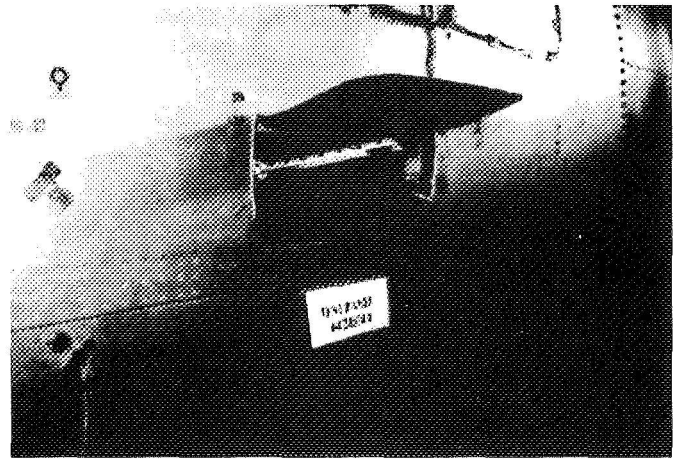


Figure 8. Final failure of multiple site damage test on panel 74-A lap joint.

revealed that several sawcuts in the same frame bay as the lead crack had grown about 0.25 inch (6 mm) during fatigue cycling. During this time, the crack showed little tendency to deviate far from the rivet line. It did however deviate from the rivet line and head toward the middle of the stringer bay as it crossed the adjacent tear straps. A fatigue crack of length 1 inch (25 mm) was detected in one of these tear straps when the skin crack was around 20 inches (510 mm) in length. This tear strap failed in fatigue when the skin crack was around 23 inches (580 mm) in length. The second tear strap failed when the skin crack was 24.5 inches (620 mm) in length. A total of 85 pressure cycles were required to fail both tear straps following the initial tear strap crack detection. The lead crack continued to grow until it reached a length of 40.2 inches (1.02 m) as shown in Figure 10. At this time, unstable crack extension resulted leading to final panel failure as shown in Figure 11. Although review of a video tape taken during the final pressure cycle is inconclusive, it is believed that final failure was precipitated by failure of one or both of the frames behind the growing crack. The crack was observed to commence growth at a differential pressure of 0.2 psi (.001 MPa) below the maximum pressure achieved during the test. Prior to final failure, the crack extended about 3 inches (76 mm).

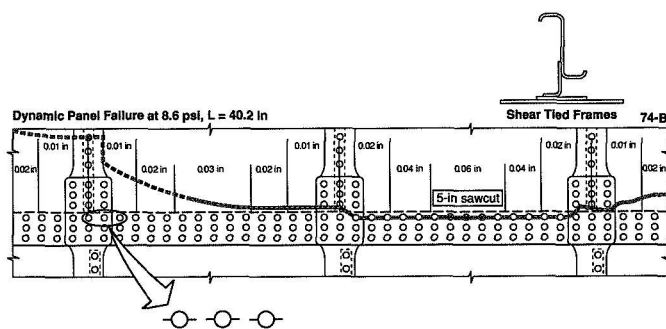


Figure 9. Multiple site damage test on panel 74-B lap joint.

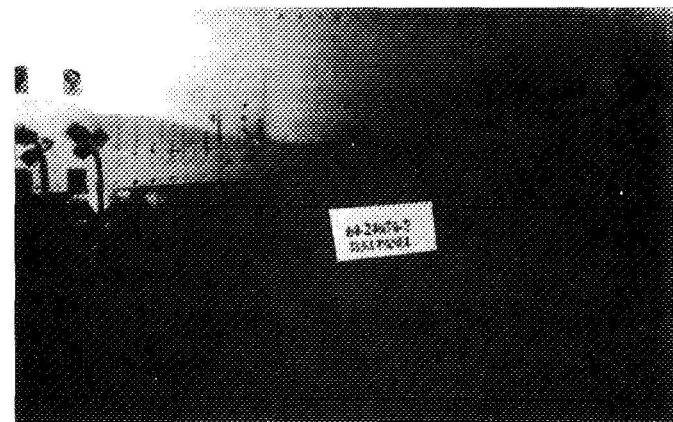


Figure 10. Crack progression immediately prior to final failure of panel 74-B.

Review of Figure 11 shows the benefit of the fusing arrangement. The frames at the upper and lower ends of the cutout broke cleanly away from the test fixture. Similarly, the stringers separated cleanly along the

vertical edges of the cutout. It can also be observed that the frames in the central region of the test panel failed at a location consistent with the last fastener in the shear-tie.

Note that in neither panel 74-A nor 74-B did the small sawcuts ahead of the main crack significantly contribute to panel failure.

A number of additional tests of cracks in lap joints in narrow-body panels are summarized in the chart in Figure 12. The data expand on results previously presented in Reference 2. All pressure cycling was at a differential pressure of 7.8 psi (.054 MPa). The illustrations in the figure describe schematically the behavior of the cracks. Some of the tests, as noted on the figure, contained multiple site damage (MSD) in the fastener holes ahead of the lead crack. A controlled decompression occurred during the first test on panel 28A only. This panel did not include any MSD. In all other cases, the lead crack continued to grow in an essentially longitudinal direction throughout the test. However in several cases, similar to Test 74-B discussed above, the crack grew out of the lap joint into the basic skin before final panel failure. No clear trends emerge from these results. However, it does appear that MSD forces the lead crack to stay in the upper fastener row of the lap joint for a longer period of time. Comparison of Test 2 on panel 28A and the test on panel 27A shows that panel behavior is independent of the method of attaching the tear strap to the skin. However, it should be noted that the tear strap is spliced using rivets at the lap joint location in such a way that both the riveted and bonded designs are locally similar.



Figure 11. Final failure of panel 74-B.

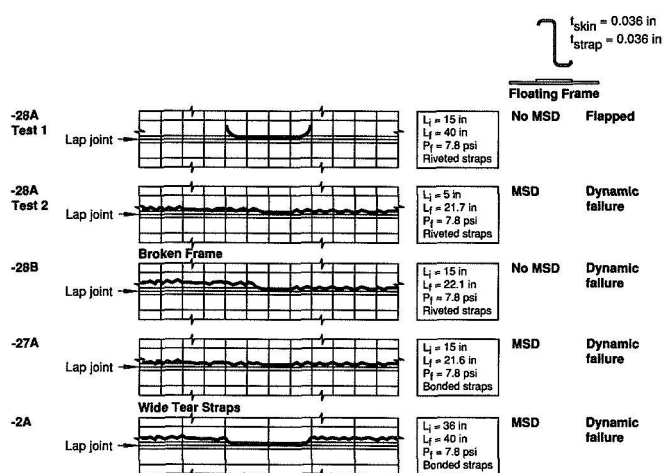


Figure 12. Summary of miscellaneous narrow-body lap joint crack growth tests.

Wide-Body Tests

A comparison of the effects of MSD on two wide-body panels is presented in Figure 13. The panels (127-B and 127-D) are 127 inch (3.23 m) in radius with frames and tear straps at a 20 inch (508 mm) spacing. The tear straps are bonded to the skin and have a stiffness ratio R_s of 0.12. The skin is 0.063 inch (1.6 mm) 2024-T3 clad sheet with the lap joint parallel to the longitudinal grain direction. The frames are shear-tied to the skin as illustrated in the figure. In each test, an initial sawcut of 5 inches (127 mm) was introduced into the upper row of fasteners in the lap joint and into the central tear strap. The central frame initially remained intact. In one case, MSD of the lengths shown in the illustration was introduced ahead of the lead crack. Each panel was subjected to fatigue cycling at a differential pressure of 8.6 psi (.059 MPa). When the cracks reached a length of 37 inches (940 mm), a differential pressure of 9.5 psi (.066 MPa) was applied. In each

case, this resulted in a small amount of crack extension. The central frame was cut and the pressure increased until panel failure. The panel with the MSD ahead of the lead crack failed at a differential pressure of 9.4 psi (.065 MPa), approximately 10% below the maximum differential pressure applied to the panel without MSD.

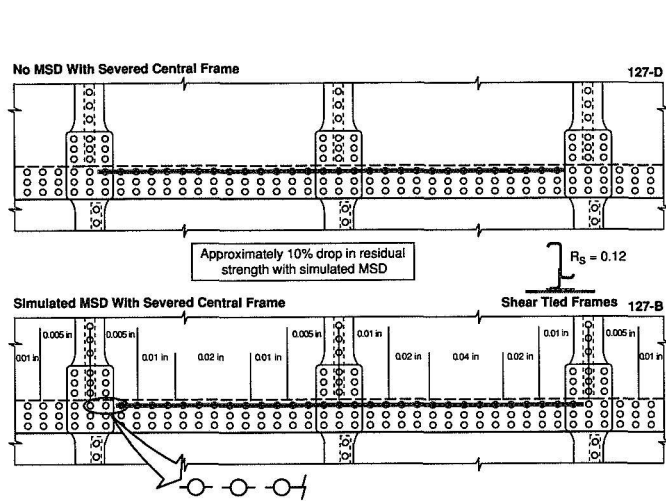


Figure 13. Effect of multiple site damage in lap joint on residual strength of wide-body panels.

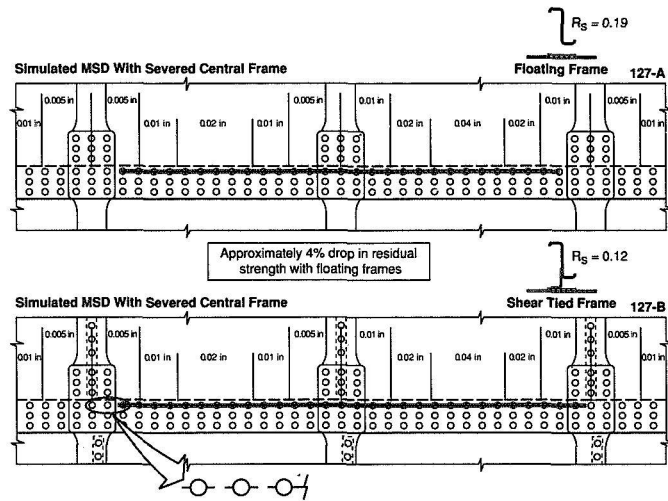


Figure 14. Effect of frame detail design on residual strength of wide-body panels with multiple site damage in lap joints.

The different capability of shear-tied against floating frame designs is illustrated in Figure 14. Test panel 127-B is as described in the previous paragraph. Test panel 127-A is similar with the exception that the frames are not shear-tied to the skin. The tear straps are bonded to the skin and have a stiffness ratio R_s equal to 0.19. The test procedure for panel 127-A was similar to 127-B with MSD introduced into the panel ahead of the lead crack as shown in the figure. This panel was subjected to fatigue cycles at a differential pressure of 8.6 psi (.059 MPa). When the crack reached a length of 37 inches (940 mm), a differential pressure of 9.5 psi (.066 MPa) was applied. Following this, the central frame was cut and the panel pressurized to failure. The condition of the panel prior to the final pressurization cycle and following the final cycle is illustrated in Figures 15 and 16.



Figure 15. Crack progression during multiple site damage test on wide-body panel 127-A lap joint.

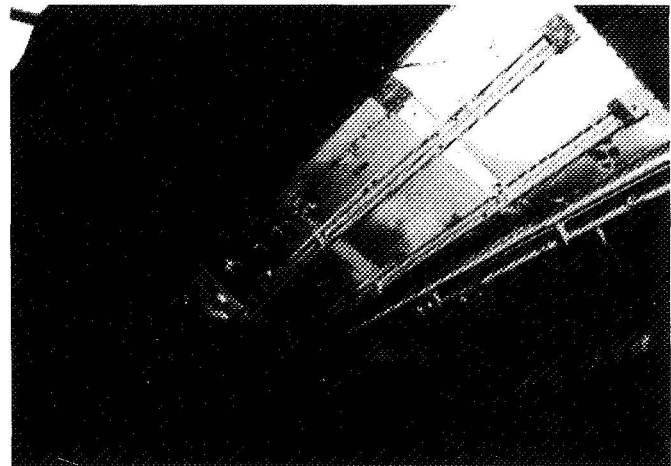


Figure 16. Final failure of multiple site damage test on panel 127-A lap joint.

The floating frame panel failed at 9.0 psi, approximately 4% less than the shear-tie panel. While this small difference could be attributed to test scatter, it is notable that this occurred despite the higher tear strap stiffness ratio. It is believed that the difference is associated with the ability of the shear-tied design to reduce the effects of out-of-plane displacements, or bulging, and to hold the crack closed.

Conceivably, MSD could occur in two or more adjacent bays. A single test on panel 16-2 was conducted to investigate the interaction of two large cracks in adjacent bays as shown in Figure 17. This panel was 127 inch (3.23 m) in radius. The skin was 0.075 inch (1.9 mm) C188-T3 clad aluminum with the lap joint parallel to the longitudinal grain direction. The panel was padded to a thickness of 0.1 inch (2.5 mm) at the lap joint. The frames were shear-tied to the skin which is locally padded to 0.1 inch (2.5 mm). Two 10 inch (254 mm) sawcuts were introduced into the upper row fasteners of the lap joint in the centers of two adjacent bays. The panel was loaded to a differential pressure of 8.6 psi (.059 MPa). The cracks were extended by sawcut one fastener at a time until each crack was about 15 inches (381 mm) in length and each crack tip was 1.25 inches (31.8 mm) from the centerline of the central shear-tie frame. At this time, 100 fatigue cycles at a differential pressure of 8.6 psi (.059 MPa) were applied to the panel. Subsequently, small sawcuts were introduced into the fastener holes to encourage re-initiation. After a further 11 fatigue cycles at the same differential pressure, the cracks linked up to form a single continuous crack of length 32.7 inches (830 mm). The test was discontinued following further fatigue cycling when the crack reached a length of 47.9 inches (1.22 m). The final condition of the crack is illustrated in Figure 18. While not conclusive, the test data indicate that cracks in adjacent bays do not automatically create an MSD concern.

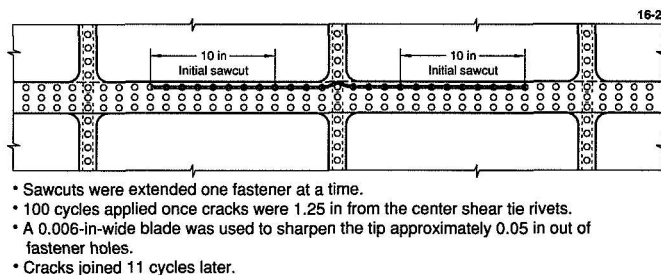


Figure 17. Test details for large interacting cracks in lap joint of wide-body panel 16-2.

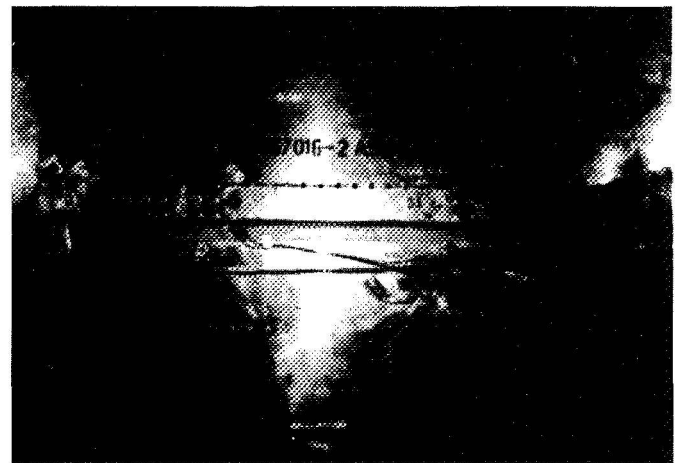


Figure 18. Final configuration of crack in lap joint of panel 16-2.

ANALYSIS PROCEDURE

The primary purpose of the analysis program is to predict the behavior of the test panels. This includes the test panel stresses (to be compared with strain gage data), the trajectory of crack growth from a sawcut, the crack growth life, and the residual strength. Residual strength can be the critical crack length under operating differential pressure or the maximum possible differential pressure for a given crack length. Successful comparisons will increase confidence in the analysis for predicting the behavior of typical fuselage structure containing cracks and for design studies.

Finite element models include the following test panel components: skin, tear straps, stringers and frames, stringer clips that attach the frames to the stringers, and, if present, shear ties that attach the frames to the skin. Eight-noded shell elements are used for the skin and tear straps, quadratic beam elements for the stringers and frames, shell elements for the shear ties, and rigid connections for the stringer clips. Fasteners are modelled with springs and rigid connections as discussed in Reference 1. Beam section coordinates are input into the model so that the nodes along the stringers are at the fastener locations and not at the neutral axis. In some cases, the tear straps are adhesively bonded to the skin. Early analysis attempts modeled the skin plus tear straps as one layer of thick shell elements. The resulting bending stresses did not correlate well with the test panels. Good results have been obtained by using two layers of shell elements. The adhesive layer is modeled with springs and rigid connections at all nodes, similar to the technique used to model riveted fasteners.

In most models, linear elastic material properties are used. In the residual strength models, material plasticity is introduced to selected elements. All analyses have been solved with ABAQUS using a geometric nonlinear solution sequence. A global analysis approach has been used so that fasteners and multiple site damage are not modelled explicitly.

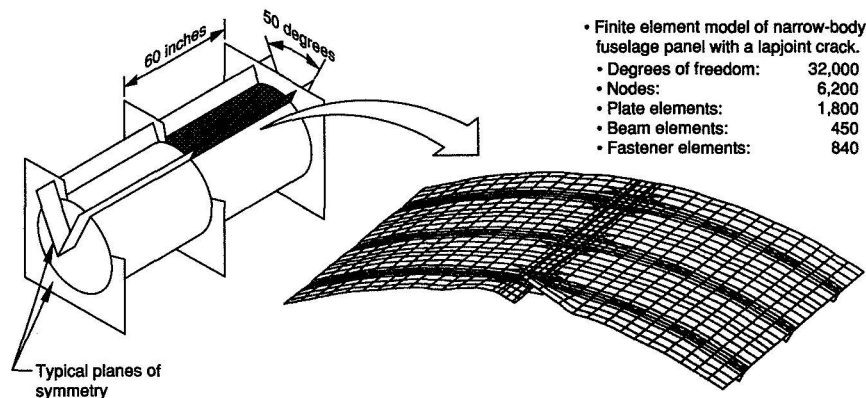


Figure 19. Finite element model of narrow-body test panel with lap joint.

A typical mesh for a narrow-body test panel containing a lap joint is shown in Figure 19. Only half of the test panel is modelled; a plane of symmetry is assumed at the crack centerline. Cylindrical symmetry is assumed at all boundaries. The circumferential boundary at the crack centerline is fixed in the longitudinal direction while the circumferential boundary away from the crack is allowed to displace uniformly in the longitudinal direction. The resultant of the pressure load in the longitudinal direction is applied at a node on this boundary.

A square-root singularity is assumed at all crack tips. Material plasticity at the crack tips is not considered since stress intensity factors are used as the basis for comparison with the experimental results. The square-root singularity is introduced into the ABAQUS models by use of collapsed eight-noded shell elements with quarter-point nodes surrounding the crack tips. Stress intensity factors are calculated using the displacements at nodes on the crack near the crack tip.

ANALYSIS RESULTS

A comparison between measured and predicted membrane hoop stresses for a narrow-body panel with floating frames is given in Figure 20. Bonded tear straps of stiffness ratio R_s equal to 0.15 coincide with the

frame locations. The data are for locations along an axial line midway between stringers and are presented in terms of the nominal hoop stress in an unstiffened cylinder of the same radius and skin thickness. The peak stress is observed to be about 85% of nominal and occurs midway between frames. The stress in the vicinity of the bonded tear straps falls to 60% of nominal. A good comparison of stresses can be observed at all locations.

A comparison between measured and predicted membrane hoop stresses in the vicinity of a lap joint in a narrow-body panel is given in Figure 21. The structure consists of floating frames at a 20 inch (508 mm) pitch and riveted tear straps at a 10 inch (254 mm) pitch. The tear strap stiffness ratio R_s is equal to 0.15. The data are for locations along an axial line adjacent to the lap joint. The data are presented in terms of the nominal hoop stress in an equivalent unstiffened cylinder of the same radius and lap joint skin gage thickness. The maximum stress of 80% of nominal occurs midway between the tear straps. A good comparison between test and analysis is obtained at this location. The stresses do not compare well at the tear straps. This may be caused by local bending at the skin and tear strap interface, or the influence of local stress concentrations around the fastener holes in the tear strap. The geometry of this panel model is similar to the test panels shown in Figure 12. Analysis results for this panel containing a 21.4 inch (540 mm) longitudinal crack show that the residual strength of the panel would be exceeded if the tear strap was broken.

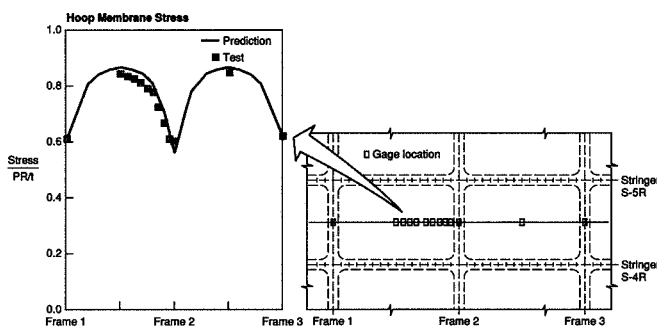


Figure 20. Test and analysis correlation for intact narrow-body panel 45-2A.

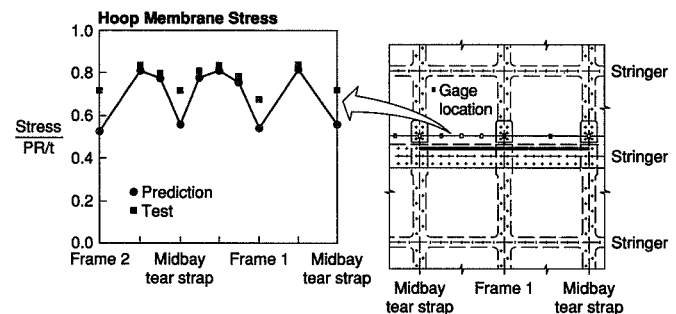


Figure 21. Test and analysis correlation for intact narrow-body panel 28-A adjacent to a lap joint.

A similar comparison of stresses is given in Figure 22 for the same panel containing a 20 inch (508 mm) crack in the upper row of fasteners in the lap joint and a broken central tear strap. As expected both measured and predicted hoop stresses behind the crack tips are close to zero. There are significant compressive membrane hoop stresses in the skin at the location of the broken tear strap. This is caused by local bending at the skin and tear strap interface. High tension stresses exist in the skin just ahead of the crack tip. Comparison with the data in Figure 21 shows the stresses are close to typical for the uncracked structure by the adjacent frame location (Frame 2 in the figure).

Panels 74-A and 74-B, discussed at length in the previous section, have also been the subjects of extensive analysis. A comparison of membrane stresses in the vicinity of the lap joint is given in Figure 23 for panel 74-B. The lap joint contains a 20 inch (508 mm) crack centered on the adjacent frame bay. The data are again presented in terms of the nominal hoop stress in an equivalent uncracked, unstiffened cylinder of the same radius and lap joint skin gage. The stresses are observed to be close to those for uncracked structure at the same locations.

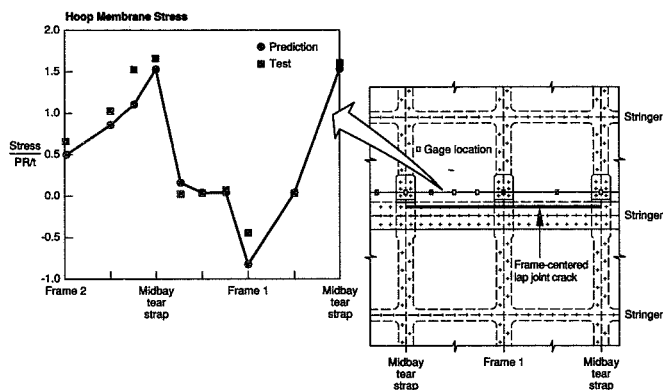


Figure 22. Test and analysis correlation for intact narrow-body panel 28-A containing a lap joint crack.

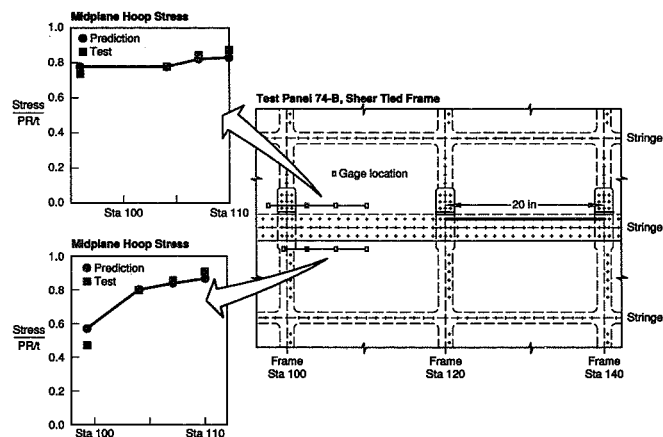


Figure 23. Test and analysis correlation for narrow-body panel 74-B containing a bay-centered lap joint crack.

Membrane stress intensity factors, non-dimensionalized with respect to the nominal membrane stress in an equivalent unstiffened cylinder, are presented in Figure 24 for panels 74-A and 74-B. Although the crack is along a lap joint, the fasteners and fastener holes are modeled only as point connections. Therefore, the stress intensity factors must be considered an approximation for lap joint configurations. It should be noted that the tear strap stiffening ratio R_s for the floating-frame panel is 0.19 and for the shear-tied panel, 0.12. Opening and sliding mode stress intensity factors are shown in the figure. In general, the opening mode stress intensity factor for the floating-frame panel is higher than for the shear-tied panel, even with the higher strap stiffness ratio. It is evident that the shear-tie helps to minimize the effect of out-of-plane displacements and to redistribute the loads around the crack. The effect of the broken tear strap is significant, causing a factor of three increase in opening mode stress intensity factor for cracks around 25 inches (635 mm) in length.

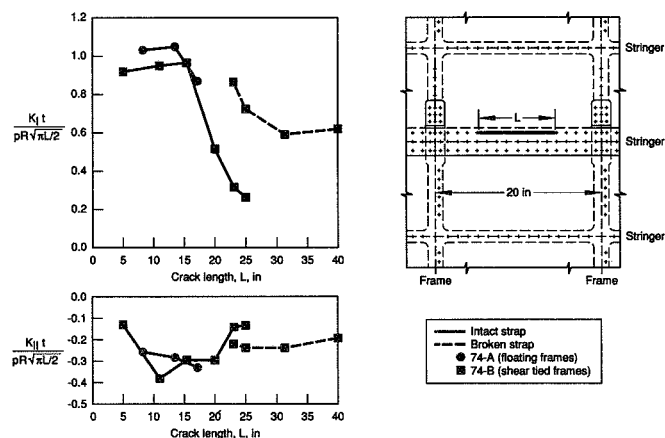


Figure 24. Non-dimensional stress intensity factors for narrow-body panels containing lap joint cracks.

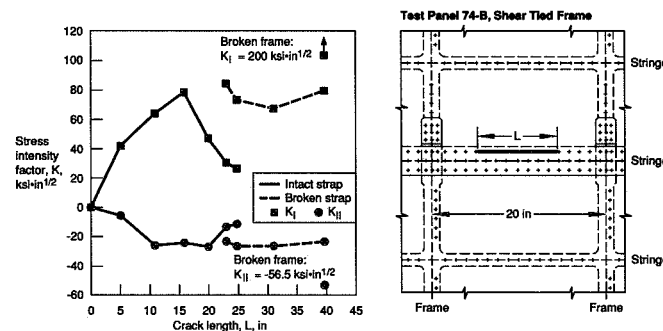


Figure 25. Stress intensity factors for narrow-body panel 74-B containing a lap joint crack.

The same data are presented as total opening and sliding mode stress intensity factors in Figure 25 for Panel 74-B. The opening mode stress intensity factor reaches a maximum of 78 ksi-in^{1/2} (86 MPa-m^{1/2}) when the skin crack is around 15 inches (380 mm) in length, before dropping as the tear strap is approached. The plane-stress fracture toughness for 0.04 inch (1.02 mm) clad 2024-T3 skin with cracks in the T-L orientation is in the range 120-130 ksi-in^{1/2} (130-140 MPa-m^{1/2}). As indicated in the discussion of the test results for this panel and as

illustrated in Figure 9, the crack remained sub-critical throughout this phase of the test. The tear straps failed in fatigue when the skin crack was 24.5 inches (620 mm) in length. At this point, the opening mode stress intensity factor in the skin was calculated to be $82 \text{ ksi}\cdot\text{in}^{1/2}$ ($90 \text{ MPa}\cdot\text{m}^{1/2}$), again well below the material toughness. The opening mode stress intensity factor is predicted to remain well below the material toughness with an intact frame. Following frame failure at a crack length of 40.2 inches (1.02 m), the opening mode stress intensity factor rises to $200 \text{ ksi}\cdot\text{in}^{1/2}$ ($220 \text{ MPa}\cdot\text{m}^{1/2}$), now well above the toughness of the material. The sliding mode stress intensity factor is presented for an assumed straight crack. This can be seen to remain fairly constant at around $25 \text{ ksi}\cdot\text{in}^{1/2}$ ($28 \text{ MPa}\cdot\text{m}^{1/2}$) for cracks longer than 10 inches (250 mm) in length, but rises significantly following frame failure.

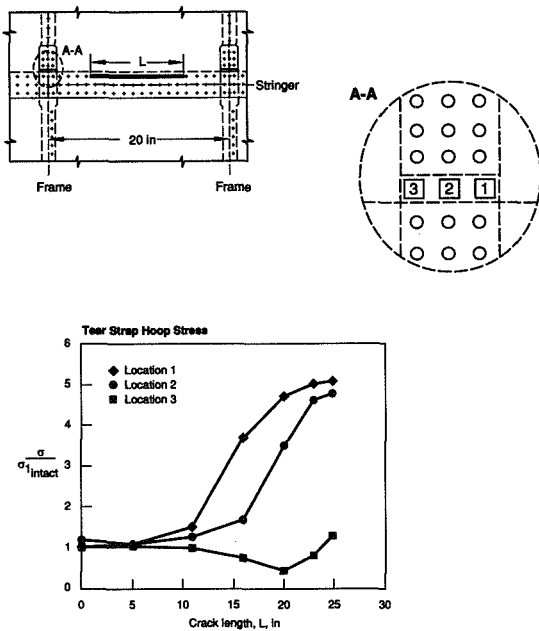


Figure 26. Stress concentration factors in tear strap for panel 74-B containing a lap joint crack.

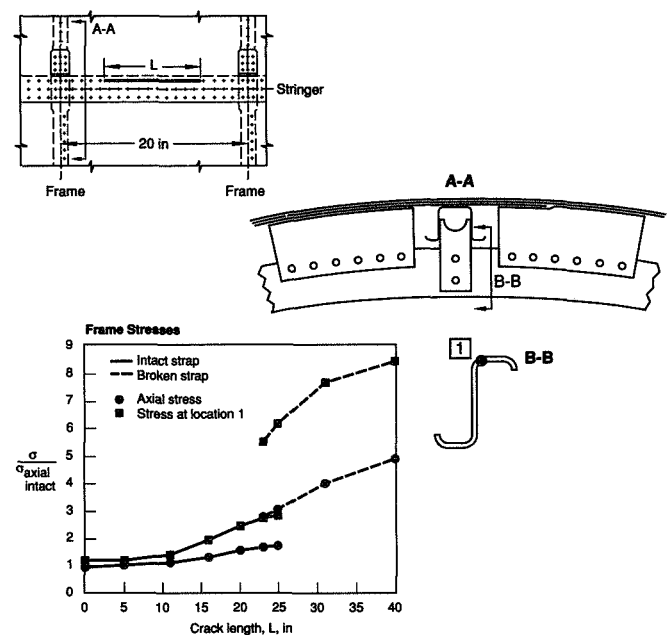


Figure 27. Stress concentration factors in frame for panel 74-B containing a lap joint crack.

The predicted tear strap stresses as a function of crack length, non-dimensionalized with respect to the stresses in the intact structure, are presented in Figure 26 for Panel 74-B. At short skin crack lengths, the stresses are uniform across the tear strap. As the crack approaches, the tear strap is subject to considerable bending in its plane. One side of the tear strap commences to yield when the skin crack is around 18 inches (460 mm) in length. In the test, the first fatigue crack was found in one of the straps when the skin crack was 20 inches (508 mm) in length. Insufficient data are available to reliably predict the fatigue life under such circumstances; however the tear straps failed in about 100 cycles during the test. Since the tear straps failed when the skin crack was 24.5 inches (620 mm) in length, no attempt was made to evaluate the tear strap stress concentration factors at longer skin crack lengths.

The predicted frame stresses as a function of crack length, non-dimensionalized with respect to the frame stresses in the intact structure are presented in Figure 27 for Panel 74-B. The stresses are provided at two locations. The first represents the average axial stress in the frame and the second represents the peak fiber stress in the outer chord of the frame just beyond the last shear-tie attachment fastener. At short skin crack lengths, the increase in stress in the frame is small. As the crack length increases, the stresses in the frame at both locations steadily increase but remain well below yield for the 7075-T6 frame material. Following tear

strap failure, the axial stress in the frame increases by about 50% but the peak fiber stress increases by 100%, indicating a significant increase in frame bending. The stresses remain below yield in the material (a yield stress of 68 ksi (470 MPa) was assumed in the analysis) until the skin crack exceeds about 35 inches (890 mm) in length. When the skin crack length is 40 inches (1.02 m), close to final panel failure, the nominal peak fiber stress in the frame exceeds 70 ksi (480 MPa). Final failure, illustrated in Figure 10, was through the last shear-tie attachment fastener. The peak fiber stress coupled with the stress concentrating effect of the fastener hole may have been sufficient to precipitate a static failure, or in a fashion similar to the tear strap, a very low-cycle fatigue failure. No observations of any fatigue cracks in the frame were recorded during the test.

A comparison between predicted and measured frame stresses in Panel 74-B is given in Figure 28. Axial stresses near the center of the frame channel, midway between two stringers are provided for two locations. The first is in the bay containing the crack and the second is in the adjacent bay, as illustrated in the figure. Stresses compare favorably while the tear strap is intact. Following tear strap failure, analysis stresses tend to be high in the bay containing the crack and low in the adjacent bay. Review of the analysis suggests that since the stringer clip attaching the stringer to the frame is modeled as a rigid connection, inaccurate predictions of load transfer into the frame result.

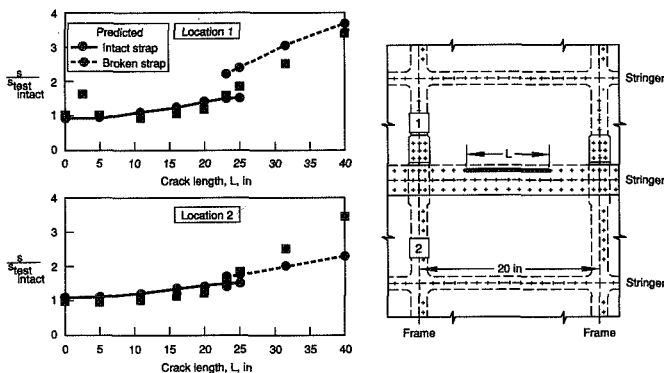


Figure 28. Comparison between test and predicted axial stresses in frame for panel 74-B as a function of skin crack length.

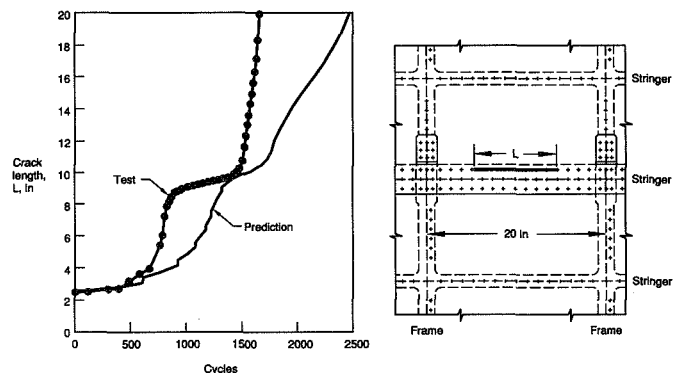


Figure 29. Comparison between test and predicted crack growth for panel 74-B containing a lap joint crack.

A comparison of skin fatigue crack growth lives for Panel 74-B is shown in Figure 29. In general, the prediction follows the test but tends to overestimate the life by about 50%. The analysis assumed fasteners behaved elastically at all times. In view of the high stresses calculated for the tear straps and frames, it is certain that several fasteners would have exceeded their yield strength. As a result, the stress intensity factor in the skin is likely to be greater than shown in Figure 25, especially for cracks beyond 20 inches (508 mm) in length. This may account for the observed differences between predicted and measured crack growth rates at the longest crack lengths.

Fully automated remeshing schemes for curving cracks are not yet available within Boeing although such a capability is under development such as the effort described in Reference 3. As a result, only a few attempts to predict crack trajectories have been made. One such attempt was made on Panel 45-2A. This narrow-body panel consisted of .036 inch (0.9 mm) 2024-T3 skin with 3 inch (76 mm) wide bonded tear straps, R_s equal to 0.15, at a 20 inch (508 mm) pitch. The panel had floating frames coincident with the tear straps. The initial damage in the panel consisted of a 5 inch (127 mm) sawcut across and including a broken tear strap. Predicted

crack trajectories are based on the maximum strain energy release rate. The predicted and measured crack trajectories are shown in Figure 30 to be in good agreement at all crack lengths. Final failure in this panel was by means of a controlled decompression. It can be observed that this failure mode can occur without the beneficial influence of nearby tear straps.

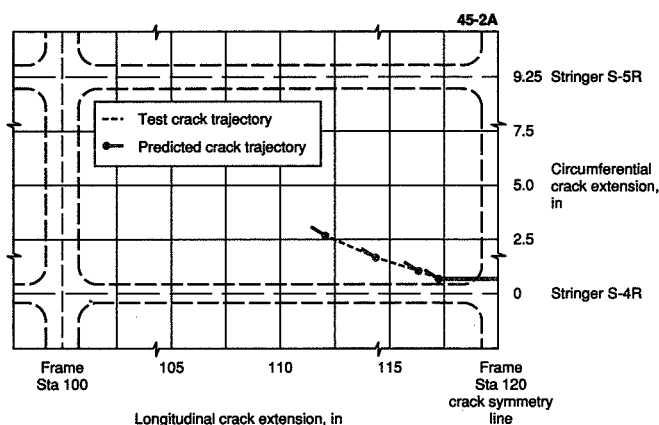


Figure 30. Comparison between test and predicted crack trajectory for narrow-body panel 45-2A containing a longitudinal crack.

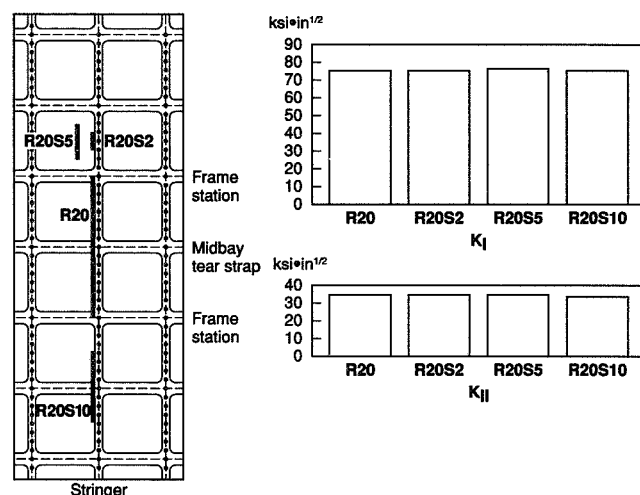


Figure 31. Effect on stress intensity factors of large interacting longitudinal cracks in a narrow-body panel.

An analysis of the interaction of large cracks in adjacent bays is given in Figure 31. The narrow-body panel consists of .036 inch (0.9 mm) thick 2024-T3 clad skin, tear straps with an R_s of 0.15 at 10 inch (254 mm) pitch, and floating frames at 20 inch (508 mm) pitch. An axial crack of length 20 inches (508 mm) centered on a broken tear strap is introduced into the structure adjacent to a stringer. An analysis is conducted for each of the different length secondary cracks located as shown in the figure. Because of the symmetry of the analysis model, each secondary crack occurs twice. Thus analysis R20S10 describes a 10 inch (254 mm) crack 5 inches (127 mm) ahead of each tip of the 20 inch (508 mm) crack. The opening and sliding mode stress intensity factors for the lead crack are shown in bar chart form for each of the crack configurations. In every case, the influence of the secondary cracks on the primary crack is negligibly small.

CONCLUSIONS AND RECOMMENDATIONS

Recent test and analysis results from an investigation into the behavior of cracks in typical fuselage structure have been discussed. In general, this has led to an increased understanding of our current capabilities. Some specific conclusions and recommendations follow.

Use of air as a pressurizing medium is necessary if the true dynamic conditions of a crack growing in representative fuselage structure are to be adequately assessed. However the risks associated with this type of testing need to be properly understood and adequate safeguards taken. Filling the cavity with polystyrene blocks and other similar material helps reduce cycling time but does not significantly reduce the energy stored in the test article. Greater air compressor capacity would help reduce cycling time. Air loss during fatigue cycling with long cracks needs to be addressed but rubber bladders have proven to be effective without significantly altering the progress of the crack through the structure. A fusing arrangement around the periphery of the test panel allows residual strength testing to destruction while minimizing damage to the test fixture.

Video recording of tests has proven to be extremely valuable, both in real time to monitor the progress of the crack allowing quick decisions to be made as the load is increased during residual strength testing, and as a permanent record for later evaluation. Strategically located strain gages also allow real-time monitoring of critical structural elements during residual strength testing.

The testing conducted to date indicates that longitudinal cracks in wide-body fuselage sections tend to grow in fatigue in a generally longitudinal direction, and do not result in a controlled decompression. On the other hand, similar cracks in narrow-body structures curve to grow circumferentially in about 50% of the cases. Exceptions are cracks midway between stringers. For the MSD pattern explored in wide-body panels with shear-tied frames, the residual strength was reduced by 10%, a smaller reduction than indicated by flat, unstiffened panel testing (see, for example, Reference 2). In narrow-body panels, the tendency of the lead crack to curve often negates the effect of MSD on final failure. Large skin cracks in adjacent frame bays need to be in close proximity before significant interaction is evident.

Structures in which the frames are tied to the skin by means of shear-ties appear to be more damage tolerant than structures with floating frames. However, additional evaluation of the relative structural efficiency needs to be conducted.

Insufficient data were available to accurately predict the fatigue life of tear straps and frames under very-low cycle fatigue conditions. Service experience shows that airline maintenance practices are more than adequate for finding long, externally visible cracks should they occur. The additional opportunities afforded by crack arrest features, such as tear straps and shear-ties, having good fatigue performance will increase opportunities for crack detection.

Future testing will include more head-to-head comparisons of cracked lap joints with or without MSD to fully characterize the loss of residual strength that might be expected. This will aid development of methods for predicting the point at which the performance of the cracked structure falls below acceptable levels. Development of a method for evaluating lap joints can then be applied to other structure susceptible to MSD for which suitable test facilities are unavailable.

Although not a primary focus of the testing discussed in this paper, the benefits to residual strength of well-bonded tear straps need to be further explored. As expected, bonded tear straps more effectively transfer load around a crack than riveted tear straps in most comparative tests. In particular, the resistance of the adhesive interface to disbonding as the crack in the skin tunnels under the tear strap needs to be understood.

A failure criterion for curving cracks in thin shells has yet to be established. While it has been shown that failure by controlled decompression is common in some typical fuselage structure, no method for sizing of structural elements such as tear straps to guarantee this type of failure is available.

Designers often increase the skin thickness of fuselage lap joints to increase the fatigue life. The effect of this local design feature on the damage tolerance of lap joints has not been the subject of systematic study, especially if the potential for MSD exists.

While the analysis approach described in this paper is more than adequate for typical structure, it is not a practical tool for the detail examination of local effects, such as loaded fastener holes and secondary bending,

that would occur in a lap joint. As a result, no attempt has been made to investigate analytically the interaction of small cracks ahead of a large crack in a lap joint.

In general, good correlation has been demonstrated between test and analysis for both intact and cracked structure. Trends observed in tests have also been confirmed by analysis. These include the observations that longitudinal cracks midway between stringers grow faster than cracks near stringers; that large cracks in adjacent frame bays do not interact significantly; and that panels with shear-tied frames tend to resist damage growth better than panels with floating frames. Crack growth rate comparisons presented in this paper and in Reference 1 are generally good at crack lengths less than 20 inches, but tend to become less satisfactory at longer lengths. The causes have not been completely identified but may include inaccurate crack growth rate data at very high stress intensity factors, or a need for additional elastic-plastic modeling of key structural elements such as fasteners, tear straps, shear-ties and stringer clips. The effects of these elements on fatigue crack growth and residual strength have been investigated for some test panels. In general, they can exceed yield as any damage approaches critical dimensions. An improved fastener load transfer model would increase confidence in the analysis of the behavior of very long cracks. The need to include skin plasticity has yet to be examined.

Future analyses will continue to focus on available test panel configurations, but will be expanded to include more parametric studies. Global-local modeling techniques will be employed to gain a better understanding of the effects of multiple site damage. Modified energy equations that include bending stress intensity factors will also be investigated to determine how they affect fatigue crack growth and residual strength.

REFERENCES

1. Miller M., Kaelber K. N., Worden R. E., "Finite Element Analysis of Pressure Vessel Panels," International Workshop on Structural Integrity of Aging Airplanes, 31 March –2 April 1992, Atlanta, Ga., USA.
2. Maclin J. R., "Performance of Fuselage Pressure Structure," Third International Conference on Aging Aircraft and Structural Airworthiness, November 19 – 21, 1991, Washington, D.C., USA.
3. Potyondy D., "A Software Framework for Simulating Curvilinear Crack Growth in Pressurized Fuselages," Doctoral Dissertation, Cornell University, 1993.

ACKNOWLEDGMENTS

The authors would like to acknowledge the graphics and publications support from Mr. W. J. Brewer and from Boeing Support Services.

ADVANCED METHOD AND PROCESSING TECHNOLOGY FOR
COMPLICATED SHAPE AIRFRAME PART FORMING

P.V. MIODUSHEVSKY
Central Aerohydrodynamic Institute
Moscow region
G.A. RAJEVSKAYA
Aviation Technology Institute
Novosibirsk

348671
533-05
23127
p. 7

SUMMARY

Slow deformation modes of forming give considerably higher residual fatigue life of the airframe part. It has been experimentally proven that fatigue life of complicated shape integral airframe panels made of high strength aluminium alloys is significantly increased after creep deformation process. To implement the slow deformation mode forming methods, universal automated equipment was developed.

Multichannel forming systems provide high accuracy of airframe part shape eliminating residual stresses and spring effect. Forming process multizone control technology was developed and experimentally proved that static/fatigue properties of formed airframe parts are increased.

1. Slow deformation processes.

It was experimentally established for many structural materials including aluminium and titanium alloys, alloys based on iron, that with the decrease of the loading velocity, the maximum strain value at the moment of material sample failure increases. This effect became more significant with the increasing of temperature [1].

Metallographic investigation of specimen microsections confirms that for high loading speed pores at the grain interfaces can be clearly observed. For specimens that were deformed at large loading speeds, pronounced porosity can be observed. On microsections of the specimens deformed up to the same values of elongations at low loading speeds these phenomena could not be seen.

A slow deformation process gives sufficient time for local peak stresses relaxation. As a result structural parts that are treated by a slow deformation process have a minimum damage of material at the production stage and have significantly better fatigue and durability properties.

2. Creep forming, thermal fixation technique.

Microscopic creep deformation has several features that are distinctive from instantaneous microscopic plastic deformation. Instantaneous plastic deformation is concentrated in narrow batches of sliding planes of dislocations, where the local shear value is very large. The areas that are located between those batches and are mostly part of the volume remain undeformed. The under creep mode sliding process is going more evenly in the many closely located atomic planes and relative displacements of neighbour planes are smallish (several distances between atoms). So creep deformation is going practically simultaneously in a whole volume of material [2]. The creep slow deformation process was successfully applied for the forming of airframe parts such as stiffened panels.

For monolithic stiffened panels made of high strength aluminium alloys mechanical properties after the creep forming process are significantly better than after instantaneous plastic forming [1].

Durability and fatigue strength of aluminium alloy integrated panels after creep forming are increased. Fig. 1 illustrates this for aluminium alloy AK4-1.

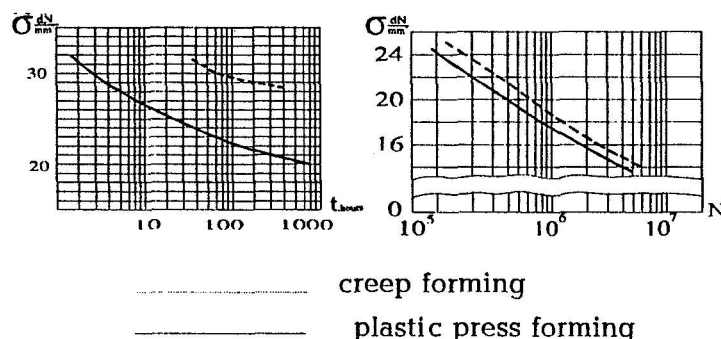


Fig. 1. Durability and fatigue strength of panels made of AK4-1 aluminium alloy.

The most widely used method of creep forming was called thermal fixation technique. This technique involves heating the blank to a specified temperature and then pressing it to the fixed surface and holding it for a determined amount of time in order to obtain a desired form. Different kinds of tools are used for loading airframe parts during thermal fixation: correspondingly shaped ribs, pads, vacuum bags, etc. Usually thermal fixation is provided inside a relatively large furnace.

In fig. 2 the airframe wing panel that was manufactured with thermal fixation technique is demonstrated.

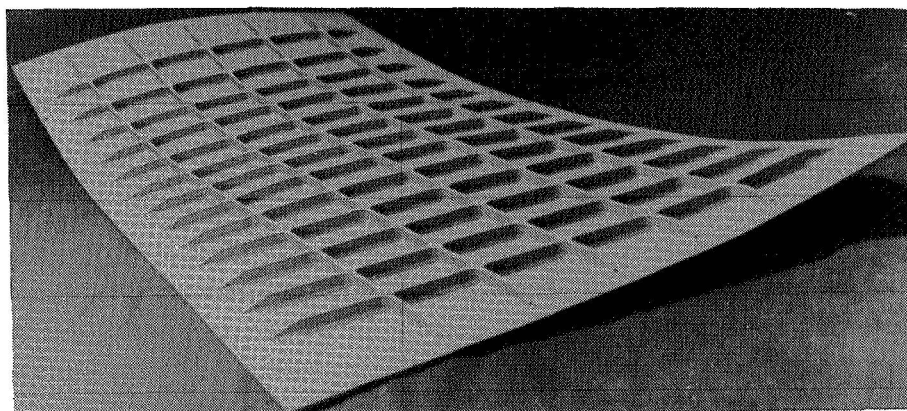


Fig. 2. Airframe wing panel.

The thermal fixation technique significantly improves the accuracy of forming and also reduces the residual stresses comparatively with other techniques. Thermal fixation provides forming a complicated shape airframe panel with double curvature [1]. However, thermal fixation does not entirely eliminate residual stresses or the spring effect and requires the manufacture of special loading and forming tools for each type of airframe panel.

Disadvantages of a thermal fixation technique originate from its advantage; that is, simplicity. In a thermal fixation technique we have only two parameters for process control: overall load (pressure) and average temperature. It is impossible to provide local monitoring and control of part shape and

residual stresses, local control of loading speed, local control of temperature, etc. So further development of creep forming method involves multichannel control of loading, relaxation, heating and cooling.

3. Local loading and relaxation

First of all it is necessary to measure and control the forming force in each zone of the workpiece. Precise forming of the workpiece must be achieved and maintained in conditions when all these forming forces are equal to zero. Forming forces are proportional to the force and moment reactions of the internal stresses in the corresponding zone of the workpiece. If these forces are equal to zero, then the actual or residual stresses inside the workpiece are self-equalizing or equal zero. Only the values of the forming forces can give us correct information on the internal stresses. Strain gauges are not useful in this application because the strain value contains significant creep component and thermal elongation.

Self-equalizing stresses do not produce resulting forces or moments and have no influence on the form of the workpiece. During annealing these self-equalizing stresses decrease to a minimum very close to zero.

Let us consider the beam model local loading control during a creep forming process. Supposing that temperature is constant during a process and across the beam and creep deformation velocity can be described by the following approximation [2]:

$$\frac{d\varepsilon_{cr}}{dt} = \varepsilon_n \left[\frac{\sigma(t)}{\sigma_n} \right]^n \cdot y, \quad (1)$$

where ε_{cr} - creep deformation,

y - distance from neutral axis of the beam,

$\varepsilon_n, \sigma_n, n$ - constants,

$\sigma(t)$ - time dependent part of stress σ ,

$\sigma = \sigma(t) \cdot y$,

Supposing that part of the beam was loaded by bending moment M that causes only elastic strain, and after that, curvature χ_0 of the beam was fixed and the beam is subjected to a creep relaxation process.

$$\sigma = E \cdot [\chi_0 - \chi(t)] \cdot y, \quad (2)$$

where E - modulus of elasticity,

$\chi_0 = \frac{M}{EJ}$ - initial beam curvature,

$\chi(t)$ - beam curvature relaxation during creep deformation process,

$J = \int_S y^2 ds$ - beam cross section area S moment of inertia.

From equations (1) and (2) follows:

$$\varepsilon_{cr} = \chi(t)y \quad (3)$$

$$\frac{d\chi(t)}{dt} = \varepsilon_n \left[\frac{\sigma(t)}{\sigma_n} \right]^n \quad (4)$$

$$\frac{d\sigma(t)}{dt} = -E\varepsilon_n \left[\frac{\sigma(t)}{\sigma_n} \right]^n \quad (5)$$

Solution of equation (5) follows:

$$\sigma(t) = \left\{ \frac{1}{(n-1) \left[E\varepsilon_n \left(\frac{1}{\sigma_n} \right)^n \cdot t + \frac{1}{n-1} \cdot \frac{1}{\sigma_0^{n-1}} \right]} \right\}^{\frac{1}{n-1}} \quad (6)$$

where $\sigma_0 = \sigma(t)$ at $t = 0$.

From equations (2) and (6) it is possible to compute $\chi(t)$:

$$\chi(t) = \chi_0 - \frac{\sigma(t)}{E} \quad (7)$$

With time growth the value of $\sigma(t)$ is tending to zero and $\chi(t)$ is tending to χ_0 .

Actual bending moment $M(t)$ can be expressed by equation (8):

$$M(t) = \int_s \sigma y ds = M - EJ\chi(t) \quad (8)$$

So $M(t)$ is tending to zero with time growth because $EJ\chi(t)$ is tending to M .

This simplified process model illustrates the importance of monitoring and control of local loads as a tool to control internal stresses and velocity of forming process and to provide high forming accuracy. Whole forming procedures may be divided by several sequential stages of loading and

relaxation for each local zone of workpiece as shown in fig. 3.

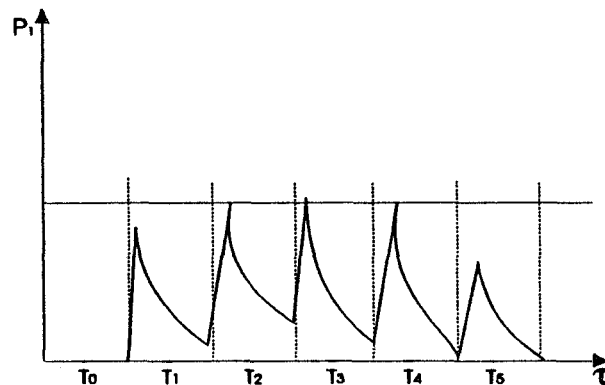


Fig. 3. Loading and relaxation stages during forming process.

4. Local temperature control.

Velocity of creep deformation is very sensitive for temperature, especially for aluminium alloys. It is possible to control a forming process by properly adjusting temperatures in local zones of the workpiece instead of load values control.

In fig. 4 a curve of equal influence of temperature and load (stress) on velocity of creep deformation is presented.

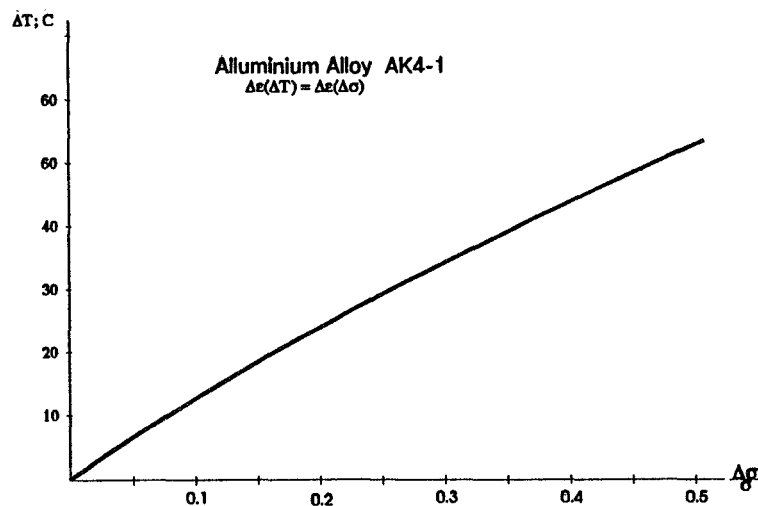


Fig. 4. Relative influence of temperature and load on creep deformation velocity.

For aluminium alloy AK4-1 a temperature variation of 10°C is equivalent to 7.5% of local load variation.

5. Multichannel creep forming process control.

Multichannel control procedure consists of:

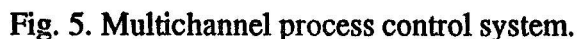
- program forming in each zone of the workpiece by electrohydraulic or electromechanical

- monitoring the force of each actuator**
- halting the program forming when any actuator force reaches the corresponding maximum allowable values**
- waiting until all actuator forces reach the corresponding minimum allowable values**
- starting the program again and repeating the forming process**
- halting and waiting until the desired form of the workpiece will be obtained**

To optimise the above procedure some useful operations can be added:

- Facility for multichannel creep forming of complicated shape airframe parts consists of multi-sectional housing in the form of a spatially flat-type surface [1]. Flat sections of the housing are connected to each other by hinges. Several sections are fixed stationary.

Forming force drives are installed at fixed angles on the flat sections of the housing. Heating and cooling devices are fixed into position on the flat sections of the housing. Forming force drives have displacement and load gauges that are connected with forming force drive controllers. Each section of the housing can serve several forming force actuators and several zones of heating and cooling means. In fig. 5 the block diagram of a multichannel control system is presented.



A multichannel creep forming procedure was successfully tested on the experimental facility. Now the industrial facility for airframe panels with width up to 2m is under construction. Length of panel is not critical because the facility is modular in the longitudinal direction.

Despite a relatively high cost of equipment, a multichannel creep forming process has several important advantages:

- the same facility can be used for forming different airframe parts (with different shapes or different materials or structures).
- manufacturing of pressforms is eliminated
- precise forming without spring-effect
- high structural quality of forming airframe parts (increase of durability and fatigue life, resistance to impact)
- applicability for airframe parts of large sizes
- possibility of forming airframe parts with changing sign double curvature shape with large geometrically nonlinear forming deflections

One interesting and prospective application of such facility is the forming of pressform panels for composite material airframe parts manufacturing.

Experiments were provided for welded panel creep forming. During the creep forming process welding stresses significantly decrease and, consequently, forming quality and structural characteristics are increased.

Conclusion

Advanced creep forming technology with multizone control of loading and temperature provides significant quality improvements of complicated shape airframe parts and gives more possibilities for airframe designers and production engineering.

References

1. P. V. Miodushevsky, G. A. Rajevskaya, O. V. Sosnin, A new production technology for complex-shaped structural element "creep forming." Proceedings of the conference STRUCOME '92, November 17-19, 1992, Paris.
2. U. N. Rabotnov, S. T. Mileico, "Short time creep," Nauka publishing house, Moscow, 1970.

REPORT DOCUMENTATION PAGE			Form Approved OMB No. 0704-0188	
Public reporting burden for this collection of information is estimated to average 1 hour per response, including the time for reviewing instructions, searching existing data sources, gathering and maintaining the data needed, and completing and reviewing the collection of information. Send comments regarding this burden estimate or any other aspect of this collection of information, including suggestions for reducing this burden, to Washington Headquarters Services, Directorate for Information Operations and Reports, 1215 Jefferson Davis Highway, Suite 1204, Arlington, VA 22202-4302, and to the Office of Management and Budget, Paperwork Reduction Project (0704-0188), Washington, DC 20503.				
1. AGENCY USE ONLY(Leave blank)	2. REPORT DATE September 1994	3. REPORT TYPE AND DATES COVERED Conference Publication		
4. TITLE AND SUBTITLE FAA/NASA International Symposium on Advanced Structural Integrity Methods for Airframe Durability and Damage Tolerance		5. FUNDING NUMBERS WU 538-02-10-01		
6. AUTHOR(S) Charles E. Harris, Editor				
7. PERFORMING ORGANIZATION NAME(S) AND ADDRESS(ES) NASA Langley Research Center Hampton, VA 23681-0001		8. PERFORMING ORGANIZATION REPORT NUMBER L-17432		
9. SPONSORING/MONITORING AGENCY NAME(S) AND ADDRESS(ES) Federal Aviation Administration Technical Center Atlantic City International Airport Center, NJ 08405 and National Aeronautics and Space Administration Washington, DC 20546-0001		10. SPONSORING/MONITORING AGENCY REPORT NUMBER NASA CP-3274, Part 1		
11. SUPPLEMENTARY NOTES				
12a. DISTRIBUTION/AVAILABILITY STATEMENT Unclassified-Unlimited Subject Category - 03, 26, 39		12b. DISTRIBUTION CODE		
13. ABSTRACT (Maximum 200 words) The international technical experts in the areas of durability and damage tolerance of metallic airframe structures were assembled to present and discuss recent research findings and the development of advanced design and analysis methods, structural concepts, and advanced materials. The principal focus of the symposium was on the dissemination of new knowledge and the peer-review of progress on the development of advanced methodologies. Papers were presented on the following topics: structural concepts for enhanced durability, damage tolerance, and maintainability; new metallic alloys and processing technology; fatigue crack initiation and small crack effects; fatigue crack growth models; fracture mechanics failure criteria for ductile materials; structural mechanics methodology for residual strength and life prediction; development of flight load spectra for design and testing; and advanced approaches to resist corrosion and environmentally assisted fatigue. About 300 people attended the symposium.				
14. SUBJECT TERMS Fatigue; Fracture mechanics; Metals; Airframe; Durability			15. NUMBER OF PAGES 509	
			16. PRICE CODE A22	
17. SECURITY CLASSIFICATION OF REPORT Unclassified	18. SECURITY CLASSIFICATION OF THIS PAGE Unclassified	19. SECURITY CLASSIFICATION OF ABSTRACT Unclassified	20. LIMITATION OF ABSTRACT	

National Aeronautics and
Space Administration
Langley Research Center
Mail Code 180
Hampton, VA 23681-00001

Official Business
Penalty for Private Use, \$300

SPECIAL FOURTH-CLASS RATE
POSTAGE & FEES PAID
NASA
Permit No. G-27